



I. R. IRAN

ISSN: 1728-1431

e-ISSN: 1735-9244



**International Journal of Engineering**

Journal Homepage: [www.ije.ir](http://www.ije.ir)



**TRANSACTIONS A: BASICS**

Volume 37, Number 04, April 2024

*Materials and Energy Research Center*

---

# INTERNATIONAL JOURNAL OF ENGINEERING

## Transactions A: Basics

---

### DIRECTOR-IN-CHARGE

H. Omidvar

### EDITOR IN CHIEF

G. D. Najafpour

### ASSOCIATE EDITOR

A. Haerian

### EDITORIAL BOARD

- |      |  |       |  |
|------|--|-------|--|
| S.B. | Adeloju, Charles Sturt University, Wagga, Australia              | A.    | Mahmoudi, Bu-Ali Sina University, Hamedan, Iran          |
| K.   | Badie, Iran Telecomm. Research Center, Tehran, Iran              | O.P.  | Malik, University of Calgary, Alberta, Canada            |
| M.   | Balaban, Massachusetts Ins. of Technology (MIT), USA             | G.D.  | Najafpour, Babol Noshirvani Univ. of Tech., Babol, Iran  |
| M.   | Bodaghi, Nottingham Trent University, Nottingham, UK             | F.    | Nateghi-A, Int. Ins. Earthquake Eng. Seis., Tehran, Iran |
| E.   | Clausen, Univ. of Arkansas, North Carolina, USA                  | S. E. | Oh, Kangwon National University, Korea                   |
| W.R. | Daud, University Kebangsaan Malaysia, Selangor, Malaysia         | M.    | Osanloo, Amirkabir Univ. of Tech., Tehran, Iran          |
| M.   | Ehsan, Sharif University of Technology, Tehran, Iran             | M.    | Pazouki, MERC, Karaj, Iran                               |
| J.   | Faiz, Univ. of Tehran, Tehran, Iran                              | J.    | Rashed-Mohassel, Univ. of Tehran, Tehran, Iran           |
| H.   | Farrahi, Sharif University of Technology, Tehran, Iran           | S. K. | Sadmezhad, Sharif Univ. of Tech, Tehran, Iran            |
| K.   | Firoozbakhsh, Sharif Univ. of Technology, Tehran, Iran           | R.    | Sahraeian, Shahed University, Tehran, Iran               |
| A.   | Haerian, Sajad Univ., Mashhad, Iran                              | A.    | Shokuhfar, K. N. Toosi Univ. of Tech., Tehran, Iran      |
| H.   | Hassanpour, Shahrood Univ. of Tech., Shahrood, Iran              | R.    | Tavakkoli-Moghaddam, Univ. of Tehran, Tehran, Iran       |
| W.   | Hogland, Linnaeus Univ, Kalmar Sweden                            | T.    | Teng, Univ. Sains Malaysia, Gelugor, Malaysia            |
| A.F. | Ismail, Univ. Tech. Malaysia, Skudai, Malaysia                   | P.    | Tiong, Nanyang Technological University, Singapore       |
| M.   | Jain, University of Nebraska Medical Center, Omaha, USA          | X.    | Wang, Deakin University, Geelong VIC 3217, Australia     |
| M.   | Keyanpour rad, Materials and Energy Research Center, Karaj, Iran | H.    | Omidvar, Amirkabir Univ. of Tech., Tehran, Iran          |

### EDITORIAL ADVISORY BOARD

- |       |  |       |   |
|-------|--|-------|---|
| S. T. | Akhavan-Niaki, Sharif Univ. of Tech., Tehran, Iran   | A.    | Kheyroddin, Semnan Univ., Semnan, Iran                  |
| M.    | Amidpour, K. N. Toosi Univ of Tech., Tehran, Iran    | N.    | Latifi, Mississippi State Univ., Mississippi State, USA |
| M.    | Azadi, Semnan university, Semnan, Iran               | H.    | Oraee, Sharif Univ. of Tech., Tehran, Iran              |
| M.    | Azadi, Semnan University, Semnan, Iran               | S. M. | Seyed-Hosseini, Iran Univ. of Sc. & Tech., Tehran, Iran |
| F.    | Behnamfar, Isfahan University of Technology, Isfahan | M. T. | Shervani-Tabar, Tabriz Univ., Tabriz, Iran              |
| R.    | Dutta, Sharda University, India                      | E.    | Shirani, Isfahan Univ. of Tech., Isfahan, Iran          |
| M.    | Eslami, Amirkabir Univ. of Technology, Tehran, Iran  | A.    | Siadat, Arts et Métiers, France                         |
| H.    | Hamidi, K.N.Toosi Univ. of Technology, Tehran, Iran  | C.    | Triki, Hamad Bin Khalifa Univ., Doha, Qatar             |
| S.    | Jafarmadar, Urmia Univ., Urmia, Iran                 |       |   |

### TECHNICAL STAFF

M. Khavarpour; M. Mohammadi; V. H. Bazzaz, R. Esfandiar; T. Ebadi

### DISCLAIMER

The publication of papers in International Journal of Engineering does not imply that the editorial board, reviewers or publisher accept, approve or endorse the data and conclusions of authors.

## CONTENTS

## Transactions A: Basics

<b>Z. N. Alabdali, F. F. Alkalid</b>	Analysis of Particle Size in Composite Materials Using Image Processing	579-587
<b>S. Buttol, B. Balaji, K. Srinivasa Rao</b>	Design and Analysis of Symmetrical Dual Gate Tunnel Field Effect Transistor with Gate Dielectric Materials in 10nm Technology	588-595
<b>M. A. Mashayekhi, M. Khanmohammadi</b>	Numerical Studies on Performance of Helical Pile-supported Embankments Over Soft Clay	596-607
<b>R. Sharafeddin, A. Gholam Abri, M. Fallah, F. Hossein Zadeh Lotfi</b>	Mathematical Model for Estimation of Return to Scale in Four-Level Green Supply Chain by using Data Envelopment Analysis	608-624
<b>R. Sreenu, S. R. Suryawanshi, A. Ashish</b>	Experimental Study on Self-compacting and Self-healing Concrete with Recycled Coarse Aggregates	625-634
<b>A. Fadlil, I. Riadi, M. A. Mu'min</b>	Mitigation from SQL Injection Attacks on Web Server using Open Web Application Security Project Framework	635-645
<b>M. Afshar, S. Y. Hadji Molana, B. Rahmani Parchicolaie</b>	A Multi Objective Optimization Model for Multi-commodity Closed-loop Supply Chain Network Considering Disruption Risk	646-661
<b>A. Dey, S. Biswas, L. Abualigah</b>	Umpire's Signal Recognition in Cricket Using an Attention based DC-GRU Network	662-674
<b>R. Mousavipoor, H. Gorji, M. Bakhshi-Jooybari, M. Shakeri</b>	Automatic Optimization of Initial Blank Shape in Production of All Kinds of Rectangular Parts in Computer Aided Hydroforming Process	675-691
<b>S. Hasyim, N. Salam, M. Saleh Pallu, F. Maricar</b>	Experimental Study of Open Channel Model of Glass Fiber Reinforced Polymer and Its Flowing Characteristics	692-710
<b>A. H. Foomani, M. Moradlou, P. Nazarian</b>	Utilizing a New Voltage Stability Index in Distribution Power System in Presence of Wind Turbine Units	711-724
<b>Y. Bahrami Kian, F. Harsej, M. Molani Aghdam, M. Sadeghpour</b>	Development of Green Product Processes in Textile Industry Using Mathematical Modeling and NSGA-II Metaheuristic Algorithm: A Case Study in Oyaz Industrial Group	725-738
<b>M. Hosseini Nasab</b>	Ash Reduction of the Tailings of Agh-Darband Coal Washing Plant by Flotation Method	739-752

<b>R. Saeed, A. J. Moradloo</b>	Seismic Assessment of Concrete Dams, Considering Anisotropy Caused by Lift Joints	753-762
<b>M. Deepak, Y. Ramalinga Reddy, R. Nagendra</b>	Experimental Investigation on Strength, Durability and Micro Structural Characteristics of Slag-Based Cement Mortar	763-778
<b>S. Ghaemifard, H. Khosravi, F. Farash Bamoharram, A. Ghannadiasl</b>	Self-healing Concrete Using Microcapsules Containing Mineral Salts	779-793
<b>S. S. Patil, Y. D. Patil</b>	Effect of Varying Glass Powder Size on Performance of Cement Mortar: Microstructural and Compressive Strength Assessment at High Temperatures	794-803
<b>P. Chupong, K. Tuchinda</b>	Computational Framework Development to Investigate Al Matrix with Low-Velocity Impact Behavior at Varied Temperatures for Cold Spray Composite Coating Design: Al/TiN Case	804-817





## Analysis of Particle Size in Composite Materials Using Image Processing

Z. N. Alabdali<sup>a</sup>, F. F. Alkhalid<sup>\*b</sup>

<sup>a</sup> Materials Engineering Department, University of Technology, Iraq

<sup>b</sup> Control and Systems Engineering Department, University of Technology, Iraq

### PAPER INFO

#### Paper history:

Received 07 November 2023

Received in revised form 13 December 2023

Accepted 23 December 2023

#### Keywords:

Composite

Materials

Computer Vision

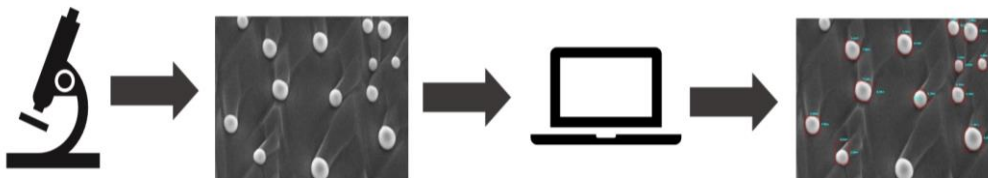
Image Processing

### ABSTRACT

Composite materials are the most important materials in materials science and engineering, which contain two or more materials. In materials engineering, the scanning electron microscopy (SEM) technique is an approach to measure the material's particle size. A new procedure was used instead of SEM is called Artificial Intelligence (AI). Artificial Intelligence (AI) is an interdisciplinary science and branch of computer science that involves solving problems that require human intelligence and capabilities. The computer vision is a subfield of AI, which uses some algorithms to detect the details of images by using computer called image processing. Detecting the particles and measuring the size of materials scanned by SEM is an essential task that helps to describe their feature, traditionally, the size is calculated manually by adding mesh to an SEM image or by drawing a diagonal line in an arbitrary particle. In this paper, a new model based on Artificial Intelligence (AI) is proposed using computer vision to analyze the size of all particles. This model is used to detect the particle size of additives in composite materials like graphene flakes and measure the size of them depending on the reference size fixed on the scanning electron microscope (SEM). The model was used based on the Open-source Computer Vision (OpenCV) library, utilizing multi-layers of canny edge detection, Sobel filter, Brightness and contrast algorithms, using Python 3. The results have achieved very satisfied indication with a very low process time = 0.2 mili-seconds.

doi: 10.5829/ije.2024.37.04a.01

### Graphical Abstract



## 1. INTRODUCTION

In the field of materials engineering, composite materials are the most important branch. Composite materials are consisting from matrix and additives like ceramic, glass, metal, and graphene (1, 2) These additives or some time called filler can be added in different amount, shape, and size to improve the mechanical and physical properties of the matrix (3-5). The size of these additives can be ranged

from micron to nanometers, which is important in the field of nanotechnology. Nanotechnology is the science that concerned with the study and preparation of materials with nanometric scale ( $10^{-9}$  meter) (6). Nanomaterials is a part of nanotechnology, which can be included organic and non-organic materials like silver, zinc, carbon nanotube, and graphene (7-9). One of the methods to characterize the nanoparticle size in the field of materials science (10) and engineering is scanning

\*Corresponding Author Email: [farah.f.alkhalid@uotechnology.edu.iq](mailto:farah.f.alkhalid@uotechnology.edu.iq)  
(F. F. Alkhalid)

electron microscopy (SEM) (11, 12). SEM imaging characterization was used to obtain the morphology of the samples as well as distinguish the particles. SEM used the beam of electrons toward the surface of the sample to generate high-resolution images with some details about the topography, composition, and distribution of the particles in the specimen (13, 14). The increasing demand for accuracy in measuring and analyzing nanoparticles within materials, and because the SEM technique is inaccurate way to measure the particle size and requires time (15, 16). The computer vision is a subfield of Artificial Intelligence (AI) (17, 18), which uses some algorithms to detect the details of images by using a computer called image processing (19). Image processing (20, 21) is the process by which one can obtain useful information about any image. Image processing was used in engineering application like cyphering (22, 23) chemistry (24, 25), materials (26), biomedical (27-29), and nanotechnology (30-32), Telcommunications (33), Covid19 detection (34). Image processing has become a radical, fast, and accurate solution for measuring the size of nanoparticles (4, 35). In this study, the image processing was used to measure the size of graphene flakes from the SEM images. In image processing technique, various alogarithms was used and compared among all these logarithms. The logarithms were used in this project include Gamma correction, Sobel (Sobel x and Sobel y), Negative, and Canny edge detection.

## 2. EXPERIMENTAL METHODS

Five famous preprocessing algorithms were applied and investigated to SEM images, which are include Gamma Correction, Sobel X, Sobel Y, Negative, and Canny edge detection.

### Preprocessing Algorithms

**2. 1. Gamma Correction** The parameter used in the power-law function that governs the correction of the image is called gamma. Gamma correction was used to adjust the intensity values of an image and to ensure that the perceived brightness in the image is closer to how the human visual system perceives light (36). Gamma correction was used to compensate the non-linear relationship between pixel values and the actual light levels captured by the imaging sensor or displayed on a screen (37). In many imaging systems, the relationship between the pixel values and the actual light intensity is not linear. The non-linearity behavior can present the images too dark or too bright, especially in the mid-tones. Therefore, to correct the non-linearity intensity by gamma correction increase the pixel values to a certain power. If the value is 1, which is mean no correction linear mapping, while if the values less than 1 (typically

between 0.5 and 2.5) indicate a nonlinear correction as shown in the following equation:

$$Y=X^\gamma \quad (1)$$

Where:

Y is the output value, X is the input value, which refers to a pixel in the plain image, and  $\gamma$  is the gamma value (36).

**2. 2. Sobel (Sobel X and Sobel Y)** The image intensity was calculated by Sobel operator at each point, so the Sobel operation was searched the maximum and minimum gradient values in the first derivative of the image. These gradients have certain magnitude as well as direction, so the value of gradient of the pixel was then calculated in a black and white image, which is use 2 kernels with 2 directions i.e., x and y. There are also a convolution masks, which is a small matrix applied to pixel value to obtain a new effect like edge detect. The Sobel filter uses two 2 x 2 kernels. One for changes in the horizontal direction  $G_x$  and the other for changes in the vertical direction  $G_y$  as shown in matrixes 2 and 3 (38, 39).

$$G_x = \begin{bmatrix} -1 & 0 & 1 \\ -2 & 0 & 2 \end{bmatrix} \quad (2)$$

$$G_y = \begin{bmatrix} -1 & -2 & -1 \\ 0 & 0 & 0 \end{bmatrix} \quad (3)$$

**2. 3. Negative** The brightest areas are converted into the darkest and the darkest areas are converted into the brightest is called negative. The negative process was occurred by subtracting each pixel's intensity value from the maximum intensity value possible for the given pixel format. For example, in an 8-bit grayscale image (with pixel values ranging from 0 to 255) (40), the negative of a pixel value P is calculated as shown in equation below. In case of color images, the negative operation was performing on each color channel independently. The apply negative operation to an image can produce an interesting artistic effect and highlight certain features or details, especially when the original image has strong contrasts or patterns (41).

$$\text{Negative}_P = 255 - P \quad (4)$$

**2. 4. Canny Edge Detection** The Canny is an essential algorithm used for multiple level image edge detection, which was proposed for the first once by Canny (42). The canny algorithm purpose was detected edges with very low error rate. The detected edges should be close to real edges by selecting the best local then labeling the concerned edges.

**2. 5. Gaussian Blur** Gaussian blur operation was applied to smooth and reduce noise in the image. It

was performed by convolving the image with a Gaussian kernel. The formula for a 2D Gaussian function as shown in Equation 5 (43):

$$G(x,y) = \frac{1}{\sqrt{2\pi\sigma^2}} e^{-\frac{x^2+y^2}{2\sigma^2}} \tag{5}$$

where:

G (x, y) is the Gaussian function at position (x, y),  
 π is the mathematical constant pi (approximately 3.14159),  
 σ is the standard deviation of the Gaussian distribution, controlling the amount of blur

**2. 6. Gradient Calculation** The Sobel operator was used to calculate gradient magnitude and orientation, which is computes the derivatives in x and y directions. Equation 6 was used to calculate the gradient magnitude (G) at each pixel and Equation 7 was used to calculate the gradient orientation (θ) at each pixel, so the angle θ indicates the direction of the edge [46]:

$$G = \sqrt{X^2 + Y^2} \tag{6}$$

$$\theta = \arctan (Gy / Gx) \tag{7}$$

where:

Gx the x-direction gradient  
 Gy the y-direction gradient

**3. METHODOLOGY**

In this manuscript, a new approach is proposed to calculate the particle size in SEM images by using Image processing. This is done by applying a preprocessing algorithm on the raw image in order to enhance the edges that help particle recognition. Figure 1 shows the process diagram of the work:

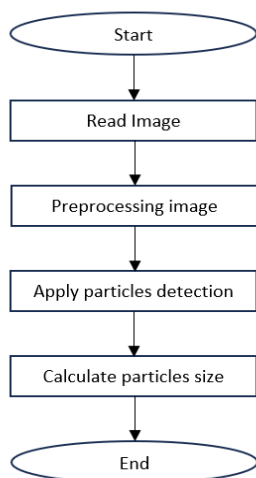


Figure 1. The process diagrams

Using an image processing approach to detect objects, these objects may have different shapes, this detection depends on the edges of them, edges detection depends on sharpening the contrast of colors, as denoted in Figure 2.

General procedure was applied to each algorithm as shown algorithm 1 below:

---

Algorithm 1: General procedure that is applied to each algorithm used in this work

---

- Step1: Start
  - Step2: Import important libraries
  - Step3: Read the input image
  - Step4: Convert to gray type
  - Step5: Apply the specific algorithm
  - Step6: Save the new image
  - Step7: Stop
- 

The philosophy of object detection and size measurement is to pass a specific mask with dimension (6x6) through over the image, this mask seeks to find edges, and the edges are detected if there is a contrast in color. This contrast is compared with a predefined threshold, in order to detect only edges. Algorithm 2 shows object detection:

---

Algorithm 2: Object Detection

---

- Step1: Start
  - Step2: Import important libraries
  - Step3: Read the input image
  - Step4: Convert to gray type
  - Step5: Apply the specific algorithm
  - Step5: Pass mask (mxm)
  - Step6: If the contrast > threshold:
    - Edges=True
    - Else
    - Edges =False
  - Step7: Draw rectangle for each closed shape
  - Step8: End
- 

Where m=6.

The object measurement is calculated after drawing a rectangle around each object (No matter how the shape looks like!), this is done by treating each rectangle

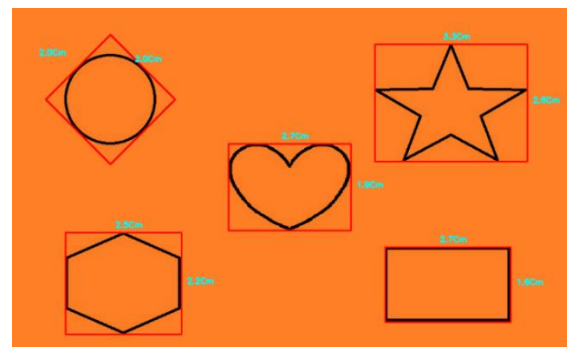


Figure 2. Different shapes object detection and size calculation

individually, the general idea for calculation and size in the image is shortened by calculating the number of pixels, number of pixels in each object is different from image to other, by referring to specific reference the number of pixels in each unit can be calculated. This can be tuned reaching to the best output.

A Python library like (OpenCV, Numpy, Matplot,) which is a reusable chunk of code were included in this project. After that, read plain image and converted to gray mode to minimize the contrast possibilities. Then each algorithm was applied and saved the new image for the program of size detection.

The object detection was applied after sharpening the edges to measure the size of the graphene flakes. Then using algorithm 3 denotes the procedure of size detection process as shown below:

---

**Algorithm 3: Size Detection**

---

```

Step1: Start
Step2: Import important libraries
Step3: Read the input image
Step4: Using Gaussian Kernel to remove unnecessary edges
Step5: Find the contours of the image, sort them, and remove those that are not large enough
Step6: Detect the objects by using contours
Step7: Draw the box and define the Width and Hight (the box dimensions can be tuned depending on the reference)
Step8: Save the new image
Step9: Stop
    
```

---

The new image which is created by algorithm was read then Gaussian Kernel algorithm was applied to remove unnecessary edges. After that sort contour sorting, which is very valuable in case of image detection or image recognition was applied. In this project two types of sorting contour were used which are included sorting by area and sorting by spatial position. The area sorting was important to extract the large contours representing important parts of an image and get rid of small contours thereby reducing the potential noise. On the other side, sorting by spatial position was also important to sort the characters to the left or right. Finally, drawing box around each graphene flakes and calculate the size from the dimensions (Height and Width), which can be tuned depending on reference object.

**3. 1. Results**

Each SEM image has a scale mentioned in the lower right of image (sometimes in the lower middle). This scale is considered as a reference to calculate the number of pixels in each 100 nm for example, as shown in Figure 3.

This reference is essential for matching the scale between pixels and units, in this work, a manual tuning is done to make matching, this matching is run one time, and then it is fixed for all images. Figure 4 denotes the measurement of the reference after make tuning, in this work the number of pixels in each 100 nm=27.8 pixels.

By Applying the proposed model on two SEM images, each has different particles, using correction algorithms to show the effect of each one on the output. Figure 5 denotes the output:

Figure 5 applying the algorithms to the two samples left column sample first and right column sample second:

Tables 1 and 2 show the approximation statistics of graphene flakes size detection from SEM image. The size detection was calculated manually by counting visually the number of particles in the two samples as shown in Figure 5.

**Scenario 1:** By applying the Canny edge algorithm on the two samples of SEM images as shown in Figure 5 (k, l) the model could detect (58 particles from 66 total particles and 12 particles from 14 total particles respectively) with a high rate of right detection percentage (95% & 100%, respectively), and low wrong detection percentage (5% and 0%, respectively).

**Scenario 2:** By applying the Negative algorithm in Figure 5 (i, j) shows the high number of graphene flakes particles detected (53 particles from 66 total particles and 13 particles from 14 total, respectively) and high rate of right detection (92% and 100%, respectively) with low wrong detection rate (8% and 0%, respectively).

**Scenario 3:** By using the Gamma correction algorithm Figure 5 (c, d) shows the number of graphene flakes detection range 47 particles from 66 total particles and 11 particles from 14 total particles, respectively), the right percentage (91% and 100%, respectively) in addition the wrong percentage (9% and 0%).

**Scenario 4:** The data obtained from Sobel x and Sobel y Figure 5 (e, f, g, h) shows the number of graphene flakes detection range (11 from 66, 3 from 14 for Sobel x and 0 from 66 and 0 from 14 for Sobel y), the percentage of right objects is 0% for all.

In general, the quality of SEM images, and the types of particle shapes may affect the process of detection and even may affect the type of the best algorithm for detection.

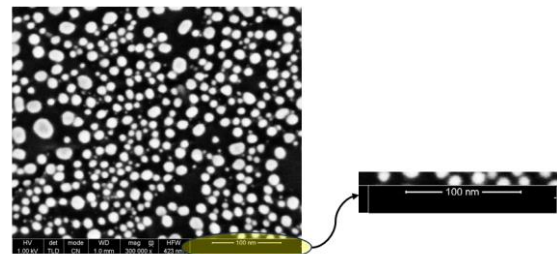
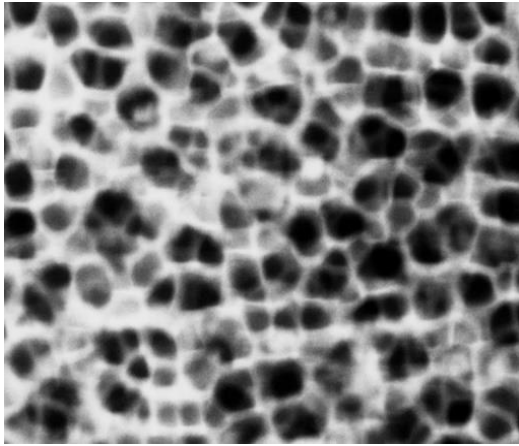


**Figure 3.** Sample of SEM image and highlighting the scale

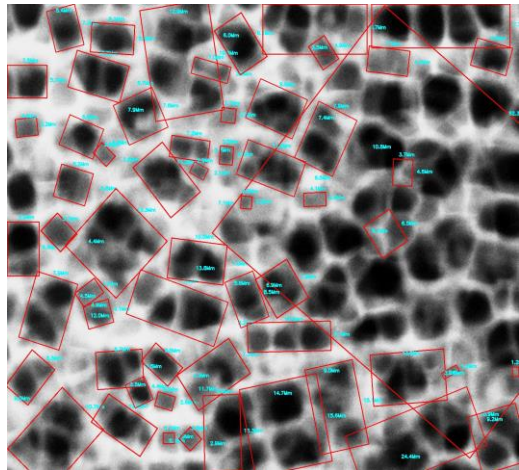


**Figure 4.** Scale measurement

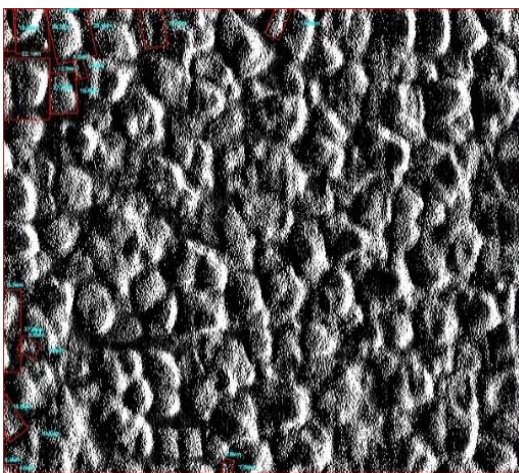
First Sample



(a)

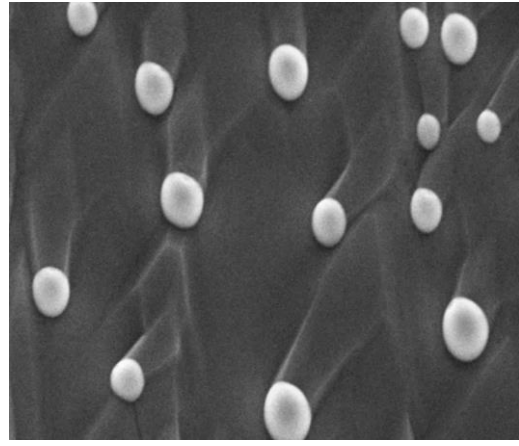


(c)

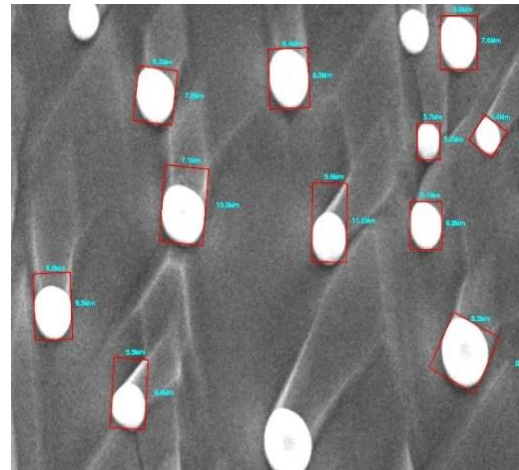


(e)

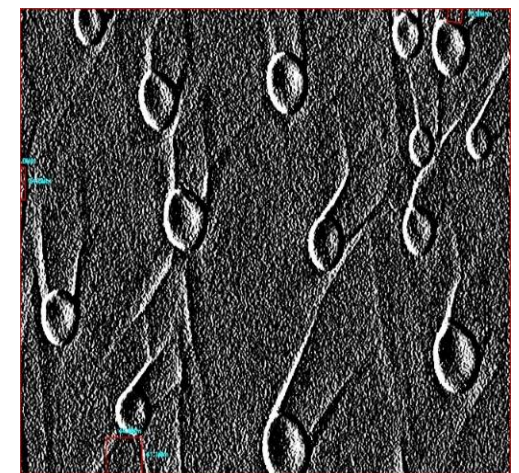
Second Sample



(b)



(d)



(f)

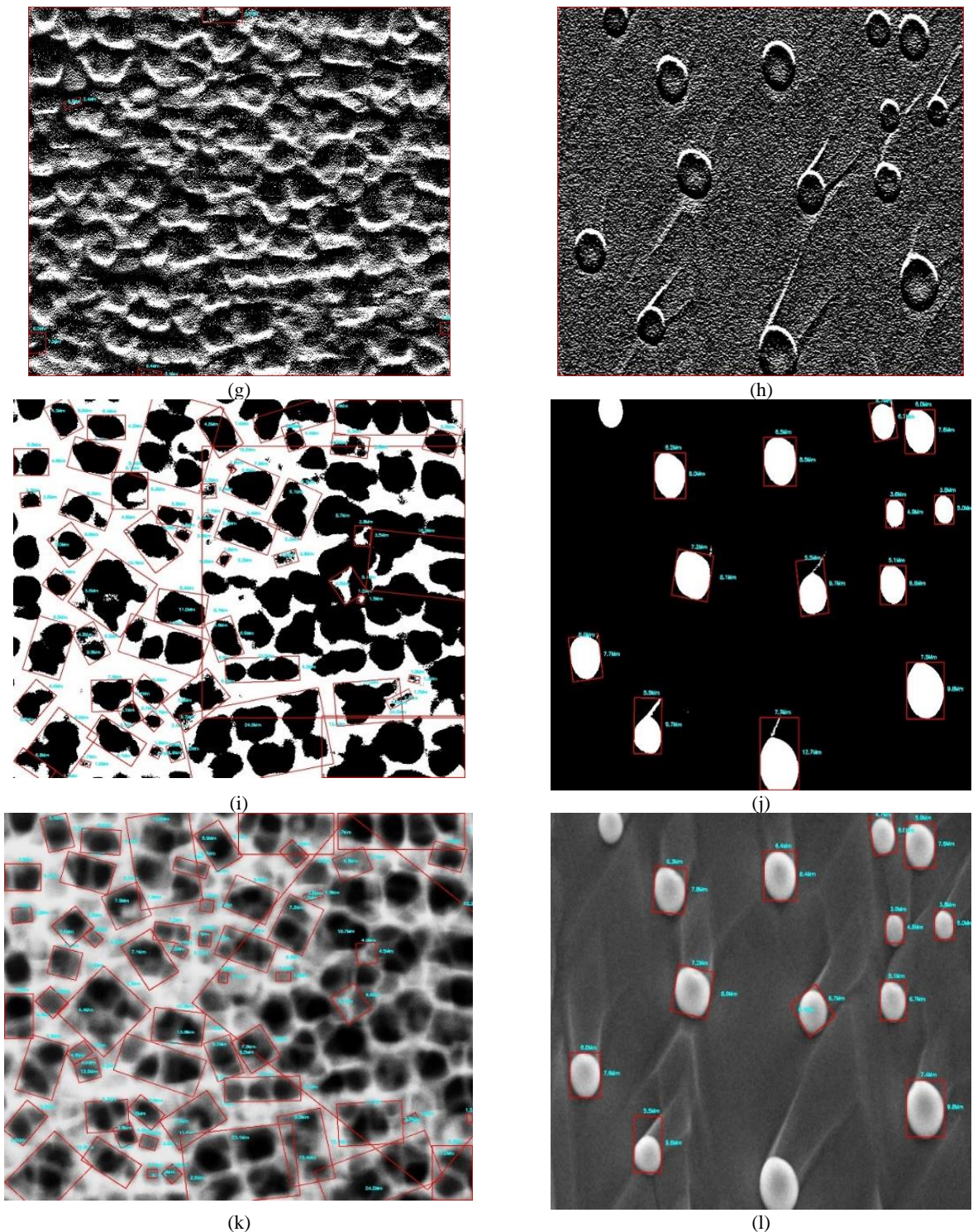


**Figure 5.** Applying the algorithms to the two samples a: Plain image (First sample) b: Plain image (Second sample) c: Particle detection with Gamma edge correction (First sample) d: Particle detection with Gamma edge correction (Second sample) e: Particle detection with Sobelx edge detection (First sample) f: Particle detection with Sobelx edge detection (Second sample) g: Particle detection with Sobely edge detection (First sample) h: Particle detection with Sobely edge detection (Second sample) i: Particle detection with Negative (First sample) j: Particle detection with Negative (Second sample) k: Particle detection with Canny edge detection (First sample) l: Particle detection with Canny edge detection (Second sample)

**TABLE 1.** The approximation statistics of graphene flakes detection for the first sample

#All Objects	# Detected	# Right	Right Percentage	# Wrong	Wrong Percentage	Algorithm
66	47	43	91 %	4	9 %	Gamma
66	11	0	0 %	11	100 %	Sobel X
66	4	0	0 %	4	100 %	Sobel Y
66	53	49	92 %	4	8 %	Negative
66	<b>58</b>	<b>55</b>	<b>95 %</b>	3	<b>5 %</b>	<b>Canny edge</b>

**TABLE 2.** The approximation statistics of graphene flakes for the second sample

#All Objects	# Detected	# Right	Right Percentage	# Wrong	Wrong Percentage	Algorithm
14	11	11	<b>100 %</b>	0	<b>0 %</b>	Gamma
14	3	0	0 %	3	100 %	Sobel X
14	0	0	0 %	0	-	Sobel Y
14	<b>13</b>	<b>13</b>	<b>100 %</b>	0	<b>0 %</b>	<b>Negative</b>
14	12	12	<b>100 %</b>	0	<b>0 %</b>	<b>Canny edge</b>

#### 4. CONCLUSION

Detecting the particles and measuring the size of materials scanned by SEM is an essential task that helps to describe their feature, traditionally, the size is calculated manually by adding mesh to an SEM image or by drawing a diagonal line in an arbitrary particle. In this work, image process technique has used, by proposing a new model with different algorithms like Gamma Correction, Sobel X, Sobel Y, Negative, and Canny edge detection. This model has many tasks, first one is to enhance the quality of SEM image by using these algorithms, hence, the detection of each particle depends on particle edges detection, when the contrast of edges is high, then the percentage of detection is high. In general, The results show that the Canny edges and Negative improve the edges rather than Gamma, Sobelx, and Sobely. This result is because of Canny edge detection approach has Gaussian Blur and Gradient calculation which make this approach good for this work. The effectiveness of each approach deeply depends on the specific characteristics of the image and the requirements of the particular application. Finally, in the future combining multiple edge detection methods or using more advanced techniques, such as the combination of Canny and Sobel, which might yield better results, also propose a new model that surround the shape as it not as rectangle.

#### 5. REFERENCES

- Ruyter I. Composites-characterization of composite filling materials: reactor response. *Advances in dental research*. 1988;2(1):122-33. 10.1177/08959374880020010
- Faraji A, Aghaali V, Rahimipour M. Effect of Al59Cu25. 5Fe12. 5B3 Quasi-crystals on Microstructure and Flexural Strength of Aluminum Matrix Composites Prepared by Spark Plasma Sintering Method. *International Journal of Engineering, Transactions A: Basics*. 2024;37(1):48-55. 10.5829/IJE.2024.37.01A.05
- Raja T, Devarajan Y, Thanappan S. Studies on the mechanical and thermal stability of Calotropis gigantea fibre-reinforced bran nano particulates epoxy composite. *Scientific Reports*. 2023;13(1):16291. 10.1038/s41598-023-42316-6
- AlMangour B, Grzesiak D, Yang J-M. In situ formation of TiC-particle-reinforced stainless steel matrix nanocomposites during ball milling: Feedstock powder preparation for selective laser melting at various energy densities. *Powder Technology*. 2018;326:467-78. 10.1016/j.powtec.2017.11.064
- Yusmaniar Y, Julio E, Rahman A, Yudanto SD, Susetyo FB. Synthesis of Polyvinyl Alcohol-Chitosan Composite Film using Nanocellulose from Coconut Fibers (Cocos nucifera). *International Journal of Engineering, Transactions B: Applications*. 2023;36(11):1993-2003. 10.5829/ije.2023.36.11b.05
- Bayda S, Adeel M, Tuccinardi T, Cordani M, Rizzolio F. The history of nanoscience and nanotechnology: from chemical-physical applications to nanomedicine. *Molecules*. 2019;25(1):112. 10.3390/molecules25010112
- Mekuye B, Abera B. Nanomaterials: An overview of synthesis, classification, characterization, and applications. *Nano Select*. 2023. 10.1002/nano.202300038
- Alshammari BH, Lashin MM, Mahmood MA, Al-Mubaddel FS, Ilyas N, Rahman N, et al. Organic and inorganic nanomaterials: fabrication, properties and applications. *RSC advances*. 2023;13(20):13735-85. 10.1039/d3ra01421e
- Rizvi M, Gerengi H, Gupta P. Functionalization of Nanomaterials: Synthesis and Characterization. *Functionalized Nanomaterials for Corrosion Mitigation: Synthesis, Characterization, and Applications*: ACS Publications; 2022. p. 1-26.
- Alabdali ZN, Reiter MP, Lynch-Branzoi JK, Mann AB. Compositional effects on mechanical properties and viscosity in UDMA-MMA blends. *Journal of Adhesion Science and*

- Technology. 2021;35(6):610-25. 10.1080/01694243.2020.1816779
11. Hodoroaba V-D, Rades S, Salge T, Mielke J, Ortel E, Schmidt R, editors. Characterisation of nanoparticles by means of high-resolution SEM/EDS in transmission mode. IOP Conference Series: Materials Science and Engineering; 2016: IOP Publishing. 10.1088/1757-899X/109/1/012006
  12. Lu P-J, Fu W-E, Huang S-C, Lin C-Y, Ho M-L, Chen Y-P, et al. Methodology for sample preparation and size measurement of commercial ZnO nanoparticles. *Journal of food and drug analysis*. 2018;26(2):628-36. 10.1016/j.jfda.2017.07.004
  13. Rianto D. Scanning Electron Microscopy for Nanostructure Analysis of Hybrid Multilayer Coating. *PILLAR OF PHYSICS*. 2022;15(2). 10.24036/14084171074
  14. Capone I, Hurlbutt K, Naylor AJ, Xiao AW, Pasta M. Effect of the particle-size distribution on the electrochemical performance of a red phosphorus-carbon composite anode for sodium-ion batteries. *Energy & Fuels*. 2019;33(5):4651-8. 10.1021/acs.energyfuels.9b00385
  15. Zhang S, Wang C. Precise analysis of nanoparticle size distribution in TEM image. *Methods and Protocols*. 2023;6(4):63. 10.3390/mps6040063
  16. Liang C, Jia Z, Chen R. An Automated Particle Size Analysis Method for SEM Images of Powder Coating Particles. *Coatings*. 2023;13(9):1547. 10.3390/coatings13091547
  17. Negaresh F, Kaedi M, Zojaji Z. Gender identification of mobile phone users based on internet usage pattern. *International Journal of Engineering*. 2023;36(2):335-47. 10.5829/ije.2023.36.02b.13
  18. Hadaeghi A, Iliyaefar M, Abdollahi Chirani A. Artificial neural network-based fault location in terminal-hybrid high voltage direct current transmission lines. *International Journal of Engineering*. 2023;36(2):215-25. 10.5829/ije.2023.36.02b.03
  19. Kumara GJJ, Hayano K, Ogiwara K. Image analysis techniques on evaluation of particle size distribution of gravel. *GEOMATE Journal*. 2012;3(5):290-7. 10.21660/2012.5.1261
  20. Surono S, Afitian MYF, Setyawan A, Arofah DKE, Thobirin A. Comparison of CNN Classification Model using Machine Learning with Bayesian Optimizer. *HighTech and Innovation Journal*. 2023;4(3):531-42. 10.28991/HIJ-2023-04-03-05
  21. Surono S, Rivaldi M, Dewi DA, Irsalinda N. New Approach to Image Segmentation: U-Net Convolutional Network for Multiresolution CT Image Lung Segmentation. *Emerging Science Journal*. 2023;7(2):498-506. 10.28991/ESJ-2023-07-02-014
  22. Jirjees SW, Alkhalid FF, Hasan AM. Text Encryption by Indexing ASCII of Characters Based on the Locations of Pixels of the Image. *Traitement du Signal*. 2023;40(2):791-6. 10.18280/ts.400240
  23. Jirjees SW, Alkalid FF, Shareef WF. Image encryption using dynamic image as a key based on multilayers of chaotic permutation. *Symmetry*. 2023;15(2):409. 10.3390/sym15020409
  24. Baum ZJ, Yu X, Ayala PY, Zhao Y, Watkins SP, Zhou Q. Artificial intelligence in chemistry: current trends and future directions. *Journal of Chemical Information and Modeling*. 2021;61(7):3197-212. 10.1021/acs.jcim.1c00619
  25. Gasteiger J. Chemistry in times of artificial intelligence. *ChemPhysChem*. 2020;21(20):2233-42. 10.1002/cphc.202000518
  26. López C. Artificial intelligence and advanced materials. *Advanced Materials*. 2023;35(23):2208683. 10.1002/adma.202208683
  27. Manickam P, Mariappan SA, Murugesan SM, Hansda S, Kaushik A, Shinde R, et al. Artificial intelligence (AI) and internet of medical things (IoMT) assisted biomedical systems for intelligent healthcare. *Biosensors*. 2022;12(8):562. 10.3390/bios12080562
  28. Singh AV, Rosenkranz D, Ansari MHD, Singh R, Kanase A, Singh SP, et al. Artificial intelligence and machine learning empower advanced biomedical material design to toxicity prediction. *Advanced Intelligent Systems*. 2020;2(12):2000084. 10.1002/aisy.202000084
  29. Walsh I, Fishman D, Garcia-Gasulla D, Titma T, Pollastri G, Harrow J, et al. DOME: recommendations for supervised machine learning validation in biology. *Nature methods*. 2021;18(10):1122-7. 10.1038/s41592-021-01205-4
  30. Kulkarni S, Bhat S, Moritz CA. Architecting for artificial intelligence with emerging nanotechnology. *ACM Journal on Emerging Technologies in Computing Systems (JETC)*. 2021;17(3):1-33. 10.1145/3445977
  31. Zhang P, Guo Z, Ullah S, Melagraki G, Afantitis A, Lynch I. Nanotechnology and artificial intelligence to enable sustainable and precision agriculture. *Nature Plants*. 2021;7(7):864-76. 10.1038/s41477-021-00946-6
  32. Winkler DA. Role of artificial intelligence and machine learning in nanosafety. *Small*. 2020;16(36):2001883. 10.1002/smll.202001883
  33. Kuklin V, Alexandrov I, Polezhaev D, Tatarkanov A. Prospects for developing digital telecommunication complexes for storing and analyzing media data. *Bulletin of Electrical Engineering and Informatics*. 2023;12(3):1536-49. 10.11591/eei.v12i3.4840
  34. Davila MH, Baldeon-Calisto M, Murillo JJ, Puente-Mejia B, Navarrete D, Riofrío D, et al. Analyzing the effect of basic data augmentation for covid-19 detection through a fractional factorial experimental design. *Emerging Science Journal*. 2022;7:1-16. 10.28991/ESJ-2023-SPER-01
  35. Baazeem R, Maheshwary P, Binjawhar DN, Gulati K, Joshi S, Ojo S, et al. Digital image processing for evaluating the impact of designated nanoparticles in biomedical applications. *Intelligent Data Analysis*. 2023(Preprint):1-12. 10.3233/ida-237435
  36. Rahman S, Rahman MM, Abdullah-Al-Wadud M, Al-Quaderi GD, Shoyaib M. An adaptive gamma correction for image enhancement. *EURASIP Journal on Image and Video Processing*. 2016;2016(1):1-13. 10.1186/s13640-016-0138-1
  37. Veluchamy M, Subramani B. Image contrast and color enhancement using adaptive gamma correction and histogram equalization. *Optik*. 2019;183:329-37. 10.1016/j.ijleo.2019.02.054
  38. Aoun A, Masadeh M, Tahar S, editors. On the Design of Approximate Sobel Filter. 2022 International Conference on Microelectronics (ICM); 2022: IEEE. 10.1109/ICM56065.2022.10005354
  39. Hu K, Yuan X, Chen S, editors. Real-time CNN-based keypoint detector with Sobel filter and descriptor trained with keypoint candidates. Fifteenth International Conference on Machine Vision (ICMV 2022); 2023: SPIE. 10.1117/12.2679944
  40. Cheng D, Li Y, Zhang D, Wang N, Gao X, Sun J. Robust single image dehazing based on consistent and contrast-assisted reconstruction. *arXiv preprint arXiv:220315325*. 2022. 10.48550/arXiv.2203.15325
  41. Zhan F, Zhang J, Yu Y, Wu R, Lu S, editors. Modulated contrast for versatile image synthesis. Proceedings of the IEEE/CVF Conference on Computer Vision and Pattern Recognition; 2022. 10.1109/CVPR52688.2022.01774
  42. Canny J. A computational approach to edge detection. *IEEE Transactions on pattern analysis and machine intelligence*. 1986(6):679-98. 10.1109/TPAMI.1986.4767851
  43. Gula T, Bertoldo JP, editors. Gaussian Image Anomaly Detection with Greedy Eigecomponent Selection. Proceedings of the IEEE/CVF International Conference on Computer Vision; 2023. 10.48550/arXiv.2308.04944

**COPYRIGHTS**

©2024 The author(s). This is an open access article distributed under the terms of the Creative Commons Attribution (CC BY 4.0), which permits unrestricted use, distribution, and reproduction in any medium, as long as the original authors and source are cited. No permission is required from the authors or the publishers.

**Persian Abstract****چکیده**

مواد کامپوزیتی مهم ترین مواد در علم و مهندسی مواد هستند که حاوی دو یا چند ماده هستند. در مهندسی مواد، تکنیک میکروسکوپ الکترونی روبشی (SEM) یکی از راه های اندازه گیری اندازه ذرات ماده است. روش جدیدی به جای SEM استفاده شد که هوش مصنوعی (AI) نام دارد. هوش مصنوعی (AI) یک علم میان رشته ای و شاخه ای از علوم کامپیوتر است که شامل حل مسائلی است که به هوش و توانایی های انسانی نیاز دارند. بینایی کامپیوتر زیرشاخه ای از هوش مصنوعی است که از الگوریتم هایی برای تشخیص جزئیات تصاویر با استفاده از رایانه به نام پردازش تصویر استفاده می کند. تشخیص ذرات و اندازه گیری اندازه مواد اسکن شده توسط SEM یک کار ضروری است که به توصیف ویژگی آنها کمک می کند. به طور سنتی، اندازه به صورت دستی با افزودن مش به یک تصویر SEM یا با کشیدن یک خط مورب در یک ذره دلخواه محاسبه می شود. در این مقاله، مدل جدیدی مبتنی بر هوش مصنوعی (AI) با استفاده از بینایی کامپیوتری برای تجزیه و تحلیل اندازه تمام ذرات پیشنهاد شده است. این مدل برای تشخیص اندازه ذرات مواد افزودنی در مواد کامپوزیتی مانند دانه های گرافن و اندازه گیری اندازه آنها بسته به اندازه مرجع ثابت شده در میکروسکوپ الکترونی روبشی (SEM) استفاده می شود. این مدل بر اساس کتابخانه منبع باز کامپیوتر Vision (OpenCV)، با استفاده از چند لایه تشخیص لبه ها، فیلتر Sobel، الگوریتم های روشنایی و کنتراست، با استفاده از Python 3 استفاده شد. نتایج به نشانه بسیار رضایت بخش با زمان فرآیند بسیار کم ۰.۲ میلی ثانیه دست یافته است.



## Design and Analysis of Symmetrical Dual Gate Tunnel Field Effect Transistor with Gate Dielectric Materials in 10nm Technology

S. Buttol, B. Balaji\*, K. Srinivasa Rao

Department of Electronics and Communication Engineering, Koneru Lakshmaiah Education Foundation, Green Fields, Vaddeswaram, Andhra Pradesh, India

### PAPER INFO

#### Paper history:

Received 25 October 2023

Received in revised form 13 November 2023

Accepted 26 November 2023

#### Keywords:

Hafnium Oxide

Titanium Dioxide

Drain Conductance

On Current

Transconductance

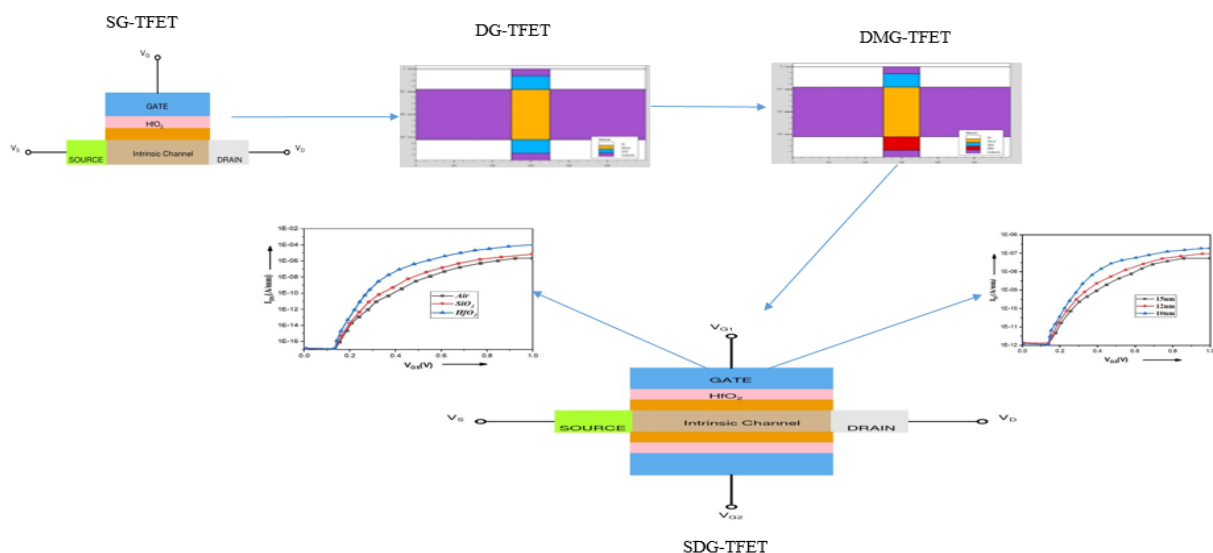
### ABSTRACT

In this work, a Symmetrical Dual Gate Tunnel Field Effect Transistor (SDGTFET) is proposed with gate dielectric materials in 10nm technology. The electrical performance parameters of this proposed device are investigated using technology computer aided design (TCAD) simulator. The new SDGTFET employing with high-k dielectric material such as hafnium oxide ( $\text{HfO}_2$ ) and interfacial layer (IL). The 2nm  $\text{HfO}_2$  with 30 dielectric constant is used between the interfacial layer and the metal gate on both sides of the device. The variation of the drain current with the varying of gate length, effective gate materials and effective oxide layer thickness of the device is evaluated in this work. By optimizing the proposed device with gate dielectric material the on current gets  $\sim 4.2$  times enhanced and the averaged subthreshold swing (SSavg) becomes reduced from 90.2 mV/dec to 53.8 mV/dec. Therefore, the SDGTFET structure has better performance than single material and double material TFET and shows a lower ambipolar current and a better on current to off current ratio.

doi: 10.5829/ije.2024.37.04a.02

### Graphical Abstract

Graphical Abstract



Corresponding Author Email: [vahividi@gmail.com](mailto:vahividi@gmail.com) (B. Balaji)

Please cite this article as: Howldar S, Balaji B, Srinivasa Rao K. Design and Analysis of Symmetrical Dual Gate Tunnel Field Effect Transistor with Gate Dielectric Materials in 10nm Technology. International Journal of Engineering, Transactions A: Basics. 2024;37(04): 588-95.

## 1. INTRODUCTION

An advanced Metal-Oxide-Semiconductor Field-Effect Transistor (MOSFET) represents a pivotal innovation in the realm of semiconductor technology, revolutionizing the design and functionality of electronic devices (1). MOSFETs are fundamental building blocks of modern integrated circuits, and advancements in their structure and materials have been crucial for achieving higher performance, increased energy efficiency, and enhanced miniaturization in electronic systems. The traditional MOSFET consists of a metal gate, an insulating silicon dioxide layer, and a semiconductor material, such as silicon. The advanced MOSFET has innovations beyond the conventional design, such as the integration of high-k dielectric material being hafnium oxide ( $\text{HfO}_2$ ), Titanium dioxide ( $\text{TiO}_2$ ) and low-k dielectric material being silicon dioxide ( $\text{SiO}_2$ ) and novel materials to overcome challenges associated with scaling down transistor dimensions (2). This shift is driven by the need to reduce the thickness of the gate oxide layer, a critical component in MOSFETs, to maintain control over the flow of electrical current while avoiding leakage current in the device. High-k dielectrics enable the creation of physically thinner gate oxides, allowing for better electrostatic control and improved transistor performance in semiconductors (3). The pursuit of smaller transistor sizes has led to the development of Fin Field-Effect Transistor (FinFET) and nanowire advanced transistor architectures. These three-dimensional structures provide better control over the flow of electrons, mitigating short-channel effects and allowing for continued transistor scaling. Advanced MOSFET technology is integral to the progress of semiconductor manufacturing processes, enabling the creation of more powerful and energy-efficient electronic devices. As semiconductor research and development continue to evolve, the exploration of new materials, advanced transistor architectures, its performance and innovative manufacturing techniques will further shape the landscape of advanced MOSFETs, influencing the capabilities and efficiency of future electronic systems (4).

The Advanced Tunnel Field-Effect Transistor (TFET) represents a cutting-edge development in semiconductor technology, pushing the boundaries of traditional transistor design to overcome challenges related to power consumption and performance scaling (5). As an innovative electronic device, the TFET devices leverages quantum mechanical tunneling phenomena to facilitate low-power operation, making it a promising device for applications demanding high energy efficiency and improved transistor scaling (6). In contrast to MOSFETs, TFETs exploit the quantum tunneling effect, allowing electrons to pass through a thin barrier without the need for high thermal energy (7). This unique an improved characteristic enables TFETs to operate at

lower voltage levels, resulting in reduced power consumption and improved overall energy efficiency. The adoption of TFETs is particularly significant in the context of power-constrained devices, such as those used in portable electronics and low-power Internet of Things (IoT) applications (8). The TFET design often incorporates materials with a narrow bandgap, enabling efficient quantum tunneling. The concept is especially relevant for addressing challenges associated with conventional MOSFETs as they approach the physical limits of scaling down in size (9). TFETs provide an alternative path to continue the advancement of transistor technology by mitigating issues like subthreshold swing, which affects the energy efficiency in small-scale nano transistors. As semiconductor research and development progress, the exploration of advanced TFET architectures, materials, and fabrication techniques continues. Engineers and researchers are working to optimize TFET designs for mainstream integration, considering factors such as manufacturability, reliability, and compatibility with existing semiconductor processes and analysis (10). The continuous evolution of TFET technology holds the promise of revolutionizing the landscape of low-power electronics, enabling the development of energy-efficient devices that are crucial for the future of computing and communication systems (11).

The dielectric constant  $\text{SiO}_2$  depends on various factors, including the crystalline structure, temperature, and frequency of the applied electric field. This material is commonly used as a dielectric material in the semiconductor industry, the dielectric constant is typically around 3.9 (12). The dielectric constant of  $\text{SiO}_2$  is relatively low compared to other dielectric materials. The lower dielectric constant helps in minimizing the capacitive coupling between adjacent conductive structures in integrated circuits (13). However, as semiconductor devices have scaled down in size, there are challenges associated with increasing capacitance and reducing leakage currents. This has led to the exploration of alternative high-k dielectric materials, such as hafnium dioxide ( $\text{HfO}_2$ ), to address these challenges in advanced semiconductor technologies (14).

The  $\text{HfO}_2$  is a metal oxide that is used as a dielectric material in the nano scale devices and manufacturing of advanced semiconductor devices, particularly in the fabrication of modern integrated circuits (15). The dielectric constant is a measure of a materials ability to store electrical energy in an electric field. The dielectric constant of  $\text{HfO}_2$  is typically in the range of 20 to 30, depending on factors such as the specific crystalline phase, the method of deposition, and the conditions of the fabrication process. This value is higher than the dielectric constants of conventional  $\text{SiO}_2$ , which has historically been used as a high-k dielectric material in semiconductor devices. The use of  $\text{HfO}_2$  as a high-k

dielectric is motivated by the need to reduce the physical thickness of the dielectric layer while maintaining a high capacitance to improve the overall performance of transistors in integrated circuits (16). High-k dielectrics are employed to overcome the limitations of traditional silicon dioxide in terms of thickness scaling and leakage current in advanced semiconductor technologies.

The Titanium dioxide ( $\text{TiO}_2$ ) is another material that is often used as a dielectric in various applications. The dielectric constant or relative permittivity of  $\text{TiO}_2$  can vary depending on factors such as the crystalline phase, temperature, and frequency of the applied electric field. The crystalline form of  $\text{TiO}_2$ , which is rutile, the dielectric constant is typically around 85. Anatase and brookite are two other crystalline phases of  $\text{TiO}_2$ , and they may have different dielectric constants. It's important to note that the dielectric constant can vary with the frequency of the electric field (17).

One of the common challenges in TFET emerging technology is the limited experimental validation. Many researchers might rely on simulations and theoretical models, and experimental verification might be lacking. Filling this gap requires more efforts in fabricating and characterizing SDGFET devices to validate the theoretical predictions and understand real-world performance for low power applications. The selection of materials is crucial in semiconductor device design. The literature may not fully explore the variety of materials that could enhance the performance of advanced TFET devices. Researchers could explore new material combinations such as high-k dielectric materials such as  $\text{HfO}_2$  and  $\text{TiO}_2$  to improve its overall device performance and reduce leakage current. The literature extensively cover the challenges associated with the fabrication processes for TFETs. Addressing this gap involves optimizing fabrication techniques and advanced to ensure reproducibility, scalability, and manufacturability in nanometer technology not behind 22nm. The SDGFET is designed for low-power applications, the literature comprehensively explore the trade-offs between power consumption and performance metrics such as speed. Addressing this gap requires a balanced approach to optimizing device parameters for specific applications in nanometer technology.

The SDGFET has gained attention in the realm of semiconductor devices is characterized by its unique dual-gate structure. It consists of two gates, each influencing the flow of charge carriers in the transistor and the symmetrical design allows for enhanced control over the transistor's behavior. The traditional TFET, the SDGFET relies on quantum tunneling for carrier transport and tunneling occurs through a thin barrier, enabling low-power operation. The primary advantage of SDGFET is their potential for extremely low-power operation due to the reliance on tunneling. The symmetrical dual-gate design provides improved control

and flexibility in tuning the transistor's characteristics. Optimizing fabrication processes and ensuring the process of compatibility with nano structures to existing advanced semiconductor manufacturing techniques are critical for TFET practical applications. Therefore, SDGFET device is a unique approach to low-power semiconductor devices, leveraging a unique dual-gate structure and quantum tunneling principles.

## 2. DEVICE STRUCTURE AND SIMULATION PARAMETERS

Two dimensional structure of SDGFET with high-k gate dielectric material and interfacial layer as shown in Figure 1. The 10nm scale, conventional TFET design face challenges such as increased leakage currents and quantum effects (18). The SDG TFET, with its enhanced symmetrical dual gate architecture, offers a potential solution by providing better control over the electrostatic field. The high-k gate dielectric materials such as  $\text{HfO}_2$  is employed for achieving optimal performance at 10nm scale. High-k dielectrics are particularly important in reducing leakage currents and enhancing gate control. The integration of advanced dielectric materials ensures that the SDG TFET can operate efficiently while maintaining a low power footprint (19). The proposed device plays a pivotal role in improving device characteristics. The design allows for a more uniform electric field distribution and tunneling barrier thickness and distance. This architecture is beneficial in achieving better ON/OFF current ratios, which are crucial for low power applications. The 10nm scale SDG TFET leverages tunneling as its fundamental mechanism of operation (20). The symmetrical gates help in optimizing tunneling processes, ensuring reliable and efficient charge through the channel and this 10nm SDG TFET is to enhance power efficiency. The combination of the symmetrical dual gate (SDG) architecture and advanced gate dielectric materials contributes to lower leakage

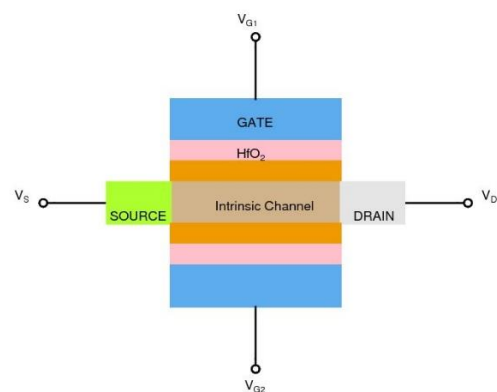


**Figure 1.** Proposed SDGFET in 10nm regime

currents, reduced power consumption, and improved overall energy efficiency (21).

Designing a SDG TFET with advanced gate dielectric materials using Technology Computer-Aided Design (TCAD) involves a comprehensive process that encompasses simulation, analysis, and optimization. TCAD tools provide engineers with a virtual environment to model and simulate semiconductor devices (3).

The SDGTFET under consideration makes use of simulation parameters as shown in Table 1. Various models and methods are applied for the simulation, employing the TCAD tool, as outlined in Tables 2 and 3.

**TABLE 1.** Utilized Parameter for the simulation of SDGTFET

Utilized Parameters	Values
Thickness of HfO <sub>2</sub>	2nm
Metal Gate-1 Work Function(W <sub>F</sub> )	4.8eV
Metal Gate-2 Work Function(W <sub>F</sub> )	4.8eV
Device Length(W <sub>L</sub> )	60 nm
Gate Length(L <sub>G</sub> )	10 nm
Source Length(L <sub>S</sub> )	25nm
Drain Length(L <sub>D</sub> )	25nm

**TABLE 2.** Models used for the device

Model	Description
commob	Specifies the mobility concentration and dependency
fldmob	Calculation of all the device field dependency
evsatmod=1	implements the carrier concentration and temperature mobility
hcte.el	to enable electric field energy balance for electrons for relaxation time
taurel.el	specifies the relaxation time in the energy balance
taumob.el	specifies the relaxation time for electrons in the temperature dependency

**TABLE 3.** Methods used for the device

Method	Description
newton	specifies the solution method
maxtrap	used as trap procedure
autonr	used to increase the speed of newton solution method
dvlimit	used as maximum magnitude
nblockit	used as the block iterations

The different design parameters to optimize the performance of SDGTFET. This could include varying the dimensions of the device in nanometer dimensions, doping concentrations, and material properties. Investigate the impact of different semiconductor materials on the device performance. Compare and analyze the characteristics of SDGTFET based on various materials, such as silicon, III-V compounds. The noise analysis to understand the impact of noise sources on the device performance. This can involve studying the thermal noise, flicker noise, and other sources that affect the signal integrity. The power consumption characteristics of the Symmetrical Dual Gate TFET under different operating conditions. Analyze the device performs in terms of energy efficiency and power dissipation. The temperature dependence of the Symmetrical Dual Gate TFET. To understand the device behaves at different temperature ranges and explore potential strategies for temperature compensation.

### 3. RESULTS AND DISCUSSION

The analysis of Id (drain current) versus Vgs (gate-source voltage) for a SDGTFET with different gate dielectric materials involved for the proposed device characteristics under varying gate voltages. SDGTFET are promising device for low-power applications due to their ability to achieve sub-threshold swing values below the limit of conventional TFET (22, 23). One of the critical parameters to analyze is the sub-threshold swing, which is a measure of the SDGTFET ability to turn on and off efficiently. A lower SS value indicates better improved performance in in the device. The threshold voltage changes with different gate dielectric materials. V<sub>th</sub> is the gate voltage at which the device starts conducting. It's essential for determining the operating region of the TFET (24). To analyze the drain current (Id) varies with different gate-source voltages. This shows the on-state behavior of the TFET as shown in Figure 2. A high Ion/Ioff ratio indicates better switching behavior and power efficiency of the proposed device (25, 26). The proposed tunneling device, the tunneling current should be a dominant factor. Analyze the impact of gate dielectric materials such as high-k HfO<sub>2</sub> on tunneling mechanisms and their influence on device performance.

The drain current (Id) versus gate-source voltage (Vgs) characteristics for a SDGTFET with variation of different technology regimes as shown in Figure 3 and investigate the proposed device characteristics scale with 10nm, 12nm and 15nm nodes (27). The 10nm node are scalable to smaller technology nodes for the limitations associated with scaling factor. The dynamic power consumption of SDGTFET during switching events and

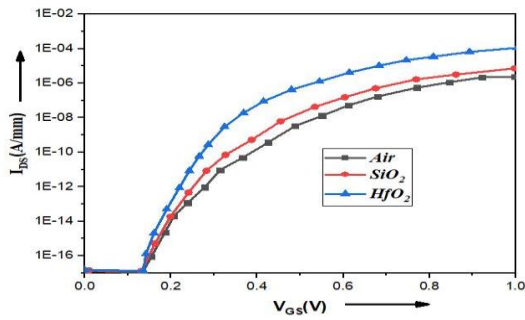


**Figure 2.** Characteristics of drain current and Gate voltage with dielectric materials

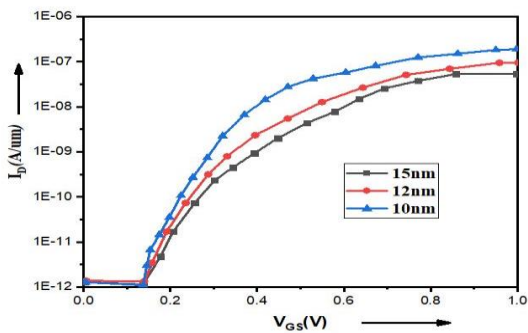


**Figure 3.** Characteristics of drain current and Gate voltage with different technology node

static power consumption in the off-state are reliable in 10nm regime. The performance of the SDGTFET with gate dielectric materials and technology nodes has improved compared to conventional TFET and double gate TFET (28).

The drain conductance ( $G_d$ ) of SDGTFET is the derivative of the drain current ( $I_d$ ) with respect to the drain-source voltage ( $V_{gs}$ ). In the characteristics of a SDGTFET with gate dielectric materials, the analysis of drain conductance involves the conductance varies with different parameters, such as improved gate voltages, gate dielectric materials, and bias conditions (29). The high-k gate dielectric materials influences the drain conductance at  $V_{gs} = 1v$ . Different dielectric materials such as high-k and low-k dielectric materials can affect the tunneling characteristics and, consequently, the conductance of the device. The sub-threshold region of this TFET is transitioning between the off and on states. A steep sub-threshold region and low drain conductance in the off state are desirable and shown in Figure 4.

Transconductance plays a critical role in understanding and characterizing the behavior of this proposed SDGTFET devices, and it is an essential concept in amplifier design, digital signal processing, and analog electronics (30). This characteristic is a measure of how much the output current of a device, changes in

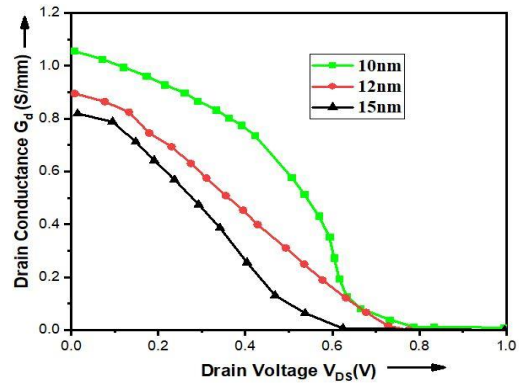


**Figure 4.** Characteristics of drain conductance with different technology node

the input voltage applied to it and it is a key factor in determining the gain and linearity of the device as it influences how effectively an electronic components can amplify an input signal. In the proposed devices, it characterizes the relationship between the input voltage and the output current when operating in the amplification or active mode. It is used to design and optimize the performance of electronic devices, ensuring they operate efficiently and accurately as shown in Figure 5.

The on resistance ( $R_{on}$ ) is to determining the power dissipation and efficiency of a TFET. It is essentially the resistance by the current flowing between the drain and source terminals when the TFET is conducting.  $R_{on}$  is a static resistance that represents the resistance of the TFET in the on-state. It is typically defined as the voltage drop across the device divided by the drain current when the device is in the on-state as shown in Figure 6.

The enhanced  $I_{on}$  and  $I_{off}$ , performance parameters of proposed device related to material and technology as shown in Tables 4 and 5. The  $G_m$  and  $G_d$  calculated parameters are shown in Tables 6 and 7. The performance parameter comparison of proposed device with existed devices are shown in Table 8.

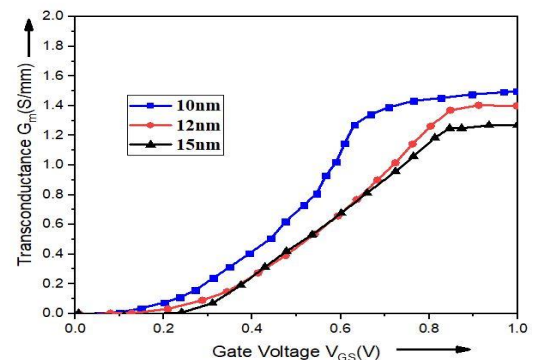


**Figure 5.** Characteristics of transconductance with different technology node

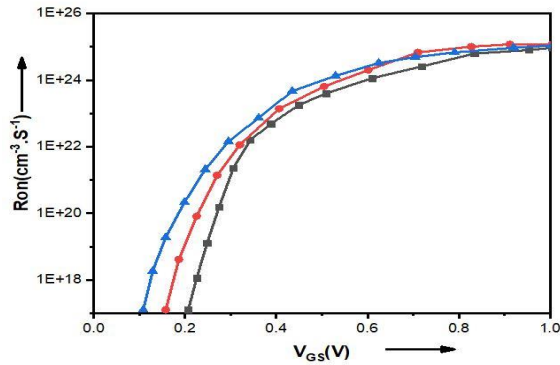


**Figure 6.** On resistance characteristics with different technology node

**TABLE 4.** On current and off current for different dielectric materials

Materials	Ion(A/μm)	Ioff(A/μm)	Ion/Ioff
Air	10e <sup>-05</sup>	10e <sup>-15</sup>	10e <sup>+12</sup>
SiO <sub>2</sub>	10e <sup>-5</sup>	10e <sup>-16</sup>	10e <sup>+11</sup>
HfO <sub>2</sub>	10e <sup>-3</sup>	10e <sup>-17</sup>	10e <sup>+12</sup>

**TABLE 5.** On current and off current for different technology node

Technology (nm)	Ion (A/μm)	Ioff (A/μm)	Ion/Ioff
10	10e <sup>-06</sup>	10e <sup>-12</sup>	10e <sup>+06</sup>
12	10e <sup>-07</sup>	10e <sup>-11</sup>	10e <sup>+05</sup>
15	10e <sup>-08</sup>	10e <sup>-11</sup>	10e <sup>+03</sup>

**TABLE 6.** Transconductance for different technology node

Technology (nm)	Gm (S/mm)
10	1.62
12	1.51
15	1.39

**TABLE 7.** Drainconductance for different technology node

Technology (nm)	Gd (S)
10	1
12	0.89
15	0.88

**TABLE 8.** Performance Parameters Comparison of SDGTFET

Parameters	C TFET	SG TFET	DG TFET	HD-DG TFET	HD-DMG-TFET	SDGTFET (10nm)
Ion(A/μm)	3.12	3.94	4.3	4.6	8.01	9.48
Ioff(A/μm)	9.40	8.99	4.50	4.22	1.34	1.16
Ion/Ioff	1.69	1.70	1.88	1.84	1.9	2.12
Gm(S/mm)	1.34	1.38	1.42	1.46	1.41	3.1
Gd(S/mm)	0.32	0.39	0.419	0.45	0.452	0.71
Ron(Ωmm)	1.41	1.61	1.32	0.88	0.6	0.51

#### 4. CONCLUSION

The SDGTFET configuration has emerged as a promising device for enhancing performance and the limitations of conventional TFET. The symmetrical dual gate TFET exhibits improved subthreshold swing, reduced leakage current and its potential for enhanced operational efficiency compared to traditional device technologies. The impact of different semiconductor materials on the device, highlighting the significance of material selection in optimizing the symmetrical dual gate TFET performance. The investigation encompassed and demonstrated the influence of material properties on device characteristics. Two dimensional structure of Symmetrical Dual Gate Tunnel Field Effect Transistor (SDGTFET) is proposed in this work. The proposed device formed by high -k gate dielectric gate dielectric material being Hafnium oxide (HfO<sub>2</sub>). The electrical characteristics of SDGTFET like drain current,

transconductance and drain conductance are calculated with the influence of varied semiconductor materials. The integration of SDG enhances the device's electrostatic control, resulting in improved ON/OFF current ratios and better overall performance. The symmetrical configuration achieving a more uniform electric field distribution and enhancing reliability. The high-k gate dielectric materials is to determining the overall efficiency of the SDGTFET. By exploring and implementing advanced dielectric materials, such as high-k dielectrics, the device can achieve lower leakage currents and improved gate control. The findings of this proposed device contribute significantly to the existing and understanding of the SDGTFET behavior and performance. These insights hold substantial promise for the advancement of semiconductor technology, as they can guide the development of refined designs and optimized utilization of SDGTFET in advanced low power applications.

## 5. REFERENCES

- Howldar S, Balaji B, Srinivasa Rao K. Design and Analysis of Hetero Dielectric Dual Material Gate Underlap Spacer Tunnel Field Effect Transistor. *International Journal of Engineering, Transactions C: Aspects.* 2023;36(12):2137-44. 10.5829/ije.2023.36.12c.01
- Krishnamurthya A, Reddy DV, Radhammac E, Jyothirmayeed B, Raoc DS, Agarwale V, et al. Design and Performance Analysis of 6H-SiC Metal-Semiconductor Field-Effect Transistor with Undoped and Recessed Area under Gate in 10nm Technology. *International Journal of Engineering, Transactions C: Aspects.* 2023;36(12):2264-71. 10.5829/ije.2023.36.12c.16
- Mehrabani AH, Fattah A, Rahimi E. Design and Simulation of a Novel Hetero-junction Bipolar Transistor with Gate-Controlled Current Gain. *International Journal of Engineering, Transactions C: Aspects.* 2023;36(03):433. 10.5829/ije.2023.36.03c
- Madan J, Pandey R, Sharma R, Chaujar R. Impact of metal silicide source electrode on polarity gate induced source in junctionless TFET. *Applied Physics A.* 2019;125(9):600. <https://doi.org/10.1007/s00339-019-2900-6>
- Musalgaonkar G, Sahay S, Saxena RS, Kumar MJ. A line tunneling field-effect transistor based on misaligned core-shell gate architecture in emerging nanotube FETs. *IEEE Transactions on Electron Devices.* 2019;66(6):2809-16. <https://doi.org/10.1109/TED.2019.2910156>
- Zare M, Peyravi F, Hosseini SE. Impact of hetero-dielectric ferroelectric gate stack on analog/RF performance of tunnel FET. *Journal of Electronic Materials.* 2020;49:5638-46. <https://doi.org/10.1007/s11664-020-08315-3>
- Raj A, Singh S, Priyadarshani KN, Arya R, Naugarhiya A. Vertically Extended Drain Double Gate Si<sub>1-x</sub>Ge<sub>x</sub> Source Tunnel FET: Proposal & Investigation For Optimized Device Performance. *Silicon.* 2021;13:2589-604. <https://doi.org/10.1007/s12633-020-00603-1>
- Radhamma E, Vemana Chary D, Krishnamurthy A, Venkatarami Reddy D, Sreenivasa Rao D, Gowthami Y, et al. Performance analysis of high-k dielectric heterojunction high electron mobility transistor for rf applications. *International Journal of Engineering, Transactions C: Aspects.* 2023;36(9):1652-8. 10.5829/ije.2023.36.09c.09
- Gowthami Y, Balaji B, Srinivasa Rao K. Performance Analysis and Optimization of Asymmetric Front and Back Pi Gates with Dual Material in Gallium Nitride High Electron Mobility Transistor for Nano Electronics Application. *International Journal of Engineering, Transactions A: Basics* 2023;36(7):1269-77. 10.5829/ije.2023.36.07a.08
- Keighobadi D, Mohammadi S, Mohtaram M. Recessed gate cylindrical heterostructure TFET, a device with extremely steep subthreshold swing. *Transactions on Electrical and Electronic Materials.* 2021;1:1-7. <https://doi.org/10.1007/s42341-021-00321-4>
- Rani CSH, Bagan KB, Roach RS. Improved drain current characteristics of germanium source triple material double gate hetero-dielectric stacked TFET for low power applications. *Silicon.* 2021;13:2753-62. <https://doi.org/10.1007/s12633-020-00556-5>
- Gowthami Y, Balaji B, Rao KS. Design and performance evaluation of 6nm hemt with silicon sapphire substrate. *Silicon.* 2022;14(17):11797-804. <https://doi.org/10.1007/s12633-022-01900-7>
- Kumar PK, Balaji B, Rao KS. Performance analysis of sub 10 nm regime source halo symmetric and asymmetric nanowire MOSFET with underlap engineering. *Silicon.* 2022;14(16):10423-36. <https://doi.org/10.1007/s12633-022-01747-y>
- Howldar S, Balaji B, Srinivasa Rao K. Design and Qualitative Analysis of Hetero Dielectric Tunnel Field Effect Transistor Device. *International Journal of Engineering, Transactions C: Aspects* 2023;36(6):1129-35. 10.5829/ije.2023.36.06c.11
- Anvarifard MK, Orouji AA. Enhancement of a nanoscale novel Esaki tunneling diode source TFET (ETDS-TFET) for low-voltage operations. *Silicon.* 2019;11(6):2547-56. <https://doi.org/10.1007/s12633-018-0043-6>
- Dixit A, Gupta N. A compact model of gate capacitance in ballistic gate-all-around carbon nanotube field effect transistors. *International Journal of Engineering, Transactions A: Basics.* 2021;34(7):1718-24. 10.5829/IJE.2021.34.07A.16
- Sharma S, Chaujar R. Band gap and gate metal engineering of novel hetero-material InAs/GaAs-based JLTFTET for improved wireless applications. *Journal of Materials Science: Materials in Electronics.* 2021;32(3):3155-66. <https://doi.org/10.1007/s10854-020-05064-1>
- Chakrabarty R, Roy S, Pathak T, Kumar Mandal N. Design of Area Efficient Single Bit Comparator Circuit using Quantum dot Cellular Automata and its Digital Logic Gates Realization. *International Journal of Engineering, Transactions C: Aspects.* 2021;34(12):2672-8. 10.5829/ije.2021.34.12c.13
- Gopal G, Varma T. Simulation-based analysis of ultra thin-body double gate ferroelectric TFET for an enhanced electric performance. *Silicon.* 2022;14(12):6553-63. <https://doi.org/10.1007/s12633-021-01428-2>
- Roy A, Mitra R, Kundu A, editors. Influence of channel thickness on analog and RF performance enhancement of an underlap DG AlGaIn/GaN based MOS-HEMT device. *2019 Devices for Integrated Circuit (DevIC); 2019: IEEE.*
- Gedam A, Acharya B, Mishra GP. Junctionless silicon nanotube TFET for improved DC and radio frequency performance. *Silicon.* 2021;13:167-78. <https://doi.org/10.1007/s12633-020-00410-8>
- Rafiee A, Nickabadi S, Nobarian M, Tagimalek H, Khatami H. Experimental investigation joining al 5083 and high-density polyethylen by protrusion friction stir spot welding containing nanoparticles using taguchi method. *International Journal of Engineering, Transactions C: Aspects.* 2022;35(6):1144-53. 10.5829/ije.2022.35.06c.06
- Alassery F, Khan AI, Shaik MS. Implementation of Advanced Tunnel Field Effect Transistor (DP-TFET) for High Power Switching Applications. *Silicon.* 2022;14(15):9589-93. <https://doi.org/10.1007/s12633-021-01647-7>
- Sahu SA, Goswami R, Mohapatra S. Characteristic enhancement of hetero dielectric DG TFET using SiGe pocket at source/channel interface: proposal and investigation. *Silicon.* 2020;12(3):513-20. <https://doi.org/10.1007/s12633-019-00159-9>
- Balaji B, Srinivasa Rao K, Girija Sravani K, Bindu Madhav N, Chandrahas K, Jaswanth B. Improved drain current characteristics of hfo<sub>2</sub>/sio<sub>2</sub> dual material dual gate extension on drain side-tfet. *Silicon.* 2022;14(18):12567-72. <https://doi.org/10.1007/s12633-022-01955-6>
- Kumar PK, Balaji B, Rao KS. Halo-Doped Hetero Dielectric Nanowire MOSFET Scaled to the Sub-10 nm Node. *Transactions on Electrical and Electronic Materials.* 2023:1-11. <https://doi.org/10.1007/s42341-023-00448-6>
- Emami N, Kuchaki Rafsanjani M. Extreme learning machine based pattern classifiers for symbolic interval data. *International Journal of Engineering, Transactions B: Applications.* 2021;34(11):2545-56. 10.5829/IJE.2021.34.11B.17
- Fouladinia F, Gholami M. Decimal to excess-3 and excess-3 to decimal code converters in QCA nanotechnology. *International Journal of Engineering, Transactions C: Aspects.* 2023;36(9):1618-25. 10.5829/ije.2023.36.09c.05

29. Gowthami Y, Balaji B, Rao KS. Design and Analysis of a Symmetrical Low- $\kappa$  Source-Side Spacer Multi-gate Nanowire Device. *Journal of Electronic Materials*. 2023;52(4):2561-8. <https://doi.org/10.1007/s11664-023-10217-z>
30. Meriga S, Bhowmick B. Deep Insight into Raised Buried Oxide SOI-Fe TFET and It's Analog/RF and Linearity Performance Parameters. *Transactions on Electrical and Electronic Materials*. 2023:1-14. <https://doi.org/10.1007/s42341-023-00480-6>

#### COPYRIGHTS

©2024 The author(s). This is an open access article distributed under the terms of the Creative Commons Attribution (CC BY 4.0), which permits unrestricted use, distribution, and reproduction in any medium, as long as the original authors and source are cited. No permission is required from the authors or the publishers.



#### Persian Abstract

##### چکیده

در این کار، یک ترانزیستور اثر میدانی تونل دو دروازه ای متقارن (SDGTFET) با مواد دی الکتریک گیت در فناوری ۱۰ نانومتر پیشنهاد شده است. پارامترهای عملکرد الکتریکی این دستگاه پیشنهادی با استفاده از شبیه‌ساز طراحی به کمک کامپیوتر (TCAD) مورد بررسی قرار گرفته است. SDGTFET جدید از مواد دی الکتریک با  $k$  بالا مانند اکسید هافنیوم ( $\text{HfO}_2$ ) و لایه سطحی (IL) استفاده می‌کند.  $\text{HfO}_2$  نانومتری با ۳۰ ثابت دی الکتریک بین لایه سطحی و دروازه فلزی در دو طرف دستگاه استفاده می‌شود. تغییر جریان تخلیه با تغییر طول دروازه، مواد موثر دروازه و ضخامت لایه اکسیدی موثر دستگاه در این کار ارزیابی می‌شود. با بهینه سازی دستگاه پیشنهادی با مواد دی الکتریک گیت، جریان روشن ۴.۲ برابر افزایش می‌یابد و میانگین نوسان زیرآستانه (SSavg) از ۹۰.۲  $\text{mV/dec}$  به ۵۳.۸  $\text{mV/dec}$  کاهش می‌یابد. بنابراین، ساختار SDGTFET عملکرد بهتری نسبت به TFET تک ماده و دو ماده دارد و جریان دوقطبی کمتر و نسبت جریان به جریان خاموش بهتر را نشان می‌دهد.



# Numerical Studies on Performance of Helical Pile-supported Embankments Over Soft Clay

M. A. Mashayekhi, M. Khanmohammadi\*

Department of Civil Engineering, Isfahan University of Technology, Isfahan, Iran

## PAPER INFO

### Paper history:

Received 18 September 2023

Received in revised from 16 November 2023

Accepted 26 November 2023

### Keywords:

Embankments

Helical Pile

Load Transfer Mechanism

Bearing Capacity

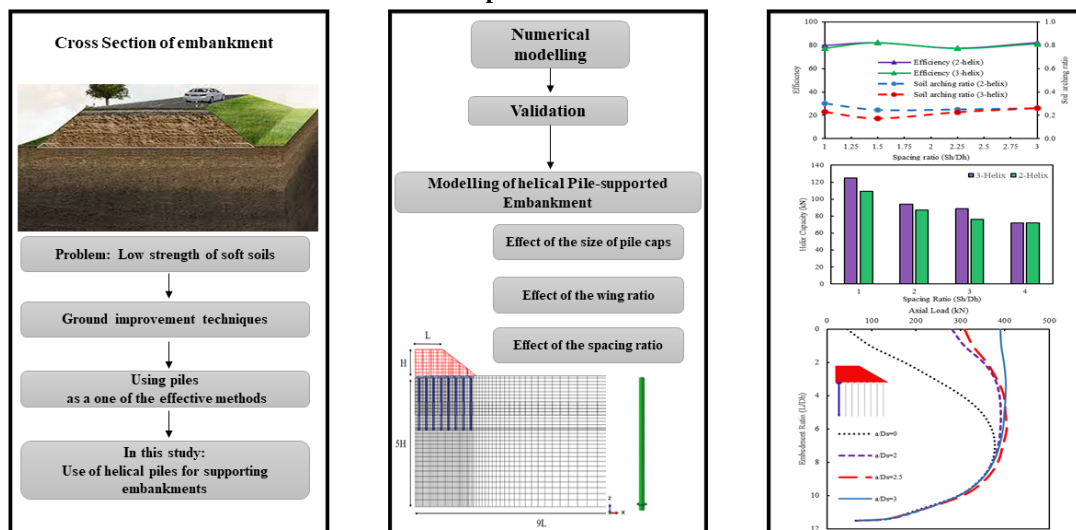
Finite Element

## ABSTRACT

The need for practical and economical solutions to increase the stability of embankments and reduce their settlement is a significant issues in geotechnical engineering. An effective approach to improve the overall performance of embankment systems is using structural elements such as piles. In recent years the use of helical piles has gained consideration due to their proper performance under compressive and tensile loads, quick and easy installation, and elimination of concreting problems. This study investigates the performance of embankments supported by helical piles through a 3D numerical study using the Abaqus software. The validation was performed according to the experimental and field data provided by other researchers. Then, 3D numerical models were developed to investigate the effects of pile caps, the ratio of helix diameter to shaft diameter, the number of helices, and the optimum spacing of helices. The finite element modeling results indicated that increasing the number of helices and changing their spacing had no significant impact on controlling the settlement. It was also found that the load transfer mechanism parameters had a direct relationship with the helix dimensions and shaft diameter. Adding helices to piles increased their bearing capacity, improving parameters of the load transfer mechanism, such that the arching in a pile with three helices decreased by 40% compared to the one with one helix. The results also revealed that on average, 80% of the load imposed on a pile was sustained by the shaft, and helices had a smaller effect on the settlement of pile-supported embankments.

doi: 10.5829/ije.2024.37.04a.03

## Graphical Abstract



\*Corresponding Author Email [mkhanmohammadi@iut.ac.ir](mailto:mkhanmohammadi@iut.ac.ir) (M. Khanmohammadi)

## 1. INTRODUCTION

The design and construction of road or railway embankments are not possible on problematic soils, such as soft soils, due to excessive total and differential settlements, low bearing capacity, high lateral displacement, and slope instability (1). As a rapid and economical solution, pile-supported embankments have been employed instead of traditional improvement methods of soft soils over recent years (2, 3). Studies have investigated different types of piles to be used in pile-supported embankments. Cast-in-place concrete piles (4, 5), precast concrete piles (6-8), prestressed concrete piles (9), steel piles (10, 11), deep mixed columns (12-14), stone columns (15, 16), sand-ash-gravel mixed columns (4, 17), and high-strength piles (18, 19) are some examples. Ahmed et al. (20) conducted a parametric study to simulate pile foundation and investigate its performance in soft clay. It was found that the performance of piled raft foundations on soft soils is significantly affected by the piles' spacing. When the ratio  $S/D$  exceeds 10, piles have little or no effect on the ultimate bearing capacity.

Liu et al. (21) conducted a study on different types of piles (rigid, rigid-flexible, flexible) in a pile embankment system. The results showed that the model test with rigid piles had the least settlement, while the model test with flexible piles experienced the largest settlement. However, it was found that using pile effectively reduced embankment settlement.

All types of conventional piles have specific issues such as construction problems, damaging the environment, and incurring large costs that make them deficient in some civil engineering projects.

A helical pile is a deep steel foundation system, consisting of one or more helices connected to a central shaft. The easy and rapid installation, recyclability and reusability, elimination of concreting issues, and low noises during installation are some merits of these piles, resulting in the widespread use of large-scale helical piles in industrial and building projects (22). The use of helical piles in pile-supported embankments is an alternative, whose performance evaluation requires further studies. The shaft diameter of a large-scale helical pile varies between 73 mm and 965 mm, and the diameter of the helices connected to it ranges from 152 to 1219 mm. Some references consider the ratio of helix diameter to shaft diameter between 2 and 3 (23-25). Most of the previous researches on helical piles have focused on the situation in which the piles are under direct loading, and by examining their geometric parameters, settlement performance and axial force distribution in the pile depth have been investigated and the results indicate that for cohesive soils, increasing the number of helices with the optimal distance of 1.5 times the diameter of the helix, by creating cylindrical shear, enhances pile's performance

(26-28). The research on the behavior of helical piles in pile-supported embankments is limited, and further studies are required.

Based on an analysis of the technical literature, embankments are now being constructed using improvement techniques for unsuitable soils. Among these techniques, the use of piles has proven to be more effective than the others. Numerous numerical, experimental, and field investigations have been conducted using various types of piles. Therefore, the objective of this research is to investigate the performance of helical piles in pile-supported embankment systems. In the present study, at first, a 3D finite element model of embankments supported by helical piles was verified using experimental and field data. Then, a parametric numerical study was performed to investigate the pile geometry including shaft diameter, number of helices, and width of pile cap.

**1. 2. Load Transfer Mechanism** The main factor governing the load transfer mechanism in pile-supported embankments is the difference between the stiffness of soil and piles and the mobilized shear strength of soil. As a result, the stress caused by the weight of embankment layers is transferred from the soft soil to the piles. Terzaghi (29) named this load transfer mechanism, the "arching effect". The arching mechanism is evaluated using the definitions of "arching ratio" and "efficiency". The arching ratio is defined as follows (30).

$$SAR = \frac{\sigma_s}{(\gamma H + q)} \quad (1)$$

In which  $\sigma_s$  is the stress imposed on the soil around the pile,  $\gamma$  is the embankment unit weight,  $H$  is the embankment height, and  $q$  is the uniform surcharge imposed on the embankment crest. The SAR ranges between zero and one.  $SAR = 0$  indicates that the whole load caused by the embankment weight is transferred to the piles, and the arching has occurred thoroughly. On the other hand,  $SAR = 1$  shows that no load has been transferred to piles. The efficiency parameter indicates the ratio of the load carried by piles to the load caused by the embankment weight and surcharge (31).

$$E = \frac{Q}{s^2(\gamma H + q)} \quad (2)$$

where  $Q$  equals the total forces imposed on a single pile and  $s$  is the spacing of piles.  $E = 0$  indicates that no arching has happened, while  $E = 100\%$  shows the occurrence of full arching.

Many parametric studies have been conducted on the load transfer mechanism in pile-supported embankments. Through field study and numerical studies, Hello and Villard (32) showed that increasing the pile cap width improved the efficiency of piles and reduced their

settlement. Investigating the impact of the length of floating piles on the degree of arching, Bhasi and Rajagopal (33) stated that the pile length can influence the degree of arching. Through 2D and 3D modeling of a pile-supported embankment, Ariyaratne and Liyanapathirana (34) studied the positive effect of increasing pile diameter and decreasing pile spacing on the increase in efficiency and reduction in the arching ratio. Conducting a parametric study, Meena et al. (35) showed that the elastic modulus of pile and embankment and the internal friction angle of embankment material play a vital role in the arching mechanism. Pham and Dias (36) present an extensive parametric study using three-dimensional numerical calculations for pile-supported embankments. The results indicated that the pile embankment system shows a good performance in reducing the embankment settlement. The results also suggested that the soil cohesion strengthens the arching effect, and increases the loading efficiency.

## 2. NUMERICAL MODELING

Figure 1 depicts a helical pile-supported embankment considered for the numerical modeling. The embankment with a height of 6 m, a crest length of 7.5m, and a lateral slope of 1:1.5 was modeled on a uniform clay layer with a depth of 30m. The steel helical piles were assumed with cylindrical sections, and the load-bearing helices were modeled as ideal disks. The effect of pile installation in the soil was ignored. In all models, the length of piles is 12m and helix diameter is fixed to 1m. In the parametric study, variables such as the dimensions of the cap width, shaft diameter, and the number of helices were considered in the modeling. During each modeling case, only one parameter was changed at a time, while keeping the other parameters at the baseline case values. The parameters and their values used in this study are summarized in Table 1. The baseline model values are presented in bold numbers. The mesh type and geometry for all the models were kept identical to eliminate the meshing size effects on the results. The meshing size was chosen to be adequately fine immediately near the piles, as well as in the contact surface between the embankment and the soft soil, and started to grow gradually with the distance from the edge of the embankment. Figure 1 depicts a sample meshing for the developed numerical model. Figure 2 demonstrates the geometry of the modeled helical pile, in which  $D_h$  and  $D_s$  denote the helix diameter and pile shaft diameter, respectively.

Regarding the boundary conditions, the displacements in the bottom boundary of the model were considered zero in three directions ( $U_x = U_y = U_z = 0$ ). Moreover, the displacements of the model were considered zero on two sides of the model along the x-axis and on two sides of the model on the y-axis ( $U_x =$

$U_y = 0$ ). To model the soil and pile, 25800 eight-node elements with reduced integration (C3D8R) were used.

The embankment material was considered to be coarse-grained, and the foundation soil layer was assumed to consist of uniform soft clay with weak geotechnical properties. Moreover, since the soft clay was considered to be fully drained, the drained parameters were used. Table 2 lists the properties of the materials used in the numerical modeling. The helical pile and the pile cap were modeled in the linear elastic mode using steel and concrete materials, respectively. To model the behavior of granular embankment and soft clay medium, the Mohr-Coulomb constitutive model has been used, which gives a precise prediction of the soil behavior (37). The soil-pile behavior at their interface was defined using the friction model of Coulomb and type Penalty, in which the relative displacement equals zero until the shear stress reaches a critical value. Sliding occurs when the shear stress exceeds the shear strength. The coefficient of friction was assumed to be equal to 0.7 (38, 39).

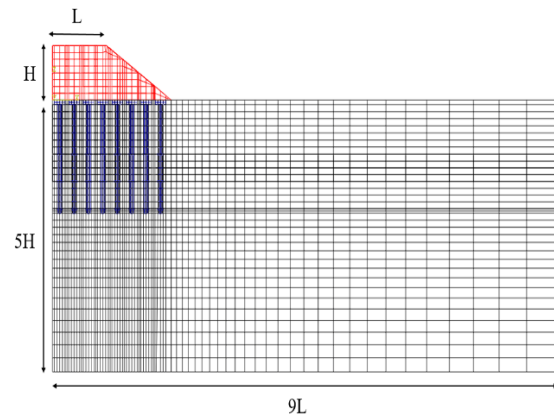
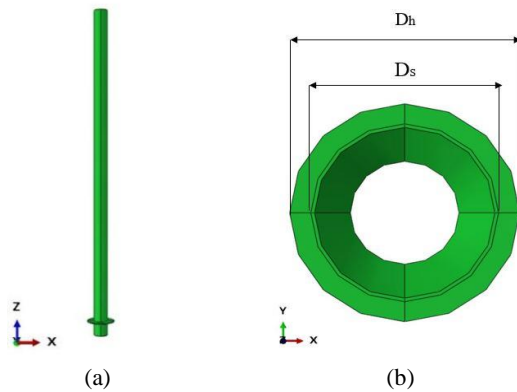


Figure 1. Schematics of the 3D model meshing

TABLE 1. Parameters values used for the parametric study

Description	Parameter	Values
Helical pile	Shaft diameter (mm)	250- <b>500</b> -667
	Depth of pile (m)	<b>12</b>
	Helix diameter (mm)	<b>1000</b>
	Number of helices	<b>1</b> -2-3
	Thickness of the shaft (mm)	<b>10</b>
	Thickness of the helix (mm)	<b>25</b>
	Vertical distance between helices (m)	1-1.5-2.25-3
	Pile spacing (m)	<b>2</b>
	Width of cap (m)	0-1-1.25- <b>1.5</b>



**Figure 2.** a) Geometry of the single-helix pile, b) Cross section of the helical pile

**TABLE 2.** Summary of the material properties used in the finite element modeling

Material	$\gamma$ (kN/m <sup>3</sup> )	E (MPa)	$\nu$	C' (kPa)	$\phi'$ (degree)	$\psi$ (degree)
Embankment	20	60	0.3	5	30	0
Soft clay	18.4	10	0.3	8	22	0
Pile	78.5	210000	0.2	-	-	-
Cap	24	35000	0.15	-	-	-

$\gamma$  = Unit weight, E = Young's modulus,  $\nu$  = Poisson's ratio, C' = Effective cohesion,  $\phi'$  = Effective friction angle,  $\psi$  = Dilation angle

### 3. VALIDATION

To validate the modeling, two studies were chosen. As the first case, the field study of TJ pile-supported embankment in China by Chen et al. (40) gives a precise description of the construction site, instrumentation, and embankment construction procedure. The cross-section of the instrumented embankment and soil profile is shown in Figure 3. The soil profile consists of a clayey soil of approximately 3m thickness underlain by a soft silty clay with a thickness of about 17m, with high water content, low permeability, and low shear strength, overlying the third layer, which is pebble. The groundwater level is at a depth of 0.5m. Figure 4 (a, b) shows a comparison between the settlement values measured in the field and the results of the numerical modeling at the soil surface and the pile cap. Comparisons of the stress at the soil surface and the pile cap are shown in Figure 5 (a, b), respectively.

The second study is based on the laboratory data in actual dimensions, related to the loading of a helical pile for the validation of numerical modeling. The helical pile modeling was validated using the data reported by Elsherbiny and El nagger (28) under compressive loading. Pile PA-1 tested in soft soil (located in northern

Alberta, Canada) was chosen for the validation. The helical pile at test site A had a cylindrical shaft with one helix affixed to it. Figure 6 shows the load-displacement curves of the helical pile for both FE modeling and field test data. The comparison of the results of full-scale compressive loading at site A with the numerical results in Figure 6 indicates that validation was accurately modeled because the load-displacement response of the numerical model is in good agreement with that of the full-scale test.

Table 3 provides the chosen parameters of the piled embankment and the helical pile validation and Table 4 summarizes the piles properties.

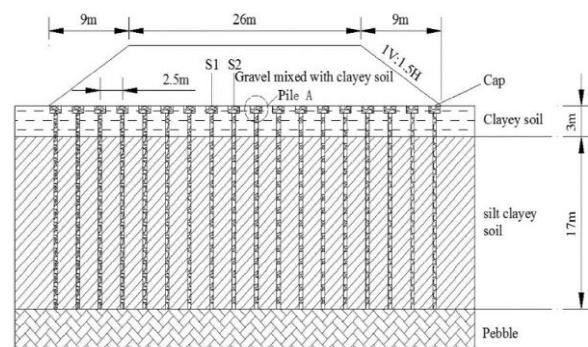


**Figure 3.** Cross-section of the test embankment of TJ Highway (Section G1)

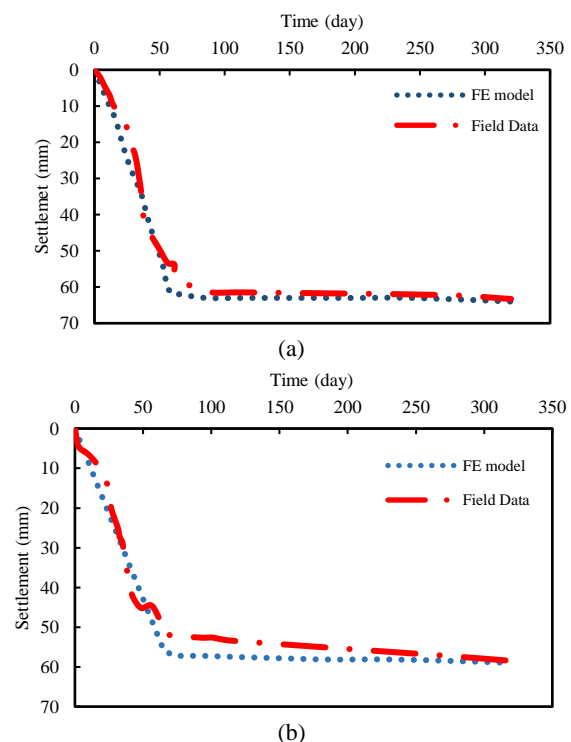


**Figure 4.** Measurements versus computed FE results: (a) settlement of the surface soil ; (b) settlement of the pile cap

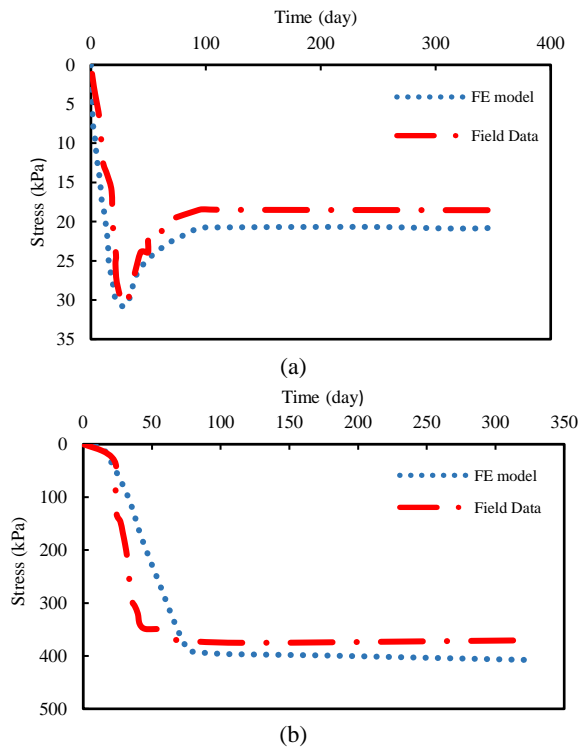


**Figure 5.** Measurements versus computed FE results: (a) Vertical stress of the surface soil; (b) Vertical stress of the pile cap

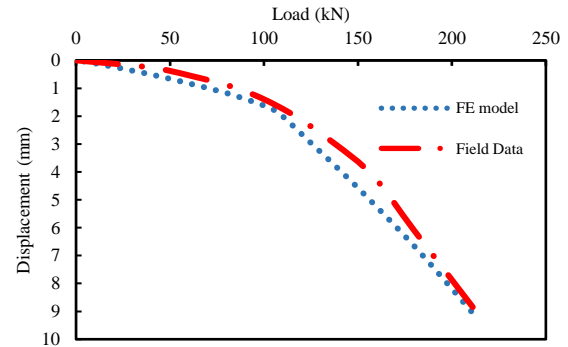


**Figure 6.** The displacement vs. load curves of the validation numerical model compared with the field compression test PA-1

## 4. RESULTS AND DISCUSSION

### 4. 1. Effect of the Size of Pile Caps

Four modes were developed to study the effect of the presence of a cap and its dimensions and evaluate its performance in helical pile-supported embankments. Figure 7 evaluates the load transfer mechanism with efficiency and arching parameters for different sizes of the pile caps. According to the results, the presence of caps and the rise in their size enhanced the load transfer mechanism in helical pile-supported embankments such that the pile

**TABLE 3.** Summary of the parameters used for model validation

Piled embankment (data from Chen et al. [41])						
Material	$\gamma$ (kN/m <sup>3</sup> )	E (MPa)	$\nu$	C' (kPa)	$\phi'$ (degree)	$e_0$
Embankment	21	15	0.30	0	32	-
ML	19.3	6.5	0.35	0	21	0.818
CL	16.7	2.4	0.30	0	24	1.286
GM	19.9	40	0.27	0	30	-
Pile and Cap	24.5	35000	0.15	-	-	-
Soil parameters (data from Elsherbiny and El Naggar . [29])						
Depth (m)	$\gamma$ (kN/m <sup>3</sup> )	E (MPa)	$\nu$	$\phi'$ (degree)	$\psi$ (degree)	-
0-5	20	50	0.3	24	10	-
5-9	20	50	0.3	21	10	-

$\gamma$  = Unit weight, E = Young's modulus,  $\nu$  = Poisson's ratio, C = Effective cohesion,  $\phi'$  = Effective friction Angle,  $\psi$  = Dilation Angle,  $e_0$  = Void ratio

**TABLE 4.** Pile parameters used in validation models

Parameter	Helical pile (Elsherbiny and El Naggar (28))	Piled embankment (Chen et al. (40))
Shaft diameter (mm)	273	400
Length of pile (m)	5.5	20
Helix diameter (mm)	610	-
Number of helix	1	-
Thickness of the shaft (mm)	9.3	-
Thickness of the helix (mm)	20	-

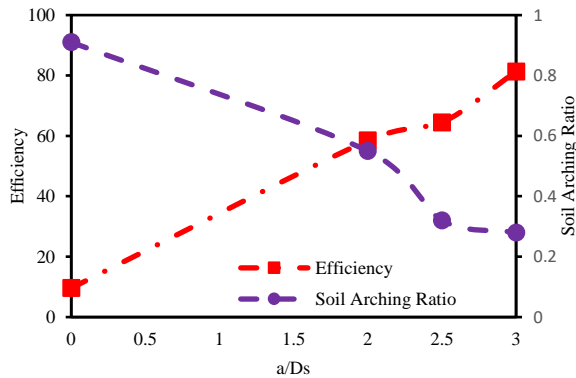


**Figure 7.** The load transfer mechanism for different  $a/D_s$  ratios of helical pile cap ( $a$ = cap width,  $D_s$ = shaft diameter)

cap efficiency and arching ratio improved to 88% and 69%, respectively, for a cap with a width of 1.5m compared to the mode with no cap.

As shown in Figure 7, the rise in the pile cap dimensions improved the load transfer mechanism in pile-supported embankments, resulting in the greater participation of the piles in sustaining the ultimate load of the embankment. Figure 8 depicts the axial force distribution along embedment depth for a helical pile with one helix connected to the pile shaft (the closest pile to the center of the embankment). Increasing the cap width enhanced the bearing capacity of the pile shaft and due to the higher load-bearing of the shaft, the load-bearing contribution of the helix connected to the shaft decreased. The load-bearing share of the helix, being 23.3% of the total load-bearing when no cap was used, reduced to 14.1% when a cap with a width of 1.5m was used (Table 5). Figure 9 indicates that the load-bearing contribution of the helix connected to the helical pile

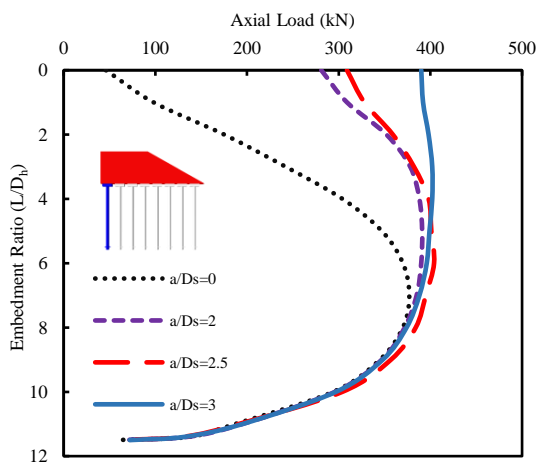


**Figure 8.** The axial load distribution along the embedment depth of piles for different  $a/D_s$  ratios of helical pile cap ( $a$ = cap width,  $D_s$ = shaft diameter)

**TABLE 5.** The load-bearing contribution of the helix and pile shaft for different ratios of cap width to helical pile shaft diameter,  $a/D_s$ .

Width Cap Ratio ( $a/D_s$ )	Portion of pile shaft (%)	Portion of helix (%)
0	76.7	23.3
2	82.3	17.7
2.5	83.4	16.6
3	85.9	14.1

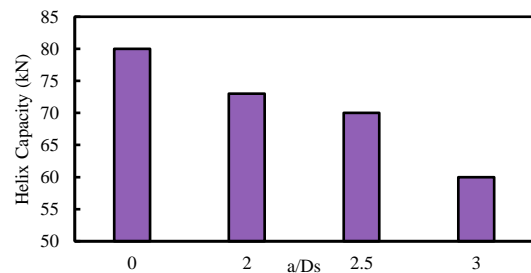


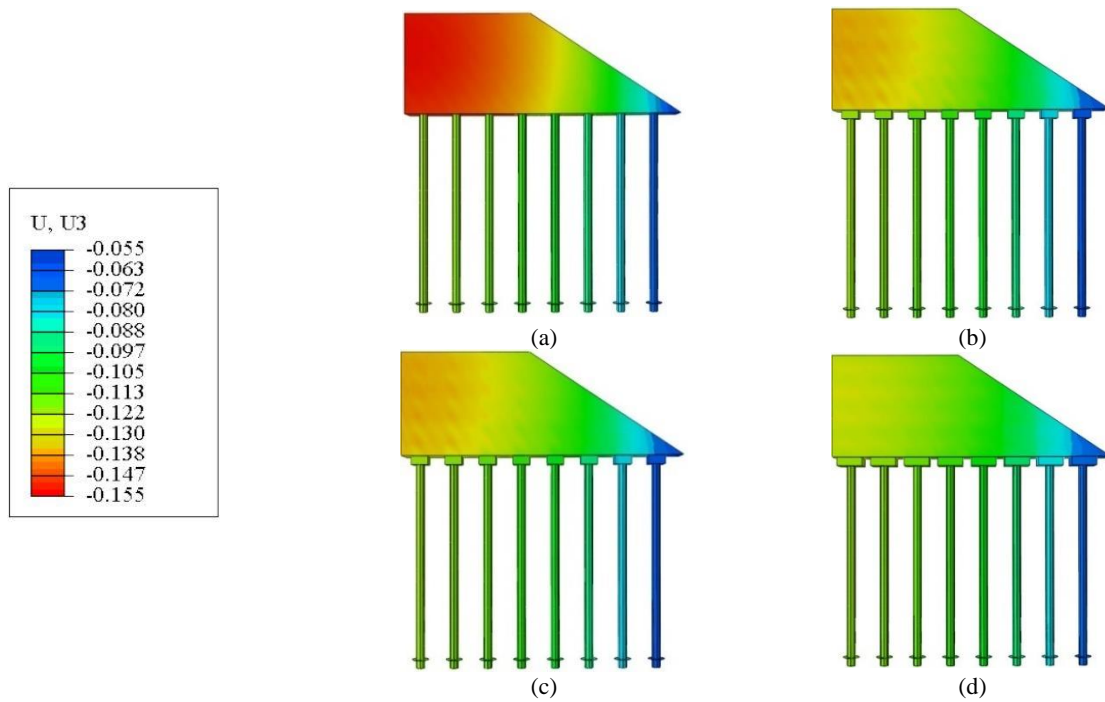
**Figure 9.** The load-bearing capacity of the helices connected to the pile shaft for different ratios of helical pile cap ( $a$ = cap width,  $D_s$ = shaft diameter)

shaft has increased with the reduction in the cap dimensions.

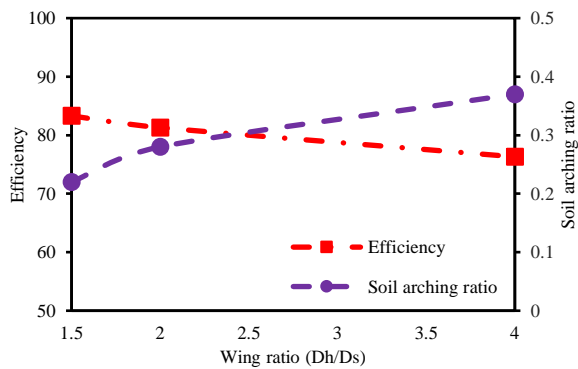
Besides enhancing the load-transfer mechanism in helical pile-supported embankments, adding caps to piles has reduced the vertical settlements of the embankment constructed on the soft soil. Figure 10 depicts the vertical displacement contours of the granular embankment, at the depth of 6 m of the embankment. The use of a cap with a width of 1 m reduced the vertical settlement of the embankment by 9.7% compared to the model with no cap on the pile. By increasing the cap width to 1.25m and 1.5m, the settlement reduced to 3.6% and 4%, respectively.

**4. 2. Effect of the Wing Ratio**

The wing ratio is defined as the ratio of the helix diameter to the shaft diameter. In this parametric study, the fixed value of 1 m was considered for the helix diameter, while the pile shaft diameter varied. Figure 10 illustrates the variations in the efficiency and arching ratio against the shaft diameter. As shown in Figure 11, increasing the wing ratio decreases the load-bearing area and parameters of the load transfer mechanism. For example, increasing the wing ratio from 2 to 4 results in the growth of the arching ratio by 24% but reversely reduces the pile efficiency by 6.2%. On the other hand, by decreasing the wing ratio, the load-bearing area of the pile has increased, resulting in greater loads imposed on piles and improving the load transfer mechanisms. Reducing the wing ratio from 2 to 1.5 has

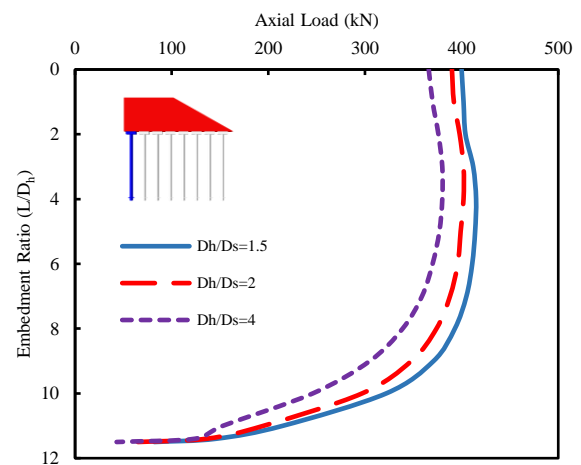


**Figure 10.** The vertical deformation contours of the granular embankment for different dimensions of the helical pile cap. a) without the cap, b) cap width = 1m, c) cap width = 1.25m, and d) cap width = 1.5m



**Figure 11.** The load transfer mechanism for different wing ratios of the helical pile ( $D_h$  = helix diameter,  $D_s$  = shaft diameter)

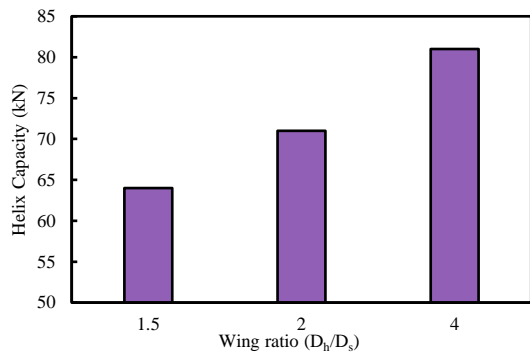
decreased the arching ratio by 24% while increasing the pile efficiency by 2.4%. The variations of axial load distribution along the embedment depth of the pile against wing ratio are plotted in Figure 12. With the reduction in the wing ratio (rise in the pile shaft diameter), the load-bearing area of the pile shaft has increased, causing to a higher axial force distribution along the pile length. Table 6 lists the load-bearing share of the pile shaft and helix. Based on the results presented in Figure 13, as the wing ratio decreases, the load-bearing area of the helix becomes smaller, leading to lower contribution against the imposed loads and less bearing capacity of the helix.



**Figure 12.** The axial load distribution along the embedment depth of piles for different wing ratios of the helical pile ( $D_h$  = helix diameter,  $D_s$  = shaft diameter)

**TABLE 6.** The load-bearing contribution of the helix and pile shaft for different wing ratios of helical pile

Wing Ratio ( $D_h/D_s$ )	Portion of pile shaft (%)	Portion of helix (%)
1.5	85.6	14.4
2	83.7	16.3
4	80.5	19.5



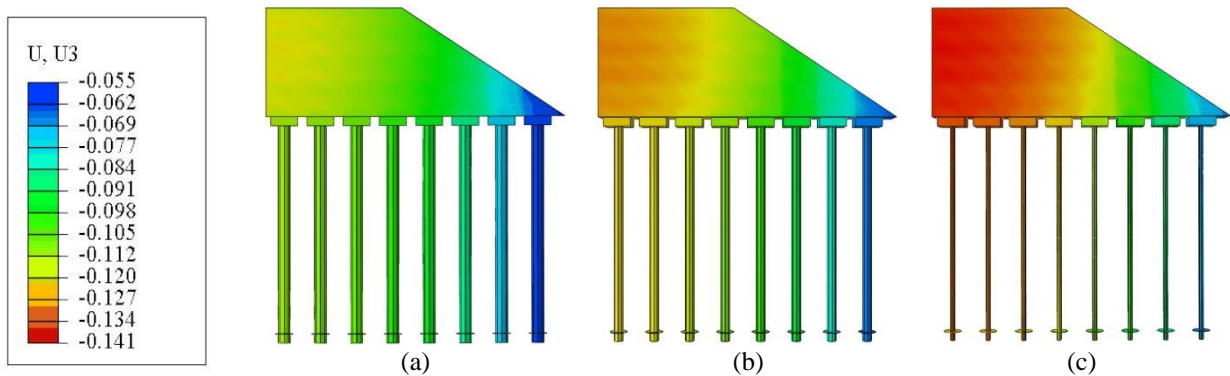
**Figure 13.** The load-bearing capacity of the helices connected to the pile shaft for different wing ratios of the helical pile

Figure 14 depicts the vertical displacement contours of the granular embankment against the wing ratio. The rise in the wing ratio means the reduction in shaft diameter, causing to reduction in soil-pile shaft resistance, and consequently, resulting in the rise in the

vertical displacements of the embankment, as can be seen in Figure 14. Vertical displacement has decreased by 6.6% and 8.1% with a reduction in the wing ratio from 2 to 1.5 and from 4 to 2, respectively.

**4. 3. Effect of the Spacing Ratio**

This section discusses effects of the the spacing between helices connected to a helical pile shaft, which is specified as the spacing ratio and defined as the ratio of the vertical distance between helices in the same pile to helix diameter. The 2- and 3-helix piles were modeled with spacing ratios of 1.5, 2.25, and 3. Figure 15 demonstrates the arching ratio and pile efficiency for different values of the spacing ratio. The results indicate that when the distance between the helices is 1.5 times the diameter of the helix, the helical pile shows cylindrical failure behavior, and the soil enclosed between the helices helps to improve the frictional resistance of the pile, so in this case, the maximum load is transferred to the piles as well as the load transfer mechanism increases. At the spacing ratio of 1.5, the 3-helix pile has reduced the arching ratio



**Figure 14.** The vertical deformation contours of the granular embankment for different wing ratios of the helical pile; a) wing ratio = 1.5, b) wing ratio = 2, and c) wing ratio = 4

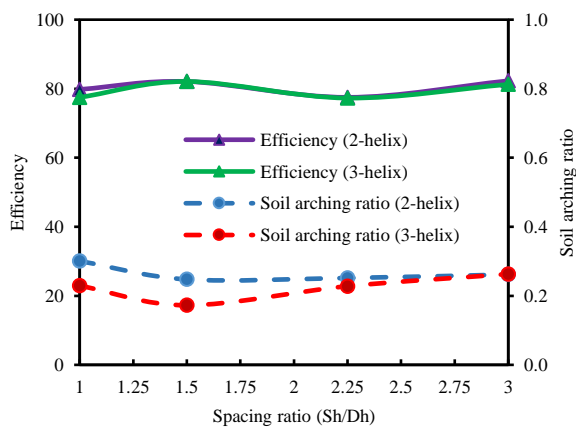


**Figure 15.** The load transfer mechanism for the different spacing ratios of the helical pile ( $S_h$  = vertical distance between helices ,  $D_h$ =helix diameter)

by 30% compared to the 2-helix one, while its efficiency has not changed. Figure 15 demonstrates the total load-bearing capacities of the helices at different spacing ratios for the 2- and 3-helix piles. The reduction in the spacing ratio of the helices is leading to higher bearing capacity. Moreover, in the 3-helix pile, the total bearing capacity of the helices was higher than that of the 2-helix pile due to the helices' greater contribution to the total load-bearing. Figure 16 shows the load-bearing capacity of the helices connected to the pile shaft for different spacing ratios of the helical pile.

The vertical settlement of the embankment does not vary significantly with the increase in the number of helices or changes in their spacing ratio. Figure 17 shows the vertical displacement contours of the granular embankment for the 3-helix pile at different spacing ratios. Similar to the 3-helix pile, the 2-helix pile shows

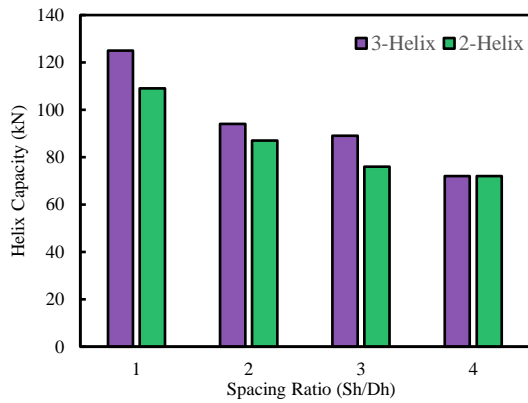


**Figure 16.** The load-bearing capacity of the helices connected to the pile shaft for different spacing ratios of the helical pile

no differences in vertical displacement at different spacing ratios. Accordingly, it can be concluded that adding helices to a helical pile does not remarkably affect the vertical displacements of a granular embankment. Table 7 lists the load-bearing contributions of the helices and pile shaft. According to the results, adding the third helix has reduced the load bearing of the upper helix and pile shaft. With increasing the spacing ratio of the helices, the pile had a separate load-bearing behavior resulting in a greater load-bearing contribution of the pile shaft. It can be concluded that regarding engineering uses and installation of helical piles, adding more than one helix to the pile shaft is not reasonable and does not significantly influence the vertical settlement of the pile-supported embankments. Thus, it is recommended to use helical piles with one helix connected to the shaft.

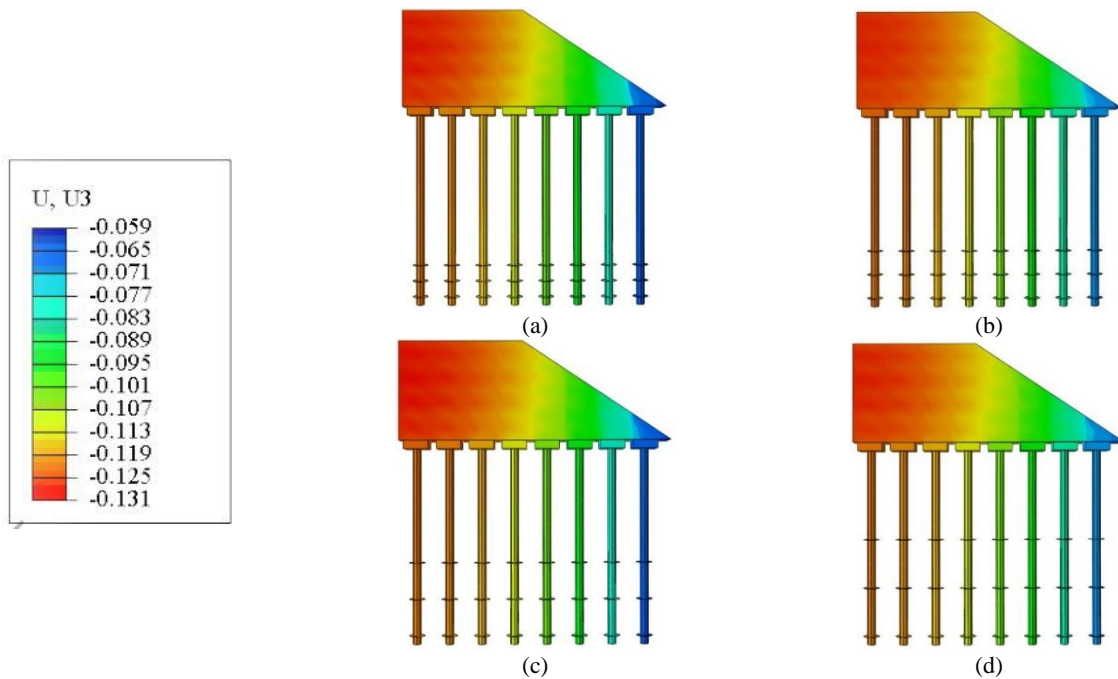


**Figure 17.** The vertical deformation contours of the granular embankment for different spacing ratios of the 3-helix piles. a) spacing ratio = 1, b) spacing ratio = 1.5, c) spacing ratio = 2.25, and d) spacing ratio = 3

**TABLE 7.** The load-bearing contribution of each helix and pile shaft for different spacing ratios of helical pile

No. Helix	Spacing ratio ( $S_h/D_h$ )	The portion of the pile shaft (%)	Portion of bottom helix (%)	Portion of Middle helix (%)	Portion of Top helix (%)
2	1	77.2	13.2	-	9.6
	1.5	81.1	13.1	-	5.9
	2.25	83.1	13.3	-	3.6
	3	84.1	12.8	-	3.1
3	1	73.9	12.7	9.2	4.2
	1.5	79.6	12.8	6.1	1.5
	2.25	80.8	11.9	6.5	0.8
	3	83.4	14	1.6	1

## 5. LIMITATIONS

(i) The current study deals with the use of cohesive-frictional materials possessing high frictional strength and coarse-grained soil for embankment fill which can largely remain in a relatively dry state. Therefore, the consolidation settlements are ignored in this study. However, consolidation can be a significant issue when dealing with saturated soft soils.

(ii) Considering the complexity of the problem investigated in this study and the difficulties in accurately determining the parameters for advanced soil models, the linearly elastic-perfectly plastic soil model with the Mohr-Coulomb strength criterion considering the dilation angle was used in this study.

(iii) The helix is idealized as a planner cylindrical disk. Therefore, modeling of the pile and surrounding soil can take advantage of the axisymmetric condition.

## 6. CONCLUSIONS

In the current study, the factors effective in the performance of helical pile-supported embankments were investigated in soft soils through FE modeling using ABAQUS software. The numerical models were validated using the field measurements on pile-supported embankments and helical pile loading in real dimensions. Afterward, a parametric study was performed to investigate the performance of helical pile-supported embankments. The following results are concluded based on the current study:

1. The results of the numerical modeling revealed that the performance of the helical piles in the pile-supported embankments depends on the cap dimensions. The vertical settlements could be reduced with the increase in the cap dimensions, and the load transfer mechanism could be improved due to the lower pressure on the soft soil surface and higher load distribution along the pile length. As a result, the load-bearing of the helices was decreased, and the pile shaft had a greater contribution to the load imposed on the pile.

2. The soil-pile interface showed a rise with the increase in the helical pile diameter, which led to the improved performance of the system and reduced settlements. Due to the greater contribution of the pile with the rise in the shaft diameter, the load transfer mechanism was improved. The evaluation of the load-bearing capacity of the pile revealed that with the rise in the pile diameter, the load-bearing capacity of the helices decreased, and a remarkable improvement occurred in the frictional capacity of the pile.

3. Evaluation of the results regarding the number and spacing of helices showed that adding helices can be ignored when controlling the vertical settlement of

granular embankments is a concern. Also, cylindrical shear failure occurred when the spacing of the helices was 1.5 times the helix diameter, which increased the pile bearing capacity and improved the load transfer mechanism. The pile with three helices connected to the shaft had a better performance than the one with two helices. Moreover, adding helices to the helical pile and reducing the spacing of the helices could cause a reduction in the load-bearing contribution of the pile shaft, and increase the load-bearing contribution of the helices.

4. The major load of the pile throughout the modeling was carried by the pile shaft, while the contribution of the helices to the ultimate load bearing was almost 20%, on average. Therefore, the design of helical piles for pile-supported embankments should focus on the pile shaft. Therefore, piles with more than 1 helix are not recommended in terms of pile installation and economic conditions.

## 7. REFERENCES

- Han J, Gabr M. Numerical analysis of geosynthetic-reinforced and pile-supported earth platforms over soft soil. *Journal of geotechnical and geoenvironmental engineering*. 2002;128(1):44-53. [https://doi.org/10.1061/\(ASCE\)10900241\(2002\)128:1\(44\)](https://doi.org/10.1061/(ASCE)10900241(2002)128:1(44))
- Chen R, Chen Y, Han J, Xu Z. A theoretical solution for pile-supported embankments on soft soils under one-dimensional compression. *Canadian Geotechnical Journal*. 2008;45(5):611-23. <https://doi.org/10.1139/t08-003>
- Brohi AS, Saand A, Sahito ZA. 3D Numerical Modeling of Pile embankment performance on Soft Soil. *International Journal*. 2021;9(6). <https://doi.org/10.30534/ijeter/2021/16962021>
- Zhang D, Zhang Y, Kim CW, Meng Y, Garg A, Garg A, et al. Effectiveness of CFG pile-slab structure on soft soil for supporting high-speed railway embankment. *Soils and Foundations*. 2018;58(6):1458-75. <https://doi.org/10.1016/j.sandf.2018.08.007>
- Ding X, Luan L, Liu H, Zheng C, Zhou H, Qin H. Performance of X-section cast-in-place concrete piles for highway constructions over soft clays. *Transportation Geotechnics*. 2020;22:100310. <https://doi.org/10.1016/j.trgeo.2019.100310>
- Briançon L, Simon B. Pile-supported embankment over soft soil for a high-speed line. *Geosynthetics International*. 2017;24(3):293-305. <https://doi.org/10.1680/jgein.17.00002>
- Xu C, Song S, Han J. Scaled model tests on influence factors of full geosynthetic-reinforced pile-supported embankments. *Geosynthetics International*. 2016;23(2):140-53. <https://doi.org/10.1680/jgein.15.00038>
- Fagundes DF, Almeida MS, Thorel L, Blanc M. Load transfer mechanism and deformation of reinforced piled embankments. *Geotextiles and Geomembranes*. 2017;45(2):1-10. <https://doi.org/10.1016/j.geotexmem.2016.11.002>
- Zhao M, Liu C, El-Korchi T, Song H, Tao M. Performance of geogrid-reinforced and PTC pile-supported embankment in a highway widening project over soft soils. *Journal of Geotechnical and Geoenvironmental Engineering*. 2019;145(11):06019014. [https://doi.org/10.1061/\(ASCE\)GT.1943-5606.0002157](https://doi.org/10.1061/(ASCE)GT.1943-5606.0002157)

10. Lee T, Lee S, Lee I-W, Jung Y-H. Quantitative performance evaluation of GRPE: a full-scale modeling approach. *Geosynthetics International*. 2020;27(3):342-7. <https://doi.org/10.1680/jgein.19.00017>
11. Bangia T, Raskar R. Cohesive methodology in construction of enclosure for 3.6 m devasthal optical telescope. *HighTech and Innovation Journal*. 2022;3(2):162-74. <https://doi.org/10.28991/HIJ-2022-03-02-05>
12. Lu W, Miao L, Wang F, Zhang J, Zhang Y, Wang H. A case study on geogrid-reinforced and pile-supported widened highway embankment. *Geosynthetics International*. 2020;27(3):261-74. <https://doi.org/10.1680/jgein.19.00024>
13. Wu P-C, Feng W-Q, Yin J-H. Numerical study of creep effects on settlements and load transfer mechanisms of soft soil improved by deep cement mixed soil columns under embankment load. *Geotextiles and Geomembranes*. 2020;48(3):331-48. <https://doi.org/10.1016/j.geotexmem.2019.12.005>
14. Phuthananon C, Jongpradist P, Jongpradist P, Dias D, Baroth J. Parametric analysis and optimization of T-shaped and conventional deep cement mixing column-supported embankments. *Computers and Geotechnics*. 2020;122:103555. <https://doi.org/10.1016/j.compgeo.2020.103555>
15. Bahrami M, Marandi S. Large-scale experimental study on collapsible soil improvement using encased stone columns. *International Journal of Engineering, Transactions B: Applications*, 2021;34(5):1145-55. <https://doi.org/10.5829/ije.2021.34.05b.08>
16. Pham TA. Design and analysis of geosynthetic-reinforced and floating column-supported embankments. *International Journal of Geotechnical Engineering*. 2022;16(10):1276-92. <https://doi.org/10.1080/19386362.2021.1997209>
17. Umravia N, Solanki CH. Numerical Analysis to Study Lateral Behavior of Cement Fly Ash Gravel Piles under the Soft Soil. *International Journal of Engineering, Transactions B: Applications*, 2022;35(11):2111-9. <https://doi.org/10.5829/ije.2022.35.11b.06>
18. Ye X, Wu J, Li G. Time-dependent field performance of PHC pile-cap-beam-supported embankment over soft marine clay. *Transportation Geotechnics*. 2021;26:100435. <https://doi.org/10.1016/j.trgeo.2020.100435>
19. Wu J, Ye X, Li J, Li G. Field and numerical studies on the performance of high embankment built on soft soil reinforced with PHC piles. *Computers and Geotechnics*. 2019;107:1-13. <https://doi.org/10.1016/j.compgeo.2018.11.019>
20. Ahmed D, bt Taib SNL, Ayadat T, Hasan A. Numerical analysis of the carrying capacity of a piled raft foundation in soft clayey soils. *Civil Engineering Journal*. 2022;8(04). <https://doi.org/10.28991/CEJ-2022-08-04-01>
21. Liu K-F, Feng W-Q, Cai Y-H, Xu H, Wu P-C. Physical model study of pile type effect on long-term settlement of geosynthetic-reinforced pile-supported embankment under traffic loading. *Transportation Geotechnics*. 2023;38:100923. <https://doi.org/10.1016/j.trgeo.2022.100923>
22. Lutenege AJ. Historical development of iron screw-pile foundations: 1836–1900. *The International Journal for the History of Engineering & Technology*. 2011;81(1):108-28. <https://doi.org/10.1179/175812109X12547332391989>
23. Sakr M. Performance of helical piles in oil sand. *Canadian Geotechnical Journal*. 2009;46(9):1046-61. <https://doi.org/10.1139/t09-044>
24. Spagnoli G, de Hollanda Cavalcanti Tsuha C. A review on the behavior of helical piles as a potential offshore foundation system. *Marine Georesources & Geotechnology*. 2020;38(9):1013-36. <https://doi.org/10.1080/1064119X.2020.1729905>
25. Elkasabgy M, El Naggar MH. Axial compressive response of large-capacity helical and driven steel piles in cohesive soil. *Canadian Geotechnical Journal*. 2015;52(2):224-43. <https://doi.org/10.1139/cgj-2012-0331>
26. Alwalan M, Alnuaim A. Axial Loading Effect on the Behavior of Large Helical Pile Groups in Sandy Soil. *Arabian Journal for Science and Engineering*. 2022;47(4):5017-31. <https://doi.org/10.1007/s13369-021-06422-9>
27. Nowkandeh MJ, Choobbasti AJ. Numerical study of single helical piles and helical pile groups under compressive loading in cohesive and cohesionless soils. *Bulletin of Engineering Geology and the Environment*. 2021;80:4001-23. <https://doi.org/10.1007/s10064-021-02158-w>
28. Elsherbiny ZH, El Naggar MH. Axial compressive capacity of helical piles from field tests and numerical study. *Canadian Geotechnical Journal*. 2013;50(12):1191-203. <https://doi.org/10.1139/cgj-2012-0487>
29. Terzaghi K. *Theoretical soil mechanics* 1943.
30. Hewlett W, Randolph M, editors. *Analysis of piled embankments*. International journal of rock mechanics and mining sciences and geomechanics abstracts; 1988: Elsevier Science.
31. Tang SK. *Arching in piled embankments* 1992.
32. Le Hello B, Villard P. Embankments reinforced by piles and geosynthetics—Numerical and experimental studies dealing with the transfer of load on the soil embankment. *Engineering geology*. 2009;106(1-2):78-91. <https://doi.org/10.1016/j.enggeo.2009.03.001>
33. Bhasi A, Rajagopal K. Numerical study of basal reinforced embankments supported on floating/end bearing piles considering pile–soil interaction. *Geotextiles and Geomembranes*. 2015;43(6):524-36. <https://doi.org/10.1016/j.geotexmem.2015.05.003>
34. Ariyaratne P, Liyanapathirana D. Review of existing design methods for geosynthetic-reinforced pile-supported embankments. *Soils and Foundations*. 2015;55(1):17-34. <https://doi.org/10.1016/j.sandf.2014.12.002>
35. Meena NK, Nimbalkar S, Fatahi B, Yang G. Effects of soil arching on behavior of pile-supported railway embankment: 2D FEM approach. *Computers and Geotechnics*. 2020;123:103601. <https://doi.org/10.1016/j.compgeo.2020.103601>
36. Pham TA, Dias D. 3D numerical study of the performance of geosynthetic-reinforced and pile-supported embankments. *Soils and Foundations*. 2021;61(5):1319-42. <https://doi.org/10.1016/j.sandf.2021.07.002>
37. Al-Tememy M, Al-Neami M, Asswad M. Finite element analysis on behavior of single battered pile in sandy soil under pullout loading. *International Journal of Engineering, Transactions C: Aspects*. 2022;35(6):1127-34. <https://doi.org/10.5829/ije.2022.35.06c.04>
38. Khanmohammadi M, Fakharian K. Evaluation of performance of piled-raft foundations on soft clay: A case study. *Geomechanics and Engineering*. 2018;14(1):43-50. <https://doi.org/10.12989/gae.2018.14.1.043>
39. Shawky O, Altahrany AI, Elmeligy M. Study of lateral load influence on behaviour of negative skin friction on circular and square piles. *Civil Engineering Journal*. 2022;8(10):2125-53. <https://doi.org/10.28991/CEJ-2022-08-10-08>
40. Chen R, Xu Z, Chen Y, Ling D, Zhu B. Field tests on pile-supported embankments over soft ground. *Journal of Geotechnical and Geoenvironmental Engineering*. 2010;136(6):777-85. [https://doi.org/10.1061/\(ASCE\)GT.1943-5606.0000295](https://doi.org/10.1061/(ASCE)GT.1943-5606.0000295)

**COPYRIGHTS**

©2024 The author(s). This is an open access article distributed under the terms of the Creative Commons Attribution (CC BY 4.0), which permits unrestricted use, distribution, and reproduction in any medium, as long as the original authors and source are cited. No permission is required from the authors or the publishers.

**Persian Abstract****چکیده**

جستجو برای راه‌حل‌های عملی و اقتصادی برای افزایش پایداری و کاهش نشست‌های کلی و تفاضلی خاکریزها ضروری است. امروزه استفاده از المان‌های سازه‌ای مانند شمع‌ها، به عنوان یک راه‌حل مؤثر در بهبود عملکرد کلی یک سیستم خاکریزی در نظر گرفته می‌شوند. در سال‌های اخیر استفاده از شمع‌های ماریپچ به دلیل عملکرد مناسب تحت بار فشاری و کششی، نصب سریع و آسان شمع و حذف مشکلات بتن‌ریزی مورد توجه قرار گرفته است. هدف در این مقاله بررسی و شناخت رفتار خاکریزهای متکی بر شمع‌های ماریپچ است که به‌همین منظور یک مطالعه عددی سه‌بعدی با استفاده از نرم‌افزار آباکوس توسعه داده شد. صحت‌سنجی با توجه به گزارش‌های میدانی و آزمایشگاهی گزارش شده توسط دیگر محققان انجام شد و در ادامه مدل‌های عددی سه‌بعدی به‌منظور بررسی اثرات کلاهک شمع، نسبت قطر پره به قطر شفت، تعداد پره‌ها و فاصله بهینه بین پره‌ها توسعه داده شد. نتایج نشان می‌دهد افزایش پره‌ها و تغییر فاصله بین آن‌ها تأثیری بر میزان کنترل نشست نخواهد داشت. همچنین پارامترهای مکانیزم انتقال بار با افزایش ابعاد کلاهک و قطر شفت شمع ارتباط مستقیم دارد. اضافه کردن پره به شمع ظرفیت باربری شمع را افزایش می‌دهد که در نتیجه باعث می‌شود پارامترهای مکانیزم انتقال بار بهبود یابد، به‌طوری‌که در شمع ماریپچ با ۳ پره نسبت قوس زدگی تا ۴۰ درصد نسبت با شمعی با ۱ پره کاهش می‌یابد. همچنین نتایج نشان می‌دهد به‌طور میانگین ۸۰ درصد سهم بار وارد بر شمع را شفت تحمل می‌کند و پره تأثیری کمتری بر عملکرد خاکریزهای متکی بر شمع خواهد داشت.



## Mathematical Model for Estimation of Return to Scale in Four-Level Green Supply Chain by using Data Envelopment Analysis

R. Sharafeddin<sup>a</sup>, A. Gholam Abri<sup>\*b</sup>, M. Fallah<sup>c</sup>, F. Hossein Zadeh Lotfi<sup>d</sup>

<sup>a</sup> Department of Industrial Engineering, Roudehen branch, Islamic Azad University, Roudehen, Iran

<sup>b</sup> Department of Mathematics, Firoozkooh Branch, Islamic Azad University, Firoozkooh, Iran

<sup>c</sup> Department of Industrial Engineering, Central Tehran Branch, Islamic Azad University, Tehran, Iran

<sup>d</sup> Department of Mathematics, Science and Research Branch, Islamic Azad University, Tehran, Iran

### PAPER INFO

#### Paper history:

Received 20 October 2023

Received in revised 30 November 2023

Accepted 12 December 2023

#### Keywords:

Data Envelopment Analysis

Return to Scale

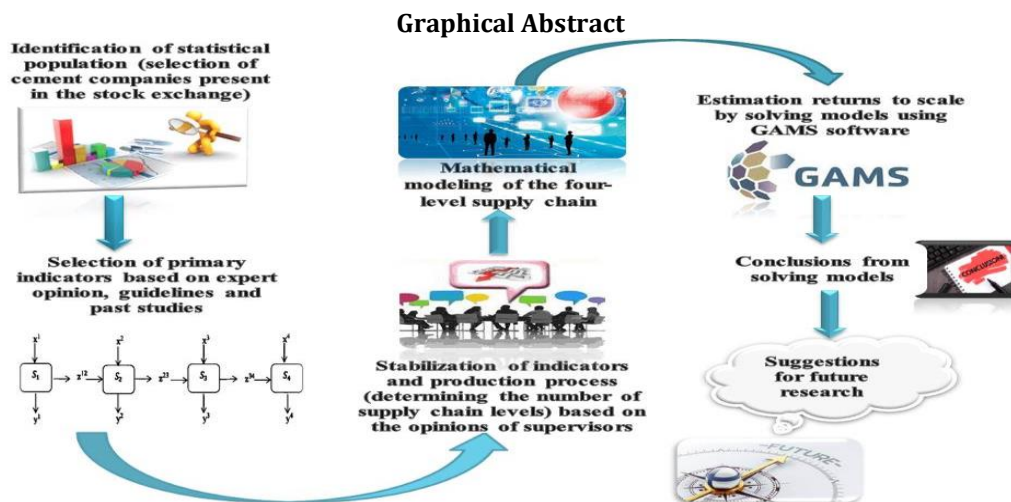
Four-level Green Supply Chain

Cement Companies

### ABSTRACT

Today, focusing on gaining a competitive edge in the global business market lies in enhancing supply chain performance. This study endeavors to examine the attainment of Returns To Scale (RTS) within a four-level green supply chain framework through the application of Data Envelopment Analysis (DEA). To achieve this objective, the Banker, Charnes, and Cooper (BCC) multiplicative model are employed to determine the return to scale at each level within the complete supply chain, ultimately culminating in estimating the overall return to scale for the entire supply chain. The statistical population for this applied research, aligned with its objectives, comprises 42 cement companies. The assessment of returns to scale in these companies, featuring a four-level chain encompassing suppliers, manufacturers, distributors, and customers, is measured. The outcomes of the model reveal that return to scale remains constant in 28 companies, exhibits a decreasing trend in 14 companies, and conversely demonstrates an increasing trajectory in 2 companies within the supplying sector, one company in manufacturing, and 14 companies in distribution. The findings underscore that an increasing return to scale renders the expansion of Decision-Making Units (DMUs) economically viable. Conversely, a diminishing return to scale suggests a rational limitation of DMUs.

doi: 10.5829/ije.2024.37.04.a.04



\* Corresponding Author Email: [amirgholamabri@gmail.com](mailto:amirgholamabri@gmail.com) (A. Gholam Abri)

**NOMENCLATURE**

$T_v$	Production possibility set	$X_{ij}^1$	Primary inputs of supply chain
$X_j$	Inputs of decision-making unit j (DMU <sub>j</sub> )	$Y_{rj}^1$	First level outputs
$Y_j$	Outputs of decision-making unit j (DMU <sub>j</sub> )	$Z_{lj}^{12}$	Intermediate data (1 <sup>st</sup> level output and 2 <sup>nd</sup> level input)
$\lambda_j$	Decision variables of decision-making unit j (DMU <sub>j</sub> )	$X_{ij}^2$	2 <sup>nd</sup> level independent inputs
$\theta$	Efficiency score of decision-making unit j (DMU <sub>j</sub> )	$Y_{rj}^2$	2 <sup>nd</sup> level outputs
$Z_{\delta}^+$	Right-hand neighborhood of the unit under evaluation (DMU <sub>o</sub> )	$Z_{lj}^{23}$	Intermediate data (2 <sup>nd</sup> level output and 3 <sup>rd</sup> level input)
$Z_{\delta}^-$	Left- hand neighborhood of the unit under evaluation (DMU <sub>o</sub> )	$X_{ij}^3$	3 <sup>rd</sup> level Independent inputs
$v$	Weights of the input data for decision-making unit j (DMU <sub>j</sub> )	$Y_{rj}^3$	Third level output
$u$	Weights of the output data for decision-making unit j (DMU <sub>j</sub> )	$Z_{lj}^{34}$	Intermediate data (3 <sup>rd</sup> level output and 4 <sup>th</sup> level input)
$w$	Weights of the intermediate data for decision-making unit j (DMU <sub>j</sub> )	$X_{ij}^4$	4 <sup>th</sup> level independent Inputs
$E$	Efficiency of supply chain levels	$Y_{rj}^4$	Final outputs
$u_o^*$	Optimal solution for return to scale in the supply chain		

**1. INTRODUCTION**

In the contemporary competitive market landscape, all enterprises, encompassing both manufacturing and service organizations, find it imperative to measure and evaluate the performance of their supply chain operations. This undertaking is essential for fostering productivity, ensuring survival, and achieving sustainable longevity.

The objective of each supply chain is to deliver a high-quality product to the end customer at minimum cost and within the shortest timeframe while concurrently adding value to all facets of the production process. In recent years, the concept of productivity has assumed a pivotal role in the ideologies and perspectives of various companies and organizations. Concurrently, researchers across diverse disciplines have increasingly employed the supply chain framework. A complete supply chain comprises four integral components: the supplier, manufacturer, distributor, and customer. It is crucial to note that the measurement and evaluation of optimal supply chain performance must be tailored to consider the unique characteristics of the chain networks and their interdependencies. Generally, assessing larger and more intricate supply chains becomes progressively more intricate and challenging.

Within the spectrum of evaluation methodologies, DEA emerges as a fitting approach for gauging the efficiency and performance of DMUs. Through the formulation of diverse models, this non-parametric method adeptly assesses DMUs that yield multiple outputs while consuming multiple inputs. DEA holds considerable significance within the literature on supply chain management.

The classical DEA methods, as delineated by Charnes et al. (1); lack of a theoretical framework for comprehending the internal operations of DMUs, treating them as a black box. These methods confine calculations to initial inputs and ultimate outputs, neglecting internal processes in their entirety.

Hence, to address this issue, several models, such as network DEA, have been introduced. The configuration of the supply chain stands out as a critical and pragmatic consideration within the context of network DEA. Methodical coordination of raw material procurement, the conception and manufacturing of suitable products, efficient distribution and transportation, and ultimately, the provision of services and customer satisfaction all hold significant importance in supply chain management. In the realm of network DEA, the emphasis extends to intermediate products and internal communications of DMUs, with performance evaluation incorporating a comprehensive examination of the internal components of a unit.

DEA serves as a tool for assessing the performance of DMUs. Within this framework, the evaluation of the return to scale for DMUs assumes paramount significance. The return to scale, in the context of DEA, holds economic importance as it signifies the maximum rate of output increase per unit increase in input. An essential consideration is that the diagnosis of the return to scale yields valuable insights into the developmental trajectory of DMUs. In economics, the concept of return to scale, whether ascending, descending, or constant, is defined as follows:

1. Ascending Return to scale occurs when, with an increase in inputs, outputs increase more than the input ratio, indicating that the expansion of DMUs is cost-effective.

2. Descending return to scale occurs when, with an increase in inputs, outputs grow proportionally less, indicating that limiting DMUs is cost-effective.

3. Constant return to scale occurs when, with an increase in inputs, the outputs also increase in the same proportion to the inputs. This implies that by expanding or limiting DMUs, we neither gain nor lose efficiency.

In this investigation, the researchers endeavor to ascertain the return to scale within a complete supply chain context, incorporating both independent and dependent inputs and outputs, utilizing the DEA method.

A seminal study addressing network structure and supply chain, dating back approximately 23 years, was introduced by Fare and Grosskopf (2, 3). Their approach to the overarching network structure involved initially establishing a Production Possibility Set (PPS) grounded in fundamental standard principles within a variable return-to-scale scenario. Subsequently, they constructed a production feasibility set within the supply chain by amalgamating the production feasibility sets of its internal components. Nevertheless, to gauge the efficacy of a supply chain, it is imperative to consider both the network properties inherent to the chain and the interrelationships among the "supplier of materials and components," "manufacturer," "distributor," and "end customer. This consideration has been prompted by Saranga and Moser (4), also by Chen and Yan (5), to present diverse models accommodating various supply chain structures. For instance, Chen and Yan (5) have delineated three network DEA models corresponding to centralized, decentralized, and hybrid organizational mechanisms for supply chain evaluation. Tavana et al. (6), introducing a network model founded on the Network Epsilon-Based Measure (NEBM), have investigated supply chain performance, simultaneously analyzing changes in inputs and outputs, both radially and non-radially within the network. In the realm of Green Supply Chain Management, Mirhedayatian et al. (7) have positioned it as a method to enhance environmental performance, asserting that companies, influenced by stakeholders, pressures, and regulations, must enhance the performance of Green Supply Chain Management (GSCM). Shafiee et al. (8), after an extensive examination of various tools for evaluating supply chain performance, have proposed a novel approach based on network DEA and the Balanced Score card (BSC) method. They have, in essence, furnished a comprehensive framework for supply chain performance evaluation through the amalgamation of BSC and DEA models. Grigoroudis et al. (9), in their work titled "Recursive Algorithm, a DEA-Based Recursive Algorithm for Optimal Design of Biomass Supply Chain Networks," have introduced an alternative method for designing supply chain networks. Khodakarami et al. (10) have conducted an evaluation of 27 Iranian companies in the sustainability realm of supply chain management, employing a two-level model. Tajbakhsh and Hassini (11) have proposed a methodology for assessing the sustainability of supply chain networks, with a sustainability approach aiming to harmonize economic, environmental, and social considerations. Tavana et al. (12) have suggested a 2-level DEA method to appraise the performance of a 3-level supply chain, encompassing the supplier, manufacturer, and distributor. This proposed model facilitates a comprehensive analysis of multi-level supply chains. Yousefi et al. (13), in their study, have introduced a

combined model of DEA and Goal Programming within a network structure to offer improvement solutions and rank units within the supply chain. Fathi and Farzipoor Saen (14) have emphasized the complexity of evaluating sustainable supply chains and articulated the use of a realistic and practical model for this purpose. This paper proposes a novel directional network DEA model for the inaugural evaluation of the stability of distribution supply chains. In this scholarly work, Darvish Motevalli et al. (15) have introduced a novel model designed to assess the efficiency of extant cement companies employing a network structure. The findings demonstrate that this innovative model is proficient in evaluating the performance of factories characterized by a network structure incorporating diverse indicators. Beyond the conventional utilization of financial and technical indicators, the model accounts for undesirable outcomes and sustainability criteria within the supply network. Simultaneously, the authors have incorporated the decision-makers perspectives on the relative importance of specific indicators, acknowledging the weighted constraints as a means to align the efficiency assessment with actual values. The examination of the computation of efficiency within the context of a green supply chain is an ongoing process. Tavassoli and Farzipoor Saen (16), in their scholarly work, have underscored that, in numerous real-life scenarios, not all inputs or outputs can be precisely determined, with some potentially being contingent or accidental. Torabi et al. (17), in their publication, introduced a novel two-stage green supply chain network. Primarily, they present an innovative multi-objective model addressing a two-level green supply chain problem. Given the intricacy of this model, a novel multi-objective interior search algorithm (MOISA) is employed. The results illustrate that the proposed algorithm MOISA yields superior Pareto solutions, affirming the efficacy of the algorithm in a majority of cases. Meanwhile, the objective of Asadpour et al. (18) in this study was to formulate a green Blood Supply Chain (BSC) network, considering expiration dates and backup facilities. The proposed model takes the form of a bi-objective Mixed Integer Programming (MIP) structure. The two primary objectives are to minimize the overall cost and mitigate the adverse environmental impacts associated with shipping between facilities and waste generation within the network. Fathollahi-Fard et al. (19) have introduced two hybrid meta-heuristic algorithms to address a dual-channel closed-loop supply chain network design problem within the tire industry under conditions of uncertainty. This study represents a pioneering effort by proposing a dual-channel, multi-product, multi-period, multi-echelon closed-loop Supply Chain Network Design (SCND) tailored to the uncertainties prevalent in the tire industry. To contend with the uncertain parameters intrinsic to the problem, such as prices and demand, a fuzzy approach,

specifically Jimenez's method, is employed. Another notable contribution of this work lies in the introduction of two innovative hybrid meta-heuristic algorithms featuring novel procedures. The integration of two contemporary nature-inspired algorithms, namely the red deer algorithm (RDA) and the whale optimization algorithm (WOA), with the genetic algorithm (GA) and simulated annealing (SA), serves to enhance the diversification and intensification phases respectively. Moosavi and Seifbarghy (20) presented a new mathematical model recognizing the significance of supply chain and environmental concerns. The model addresses a green closed-loop supply chain network with the primary objectives of maximizing profits, job creation, and reliability. The practical application of the model to a real case study within the Iranian engine oil industry demonstrates the efficacy of the derived solutions for this network. In this study, Sahraeian et al. (21) emphasize the critical significance of designing an efficient and reliable cold supply chain for the benefit of the company, suppliers, customers, and society. The research delves into all facets of the cost of quality within the design of a cold supply chain, encompassing considerations such as the cost of quality associated with suppliers and the cost of distribution service quality. Notably, the study takes a holistic approach by simultaneously evaluating the quality of suppliers, manufacturers, and distributors across the entirety of the supply chain. To address this, the problem is formally expressed as a mathematical model, accommodating multi-item and multi-period scenarios while considering two distinct objective functions. In this article, Gholizadeh et al. (22) highlight the significant impact of an electrical discharge machine (EDM) on production management. The study delves into the investigation of EDM machining parameters and their influence on the volumetric flow rate, electrode corrosion percentage, and surface roughness. These parameters play a crucial role in determining the quality of the final product, thereby enhancing customer satisfaction and increasing the company's market share. Given the dynamic nature of machine parameters and the variations in production environments, the use of an uncertain model becomes imperative. To address the machining data under uncertainty, the study introduces a mathematical modeling approach based on the fuzzy possibility regression integrated (FPRI) model. Considering the uncertainty and unclear distribution of results and numbers obtained from the neural network, a robust data envelopment analysis approach (RDEA) is applied to identify the optimal tuning level of the parameters. The findings substantiate the accuracy and reliability of the proposed method for predicting and optimizing EDM parameters. In this study, Moosavi et al. (23) present a comprehensive set of contemporary bibliometric, network, and thematic analyses aimed at discerning

influential contributors, principal research streams, and strategies for disruption management concerning supply chain (SC) performance within the context of the COVID-19 pandemic. The analyses conducted unveil resilience and sustainability as the predominant SC topics. Additionally, the primary research themes identified are centered around food, health-related supply chains, and technology-aided tools such as artificial intelligence (AI), the Internet of Things (IoT), and blockchains.

In this article authored by Berlin et al. (24), the discussion revolves around the configuration of closed-loop supply chains (CLSCs) for original equipment manufacturers (OEMs) to recover and remarket products, representing a pivotal avenue in the transition towards the circular economy (CE). Through a systematic literature review spanning from 2007 to 2021, this paper contributes to the literature by delineating the characteristics of open-loop supply chains (OLSC), providing empirical illustrations, and constructing a conceptual framework for the open- and closed-loop supply chain continuum. In this scholarly article, Haghshenas et al. (25) assert that the primary aim of supply chain design is the enhancement of profitability. Consequently, they introduced a cutting-edge model for a three-echelon closed-loop supply chain comprising the manufacturer, retailer, and collection centers. Notably, this model pioneers a distinct and autonomous channel dedicated to the sale of Reman products strategically aimed at augmenting manufacturer profitability. The model also incorporates considerations for the location, inventory, and pricing of the product, contributing to a comprehensive approach.

In this research, Asghari et al. (26) focused on pricing and advertising decisions within a closed-loop supply chain network. While pricing decisions have been extensively studied in this context, advertising decisions have received comparatively little attention. It is widely acknowledged that advertising plays a significant role in influencing customer behavior regarding the return of end-of-life products in a closed-loop supply chain. The primary novelty of this paper lies in the development of a new optimization model that incorporates both pricing and advertising decisions within a direct-sales closed-loop supply chain.

The study conducted by Simonetto et al. (27) directs its attention to the analysis of the benefits that Industry 4.0 technologies can offer in terms of mitigating risks in Closed Loop Supply Chains (CLSCs), specifically focusing on operational risks. Through two systematic literature reviews, the paper identifies the primary operational risks associated with CLSC activities and elucidates the impact of Industry 4.0 technologies on mitigating these identified risks. To summarize the reviews and support future managerial initiatives in the CLSC domain, the paper proposes a conceptual

framework and a new cross-sectional matrix. The conclusion of the paper outlines identified open research opportunities.

Technical analysis indicators serve as widely used tools in financial markets, aiding investors in discerning buy and sell signals with a margin of error. The primary objective of this study is to develop novel and practical methods for identifying false signals emanating from technical analysis indicators within the precious metals market. As articulated by Fathollahi-Fard and Soleimani (28) in this article, the key innovation of this research lies in proposing hybrid neural network-based metaheuristic algorithms for accurate analysis while enhancing the performance of signals derived from technical analysis indicators. The ultimate finding underscores that the suggested neural network-based metaheuristics can function as valuable decision-support tools for investors, addressing and managing the significant uncertainties inherent in financial and precious metals markets.

In their paper, Ali et al. (29) assert that closed-loop supply chain (CLSC) networks offer a viable solution for effective waste management by facilitating the recycling, reassembly, and reuse of waste products. They tackle these challenges by presenting a comprehensive CLSC network that optimizes environmental, economic, and social footprints through a multi-objective optimization approach. To address the proposed model's scenario-based stochastic nature, they transform the multi-objective formulation into a single-objective model using a weighted sum method, incorporating a set of problem-specific heuristics. Additionally, they leverage Lagrangian relaxation theory to formulate various problem reformulations, aiming to achieve an optimal lower bound for the CLSC problem. This is complemented by a neighborhood-based algorithm designed to identify a feasible upper bound.

As highlighted earlier, the assessment of green supply chain efficiency has been explored in various scenarios; however, there has been a relatively limited emphasis on estimating the return to scale within green supply chains.

In this context, a seminal work by Banker et al. (30) has introduced a significant approach, emphasizing that extending the measurement of return to scale from a single number to an interval could broaden its applicability to Data Envelopment Analysis (DEA) domains with multiple inputs and outputs. They delineate an optimal boundary consisting of three segments representing increasing, constant, and decreasing returns to scale, respectively. The paper establishes a precise framework facilitating the identification of several optimal solutions.

Gholam Abri (31) has contributed a paper addressing the determination of "stability radius." A noteworthy aspect of this work is the introduction of a novel method for calculating the 'stability radius,' wherein variations in data neither alter the class of efficiency units nor the class

of return to scale. The method's value lies in its capacity to discuss input and output changes through various strategies, subsequently fostering the enhancement of evaluated Decision Making Unit (DMU) performance via diverse options.

Zhang and Yang (32) have presented a paper on the calculation of network return to scale in two stages. They expound on network DEA as a non-parametric method for determining the return to scale of Decision-Making Units (DMUs) with multi-stage structures, examining a two-stage production process using network DEA techniques.

Alirezaee et al. (33), in their study, address a critical issue in developing a DEA model, specifically the identification of relevant returns to scale for the data. They introduced a purposeful, non-statistical method named the Angles method to identify technological return to scale in the data.

In a comprehensive investigation, Wang et al. (34) delve into the performance of energy in terms of CO<sub>2</sub> pollution and emission, employing variable return to scale and a non-radial model. Three main conclusions emerge:

- 1) Performance varies across the economic levels of the members,
- 2) Development of the members holds potential for further reduction in energy consumption and CO<sub>2</sub> emissions and
- 3) Reduction in energy and CO<sub>2</sub> emission intensity, coupled with the contribution of industrial-added value to total GDP, can effectively enhance energy performance and reduce CO<sub>2</sub> emissions.

This paper examines the use of DEA to determine the return to scale in the structure of green supply chains and considers the relationship between intermediate products. A new model is presented to estimate the return to scale at each stage and in the entire chain, thus estimating the return to scale for cement companies.

In continuation of this article, we will review basic concepts. Then, we will introduce suitable models for estimating return to scale in the structure of a four-level supply chain network. In this regard, we provide a practical example in the cement industry to illustrate the proposed models, and finally, we discuss and analyze the results obtained from model execution in the conclusion.

## 2. BASIC CONCEPTS

A set of production possibilities is defined as follows:

$\{T = (X, Y) \text{ output } Y \text{ can be generated by input } X\}$

It is observed that the set of production possibilities  $T$  is determined when the production function is known. Suppose  $n$  is an existing DMU that  $Y_j = (y_{1j}, \dots, y_{sj})^t$ ,  $X_j = (x_{1j}, \dots, x_{mj})^t$  are the input and output

vectors of DMU<sub>j</sub>, respectively and  $Y_j \neq 0, Y_j \geq 0, X_j \neq 0, X_j \geq 0$ .

In general, the production function is not available. Therefore, by accepting the principles of inclusion of

$$T_v = \left\{ \left( \begin{matrix} X \\ Y \end{matrix} \right) \mid X \geq \sum_{j=1}^n \lambda_j X_j, Y \leq \sum_{j=1}^n \lambda_j Y_j, \sum_{j=1}^n \lambda_j = 1, \lambda_j \geq 0, j = 1, 2, \dots, n \right\} \tag{1}$$

Now, suppose the unit under evaluation, DMU<sub>o</sub>, is in  $T_v$ . For evaluating DMU<sub>o</sub>, the following model, by an input nature, must be solved.

$$\begin{aligned} & \text{Min } \theta, \\ & \text{s.t:} \\ & \left( \begin{matrix} \theta X_o \\ Y_o \end{matrix} \right) \in T_v. \\ & \text{Min } \theta, \\ & \text{s.t:} \\ & \sum_{j=1}^n \lambda_j x_{ij} \leq \theta x_{io}, \quad i = 1, 2, \dots, m \\ & \sum_{j=1}^n \lambda_j y_{rj} \geq y_{ro}, \quad r = 1, 2, \dots, s \\ & \sum_{j=1}^n \lambda_j = 1, \\ & \lambda_j \geq 0 \quad j = 1, 2, \dots, n \end{aligned} \tag{2}$$

Model 2, identified as BCC in terms of input, was introduced by Banker et al. (30). It is evident that DMU<sub>o</sub> achieves "strong efficiency" or "Pareto-Koopmans Efficiency" if and only if  $\theta^* = 1$  and in every optimal solution of Model 2, the value of all auxiliary variables is zero.

**Definition 1.** Return to scale in the Black Box. To define the return to scale in Black Box, suppose,  $(x_o, y_o) \in T_v$ .

**a.** If  $\delta_1^* > 0$ , so that,  $0 \leq \delta < \delta_1^*$ :

$$\begin{aligned} Z_\delta &= ((1+\delta) x_o, (1+\delta) y_o) \in T_v, \\ Z'_\delta &= ((1-\delta) x_o, (1-\delta) y_o) \notin T_v \end{aligned} \tag{3}$$

Then, "return to scale" will be increasing at this point.

**b.** If  $\delta_2^* > 0$ , so that,  $0 \leq \delta < \delta_2^*$ :

$$\begin{aligned} Z_\delta &= ((1+\delta) x_o, (1+\delta) y_o) \notin T_v, \\ Z'_\delta &= ((1-\delta) x_o, (1-\delta) y_o) \in T_v \end{aligned} \tag{4}$$

Then, "return to scale" will be descending at this point.

**c.** whereas DMU<sub>o</sub> does not apply in **definition (a)** increasing and **(b)** descending return to scale does not apply, then, "return to scale" will be constant at this point. Banker and Thrall (35) have articulated and substantiated the following two propositions regarding the estimation of return to scale in the Black Box using the BCC multiplicative model when the solutions are distinct and singular:

**Theorem 1:** Suppose  $(x_o, y_o)$  is an efficient DMU in the BCC model (on BCC border) and  $(v^*, u^*, u_o^*)$ , the optimal

observations, convexity, feasibility and the minimum of interpolation, a set of production possibilities will be defined as follows:

answer is the BCC multiplicative model in the evaluation of this DMU. In addition, suppose the optimal answer  $u_o^*$  is unique, in which:

\* Return to scale is increasing at the point  $(x_o, y_o)$ , if and only if  $u_o^* > 0$ .

\* Return to scale is constant at the point  $(x_o, y_o)$ , if and only if  $u_o^* = 0$ .

\* Return to scale is descending at the point  $(x_o, y_o)$ , if and only if  $u_o^* < 0$ .

**Proof:** To prove above the theorem, refer to Banker and Thrall (35).

**Theorem 2:** Suppose,  $(x_o, y_o)$  is an efficient DMU in the BCC model (on the BCC border), and  $(v^*, u^*, u_o^*)$  is the optimal answer to the BCC multiplicative model in the evaluation of this DMU. In addition, suppose  $u_o^*$  is not unique; that is, we have multiple answers. Now, to calculate the return to scale, we consider models 5 and 6:

$$\begin{aligned} u_o^{*+} &= \max u_o, \\ & \text{s.t:} \\ & v^t x_o = 1, \\ & u^t y_j - v^t x_j + u_o \leq 0, \quad j = 1, 2, \dots, n \\ & u^t y_o - v^t x_o + u_o = 0, \\ & u \geq 0, v \geq 0, u_o \text{ free} \end{aligned} \tag{5}$$

$$\begin{aligned} u_o^{*-} &= \min u_o, \\ & \text{s.t:} \\ & v^t x_o = 1, \\ & u^t y_j - v^t x_j + u_o \leq 0, \quad j = 1, 2, \dots, n \\ & u^t y_o - v^t x_o + u_o = 0, \\ & u \geq 0, v \geq 0, u_o \text{ free} \end{aligned} \tag{6}$$

where in,  $u_o^{*-} < u_o^{*+}$  and  $u_o^* \in [u_o^{*-}, u_o^{*+}]$ .

Whereas,

- If  $u_o^{*+} > 0$  and  $u_o^{*-} > 0$ , the return to scale will be increasing at the point  $(x_o, y_o)$ .
- If  $u_o^{*+} \geq 0$  and  $u_o^{*-} \leq 0$ , the return to scale will be constant at the point  $(x_o, y_o)$ .
- If  $u_o^{*+} < 0$  and  $u_o^{*-} < 0$ , the return to scale will be descending at the point  $(x_o, y_o)$ .

**Proof:** To prove the above theorem, refer to Banker and Thrall (35).

**Definition2.** Return to scale in the network: to define return to scale efficiency in the supply chain network, suppose  $(x_o^1, y_o^1, z_o^{12}) \in T_v$  is the vector of the first level of the supply chain in DMU<sub>o</sub>.

a. If  $\delta_1^* > 0$ , so that,  $0 \leq \delta < \delta_1^*$ :

$$\begin{aligned} Z_{\delta} &= ((1+\delta) x_o^1, (1+\delta) y_o^1, (1+\delta) z_o^{12}) \in T_v, \\ Z'_{\delta} &= ((1-\delta) x_o^1, (1-\delta) y_o^1, (1-\delta) z_o^{12}) \notin T_v \end{aligned} \tag{7}$$

In that case, the "return to scale of the first level" will increase at the points  $(x_o^1, y_o^1, \text{ and } z_o^{12})$ .

b. If  $\delta_2^* > 0$ , so that,  $0 \leq \delta < \delta_2^*$ :

$$\begin{aligned} Z_{\delta} &= ((1+\delta) x_o^1, (1+\delta) y_o^1, (1+\delta) z_o^{12}) \notin T_v, \\ Z'_{\delta} &= ((1-\delta) x_o^1, (1-\delta) y_o^1, (1-\delta) z_o^{12}) \in T_v \end{aligned} \tag{8}$$

Where the "return to scale of the first level" will be descending at the points  $(x_o^1, y_o^1, z_o^{12})$ .

c. If DMU<sub>o</sub> does not apply in the **definition (a)** increasing return to scale and **(b)** descending return to scale, then, "return to scale" is constant at the point  $(x_o^1, y_o^1, z_o^{12})$ . The definition of return to scale in levels 2, 3 and 4, as well as the return to scale of the whole supply chain, is done similarly. Further explanation is avoided to summarize the issue.

Subsequently, the proposed method will be examined utilizing the aforementioned definitions and theorems pertaining to return to scale in the Black Box and supply chain network.

### 3. PROPOSED METHOD

In traditional DEA models, the consideration of intermediate products and the interactions among different components within the system is often neglected. Addressing this limitation, network DEA models are employed. In these instances, the output of one level may be computed as the input of the subsequent level, and conversely, each level may possess independent inputs. The return to scale is an economic concept within DEA, denoting the maximum increase in output per unit increase in input. The identification of return to scale holds particular significance in developing DMU<sub>o</sub>.

In order to draw the figure and to construct the framework, relevant supply chain literature, including the work of Darvish Motevalli et al. (15), has preferred from the available sources. This paper aims to estimate the return to scale of a green supply chain under various conditions within the cement industry using DEA methodology. The exploration follows the outlined structure:

In the above complete supply chain:

- $L_1, L_2, L_3$  and  $L_4$  represent the supplier, manufacturer, distributor, and customer respectively.
- $X^f = (x_{ij}^f, i = 1, 2, \dots, m)$  for  $f = 1, 2, 3, 4$  of input vector DMU<sub>j</sub>, including independent inputs to the level  $L_f$ .
- $Z^{k_1 k_2} = (z_{lj}^{k_1 k_2}, l = 1, 2, \dots, p)$  for  $k_1 = 1, 2, 3$  and  $k_2 = 2, 3, 4$  intermediate data from the level  $L_{k_1}$  to  $L_{k_2}$  is the unit j, or, in other words, the output vector of the level  $L_{k_1}$  in the unit j, is also the input vector of level  $L_{k_1+1}$ .
- $Y^{k_3} = (y_{rj}^{k_3}, r = 1, 2, \dots, s)$  for  $k_3 = 1, 2, 3, 4$  is the output vector of the level  $L_{k_3}$ .

Consider a set of n identical supply chains similar to the configuration depicted in Figure 1, denoted as n Decision-Making Units (DMUs) as DMU<sub>1</sub>, DMU<sub>2</sub>, ..., DMU<sub>n</sub> in the DEA literature. The development of a novel network DEA model is imperative to assess the return to scale of the supply chain under varying conditions. Notably, the BCC model proves insufficient in identifying the corresponding black box returns to scale of the supply chain illustrated in Figure 1. This inadequacy arises due to its exclusive consideration of the inputs and outputs of the supply chain, disregarding the intermediate products generated at different levels within the supply chain. Hence, this study introduces a network BCC model for the complete supply chain, structured according to the nature of input. This model aims to calculate the return to scale at each level and, ultimately, for the entire supply chain. The model is articulated as follows:

Min  $\theta$ , s.t:

$$\begin{aligned} \sum_{j=1}^n \lambda_j^1 x_{ij}^1 &\leq \theta x_{io}^1, & i = 1, 2, \dots, m_1 \\ \sum_{j=1}^n \lambda_j^1 z_{lj}^{12} &\geq \sum_{j=1}^n \lambda_j^2 z_{lj}^{12}, & l = 1, 2, \dots, p_1 \\ \sum_{j=1}^n \lambda_j^1 y_{rj}^1 &\geq y_{ro}^1, & r = 1, 2, \dots, s_1 \\ \sum_{j=1}^n \lambda_j^2 x_{ij}^2 &\leq \theta x_{io}^2, & i = 1, 2, \dots, m_2 \\ \sum_{j=1}^n \lambda_j^2 z_{lj}^{23} &\geq \sum_{j=1}^n \lambda_j^3 z_{lj}^{23}, & l = 1, 2, \dots, p_2 \\ \sum_{j=1}^n \lambda_j^2 y_{rj}^2 &\geq y_{ro}^2, & r = 1, 2, \dots, s_2 \\ \sum_{j=1}^n \lambda_j^3 x_{ij}^3 &\leq \theta x_{io}^3, & i = 1, 2, \dots, m_3 \\ \sum_{j=1}^n \lambda_j^3 z_{lj}^{34} &\geq \sum_{j=1}^n \lambda_j^4 z_{lj}^{34}, & l = 1, 2, \dots, p_3 \\ \sum_{j=1}^n \lambda_j^3 y_{rj}^3 &\geq y_{ro}^3, & r = 1, 2, \dots, s_3 \\ \sum_{j=1}^n \lambda_j^4 x_{ij}^4 &\leq \theta x_{io}^4, & i = 1, 2, \dots, m_4 \\ \sum_{j=1}^n \lambda_j^4 y_{rj}^4 &\geq y_{ro}^4, & r = 1, 2, \dots, s_4 \\ \sum_{j=1}^n \lambda_j^1 &= 1, \quad \sum_{j=1}^n \lambda_j^2 = 1, \quad \sum_{j=1}^n \lambda_j^3 = 1, \quad \sum_{j=1}^n \lambda_j^4 = 1, \\ \lambda_j^1, \lambda_j^2, \lambda_j^3, \lambda_j^4 &\geq 0, \quad j = 1, 2, \dots, n, \quad \theta \text{ free} \end{aligned} \tag{9}$$

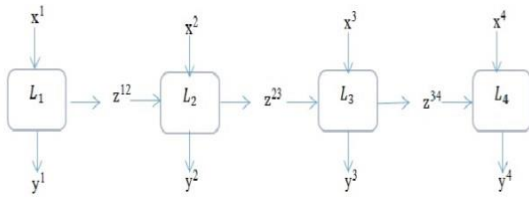


Figure 1. Four-level supply chain

Where in:

1. For  $f = 1, 2, 3, 4$  the constraints  $\sum_{j=1}^n \lambda_j^f x_{ij}^f \leq \theta x_{i0}^f, i = 1, 2, \dots, m$  are written corresponding to the independent inputs of the level  $S_f$ .

2. For  $k_1 = 1, 2, 3$  and  $k_2 = 2, 3, 4$  the constraints  $\sum_{j=1}^n \lambda_j^{k_1} z_{ij}^{k_1 k_2} \geq \sum_{j=1}^n \lambda_j^{k_2} z_{ij}^{k_1 k_2}, l = 1, 2, \dots, p$  corresponding to the output of the level  $S_{k_1}$  is written in unit  $j$ th and indicates that the convex combination of these outputs as the inputs of the level  $S_{k_2}$  must be less or equal to the production of the level  $S_{k_1}$ .

3. For  $k_3 = 1, 2, 3, 4$  the constraints  $\sum_{j=1}^n \lambda_j^{k_3} y_{rj}^{k_3} \geq y_{r0}^{k_3}, r = 1, 2, \dots, s$  corresponding to the output of the level  $S_{k_3}$  is written.

Employing model 9, the dual formulation of the BCC model within a complete supply chain (represented in multiplicative form) is articulated as follows. This formulation serves as a tool for estimating the efficiency of a complete supply chain:

$$\begin{aligned} \text{Max } Z &= \sum_{r=1}^{s_1} u_{r1} y_{r0}^1 + \sum_{r=1}^{s_2} u_{r2} y_{r0}^2 + \sum_{r=1}^{s_3} u_{r3} y_{r0}^3 + \sum_{r=1}^{s_4} u_{r4} y_{r0}^4 + u_{o1} + u_{o2} + u_{o3} + u_{o4}, \\ \text{s.t:} \\ - \sum_{i=1}^{m_1} v_{i1} x_{ij}^1 + \sum_{l=1}^{p_1} w_{l1} z_{lj}^{12} + \sum_{r=1}^{s_1} u_{r1} y_{rj}^1 + u_{o1} &\leq 0, \quad j = 1, 2, \dots, n \\ - \sum_{l=1}^{p_1} w_{l1} z_{lj}^{12} - \sum_{i=1}^{m_2} v_{i2} x_{ij}^2 + \sum_{l=1}^{p_2} w_{l2} z_{lj}^{23} + \sum_{r=1}^{s_2} u_{r2} y_{rj}^2 + u_{o2} &\leq 0, \quad j = 1, 2, \dots, n \\ - \sum_{l=1}^{p_2} w_{l2} z_{lj}^{23} - \sum_{i=1}^{m_3} v_{i3} x_{ij}^3 + \sum_{l=1}^{p_3} w_{l3} z_{lj}^{34} + \sum_{r=1}^{s_3} u_{r3} y_{rj}^3 + u_{o3} &\leq 0, \quad j = 1, 2, \dots, n \\ - \sum_{l=1}^{p_3} w_{l3} z_{lj}^{34} - \sum_{i=1}^{m_4} v_{i4} x_{ij}^4 + \sum_{r=1}^{s_4} u_{r4} y_{rj}^4 + u_{o4} &\leq 0, \quad j = 1, 2, \dots, n \end{aligned} \tag{10}$$

$$\sum_{i=1}^{m_1} v_{i1} x_{i0}^1 + \sum_{i=1}^{m_2} v_{i2} x_{i0}^2 + \sum_{i=1}^{m_3} v_{i3} x_{i0}^3 + \sum_{i=1}^{m_4} v_{i4} x_{i0}^4 = 1,$$

$$v_{i1}, v_{i2}, v_{i3}, v_{i4} \geq 0,$$

$$u_{r1}, u_{r2}, u_{r3}, u_{r4} \geq 0,$$

$$w_{l1}, w_{l2}, w_{l3} \geq 0,$$

$$u_{o1}, u_{o2}, u_{o3}, u_{o4} \text{ free}$$

To estimate the return to scale of levels 1, 2, 3, and 4 under distinct or identical conditions utilizing the BCC

multiplicative model, let  $DMU_o$  represent an arbitrary complete supply chain in accordance with the structure depicted in Figure 1.

Initially, the return to scale of the first level is estimated, and subsequently, the estimations for levels 2, 3, and 4 are derived, mirroring the procedure applied to the first level.

### 3. 1. Estimation of the Return to Scale of the First Level (supplier)

For estimation of the return to scale of the first level, model 10 is first solved.

To do this, the target function of model 10 is considered in the optimization of  $Z^*$ . On  $Z^*$ , the efficiency of the first level ( $E_1^*$ ) or ( $\theta_1^*$ ) will be obtained from the following model.

In order to determine the efficiency of the first level, the following model is solved:

$$\begin{aligned} \text{Max } E_1 &= \sum_{l=1}^{p_1} w_{l1} z_{l0}^{12} + \sum_{r=1}^{s_1} u_{r1} y_{r0}^1 + u_{o1}, \\ \text{s.t:} \\ \sum_{i=1}^{m_1} v_{i1} x_{i0}^1 &= 1, \\ - \sum_{i=1}^{m_1} v_{i1} x_{ij}^1 + \sum_{l=1}^{p_1} w_{l1} z_{lj}^{12} + \sum_{r=1}^{s_1} u_{r1} y_{rj}^1 + u_{o1} &\leq 0, \quad j = 1, 2, \dots, n \\ - \sum_{l=1}^{p_1} w_{l1} z_{lj}^{12} - \sum_{i=1}^{m_2} v_{i2} x_{ij}^2 + \sum_{l=1}^{p_2} w_{l2} z_{lj}^{23} + \sum_{r=1}^{s_2} u_{r2} y_{rj}^2 + u_{o2} &\leq 0, \quad j = 1, 2, \dots, n \\ - \sum_{l=1}^{p_2} w_{l2} z_{lj}^{23} - \sum_{i=1}^{m_3} v_{i3} x_{ij}^3 + \sum_{l=1}^{p_3} w_{l3} z_{lj}^{34} + \sum_{r=1}^{s_3} u_{r3} y_{rj}^3 + u_{o3} &\leq 0, \quad j = 1, 2, \dots, n \\ - \sum_{l=1}^{p_3} w_{l3} z_{lj}^{34} - \sum_{i=1}^{m_4} v_{i4} x_{ij}^4 + \sum_{r=1}^{s_4} u_{r4} y_{rj}^4 + u_{o4} &\leq 0, \quad j = 1, 2, \dots, n \end{aligned} \tag{11}$$

$$Z^* = \frac{\sum_{r=1}^{s_1} u_{r1} y_{r0}^1 + \sum_{r=1}^{s_2} u_{r2} y_{r0}^2 + \sum_{r=1}^{s_3} u_{r3} y_{r0}^3 + \sum_{r=1}^{s_4} u_{r4} y_{r0}^4 + u_{o1} + u_{o2} + u_{o3} + u_{o4}}{\sum_{i=1}^{m_1} v_{i1} x_{i0}^1 + \sum_{i=1}^{m_2} v_{i2} x_{i0}^2 + \sum_{i=1}^{m_3} v_{i3} x_{i0}^3 + \sum_{i=1}^{m_4} v_{i4} x_{i0}^4}$$

$$v_{i1}, v_{i2}, v_{i3}, v_{i4} \geq 0,$$

$$u_{r1}, u_{r2}, u_{r3}, u_{r4} \geq 0,$$

$$w_{l1}, w_{l2}, w_{l3} \geq 0,$$

$$u_{o1}, u_{o2}, u_{o3}, u_{o4} \text{ free}$$

In these conditions, two cases will be considered:

1. Where  $u_{o1}$  is unique;
2. Where  $u_{o1}$  has multiple answers.

To identify the uniqueness of  $u_{o1}$ , models 12 and 13 are considered.

In fact, to estimate the return to scale in  $u_{o1}$ , the following two models by the same achievable area and two target functions are used to estimate  $u_{o1}^-$  and  $u_{o1}^+$ .

$$\begin{aligned} u_{o1}^+ &= \max u_{o1}, \\ \text{s.t:} \\ \sum_{i=1}^{m_1} v_{i1} x_{i0}^1 &= 1, \end{aligned} \tag{12}$$

$$\begin{aligned}
 & -\sum_{i=1}^{m_1} v_{i1} x_{ij}^1 + \sum_{i=1}^{p_1} w_{i1} z_{ij}^{12} + \sum_{r=1}^{s_1} u_{r1} y_{rj}^1 + u_{o1} \leq 0, \quad j = 1, 2, \dots, n \\
 & -\sum_{i=1}^{p_1} w_{i1} z_{ij}^{12} - \sum_{i=1}^{m_2} v_{i2} x_{ij}^2 + \sum_{i=1}^{p_2} w_{i2} z_{ij}^{23} + \sum_{r=1}^{s_2} u_{r2} y_{rj}^2 + u_{o2} \leq 0, \quad j = 1, 2, \dots, n \\
 & -\sum_{i=1}^{p_2} w_{i2} z_{ij}^{23} - \sum_{i=1}^{m_3} v_{i3} x_{ij}^3 + \sum_{i=1}^{p_3} w_{i3} z_{ij}^{34} + \sum_{r=1}^{s_3} u_{r3} y_{rj}^3 + u_{o3} \leq 0, \quad j = 1, 2, \dots, n \\
 & -\sum_{i=1}^{p_3} w_{i3} z_{ij}^{34} - \sum_{i=1}^{m_4} v_{i4} x_{ij}^4 + \sum_{r=1}^{s_4} u_{r4} y_{rj}^4 + u_{o4} \leq 0, \quad j = 1, 2, \dots, n \\
 & Z^* = \frac{\sum_{r=1}^{s_1} u_{r1} y_{r0}^1 + \sum_{r=1}^{s_2} u_{r2} y_{r0}^2 + \sum_{r=1}^{s_3} u_{r3} y_{r0}^3 + \sum_{r=1}^{s_4} u_{r4} y_{r0}^4 + u_{o1} + u_{o2} + u_{o3} + u_{o4}}{\sum_{i=1}^{m_1} v_{i1} x_{i0}^1 + \sum_{i=1}^{m_2} v_{i2} x_{i0}^2 + \sum_{i=1}^{m_3} v_{i3} x_{i0}^3 + \sum_{i=1}^{m_4} v_{i4} x_{i0}^4}, \\
 & E_1^* = \sum_{i=1}^{p_1} w_{i1} z_{i0}^{12} + \sum_{r=1}^{s_1} u_{r1} y_{r0}^1 + u_{o1}, \\
 & v_{i1}, v_{i2}, v_{i3}, v_{i4} \geq 0, \\
 & u_{r1}, u_{r2}, u_{r3}, u_{r4} \geq 0, \\
 & w_{i1}, w_{i2}, w_{i3} \geq 0, \\
 & u_{o1}, u_{o2}, u_{o3}, u_{o4} \text{ free.}
 \end{aligned}$$

Also, model 13 is estimated with the same achievable area and different target function as model 12 to estimate  $u_{o1}^-$ .

$$\begin{aligned}
 & u_{o1}^- = \min u_{o1}, \\
 & \text{s.t:} \\
 & \sum_{i=1}^{m_1} v_{i1} x_{i0}^1 = 1, \\
 & -\sum_{i=1}^{m_1} v_{i1} x_{ij}^1 + \sum_{i=1}^{p_1} w_{i1} z_{ij}^{12} + \sum_{r=1}^{s_1} u_{r1} y_{rj}^1 + u_{o1} \leq 0, \quad j = 1, 2, \dots, n \\
 & -\sum_{i=1}^{p_1} w_{i1} z_{ij}^{12} - \sum_{i=1}^{m_2} v_{i2} x_{ij}^2 + \sum_{i=1}^{p_2} w_{i2} z_{ij}^{23} + \sum_{r=1}^{s_2} u_{r2} y_{rj}^2 + u_{o2} \leq 0, \quad j = 1, 2, \dots, n \\
 & -\sum_{i=1}^{p_2} w_{i2} z_{ij}^{23} - \sum_{i=1}^{m_3} v_{i3} x_{ij}^3 + \sum_{i=1}^{p_3} w_{i3} z_{ij}^{34} + \sum_{r=1}^{s_3} u_{r3} y_{rj}^3 + u_{o3} \leq 0, \quad j = 1, 2, \dots, n \\
 & -\sum_{i=1}^{p_3} w_{i3} z_{ij}^{34} - \sum_{i=1}^{m_4} v_{i4} x_{ij}^4 + \sum_{r=1}^{s_4} u_{r4} y_{rj}^4 + u_{o4} \leq 0, \quad j = 1, 2, \dots, n \\
 & Z^* = \frac{\sum_{r=1}^{s_1} u_{r1} y_{r0}^1 + \sum_{r=1}^{s_2} u_{r2} y_{r0}^2 + \sum_{r=1}^{s_3} u_{r3} y_{r0}^3 + \sum_{r=1}^{s_4} u_{r4} y_{r0}^4 + u_{o1} + u_{o2} + u_{o3} + u_{o4}}{\sum_{i=1}^{m_1} v_{i1} x_{i0}^1 + \sum_{i=1}^{m_2} v_{i2} x_{i0}^2 + \sum_{i=1}^{m_3} v_{i3} x_{i0}^3 + \sum_{i=1}^{m_4} v_{i4} x_{i0}^4}, \\
 & E_1^* = \sum_{i=1}^{p_1} w_{i1} z_{i0}^{12} + \sum_{r=1}^{s_1} u_{r1} y_{r0}^1 + u_{o1}, \\
 & v_{i1}, v_{i2}, v_{i3}, v_{i4} \geq 0, \\
 & u_{r1}, u_{r2}, u_{r3}, u_{r4} \geq 0, \\
 & w_{i1}, w_{i2}, w_{i3} \geq 0, \\
 & u_{o1}, u_{o2}, u_{o3}, u_{o4} \text{ free.}
 \end{aligned} \tag{13}$$

1. If  $u_{o1}^+ = u_{o1}^-$  that is,  $u_{o1}^*$  is unique and **theorem 1** will be correct.

2. If  $u_{o1}^- < u_{o1}^+$  then  $u_{o1}^* \in [u_{o1}^-, u_{o1}^+]$  and **theorem 2** will be.

**Tip 1:** To get the returns to scale of the level 2, 3 and 4, the same procedure is followed.

### 3. 2. Examining the Conformity of the Calculation of the Return to Scale to its Definition in a Green Supply Chain

Suppose  $DMU_o$  is a supply chain with an intended structure as shown in Figure 1. This chain can be considered as follows:

$$\left( \begin{array}{cc} \underbrace{(x_0^1, y_0^1, z_0^{12})}_{\text{Input and output vector in level (1)}} & , \quad \underbrace{(x_0^2, z_0^{12}, y_0^2, z_0^{23})}_{\text{Input and output vector in level (2)}} \\ \underbrace{(x_0^3, z_0^{23}, y_0^3, z_0^{34})}_{\text{Input and output vector in level (3)}} & , \quad \underbrace{(x_0^4, z_0^{34}, y_0^4)}_{\text{Input and output vector in level (4)}} \end{array} \right)$$

In this section, it is necessary to examine the conformity of the definition of return to scale in all four levels and finally, the return to scale of the whole chain and the way of estimation. In other words, the relationship between definition 1 and theorems 1 and 2 in Black Box will be studied in each level of the chain and finally the whole supply chain.

**Theorem 3:** The return to scale of the first level is increasing at the point  $(x_0^1, y_0^1, z_0^{12})$ , if and only if  $u_{o1}^* > 0$ .

The return to scale of the first level is constant at the point  $(x_0^1, y_0^1, z_0^{12})$ , If and only if  $u_{o1}^* = 0$ .

The return to scale of the first level is descending at the point  $(x_0^1, y_0^1, z_0^{12})$ , If and only if  $u_{o1}^* < 0$ .

**Proof:** Suppose  $(x_0^1, y_0^1, z_0^{12})$  is the vector of the first level in the supply chain of  $DMU_o$ . In order to represent that the return to scale is increasing at this level, it is sufficient, by definition 1, to show that  $\delta_1^* > 0$ , that for every  $0 \leq \delta < \delta_1^*$

We have:

$$\text{a) } Z_\delta = \left( (1+\delta) x_0^1, (1+\delta) y_0^1, (1+\delta) z_0^{12} \right) \in T_v,$$

$$\text{b) } Z'_\delta = \left( (1-\delta) x_0^1, (1-\delta) y_0^1, (1-\delta) z_0^{12} \right) \notin T_v$$

To show the relation (a) by using the second constraint of model 12, we have:

$$\begin{aligned}
 & -v^*(1+\delta) x_0^1 + w^*(1+\delta) z_0^{12} + u^*(1+\delta) y_0^1 + u_{o1}^* = \\
 & (1+\delta) [-v^* x_0^1 + w^* z_0^{12} + u^* y_0^1 + u_{o1}^*] - \delta u_{o1}^*
 \end{aligned}$$

But, in the above equation:  $1+\delta > 0$  and  $[-v^* x_0^1 + w^* z_0^{12} + u^* y_0^1 + u_{o1}^*] \leq 0$ . Because,  $(x_0^1, y_0^1, z_0^{12})$  is in the set of product possibilities. Therefore,  $Z_\delta \in T_v$ , if and only if  $-\delta u_{o1}^* \leq 0$ . So  $-\delta \leq 0$ , it should be  $u_{o1}^* \geq 0$ .

On the other hand, to show the relation (b) by using the second constraint of model 12, we have:

$$-v^*(1-\delta)x_0^1 + w^*(1-\delta)z_0^{12} + u^*(1-\delta)y_0^1 + u_{01}^* = (1-\delta)[-v^*x_0^1 + w^*z_0^{12} + u^*y_0^1 + u_{01}^*] + \delta u_{01}^*$$

But, in the above equation:  $1-\delta > 0$  and  $[-v^*x_0^1 + w^*z_0^{12} + u^*y_0^1 + u_{01}^*] \leq 0$ . Because,  $(x_0^1, y_0^1, z_0^{12})$  is in the set of product possibilities. Therefore,  $Z_\delta \notin T_v$  if and only if  $\delta u_{01}^* > 0$ . So  $\delta > 0$ , it should be  $u_{01}^* \geq 0$ .

As a result, by the relation  $u_{01}^* \geq 0$  and  $u_{01}^* > 0$  proved previously, we conclude  $u_{01}^* > 0$ . Exactly by this argument and simply, it can be possible to prove the return to scale in a fixed and descending state.

**Theorem 4:** The returns to scale in the second level increase at the point  $(x_0^2, z_0^{12}, y_0^2, z_0^{23})$ , if and only if  $u_{02}^* > 0$ .

The returns to scale in 2<sup>nd</sup> level are constant at the point  $(x_0^2, z_0^{12}, y_0^2, z_0^{23})$ , if and only if  $u_{02}^* = 0$ .

The returns to scale in 2<sup>nd</sup> level is descending at the point  $(x_0^2, z_0^{12}, y_0^2, z_0^{23})$ , if and only if  $u_{02}^* < 0$ .

**Proof:** It is exactly the same as proving theorem 3.

**Theorem 5:** The returns to scale of the 3<sup>rd</sup> level are increasing at the point  $(x_0^3, z_0^{23}, y_0^3, z_0^{34})$ , if and only if  $u_{03}^* > 0$ .

The return to scale of 3<sup>rd</sup> level is constant at the point  $(x_0^3, z_0^{23}, y_0^3, z_0^{34})$ , if and only if  $u_{03}^* = 0$ .

The return to scale of 3<sup>rd</sup> level is descending at the point  $(x_0^3, z_0^{23}, y_0^3, z_0^{34})$ , if and only if  $u_{03}^* < 0$ .

**Proof:** It is exactly the same as proving theorem 3.

**Theorem 6:** The return to scale in the 4<sup>th</sup> level is increasing at the point  $(x_0^4, z_0^{34}, y_0^4)$ , if and only if  $u_{04}^* > 0$ .

The returns to scale of the 4<sup>th</sup> level scale are constant at the point  $(x_0^4, z_0^{34}, y_0^4)$ , if and only if  $u_{04}^* = 0$ .

The returns to scale of the 4<sup>th</sup> level are descending at the point  $(x_0^4, z_0^{34}, y_0^4)$ , if and only if  $u_{04}^* < 0$ .

**Proof:** It is exactly the same as proving Theorem 3.

**Note 2:** Theorems 3, 4, 5 and 6, regarding the method of estimating four-level return to scale, were proved in the case that the optimal answer is unique. It can be easily proved that these 4 theorems are correct in the case that the optimal answer is not unique. To prove the case, for example, for the level 1, that is,  $u_{01}^*$  is an optimal answer of models 12 and 13, that is,  $u_{01}^{*+}$  and  $u_{01}^{*-}$  and similar to the process of proving theorem 3. The proof of the theorem in levels 2, 3 and 4 is also similar. it is avoided to be written for the sake of summary.

Now, we will study the way of estimating the return to scale of the whole chain( $u_0^*$ ).

**Note 3:** As we know, we no longer solve the model

to estimate the return to scale of the whole supply chain.

But, we estimate the return to scale of the whole supply chain( $u_0^*$ ) through the following relation:

$$u_0^* = u_{01}^* + u_{02}^* + u_{03}^* + u_{04}^* \tag{14}$$

1. If  $u_{01}^*, u_{02}^*, u_{03}^*, u_{04}^*$  all are unique,  $u_0^*$  is unique and **theorem 1** will be correct.

2. If at least one of  $u_{01}^*, u_{02}^*, u_{03}^*, u_{04}^*$  is not unique, so  $u_0^*$  (return to scale of the whole chain) will certainly not be unique and due to interval operations,  $u_0^*$  will be calculated.

Alefeld and Herzberger (36), in the first part (the calculation of real distances) of the book Preliminary Distance Estimations, have talked about the estimations of interval operations (distances):

The operations can be explicitly estimated in the ranges  $A = [a_1, a_2]$  and  $B = [b_1, b_2]$ , so that:

$$A + B = [a_1 + b_1, a_2 + b_2].$$

So, to calculate  $u_0^*$ , we have:

$$u_0^* = u_{01}^* + u_{02}^* + u_{03}^* + u_{04}^*,$$

$$[u_0^-, u_0^+] = [u_{01}^-, u_{01}^+] + [u_{02}^-, u_{02}^+] + [u_{03}^-, u_{03}^+] + [u_{04}^-, u_{04}^+], \tag{15}$$

$$\Rightarrow [u_0^-, u_0^+] = [u_{01}^- + u_{02}^- + u_{03}^- + u_{04}^-, u_{01}^+ + u_{02}^+ + u_{03}^+ + u_{04}^+]$$

**Theorem 7:** Suppose  $u_0^* = u_{01}^* + u_{02}^* + u_{03}^* + u_{04}^*$ , in that case:

- The return to scale of the whole supply chain is increasing, if and only if  $u_0^* > 0$ .

- The return to scale of the whole supply chain is constant if and only if  $u_0^* = 0$ .

- The return to scale of the whole supply chain is descending, if and only if  $u_0^* < 0$ .

**Proof:** Suppose DMU<sub>0</sub> is a supply chain with an assumptive structure. In order to represent that the return to scale of the whole chain is increasing, it is enough, by definition 1, to show that if  $\delta_1^* > 0$  for each  $0 \leq \delta < \delta_1^*$ , we have:

a)  $Z_\delta \in T_v,$

b)  $Z_\delta \notin T_v$

To show the relation (a), we, from the sum of 4 constraints including the second to fifth, will have model 12:

$$-v_1^* x_j^1 + w_1^* z_j^{12} + u_1^* y_j^1 + u_{01}^* - w_1^* z_j^{12} - v_2^* x_j^2 + w_2^* z_j^{23} + u_3^* y_j^3 + u_{02}^* - w_2^* z_j^{23} - v_3^* x_j^3 + w_3^* z_j^{34} + u_3^* y_j^3 + u_{03}^* - w_3^* z_j^{34} - v_4^* x_j^4 + u_4^* y_j^4 + u_{04}^* \leq 0.$$

Now, we will construct  $Z_\delta$  as follows:

$$\begin{aligned}
 & [-v_1^*(1+\delta) x_0^1 + w_1^*(1+\delta) z_0^{12} + u_1^*(1+\delta) y_0^1 + u_{01}^*] + [-w_1^*(1+\delta) z_0^{12} - v_2^*(1+\delta) x_0^2 + w_2^*(1+\delta) z_0^{23} + u_2^*(1+\delta) y_0^2 + u_{02}^*] \\
 & + [-w_2^*(1+\delta) z_0^{23} - v_3^*(1+\delta) x_0^3 + w_3^*(1+\delta) z_0^{34} + u_3^*(1+\delta) y_0^3 + u_{03}^*] + [-w_3^*(1+\delta) z_0^{34} - v_4^*(1+\delta) x_0^4 + u_4^*(1+\delta) y_0^4 + u_{04}^*] \\
 & = (1+\delta) \left[ \overbrace{-v_1^* x_0^1 + w_1^* z_0^{12} + u_1^* y_0^1 + u_{01}^*}^{\text{The first sentence}} \right] + (1+\delta) \left[ \overbrace{-w_1^* z_0^{12} - v_2^* x_0^2 + w_2^* z_0^{23} + u_2^* y_0^2 + u_{02}^*}^{\text{The second sentence}} \right] + \\
 & (1+\delta) \left[ \overbrace{-w_2^* z_0^{23} - v_3^* x_0^3 + w_3^* z_0^{34} + u_3^* y_0^3 + u_{03}^*}^{\text{The third sentence}} \right] + (1+\delta) \left[ \overbrace{-w_3^* z_0^{34} - v_4^* x_0^4 + u_4^* y_0^4 + u_{04}^*}^{\text{The fourth sentence}} \right] - \delta \left( \overbrace{u_{01}^* + u_{02}^* + u_{03}^* + u_{04}^*}^{\text{The fifth sentence}} \right)
 \end{aligned} \tag{16}$$

But, since  $(1+\delta) > 0$  and  $DMU_0$  is a supply chain, in the last sentence of the above 5 sentences, the first 4 sentences are less than or equal to zero. Therefore,  $Z_\delta \in T_v$ , if and only if  $-\delta u_0^* \leq 0$ , and because  $-\delta < 0$ , so, it must be  $u_0^* \geq 0$ .

On the other hand, to represent the relation (b) in a similar way to the above process and to prove theorem (3), we will obtain  $u_0^* > 0$ . As a result, we conclude  $u_0^* > 0$  by the relations  $u_0^* \geq 0$  and  $u_0^* > 0$ . The return to scale can be easily proved in the case of constant and increasing.

#### 4. CASE STUDY

The effective management of a green supply chain stands as a critical concern for organizations, necessitating managerial efforts to formulate suitable models for performance estimation.

This study examines 42 companies operating within the cement industry to ascertain the overall return to scale across various levels. The comprehensive costs encompass annual expenditures associated with green

training, eco-friendly design (pertaining to economic sustainability), personnel costs (relating to social sustainability), and environmental costs (reflecting environmental sustainability).

These factors manifest at different stages of the supply chain. The impetus for undertaking this research lies in the need to estimate the return to scale for cement factories, treating them as complete supply chains while accounting for these environmental considerations, where changes lie either entirely or partially beyond managerial control.

Validation of the proposed model is executed using real data from the cement industry in 2021. The model adeptly estimates the return to scale for the supply chain within this industry.

Additionally, the supporting source used to determine input, output, and intermediate data indicators, are determined based on authoritative sources and expert opinions, prominently featuring the work of Darvish Motevalli et al. (15), which is duly referenced.

Subsequently, the indicators outlined in Table 1 encompass financial, economic, and production metrics.

**TABLE 1.** Introduction of indicators and their definitions for J th DMU in independent inputs, intermediate data and outputs

Symbols	Classification of indicators	Title of Indicators
$x_{1j}^1$		Quality of suppliers in terms of stability in supplying raw materials and consumables
$x_{2j}^1$		Cost of green training and sustainability for addressing related issues along the supply chain
$x_{3j}^1$		Total initial investment in mining and factory operation
$x_{4j}^1$	Primary inputs of supply chain	Total cost of purchasing minerals, chemicals and other consumables
$x_{5j}^1$		Total cost paid to contractors for mining extraction
$x_{6j}^1$		Total transportation costs paid
$x_{7j}^1$		Total financial costs
$x_{8j}^1$		Total cost of salaries and wages paid
$y_{1j}^1$	First level outputs	Factory performance impact on creating adverse environmental effects in mining
$y_{2j}^1$		Total mineral reserves available
$z_{1j}^{12}$	Intermediate data (1 <sup>st</sup> level output and 2 <sup>nd</sup> level input)	Total tonnage of chemical and mineral additives in the production process
$z_{2j}^{12}$		Total mineral raw materials stored to use in cold season
$z_{3j}^{12}$		Quality of training programs for suppliers and employees for sustainable production and TQM

Symbols	Classification of indicators	Title of Indicators
$Z_{4j}^{12}$		Total research and development costs
$Z_{5j}^{12}$		Industry's actual capacity
$X_{1j}^2$		Suppliers flexibility
$X_{2j}^2$		Improvement of relationships throughout the supply chain
$X_{3j}^2$		Total cost to increase reliability in the supply chain
$X_{4j}^2$	2 <sup>nd</sup> level independent inputs	Paying attention to principles of legal standards and government regulations along the chain
$X_{5j}^2$		Total energy payment costs
$X_{6j}^2$		Electricity consumption per year in kilowatt-hours (kw/h)
$X_{7j}^2$		Gas consumption per year in cubic meters per ton (m3/ton)
$X_{8j}^2$		Mazut fuel energy consumption per year in liters per ton (liters/ton)
$Y_{1j}^2$		Total dust particles produced in milligrams per cubic meter (mg / m3)
$Y_{2j}^2$		Annual average of emitted NOX greenhouse gases (mg/m3)
$Y_{3j}^2$		Annual average of emitted CO greenhouse gases (mg/m3)
$Y_{4j}^2$	2 <sup>nd</sup> level outputs	Annual average of emitted SO2 greenhouse gases (mg/m3)
$Y_{5j}^2$		Impact of total infiltrated water consumption and wastewater on groundwater
$Z_{1j}^{23}$		Intermediate data (2 <sup>nd</sup> level output and 3 <sup>rd</sup> level input)
$Z_{2j}^{23}$	Total tonnage of the cement production by the factory	
$X_{1j}^3$	3 <sup>rd</sup> level Independent inputs	Reverse logistics
$X_{2j}^3$		Efforts to use advanced technologies and alternative raw materials
$X_{3j}^3$		Total marketing costs
$X_{4j}^3$		Cost of environmentally compatible design
$X_{5j}^3$	Third level output	Number of consumed cement bags per year of type pp
$Y_{1j}^3$		Total value of assets and inventory held ready for sale in Rials
$Z_{1j}^{34}$	Intermediate data (3 <sup>rd</sup> level output and 4 <sup>th</sup> level input)	Total tonnage of bagged and bulk cement sales in the domestic and export markets
$Z_{2j}^{34}$		Total tonnage of clinker sold
$Z_{3j}^{34}$		Total finished product cost
$X_{1j}^4$	4 <sup>th</sup> level independent Inputs	Implementation of quality of life principles and social welfare for personnel
$X_{2j}^4$		Factory's impact in the area of activity
$X_{3j}^4$		Social responsiveness
$Y_{1j}^4$		Total assets
$Y_{2j}^4$		Competitiveness and globalization of the factory brand
$Y_{3j}^4$		Cultural attitude towards creating green spaces
$Y_{4j}^4$		Total revenue from products sales
$Y_{5j}^4$		Total profit earned
$Y_{6j}^4$		Annual growth rate based on performance
$Y_{7j}^4$	Returns on assets (ROA)	
$Y_{8j}^4$	Final outputs	Return on equity owners' accounts
$Y_{9j}^4$		Customer satisfaction

To exemplify the application of the proposed method, authentic data from 42 cement companies in the year 2021 is meticulously scrutinized, encompassing inputs, outputs, and intermediate data.

Subsequently, the implementation of models 10 and 11 is effectuated through GAMS software. Following the execution of models 10 and 11 using the GAMS software, the overall efficiency of the supply chain and the efficiency of levels one through four were estimated. According to the basic DEA definitions and principles mentioned by Banker et al. (30), a value of “1.00000” in

Table 2 indicates "strong efficiency" or "Pareto-Koopmans Efficiency" for DMUs. The results are presented in Table 2.

By implementing models 12 and 13 using the GAMS software and considering theorem 2 proposed by Banker and Thrall (35), the return to scale of levels one to four was estimated. Finally, based on the relationship presented by Alfield and Herzberger (36), the return to scale of complete supply chain was estimated. The results are illustrated in Table 3.

**TABLE 2.** The efficiency of the whole supply chain and the efficiency of the first to fourth level

Company Name		Z	E1	E2	E3	E4
Sabad	DMU1	1.000000	1.000000	1.000000	1.000000	1.000000
Sabik	DMU2	1.000000	1.000000	1.000000	1.000000	1.000000
Sarab	DMU3	0.9981847	0.9993864	1.000000	1.000000	0.9817792
Sarbil	DMU4	0.9986577	1.000000	1.000000	0.9342312	1.000000
Sarum	DMU5	1.000000	1.000000	1.000000	1.000000	1.000000
Saveh	DMU6	1.000000	1.000000	1.000000	1.000000	1.000000
Sebagher	DMU7	1.000000	1.000000	1.000000	1.000000	1.000000
Sebajnu	DMU8	0.9978771	1.000000	1.000000	0.9835436	1.000000
Sabzeva	DMU9	0.9993072	1.000000	1.000000	0.9485462	1.000000
Sebahan	DMU10	0.9985984	0.9985984	1.000000	1.000000	1.000000
Sepaha	DMU11	1.000000	1.000000	1.000000	1.000000	1.000000
Satran	DMU12	1.000000	1.000000	1.000000	1.000000	1.000000
Sajam	DMU13	0.9966413	1.000000	0.9989980	0.9198612	1.000000
Sakhash	DMU14	0.9996298	1.000000	1.000000	1.000000	0.9900012
Sakhrom	DMU15	1.000000	1.000000	1.000000	1.000000	1.000000
Sekhazar	DMU16	0.9999267	1.000000	1.000000	1.000000	1.000000
Sakhvaf	DMU17	1.000000	1.000000	1.000000	1.000000	1.000000
Sakhuz	DMU18	1.000000	1.000000	1.000000	1.000000	1.000000
Sedasht	DMU19	1.000000	1.000000	1.000000	1.000000	1.000000
Sadur	DMU20	0.9986574	1.000000	1.000000	0.9541445	1.000000
Sarud	DMU21	0.9996711	1.000000	1.000000	0.9720452	1.000000
Seshargh	DMU22	0.9985093	1.000000	1.000000	0.9765528	1.000000
Seshomal	DMU23	1.000000	1.000000	1.000000	1.000000	1.000000
Sesafha	DMU24	1.000000	1.000000	1.000000	1.000000	1.000000
Sesufi	DMU25	0.9981047	1.000000	1.000000	0.9686542	1.000000
Saghrab	DMU26	0.9948798	1.000000	1.000000	0.9525511	1.000000
Sefar	DMU27	1.000000	1.000000	1.000000	1.000000	1.000000
Sefars	DMU28	0.9987711	1.000000	1.000000	0.9965400	1.000000
Sefarum	DMU29	1.000000	1.000000	1.000000	1.000000	1.000000
Sefanu	DMU30	0.9989667	0.9994331	1.000000	0.9912634	1.000000
Sefiruz	DMU31	1.000000	1.000000	1.000000	1.000000	1.000000

Company Name		Z	E1	E2	E3	E4
Seghain	DMU32	0.9990562	1.0000000	1.0000000	0.9853776	0.9505419
Sekarun	DMU33	0.9990175	1.0000000	1.0000000	0.9998777	1.0000000
Sekard	DMU34	0.9976153	1.0000000	0.9991167	0.9204183	1.0000000
Sekarma	DMU35	0.9990327	1.0000000	1.0000000	0.9139310	1.0000000
Selaar	DMU36	1.0000000	1.0000000	1.0000000	1.0000000	1.0000000
Semazen	DMU37	1.0000000	1.0000000	1.0000000	1.0000000	1.0000000
Samtaz	DMU38	0.9987039	0.9989622	1.0000000	1.0000000	1.0000000
Senir	DMU39	1.0000000	1.0000000	1.0000000	1.0000000	1.0000000
Sehormoz	DMU40	1.0000000	1.0000000	1.0000000	1.0000000	1.0000000
Sehegmat	DMU41	0.9995315	0.9995318	1.0000000	1.0000000	1.0000000
Silam	DMU42	0.9990813	0.9990813	1.0000000	1.0000000	1.0000000

**TABLE 3.** Estimating the returns to scale of the first to fourth levels and estimating the return to scale of the whole supply chain

Company Name		$u_{01}^+$	$u_{01}^-$	1 <sup>st</sup> level return to scale	$u_{02}^+$	$u_{02}^-$	2 <sup>nd</sup> level return to scale	$u_{03}^+$	$u_{03}^-$	3 <sup>rd</sup> level return to scale	$u_{04}^+$	$u_{04}^-$	4 <sup>th</sup> level return to scale	$u_0^+$	$u_0^-$	Total return to scale
Sabad	DMU1	+	-	constant	+	-	constant	+	+	increasing	+	-	constant	+	-	constant
Sabik	DMU2	+	+	increasing	+	-	constant	+	-	constant	+	-	constant	+	-	constant
Sarab	DMU3	-	-	decreasing	+	-	constant	+	-	constant	-	-	decreasing	-	-	decreasing
Sarbil	DMU4	+	-	constant	+	-	constant	+	+	increasing	-	-	decreasing	-	-	decreasing
Sarum	DMU5	+	-	constant	+	-	constant									
Saveh	DMU6	+	-	constant	+	-	constant									
Sebagher	DMU7	+	-	constant	+	-	constant	+	-	constant	-	-	decreasing	-	-	decreasing
Sebajnu	DMU8	+	-	constant	+	-	constant	-	-	decreasing	+	-	constant	+	-	constant
Sabzeva	DMU9	-	-	decreasing	+	-	constant	+	+	increasing	+	-	constant	+	-	constant
Sebahan	DMU10	-	-	decreasing	+	-	constant	+	-	constant	+	-	constant	+	-	constant
Sepaha	DMU11	+	-	constant	+	-	constant									
Satran	DMU12	+	-	constant	+	-	constant									
Sajam	DMU13	+	-	constant	+	+	increasing	+	+	increasing	+	-	constant	+	-	constant
Sakhash	DMU14	+	-	constant	+	-	constant	+	-	constant	-	-	decreasing	-	-	decreasing
Sakhrom	DMU15	+	-	constant	+	-	constant									
Sekhazar	DMU16	+	-	constant	+	-	constant	+	-	constant	-	-	decreasing	-	-	decreasing
Sakhvaf	DMU17	+	-	constant	+	-	constant									
Sakhuz	DMU18	+	-	constant	+	-	constant									
Sedasht	DMU19	+	-	constant	+	-	constant									
Sadur	DMU20	+	-	constant	+	-	constant	+	+	increasing	-	-	decreasing	-	-	decreasing
Sarud	DMU21	+	-	constant	+	-	constant	+	+	increasing	+	-	constant	+	-	constant
Seshargh	DMU22	+	-	constant	+	-	constant	+	+	increasing	+	-	constant	+	-	constant
Seshomal	DMU23	+	-	constant	+	-	constant									
Sesafha	DMU24	+	-	constant	+	-	constant									
Sesufi	DMU25	-	-	decreasing	+	-	constant	+	+	increasing	-	-	decreasing	-	-	decreasing
Saghrab	DMU26	+	-	constant	+	-	constant	+	+	increasing	-	-	decreasing	-	-	decreasing
Sefar	DMU27	+	-	constant	+	-	constant	+	-	constant	-	-	decreasing	-	-	decreasing
Sefars	DMU28	-	-	decreasing	+	-	constant	+	+	increasing	+	-	constant	+	-	constant
Sefarum	DMU29	+	-	constant	+	-	constant									

Company Name	DMU	$u_{01}^+$ $u_{01}^-$		1 <sup>st</sup> level return to scale		$u_{02}^+$ $u_{02}^-$		2 <sup>nd</sup> level return to scale		$u_{03}^+$ $u_{03}^-$		3 <sup>rd</sup> level return to scale		$u_{04}^+$ $u_{04}^-$		4 <sup>th</sup> level return to scale		$u_0^+$ $u_0^-$		Total return to scale
Sefanu	DMU30	-	-	decreasing	+	-	constant	-	-	decreasing	-	-	decreasing	-	-	decreasing	-	-	decreasing	decreasing
Sefiruz	DMU31	+	-	constant	+	-	constant	+	-	constant	-	-	decreasing	+	-	constant	+	-	constant	constant
Seghain	DMU32	-	-	decreasing	+	-	constant	+	+	increasing	-	-	decreasing	-	-	decreasing	-	-	decreasing	decreasing
Sekarun	DMU33	+	-	constant	+	-	constant	+	+	increasing	-	-	decreasing	-	-	decreasing	-	-	decreasing	decreasing
Sekard	DMU34	+	-	constant	-	-	decreasing	+	+	increasing	-	-	decreasing	-	-	decreasing	-	-	decreasing	decreasing
Sekarma	DMU35	+	-	constant	+	-	constant	+	+	increasing	+	-	constant	+	-	constant	+	-	constant	constant
Selaar	DMU36	+	-	constant	+	-	constant	+	-	constant	+	-	constant	+	-	constant	+	-	constant	constant
Semazen	DMU37	+	-	constant	+	-	constant	+	-	constant	+	-	constant	+	-	constant	+	-	constant	constant
Samtaz	DMU38	-	-	decreasing	+	-	constant	+	-	constant	+	-	constant	+	-	constant	+	-	constant	constant
Senir	DMU39	+	-	constant	+	-	constant	+	-	constant	+	-	constant	+	-	constant	+	-	constant	constant
Sehormoz	DMU40	+	-	constant	+	-	constant	+	-	constant	+	-	constant	+	-	constant	+	-	constant	constant
Sehegmat	DMU41	-	-	decreasing	+	-	constant	+	-	constant	-	-	decreasing	-	-	decreasing	-	-	decreasing	decreasing
Silam	DMU42	+	+	increasing	+	-	constant	+	-	constant	+	-	constant	+	-	constant	+	-	constant	constant

## 5. CONCLUSION

In a broader context, the estimation of returns to scale furnishes valuable insights into the progression or constraints within Decision-Making Units (DMUs). An escalating return to scale implies that when the input is doubled, the output surpasses a twofold increase. This signifies that the expansion of DMUs is cost-effective. Conversely, a diminishing return to scale indicates that when the input is doubled, the output falls short of doubling. In this scenario, the constraints on DMUs are deemed reasonable.

In the contemporary business landscape, the enhancement of supply chain performance stands as the sole avenue to attain a competitive advantage in the global market. Thus, leveraging the Multiple BCC model within a complete supply chain, the initial step involves estimating the overall efficiency model and the efficiency at each level within the supply chain. Subsequently, the return-to-scale model of each level was estimated. Finally the return to scale model for complete supply chain was estimated. Given the pivotal role of the cement industry in national development, a thorough examination of total efficiency, efficiency at various levels, and the return to scale at each level and for the entire cement industry is conducted. This examination is based on the data from 2021 and employs the models and theorems expounded in this paper. The return to scale for 42 cement companies listed on the Stock Exchange, each comprising four levels (supplier, producer, distributor, and customer), is meticulously estimated.

The results of model execution indicate that, in the entire supply chain, 28 Companies exhibit constant return to scale. This implies that if inputs increase, the outputs also increase in the same proportion to the inputs. Therefore, economically, expanding or limiting DMUs

results in neither profit nor loss. However, based on the defined input indices in Table 1, various decision-making approaches can be considered. For instance:

1) Considering the eighth input index, "Total cost of salaries and wages paid" if the development of these 28 Companies leads to increased employment, it may not be financially beneficial for the company. Still, it could be considered a socially and culturally beneficial activity, contributing to job creation and preventing social harm overall.

2) Regarding the second input index, "Cost of green training and sustainability for addressing related issues along the supply chain", if the development of these 28 companies results in a healthier environment and a reduction in harmful effects from factory activities, it may not yield financial benefits for the company. However, it can be considered a useful activity for health and environmental sustainability, serving future generations.

Based on the above examples, the decision regarding whether a DMU should expand or not depends on the decision-maker.

The results of the model execution indicate that, in the entire supply chain, 14 remaining companies exhibit decreasing return to scale. This implies that if inputs increase, outputs increase less than the input ratio, economically justifying the limitation of DMUs.

Furthermore, executing the model using GAMS software revealed that 2 cement companies at the supplying level, 1 company at the production level, and 14 companies at the distributing level have ascending return to scale. It means that while the overall return to scale of these 42 companies is either constant or decreasing, some companies, according to the results in Table 3, exhibit ascending return to scale at various levels. In economic terms, this indicates that developing

these DMUs at specific levels within the supply chain is economically viable.

The analysis suggests that if a company's return to scale is upward at a specific level, it needs to be investigated whether the overall return to scale of that company is constant or decreasing. If the overall return to scale of the company throughout the supply chain is decreasing, and the return to scale at one of the levels is increasing, the development of this DMU at the intended level is not economically feasible. This means that by expanding a specific level of the company's chain where its return to scale has increased, the overall return to scale of the chain in the company remains reduced.

However, if the overall return to scale of the company throughout the supply chain is constant and the return to scale at one of the levels is increasing, the development of the company can be considered, depending on the decision-maker's perspective. It is recommended to consider relevant indicators regarding employment generation, reduction of social damages, health, environmental sustainability, etc.

The following topics are proposed for consideration as future research needs:

- Estimating return to scale in a four-level supply chain in the presence of uncontrollable and undesirable factors;
- Determining units with the Most Productive Scale Size (MPSS) in the green supply chain using data envelopment analysis;
- Presenting non-radial models for evaluating the performance of the complete supply chain with dependent and independent inputs and outputs;
- Determining left and right scale efficiencies in the 4-level green supply chain using data envelopment analysis;
- Furthermore, in future research, it would be possible to investigate the waste of intermediate outputs in the supply chain, resulting from the

imbalance between supply and demand in internal sectors. A comprehensive study on resource efficiency for the supply chain could also be presented.

## 6. REFERENCES

1. Charnes A, Cooper WW, Rhodes E. Measuring the efficiency of decision making units. *European journal of operational research*. 1978;2(6):429-44. [https://doi.org/10.1016/0377-2217\(78\)90138-8](https://doi.org/10.1016/0377-2217(78)90138-8)
2. Färe R, Grosskopf S. Intertemporal production frontiers: with dynamic DEA. *Journal of the operational research society*. 1997;48(6):656-. <https://doi.org/10.1057/palgrave.jors.2600779>
3. Färe R, Grosskopf S, Whittaker G. Network Dea II. Data Envelopment Analysis: A Handbook on the Modeling of Internal Structures and Networks. 2014:307-27. [https://doi.org/10.1016/S0038-0121\(99\)00012-9](https://doi.org/10.1016/S0038-0121(99)00012-9)
4. Saranga H, Moser R. Performance evaluation of purchasing and supply management using value chain DEA approach. *European journal of operational research*. 2010;207(1):197-205. <https://doi.org/10.1016/j.ejor.2010.04.023>
5. Chen C, Yan H. Network DEA model for supply chain performance evaluation. *European journal of operational research*. 2011;213(1):147-55. <https://doi.org/10.1016/j.ejor.2011.03.010>
6. Tavana M, Mirzagoltabar H, Mirhedayatian SM, Saen RF, Azadi M. A new network epsilon-based DEA model for supply chain performance evaluation. *Computers & Industrial Engineering*. 2013;66(2):501-13. <https://doi.org/10.1016/j.cie.2013.07.016>
7. Mirhedayatian SM, Azadi M, Saen RF. A novel network data envelopment analysis model for evaluating green supply chain management. *International Journal of Production Economics*. 2014;147:544-54. <https://doi.org/10.1016/j.ijpe.2013.02.009>
8. Shafiee M, Lotfi FH, Saleh H. Supply chain performance evaluation with data envelopment analysis and balanced scorecard approach. *Applied mathematical modelling*. 2014;38(21-22):5092-112. <https://doi.org/10.1016/j.apm.2014.03.023>
9. Grigoroudis E, Petridis K, Arabatzis G. RDEA: A recursive DEA based algorithm for the optimal design of biomass supply chain networks. *Renewable Energy*. 2014;71:113-22. <https://doi.org/10.1016/j.renene.2014.05.001>
10. Khodakarami M, Shabani A, Saen RF, Azadi M. Developing distinctive two-stage data envelopment analysis models: An application in evaluating the sustainability of supply chain management. *Measurement*. 2015;70:62-74. <https://doi.org/10.1016/j.measurement.2015.03.024>
11. Tajbakhsh A, Hassini E. A data envelopment analysis approach to evaluate sustainability in supply chain networks. *Journal of Cleaner Production*. 2015;105:74-85. <https://doi.org/10.1016/j.jclepro.2014.07.054>
12. Tavana M, Kaviani MA, Di Caprio D, Rahpeyma B. A two-stage data envelopment analysis model for measuring performance in three-level supply chains. *Measurement*. 2016;78:322-33. <https://doi.org/10.1016/j.measurement.2015.10.023>
13. Yousefi S, Soltani R, Saen RF, Pishvaei MS. A robust fuzzy possibilistic programming for a new network GP-DEA model to evaluate sustainable supply chains. *Journal of Cleaner Production*. 2017;166:537-49. <https://doi.org/10.1016/j.jclepro.2017.08.054>
14. Fathi A, Saen RF. A novel bidirectional network data envelopment analysis model for evaluating sustainability of distributive supply chains of transport companies. *Journal of Cleaner Production*. 2018;184:696-708. <https://doi.org/10.1016/j.jclepro.2018.02.256>
15. Darvish Motevalli MH, Hosseinzadeh Lotfi F, Shoja N, Gholamabari A. A new model for calculating the efficiency of existing cement companies with a network structure (an application of data envelopment analysis). *Financial engineering and portfolio management*. 2019;10(38):65-93. <https://doi.org/10.1007/s12251-019-165-1398-10.38.4.0>
16. Tavassoli M, Saen RF. Predicting group membership of sustainable suppliers via data envelopment analysis and discriminant analysis. *Sustainable Production and Consumption*. 2019;18:41-52. <https://doi.org/10.1016/j.spc.2018.12.004>
17. Torabi N, Tavakkoli-Moghaddam R, Najafi E, Hosseinzadeh-Lotfi F. A two-stage green supply chain network with a carbon emission price by a multi-objective interior search algorithm. *International Journal of Engineering, Transactions C: Aspects*. 2019;32(6):828-34. [10.5829/ije.2019.32.06c.05](https://doi.org/10.5829/ije.2019.32.06c.05)
18. Asadpour M, Boyer O, Tavakkoli-Moghaddam R. A blood supply chain network with backup facilities considering blood groups and expiration date: a real-world application. *International*

- Journal of Engineering, Transactions B: Applications. 2021;34(2):470-9. 10.5829/ije.2021.34.02b.19
19. Fathollahi-Fard AM, Dulebenets MA, Hajiaghahi-Keshteli M, Tavakkoli-Moghaddam R, Safaeian M, Mirzahosseini H. Two hybrid meta-heuristic algorithms for a dual-channel closed-loop supply chain network design problem in the tire industry under uncertainty. *Advanced engineering informatics*. 2021;50:101418. <https://doi.org/10.1016/j.aei.2021.101418>
  20. Moosavi S, Seifbarghy M. A robust multi-objective fuzzy model for a green closed-loop supply chain network under uncertain demand and reliability (a case study in engine oil industry). *International Journal of Engineering, Transactions C: Aspects*. 2021;34(12):2585-603. 10.5829/ije.2021.34.12c.03
  21. Sahraeian R, Afshar MA, Hosseini SMH. A bi-objective cold supply chain for perishable products considering quality aspects: a case study in Iran dairy sector. *International Journal of Engineering Transactions B: Applications*. 2022;35(2). 10.5829/ije.2022.35.02b.22
  22. Gholizadeh H, Fathollahi-Fard AM, Fazlollahtabar H, Charles V. Fuzzy data-driven scenario-based robust data envelopment analysis for prediction and optimisation of an electrical discharge machine's parameters. *Expert Systems with Applications*. 2022;193:116419. <https://doi.org/10.1016/j.eswa.2021.116419>
  23. Moosavi J, Fathollahi-Fard AM, Dulebenets MA. Supply chain disruption during the COVID-19 pandemic: Recognizing potential disruption management strategies. *International Journal of Disaster Risk Reduction*. 2022;75:102983. <https://doi.org/10.1016/j.ijdrr.2022.102983>
  24. Berlin D, Feldmann A, Nuur C. The relatedness of open and closed-loop supply chains in the context of the circular economy; framing a continuum. *Cleaner Logistics and Supply Chain*. 2022;4:100048. <https://doi.org/10.1016/j.ijdrr.2022.102983>
  25. Haghshenas P, Sahraeian R, Golmohammadi A-M. A state-of-the-art model of location, inventory, and pricing problem in the closed-loop supply chain network. *International Journal of Engineering, Transactions B: Applications*. 2022;35(8):1558-70. 10.5829/ije.2022.35.08b.12
  26. Asghari M, Afshari H, Mirzapour Al-e-hashem S, Fathollahi-Fard AM, Dulebenets MA. Pricing and advertising decisions in a direct-sales closed-loop supply chain. *Computers & Industrial Engineering*. 2022;171:108439. <https://doi.org/10.1016/j.cie.2022.108439>
  27. Simonetto M, Sgarbossa F, Battini D, Govindan K. Closed loop supply chains 4.0: From risks to benefits through advanced technologies. A literature review and research agenda. *International Journal of Production Economics*. 2022:108582. <https://doi.org/10.1016/j.ijpe.2022.108582>
  28. Mousapour Mamoudan M, Ostadi A, Pourkhodabakhsh N, Fathollahi-Fard AM, Soleimani F. Hybrid neural network-based metaheuristics for prediction of financial markets: a case study on global gold market. *Journal of Computational Design and Engineering*. 2023;10(3):1110-25. <https://doi.org/10.1093/jcde/qwad039>
  29. Ali SM, Fathollahi-Fard AM, Ahnaf R, Wong KY. A multi-objective closed-loop supply chain under uncertainty: An efficient Lagrangian relaxation reformulation using a neighborhood-based algorithm. *Journal of Cleaner Production*. 2023;423:138702. <https://doi.org/10.1016/j.jclepro.2023.138702>
  30. Banker RD, Charnes A, Cooper WW. Some models for estimating technical and scale inefficiencies in data envelopment analysis. *Management science*. 1984;30(9):1078-92. <https://doi.org/10.1287/mnsc.30.9.1078>
  31. Abri AG. An investigation on the sensitivity and stability radius of returns to scale and efficiency in data envelopment analysis. *Applied mathematical modelling*. 2013;37(4):1872-83. <https://doi.org/10.1016/j.apm.2012.04.047>
  32. Zhang Q, Yang Z. Returns to scale of two-stage production process. *Computers & industrial engineering*. 2015;90:259-68. <https://doi.org/10.1016/j.cie.2015.09.009>
  33. Alirezaee M, Hajinezhad E, Paradi JC. Objective identification of technological returns to scale for data envelopment analysis models. *European journal of operational research*. 2018;266(2):678-88. <https://doi.org/10.1016/j.ejor.2017.10.016>
  34. Wang Z, He W, Wang B. Performance and reduction potential of energy and CO2 emissions among the APEC's members with considering the return to scale. *Energy*. 2017;138:552-62. <https://doi.org/10.1016/j.energy.2017.07.059>
  35. Banker RD, Thrall RM. Estimation of returns to scale using data envelopment analysis. *European Journal of operational research*. 1992;62(1):74-84. [https://doi.org/10.1016/0377-2217\(92\)90178-C](https://doi.org/10.1016/0377-2217(92)90178-C)
  36. Alefeld G, Herzberger J. *Introduction to interval computation*: Academic press; 2012.

## COPYRIGHTS

©2024 The author(s). This is an open access article distributed under the terms of the Creative Commons Attribution (CC BY 4.0), which permits unrestricted use, distribution, and reproduction in any medium, as long as the original authors and source are cited. No permission is required from the authors or the publishers.



## Persian Abstract

### چکیده

امروزه، تمرکز بر کسب مزیت رقابتی در بازار جهانی کسب و کار در بهبود عملکرد زنجیره تامین نهفته است. در این مقاله سعی شده است نحوه بدست آوردن بازده به مقیاس در ساختار زنجیره تامین سبز چهار سطحی با استفاده از تحلیل پوششی داده‌ها مورد بررسی قرار گیرد. برای دستیابی به این هدف، با استفاده از مدل مضربی زنجیره تامین کامل، ابتدا بازده به مقیاس هر مرحله از زنجیره تخمین زده می‌شود و در نهایت منجر به تخمین بازده به مقیاس کل زنجیره تامین می‌گردد. جامعه آماری این پژوهش کاربردی، همسو با اهداف آن، ۴۲ شرکت سیمان می‌باشد. بازده به مقیاس این شرکتها که زنجیره متناظر هر یک از آنها دارای چهار سطح تامین کننده، تولیدکننده و توزیع کننده و مشتری می‌باشد، مورد ارزیابی قرار گرفتند. نتایج اجرای مدل نشان داد که در کل زنجیره، بازده به مقیاس ۲۸ شرکت ثابت و ۱۴ شرکت کاهش می‌باشد و از طرفی تعداد ۲ شرکت در بخش تامین کننده، ۱ شرکت در بخش تولیدکننده و ۱۴ شرکت در بخش توزیع کننده بازده به مقیاس صعودی دارند. یافته‌ها تأکید می‌کنند که از نظر اقتصادی افزایش بازده به مقیاس، گسترش واحدهای تصمیم‌گیری را مقرون‌به‌صرفه می‌کند و برعکس، کاهش بازده به مقیاس، محدودیت منطقی DMU ها را مقرون‌به‌صرفه می‌کند.



## Experimental Study on Self-compacting and Self-healing Concrete with Recycled Coarse Aggregates

R. Sreenu<sup>\*a</sup>, S. R. Suryawanshi<sup>b</sup>, A. Ashish<sup>a</sup>

<sup>a</sup> Department of Civil Engineering, Anurag University, Ghatkesar, Hyderabad, Telangana, India

<sup>b</sup> Department of Civil Engineering, SVNIT-Surat, Gujarat, India

### PAPER INFO

#### Paper history:

Received 21 August 2023

Received in revised form 25 September 2023

Accepted 26 September 2023

#### Keywords:

Bacteria

Self-healing

Cell Concentration

Bacillus Licheniformis

Fly Ash

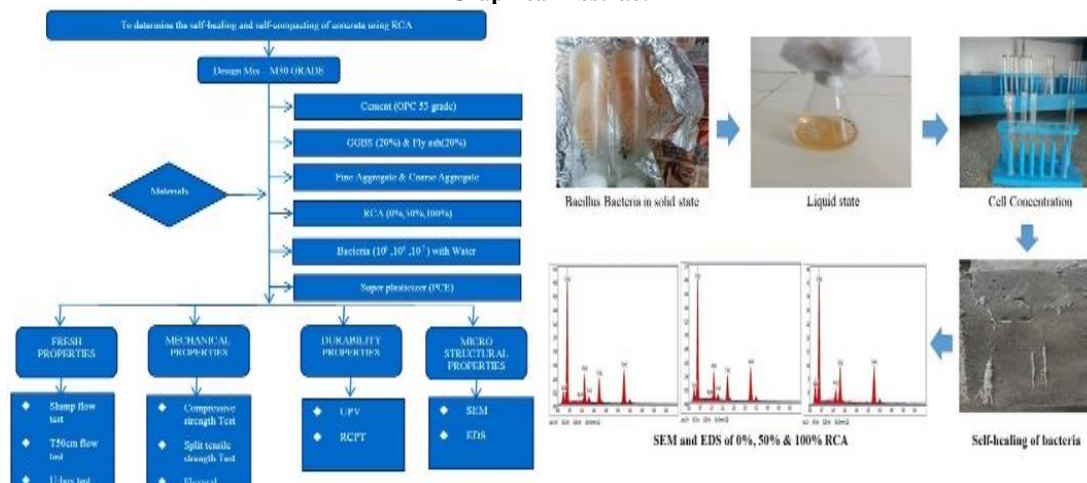
Ground Granulated Blast Furnace Slag

### ABSTRACT

This study focuses on evaluating the effectiveness of various cell concentrations of bacillus bacteria in mending cracks within recycled concrete containing coarse aggregates. In this investigation, the introduction of bacillus bacterial sustainable concrete as a solution for addressing crack repairs. This innovative concrete formulation not only provides environmentally friendly alternatives but also offers economic benefits. This research involves the incorporation of coarse aggregates into the concrete mix, along with the partial substitution of cement by Fly ash and Ground Granulated Blast Furnace Slag (GGBS), each accounting for 20% of the mix. The coarse aggregates consist of Recycled Concrete Aggregate (RCA) in varying proportions: 0%, 50%, and 100%. Additionally, *Bacillus licheniformis* was used at concentrations of  $10^3$ ,  $10^5$ , and  $10^7$  cells/mL, respectively. The findings indicate a positive correlation between the healing percentage of cracks, as measured by Ultrasonic Pulse Velocity (UPV), and the concentration of bacteria. Furthermore, it is observed that recycled aggregates possess inherent pores that allow for water absorption through these pores. Therefore, RCA is subjected to a 24-hour water immersion process before its incorporation into the concrete mix. While the compressive strength of the concrete remains consistent between RCA 0% and RCA 50%, it decreases significantly at RCA 100%. However, the performance of the bacteria exhibits proportionality to cell concentration. Notably, the effectiveness of the bacteria remains consistent regardless of changes in RCA proportions. This study underscores the promising potential of Bacillus bacteria in enhancing the durability and sustainability of concrete structures, with particular relevance to RCC applications.

doi: 10.5829/ije.2024.37.04a.05

### Graphical Abstract



\*Corresponding Author Email: [d19am002@amd.svni.ac.in](mailto:d19am002@amd.svni.ac.in) (R. Sreenu)

Please cite this article as: Sreenu R, Suryawanshi SR, Ashish A. Experimental Study on Self-compacting and Self-healing Concrete with Recycled Coarse Aggregates. International Journal of Engineering, Transactions A: Basics. 2024;37(04):625-34.

**NOMENCLATURE**

RCA	Recycled coarse aggregates	UPV	Ultrasonic Pulse Velocity
SCC	Self-compacting concrete	RCPT	Rapid Chloride Permeability Test
CaCO <sub>3</sub>	Calcium carbonate	C	Calcite
SCMs	Supplementary cementitious materials	CSH	Calcium Silicate Hydrate

**1. INTRODUCTION**

The emergence of self-compacting concrete (SCC) has sparked a revolution in concrete technology, offering unparalleled filling capacity and ease of placement without the need for traditional compaction methods. SCC's unique properties make it adept at maintaining stability and workability while minimizing issues such as bleeding and segregation, resulting in significant labour and cost savings in construction processes (1). However, these advantages often come at the expense of durability and strength, critical design criteria for structural applications (2). One of the key challenges associated with SCC is the presence of free water, which can adversely affect the strength and durability of concrete. This is due to its impact on the microstructure of the aggregate paste's interfacial transition zone (ITZ) and increased capillary porosity of the hardened paste (3). To address this issue, supplementary cementitious materials (SCMs) like fly ash, ground granulated blast furnace slag (GGBS), pozzolans, cement kiln dust, sugarcane bagasse ash, and rice husk ash (RHA) are commonly employed to enhance both the mechanical and durability properties of concrete while reducing CO<sub>2</sub> emissions (4). The environmental concern surrounding construction waste management (CWM) has taken centre stage in many Indian municipalities, as they grapple with the disposal of an annual production of 150 million tons of construction waste, accounting for 35%–40% of the world's construction and demolition (C&D) trash (5). These wastes often end up in landfills, causing significant negative environmental impacts. Recycling concrete waste into aggregates provides an environmentally friendly solution, reducing construction costs while mitigating environmental issues. However, recycled concrete aggregate (RCA) presents challenges due to the presence of micro-cracks and increased porosity resulting from the crushing process (6). Moreover, the old cement paste in RCA accounts for approximately 30–35% of its volume, complicating the microstructure of RCA concrete/mortar by forming a dual ITZ when mixed with new mortar/cement (6). Previous research has shown that using RCA to replace natural aggregates, either partially or entirely, leads to a 20% reduction in compressive strength, further highlighting the need for innovative solutions. To enhance the properties of RCA concrete/mortar, various methods have been explored, including surface treatments to remove adhered mortar, bio-deposition techniques to reduce RCA porosity, and

the use of SCMs such as fly ash, silica fume, and GGBS to densify the pore system by promoting the formation of calcium silicate hydrate. Additionally, immersing RCA in acidic solutions to reduce adhered mortar and allowing dehydrated cement paste to hydrate in water have shown promise in improving RCA's properties (7). Concrete cracks pose further challenges as they expose reinforcement to the environment, potentially leading to corrosion. To address this issue, bacteria have been harnessed to facilitate crack healing in what is commonly referred to as "Bio concrete" or "Bacterial concrete." These bacteria, including non-pathogenic species like *Bacillus subtilis*, *Bacillus cereus*, *Bacillus licheniformis*, and *Bacillus halodurans*, are incorporated into concrete to initiate bio-calcification, a process where microorganisms secrete calcium precipitate externally. This calcium precipitate, typically in the form of CaCO<sub>3</sub>, fills the cracks, increasing the concrete's compactness and preventing the formation of new cracks (8). Moreover, this bio-calcification process reduces carbon dioxide emissions, aligning with sustainability goals. The effectiveness of these bacteria in crack repair has been demonstrated through increased strength in concrete samples containing them, and their indirect use allows for greater flexibility and cost-effectiveness (9). In summary, the concrete industry has seen a transformation with the advent of SCC and the pursuit of sustainable solutions in the face of CWM challenges and concrete cracks. These advancements, from the use of SCMs in SCC to the innovative approaches for improving RCA and the incorporation of bacteria for crack healing, offer promising avenues for enhancing the performance and sustainability of concrete in construction. This study explores these developments in detail and assesses their potential to shape the future of concrete technology.

**2. RESEARCH SIGNIFICANCE**

Pachaivannan et al. (10) conducted an experimental analysis of the self-healing properties of bacterial concrete, shedding light on the material's ability to autonomously repair cracks and fissures. The study provided valuable insights into the practical application of this innovative construction material.

Iswarya and Adalarasan (11) focused on the strength and durability of lightweight bacterial concrete, exploring its potential to meet the structural requirements of various construction projects. Their investigation

emphasized the importance of optimizing bacterial concentration for improved performance. Jagannathan (12) studied the mechanical properties of bacterial concrete using two different bacterial species, expanding our understanding of the role of microorganisms in enhancing concrete strength and resilience. Ameri et al. (13) investigated the optimum content of rice husk ash and bacterial concentration in self-compacting concrete, contributing to the sustainability aspect of bacterial concrete production. David et al. (14) explored the utilization of medical vial glass waste in bio-concrete, showcasing the potential to incorporate waste materials into construction processes. Rautray et al. (15) delved into the performance of self-compacting geopolymer concrete using *Bacillus licheniformis*, offering an alternative perspective on the application of bacteria in sustainable construction materials. On silica-based immobilization, Agarwal et al. (16) investigated bacterial concrete with micronized biomass silica, highlighting the importance of immobilization techniques for ensuring bacterial activity and longevity. Druga et al. (17) conducted comprehensive microbiological studies to screen bacteria for self-healing concrete, emphasizing the significance of selecting suitable bacterial strains for optimal results. On impact of compressive strength, Rao et al. (18) explored the impact of bacteria on the compressive strength of cement mortar and concrete, providing valuable data for structural engineers and designers. Vaezi et al. (19) examined recycled microbial mortar and assessed the effects of bacterial concentration and calcium lactate content, contributing to the sustainable utilization of bacteria in construction. Rohini and Padmapriya (20) studied the effect of *Bacillus subtilis* on e-waste concrete, showcasing the versatility of bacterial concrete in diverse applications. About encapsulation in expanded clay, Lucas et al. (21) investigated self-healing properties in concrete with bacteria encapsulated in expanded clay, offering innovative approaches to delivering bacteria within the concrete matrix. Xu and Wang (22) explored the use of bacteria-containing low-alkali cementitious materials for the self-healing of concrete cracks, paving the way for novel approaches to bacterial concrete production. Rauf et al. (23) compared the performance of different bacteria immobilized in natural fibres, contributing to the development of modified bacterial concrete solutions. Wang et al. (24) studied polymeric healing materials, and bacterial  $\text{CaCO}_3$  precipitation may also be exploited for self-healing. It is more environmentally friendly and more suited to the concrete matrix. Seifan et al. (25) highlighted the potential of bio concrete as the next generation of self-healing construction materials, emphasizing its role in sustainable and resilient infrastructure. Onyelowe et al. (26). carried out by studying the compressive strength of concrete formed from recycled aggregate and utilizing a unique artificial

neural network (ANN), which makes use of a sigmoid function and allows the formulation of closed-form equations, an intelligent prediction is made. Akhtar et al. (27) investigated ways to improve the self-healing capacity of concrete by introducing various bacteria either separately or in combination with various mineral additions. It has been observed that a number of renovated approaches are awaiting approval in order to address the shortcomings of concrete and boost its toughness and longevity. Balamuralikrishnan et al. (28) conducted on a new ultrafine material called Alccofine (AF), produced from glass waste, and it was carried out as testing materials for the partial replacement. The vast array of experimental studies in the realm of self-healing concrete, coupled with advancements in sustainability and waste utilization, underscores the transformative potential of bacterial concrete in the construction industry. These studies not only expand our knowledge but also provide practical insights and solutions that hold the promise of a more resilient, eco-friendly, and durable infrastructure. The ongoing debate and exploration in this field signal an exciting future for construction materials and their impact on the built environment.

### 3. EXPERIMENTAL PROGRAM

#### 3. 1. Materials

**3. 1. 1. Cement** Grade 53 ordinary Portland cement (OPC) that complies with IS:269-2015 specifications has a specific gravity of 3.10, a fineness of 6%, a standard consistency of 34%, an initial setting time of 36.3 minutes, and a soundness of 9 mm.

**3. 1. 2. Fly Ash** From PRISM JOHNSON LIMITED, IDA Nacharam, the fly ash is collected. With a specific gravity of 2.91, fineness of 5%, standard consistency of 26%, and an initial setting of 30 minutes, Class-F fly ash is utilized.

**3. 1. 3. GGBS** PRISM JOHNSON LIMITED, IDA Nacharam, also contributes to the GGBS collection. The GGBS's initial setting was 38 minutes, with a specific gravity of 2.91, fineness of 5%, and standard consistency of 32%.

**3. 1. 4. Fine Aggregate** The river sand in grading zone 2 of IS:383-2016 has a fineness modulus of 2.56, specific gravity of 2.89, bulk density of  $0.788 \text{ kg/m}^3$ , void ratio of 5.549, porosity of 72, and water absorption of 2%. Therefore, fine aggregate forms the S-curve.

**3. 1. 5. Coarse Aggregate** According to IS:383-2016, with a maximum dimension of 16 mm for the crushed stone and the following specifications was utilized as coarse aggregate: specific gravity of 2.781,

bulk density of  $0.665 \text{ kg/m}^3$ , void ratio of 5.959, porosity of 76, and water absorption of 0.4% (29).

**3. 1. 6. Recycled Coarse Aggregates (RCA)** The construction and demolition (C&D) company Nagole is where the recycled coarse aggregates (RCA) are gathered. 16mm-sized aggregates are used.

**3. 1. 7. Water** According to IS:456-2000, to combine and cure, portable water is employed and has a pH of 6.98, 360 mg/L of alkalinity, 45 mg/L of acidity, and 685.8 mg/L of total dissolved solids (TDS). The ratio of water to cement is 0.47.

**3. 1. 8. Bacteria** The microbial type culture collection (MTCC), Hyderabad, is where the bacteria *Bacillus licheniformis* (MTCC NO: 2588) was found. It is a mesophilic, gram-positive bacterium. The "Bacteria culturing" method is used to transfer and propagate the organism from nutrient agar media to both culture of the bacteria into a liquid phase. Cell concentration is then carried out to determine the capacity of cells/mL.

**3. 2. Mix Design** The SCC mixture ratios that were following the IS 10262:2019 process (30). In every combination, Fly ash and GGBS replace cement to the amount of 20%. At 0%, 50%, and 100%, RCA replaces the coarse aggregates. Bacteria are used in every mix at  $10^3$ ,  $10^5$ , and  $10^7$  cells/mL proportions. As per IS: 516:2019, the freshly mixed composites are cast into cubes, cylinders, and prisms after being assessed for their fresh properties. The materials are cured for 7 and 28 days. Every bacterial sample is subjected to the UPV test to assess the bacteria's capacity for self-healing. The sample is once more put in a curing tank to repair the cracks after being tested under compression. The UPV test is then performed 28 days later. According to ASTM C1202, the RCPT is done to determine whether a material is resistant to chloride ions penetrating it. The RCA 0%, 50%, and 100% samples were cast for 28 days.



Figure 1. Bacillus Bacteria in solid phase



Figure 2. Liquide phase



Figure 3. Cell Concentration

**3. 3. METHODOLOGY** The main focus of the current experiment was RCA in self-healing and self-compacting concrete. The study's primary interest was in the physical, fresh, mechanical, durability and microstructural characteristics of various RCA mix percentages and bacterial cell concentrations. M30 grade concrete was taken into consideration since an additional parametric study included a rise in the percentage of RCA in SCC. The majority of the characteristics of SCC is fresh features. The basic objective of the mix design is to preserve uniformity without segregation, flow through densely packed reinforcement without vibrating, and flow under its own weight. SCC is more workable than what is meant by "very high" workability in IS: 456: 2000 (30). For concrete that is referred to as self-compacting, it must have the following qualities: "Filling ability," "Passing ability," and "Resistance to segregation." In an effort to define these qualities, many test procedures have been developed. Nevertheless, the EFNARC standard and recommendations served as the basis for, the set of test procedures for the SCC's workability qualities. The permeability of the surface layer, which should prevent the entry of substances that can start or spread possibly harmful processes, is closely linked to the durability of a concrete structure. ( $\text{CO}_2$ , chloride, sulphate, water, oxygen, alkalis, acids, etc.). In fact, resilience is influenced by the type of materials used, the composition

of the concrete, and the level of supervision utilized during placement, compaction, finishing, and curing. The formwork and re-bars or other components are in close proximity, which causes vibration issues, honeycomb and lack of compaction of the surface layer have been linked in part to the inferior durability performance of reinforced concrete structures subjected to hard circumstances. To prevent this, SCC was initially created in Japan for several reasons, among them. Tamping is a discontinuous procedure that vibrates the material to compact it in traditional vibrated concrete. Internal vibration, even when done correctly, does not lead to an even distribution of compaction energy across the whole volume of concrete inside the vibrator's area of effect. This suggests that there is still area of vibrated concrete that are over and under-vibrated. Depending on where the vibration sources are located, external vibration produces essentially heterogeneous compaction, much like internal vibration does. The vibration causes the concrete in the structure to have uneven compaction and varying permeabilities, which makes it easier for harmful substances to be absorbed selectively. It should go without saying that inappropriate vibration's effects segregation, honeycombing, bleeding, etc. have a significantly higher detrimental effect on permeability

and, consequently, durability. Self-compacting concrete will be free of these problems provided it possesses the necessary characteristics. It will also offer a material with consistently low and uniform permeability, fewer weak spots for the damaging impacts of the environment, and improved durability. The greater durability of self-compacting concrete satisfies the need for sustainability because maintenance and repairs can be delayed or minimized. As a result, it can be argued that SCC structures and elements endure longer because of the material's increased durability, which comes directly from its higher interfacial transition zone quality and lower inclination to crack in comparison to standard concrete. The various materials used to mix the concrete, mixed design and test conducted on bacterial concrete are clearly shown in Figure 4.

#### 4. BACTERIA CULTURING

Bacteria exhibited greater strength. The usage of bacteria is indirect. There is an improvement in healing by employing bacteria in cell concentration. Using this procedure, we can employ more bacteria, and the cost is

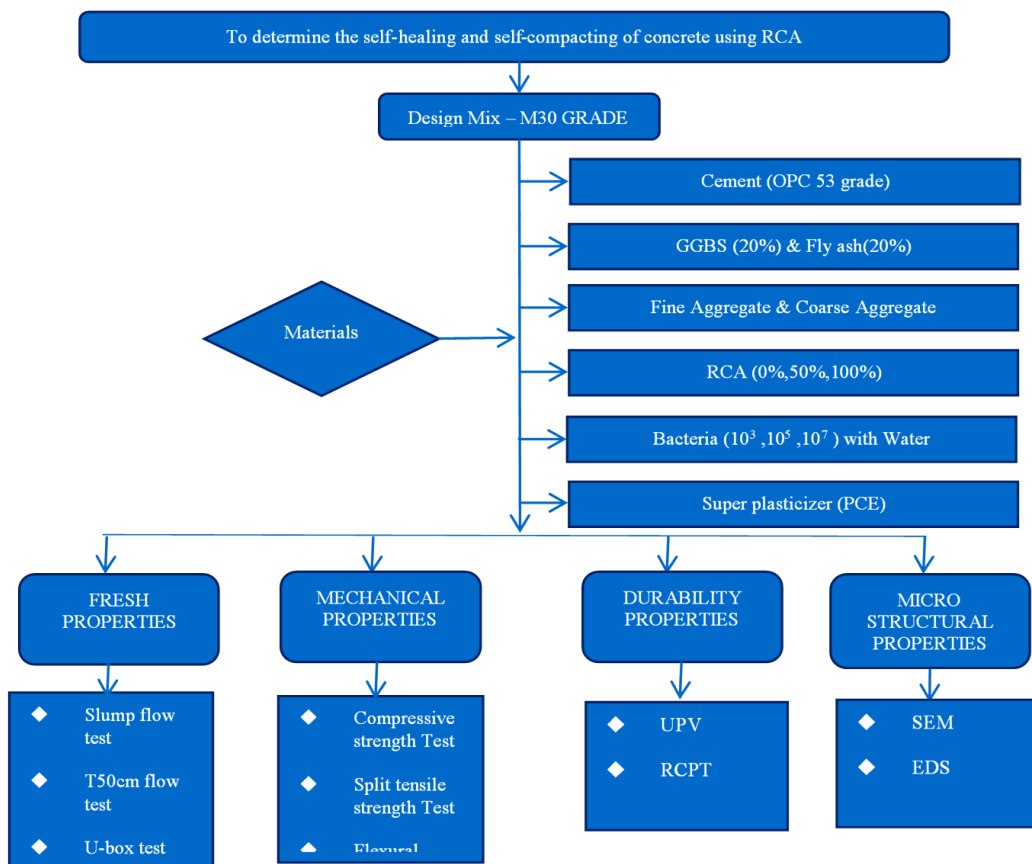


Figure 4. Schematic representation of methodology and characterizations

lower. Liquid culture is one way to cultivate bacteria. In this technique, in an upright flask, the preferred bacteria are suspended in a liquid nutrient media, such as Luria Broth. This enables the growth of numerous microorganisms for use in numerous subsequent processes. Liquid cultures are perfect for the preparation of an antimicrobial assay, which entails inoculating liquid broth with bacteria and allowing it to grow overnight. They may use a shaker for uniform growth. Afterwards, they would remove a piece of the sample to conduct a particular drug or protein's antibacterial activity (antimicrobial peptides). These cultures don't shake and offer an oxygen gradient to the microorganisms. The microbial type culture collection (MTCC), Hyderabad, is where the bacteria *Bacillus licheniformis* (MTCC NO: 2588) was supplied. It is a mesophilic, gram-positive bacterium. The "Bacteria culturing" method is used to change the solid phase of the bacteria into a liquid phase. As shown in Figures 1, 2 and 3. Cell concentration is then conducted to ascertain the capacity of cells/mL.

**4. 1. Fresh Properties** All combinations are picked to fall in the SF2 class of slump. The range of the slump flow is from a diameter of 710 to 745. To improve the slump flow, the superplasticizer PCE is utilized. There is an increase in slump flow depending on how much RCA is used. This is because RCA aggregates are entirely different from natural aggregates. Natural aggregates have sharp edges, whereas RCA has smooth edges. Because RCA contains materials that have been used before. Because of its smooth surface, it flows readily, increasing the slump. However, RCA notices more water because of its porous nature. In this instance, the RCA is cleaned and soaked in water for a day before casting. According to the addition of RCA, the time of T50 flow differs. It received a range of 3.2 to 3.9 seconds. The amount of RCA increases as the time decreases. According to EFNARC, it corresponds to VF2 in the V-funnel. The data spans between 9 and 10 seconds. As the RCA rises, the outcomes of the V-funnel duration shorten. U-box is used to determine the filling capacity. It includes data between 20 and 25. The U-box values drop as the RCA rises. The passing ability is located using the L-box method. The values, which fall within the PA2 class, range from 0.88 to 0.96. L-box values are raised as the RCA rises. EFNARC regulations are applied to all fresh properties.

**4. 2. Mechanical Properties** Results for the SCC mixes with RCA's 7 and 28 days, the results of experiments for compressive strength, with values ranging from 19.84 to 51.84 Mpa. The 50% RCA addition has strength that is roughly equivalent to that of a conventional mix, but a 100% RCA addition has the



Figure 5. Self-healing of bacteria

least strength. Up to 50% can be used with RCA. Bacteria in this instance have no impact on strength. Samples including and excluding bacteria both have equivalent strengths. The samples had good results because Flyash and GGBS work to increase the strength. The split tensile strength test results for SCC mixes with RCA, demonstrate that 50% RCA produces better results than 100% RCA. The results fall in the 1.74 to 4.14 MPa range. It shows that an increase in RCA decreases the strength. The flexural strength tests for the RCA SCC mixtures, with results in the range of 2.16 to 5.46 MPa according to the findings, a rise in RCA reduces concrete's strength.

**4. 3. Durability Properties** To find bacteria that are capable of self-healing, ultrasonic pulse velocity (UPV) is been used. The quality of concrete is produced by transmitting electronic waves. On these bacterial cubes, UPV is tested. The UPV value drops when a crack appears in concrete; after that, bacteria fill the gap and it heals itself.  $\text{CaCO}_3$  precipitation takes place to repair the cracks. The cube is tested before and after the compressive test. The curing tank is next used to preserve it. The same sample is analyzed after 7 and 28 days.

Bacteria cell concentrations of  $10^3$ ,  $10^5$ , and  $10^7$  are tested using the UPV method. The self-healing cube after 28 days is shown in Figure 5. Due to its ease of use and speed, the Rapid Chloride Permeability Test (RCPT) gauges concrete's resistance to chloride ion infiltration. The RCA 0%, 50%, and 100% samples were evaluated. It demonstrates that a rise in RCA decreases chloride permeability.

#### 4. 4. Microstructural Properties

**4. 4. 1. SEM Analysis** From Figure 6, it is observed that the control mix's SEM image of 0% RCA, where precipitation of calcite (C) and calcium silicate hydrate (CSH) can be seen. Due to the normal aggregate's presence in the mix, the binding properties between gel and aggregates are more effective, these are leads to better- resisting properties. Figure 7 demonstrates the

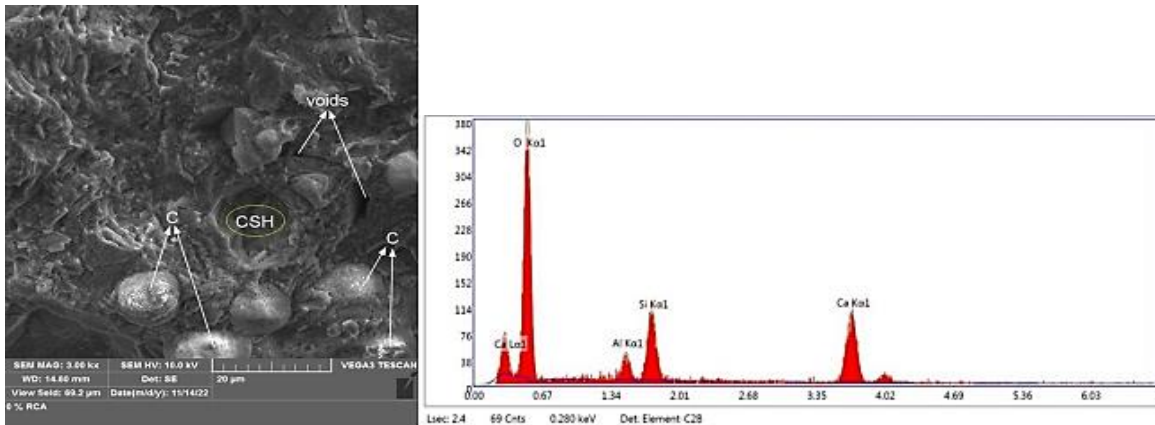


Figure 6. SEM and EDS of 0% RCA

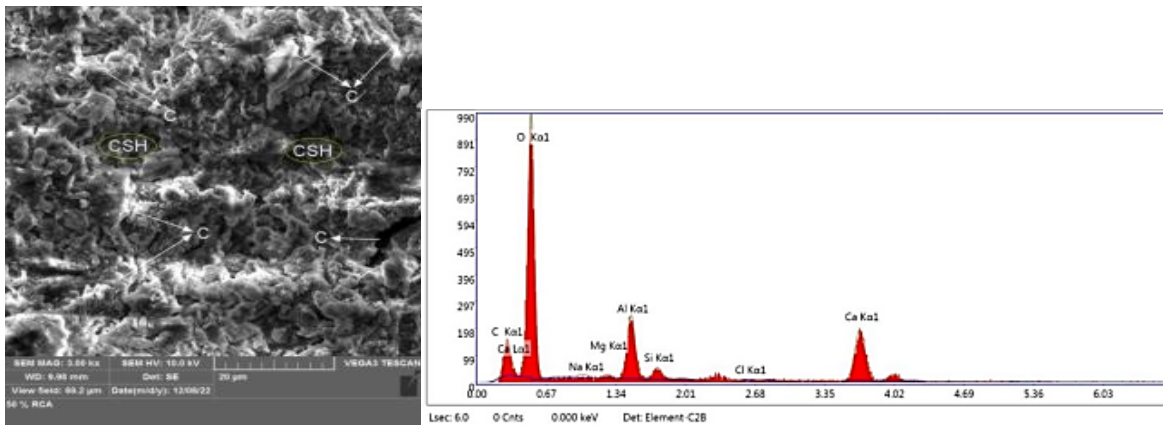


Figure 7. SEM and EDS of 50% RCA

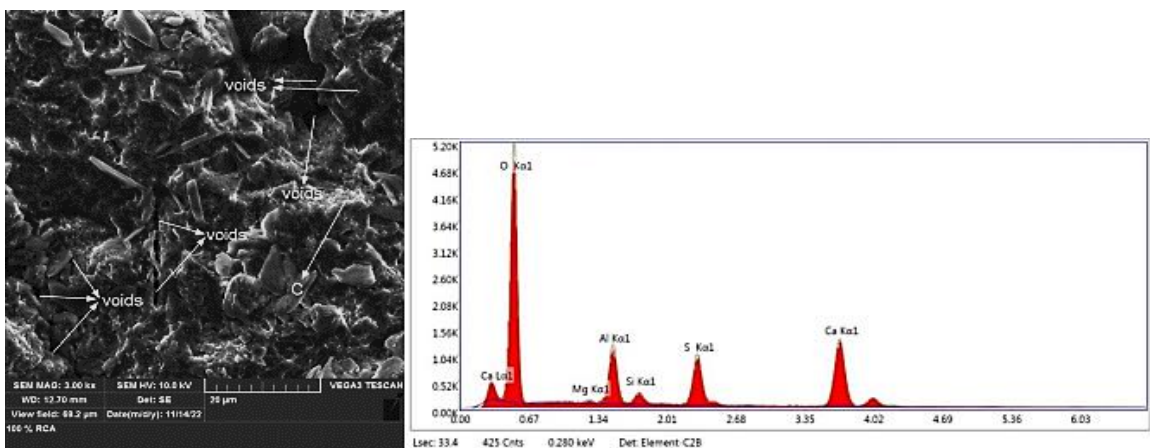


Figure 8. SEM and EDS of 100% RCA

increased CSH gel formation and calcite (C) precipitation by bacterial cells in the sample with 50% RCA. The 50% RCA concrete's pore reinforcing, water absorption, and permeability were all dramatically reduced as a result of

the CSH gel formation, and a higher strength was attained. Calcite filled in spaces and pores in the concrete, improving the pore structure, which led to increased strength development and decreased

permeability. There are numerous voids and microspores visible in Figure 7, which is 100% RCA. Due to the Recycled Aggregate presence in the mix, the binding properties between gel and aggregates are less effective, which leads to a reduction in resisting properties. In comparison to mixtures of  $10^3$  and  $10^5$  cells/mL, more densification pore structure, and a uniform concrete matrix were created as a result created. Because of this, a larger cell concentration causes more calcite to precipitate. This is a result of how quickly bacteria's cell membranes cause calcium hydroxide to carbonate. Even yet, several pores and cracks are visible, which may have developed during the compression test due to the RCA's complete replacement with a less dense matrix. As seen in the above Figures, the EDS spectra match the sample's scanned areas. The elements that were found and their associated percentages.

**4. 4. 2. EDS Spectra** Together with the discovered elements and their associated percentages, EDS spectra for the scanned areas of RCA 0% (control concrete), RCA 50%, and RCA 100% containing bacteria are displayed. The primary elements in the control concrete were silicon (Si; 9.24%), calcium (Ca; 36.97%), and oxygen ( $O_2$ ; 50.45%). The amount of  $O_2$  was raised in the RCA of 50% and the amount of  $O_2$  was reduced in the RCA of 100%. For illustrative purposes, the calcium content was reduced from 36.94% in RCA0% to 30.86% in RCA 50% correspondingly. However, there was a decrease in the silicon concentration of the RCA mix, going from 9.24% in RCA 0% to 1.63%. As was previously mentioned, pore obstruction at the specimen's surface prevented the formation of calcite and CSH gel.

The calcium content and silicon content of the RCA 100% mix were lower than those of the RCA 50% and RCA 100% as samples were obtained from the inside of the concrete specimens for SEM and EDS analyses.

## 5. CONCLUSION

The results of the presented parametric experimental study enable the following inferences:

- While the amount of material produced from some of the mixes surpassed the EFNARC's maximum limit, all of the mixes had acceptable flowability and self-compaction properties. Addition of RCA increased the fresh characteristics by 5%. The filling and passing performance of concrete that uses RCA as a partial replacement for coarse aggregates is good. The fresh concrete's characteristics are not dramatically changed by addition of bacteria cells.
- Compared to 100% RCA, RCA of 50% replacement has good strength. Nearly equal to conventional

concrete is the 50% RCA. Similar to mechanical characteristics, 50% RCA content yields the optimum durability characteristics.

- The durability and strength of the concrete are unaffected by the addition of bacteria. Bacteria recover faster when cell concentration is higher. Compared to  $10^3$  and  $10^5$ , a bacterial cell concentration of  $10^7$  has greater healing potential.
- According to the UPV test, the cracks have healed more for the 28-day sample than for the 7-day sample. The bacteria, therefore, requires time to recover. The period of time increases the rate of bacterial growth increases.
- SEM examination findings reveal that concrete with an RCA concentration of 50% has a denser matrix than concrete with an RCA level of 100%. The pores and spaces within the specimen are further diminished by the addition of bacterial cells through calcite precipitation.
- However, the results of the EDS analysis show that the excessive precipitated calcite on the specimen's surface stops water from penetrating into the inner matrix, lowering the hydration of cement and calcite precipitation inside the specimen, even at a high bacterial cell concentration of  $10^7$  cells/ mL.
- The result of this study demonstrates that higher bacterial cell concentration increases concrete's resistance to water infiltration and other damaging substances. The experimental analysis of self-healing properties in concrete using recycled coarse aggregates and bacteria presents a compelling case for the feasibility and advantages of this innovative construction material. These findings suggest that such concrete formulations can offer structural robustness and self-healing capabilities, contributing to the sustainability and longevity of concrete structures in various applications such as buildings and other civil engineering structures.

The future scope of experimental studies on self-compacting and self-healing concrete with recycled coarse aggregates holds significant potential. Research in this field can evolve to address critical challenges, such as fine-tuning the incorporation of recycled aggregates for optimal mechanical properties, advancing bacterial strains and immobilization techniques for improved healing efficiency, and expanding the application of this innovative concrete in large-scale infrastructure projects. Furthermore, exploring the integration of smart technologies for real-time monitoring, standardizing production processes, and conducting extensive field trials can pave the way for the widespread adoption of this sustainable and resilient construction material, making a substantial contribution to the construction industry's environmental and structural advancements.

## 6. REFERENCES

- Santos S, Da Silva P, De Brito J. Self-compacting concrete with recycled aggregates—a literature review. *Journal of Building Engineering*. 2019;22:349-71. <https://doi.org/10.1016/j.jobe.2019.01.001>
- Faraj RH, Ali HFH, Sherwani AFH, Hassan BR, Karim H. Use of recycled plastic in self-compacting concrete: A comprehensive review on fresh and mechanical properties. *Journal of Building Engineering*. 2020;30:101283. <https://doi.org/10.1016/j.jobe.2020.101283>
- Kavyateja BV, Jawahar J, Sashidhar C. Durability performance of self compacting concrete incorporating alccofine and fly ash. *International Journal of Engineering, Transactions B: Applications*. 2020;33(8):1522-8. 10.5829/IJE.2020.33.08B.10
- Ndahirwa D, Zmamou H, Lenormand H, Leblanc N. The role of supplementary cementitious materials in hydration, durability and shrinkage of cement-based materials, their environmental and economic benefits: A review. *Cleaner Materials*. 2022:100123. <https://doi.org/10.1016/j.clema.2022.100123>
- Elshaboury N, Al-Sakkaf A, Mohammed Abdelkader E, Alfalah G. Construction and demolition waste management research: A science mapping analysis. *International journal of environmental research and public health*. 2022;19(8):4496. <https://doi.org/10.3390/ijerph19084496>
- Kim J, Grabiec AM, Ubysz A. An experimental study on structural concrete containing recycled aggregates and powder from construction and demolition waste. *Materials*. 2022;15(7):2458. <https://doi.org/10.3390/ma15072458>
- Senaratne S, Lambrousis G, Mirza O, Tam VW, Kang W-H. Recycled concrete in structural applications for sustainable construction practices in Australia. *Procedia engineering*. 2017;180:751-8. <https://doi.org/10.1016/j.proeng.2017.04.235>
- Mahmod AK, Al-Jabbar LA, Salman MM, editors. *Bacteria Based Self-Healing Concrete: A Review*. 2<sup>nd</sup> online Scientific conference for Graduate Engineering Students, Journal of Engineering and Sustainable Development; 2021.
- Van Tittelboom K, De Belie N, De Muynck W, Verstraete W. Use of bacteria to repair cracks in concrete. *Cement and concrete research*. 2010;40(1):157-66. <https://doi.org/10.1016/j.cemconres.2009.08.025>
- Pachaivannan P, Hariharasudhan C, Mohanasundram M, Bhavani MA. Experimental analysis of self healing properties of bacterial concrete. *Materials Today: Proceedings*. 2020;33:3148-54. 10.1016/j.matpr.2020.03.782
- Iswarya N, Adalarasan R. Experimental investigation on strength and durability of light weight bacterial concrete. *Materials Today: Proceedings*. 2020;22:2808-13. <https://doi.org/10.1016/j.matpr.2020.03.412>
- Jagannathan P. Studies on the mechanical properties of bacterial concrete with two bacterial species. *Materials Today: Proceedings*. 2018;5(2):8875-9. <https://doi.org/10.1016/j.matpr.2017.12.320>
- Ameri F, Shoaie P, Bahrami N, Vaezi M, Ozbakkaloglu T. Optimum rice husk ash content and bacterial concentration in self-compacting concrete. *Construction and Building Materials*. 2019;222:796-813. 10.1016/j.conbuildmat.2019.06.190
- Franchis David M, Mohan kumar G, Raambalaji C, Subaranjani S, Muthusivashankar A, Chandra Bose J. Experimental investigation on bio-concrete with medical vial glass waste. *Asian Journal of Civil Engineering*. 2021;22:59-71. 10.1007/s42107-020-00298-0
- Rautray SS, Mohanty BN, Das MR. Performance of self-compacting geopolymer concrete using *Bacillus Licheniformis*. *Materials Today: Proceedings*. 2020;26:2817-24. 10.1016/j.matpr.2020.02.587
- Agarwal A, Bhusnur S, Chaudhary K, Priya TS. Experimental investigation on bacterial concrete with micronized biomass silica. *Materials Today: Proceedings*. 2020;22:2475-81. 10.1016/j.matpr.2020.03.375
- Durga CSS, Ruben N, Chand MSR, Indira M, Venkatesh C. Comprehensive microbiological studies on screening bacteria for self-healing concrete. *Materialia*. 2021;15:101051. 10.1016/j.mtla.2021.101051
- Rao PP, Asadi S, Krishna MR, Babu AS, Alla S. An experimental investigation of bacteria impact on compressive strength of cement mortar and concrete. *Materials Today: Proceedings*. 2021;43:1949-55. 10.1016/j.matpr.2020.11.213
- Vaezi M, Zareei SA, Jahadi M. Recycled microbial mortar: Effects of bacterial concentration and calcium lactate content. *Construction and Building Materials*. 2020;234:117349. <https://doi.org/10.1016/j.conbuildmat.2019.117349>
- Rohini I, Padmapriya R. Effect of bacteria subtilis on e-waste concrete. *Materials Today: Proceedings*. 2021;42:465-74. <https://doi.org/10.1016/j.matpr.2020.10.192>
- Lucas SS, Moxham C, Tziviloglou E, Jonkers H. Study of self-healing properties in concrete with bacteria encapsulated in expanded clay. *Science and Technology of Materials*. 2018;30:93-8. 10.1016/j.stmat.2018.11.006
- Xu J, Wang X. Self-healing of concrete cracks by use of bacteria-containing low alkali cementitious material. *Construction and Building Materials*. 2018;167:1-14. <https://doi.org/10.1016/j.conbuildmat.2018.02.020>
- Rauf M, Khaliq W, Khushnood RA, Ahmed I. Comparative performance of different bacteria immobilized in natural fibers for self-healing in concrete. *Construction and Building Materials*. 2020;258:119578. 10.1016/j.conbuildmat.2020.119578
- Wang J, Van Tittelboom K, De Belie N, Verstraete W. Use of silica gel or polyurethane immobilized bacteria for self-healing concrete. *Construction and building materials*. 2012;26(1):532-40. <https://doi.org/10.1016/j.conbuildmat.2011.06.054>
- Seifan M, Samani AK, Berenjian A. Bioconcrete: next generation of self-healing concrete. *Applied microbiology and biotechnology*. 2016;100:2591-602. 10.1007/s00253-016-7316-z
- Onyelowe KC, Gnananandarao T, Ebid AM, Mahdi HA, Ghadikolaee MR, Al-Ajamee M. Evaluating the compressive strength of recycled aggregate concrete using novel artificial neural network. *Civil Engineering Journal*. 2022;8(8):1679-93. 10.28991/CEJ-2022-08-08-011
- Akhtar J, Khan RA, Khan RA, Akhtar MN, Nejem JK. Influence of natural zeolite and mineral additive on bacterial self-healing concrete: a review. *Civil Engineering Journal*. 2022;8(5):1069-85. 10.28991/CEJ-2022-08-05-015
- Balamuralikrishnan R, Saravanan J. Effect of addition of alccofine on the compressive strength of cement mortar cubes. *Emerging Science Journal*. 2021;5(2):155-70. 10.28991/esj-2021-01265
- Standard I. IS: 383 (2016) Coarse and fine aggregate for concrete-specification. Bureau of Indian Standards, New Delhi. 2016. <http://icikbc.org/docs/IS383-2016.pdf>
- Standard I. Plain and reinforced concrete-code of practice. New Delhi: Bureau of Indian Standards. 2000. <https://law.resource.org/pub/in/bis/S03/is.456.2000.pdf>

**COPYRIGHTS**

©2024 The author(s). This is an open access article distributed under the terms of the Creative Commons Attribution (CC BY 4.0), which permits unrestricted use, distribution, and reproduction in any medium, as long as the original authors and source are cited. No permission is required from the authors or the publishers.

**Persian Abstract****چکیده**

این مطالعه بر ارزیابی اثربخشی غلظت‌های مختلف سلولی باکتری‌های باسیلوس در ترمیم ترک‌های بتن بازیافتی حاوی سنگدانه‌های درشت تمرکز دارد. در این تحقیق، معرفی بتن پایدار باکتریایی باسیلوس به عنوان راه حلی برای پرداختن به ترمیم ترک است. این فرمول ابتکاری بتن نه تنها جایگزین‌های سازگار با محیط زیست را ارائه می‌دهد، بلکه مزایای اقتصادی نیز ارائه می‌دهد. این تحقیق شامل ادغام سنگدانه‌های درشت به مخلوط بتن، همراه با جایگزینی جزئی سیمان با خاکستر بادی و سربراه کوره بلند دانه بندی شده زمینی (GGBS) است که هر کدام ۲۰ درصد از مخلوط را تشکیل می‌دهند. سنگدانه‌های درشت از سنگدانه‌های بتن بازیافتی (RCA) در نسبت‌های مختلف تشکیل شده‌اند: ۰٪، ۵۰٪ و ۱۰۰٪. علاوه بر این، باسیلوس لیکنیفورمیس به ترتیب در غلظت‌های ۱۰۳، ۱۰۵ و ۱۰۷ سلول در میلی لیتر استفاده شد. یافته‌ها نشان‌دهنده همبستگی مثبت بین درصد بهبودی ترک‌ها، همانطور که با سرعت پالس اولتراسونیک (UPV) اندازه‌گیری می‌شود، و غلظت باکتری‌ها است. علاوه بر این، مشاهده می‌شود که سنگدانه‌های بازیافتی دارای منافذ ذاتی هستند که امکان جذب آب از طریق این منافذ را فراهم می‌کند. بنابراین، RCA قبل از ادغام آن در مخلوط بتن تحت یک فرآیند غوطه‌وری ۲۴ ساعته در آب قرار می‌گیرد. در حالی که مقاومت فشاری بتن بین ۰٪ RCA و ۵۰٪ RCA ثابت می‌ماند، در ۱۰۰٪ RCA به طور قابل توجهی کاهش می‌یابد. با این حال، عملکرد باکتری نسبت به غلظت سلولی را نشان می‌دهد. قابل ذکر است، اثربخشی باکتری بدون توجه به تغییرات در نسبت RCA ثابت باقی می‌ماند. این مطالعه بر پتانسیل امیدوارکننده باکتری باسیلوس در افزایش دوام و پایداری سازه‌های بتنی، با ارتباط خاص با کاربردهای RCC تاکید می‌کند.



## Mitigation from SQL Injection Attacks on Web Server using Open Web Application Security Project Framework

A. Fadlil<sup>a</sup>, I. Riadi<sup>b</sup>, M. A. Mu'min<sup>\*b</sup>

<sup>a</sup> Department of Electrical Engineering, Universitas Ahmad Dahlan, Yogyakarta, Indonesia

<sup>b</sup> Department of Information System, Universitas Ahmad Dahlan, Yogyakarta, Indonesia

### PAPER INFO

#### Paper history:

Received 20 September 2023

Received in revised form 03 November 2023

Accepted 04 November 2023

#### Keywords:

Mitigation

Open Web Application Security Project

Database

Data security

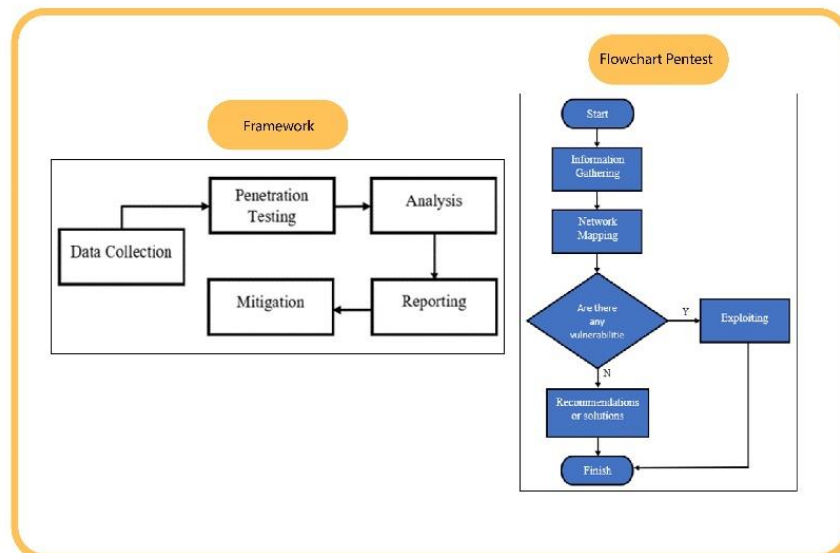
Web server

### ABSTRACT

SQL injection (SQLi) is one of the most common attacks against database servers and has the potential to threaten server services by utilizing SQL commands to change, delete, or falsify data. In this study, researchers tested SQLi attacks against websites using a number of tools, including Whois, SSL Scan, Nmap, Open Web Application Security Project (OWASP) Zap, and SQL Map. Then, researchers identified SQLi vulnerabilities on the tested web server. Next, researchers developed and implemented mitigation measures to protect the website from SQLi attacks. Test results using OWASP Zap identified 14 vulnerabilities, with five of them at a medium level of 35%, seven at a low level of 50%, and two at an informational level of 14%. Meanwhile, testing using SQL Map succeeded in gaining access to the database and username on the web server. The next step in this research is to provide recommendations for installing a firewall on the website as a mitigation measure to reduce the risk of SQLi attacks. The main contribution of this research is the development of a structured methodology to identify and address SQLi vulnerabilities in web servers, which play an important role in maintaining data security and integrity in a rapidly evolving online environment.

doi: 10.5829/ije.2024.37.04a.06

### Graphical Abstract



\*Corresponding Author Email: [mumin2008048038@webmail.uad.ac.id](mailto:mumin2008048038@webmail.uad.ac.id) (M. A. Mu'min)

## 1. INTRODUCTION

The rapid development of technology and information has entered all walks of life for various purposes and interests (1, 2). Therefore in recent years, hacking of web servers has dramatically increased (3). This causes more and more companies or organizations to require security in maintaining web servers (4, 5). However, with this development and convenience, it becomes the biggest threat if the security aspect is not given special attention (6, 7). One of the toughest problems faced by web owners is ensuring that the web server is safe from attacks and misuse (8, 9). According to Open Web Application Security Project (OWASP) top 10 (10) SQL injection (SQLi) is one of the most numerous and common attacks that attacks database servers (11) and compromises server services such as: confidentiality, authentication, authorization and integrity (12, 13). This technique is commonly used to exploit web-based applications (14, 15). Injection attacks allow attackers to fake identities, change and delete existing data in the server database by inserting SQL commands into the query string (16, 17). Attackers exploit website application vulnerabilities by entering or injecting special commands into websites that have security holes (18). Improper validation of user input can lead to SQLi attacks (19). Thus, it can cause important user data to be deleted or changed from the web application (20, 21).

In order to maintain security from SQLi attacks, mitigation needs to be implemented as a very important step taken to reduce the risk and impact of SQLi attacks on an application or system (22). The main goal of SQLi mitigation is to prevent attackers from successfully injecting malicious SQL commands into an application or system, so that sensitive data is not exposed or corrupted (23). One effective way of mitigation is to install a firewall layer on the website (24). These firewalls play a key role in protecting websites by implementing specific rules aimed at blocking and eliminating potentially malicious traffic (25). The rules implemented by this firewall are designed to combat various types of attacks, including cross-site scripting and SQL injection (26). With a firewall, websites are better able to detect and respond quickly to SQLi attack attempts that can compromise the integrity and confidentiality of the data stored therein. Thus, implementing a firewall is one of the key components in a mitigation strategy that can help maintain the security and integrity of a website from various SQLi attacks that can arise (27).

Agreindra et al. (8) investigated the Analysis of Web Security Using Open Web Application Security Project 10, their research analyzes and tests web security along with six subdomains with the aim of knowing and assessing the level of security of a website, whether

additional security is needed, and recommendations on the website. The results of their work showed that the web has a security level of 80%, the web informatics engineering subdomain 60%, information systems 60%, informatics management 60%, integrated academic systems 80%, student acceptance 80% and e-learning 80%.

Alanda et al. (28) introduced the title Mobile Application Security Penetration Testing Based on OWASP, the aim of their research was to determine vulnerabilities and the techniques used to find these vulnerabilities on the Android operating system and Android applications. In addition, it provides recommendations and prevention of these vulnerabilities. The techniques and methods used are based on research from the OWASP Foundation which consists of the 10 main vulnerabilities in Android applications. Results from testing five applications downloaded from the Play Store. Four application based vulnerabilities in the OWASP Mobile Top Ten documentation. OWASP documentation can provide an overview of the most commonly found vulnerabilities in Android applications from the market.

Priyawati et al. (29) investigated Website Vulnerability Testing and Analysis of Internet Management Information System Using OWASP; they have carried out gray box penetration testing techniques using the OWASP method and the OWASP ZAP tool. The test results showed that the target application website has 12 vulnerabilities with details of 8.3% at a high level of vulnerability or 1 warning, 41.7% at a medium level or 5 warnings, 33.3% at a low level or 4 warnings, and 16.7% at information level or 2 warnings. These vulnerabilities relate to matters related to A01-Broken Access Control, A03-Injection, A05-Security Misconfiguration, and A08-Software and Data Integrity Failures.

Alanda et al. (30) studied Web Application Penetration Testing Using SQL Injection Attack, this research randomly tests several websites such as government, school and other commercial sites with several SQL injection attack techniques. Testing was carried out on ten random websites by looking for loopholes to test security using SQL injection attacks. The test results carried out 80% of the websites tested had weaknesses against SQL injection attacks.

In contrast to previous research, the research only focuses on testing and identifying vulnerabilities without carrying out mitigation. In addition, the tools used in previous research did not involve all the stages contained in the OWASP Framework. Therefore, in this research, tools are involved that cover all the stages defined in the OWASP framework, including Information Collection using the Whois tool, SSL Scanning, Network Mapping using Nmap and OWASP Zap, as well as exploiting using

SQL Map. This research has the aim of testing website security against SQLi attacks using various network forensic tools in accordance with the guidelines set out in the OWASP framework and implementing mitigation measures by recommending that the website install a firewall to reduce attacks on the web server. The results of this research are expected to provide valuable guidance for institutions or entities that use websites as information platforms, assisting them in selecting appropriate and effective web security tools.

One of the frameworks used is OWASP, which is a structured framework with several steps in grouping information for security test plans for websites, assessments and verified and analyzed domain reports (31, 32). This framework is for analyzing various vulnerabilities issued by the OWASP Top 10 2021 (33, 34), including: Broken Access Control, Security Misconfiguration, Insecure Deserialization, Injection, Sensitive Data Exposure, XML External Entities, Broken Authentication, Cross Site Scripting, Using Components with Known Vulnerabilities, and Insufficient Logging and Monitoring. There are four tools used to find these vulnerabilities in this framework, namely: Whois, SSL Scan, Nmap, OWASP Zap, and SQL Map. Most tools used to detect vulnerabilities classify vulnerabilities into four categories: High, Medium, Low, and Information (32).

**2. MATERIALS AND METHOD**

In carrying out penetration testing on web servers, this research uses the OWASP framework to categorize threats and weaknesses in web servers (35, 36). Using the OWASP framework has the benefit of checking web-based application security standards, so that data theft and dissemination by irresponsible parties can be avoided so that it can continue to be used in the long term (37).

The use of the OWASP framework in Penetration Testing on web servers is important because it provides proven security standards, covers various types of threats, is relevant to current challenges, protects data and privacy, and ensures long-term sustainability. The stages in this research can be seen in Figure 1.

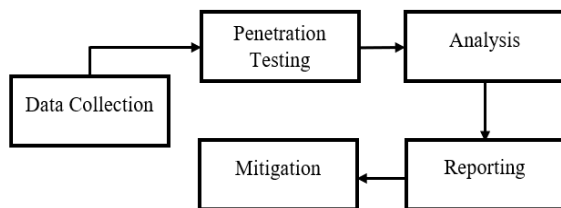


**Figure 1.** Research stages using the OWASP framework

Data Collection, in this step, collects information about the selected topic and completes the survey. Penetration Testing, at this stage testing is carried out on websites with the aim of security testing carried out by pentesters by imitating actual attacks to damage the security features of an application, system or network so that vulnerabilities are known. There are three stages in carrying out PENTEST, which can be seen in Figure 2. Analysis, at this stage, performs an analysis of the Web Server to find vulnerabilities. Reporting, at this stage describes in detail the results of the analysis that has been processed and writes a report. This mitigation stage involves assessing the website and providing recommendations regarding firewall configurations that need to be implemented to improve web security by preventing injection attacks.

Figure 2. involves the use of the OWASP framework. In the first stage, data is collected using Whois and SSL Scan. Then, in the second stage, network mapping is carried out by carrying out vulnerability scanning using the Nmap and OWASP ZAP tools. Once completed with a comprehensive vulnerability scan, the research proceeds to the third phase, which includes exploitation, using tools to identify SQL vulnerabilities.

The testing process using the OWASP Framework after the completion and implementation stages, the tools used and the functionality of the tools will be explained in Table 1.

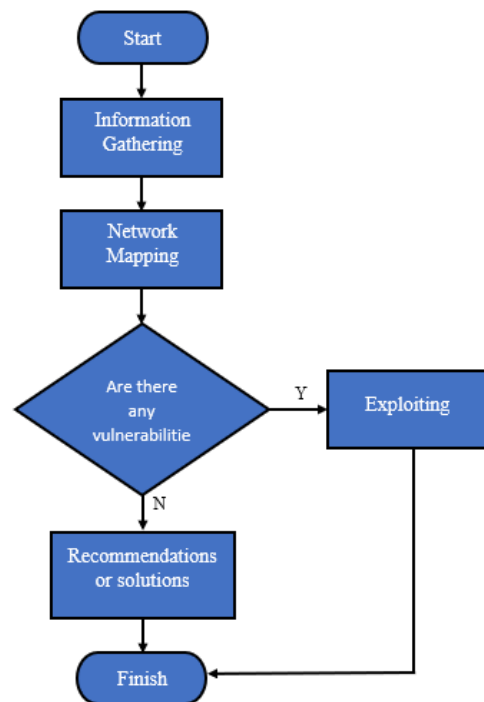


**Figure 2.** Flowchart of penetration testing stages using the OWASP framework

**TABLE 1.** Tools in the OWASP Framework

Tools	Information
Whois, and SSL Scan	Used to obtain data about a website.
Nmap	Functions to check the ports on the network.
OWASP Zap	Used to identify potential vulnerabilities in web application testing.
SQL Map	Used to identify the existence of a database on a website.

### 3. RESULTS AND DISCUSSION

According to the framework established by OWASP, the process of assessing and aggregating the risk level of vulnerabilities on a web server involves several structured stages. This stage includes Data Collection to understand the vulnerability, carrying out Penetration Testing to identify the vulnerability in more depth, analysis the findings found, compiling a Report with a summary of the results and recommendations, and finally implementing the necessary Mitigation steps to reduce the risk of the vulnerability.

**3.1. Data Collection** In this phase, the information collected to support the experiments in this research comes from data found on the website designlink.com.hk. The OWASP framework is used as a tool to identify vulnerabilities contained in the website.

**3.2. Penetration Testing** Penetration testing is a testing process carried out on websites to detect potential vulnerabilities, identify poor system configurations, find hardware and software weaknesses, and uncover technical weaknesses in the information system being tested (38). Penetration testing is useful for identifying and addressing vulnerabilities in an infrastructure network, illustrating the level of vulnerability to malicious attacks on a network. There are three main steps in penetration testing, namely Information Gathering, Network Mapping, and exploitation.

**3.2.1. Information Gathering** The purpose of the information gathering is to better understand the web server and any potential issues with it, as shown in Figure 3.

Figure 3 These results come from the process of searching for information via the online Whois tool. This stage aims to collect important data about a web server, including the domain name, registrar name, registrar contact email address, email address, telephone number, country, and related account names. Figure 4. illustrates the outcome of utilizing SSL Scan tools.

Figure 4 shows the use of SSL Scan tool aims to check information about SSL security on a web server;

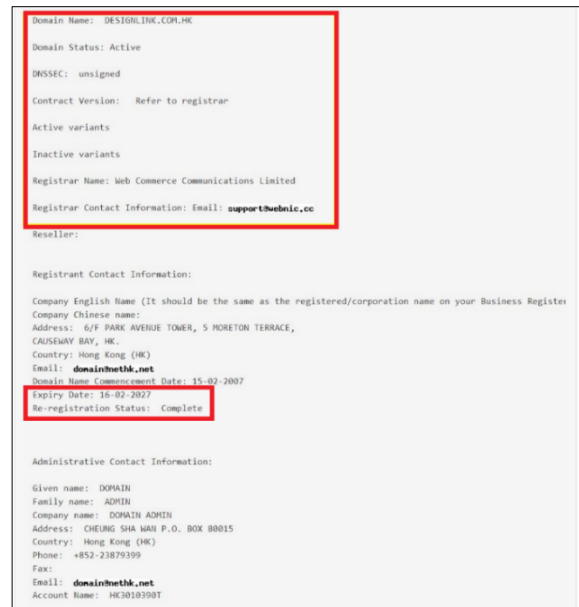


**Figure 3.** Results of a search using Whois tools



**Figure 4.** Results of employing tools for online SSL scans

findings indicating inactivity of the SSL security layer on a web server may increase the risk of sensitive data theft, Man-in-the-Middle attacks, vulnerability to credential theft, data integrity risks, and vulnerability to malware attacks.

**3.2.2. Network Mapping** Network mapping is the stage of a web network's mapping process where it is determined which ports have security flaws. The Nmap utility can be used to scan. The outcomes are shown in Figure 5.

Figure 5 depicts the outcome comes from utilizing the Nmap program to perform a port scan on the web server. Ten ports in all were examined based on the scan results. Out of the ten ports, seven are marked as "open," meaning that you can access them; the remaining three are marked as "closed," meaning that you cannot access them.

**3.2.3. Exploit** The data gathered in the first phase can be used as test data in the exploitation phase, which entails testing the identified security flaws. OWASP Zap

Port	Protocol	State	Service	Version
21	tcp	open	ftp	vsftpd 3.0.2
53	tcp	open	domain	(unknown banner: get lost)
80	tcp	open	http	nginx
443	tcp	open	http	nginx
2121	tcp	open	ssh	OpenSSH 7.4 (protocol 2.0)
3306	tcp	open	mysql	MySQL (blocked - too many connection errors)
5432	tcp	closed	postgresql	
8000	tcp	closed	http-alt	
8083	tcp	open	http	nginx
12000	tcp	closed	cce4x	

Figure 5. Utilizing Nmap tools results

and SQL Map are two tools that are currently in use in this situation. Figure 6 demonstrates how users can examine the scan results using the OWASP Zap tool.

Figure 6 shows the purpose of this scanning procedure is to perform a thorough assessment of the web server in order to determine the degree of security or vulnerability of the data and information passing through the server. This procedure is also intended to identify potential risks related to the web server and find any threats or vulnerabilities that might be concealed in the setup and configuration of the web server, allowing for the implementation of the necessary mitigating actions to improve security and lower existing risks. The scanning results can be seen in Figure 7.

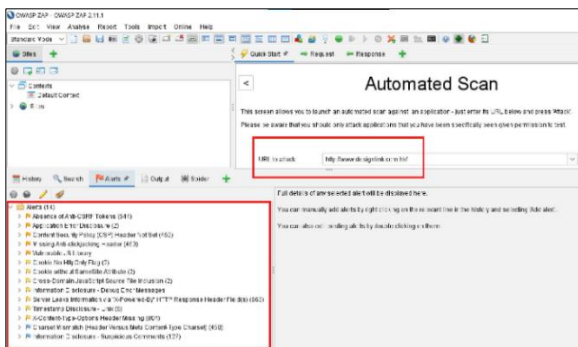


Figure 6. Technique of scanning using the OWASP Zap tool

Alerts (14)
Absence of Anti-CSRF Tokens (544)
Application Error Disclosure (2)
Content Security Policy (CSP) Header Not Set (452)
Missing Anti-clickjacking Header (450)
Vulnerable JS Library
Cookie No HttpOnly Flag (2)
Cookie without SameSite Attribute (2)
Cross-Domain JavaScript Source File Inclusion (2)
Information Disclosure - Debug Error Messages
Server Leaks Information via "X-Powered-By" HTTP Response Header Field(s) (663)
Timestamp Disclosure - Unix (5)
X-Content-Type-Options Header Missing (804)
Charset Mismatch (Header Versus Meta Content-Type Charset) (450)
Information Disclosure - Suspicious Comments (127)

Figure 7. OWASP Zap results of scanning

There were a total of 14 vulnerabilities found in the web server's vulnerability assessment reports (see Figure 7). Five of these vulnerabilities have a moderate risk (medium), seven have a low risk (low), and two have information that is just marginally useful (informational). This scan did not find any vulnerabilities with a high risk level, however it did find a number of medium risk vulnerabilities that needed to be fixed right away to improve server security.

Using SQL Map is the next step in the web server security evaluation procedure. After using OWASP Zap for an initial scan, this SQL Map is used. SQL Map is especially used on web servers to assess security risks linked to SQL. This allows for more thorough testing to be done in order to find possible SQL-related security flaws and take the necessary mitigation steps to improve server security. The SQL Map command used in this procedure is shown in Figure 8.

Figure 8 illustrate an attempt was made to execute SQL statements into the server using the `-u` command to indicate the target URL and the `-dbs` command to query a list of accessible databases in an effort to test the web server's security. Thus, it was effective in locating the `'id'` parameter, which was open to SQL injection. Table 2 contains more details regarding the experiment's outcomes.

Table 2 demonstrates the `designlink_jack` and `information_schema` databases are present on the web server as a result of the `--dbs` command utilizing SQL Map. Web servers are not protected in a way that makes it simple for attackers to get access to such data. Once the database has been located, provide a command to retrieve the table's contents from the database. Figure 9 demonstrates it clearly.

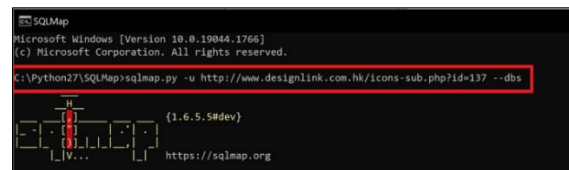


Figure 8. Using SQL Map as a SQL command

TABLE 2. Search results -dbs

No.	Database name
1	designlink_jack
2	information_schema



Figure 9. Activate the -tables command.

Figure 9 shows the use of `-tables` command on the `designlink_jack` database to access SQL Map tools. This command is used to view the database's contents. The outcomes are shown in Table 3.

Table 3 displays the outcomes of the query after identifying eight tables in the `designlink_jack` database using the `-tables` command. Figure 10 shows a method for calling a table's contents from `dnd_adminlogin`.

Figure 10 shows the `dnd_adminlogin` table's contents can be viewed by using the `-T` command, and its columns' contents can be viewed by using the `-dump` command. The outcomes are shown in Table 4.

Table 4 summarized the performing SQL requests in the SQL Map tool, it can be shown that it was successful in retrieving the data or information present in the web server. If there is insufficient security, this leaves the program open to the web server. Mysqli security makes it very difficult for injection attacks to succeed since the validation is so rigorous that the SQL command that is being injected cannot run.

**3. 3. Analysis** A thorough analysis process will be applied to vulnerabilities found during the earlier phases of web server testing, with a special emphasis on the web server under investigation. The OWASP Framework was used to conduct this analysis, and the results are available in Table 5 and will be thoroughly documented.

Table 5 shows that three ports are listed as "closed" and seven ports are listed as "open" on the website's port scan results. This data offers crucial insight into the security flaws of the website and the degree to which its security systems are ready to thwart unauthorized access

**TABLE 3.** Search results from the `-tables` command

Number	Table names
1	Dnd_adminlogin
2	Dnd_blog
3	Dnd_blog_categories
4	Dnd_brands
5	Dnd_contactus



**Figure 10.** Call a table's contents "dnd\_adminlogin"

**TABLE 4.** Table results "dnd\_adminlogin"

Id	Username	Password
1	dndlink	SSGBCj6Tuy

**TABLE 5.** Results of port mapping found

Port	Protocol	Status	Service
21	tcp	Open	ftp
53	tcp	Open	Domain
80	tcp	Open	http
443	tcp	Open	http
2121	tcp	Open	Ssh
3306	tcp	Open	Mysql
5432	tcp	Closed	Postgresql
8000	tcp	Closed	http-alt
8083	tcp	Open	http
12000	tcp	Closed	Ccc4x

attempts. Attackers may attempt to gain access to resources or services on a website by trying to leverage open ports as possible points of entry. A closed port, on the other hand, shows that the security system has effectively controlled access to the port, lowering the likelihood of attacks or penetration that could jeopardize the confidentiality and integrity of data on the website. Website owners will therefore be able to take proactive measures to fortify their security defenses and protect the integrity of their websites from potential threats by having a better understanding of the status of these ports. Table 6 summarized the results of the vulnerability recapitulation.

Based on Table 6. which is depicted in percentage form, namely the risk level of vulnerability at high gets a value of 0% or no vulnerability was found in it, at the medium level it gets a value of 35% (5), namely: Absence of Anti-CSRF Tokens, Application Error Disclosure, Content Security Policy (CSP) Header Not Set, Missing Anti-Clickjacking Header, Vulnerable JS Library. At the low level, it gets a score of 50% (7), namely: Cookie Without Samesite Attribute, Cross-Domain Javascript Source File Inclusion, Information Disclosure-Debug Error Messages, Server Leaks Information Via "X-Powered-By" HTTP Response Header Field(s), Timestamp Disclosure-Unix, X-Content-Type-Options Header Missing. And at the informational level, it gets a value of 14% (2) vulnerabilities, namely: Charset Mismatch (Header Versus Meta Content-Type Charset),

**TABLE 6.** Recapitulation of discovered vulnerabilities

Risk Level	Number of Alerts	Presentase
High	-	0%
Medium	5	35%
Low	7	50%
Informational	2	14%

Information Disclosure-Suspicious Comments. The results of security testing analysis based on the OWASP Top 10 in 2021 are presented in Table 5.

Table 7. The results of system testing using tools such as OWASP ZAP have identified four vulnerabilities that require urgent repair, namely "broken access control," "security misconfiguration," "vulnerable and outdated components," and "software and data integrity failures." Not addressing these vulnerabilities may result in serious risks to the system and associated applications.

Failure to address vulnerabilities such as "Broken Access Control" may result in unauthorized access and privacy breaches, "Security Misconfiguration" may result in exposure of sensitive data and denial of service, "Vulnerable and Outdated Components" increases the risk of vulnerability exploitation and data theft, and "Software and Data Integrity Failures" can result in data loss and reduced service quality and damage data integrity.

Addressing and remediating these vulnerabilities is critical to maintaining system security, integrity, and availability, as well as protecting user data and privacy.

**TABLE 7.** Vulnerability results on web servers based on OWASP Top 10 2021

Vulnerability	Solution
Broken Access Control	Implement access control system work and reuse it in all applications so as to minimize CORS (Cross Origin Resource Sharing) users, so that users cannot create, read, update or delete records freely, the access control model should limit this by using ownership for each record, and disable the web server directory listing.
Cryptographic Failures	Not found
Injection	Not found
Insecure Design	Not found
Security Misconfiguration	System management can review and update the appropriate configuration for all security notes, updates and patches as part of the patch management process
Vulnerable and Outdated Components	Remove unused dependencies, unnecessary features, components, files and documentation.
Identification and Authentication Failures	Not found
Software and Data Integrity Failures	Use digital signatures or similar mechanisms to verify that software or data comes from the intended source and has not been manipulated
Security Logging and Monitoring Failures	Not found
Server-Side Request Forgery	Not found

That's why fixing these vulnerabilities must be prioritized in information security and application development strategies.

### 3. 4. Reporting

At this stage, take an important step in summarizing the results of the analysis that has been carried out during the OWASP Framework implementation process. This report aims to present the key findings found on the web servers that have been studied. Table 8. presented below, is a representation of research data obtained through the implementation of the OWASP Framework. This report will provide a more detailed and structured picture of the security condition of the web servers that have been analyzed.

Table 8. shows the results of a report on a series of penetration tests and vulnerability analysis carried out using a framework that complies with the security guidelines and standards recommended by OWASP. Through this report, we hope to provide deeper insight into the state of web server security that has been researched, so that appropriate corrective steps can be taken to reduce risks and improve system integrity.

### 3. 5. Mitigation

According to CERT/CC, 90% of security flaws are found during the program development process. This is a result of most developers' ignorance of security-related information and an ineffective strategy for maintaining software security. Web-based assaults are increasing as a result of a number of causes, including poor design, insufficient security requirements, configuration issues, unsafe coding practices, uncontrolled input controls, and password management flaws.

Implementing a framework for "secure software design" is one efficient remedy. But diverse groups of security experts have different perspectives, which makes developing secure software difficult. Network administrators typically concentrate on the use of firewalls, intrusion detection systems, and management systems, whereas software engineers frequently concentrate on aspects of code quality with an eye toward security. The concept of security may be abstracted by software developers from design or architectural principles, security patterns, or other elements.

**TABLE 8.** Summarize research findings using the OWASP Framework.

Stage	Parameter	Tools	Result
Information Gathering	Domain name, domain status, email expiry date	Whois	Success
	Overall Rating	SSL Scan	Success
Network Mapping	Vulnerability	OWASP Zap	Success
Exploiting	Username and password	SQL Map	Success

It is crucial to keep in mind that developing secure software requires appropriate data security requirements, careful design, meticulous execution, and thorough testing. To achieve effective protection, security must be considered at every stage of the system development life cycle (SDLC). Keep in mind that by offering an additional, comprehensive layer of protection, investing in information security can help lower future expenditures (39, 40).

One step that may be taken to lessen the risk of web attacks is to install a firewall, as depicted in Figure 11. In a defense system, firewalls function as the first line of defense, regulating incoming and outgoing data traffic to guarantee that only approved and permitted traffic may get to the server. As a result, it is a crucial step in enhancing system security and guarding against future cyberattacks and threats.

Figure 11 demonstrates attackers who have access to the Internet attempt to initiate assaults against network-connected websites and web servers. The firewall that had been installed on the network, however, prevented the attack attempt. This firewall acts as a powerful defense against intrusions that could jeopardize the availability, integrity, and confidentiality of the services being offered. Attackers are prevented from accessing or corrupting data kept on web servers and from interfering with the availability of such websites to authorized users when an effective firewall is in place. This adds a crucial layer of security for preserving the network's security and stability as well as safeguarding any sensitive data that might be kept on the web server. In other words, the presence of a firewall has successfully stopped assaults on websites and web servers running on the firewall-protected network. It can be seen in Figure 12 attacks on websites that have firewalls.

Figure 12 shows the research attempts to conduct a SQL Injection (SQLi) attack using the SQL Map tool in order to evaluate the efficacy of the firewall that has been put in place on the website. The experiment's findings demonstrate that, despite careful application, the SQL Map tool is unable to locate the "id" parameter on websites that have firewalls.

These unfavorable outcomes offer an intriguing hint about how reliable the security system that was put in place is. This shows that the firewall that was put in place has been successful in thwarting attempts at SQLi

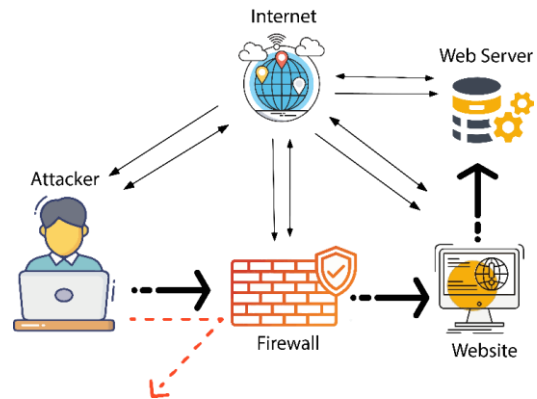


Figure 11. Mitigation of hacker attacks

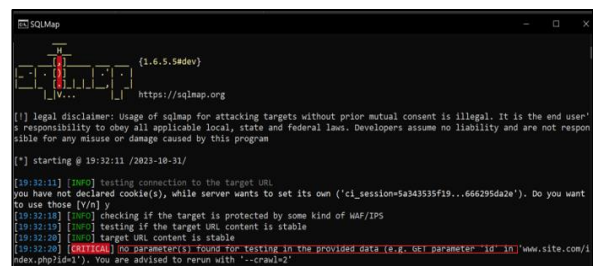


Figure 12. Web server with firewall installed

attacks, which typically look for and take advantage of parameters like "id" in an effort to replace or access private information on the internet. Consequently, these results bolster the notion that the security mitigation strategy employed in this study—installing a firewall, for example—can be regarded as a successful means of shielding websites against potentially harmful SQL Injection attacks. Table 7. presents a comparison of research findings from other studies that used the OWASP framework.

Table 9. illustrates an interesting comparison various studies regarding the use of the OWASP framework in carrying out SQLi attacks. Different research results show various levels of security gaps on the web. In 2020, a study by Agreindra et al. (8) in testing security obtained a security level of 60%. Then Alanda, et al. (28) in 2020, obtained test results with a vulnerability value of 80%. Priyawati et al. (29) in 2022 found 12 vulnerabilities. In 2021, research conducted by Alanda, et al. (30) found that 80% of the websites tested had weaknesses.

TABLE 9. Comparison with earlier studies

Ref.	Method	Object	Tools	Results	Year
[8]	OWASP	Website	Nmap and OWASP Zap	This website is generally safe from security testing, but some subdomains have a security level of 60%.	2020
[28]	OWASP	Mobile Application	Burp suite	The test results show a vulnerability with a value of 80%	2020

[29]	OWASP	Website	OWASP Zap	The test results show that the target application website has 12 vulnerabilities with details of 8.3% at a high level of vulnerability or 1 warning, 41.7% at a medium level or 5 warnings, 33.3% at a low level or 4 warnings, and 16.7 at information level or 2 warnings.	2022
[30]	OWASP	Website	SQL Map	The test results carried out were 80% of the tested website is vulnerable to SQL injection attacks.	2021
This research	OWASP	Web Servers	Whois, SSL Scan, Nmap, OWASP Zap, and SQL Map	The results of using the Whois tool get a web identity, SSL Scan gets an Overall rating value, Nmap finds three ports with closed status and seven ports with open status, OWASP Zap finds 14 vulnerabilities including; five medium levels, seven low levels, and two information levels, and the SQL Map tool successfully retrieved user names and passwords on the web	2023

This research in 2023 found 14 vulnerabilities including; five medium levels, seven low levels, and two information levels. Then successfully get the username and password on the website. This research also provides a mitigation solution by installing a firewall on the web to protect against injection attacks.

#### 4. CONCLUSIONS

SQLi attacks are one of the main threats that lurk on any web server that is not sufficiently protected. Based on the results of analysis of testing against SQLi attacks using the OWASP framework. The results of using the Whois tool get a web identity, SSL Scan gets an Overall rating value, Nmap finds three ports with closed status and seven ports with open status, OWASP Zap finds 14 vulnerabilities including; five medium levels with a percentage value of 35%, seven at the low level with a percentage value of 50%, and two at the information level with a percentage value of 14%, and the SQL Map tool succeeded in retrieving user names and passwords on the web. This illustrates that the web server does not have adequate security and validation layers to protect itself from various attacks, especially injection attacks. On websites that have a firewall installed, attacks often fail and attempts to find the ID parameter on the web are unsuccessful.

For future research, more in-depth research is needed to reveal mitigation measures other than firewalls in maintaining website security from SQLi attacks. This approach can include the implementation of various frameworks and tools used. Thus, future research will provide deeper and more comprehensive insight into stronger efforts to reduce the risk of attacks on the web.

#### 5. REFERENCES

1. Wang B, Yao Y, Shan S, Li H, Viswanath B, Zheng H, et al., editors. Neural cleanse: Identifying and mitigating backdoor

- attacks in neural networks. 2019 IEEE Symposium on Security and Privacy (SP); 2019: IEEE. 10.1109/SP.2019.00031
2. Bora A, Bezboruah T. Investigation on reliability estimation of loosely coupled software as a service execution using clustered and non-clustered web server. *International Journal of Engineering, Transactions A: Basics.* 2020;33(1):75-81. 10.5829/ije.2020.33.01a.09
3. Abdullah HS. Evaluation of open source web application vulnerability scanners. *Academic Journal of Nawroz University.* 2020;9(1):47-52. 10.25007/ajnu.v9n1a532
4. Sargolzaei A, Yazdani K, Abbaspour A, Crane III CD, Dixon WE. Detection and mitigation of false data injection attacks in networked control systems. *IEEE Transactions on Industrial Informatics.* 2019;16(6):4281-92. 10.1109/TII.2019.2952067
5. Thepade S, Dindorkar M, Chaudhari P, Bang S. Enhanced face presentation attack prevention employing feature fusion of pre-trained deep convolutional neural network model and thepade's sorted block truncation coding. *International Journal of Engineering, Transactions A: Basics.* 2023;36(4):807-16. 10.5829/ije.2023.36.04a.17
6. Thakre S, Bojewar S, editors. Studying the effectiveness of various tools in detecting the protecting mechanisms implemented in web-applications. 2018 International Conference on Inventive Research in Computing Applications (ICIRCA); 2018: IEEE. 10.1109/ICIRCA.2018.8597363
7. Nasirae H, Ashouri-Talouki M. DoS-Resistant Attribute-Based Encryption in Mobile Cloud Computing with Revocation. *International Journal of Engineering, Transactions C: Aspects.* 2019;32(9):1290-8. 10.5829/ije.2019.32.09c.09
8. Helmiawan MA, Firmansyah E, Fadil I, Sofivan Y, Mahardika F, Guntara A, editors. Analysis of web security using open web application security project 10. 2020 8th International Conference on Cyber and IT Service Management (CITSM); 2020: IEEE. 10.1109/CITSM50537.2020.9268856
9. Dalai AK, Jena SK. Neutralizing SQL injection attack using server side code modification in web applications. *Security and Communication Networks.* 2017;2017. 10.1155/2017/3825373
10. Lala SK, Kumar A, Subbulakshmi T, editors. Secure web development using owasp guidelines. 2021 5th International Conference on Intelligent Computing and Control Systems (ICICCS); 2021: IEEE. 10.1109/ICICCS51141.2021.9432179
11. Alghawazi M, Alghazzawi D, Alarifi S. Detection of sql injection attack using machine learning techniques: a systematic literature review. *Journal of Cybersecurity and Privacy.* 2022;2(4):764-77. 10.3390/jcp2040039
12. Kareem FQ, Ameen SY, Salih AA, Ahmed DM, Kak SF, Yasin HM, et al. SQL injection attacks prevention system technology. *Asian Journal of Research in Computer Science.* 2021;10(3):13-32. 10.9734/ajrcos/2021/v10i330242

13. Chen D, Yan Q, Wu C, Zhao J, editors. Sql injection attack detection and prevention techniques using deep learning. *Journal of Physics: Conference Series*; 2021: IOP Publishing. 10.1088/1742-6596/1757/1/012055
14. Mokbal FMM, Dan W, Imran A, Jiuchuan L, Akhtar F, Xiaoxi W. MLPXSS: an integrated XSS-based attack detection scheme in web applications using multilayer perceptron technique. *IEEE Access*. 2019;7:100567-80. 10.1109/ACCESS.2019.2927417
15. Hu J, Zhao W, Cui Y, editors. A survey on sql injection attacks, detection and prevention. *Proceedings of the 2020 12th International Conference on Machine Learning and Computing*; 2020. 10.1145/3383972.3384028
16. Pattewar T, Patil H, Patil H, Patil N, Taneja M, Wadile T. Detection of SQL injection using machine learning: a survey. *Int Res J Eng Technol(IRJET)*. 2019;6(11):239-46.
17. Alenezi M, Nadeem M, Asif R. SQL injection attacks countermeasures assessments. *Indonesian Journal of Electrical Engineering and Computer Science*. 2021;21(2):1121-31. 10.11591/ijeecs.v21.i2.pp1121-1131
18. Ravindran U, Potukuchi RV. A Review on Web Application Vulnerability Assessment and Penetration Testing. *Review of Computer Engineering Studies*. 2022;9(1). 10.18280/rces.090101
19. Syamasudha V, Syed A, Gayatri E. The Solutions of SQL Injection Vulnerability in Web Application Security. no. 2019;6:3803-8. 10.35940/ijeat.F9395.088619
20. Sharma K, Bhatt S. SQL injection attacks-a systematic review. *International journal of information and computer security*. 2019;11(4-5):493-509. 10.1504/IJICS.2019.101937
21. Akbar M, Ridha MAF. Sql injection and cross site scripting prevention using owasp modsecurity web application firewall. *JOIV: International Journal on Informatics Visualization*. 2018;2(4):286-92. 10.30630/joiv.2.4.107
22. Jana A, Maity D, editors. Code-based analysis approach to detect and prevent SQL injection attacks. *2020 11th International Conference on Computing, Communication and Networking Technologies (ICCCNT)*; 2020: IEEE. 10.1109/ICCCNT49239.2020.9225575
23. Alotaibi FM, Vassilakis VG. Toward an SDN-Based Web Application Firewall: Defending against SQL Injection Attacks. *Future Internet*. 2023;15(5):170. 10.3390/fi15050170
24. Rankothge W, Randeniya M, Samaranyaka V, editors. Identification and mitigation tool for Sql injection attacks (SQLIA). *2020 IEEE 15th International Conference on Industrial and Information Systems (ICIIS)*; 2020: IEEE. 10.1109/ICIIS51140.2020.9342703
25. Xiao M, Guo M. Computer network security and preventive measures in the age of big data. *Procedia Computer Science*. 2020;166:438-42. 10.1016/j.procs.2020.02.068
26. Krishnan S, Zolkipli MF. Survey on SQL Injection and Cross-Site Scripting Malware Injection Attacks. 10.35629/5252-0502822833
27. Hasan M, Balbahaith Z, Tarique M, editors. Detection of SQL injection attacks: a machine learning approach. *2019 International Conference on Electrical and Computing Technologies and Applications (ICECTA)*; 2019: IEEE. 10.1109/ICECTA48151.2019.8959617
28. Alanda A, Satria D, Mooduto H, Kurniawan B, editors. Mobile application security penetration testing based on OWASP. *IOP Conference Series: Materials Science and Engineering*; 2020: IOP Publishing. 10.1088/1757-899X/846/1/012036
29. Priyawati D, Rokhmah S, Utomo I. Website Vulnerability Testing and Analysis of Internet Management Information System Using OWASP. *International Journal of Computer and Information System (IJCIS) Peer Reviewed-International Journal*. 2022;3(03):2745-9659. 10.29040/ijcis.v3i3.90
30. Alanda A, Satria D, Ardhana MI, Dahlan AA, Mooduto HA. Web application penetration testing using SQL Injection attack. *JOIV: International Journal on Informatics Visualization*. 2021;5(3):320-6. 10.30630/joiv.5.3.470
31. Wiradarma AABA, Sasmita GMA. IT Risk Management Based on ISO 31000 and OWASP Framework using OSINT at the Information Gathering Stage (Case Study: X Company). *International Journal of Computer Network and Information Security*. 2019;10(12):17. 10.5815/ijcnis.2019.12.03
32. Wijayanto A, Utami E, Prasetio AB, editors. Analysis of Vulnerability Webserver Office Management of Information And Documentation Diskominfo using OWASP Scanner. *2020 2nd International Conference on Cybernetics and Intelligent System (ICORIS)*; 2020: IEEE. 10.1109/ICORIS50180.2020.9320833
33. Wibowo RM, Sulaksono A. Web vulnerability through Cross Site Scripting (XSS) detection with OWASP security shepherd. *Indonesian Journal of Information Systems*. 2021;3(2):149-59. 10.24002/ijis.v3i2.4192
34. Ferrara P, Mandal AK, Cortesi A, Spoto F. Static analysis for discovering IoT vulnerabilities. *International Journal on Software Tools for Technology Transfer*. 2021;23:71-88. 10.1007/s10009-020-00592-x
35. Qian K, Parizi RM, Lo D, editors. Owasp risk analysis driven security requirements specification for secure android mobile software development. *2018 IEEE Conference on Dependable and Secure Computing (DSC)*; 2018: IEEE. 10.1109/DESEC.2018.8625114
36. Mateo Tudela F, Bermejo Higuera J-R, Bermejo Higuera J, Sicilia Montalvo J-A, Argyros MI. On Combining Static, Dynamic and Interactive Analysis Security Testing Tools to Improve OWASP Top Ten Security Vulnerability Detection in Web Applications. *Applied Sciences*. 2020;10(24):9119. 10.3390/app10249119
37. Kellezi D, Boegelund C, Meng W. Securing open banking with model-view-controller architecture and OWASP. *Wireless communications and mobile computing*. 2021;2021:1-13. 10.1155/2021/8028073
38. Ghanem MC, Chen TM. Reinforcement learning for efficient network penetration testing. *Information*. 2019;11(1):6. 10.3390/info11010006
39. Silva RF, Barbosa R, Bernardino J. Intrusion detection systems for mitigating sql injection attacks: review and state-of-practice. *International Journal of Information Security and Privacy (IJISP)*. 2020;14(2):20-40. 10.4018/IJISP.2020040102
40. Khalaf M, Youssef A, El-Saadany E. Joint detection and mitigation of false data injection attacks in AGC systems. *IEEE Transactions on Smart Grid*. 2018;10(5):4985-95. 10.1109/TSG.2018.2872120

## COPYRIGHTS

The author(s). This is an open access article distributed under the terms of the Creative Commons 2024© Attribution (CC BY 4.0), which permits unrestricted use, distribution, and reproduction in any medium, as long as the original authors and source are cited. No permission is required from the authors or the publishers



## Persian Abstract

## چکیده

تزریق SQL (SQLi) یکی از رایج ترین حملات علیه سرورهای پایگاه داده است و با استفاده از دستورات SQL برای تغییر، حذف یا جعل داده ها، می تواند خدمات سرور را تهدید کند. در این مطالعه، محققان با استفاده از تعدادی ابزار، از جمله Whois، SSL Scan، Nmap، OWASP Zap و SQL Map، حملات SQLi را علیه وب سایت ها آزمایش کردند. سپس، محققان آسیب پذیری های SQLi را در وب سرور آزمایش شده شناسایی کردند. در مرحله بعد، محققان اقدامات کاهش را برای محافظت از وب سایت در برابر حملات SQLi ایجاد و اجرا کردند. نتایج آزمایش با استفاده از OWASP Zap 14 آسیب پذیری را شناسایی کرد که پنج مورد از آنها در سطح متوسط ۳۵٪، هفت مورد در سطح پایین ۵۰٪ و دو مورد در سطح اطلاعاتی ۱۴٪ بودند. در همین حال، آزمایش با استفاده از SQL Map موفق به دسترسی به پایگاه داده و نام کاربری در وب سرور شد. گام بعدی در این تحقیق ارائه توصیه هایی برای نصب فایروال در وب سایت به عنوان یک اقدام کاهش برای کاهش خطر حملات SQLi است. سهم اصلی این تحقیق توسعه یک روش ساختار یافته برای شناسایی و رسیدگی به آسیب پذیری های SQLi در سرورهای وب است که نقش مهمی در حفظ امنیت و یکپارچگی داده ها در یک محیط آنلاین به سرعت در حال تکامل دارند.



## A Multi Objective Optimization Model for Multi-commodity Closed-loop Supply Chain Network Considering Disruption Risk

M. Afshar<sup>a</sup>, S. Y. Hadji Molana<sup>\*b</sup>, B. Rahmani Parchicolaie<sup>c</sup>

<sup>a</sup> Department of Industrial Engineering, Central Tehran Branch, Islamic Azad University, Tehran, Iran

<sup>b</sup> Department of Industrial Engineering, Science and Research Branch, Islamic Azad University, Tehran, Iran

<sup>c</sup> Department Mathematics, Noor branch, Islamic Azad University, Noor, Iran

### PAPER INFO

#### Paper history:

Received 31 October 2023

Received in revised form 16 December 2023

Accepted 24 December 2023

#### Keywords:

X-band

Closed-loop Supply Chain

Sustainability

Boom-Bust Cycle

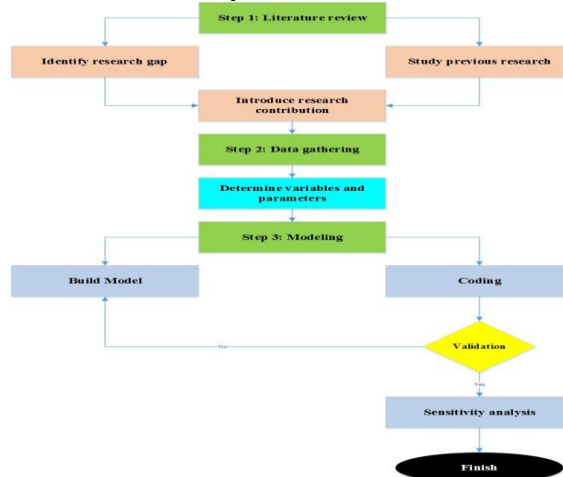
Optimization Model

### ABSTRACT

Recently, the difference in the most effective competencies is considered the main competitive factor in organizations. To this end, organizations seek to improve a number of their functional capabilities, expertise, and capacities to enhance their operational area. Therefore, when an organization focuses on the quality of its services or products, it is trying to improve maintainability to gain a competitive advantage. In this study, a closed-loop, multi-objective, multi-level, multi-commodity, and multi-period mathematical model for a supply chain with producer, and distributor components is presented to locate and allocate items. The presented model can control environmental, economic, and social factors along the chain. One of the most important and unique aspects of the current study is considering different scenarios in the closed-loop supply chain (CLSC) so that the quality of the produced and transported products is paid attention to according to perishability. In addition, to control environmental effects, the model can minimize total CO<sub>2</sub> emissions. The problem is solved on small, medium, and large scales using Epsilon Constraint and NSGA-II methods. According to the obtained results, the flow according to the boom scenario is more than the stagnation scenario. Finally, according to the sensitivity analysis, the number of centers established increases with an increase in demand. The results show that the non-dominated sorting genetic algorithm (NSGA-II) model can predict the behavior of the model well in the long term. For this purpose, Mean ideal distance (MID) index, has been used for evaluation of calculation. the value of standard MID is equal to 6.56 that shows the model accuracy is adequate.

doi: 10.5829/ije.2024.37.04a.07

### Graphical Abstract



\*Corresponding Author Email: [molana@srbiau.ac.ir](mailto:molana@srbiau.ac.ir) (S. Y. Hadji Molana)

Please cite this article as: Afshar M, Hadji Molana SY, Rahmani Parchicolaie B. A Multi Objective Optimization Model for Multi-commodity Closed-loop Supply Chain Network Considering Disruption Risk. International Journal of Engineering, Transactions A: Basics. 2024;37(04):646-61.

## 1. INTRODUCTION

Supply chain (SC) systems encompass a cohesive network of goods, services, and interrelated activities. Among the pivotal considerations in designing an efficient supply chain is the judicious selection of suppliers responsible for producing goods or delivering services. Thus, the act of choosing the right supplier emerges as a critical facet that enhances and optimizes the flow within the supply chain (1). In the contemporary landscape, supply chains have evolved into structured circuits that, in addition to their forward flows, also accommodate reverse flows. This paradigm is known as a closed-loop supply chain (CLSC), comprising a collaborative network of components operating in unison (2). CLSCs play a significant role in conserving substantial quantities of fossil fuels, non-renewable resources, water, and land through resource recycling; thus, leaving a noteworthy impact on the environment (3). Given the growing significance of environmental concerns, manufacturers and retailers have begun to collaborate on shared responsibilities to enhance the environmental design of products and CLSC efficiency (4). The quest for a more effective collaborative model to encompass various aspects has become a focal point of research (5). Furthermore, in numerous developed and progressive nations, attention has been directed towards the reverse supply chain and its implications on environmental sustainability (6). The reverse supply chain and reverse logistics, by considering the environmental impact of product manufacturing, have garnered significant attention (7-9). Dealing with yield management in a supply chain is a multifaceted endeavor that necessitates decision-making at both strategic and operational levels. High-level decisions encompass determinations regarding facility types, locations, and the control of planned returns (10, 11). Conversely, lower-level planning addresses issues such as intervals between waste material collection, the number and capacity of transportation vehicles, and the determination of optimal routes (12). These two management levels are intertwined, often necessitating separate reviews due to their closeness. Strategic decisions are typically imposed by upstream government institutions on downstream organizations, while operational decisions are enacted through downstream institutions. Therefore, the management of recycling-related issues must be studied concerning various product types (13-15). New logistics structures illustrate the utilization of closed-loop supply chain concepts, showcasing significant improvements in resource utilization efficiency (16, 17). In today's context, returned products have gained substantial importance, being recognized as valuable assets within the supply chain components (18). Reducing environmental impacts to preserve the environment represents one of the primary objectives of the reverse

supply chain. Environmental conservation has taken precedence over the costs associated with collecting returned products, primarily due to the detrimental consequences of excessive carbon emissions from waste disposal on the environment and its resources (19). While reverse logistics focuses on the flow of returned products, a CLSC comprehensively addresses both forward and reverse supply chain operations. Therefore, not only are the two terms distinct, but reverse logistics also falls under the umbrella of the CLSC (20, 21). To ensure the success of any organization, proactive and continuous risk management throughout a project is imperative (22). Managing risk effectively across all levels of the supply chain's life cycle is essential. It's worth noting that project risk exists from the project's inception, and neglecting risk management can hinder project progress. Project risk encompasses uncertain events that can lead to damage or loss, posing threats to project objectives such as schedule, cost, and quality. Often, project managers have limited information about risks associated with individual activities during the planning phase, which can result in delays and increased costs that affect budgets and quality. Addressing risks correctly is crucial, as not doing so can diminish the effectiveness of risk identification and assessment. The risk response stage typically involves four strategies: risk avoidance, risk transfer, risk reduction, and risk acceptance. These strategies vary based on risk severity, resource availability, and other factors relevant to project managers. Risk avoidance entails eliminating potential risks from the environment, while risk reduction aims to minimize the likelihood of these risks. Implementing risk avoidance may introduce complexities to project management (23).

Furthermore, political issues, shifts in demand, technological advancements, and financial considerations introduce uncertainty into the supply chain (24). Sustainable supply chains and their resilience to disruptions have been examined in numerous studies (25). Managing disruptions involves risk identification, assessment, decision-making, and monitoring (26). Fuzzy logic is a valuable method for addressing uncertainties in supply chain management, enabling more precise statistical and mathematical analyses of complex systems and decisions (27). Fuzzy logic has found applications in a wide array of problems, including newly defined fuzzy post-quantum Bernstein polynomials and extended properties of the Bernstein-Klodowski operators, from real function spaces to fuzzy function spaces (28-30).

The present study seeks to address several significant research gaps within the domain of closed-loop supply chains. Notably, prior models have overlooked the product quality, failed to consider diverse scenarios, omitted capacity constraints in distribution and production centers, neglected the natural impact on CO<sub>2</sub> emissions, and disregarded the vulnerability of critical

parameters. This research strives to bridge these gaps by formulating a multi-objective mathematical model that optimizes a sustainable closed-loop supply chain network while factoring in the risk of disruptions in uncertain conditions. To mitigate the risk of disruption in the supply chain network, the study employs sensitivity analysis and numerical tests. By presenting this mathematical model, the research provides a robust decision-making tool for the design and optimization of a sustainable closed-loop supply chain network. In essence, the primary contributions of this research lie in its holistic approach to sustainability considerations and its emphasis on minimizing disruption risk in uncertain conditions. Evaluation of product quality and haulage considerations is incorporated. Various unpredictable scenarios in closed-loop supply chains are accounted for. Capacity constraints in distribution and production centers are considered. Sustainability and resilience in both reverse and direct supply chain flows are explored. The primary objectives include reducing CO<sub>2</sub> emissions, total network costs, and overall risk. Uncertainty in diverse parameters of the mathematical model is addressed.

General limitations of existing models in the field of multi-objective optimization for multi-commodity closed-loop supply chain network with disruption risk is as follow:

- Existing models often simplify the supply chain network by considering only a limited number of factors or assume simplified scenarios. They may not fully capture the complex nature of real-world supply chain systems, including uncertainties, dynamic disruptions, and multiple objectives.
- Many models focus on optimizing a single objective or a predefined set of objectives, which may not be suitable for addressing the dynamic nature of disruptions in a closed-loop supply chain network. These models may not provide robust solutions that can adapt effectively to unforeseen disruptions.
- While disruption risk is an important factor in closed-loop supply chain network design, existing models may not adequately incorporate probabilistic models or stochastic optimization techniques to handle risks and uncertainties associated with disruptions.
- Some models may focus on a single product or commodity, neglecting the complexities that arise when dealing with a wide range of commodities with different characteristics and requirements within a closed-loop supply chain network.

This paper is structured into five sections. The subsequent section offers an overview of the relevant literature. Section three presents the problem statement and the mathematical model. Next, the paper presents the computational results, and the concluding section wraps up the paper.

## 2. LITERATURE REVIEW

This section delves into a literature review pertaining to supply chain management, with a specific focus on both reverse and direct supply chains, uncertainty within the supply chain, and sustainability and risk considerations (31, 32). Numerous studies have put forth mathematical models to tackle these challenges. For instance, Pishvaei et al. (33) concentrated on crisis management in a sustainable pharmaceutical supply chain network; while, Khalifehzadeh et al. (34) aimed to minimize costs and maximize system reliability within a four-level supply chain. Zhalechian et al. (35) investigated environmental effects in a location-routing-inventory problem within a sustainable closed-loop supply chain. Rahmani and Mahoodian (36) factored in CO<sub>2</sub> emissions and reliability within their supply chain network design model. Nasr et al. (37) presented a multi-objective fuzzy model that strives to reduce costs, maximize employment opportunities, and incorporate sustainability considerations within the supply chain. Dong et al. (38) put forth a model that takes into account random demand and reproduction systems, with three primary objectives: identifying profitable producers, allocating distributors to customers, and assessing the flow across various supply chain tiers. Diabat and Jebali (13) introduced a multi-period, multi-commodity models that grapples with uncertainty and recovery based on product quality. Wu (39) devised a dynamic competitive game framework, inclusive of government intervention, with the aim of minimizing environmental costs. In contrast, finally, Moradi and Sangari (40) outlined a multi-level supply chain network, accounting for uncertain parameters and employing robust optimization techniques to mitigate fixed and transportation costs. Kalantari et al. (41) employed a fuzzy robust stochastic optimization approach to reduce environmental impacts while maximizing net present value and social impacts within a sustainable closed-loop supply chain. In recent years, several mathematical models have emerged in the field of closed-loop supply chain management. For instance, Salehi-Amiri et al. (42) developed a mixed-integer programming (MIP) model that considers employment-related costs and opportunities in the avocado industry. Kalantari et al. (43) formulated a stable closed-loop supply chain problem with a dual aim of maximizing net present value (NPV) while minimizing carbon emissions, accounting for inherent uncertainties. Garai & Sarkar (44) delved into the realm of independent economic reverse logistics in a customer-centric closed-loop supply chain, focusing on herbal medicines and biotech fuels. Abolghasemian & Darabi (45), Abolghasemian et al. (46) focused on optimization of hauling system of open-pit mine modeling. Additionally, Devika et al. (47) developed a mixed integer programming model multi-objective CLSC problem. Based on built model, three

novel hybrid metaheuristic methods are developed which are based on adapted imperialist competitive algorithms and variable neighborhood search. Fatollahi-Fard et al. (48) proposed a dual-channel, multi-product, multi-period, multi-echelon CLSC network design under uncertainty for the tire industry. Ali et al. (49) proposed a comprehensive CLSC network that optimizes environmental, economic, and social footprints through a multi-objective optimization approach. To account for parameter uncertainties, employed scenario generation using a scenario-based stochastic programming procedure.

Upon reviewing the existing literature and prior research, this study addresses the following research gaps:

1. Failure to incorporate sustainability considerations within supply chain management, often concentrating solely on economic and environmental aspects.
2. Neglect of the diverse scenarios and possibilities that may arise in closed-loop supply chains due to the presence of uncertainty.
3. Overlooking the capacity constraints in supply chain centers and neglecting discussions on handling multiple commodities.
4. Disregarding the significance of product quality as a critical factor in closed-loop supply chain models.
5. Ignoring the element of parameter uncertainty, which can significantly impact the effectiveness of closed-loop supply chain operations.

### 3. PROPOSED MODEL

**3.1. Problem Definition** In the scope of this research, a sustainable closed-loop supply chain (CLSC) network is developed, encompassing multiple levels, products, and time periods. The research takes into account the risks associated with returned products within the context of production and distribution-related disruptions in the supply chain. This comprehensive supply chain includes various components, such as markets, collection points, production facilities, distribution centers, suppliers, and recycling and disposal sites. Moreover, different production process levels are identified to facilitate cleaner production processes and minimize manufacturing impacts. Diverse technologies are designed to enable the production of reusable products, reducing the demand for natural resources.

Within this examined supply chain, various disturbances faced by distributors are considered. This includes factors like disruptions caused by issues such as drivers' stress during the distribution process. Additionally, the research delves into the impact of economic sanctions on producers, as these risks can hinder meeting customer demands and disrupt supply

chain performance. Factors like outdated technology in industries, unsuitable raw materials, inadequate equipment, and a lack of focus on market requirements can adversely affect the industry in question. Therefore, this study addresses the type of technology utilized in production centers and the costs associated with its use. Consequently, within such a framework, the selection of production and distribution center locations and the establishment of appropriate network flows are deemed of paramount importance. Total supply chain costs encompass facility costs, transportation expenses, procurement, and production costs. Furthermore, the research takes into account the risk stemming from returned products, aligning with a resilience strategy within the reverse supply chain, and considers the social impacts arising from these measures. Given that real-world data required for the mathematical model's parameters are fraught with uncertainties, this research leverages fuzzy set theory to manage these uncertainties. Additionally, to tackle repair-related risks, repair teams are dispatched to designated locations, with the associated repair costs integrated into the supply chain. Lastly, the study examines the supply chain's state under two scenarios: recession and economic boom.

To design a multi-product sustainable CLSC network and create a multi-objective mathematical model that accounts for disruption risks in uncertain conditions, a set of modeling techniques and methods are utilized. These techniques enable the simultaneous pursuit of various objectives, including cost reduction, environmental pollution mitigation resulting from facility creation and product transport, and the enhancement of social welfare within a sustainable multi-product closed-loop supply chain.

To achieve this, a mixed-integer multi-objective mathematical programming model has been formulated. Both deterministic and meta-heuristic methods have been employed to solve the model. The deterministic solution relies on the epsilon-constrained method implemented with GAMS software, while the NSGA-II meta-heuristic solution is executed using MATLAB for the formulation and coding.

The key assumptions underlying the model are as follows:

- Fuzzy demand is considered to accommodate real-world uncertainties.
- Uncertainty in the quality factor of returned products is accounted for.
- The model is multi-period, multi-product, and multi-objective in nature.
- Facility location is assumed to be fixed, and the model selects these locations from among all potential alternatives.

The cost of goods and product transportation between centers is treated as fixed within each scenario. The structural representation of the proposed model is

depicted in Figure 1, which is illustrating the cycle pertaining to the CLSC examined in this research. According to this cycle, products produced are distributed to customers through various distributors. Some of these sold products are returned, refurbished, and reutilized, while others may be discarded as waste or

reintroduced into the production cycle as recycled products.

**3. 2. Notation** In this section, all the symbols used to describe sets, parameters, and variables of the problem are explained in Tables 1-3.

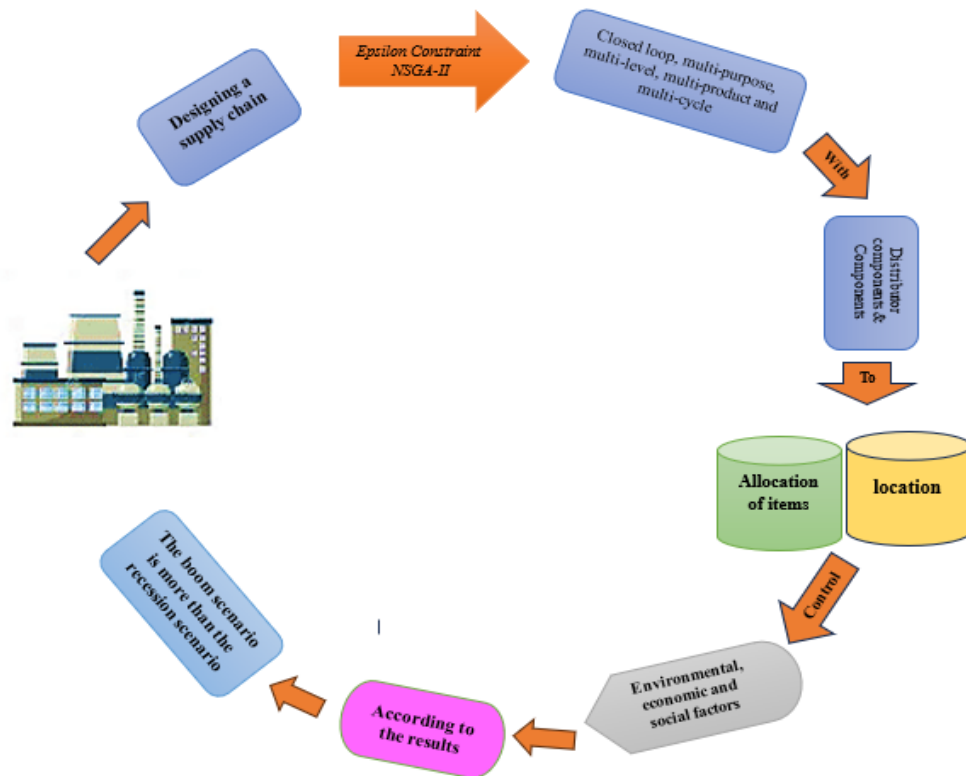


Figure 1. The structure of proposed model

TABLE 1. Notation for indices in the Mathematical Model

Indices	
Symbol	Explanation
$K$	The set of customers $k \in \{1, 2, 3\}$
$R$	The set of re-use centers $r \in \{1, 2\}$
$J$	The set of distributors $j \in \{1, 2\}$
$P$	The set of products $p \in \{1, 2\}$
$I$	The set of collection centers $i \in \{1, 2, 3\}$
$W$	The set of burial and disposal sites $w \in \{1\}$
$Y$	The set of suppliers $y \in \{1, 2\}$
$H$	The set of manufacturers $h \in \{1, 2\}$

TABLE 2. Notation for parameters in the Mathematical Model

$li_y$	Center y's volume capability
$li'_{hv}$	Center h's ability to revamp products using technology v

$li_w$	Capacity of establishment w
$li_{hv}$	Center h's capacity to utilize technology v
$li_i$	Maximum potential of center i
$li_r$	Capability of center r
$li_j$	Capacity of establishment j
$cb_w$	Center w's carbon footprint
$cb_i$	CO2 emissions from center i's operations
$cb_r$	The amount of CO2 emitted by center r
$cb_j$	Carbon emissions associated with center j
$cpk$	Emissions resulting from delivering one unit of product per distance unit
$h_w$	Establishment costs of center w
$h_p$	Center p's fixed establishment cost
$h_i$	The initial expense of setting up center i
$h_j$	Fixed start-up cost for center j

$vl_{ps}$	Quantity of product p in scenario s following recycling
$\widetilde{d}_{ks}^{pt}$	Customer demand for product p in period t from segment k in scenario s
$fo_{ps}$	Unit production cost of product p under scenario s
$f'o_{ps}$	The expense of collecting one unit of product p in scenario s
$pg_{pq}^s$	The price of returned product p with quality q in scenario s
$d_{ihvqs}^p$	Transportation distance/cost of delivering product p with quality q from center i to center h using technology v in scenario s
$d_{yhs}^p$	Shipping costs/distance for product p from center y to center h in scenario s
$d_{hjs}^p$	Transporting product p from center h to center j, including distance and cost, in scenario s
$d_{kis}^p$	Transportation costs/distance for delivering product p from customer k to center i in scenario s
$d_{irqs}^p$	Shipping expenses/distance for delivering product p from center i to center r with quality q in scenario s
$d_{iwqs}^p$	Distance/travel cost for transporting product p from center i to center w with quality q in scenario s
$d_{rhqs}^p$	Shipping costs/distance for delivering product p from center r to center h with quality q in scenario s
$d_{jks}^p$	Distance/cost of product transportation from center to customer in scenario s
$pr_s$	Probability of occurrence for scenario s
$r_{k,q,s}^{pt}$	Return rate of product p with quality q from customer site k during period t in scenario s
$rr^{'pt}$	Return rate of product p from collection center to burial site during period t
$rr^{pt}$	Return rate of product p from collection center to the manufacturer during period t
$rr''^{pt}$	Return rate of product p from collection center to recycling center during period t
$pol_{jt}$	Total pollution emitted during establishment of center j in period t
$pol_{it}$	Total pollution emitted during establishment of center i in period t

$pol_{rt}$	Total pollution emitted during establishment of center r in period t
$pol_{wt}$	Total pollution emitted during establishment of center w in period t
$\alpha_{hts}$	1 if there is no disruption in production center h during period t in scenario s, otherwise 0
$\beta_{yts}$	1 if there is no disruption in supply center y during period t in scenario s, otherwise 0
$cm_{hts}$	Repair cost of manufacturing center h during period t in scenario s
$cm_{yts}$	Repair cost of supply center y during period t in scenario s

**TABLE 3.** Notation for Variables of the Mathematical Model.

$x_j$	If center d is formed, it will be assigned a value of 1; otherwise, it will be assigned a value of 0.
$x_i$	In the event that center g is established, its assigned value will be 1; if not, its value will be 0.
$x_r$	Center b will have a value of 1 if it is established; otherwise, it will have a value of 0.
$x_w$	Should center e be established, its value will be 1; otherwise, it will be 0.
$z_{ihvqs}^{pt}$	Number of product p sent from center i to center h by technology v with quality q during period t in scenario s
$z_{hvjs}^{pt}$	Number of product p sent from center h to center j by technology v during period t in scenario s
$z_{jks}^{pt}$	Number of product p sent from center j to customer k during period t in scenario s
$z_{rhqs}^{pt}$	Number of product p sent from customer j to center k with quality q during period t in scenario s
$z_{iwqs}^{pt}$	Number of product p sent from center j to center w with quality q during period t in scenario s
$z_{yhs}^{pt}$	Number of product p sent from center y to center h during period t in scenario s
$z_{irqs}^{pt}$	Number of product p sent from center i to center r with quality q during period t in scenario s
$y_{ht}$	If repair group f is sent to center h during period t, it's 1
$y_{yt}$	If repair group f is sent to center y during period t, it's 1

**3. 3. Model Formulation**

In this section, all equation used to describe mathematical modeling, are explained.

$$Min f_1 = (\sum_{j \in J} h_j x_j + \sum_{i \in I} h_i x_i + \sum_{r \in R} h_r x_r + \sum_{w \in W} h_w x_w) + pr_s (\sum_t \sum_s (\sum_{p \in P} \sum_{y \in Y} \sum_{h \in H} \beta_{hts} \cdot d_{yhs}^p z_{yhs}^{pt} + \sum_{p \in P} \sum_{y \in Y} \sum_{j \in J} md x_{jks}^{st} + \sum_{p \in P} \sum_{j \in J} \sum_{k \in K} d_{jks}^p z_{jks}^{pt} + \sum_{h \in H} \sum_{s \in S} \sum_{t \in T} y_{ht} \cdot cm_{hts} + \sum_{y \in Y} \sum_{s \in S} \sum_{t \in T} y_{yt} \cdot cm_{yts}) \tag{1}$$

$$Min f_2 = \sum_{r \in R} x_r \cdot cb_r + \sum_{i \in I} x_i \cdot cb_i + \sum_{w \in W} x_w \cdot cb_w + \sum_{j \in J} x_j \cdot cb_j + \sum_{s \in S} w_{sen} \cdot \sum_{t \in T} CEM [\sum_t \sum_s (\sum_{p \in P} \sum_{y \in Y} \sum_{h \in H} d_{yhs}^p z_{yhs}^{pt} + \sum_{p \in P} \sum_{y \in Y} \sum_{j \in J} md x_{jks}^{st} + \sum_{p \in P} \sum_{j \in J} \sum_{k \in K} d_{jks}^p z_{jks}^{pt} + \sum_{s \in S} (\sum_{p \in P} \sum_{k \in K} \sum_{h \in H} d_{kis}^p z_{kis}^{pt} + \sum_{p \in C} \sum_{q \in Q} \sum_{i \in I} \sum_{r \in R} d_{irqs}^p z_{irqs}^{pt} + \sum_{p \in P} \sum_{q \in Q} \sum_{i \in I} \sum_{w \in W} d_{iwqs}^p z_{iwqs}^{pt} + \sum_{v \in V} \sum_{p \in P} \sum_{q \in Q} \sum_{i \in I} \sum_{h \in H} d_{ihqs}^c z_{ihvqs}^{ct} + \sum_{p \in P} \sum_{q \in Q} \sum_{r \in R} \sum_{h \in H} d_{rhqs}^p z_{rhqs}^{pt})] \tag{2}$$

$$Min f_3 = \sum_{t \in T} \sum_{j \in J} pol_{jt} \cdot x_j + \sum_{i \in I} \sum_{t \in T} pol_{it} \cdot x_i + \sum_{r \in R} \sum_{t \in T} pol_{rt} \cdot x_r + \sum_{w \in W} \sum_{t \in T} pol_{wt} \cdot x_w \tag{3}$$

Subject to:

$$\sum_{w \in W} x_w \geq 1 \quad (4)$$

$$\sum_{i \in I} x_i \geq 1 \quad (5)$$

$$\sum_{j \in J} x_j \geq 1 \quad (6)$$

$$\sum_{r \in R} x_r \geq 1 \quad (7)$$

$$\sum_{q_2} \sum_{y \in Y} z_{irqs}^{pt} = rr^{pt} \sum_q (\sum_{k \in K} z_{kiqs}^{pt}) \quad \forall i \in I, p \in P, t \in T, s \in S \quad (8)$$

$$\sum_{i \in I} z_{kiqs}^{pt} = r_{ks}^p \cdot \sum_{p \in P} \sum_{k \in K} z_{jks}^{pt} \quad \forall k \in K, j \in J, t \in T, q \in Q, s \in S \quad (9)$$

$$\sum_{q_1} \sum_{h \in H} \alpha_{hts} \cdot z_{ihvqs}^{pt} = rr^{pt} \sum_q (\sum_{k \in K} z_{kiqs}^{pt}) \quad \forall i \in I, v \in V, p \in P, t \in T, s \in S \quad (10)$$

$$\sum_{h \in H} (\alpha_{hts} \cdot z_{hvjts}^{pt} + w_{hjs}^{pt}) = \sum_{l \in L} z_{ljts}^{pt} \quad \forall j \in J, v \in V, p \in P, t \in T, s \in S \quad (11)$$

$$\sum_{q_2} \sum_{w \in W} z_{iwqs}^{pt} = rr^{pt} \sum_q (\sum_{k \in K} z_{kiqs}^{pt}) \quad \forall p \in P, t \in T, i \in I, s \in S \quad (12)$$

$$\sum_{q_2} \sum_{i \in I} z_{irqs}^{pt} = \sum_q \sum_{h \in H} z_{rhqs}^{pt} \quad \forall r \in R, p \in P, t \in T, s \in S \quad (13)$$

$$\sum_{q_1} \sum_{h \in H} \alpha_{hts} \cdot z_{ihvqs}^{pt} + \sum_{q_2} \sum_{r \in R} z_{irqs}^{pt} + \sum_{q_3} \sum_{w \in W} z_{iwqs}^{pt} = \sum_q \sum_{k \in K} z_{kiqs}^{pt} \quad (14)$$

$$\sum_{y \in Y} z_{yhs}^{pt} + \sum_{q_1} \sum_{i \in I} \alpha_{hts} \cdot z_{ihvqs}^{pt} + \sum_{q \in Q} \sum_{r \in R} z_{rhqs}^{pt} = \sum_{j \in J} \alpha_{hts} \cdot z_{hvjs}^{pt} \quad \forall h \in H, v \in V, p \in P, t \in T, s \in S \quad (15)$$

$$rr^{pt} + rr^{pt} + rr^{pt} = 1 \quad \forall p \in P, t \in T \quad (16)$$

$$\sum_{j \in J} z_{jks}^{pt} \geq d_{ks}^{pt} \quad \forall k \in K, p \in P, t \in T, s \in S \quad (17)$$

$$\sum_{p \in P} \sum_{h \in H} z_{yhs}^{pt} \leq li_y \quad \forall y \in Y, t \in T, s \in S \quad (18)$$

$$\sum_{p \in P} \sum_{j \in J} z_{hvjts}^{pt} \leq li_{hv} \quad \forall h \in H, v \in V, t \in T, s \in S \quad (19)$$

$$\sum_{p \in P} \sum_{k \in K} z_{jks}^{pt} \leq li_j x_j \quad \forall j \in J, t \in T, s \in S \quad (20)$$

$$\sum_{q_3} \sum_{p \in P} \sum_{i \in I} z_{iwqs}^{pt} \leq li_w x_w \quad \forall w \in W, t \in T, s \in S \quad (21)$$

$$\sum_{p \in P} (\sum_{q_1} \sum_{i \in I} \alpha_{hts} \cdot z_{ihvqs}^{pt} + \sum_q \sum_{r \in R} z_{rhqs}^{pt}) \leq li_{hv} \quad \forall h \in H, v \in V, t \in T, s \in S \quad (22)$$

$$\sum_{q_2} \sum_{p \in P} \sum_{i \in I} z_{irqs}^{pt} \leq li_r x_r \quad \forall r \in R, t \in T, s \in S \quad (23)$$

$$\sum_{q_1} \sum_{p \in P} \sum_{i \in I} \alpha_{hts} \cdot z_{ihvqs}^{pt} + \sum_{q_3} \sum_{p \in P} \sum_{w \in W} z_{iwqs}^{pt} + \sum_{q_2} \sum_{p \in P} \sum_{r \in R} z_{rhqs}^{pt} \leq li_r x_r \quad \forall i \in I, v \in V, t \in T, s \in S \quad (24)$$

$$1 - \alpha_{hts} \leq y_{ht} \quad \forall h \in H, t \in T, s \in S \quad (25)$$

$$1 - \beta_{yts} \leq y_{yt} \quad \forall y \in Y, t \in T, s \in S \quad (26)$$

$$z_{ihvqs}^{pt}, z_{hvjts}^{pt}, z_{jks}^{pt}, z_{rhqs}^{pt}, z_{kiqs}^{pt}, z_{iwqs}^{pt}, z_{yhs}^{pt}, z_{irqs}^{pt} \geq 0 \quad (27)$$

$$x_j, x_i, x_r, x_w, y_{ht}, y_{yt} \in \{1, 0\} \quad \forall j \in J, i \in I, r \in R, w \in W \quad (28)$$

The objective Function 1 in the above model minimizes the cost of the entire supply chain, which is related to the construction, flow of goods, transportation, return of returned products, burial, collection and production. The objective Function 2 reduce the amount of CO<sub>2</sub> gas emitted from newly established centers and product transportation equipment. The objective Function 3 reduce the occurrence of risks. By considering the above three functions in this research, the highest social level is achieved. Constraint 4 ensures that there is at least one place to bury waste products. Constraint 5 guarantees that there is a center for the collection of return products identified by the model. Constraint 6 guarantees that there is at least one center for the distribution of goods. Constraint 7 guarantees that there is at least one recycling center for the returned products to be recycled. Constraint 8 ensures that there is an equilibrium between collection and recycling centers. Limitation 9 guarantees that no return products are left before customers and are completely collected. Limitation 11 shows the amount of goods sent to customers. Limitation 12 shows the balance between the place of collection and burial of reversible products. Limitation 13 guarantees balance at the recycling node. Limitation 14 guarantees the quantity of goods sent to collection centers from customers. Limitation 15 guarantees the quantity of goods sent to distributors from manufacturers. Limitation 16 guarantees that the sum of the coefficients of the returned products is equal to 1. Limitation 17 guarantees that the demand must be fully satisfied. Limitation 18 guarantees that the capacity of suppliers is not exceeded. Limitation 19 guarantees not to exceed the capacity of constructors. Limitation 20 shows not exceeding the capacity of distributors. Limitation 21 shows that burial centers must be used if they are created. Limitation 22 shows the capacity of production centers to reproduce products. Limitation 23 guarantees that recycling centers are used. Limitation 24 shows the number of collection centers. It can also be used if a collection center is created. Limitation 25 and 26 indicate that if a center breaks down, it must be rebuilt by the repair group. Limitations 27 and 28 indicate the type of decision variables.

**3. 4. Proposed Fuzzy Model** This research the fuzzify the model is used. A triangular fuzzy approach is employed concerning the existing uncertainty in demand, establishment costs of centers, and CO<sub>2</sub> emissions from established centers. The definition of these uncertain parameters are as follows:

- $(j_1, j_2, j_3)_{is}^{pt}$  The imprecise product p demand from customer i during period t in scenario s
- $(h_1, h_2, h_3)_j$  The vague cost of creating center j
- $(h_1, h_2, h_3)_p$  The uncertain expenses for setting up center p

- $(h_1, h_2, h_3)_i$  The ambiguous costs associated with establishing center i
- $(h_1, h_2, h_3)_w$  The imprecise cost of creating center w
- $(cb_1, cb_2, cb_3)_j$  The uncertain quantity of CO<sub>2</sub> emitted during the establishment of center j
- $(cb_1, cb_2, cb_3)_p$  The ambiguous amount of CO<sub>2</sub> released when setting up center p
- $(cb_1, cb_2, cb_3)_i$  The vague emissions associated with establishing center i
- $(cb_1, cb_2, cb_3)_w$  The fuzzy environmental impact of creating center w

Let's say we want to solve a linear mathematical model using classical methods. We can do this by following these steps:

$$\begin{aligned} & \text{Max } C^t x \\ & \text{Subject to:} \end{aligned} \tag{29}$$

$$A_i x \leq b_i, \quad x \geq 0, \quad (i = 1, \dots, m)$$

The values of A, b, and c are fixed in this context. To convert a fuzzy limitation into a clear membership function, the proposed approach is employed. Tan and Cao present a linear normal fuzzy model by defining the objective function in the following manner:

$$\begin{aligned} & LP(\alpha) \\ & \text{Max } C^t x \\ & \text{Subject to:} \end{aligned} \tag{30}$$

$$A_i x \leq b_i + (1 - \alpha)p_i, \quad i = 1, 2, \dots, m, \quad x \geq 0, \quad \alpha \in [0, 1]$$

The optimization problem involves a parameter  $\alpha$  that takes values between 0 and 1. The linear-term coefficient  $p_i \geq 0$  is non-negative, while  $LP_\alpha$ ,  $B_\alpha$  and  $z_\alpha$  denote the optimal value, vector, and solution of the equation  $LP_\alpha$  respectively. The right coefficient  $b + (1 - \alpha)p$  varies depending on the chosen  $\alpha$ , and  $P_0$  represents the difference between the optimal and secondary vectors. To implement the proposed algorithm, one selects  $z_1$  and  $z_0$  as the optimal values of  $LP_1$  and  $LP_0$ , respectively, subject to the condition  $p_0 = z_0 - z_1 > 0$ .

**4. PROPOSED SOLUTION ALGORITHM**

**4. 1.  $\epsilon$  –Constraint Method** One of the popular methods in multi-objective optimization, which will be used in this research, is the  $\epsilon$  –constraint method, in which one of the objective functions is selected for optimization, and other objective functions become constraints with an upper limit of  $\epsilon$  (6, 46, 47). In the epsilon method, the limitation is that one of the contradictory goals is kept in the objective function and other functions are limited by defining an upper bound.

In fact, in this way, the multi-objective problem becomes a single-objective problem. The limit of the objective functions for the problem is such that by changing the vector on the right side of the problem, all possible Pareto solutions for the multi-objective problem are repeated from the upper limit to the lower limit, and the problem is solved. Then, an optimal solution for the problem is produced. By changing the epsilons, we can get different values for the main objective function. All possible Pareto solutions for the multi-objective problem are generated. The general form of the  $\epsilon$ -constraint problem is as follows.

$$\begin{aligned}
 & \max f_i(x) \\
 & \text{s.t.} \\
 & f_j(x) \leq \epsilon_i \quad \forall i \neq j \\
 & x \in X
 \end{aligned} \tag{31}$$

**4. 2. NSGA-II** Based on the genetic algorithm that is in accordance with the natural property of reproduction, first a potential population P is considered as a productive population. Therefore, the community is sorted based on this sorting algorithm and a Pareto rank is assigned to each individual. At this stage, various optimization problems become a Pareto optimization problem. For this purpose, the mutation and crossover operators to create the resulting number of children are specified using the Q and N sets. Next, a mixed population is created by assigning each child to one parent. Finally, the combined population is sorted and the N best individuals are considered as the population for the next generation.

**4. 2. 1. Solution Representation** In Figure 2, the rows and columns represent manufacturers and suppliers and the duration of repairs, respectively. The numbers of each cell also guarantee the dispatch or non-dispatch of the work service to the place.

For the crossover operation, the suitable parents for each child must first be selected from the generated population, for this purpose, the Roulette cycle structure is used. Based on this, the selection criterion is based on solutions that have a greater density distance.

		$t_1$	$t_2$	$t_3$	$t_1$	$t_2$	$t_3$
$m_1$		1	1	0	0	0	1
$m_2$		0	0	1	1	0	1
$n_1$		1	1	0	1	0	1
$n_2$		0	1	1	1	1	0

Figure 2. Chromosome representation

**4. 2. 2. Crossover and Mutation Operators** The crossover operation is performed point by point for location variables. This location selection structure leads to the creation of convergent solutions for the problem based on the algorithm. In this study, creating two points for chromosome selection is used for crossover operation (49-52).

For the mutation operation, a chromosome is randomly selected. Because, the random selection of chromosomes increases the variety of solutions and presents different situations. In this research, a set of chromosomes are randomly selected, but they are used for reverse mutation operations (Figure 3).

Setting the parameters used in this study is reported based on Taguchi approach stated in Tables 4 and 5.

Then, according to Taguchi L9 design, the following NSGA-II algorithm is implemented. After entering data in MINITAB software and implementing Taguchi method, the S / N diagram is presented in Figure 4.

**4. 2. 3. Full Algorithm** There are deference methods to analyze the efficiency of genetic algorithm. For example, one of these indicators is the average distance from the average ideal distance (MID) metric. This index is calculated using equation 32. In equation 35, n is equal to the number of Pareto points, and  $f_{1,total}^{max}$  and  $f_{1,total}^{min}$  are the highest and lowest values of the objective function in the algorithm.

Parent	81	54	46	62	71	48
	6	61	28	95	401	100
	47	44	57	401	461	75
	100	321	32	63	123	91
Child	81	54	46	62	71	47
	100	401	95	28	61	6
	47	44	57	401	461	75
	100	321	32	63	123	91

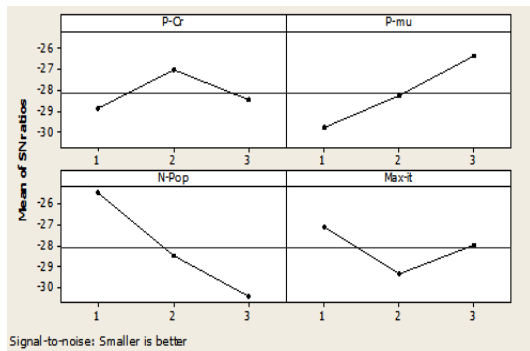
Figure 3. Mutation operator

TABLE 4. Parameters and their value levels for the NSGA-II algorithm

Parameters	Values of each level		
	Level 1	Level 2	Level 3
Rate of Crossover (RC)	0.5	0.6	0.7
Rate of Mutation (Rm)	0.4	0.5	0.6
Number of potential in the Population (N-pop)	50	100	150
Maximum iteration (Max-iteration)	50	150	200

**TABLE 5.** Tuning the parameters

Parameters	Description	Value
nPop	Population number	150
MaxIt	Iteration number	80
Rc	Cross over rate	0.6
Rm	Mutation rate	0.5



**Figure 4.** Output of Taguchi method in NSGA-II algorithm

$$MID = \frac{\sum_{i=1}^n \sqrt{\left(\frac{f_{1i}-f_1^{best}}{f_{1,max}-f_{1,min}}\right)^2 + \left(\frac{f_{2i}-f_2^{best}}{f_{2,max}-f_{2,min}}\right)^2}}{n} \quad (32)$$

where the ideal point's coordinates are  $(f_1^{best}, f_2^{best})$ .

## 5. COMPUTATIONAL RESULTS

**5.1. Simulated Instances** In this part of the research, the results of the mathematical model are presented to measure the efficiency of the model. In

Table 6, numerical examples are considered in different dimensions. For this purpose, 10 problems have been considered as examples, which are numerical problems 1-4 on a small scale, numerical problems 5-7 on a medium scale, and numerical examples 8-10 on a large scale, respectively.

Table 7 shows the findings of solving the model in small, medium and large dimensions. The solved results have been solved based on classification of problem dimensions; also, based on the epsilon constraint method and genetic meta-heuristic method. According to the obtained results, the problem-solving time using the epsilon constraint method increases, while the solving time using the genetic meta-heuristic method is less than the deterministic  $\epsilon$ constraint method. In addition, the deterministic  $\epsilon$ constraint method is not able to solve the problem in large scales, but considering that the calculation error between the meta-heuristic method and the deterministic method in the first and third objective function is less than 1% and in the second objective function less than 6%. It is possible to use the results of meta-heuristic method in large dimensions instead of exact solution to solve problems. Therefore, considering that the calculation error between the epsilon constraint method and NSGA-II is less than 0.1 in the 95% confidence interval; therefore, we can conclude that from the meta-heuristic method in the long run and in very large problems that the epsilon limit method is able to handle it. We should not use it to solve and estimate the value of the objective function.

Table 8 presents the results of the implementation of the evaluation criteria to measure the performance of the NSGA-II approach. According to the obtained results, the standard average of MID is equal to 6.56. Therefore, the results obtained from the proposed solution method can be trusted to solve large-scale problems.

**TABLE 6.** Various scales examples

Scale	Examples	Disposal centers	Collection centers	Manufacturers	Recycling centers	Customers	Distribution centers	Supplier
<b>Small Scale</b>	Example 1	1	2	1	1	1	2	1
	Example 2	2	1	1	1	1	2	2
	Example 3	2	2	2	2	2	2	3
	Example 4	3	2	3	3	2	2	3
<b>Medium Scale</b>	Example 5	3	2	3	4	2	3	3
	Example 6	3	3	4	4	3	3	4
	Example 7	4	3	4	4	3	3	4
<b>Large Scale</b>	Example 8	4	4	4	4	3	4	4
	Example 9	5	5	5	4	3	4	5
	Example 10	6	6	5	5	4	5	6

**TABLE 7.** Comparison between finding for exact and meta-heuristic method

Error%			NSGA-II				Epsilon constraint			No	
$f_3$	$f_2$	$f_1$	Time(s)	$f_3$	$f_2$	$f_1$	Time(s)	$f_3$	$f_2$	$f_1$	
0.001	0.05	0.009	1.01	3.46	225.3	631	1.11	3.11	213.6	625	1
0.004	0.03	0.008	3.6	4.77	364.1	674	25.69	4.58	358.3	661	2
0.009	0.04	0.007	5.14	5.39	371.5	697	36.14	5.17	365.3	684	3
0.008	0.05	0.007	12.17	6.14	382.1	702	84.74	5.98	371.8	689	4
0.008	0.04	0.006	22.17	6.25	621.7	1022	657.11	6.10	583.9	978	5
0.009	0.03	0.005	33.69	7.94	647.5	1125	974.12	7.87	614.9	1058	6
0.008	0.05	0.005	37.17	8.07	751.6	1361	1473.8	7.93	728.3	1236	7
0.007	0.05	0.004	42.57	8.66	911.6	1911	1971.7	8.47	892.4	1894	8
0.005	0.04	0.002	56.33	9.11	1162.4	2230	2037.11	8.98	1034.1	2068	9
0.002	0.02	0.002	61.28	9.68	1319.7	2487	2975.64	9.51	1298.7	2540	10

**TABLE 8.** Performance evaluation standards

MID	0	6.13	6.16	6.32	6.51	6.59	6.65	6.76	6.81
-----	---	------	------	------	------	------	------	------	------

Figures 5 and 6 show the solution time for small, medium, and large-scale problems. As observed, the solution time of the Epsilon constraint method increases at a higher level than in the NSGA-II method. In contrast, in the NSGA-II method, increase in solution time is the more stable level.

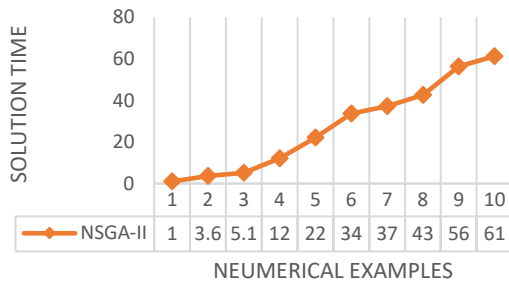


**Figure 5.** Solution time in NSGA-II method

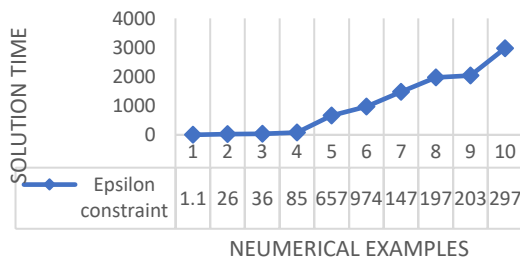


**Figure 6.** Solution time in Epsilon constraint method

**5. 2. Calibration Analysis**

This research has been implemented as a pilot in the plastic industry, including five suppliers, five types of product variety, four distributors, five collection centers and 10 major customers. As an output from this chain, plastic nylon reaches customers after collecting the raw materials. Then, the gathering waste and classified as scrap materials based on their quality from customers. Some of these wastes are buried and the rest are recycled for reproduction. In this study, based on the defined goals, we intend to reduce the environmental effects emanating from them in order to improve the social effects. Table 9 depict the numerical finding of applying the mathematical model in the real study. According to Table 9, the amount of product supply flow to production centers is shown based on recession and boom scenarios in each time period. The first scenario is considered as a boom scenario and the second scenario as a recession scenario. Based on the obtained results, the shipment flow from supply center number 1 to production center 1 according to the recession scenario is equal to 98 and 124 during two periods. This is despite the fact that according to the boom scenario, this flow transfer is equal to 124 and 395.

**5. 3. Sensitivity Analysis**

In this part of the research, we make changes in the basic parameters of the model to assess the effect of changing the parameters on the value of the objective function. Figure 7 shows the number of centers for building recycling centers with increasing demand. Because, the increase in the amount of demand makes more recycling centers to be built. This issue is much more when we are facing a recession scenario. For example, if demand increases by 5%, the number of recycling centers that can be established increases from one to three.

**TABLE 9.** The product flows from supplier center to producer centers

Producer and supplier	Type/ Cycle	Type 2-Cycle2	Type2-Cycle1	Type1-Cycle2	Type1-Cycle1
Supplier1 – Producer 1		98	124	124	365
Supplier1 – Producer 3		258	279	419	478
Supplier2- Producer 2		457	364	574	578
Supplier2- Producer 4		689	398	916	574
Supplier3- Producer 1		367	405	589	368
Supplier3 – Producer 4		714	458	1287	475
Supplier4 – Producer 3		513	517	873	366
Supplier4 – Producer 4		657	598	987	314
Supplier5 – Producer 2		698	687	573	755
Supplier5 – Producer 5		547	697	429	719

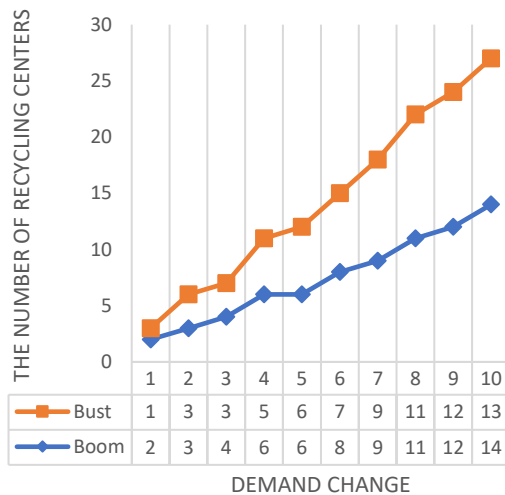


**Figure 7.** Changing demand and its effect to the costs

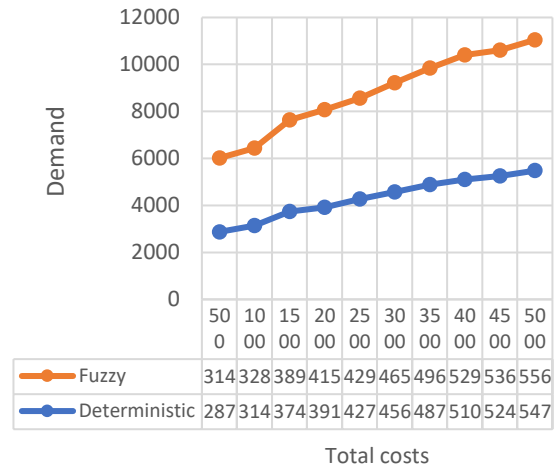


**Figure 8.** The effect of demand’s change on costs in deterministic and fuzzy models

Figure 8 shows that the total costs vary based on demand changes in two deterministic and fuzzy model cases. As observed, the increase in demand raises the total costs in two cases. The amount of costs in an uncertain situation is higher than that in a deterministic situation. Also, the increase in costs by increasing the demand is higher in a fuzzy environment rather than in a deterministic environment.

**5. 4. Discussion and Managerial Insights**

According to the numerical findings obtained in this research, the suggested model has been solved using two methods, epsilon, constraint and genetics. The duration of solving the model using the epsilon method is more limited than the meta-heuristic method. Moreover, the calculation error between the limit epsilon method and

the meta-heuristic algorithm in small and medium dimensions for the first and third objective function is less than 1% and for the third objective function is less than 6%, which can be a proof of the reliability of the meta-heuristic algorithm in large dimensions are the limit for solving the problem instead of the epsilon method. In addition, in the meta-heuristic method, the standard mean of MID is equal to 6.56. Based on the obtained results, the shipment flow from supply center number 1 to production center 1 according to the recession scenario is equal to 98 and 124 during two periods. This is despite the fact that according to the boom scenario, this flow transfer is equal to 124 and 395. As observed, the increase in demand raises the total costs in two cases of deterministic and fuzzy models. The amount of costs in an uncertain situation is higher than that in a deterministic

situation. Also, the increase in costs by increasing the demand is higher in a fuzzy environment rather than in a deterministic environment. According to above mentioned building a multi-objective mathematical model of a multi-product sustainable CLSC network, taking into account the risk of disruption in the conditions of uncertainty, is one of the complex and challenging issues in the field of SCM. In this context, the most important managerial insights are:

1. Productivity: Gain more productivity in using resources in real time.
2. Flexibility: designing a system that can adapt to different conditions.
3. Sustainability: planning and implementing activities in a way that indicates financial, environmental, social and process sustainability.
4. Optimism: obtaining the most optimal solution for the balance between cost and performance, improving internal and external processes of the organization.
5. Risk management: identifying, measuring and controlling risks, taking into account uncertainty and environmental changes.
6. Cooperation: providing cooperation and coordination between employees, departments and business partners.
7. Strategizing: designing appropriate strategies to maintain and develop the organization's competitive ability.
8. Energy efficiency: Economizing the use of energy in the SC in a way that leads to cost reduction and environmental protection.
9. Technology: Using new technologies in various fields such as tag identification, IoT and goods circulation to improve the performance and sustainability of the SC.
10. Transparency: ensuring transparency in processes and information to increase the trust of customers and business partners.

## 5. CONCLUSION AND FUTURE STUDIES

In modern business, the ability to differentiate key competencies has become critical for companies' competitiveness. To achieve this, companies often focus on their strengths and seek to improve sustainability to gain a competitive advantage. The innovative aspects of this study include considering product quality, vulnerability scenarios, production and distribution capacity, and sustainability in the supply chain. The problem was solved using the Epsilon Constraint and NSGA-II methods on small, medium, and large scales. The results showed that costs increase as demand increases, especially during boom cycles. The number of built-up centers also increases with demand, particularly during boom cycles. Additionally, the study compared deterministic and fuzzy models, and emphasized the importance of considering returned goods as valuable assets in the CLSC. Also, the resilience of the designed

network was viewed by this assumption that facilities may fail in the SC, and the disruption risk is removed. In addition, in this study, we developed the mathematical model for a cleaner production process and minimizing possible environmental and human health damage. The suggested model tries to reduce the SC costs and environmental effects. Main obtained results of the research is as follow:

- The model was solved on various dimension using the  $\varepsilon$ -Constraint and NSGA-II algorithm.
- Also, using a case study, Sunny Plats Industries, the validity of the model was investigated.
- MID ration calculates 6.48 for NSGA-II.
- In addition, according to the numerical results, the flow in the Boom Scenario is more than that in the Bust Scenario.
- By increasing the demand, the number of established centers gets higher.

In the research design a mathematical model of the multi-product sustainable CLSC network, taking into account the risk of disruption in the conditions of uncertainty, there are important limitations that should be considered. Some of the most important research limitations are:

1. Time limit: There is a limited time for data collection and mathematical model design. This limitation can put a lot of pressure on the researcher due to the scarcity of resources.
2. Data limitation: It may be difficult to collect enough data to cover all possible conditions in a state of uncertainty.
3. Mathematical limitation: Mathematical methods for modeling the multi-product sustainable CLSC network considering the risk of disruption in conditions of uncertainty are very complex and time-consuming.
4. Communication limitation: In designing a mathematical model, there is a need for coordination between real people, which can be a limitation due to geographical distance, time and cost.
5. Resource limitation: To design a mathematical model, there is a need to access various resources, including powerful computers and specialized software to solve mathematical problems. This limitation may cause the cost of model design to increase dramatically.

This study primarily used the epsilon constraint and NSGA-II methods for the decision problem under study. For future research, the authors suggest using more advanced optimization algorithms for this decision problem. Therefore, it is proposed to develop a general discussion on the importance of advanced optimization algorithms (eg, hybrid heuristics and meta-heuristics, adaptive algorithms, self-adaptive algorithms, island algorithms, polyploid algorithms, hyper-heuristics) for challenging decision problems. For this purpose, there are various fields in which advanced optimization algorithms are used as solution approaches, such as

machine learning, scheduling, multi-objective optimization, transportation, medicine, data classification, and other things. Therefore, it is proposed to develop a discussion that highlights the effectiveness of advanced optimization algorithms in the aforementioned domains and their potential applications for the decision problem investigated in this study.

## 6. REFERENCES

- Ghasempoor Anaraki M, Vladislav DS, Karbasian M, Osintsev N, Nozick V. Evaluation and selection of supplier in supply chain with fuzzy analytical network process approach. *Journal of fuzzy extension and applications*. 2021;2(1):69-88. 10.22105/jfea.2021.274734.1078
- Yun Y, Chuluunsukh A, Gen M. Sustainable closed-loop supply chain design problem: A hybrid genetic algorithm approach. *Mathematics*. 2020;8(1):84. 10.3390/math8010084
- Vidergar P, Perc M, Lukman RK. A survey of the life cycle assessment of food supply chains. *Journal of cleaner production*. 2021;286:125506. <https://doi.org/10.1016/j.jclepro.2020.125506>
- Haghshenas P, Sahraeian R, Golmohammadi A-M. A state-of-the-art model of location, inventory, and pricing problem in the closed-loop supply chain network. *International Journal of Engineering, Transactions B: Applications*. 2022;35(8):1558-70. 10.5829/ije.2022.35.08B.12
- Wang Z, Wang Y, Li B, Cheng Y. Responsibility sharing strategy of product ecological design and collection in manufacturer-retailer closed-loop supply chain. *Computers & Industrial Engineering*. 2023;176:108926. <https://doi.org/10.1016/j.cie.2022.108926>
- Abolghasemian M, Kanafi AG, Daneshmand-Mehr M. Simulation-based multiobjective optimization of open-pit mine haulage system: a modified-NBI method and meta modeling approach. *Complexity*. 2022;2022. <https://doi.org/10.1155/2022/3540736>
- Chkanikova O, Sroufe R. Third-party sustainability certifications in food retailing: Certification design from a sustainable supply chain management perspective. *Journal of Cleaner Production*. 2021;282:124344. <https://doi.org/10.1016/j.jclepro.2020.124344>
- Ghasemi P, Hemmaty H, Pourghader Chobar A, Heidari MR, Keramati M. A multi-objective and multi-level model for location-routing problem in the supply chain based on the customer's time window. *Journal of Applied Research on Industrial Engineering*. 2023;10(3):412-26. 10.22105/jarie.2022.321454.1414
- Ostad-Ali-Askari K. Management of risks substances and sustainable development. *Applied Water Science*. 2022;12(4):65. 10.1007/s13201-021-01562-7
- Dai J, Xie L, Chu Z. Developing sustainable supply chain management: The interplay of institutional pressures and sustainability capabilities. *Sustainable Production and Consumption*. 2021;28:254-68. <https://doi.org/10.1016/j.spc.2021.04.017>
- Jahangiri S, Abolghasemian M, Ghasemi P, Chobar AP. Simulation-based optimisation: analysis of the emergency department resources under COVID-19 conditions. *International journal of industrial and systems engineering*. 2023;43(1):1-19. <https://doi.org/10.1504/IJISE.2023.128399>
- Moosavi S, Seifbarghy M. A robust multi-objective fuzzy model for a green closed-loop supply chain network under uncertain demand and reliability (a case study in engine oil industry). *International Journal of Engineering, Transactions C: Aspects* 2021;34(12):2585-603. 10.5829/ije.2021.34.12c.03
- Diabat A, Jebali A. Multi-product and multi-period closed loop supply chain network design under take-back legislation. *International Journal of Production Economics*. 2021;231:107879. <https://doi.org/10.1016/j.ijpe.2020.107879>
- Pourghader Chobar A, Adibi MA, Kazemi A. A novel multi-objective model for hub location problem considering dynamic demand and environmental issues. *Journal of industrial engineering and management studies*. 2021;8(1):1-31. <https://doi.org/10.22116/jiems.2021.239719.1373>
- Ramesh A, Ostad-Ali-Askari K. Effect of effluent and magnetized effluent on Manning roughness coefficient in furrow irrigation. *Applied Water Science*. 2023;13(1):21. 10.1007/s13201-022-01818-w
- Emenike SN, Falcone G. A review on energy supply chain resilience through optimization. *Renewable and Sustainable Energy Reviews*. 2020;134:110088. 10.1016/j.rser.2020.110088
- Pourghader Chobar A, Sabk Ara M, Moradi Pirbalouti S, Khadem M, Bahrami S. A multi-objective location-routing problem model for multi-device relief logistics under uncertainty using meta-heuristic algorithm. *Journal of Applied Research on Industrial Engineering*. 2022;9(3):354-73. <https://doi.org/10.22105/jarie.2021.299798.1365>
- Sajedi S, Sarfaraz A, Bamdad S, Khalili-Damghani K. Designing a sustainable reverse logistics network considering the conditional value at risk and uncertainty of demand under different quality and market scenarios. *International Journal of Engineering, Transactions B: Applications* 2020;33(11):2252-71. 10.5829/ije.2020.33.11b.17
- Ullah M. Impact of transportation and carbon emissions on reverse channel selection in closed-loop supply chain management. *Journal of Cleaner Production*. 2023;394:136370. <https://doi.org/10.1016/j.jclepro.2023.136370>
- Fu R, Qiang QP, Ke K, Huang Z. Closed-loop supply chain network with interaction of forward and reverse logistics. *Sustainable Production and Consumption*. 2021;27:737-52. <https://doi.org/10.1016/j.spc.2021.01.037>
- Afshar M, Hadji Molana SM, Rahmani Parchicolaie B. Developing multi-objective mathematical model of sustainable multi-commodity, multi-level closed-loop supply chain network considering disruption risk under uncertainty. *Journal of Industrial and Systems Engineering*. 2022;14(3):280-302. 20.1001.1.17358272.2022.14.3.13.2
- Heydari Kushalshah T, Daneshmand-Mehr M, Abolghasemian M. Hybrid modelling for urban water supply system management based on a bi-objective mathematical model and system dynamics: A case study in Guilan province. *Journal of Industrial and Systems Engineering*. 2023;15(1):260-79.
- Ghasemi P, Abolghasemian M. A Stackelberg game for closed-loop supply chains under uncertainty with genetic algorithm and gray wolf optimization. *Supply Chain Analytics*. 2023;4:100040. <https://doi.org/10.1016/j.sca.2023.100040>
- Negri M, Cagno E, Colicchia C, Sarkis J. Integrating sustainability and resilience in the supply chain: A systematic literature review and a research agenda. *Business Strategy and the environment*. 2021;30(7):2858-86. <https://doi.org/10.1002/bse.2776>
- Chobar AP, Adibi MA, Kazemi A. Multi-objective hub-spoke network design of perishable tourism products using combination machine learning and meta-heuristic algorithms. *Environment, Development and Sustainability*. 2022:1-28. 10.1007/s10668-022-02350-2
- Zavala-Alcivar A, Verdecho M-J, Alfaro-Saiz J-J, editors. Assessing and selecting sustainable and resilient suppliers in agri-food supply chains using artificial intelligence: a short review. *Boosting Collaborative Networks 40: 21st IFIP WG 55 Working Conference on Virtual Enterprises, PRO-VE 2020, Valencia*,

- Spain, November 23–25, 2020, Proceedings 21; 2020: Springer. 10.1007/978-3-030-62412-5\_41
27. Rezaei Kallaj M, Abolghasemian M, Moradi Pirbalouti S, Sabk Ara M, Poughader Chobar A. Vehicle routing problem in relief supply under a crisis condition considering blood types. *Mathematical Problems in Engineering*. 2021;2021:1-10. 10.1155/2021/7217182
  28. Özkan EY. Inequalities for approximation of new defined fuzzy post-quantum Bernstein polynomials via interval-valued fuzzy numbers. *Symmetry*. 2022;14(4):696. <https://doi.org/10.3390/sym14040696>
  29. Ozkan EY. Approximation by Fuzzy  $S(p, q)$ -Bernstein-Chlodowsky Operators. *Sahand Communications in Mathematical Analysis*. 2022;19(2):113-32. <https://doi.org/10.22130/scma.2022.524506.910>
  30. Özkan EY, Hazarika B. Approximation results by fuzzy Bernstein type rational functions via interval-valued fuzzy number. *Soft Computing*. 2023;27(11):6893-901. 10.1007/s00500-023-08013-2
  31. Pasandideh SHR, Niaki STA, Asadi K. Bi-objective optimization of a multi-product multi-period three-echelon supply chain problem under uncertain environments: NSGA-II and NRGA. *Information Sciences*. 2015;292:57-74. <https://doi.org/10.1016/j.ins.2014.08.068>
  32. Ghomi-Avili M, Naeini SGJ, Tavakkoli-Moghaddam R, Jabbarzadeh A. A fuzzy pricing model for a green competitive closed-loop supply chain network design in the presence of disruptions. *Journal of Cleaner Production*. 2018;188:425-42. 10.1016/j.jclepro.2018.03.273
  33. Pishvaei MS, Razmi J, Torabi SA. An accelerated Benders decomposition algorithm for sustainable supply chain network design under uncertainty: A case study of medical needle and syringe supply chain. *Transportation Research Part E: Logistics and Transportation Review*. 2014;67:14-38. <https://doi.org/10.1016/j.tre.2014.04.001>
  34. Khalifehzadeh S, Seifbarghy M, Naderi B. A four-echelon supply chain network design with shortage: Mathematical modeling and solution methods. *Journal of Manufacturing Systems*. 2015;35:164-75. <https://doi.org/10.1016/j.jmsy.2014.12.002>
  35. Zhalechian M, Tavakkoli-Moghaddam R, Zahiri B, Mohammadi M. Sustainable design of a closed-loop location-routing-inventory supply chain network under mixed uncertainty. *Transportation research part E: logistics and transportation review*. 2016;89:182-214. <https://doi.org/10.1016/j.tre.2016.02.011>
  36. Rahmani D, Mahoodian V. Strategic and operational supply chain network design to reduce carbon emission considering reliability and robustness. *Journal of Cleaner Production*. 2017;149:607-20. <https://doi.org/10.1016/j.jclepro.2017.02.068>
  37. Nasr AK, Tavana M, Alavi B, Mina H. A novel fuzzy multi-objective circular supplier selection and order allocation model for sustainable closed-loop supply chains. *Journal of Cleaner production*. 2021;287:124994.
  38. Dong J, Jiang L, Lu W, Guo Q. Closed-loop supply chain models with product remanufacturing under random demand. *Optimization*. 2021;70(1):27-53. <https://doi.org/10.1016/j.jclepro.2020.124994>
  39. Wu C-H. A dynamic perspective of government intervention in a competitive closed-loop supply chain. *European Journal of Operational Research*. 2021;294(1):122-37. <https://doi.org/10.1016/j.ejor.2021.01.014>
  40. Moradi S, Sangari MS. A robust optimisation approach for designing a multi-echelon, multi-product, multi-period supply chain network with outsourcing. *International Journal of Logistics Systems and Management*. 2021;38(4):488-505. <https://doi.org/10.1504/IJLSM.2021.114759>
  41. Kalantari S, Kazemipoor H, Sobhani FM, Molana SMH. A neutrosophical model for optimal sustainable closed-loop supply chain network with considering inflation and carbon emission policies. *Decision Making: Applications in Management and Engineering*. 2022;5(2):46-77. <https://doi.org/10.31181/dmame03051020224k>
  42. Salehi-Amiri A, Zahedi A, Gholian-Jouybari F, Calvo EZR, Hajiaghahi-Keshteli M. Designing a closed-loop supply chain network considering social factors; a case study on avocado industry. *Applied Mathematical Modelling*. 2022;101:600-31. 10.1016/j.apm.2021.08.035
  43. Kalantari S, Kazemipoor H, Sobhani FM, Molana SMH. Designing sustainable closed-loop supply chain network with considering spot-to-point inflation and carbon emission policies: A case study. *Computers & Industrial Engineering*. 2022;174:108748. <https://doi.org/10.1016/j.cie.2022.108748>
  44. Garai A, Sarkar B. Economically independent reverse logistics of customer-centric closed-loop supply chain for herbal medicines and biofuel. *Journal of Cleaner Production*. 2022;334:129977. <https://doi.org/10.1016/j.jclepro.2021.129977>
  45. Abolghasemian M, Darabi H. Simulation based optimization of haulage system of an open-pit mine: Meta modeling approach. *Organizational resources management researchs*. 2018;8(2):1-17. 20.1001.1.22286977.1397.8.2.2.6
  46. Abolghasemian M, Ghane Kanafi A, Daneshmandmehr M. A two-phase simulation-based optimization of hauling system in open-pit mine. *Iranian journal of management studies*. 2020;13(4):705-32. 0.22059/IJMS.2020.294809.673898
  47. Devika K, Jafarian A, Nourbakhsh V. Designing a sustainable closed-loop supply chain network based on triple bottom line approach: A comparison of metaheuristics hybridization techniques. *European journal of operational research*. 2014;235(3):594-615. <https://doi.org/10.1016/j.ejor.2013.12.032>
  48. Fathollahi-Fard AM, Dulebenets MA, Hajiaghahi-Keshteli M, Tavakkoli-Moghaddam R, Safaeian M, Mirzahasseinian H. Two hybrid meta-heuristic algorithms for a dual-channel closed-loop supply chain network design problem in the tire industry under uncertainty. *Advanced engineering informatics*. 2021;50:101418. <https://doi.org/10.1016/j.aei.2021.101418>
  49. Ali SM, Fathollahi-Fard AM, Ahnaf R, Wong KY. A multi-objective closed-loop supply chain under uncertainty: An efficient Lagrangian relaxation reformulation using a neighborhood-based algorithm. *Journal of Cleaner Production*. 2023;423:138702. <https://doi.org/10.1016/j.jclepro.2023.138702>
  50. Li B, Liu K, Chen Q, Lau Y-y, Dulebenets MA. A Necessity-Based Optimization Approach for Closed-Loop Logistics Considering Carbon Emission Penalties and Rewards under Uncertainty. *Mathematics*. 2023;11(21):4516. <https://doi.org/10.3390/math11214516>
  51. Asghari M, Afshari H, Mirzapour Al-e-hashem S, Fathollahi-Fard AM, Dulebenets MA. Pricing and advertising decisions in a direct-sales closed-loop supply chain. *Computers & Industrial Engineering*. 2022;171:108439. <https://doi.org/10.1016/j.cie.2022.108439>
  52. Moosavi J, Fathollahi-Fard AM, Dulebenets MA. Supply chain disruption during the COVID-19 pandemic: Recognizing potential disruption management strategies. *International Journal of Disaster Risk Reduction*. 2022;75:102983. <https://doi.org/10.1016/j.ijdrr.2022.102983>

**COPYRIGHTS**

©2024 The author(s). This is an open access article distributed under the terms of the Creative Commons Attribution (CC BY 4.0), which permits unrestricted use, distribution, and reproduction in any medium, as long as the original authors and source are cited. No permission is required from the authors or the publishers.

**Persian Abstract****چکیده**

اخیراً تفاوت در مؤثرترین شایستگی‌ها عامل اصلی رقابتی در سازمان‌ها تلقی می‌شود. برای این منظور، سازمان‌ها به دنبال بهبود تعدادی از قابلیت‌های عملکردی، تخصص و ظرفیت‌های خود برای ارتقای حوزه عملیاتی خود هستند. بنابراین، زمانی که یک سازمان بر کیفیت خدمات یا محصولات خود تمرکز می‌کند، در تلاش است تا قابلیت نگهداری را بهبود بخشد تا مزیت رقابتی به دست آورد. در این مطالعه، یک مدل ریاضی حلقه بسته، چند هدفه، چند سطحی، چند کالایی و چند چرخه برای یک زنجیره تامین با اجزای سازنده و توزیع کننده برای مکان یابی و تخصیص اقلام ارائه شده است. مدل ارائه شده می‌تواند عوامل محیطی، اقتصادی و اجتماعی را در طول زنجیره کنترل کند. یکی از مهمترین و منحصر به فردترین جنبه‌های مطالعه حاضر، در نظر گرفتن سناریوهای مختلف در زنجیره تامین حلقه بسته (CLSC) است تا کیفیت محصولات تولیدی و حمل شده با توجه به فسادپذیری مورد توجه قرار گیرد. علاوه بر این، برای کنترل اثرات زیست محیطی، مدل می‌تواند انتشار کل CO<sub>2</sub> را به حداقل برساند. این مشکل در مقیاس‌های کوچک، متوسط و بزرگ با استفاده از روش‌های Epsilon Constraint و NSGA-II حل می‌شود. با توجه به نتایج به دست آمده، جریان بر اساس سناریوی رونق بیشتر از سناریوی رکود است. در نهایت، با توجه به تحلیل حساسیت، تعداد مراکز تأسیس شده با افزایش تقاضا افزایش می‌یابد. نتایج نشان می‌دهد که مدل NSGA-II می‌تواند رفتار مدل را به خوبی در بلندمدت پیش‌بینی کند. برای این منظور از دو شاخص MID و SM استفاده شده است که مقدار استاندارد MID برابر با ۶.۵۶ و SM استاندارد برابر با ۰.۱۳۹ است.



## Umpire's Signal Recognition in Cricket Using an Attention based DC-GRU Network

A. Dey<sup>\*a</sup>, S. Biswas<sup>a</sup>, L. Abualigah<sup>b,c,d,e</sup>

<sup>a</sup> Department of Computer Science and Technology, Indian Institute of Engineering Science and Technology, Shibpur, Howrah, India

<sup>b</sup> Computer Science Department, Prince Hussein Bin Abdullah Faculty for Information Technology, Al al-Bayt University, Mafra, Jordan

<sup>c</sup> Department of Electrical and Computer Engineering, Lebanese American University, Byblos, Lebanon

<sup>d</sup> Hourani Center for Applied Scientific Research, Al-Ahliyya Amman University, Amman, Jordan

<sup>e</sup> MEU Research Unit, Middle East University, Amman, Jordan

### PAPER INFO

#### Paper history:

Received 13 August 2023

Received in revised form 02 November 2023

Accepted 04 November 2023

#### Keywords:

Action Recognition

Umpire Signal

Cricket Game

Attention

DC-GRU

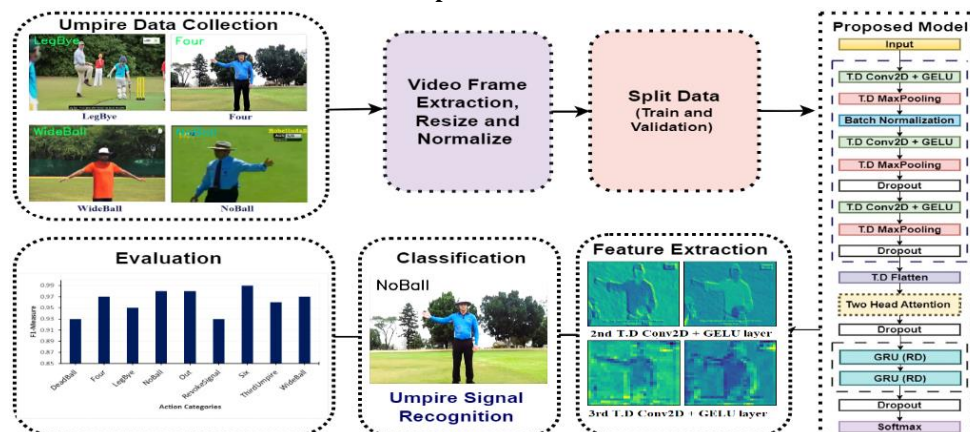
Video Sequences

### ABSTRACT

Computer vision has extensive applications in various sports domains, and cricket, a complex game with different event types, is no exception. Recognizing umpire signals during cricket matches is essential for fair and accurate decision-making in gameplay. This paper presents the Cricket Umpire Action Video dataset (CUAVd), a novel dataset designed for detecting umpire postures in cricket matches. As the umpire possesses the power to make crucial judgments concerning incidents that occur on the field, this dataset aims to contribute to the advancement of automated systems for umpire recognition in cricket. The proposed Attention-based Deep Convolutional GRU Network accurately detects and classifies various umpire signal actions in video sequences. The method achieved remarkable results on our prepared CUAVd dataset and publicly available datasets, namely HMDB51, Youtube Actions, and UCF101. The DC-GRU Attention model demonstrated its effectiveness in capturing temporal dependencies and accurately recognizing umpire signal actions. Compared to other advanced models like traditional CNN architectures, CNN-LSTM with Attention, and the 3DCNN+GRU model, the proposed model consistently outperformed them in recognizing umpire signal actions. It achieved a high validation accuracy of 94.38% in classifying umpire signal videos correctly. The paper also evaluated the models using performance metrics like F1-Measure and Confusion Matrix, confirming their effectiveness in recognizing umpire signal actions. The suggested model has practical applications in real-life situations such as sports analysis, referee training, and automated referee assistance systems where precise identification of umpire signals in videos is vital.

doi: 10.5829/ije.2024.37.04a.08

### Graphical Abstract



\*Corresponding Author Email: [arnabdey@ gmail.com](mailto:arnabdey@ gmail.com) (A. Dey)

Please cite this article as: Dey A, Biswas S, Abualigah L. Umpire's Signal Recognition in Cricket Using an Attention based DC-GRU Network. International Journal of Engineering, Transactions A: Basics. 2024;37(04):662-74.

## 1. INTRODUCTION

Umpires play a critical role in cricket, ensuring fair play and making important decisions throughout a match. They serve as impartial arbiters, upholding the game's rules and regulations. Their judgments not only ensure fairness but also boost player confidence, enhance the spectator experience, and contribute to the smooth functioning of cricket tournaments. Cricket umpire signals play a vital role in maintaining fairness and making accurate decisions during matches (1). The use of computer vision techniques to recognize and analyze these signals in videos has practical applications across various aspects of cricket. Identifying cricket umpire signals using deep learning can provide valuable insights (2) to players, coaches, and spectators. By integrating umpire signal recognition with broadcast technologies, real-time graphics and overlays can be generated, improving the visual presentation of the game and helping viewers understand the decision-making process. Recognizing umpire signals from video sequences is complex, but advancements in deep learning techniques offer promising solutions. The proposed Two-Head Attention based Deep Convolutional Gated Recurrent Unit (DC-GRU) network shows promise in accurately identifying cricket umpire signals. The proposed model's lightweight design makes it suitable to run on devices with low memory requirements. This means that even general-purpose desktops or laptops can effectively run the proposed model without the need for extensive computational resources. Furthermore, the proposed model can robustly detect and interpret umpire signals. This technology aims to enhance decision-making accuracy and minimize human errors in crucial match situations. In cricket, umpires play a pivotal role in making critical on-field decisions, communicating through unique hand signals and gestures. From sports analysis to referee training and automated referee assistance systems, the applications are diverse and have the potential to significantly enhance the quality of cricket matches, benefiting players, officials, and spectators alike. Recognizing the umpire's signals in cricket is challenging due to similarities and complexities in postures and gestures. One significant obstacle is the lack of publicly accessible datasets designed explicitly for classifying umpire's signals. Due to the absence of an existing video dataset for umpire's signals, we have taken the initiative to create a new video dataset comprising 1179 videos showcasing umpire's signals. The model under consideration has undergone training using a custom dataset that we created. The proposed DC-GRU Attention model mainly classifies the videos into nine umpire signal classes: DeadBall, Four, LegBye, NoBall, Out, RevokeSignal, Six, ThirdUmpire and WideBall.

This research offers the following notable contributions: a) Development of a new video dataset for

Cricket Umpire Action (CUAVd) with proper annotations. b) Recognition of Umpire Signals in videos is carried out using the proposed Two-Head Attention based DC-GRU network. c) The proposed DC-GRU Attention model has been evaluated over three standard related benchmark datasets, namely Youtube Actions, HMDB51, and UCF101 action datasets during experimentations, resulting in a high recognition performance of 93.82%, 83.67%, and 92.65%, respectively. d) The effectiveness of the proposed approach is assessed through rigorous evaluation using various well-known classifiers.

## 2. RELATED WORKS

In this section we delve into the realm of prior research endeavors concerning the domain of action recognition. Conventional machine learning (ML) based action recognition systems typically follow a three-step process: feature extraction using manually crafted feature descriptors, feature representation, and feature classification using suitable ML algorithms. In their research, Shi et al. (3) presented a new local spatiotemporal descriptor known as gradient boundary histograms (GBH). The authors showed that the GBH descriptor surpasses other gradient-based descriptors in representing both local structure and motion. The paper focuses on action recognition and introduces the GBH descriptor as a spatiotemporal feature. They have attained 63.2% accuracy on HMDB51 and 86.6% on UCF101 dataset. Challenges associated with handcrafted-based action recognition methods include time-consuming feature selection, labor-intensive processes, and difficulties in determining suitable features (4). To overcome the shortcomings and challenges of handcrafted-based methods, researchers turned to deep learning to develop effective and innovative approaches for cutting-edge action recognition systems based on videos. Deep learning techniques directly analyze videos to identify human actions, using an end-to-end approach. The spatiotemporal and the two-stream networks stand out among deep learning techniques. Xin et al. (5) introduced an adaptive recurrent-convolutional hybrid (ARCH) network. Their approach effectively handles variations in the spatial and temporal domains, as well as intra- and inter-class diversities. This architecture incorporates Temporal-Spatial fusion-Convolutional Neural Networks (CNN) to gather local static and dynamic information, and Recurrent neural network (RNN) focus on global sequence pattern modeling. The seamless connectivity between local feature extraction and global pattern modelling enhances the network's adaptability to actions with varying speeds and durations. Simonyan and Zisserman (6) presented a two-stream CNN model comprising a spatial stream, responsible for

processing individual video frames to capture spatial information, and a temporal stream, dedicated to capturing temporal information within the video sequences. Xiong et al. (7) further extended this concept by proposing a transferable two-stream CNN technique that combined motion and spatial features. The model was trained on the UCF101 dataset, yielding satisfactory results. Wang et al. (8) have implemented action recognition by employing Temporal Segment Network (TSN). This approach uses unique segment-based sampling and aggregation techniques to mimic the patterns and relationships that exist over a longer period of time in a temporal sequence. TSNs divide the input video into multiple segments and independently classify each segment. The classification scores obtained from all segments are then combined to generate the final output. Li et al. (9) introduced a new architecture named VideoLSTM, designed specifically for learning action sequences from videos. VideoLSTM addresses the distinctive characteristics of video data by incorporating convolutions to leverage spatial relationships within images, and it integrates a shallow CNN to capture motion information and produce attention maps-based motion maps. Ge et al. (10) introduced CNN-LSTM with an attention model to recognize human actions. GoogleNet is used to extract features from video sequences. A spatial transformer network is then applied to focus on important regions by transforming the feature maps. The convolutional LSTM module captures sequential information for action classification. Redundant features extracted by GoogleNet are reduced using temporal coherence analysis during training, maintaining high accuracy. Minhas et al. (11) introduced a method to classify shots in field sports videos utilizing AlexNet CNN. The proposed approach achieved 94.07% accuracy. In another study, Rafiq et al. (12) presented a method to classify sports videos and video summarization utilizing transfer learning. By employing an AlexNet CNN-based approach on a relatively smaller dataset exclusively comprised of cricket scenes, they attained an impressive accuracy of 99.26%. Sanchez-Caballero et al. (13) have proposed a real-time method to detect human actions. Their method utilizes a 3D-CNN that can automatically extract spatio-temporal patterns from unprocessed depth sequences. The 3DFCNN classifies the activities based on the spatial and temporal data from depth sequences, without the need to identify people's identities, ensuring privacy is maintained. Savadi Hosseini et al. (14) have introduced a hybrid deep learning architecture that merges the multiple GRU layers with a two-stream inflated CNN network to address action recognition challenges. By combining the strengths of gated recurrent unit (GRU) layers and the two-stream inflated 3D Convolutional neural network (3DCNN), the proposed hybrid architecture enables the

model to process video data, extract both local and global features, and improve its understanding of the temporal and spatial characteristics present in the video content. Kavimandan et al. (15) presented a methodology aimed at enhancing the recognition accuracy of actions utilizing only one camera in multi-camera environments. They suggested a modified bag-of-visual-words method, employing Support Vector Machine (SVM) to detect and categorize human actions. Foyisal et al. (16) put forward a CNN based model designed to categorize six distinct cricket shots. Using their curated dataset, they have attained good results. In our earlier research concerning the identification of workout-related actions from images (17), we have achieved a validation accuracy of 92.75% on the WAId dataset prepared by us, and an accuracy of 89% on the Sports Image dataset using the proposed WorkoutNet architecture. In another research (18), we successfully identified diverse human interactions from image data by implementing the AdaptiveDRNet, enhanced with a multi-level attention mechanism. Wu et al. (19) have provided a survey that delves into the realm of video-based sports action recognition, shedding light on the existing datasets and methodologies in this field. Li et al. (20) introduced a framework that tackles the challenge of selecting important spatial parts and modelling temporal motion in action recognition. Their approach involves selecting the most discriminative spatial parts within video clips and effectively modelling temporal motion by incorporating bidirectional temporal information across multiple layers of an LSTM model. Hussain et al. (21) introduced a convolution-free approach that successfully overcomes previous challenges by accurately encoding relative spatial information. The proposed method employs a pre-trained Vision Transformer to extract features at the frame level. These extracted features are subsequently fed into a multilayer LSTM network, enabling the capture of long-range dependencies within videos. Ravi et al. (22) proposed a new image dataset called SNOW, aimed at detecting umpire poses in cricket. The study's main objective was to identify and categorize four important umpire events: WIDE, OUT, NO BALL and SIX. To extract relevant features, the researchers employed pre-trained CNN models like InceptionV3 and VGG19 to extract features from the umpires pose images and then fed them into a linear SVM classifier. Ahmad et al. (23) proposed a technique to recognize human actions by employing a combination of CNN and Bidirectional-GRU (BD-GRU). The approach involves two main steps. Firstly, they utilized CNN to extract deep features from the frame sequences in human activity videos. Secondly, to capture the temporal dynamics within the sequence of frames, the researchers introduce Bi-GRU. The deep and informative features extracted from the frame sequence are fed into the Bi-GRU, which learns the temporal

motions in both forward and backward directions at every time step. In addition, Wickramasinghe (24) conducted a comprehensive review of the diverse applications of machine learning within the realm of cricket. Reddy and Santhosh (25) propose a two-stream spatial CNN method for recognizing human actions in long video datasets. The first stream extracts spatial information from the RGB frames, while another stream incorporates graph-based visual saliency (GBVS) maps produced using the GBVS technique. The outputs of these spatial streams are concatenated utilizing various feature fusion techniques such as sum, max, average, and product. Pan et al. (26) have proposed a sensor based approach for sports referee training. Several recent studies have placed emphasis on enhancing the detection of cricket events (27, 28) and the summarization of cricket videos (29, 30). Nandyal and Kattimani (31) prepared a new dataset named SNWOLF, designed specifically to identify umpire poses in cricket matches. The proposed method focuses on detecting umpire stances from cricket video frames and classifying them into the six events namely WIDE, LEG BYE, FOUR, SIX, NO BALL and OUT using CNN based framework. They have achieved an accuracy of 98.20% on their prepared SNWOLF data.

The majority of studies in the domain of image or video-based action recognition tend to primarily focus on the recognition of everyday actions (14) or the classification of sports events (32). However, due to the absence of a publicly available standardized video dataset for umpire's signal in cricket, we have taken the initiative to develop our own comprehensive Cricket Umpire Action Video Dataset (CUAVd). This dataset serves as a benchmark resource for evaluating and advancing the field of umpire signal recognition in cricket, providing researchers with a valuable tool for further exploration and development.

### 3. PROPOSED METHOD

The method commenced by gathering videos featuring umpire actions and subsequently trimming them based on the action performed. And then data augmentation is applied. The frame extraction function receives a video path as input and extracts frames from the video. It utilizes the Video Capture object to read the video, determines the total number of frames within the video, and calculates the interval at which frames will be added to the frames list. The frames will be extracted based on a specified sequence length. It then iterates through the frames, resizes them to 64 X 64 height and width, normalizes them by dividing by 255, and appends the normalized frames to the frames list. Finally, it releases the Video Capture object and returns the frames list containing the extracted frames. Next, the dataset is

divided into training and validation set in 75:25 ratio. The block diagram illustrating the sequential steps involved in the proposed method is depicted in Figure 1. This study introduces a Two-Head Attention based Deep Convolutional GRU (DC-GRU) network for umpire's signal recognition in cricket.

Utilizing the proposed DC-GRU Attention model with Callback functions, we train the umpire dataset, extract video frame features, and classify umpire signals with the last layer of the proposed model namely the Softmax layer. The proposed approach effectively analyze both spatial and temporal features extracted from video data, resulting in accurate action predictions. The following subsections explain: A) Training dataset preparation, B) DC-GRU Attention: Model Architecture, C) Loss Function and Optimizer Details, and D) Importance of Attention Mechanism in Umpire Signal Recognition.

**3. 1. Training Dataset Preparation** Initially, we collected the umpire signal dataset and used data augmentation to enhance the model's performance by increasing the training data and reducing overfitting. We have implemented random transformations as part of video data augmentation, including zooming within a range of 0.2 factor, rotation range of 20 degrees, adjusting brightness within a range of 0.5 to 0.9 and applying a contrast range of 1.5. To generate augmented video data, we have utilized the Moviepy python library. Data augmentation, through random transformations applied to the training videos, generates additional training data. This technique perform effectively on unseen data.

**3. 2. DC-GRU Attention: Model Architecture** The proposed Two-Head Attention based DC-GRU Model comprises of a total of 16 layers, including Time Distributed (T.D) Conv2D layers, T.D max pooling layers, T.D dropout layers, T.D Flatten layer, Two Head Attention mechanism, GRU layers and a dense output layer. The proposed model utilized for implementing the proposed work to recognize umpire signals in cricket is depicted in Figure 2. Time-distributed (T.D) layers give more importance to temporal dynamics in video based umpire signal recognition by applying convolution and pooling operations across the time dimension.

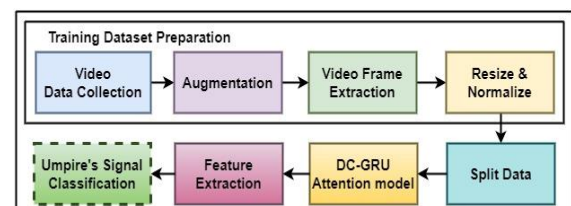


Figure 1. Overview of the Proposed Method

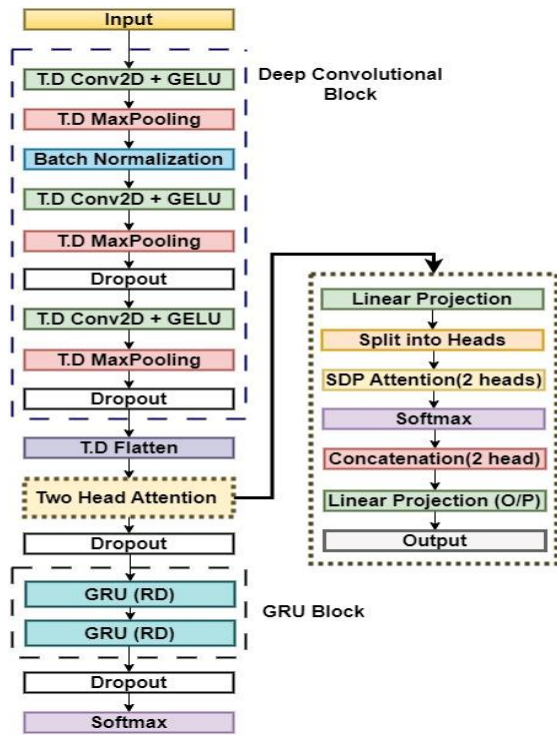


Figure 2. Proposed DC-GRU Attention Model

The breakdown of the model architecture are as follows:

**3. 2. 1. Input Layer** The input layer accepts a sequence of video frames with a shape of (SeqLength, FrameHeight, FrameWidth, nChannels), where SeqLength represents the number of frames considered as a sequence, FrameHeight and FrameWidth are the dimensions of each frame and nChannels are the number of channels. Here, the SeqLength, FrameHeight, FrameWidth are taken as 15, 64, 64 and 3 respectively.

**3. 2. 2. Deep Convolutional Block** This block applies several convolutional layers to each frame in the input sequence, capturing spatial features from the frames. This branch uses three sets of convolutional layers, with 32, 64, and 64 filters, respectively. In the first block, the input sequences of video frames are processed through three layers. The initial Time distributed (T.D) Conv2D+GELU layer (Layer 1) applies 32 filters with a 3x3 kernel size to capture local features in each frame. A TimeDistributed (T.D) wrapper allows each frame in the sequence to be treated independently. The T.D Conv2D layer is mathematically represented using Equation 1. Here,  $I(t-i)$  denotes the input sequence at time step  $(t-i)$ ,  $W_i$  denotes the convolutional kernel at time step  $i$  and  $Y(t)$  represent the output at time step  $t$ .

$$Y(t) = \sum_i W_i * I(t - i) \quad (1)$$

Following this, a MaxPooling2D layer (Layer 2) with a pool size of 4x4 reduces spatial dimensions, emphasizing key features while reducing computation. Each T.D convolutional layer is followed by an Gaussian Error Linear Unit (GELU) activation function and max pooling to reduce the spatial dimensions. The GELU activation (GA) utilized in this study is mathematically represented using Equations 2 and 3, where  $u$  denote the input to the activation function. GA offers a smooth transition from linear to non-linear behavior, addressing vanishing gradient problems while providing superior performance.

$$GA(u) = 0.5 u (1 + \tanh(CT)) \quad (2)$$

$$CT = \left( \sqrt{\frac{2}{\pi}} (u + 0.044715 u^3) \right) \quad (3)$$

BatchNormalization (Layer 3) is used to normalize the batches. The subsequent layers continues feature extraction with deeper layers. Another T.D Conv2D+GELU layer (Layer 4) applies 64 filters, maintaining the 3x3 kernel size for local feature extraction. Subsequently, a MaxPooling2D layer (Layer 5) further compresses feature maps spatially, improving computational efficiency. A Dropout (0.15 rate) layer (Layer 6) is applied for regularization, randomly deactivating portions of the network during training to prevent overfitting. In this block, the complexity of the features is increased. And the third T.D Conv2D+GELU layer (Layer 7) applies 64 filters to capture more intricate patterns. MaxPooling2D (Layer 8) further reduces spatial dimensions, while Dropout (0.15 rate) (Layer 9) maintains regularization. Then T.D flatten layer (Layer 10) is added to reshape the 2D feature maps into a 1D vector format.

**3. 2. 3. Two Head Attention Block** After feature extraction, the sequence of flattened features enters an attention mechanism (Layer 11). The proposed model for recognizing umpire actions in video sequences incorporates a pivotal element known as the scaled dot product mechanism with two attention heads. In a two-head attention mechanism, two distinct sets of query, key, and value vectors facilitate simultaneous focus on different sequence parts. Each set acts as an individual head, allowing the model to learn distinct relationships and extract various sequence features. Computation occurs in parallel across these two heads, and their results are usually combined before progressing through subsequent model layers. This method significantly improves the model's capability to capture diverse sequence relationships and patterns.

The dimensionality of the model ( $d_{\text{model}}$ ) is set to 128, which defines the size of hidden layers of the Two-

Head attention. Here's a breakdown of this Two-Head Attention mechanism:

**1. Utilizing Query, Key, and Value Vectors with Two Attention Heads:** The scaled dot product (SDP) mechanism employs three distinct sets of vectors: Queries (R), Keys (K) and Values (U). In the specific context of the umpire action recognition model, these vectors are derived from the flattened features that are extracted by the preceding convolutional layers of the model. Linear Projections for R, K and U are represented using Equation 4. Here,  $I$  denote the input sequence,  $h$  is the number of attention heads (two here), and  $W_R, W_K, W_U$  are learnable weight matrices specific to R, K, V and it is computed for  $h=1$ , and  $h=2$ .

$$R, K, U = I \cdot W_{R_h}, I \cdot W_{K_h}, I \cdot W_{V_h} \quad (4)$$

**2. Dot Product and Scaling with Two Attention heads:**

This mechanism proceeds by computing the dot product between the Query and Key vectors. Attention scores (AS) are computed using the expression given in Equation 5. This computation quantifies the similarity between various elements in the sequence. To maintain the dot product within manageable bounds, it scales down the values by the square root of the dimension of the K vectors ( $dim_k$ ) as shown in Scaled AS expression represented in Equation 6.  $AS_h$  is computed for  $h=1,2$ .

$$AS_h = R_h K_h^T \quad (5)$$

$$Scaled\ AS_h = \frac{Q_h K_h^T}{\sqrt{dim_k}} \quad (6)$$

**3. Attention Weights (AW) with Two Attention Heads:**

Subsequently, the scaled dot product mechanism applies a softmax function to the SDP, producing the attention weights (AW) as represented in Equation 7. These weights signify the significance and relevance of each element within the sequence relative to the others. Higher attention weights denote that a given element bears greater importance in the context of the task at hand.  $AW_h$  is computed for  $h=1$ , and  $h=2$ .

$$AW_h = Softmax(Scaled\ AS_h) \quad (7)$$

**4. Weighted Summation with Two Attention Heads:**

Finally, the mechanism computes a weighted sum of the Value vectors (U) by leveraging the attention weights (AW) represented using Equation 8. This weighted summation effectively captures vital sequence information, allowing focused attention on crucial segments while disregarding noise. AO represents the Attention Output for  $h=1$ , and  $h=2$ , resulting in concatenated weighted sum outcomes.

$$AO_h = WS_h = (AW_h) \cdot U_h \quad (8)$$

In the realm of umpire action recognition, this mechanism equips the model with the ability to discern which frames or moments in the video sequence hold the utmost relevance for identifying specific umpire actions. By directing its attention towards the pertinent segments of the video data, the model can furnish more precise predictions. The utilization of self-attention mechanisms, such as the scaled dot product attention with two attention heads, emerges as a potent tool for modeling intricate relationships within sequential data. Scaled Dot Product (SDP) Attention layer computes attention scores between the feature vectors from different frames within the sequence. This operation applies attention to the features, assigning higher importance to elements that have higher attention scores. This step results in attention-enhanced features that are more focused on the relevant parts of the sequence. This process is followed by a Dropout layer with 0.18 dropout rate to promote regularization.

**3.2.4. GRU Block** Two GRU layers (Layers 13 and 14) with 128 units each and recurrent dropout (0.23) process the attention-enhanced features, capturing temporal dependencies among the frames in the video sequence. The GRU, a variant of the recurrent neural network (RNN), excels in capturing temporal dependencies and sequence-related information. It operates by processing the current input and the hidden state inherited from the preceding node. This process results in the generation of output, and the updated hidden state is subsequently transmitted to the subsequent node. GRU only needs one unit to complete forget and selecting memory operations. The updated equation of GRU can be represented as depicted in Equations 9 and 10, where  $X_t$  is the external input vector, the update gate is denoted as  $U$  and reset gate as  $rs$ , the hidden state from the previous node ( $hs^{t-1}$ ) are fed through GRU, the updated hidden state ( $hs^t$ ) which is then passed to the next node, the parameters for two matrices  $W$  and  $U$ , bias vector  $b$ .

$$hs^t = (1 - U) \odot hs^{t-1} + U \odot hs' \quad (9)$$

$$hs' = \tanh(W_h X_t + (rs_t * U_{hs} hs_{t-1}) + b_{hs}) \quad (10)$$

In this context, the initial GRU layer, comprising 128 units, is harnessed for the purpose of capturing temporal dependencies embedded within the sequence. Subsequently, a second GRU layer, also featuring 128 units, is employed to derive the ultimate output sequence. In the model, the initial GRU layer is configured to return sequences rather than a single output. This empowers the model to grasp temporal nuances spanning across frames while preserving the output sequence. The second GRU layer does not return sequences, so it returns a single output. Then a dropout layer (Layer 15) with 0.23 dropout rate is applied.

**3. 2. 5. Output Layer** Dense layer with softmax activation (Layer 16) is used to produce the final output probabilities for the nine umpire's signal classes. This layer maps the concatenated features to the corresponding class probabilities. The sum of those probabilities, expressed in decimal form, equals 1. In this study, we are dealing with a multi-class problem. During training, the model employs the Categorical cross-entropy loss function, serving as the metric to gauge the error the model endeavors to reduce.

The proposed Attention based DC-GRU model offers significant utility in recognizing umpire's signals within video sequences, leveraging the distinct strengths of its constituent layers. Time-Distributed (T.D) Conv2D layers perform spatial feature extraction, using 2D convolutional filters that slide across frames, capturing spatial patterns, edges, and textures. As the filters convolve over the frames, they generate feature maps. Each feature map signifies the activation patterns of a distinct filter across various spatial positions within individual frames. These feature maps capture spatial information such as local patterns, object boundaries, and spatial relationships within the frames. The time-distributed convolutional layers are responsible for extracting spatial features from each frame within the sequence. They operate on each frame independently within the sequence. The feature map(s) derived from the three T.D Conv2D+GELU layers when applied to a sample frame containing the 'No Ball' umpire signal are highlighted in Figure 3. Multiple layers hierarchically abstract spatial features, ranging from low-level patterns to complex spatial structures.

Shared weights across frames ensure consistency over time, crucial for recognizing umpire signals. This is particularly useful for tasks that require understanding how spatial patterns evolve across a sequence. The integration of an attention mechanism further enhances the model's ability to focus on relevant frames where

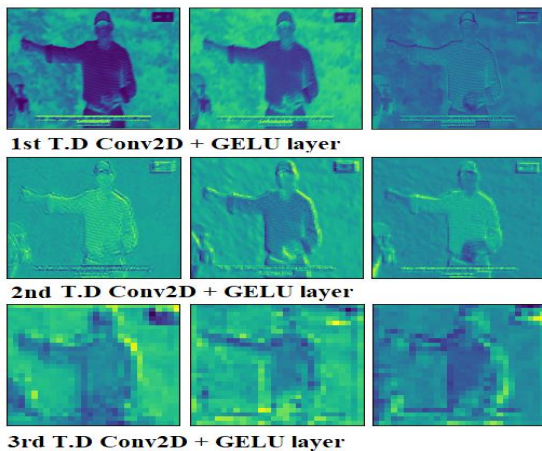


**Figure 3.** Feature map results of 'No Ball' umpire signal

signals are likely to occur for making predictions. On the other hand, the recurrent layers, particularly the GRU components, specialize in capturing temporal dependencies and context across frames present within the sequence. The combination of convolutional layers, attention mechanism, and recurrent layers allows the model to extract both spatial features from individual frames and temporal features from the entire sequence. The proposed Two-Head Attention based DC-GRU architecture is particularly effective in modeling short-term dependencies and intricate temporal dynamics. By combining these layers, the proposed model achieves a comprehensive understanding of umpire signals, encompassing both the complex temporal evolution of these signals. Its ability to learn intricate spatial and temporal features, coupled with its capacity to focus on relevant segments, positions it as a valuable tool for automating the recognition of umpire's signals, thereby enhancing the efficiency and accuracy of sports match analysis and decision-making. With a total number of trainable parameters of 297,097 and a model size of approximately 1.13 MB, the proposed model is suitable for running on low-memory requirement devices like general purpose desktops or laptops.

**3. 3. Loss Function and Optimizer Details** In the proposed work, we are dealing with a multi-class problem. To measure the training error, we utilized the Categorical Cross-Entropy (CCE) loss function. This function minimizes the disparity between expected and actual probability distributions, computing the error as shown in Equation 11 for each instance.

$$Loss_{cce} = \sum_{c=1}^9 t_c \cdot \log f(U S_c) \quad (11)$$

Here,  $t_c$  denotes the ground truth label of  $c^{th}$  class,  $f(U S_c)$  denotes the softmax probability value for  $c^{th}$  class, and  $c$  signifies the overall count of scalar values contained within the model's output. The proposed model utilizes the Nadam optimizer with initial learning rate of 0.01 to minimize the error function. The Nadam optimizer (33) combines elements of two popular optimization methods, namely Nesterov Accelerated Gradient (NAG) and Adam optimizer.

$$\theta_{t+1} = \theta_t - \frac{\eta}{\sqrt{\hat{v}_t + \epsilon}} \left( \beta_1 \frac{m_t}{1 - \beta_1} + \frac{(1 - \beta_1) \nabla L(\theta_t)}{1 - \beta_1^t} \right) \quad (12)$$

In Equation 12,  $\theta_{t+1}$  denotes the parameter updated at the next time step,  $t+1$ , while  $\theta_t$  represents the parameter at the current time step,  $t$ . The symbol  $\eta$  corresponds to the learning rate, determining the step size of the parameter updates. Furthermore,  $\hat{v}_t$  signifies the exponentially weighted average of the squared gradients, offering insights into both the direction and magnitude of the parameter updates,  $\epsilon$  serves as a minuscule value essential for averting division by zero,  $\beta_1$  is the first momentum decay term,  $m_t$  is the exponentially weighted

average of the gradients, and  $\nabla L(\theta_t)$  represents the gradient of the loss function w.r.t the parameter at time step  $t$ .

The Nadam optimizer exhibits several advantages compared to other optimizers such as Adam. Firstly, it incorporates NAG, which enables faster convergence by including momentum in the gradient descent process. This momentum helps the optimizer to navigate areas with steep gradients more efficiently, leading to quicker convergence and improved optimization. Secondly, Nadam combines the benefits of NAG with the adaptive learning rate capabilities inherent in the Adam optimizer. This dynamic learning rate adjustment feature enables the optimizer to fine-tune the learning rates for individual parameters, guided by their gradients and past updates.

### 3. 4. Importance of Attention Mechanism in Umpire Signal Recognition

Attention mechanisms are of paramount importance when it comes to the identification and recognition of umpire signals, such as "FOUR", "SIX", "NO BALL", "WIDE", and others in the context of cricket matches. The diverse array of umpire signals involves distinct visual representations, each conveying specific game events. For instance, signaling a "FOUR" entails raising both arms with all fingers extended, while a "SIX" is typically indicated by both arms raised above the head. The ability to recognize and differentiate these unique visual cues is fundamental in comprehending the dynamics of the ongoing match. Umpire signals sometimes involve subtle hand movements, which can be challenging to detect, particularly when the frame includes other players or objects. Attention mechanisms help the model to concentrate on the umpire's hand or the pertinent area, improving recognition. They enhance robustness to lighting, camera angles, and clutter for effective operation in various conditions. They also allocate computational resources efficiently, reducing processing costs. In complex cases with gesture combinations, attention mechanisms excel at identifying components and their sequence, ensuring accurate signal interpretation. Thus, attention mechanisms are indispensable in the recognition of umpire signals in cricket matches for dynamic focus, capturing dependencies, enhance robustness to variations and ensuring context-aware recognition, making them invaluable for diverse and context-dependent umpire signals in cricket game.

## 4. EXPERIMENTAL RESULTS

This section provides a comprehensive overview of the dataset, conducts a thorough performance evaluation, and

finally analyses the results. The study was conducted on the Google Colab platform without utilizing any GPU. This research has involved a comprehensive investigation of relevant literature and the exploration of various well-established deep learning models. In order to evaluate the overall classification performance of our approach, we have reported the training and validation accuracy, along with the F1-score.

### 4. 1. Dataset Details

Several publicly accessible datasets that are related to the proposed work include HMDB51, UCF50, Youtube Actions and UCF101. These datasets provide valuable resources for conducting research and analysis in the area.

We have created a unique dataset called Cricket Umpire Action Video dataset (CUAVd)<sup>1</sup> by gathering videos from different social media platforms, cricket tournaments and some YouTube videos. Once the data collection phase was completed, we manually identified and extracted the specific segments of the videos that showcase umpire actions. These videos were then organized into separate directories based on different categories to ensure proper labelling. The dataset primarily focuses on umpire signals performed by various umpires during cricket matches. Figure 4 illustrates sample video frames showcasing the LegBye, Four, WideBall, and NoBall umpire signals extracted from the umpire signals video dataset.

In the CUAVd dataset, various umpire signals in cricket have been given by various umpires. Within the proposed dataset, there are 9 distinct categories encompassing various umpire actions, and it comprises a total of 1179 RGB videos. The umpire's signal categories are DeadBall, Four, LegBye, NoBall, Out, RevokeSignal, Six, ThirdUmpire and WideBall. The training dataset is collected from various Cricket tournaments, TV episodes



Figure 4. Sample video frames of CUAVd dataset

<sup>1</sup> CUAVd : <https://sites.google.com/view/cuavd/home>

and Youtube videos. Data collection is a vital step in the proposed work for maintaining the integrity of the research due to the unavailability of various umpire action videos.

**4. 2. Performance Evaluation** Python libraries such as TensorFlow-Keras, Callbacks, and Optimizers have been employed to construct the models on the Google Colab platform. These libraries offer a wide array of functionalities and tools that facilitate creating and training deep learning models. In addition, the Sklearn and Matplotlib libraries have been used for analysis. Sklearn offers various machine learning algorithms and evaluation metrics, while Matplotlib provides visualization capabilities, allowing for the creation of informative and visually appealing plots. Figure 5 exhibits the accuracy curve for the Two-Head Attention based DC-GRU model under consideration, with a training accuracy of 96.17% and a corresponding validation accuracy of 94.38%.

The model's performance did not significantly improve over several consecutive epochs, so the training process was halted at 24 epochs using callback functions.

The proposed study has undergone evaluation using several advanced benchmark deep learning models on the CUAVD dataset. Table 1 showcases the accuracy and F1-Measure achieved by these models, namely VidLSTM [9], CNN-LSTM with Attention [10], 3DFCNN [13], BD-LSTM [20], the DC-LSTM, the DC-GRU model (without attention), and our proposed model. Through extensive experimentation and analysis, it was observed that our proposed DC-GRU Attention model outperformed all the baseline models considered in this study. Moreover, the BD-LSTM [20], 3DFCNN [13], DC-GRU model (without attention), and CNN-LSTM with Attention model [10] also displayed noteworthy performance in classifying Cricket Umpire action videos (CUAVd), achieving validation accuracies of 91.82%, 89.69%, 93.86%, and 90.35% respectively.

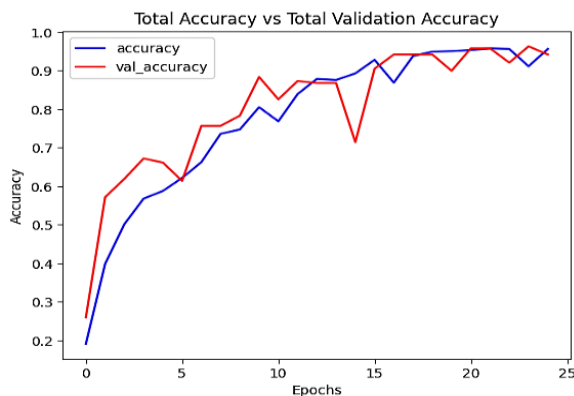


Figure 5. Model Accuracy Trend on CUAVD Dataset

TABLE 1. Experimental Results with Various deep learning models on our CUAVD dataset

Model	Train Accuracy	Validation Accuracy	F1-Score
VidLSTM [9]	94.20%	87.40%	0.87
CNN-LSTM + Attention [10]	93.57%	90.35%	0.90
3DFCNN [13]	94.61%	89.69%	0.89
BD-LSTM [20]	95.36%	91.82%	0.91
DC-LSTM	94.85%	91.43%	0.90
DC-GRU	95.69%	93.86%	0.94
Proposed Model	96.17%	94.38%	0.96

The classification performance report depicted in Figure 6 indicates that the proposed model demonstrates strong performance, achieving an impressive Average F1-Score of 0.96.

In Figures 7 and 8, the confusion matrices for both the DC-GRU model and our proposed model when tested on our CUAVD dataset is shown. Notably, our proposed model outperforms the DC-GRU model (without Attention) in terms of classification accuracy.

The Receiver Operating Characteristic (ROC) curve for the proposed DC-GRU Attention model on the CUAVD dataset is depicted in Figure 9. Notably, all umpire signal categories achieve a perfect AUC of 1, indicating ideal performance. This is evident in intersecting ROC curves, showcasing optimal performance for each category. The Attention-based DC-GRU Model demonstrates outstanding classification performance, with each color on the ROC curve representing a specific umpire signal class, offering valuable insights into its proficiency at different classification thresholds.

Our proposed model has been evaluated on various video-based action recognition datasets using established performance metrics, generating promising results. To

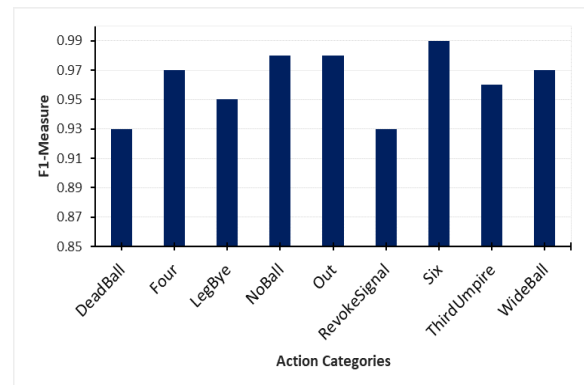


Figure 6. Classification accuracy of proposed model on CUAVD

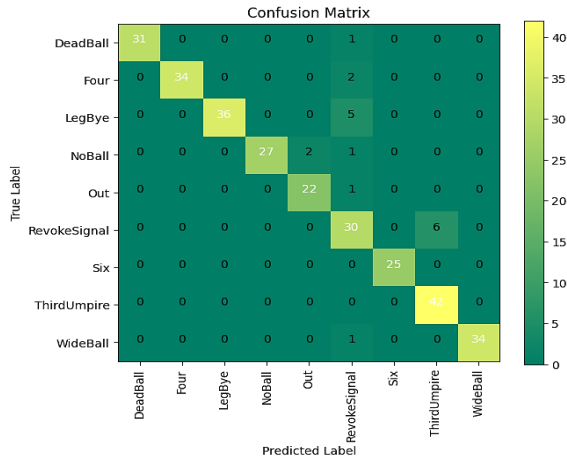


Figure 7. Confusion Matrix of DC-GRU model on CUAVD

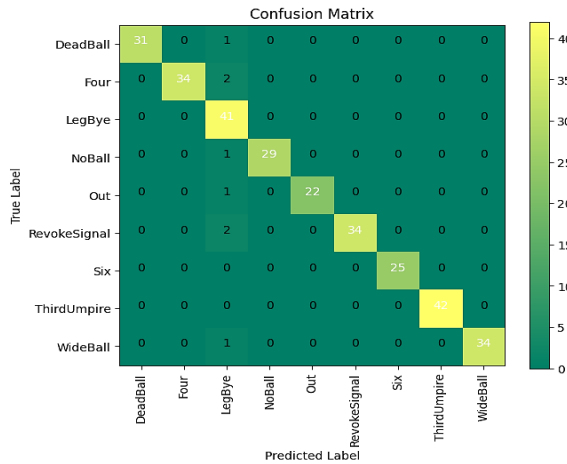


Figure 8. Confusion Matrix of Proposed model on CUAVD

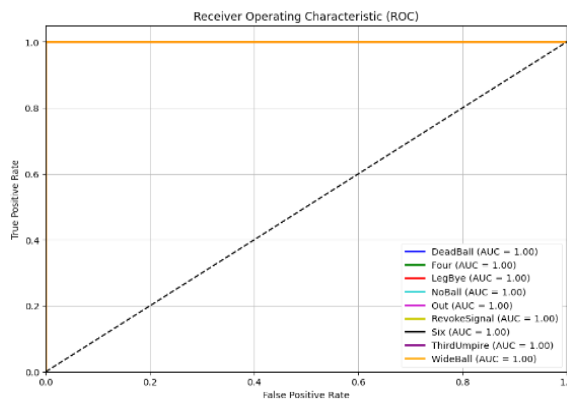


Figure 9. ROC curve of proposed model on CUAVD

thoroughly assess the effectiveness of our proposed approach, we computed F1-score, precision and recall values across different related action datasets. A detailed

summary of these values can be found in Table 2. Notably, our proposed model performs well when tested on well-known datasets, namely Youtube Actions, HMDB51, UCF50 and UCF101. The precision and recall scores achieved by our technique are well-balanced across the benchmark datasets, highlighting a reduced number of both the true and false negatives. Additionally, the proposed Two-Head Attention based DC-GRU model achieved impressive F1-measures of 0.83, 0.93, 0.94, and 0.91 for the HMDB51, UCF50, Youtube Actions, and UCF101 respectively. The F1-score obtained illustrates its effectiveness, further reinforcing its superiority in action recognition tasks.

The performance of our proposed DC-GRU Attention model was further assessed by introducing random noise to our CUAVD dataset, as illustrated in Table 3. The model's performance showed a minor decline with the introduction of noise in the data, achieving an F1-score of 0.91. In contrast, the DC-GRU model without attention attain F1-score of 0.88.

Confusion matrix of Youtube Actions and UCF50 dataset utilizing proposed model is depicted in Figures 10 and 11, respectively. It shows remarkable performance.

The efficacy of the proposed DC-GRU Two-Head Attention model is evaluated by comparing it with a range of existing standard approaches. Table 4 presents the outcomes of this comparison, showcasing the performance of different deep learning-based models on related benchmark action datasets, namely HMDB51, YouTube Actions, and the UCF101 dataset.

The model proposed in this study demonstrated an impressive accuracy rate of 93.82% when evaluated on the YouTube Actions dataset. Our method demonstrated

TABLE 2. Evaluating the Proposed Model's Performance on various Existing Action Datasets

Dataset	Action Classes	Net Precision	Net Recall	Net F1-Score
Youtube Actions	11	0.94	0.95	0.94
HMDB51	51	0.83	0.84	0.83
UCF50	50	0.93	0.94	0.93
UCF101	101	0.92	0.91	0.91
Our CUAVD Dataset	9	0.97	0.95	0.96

TABLE 3. Experimental Results with Effect of random Noise on our CUAVD dataset

Model	Train Accuracy	Validation Accuracy	F1-Score
DC-GRU	90.39%	88.26%	0.88
Proposed Model	92.57%	90.42%	0.91

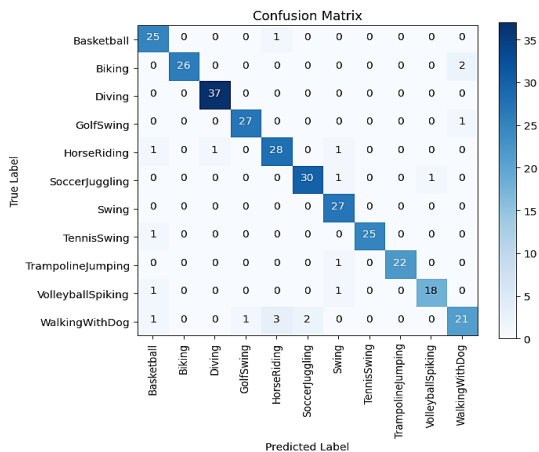


Figure 10. Confusion Matrix of Youtube Actions dataset utilizing Proposed model

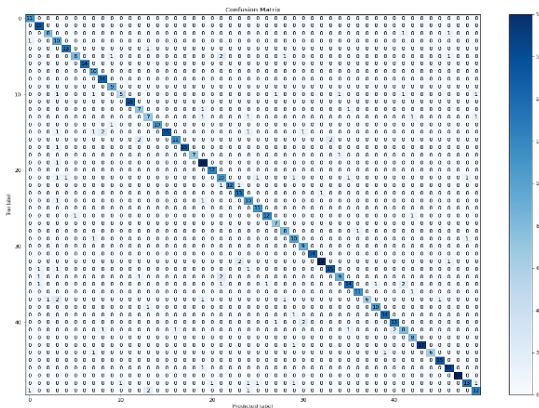


Figure 11. Confusion Matrix of UCF50 dataset using Proposed model

TABLE 4. Comparative Analysis of Various Benchmark Video based Action Recognition methods

Model	HMDB51	Youtube Actions	UCF101
GBH+BoW [3]	63.2%	83.40%	83%
ARCH [5]	58.2%	---	85.30%
CNN Two Stream [6]	76%	88.46%	84.65%
TSN [8]	71%	---	94.90%
VidLSTM [9]	56.40%	---	92.20%
CNN-LSTM + Attention [10]	67.10%	93.48%	92.50%
3DFCNN [13]	72.54%	89.18%	87.41%
3DCNN+ GRU [14]	81.87%	86.64%	---
BD-LSTM [20]	70.40%	91.80%	94.20%
ViT+LSTM [21]	73.71%	---	96.14%
Bi-GRU [23]	71.89%	93.28%	91.79%
<b>Proposed Model</b>	<b>83.67%</b>	<b>93.82%</b>	<b>92.65%</b>

high classification scores on both the YouTube Actions dataset and HMDB51 dataset, yielding remarkable accuracies. The ViT+LSTM [21] achieved the highest accuracy of 96.14%, and TSN [8] model achieved an accuracy of 94.90% on UCF101 dataset. Out of all the models evaluated, the proposed DC-GRU Attention model secured exceptional accuracy on the UCF101 dataset, ranking among the top three performers with an impressive accuracy of 92.65%. For the YouTube Actions dataset, our proposed model achieved the topmost accuracy of 93.82%, followed by the CNN-LSTM with Attention [10] and Bi-GRU [23] and BD-LSTM [20]. In terms of the HMDB51 dataset, the ViT+LSTM [21], 3DFCNN [13], CNN Two-Stream Fusion [6] and 3DCNN+GRU [14] achieved accuracies of 73.71%, 72.54%, 76% and 81.87% respectively.

However, ARCH [5] and GBH+BoW [3] achieved accuracies of 58.2% and 63.2%, respectively, on the HMDB51 dataset. In comparison, our proposed technique achieved 83.67% accuracy on HMDB51, which surpassed all others, securing the top position in Table 4. The proposed model has undergone rigorous testing with multiple video samples, demonstrating its ability to accurately classify umpire signals by correctly labelling the videos using the trained model. The classification result on a realistic video sample with the 'Six' umpire signal category is indicated in Figure 12.

The experimental findings indicate that the proposed model excels in accurately detecting the umpire's signal from the videos. So, the proposed model can also be utilized to detect the umpire signals from the video sequences in real-life.

### 5. CONCLUSION AND FUTURE SCOPE

Cricket umpire's signal recognition in videos is a captivating and rapidly evolving field within computer vision. The ability to automatically identify and classify umpire signal actions in cricket matches has immense practical applications. It contributes to fair decision-making, enhances the game flow, and provides valuable

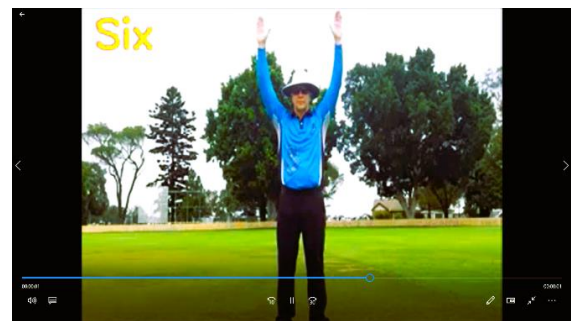


Figure 12. Test Video of 'Six' umpire signal recognized using proposed model

insights for players, coaches, and spectators. The proposed Two-Head Attention based Deep Convolutional GRU framework has shown great promise in accurately recognizing and classifying umpire signal actions. With a high accuracy rate of 94.38% and a Net F1-Score of 0.96, this model stands out as an effective solution. This framework can serve as a virtual trainer for novice umpires, assisting them in practising their cricket umpire signal actions effectively. A significant contribution of this research is the creation of the Cricket Umpire Action Video dataset (CUAVd), which provides a comprehensive collection of videos showcasing the umpire's signals in cricket. This dataset enables the training and evaluation of the proposed DC-GRU Attention model. The model's lightweight design ensures efficient performance even on devices with limited memory, enabling its widespread usage. The proposed approach has been extensively tested and evaluated using three well-established benchmark action datasets, consistently showcasing remarkable recognition performance. Moreover, the effectiveness of the proposed model has been confirmed through successful testing on a diverse range of sample videos, accurately identifying and labelling the umpire signals.

The future scope of this research lies in refining the proposed model, expanding the dataset size to encompass a wider range of umpire signal actions, generalizing to other sports, integrating with sports technology, collaborating with sports organizations, and addressing ethical considerations. Further optimization of the model's architecture and network combinations can enhance its performance.

## 6. REFERENCES

1. Oslear D. Wisden's The Laws Of Cricket: Random House; 2010.
2. Naik BT, Hashmi MF, Bokde ND. A comprehensive review of computer vision in sports: Open issues, future trends and research directions. *Applied Sciences*. 2022;12(9):4429. 10.3390/app12094429
3. Shi F, Laganiere R, Petriu E, editors. Gradient boundary histograms for action recognition. 2015 IEEE Winter Conference on Applications of Computer Vision; 2015: IEEE. 10.1109/WACV.2015.152
4. Kong Y, Fu Y. Human action recognition and prediction: A survey. *International Journal of Computer Vision*. 2022;130(5):1366-401. 10.1007/s11263-022-01594-9
5. Xin M, Zhang H, Wang H, Sun M, Yuan D. Arch: Adaptive recurrent-convolutional hybrid networks for long-term action recognition. *Neurocomputing*. 2016;178:87-102. 10.1016/j.neucom.2015.09.112
6. Simonyan K, Zisserman A. Two-stream convolutional networks for action recognition in videos. *Advances in neural information processing systems*. 2014;27. 10.48550/arXiv.1406.2199
7. Xiong Q, Zhang J, Wang P, Liu D, Gao RX. Transferable two-stream convolutional neural network for human action recognition. *Journal of Manufacturing Systems*. 2020;56:605-14. 10.1016/j.jmsy.2020.04.007
8. Wang L, Xiong Y, Wang Z, Qiao Y, Lin D, Tang X, et al. Temporal segment networks for action recognition in videos. *IEEE transactions on pattern analysis and machine intelligence*. 2018;41(11):2740-55. 10.1109/TPAMI.2018.2868668
9. Li Z, Gavriluk K, Gavves E, Jain M, Snoek CG. Videolstm convolves, attends and flows for action recognition. *Computer Vision and Image Understanding*. 2018;166:41-50. 10.1016/j.cviu.2017.10.011
10. Ge H, Yan Z, Yu W, Sun L. An attention mechanism based convolutional LSTM network for video action recognition. *Multimedia Tools and Applications*. 2019;78:20533-56. 10.1007/s11042-019-7404-z
11. Minhas RA, Javed A, Irtaza A, Mahmood MT, Joo YB. Shot classification of field sports videos using AlexNet Convolutional Neural Network. *Applied Sciences*. 2019;9(3):483. 10.3390/app9030483
12. Rafiq M, Rafiq G, Agyeman R, Choi GS, Jin S-I. Scene classification for sports video summarization using transfer learning. *Sensors*. 2020;20(6):1702. 10.3390/s20061702
13. Sanchez-Caballero A, de López-Diz S, Fuentes-Jimenez D, Losada-Gutiérrez C, Marrón-Romera M, Casillas-Perez D, et al. 3dfcnn: Real-time action recognition using 3d deep neural networks with raw depth information. *Multimedia Tools and Applications*. 2022;81(17):24119-43. 10.1007/s11042-022-12091-z
14. Savadi Hosseini M, Ghaderi F. A hybrid deep learning architecture using 3d cnns and grus for human action recognition. *International Journal of Engineering, Transactions B: Applications*. 2020;33(5):959-65. 10.5829/ije.2020.33.05B.29
15. Kavimandan PS, Kapoor R, Yadav K. Human action recognition using prominent camera. *International Journal of Engineering, Transactions B: Applications*. 2021;34(2):427-32. 10.5829/ije.2021.34.02b.14
16. Foysal MFA, Islam MS, Karim A, Neehal N, editors. Shot-Net: A convolutional neural network for classifying different cricket shots. *Recent Trends in Image Processing and Pattern Recognition: Second International Conference, RTIP2R 2018, Solapur, India, December 21–22, 2018, Revised Selected Papers, Part I 2*; 2019: Springer. 10.1007/978-981-13-9181-1\_10
17. Dey A, Dutta A, Biswas S, editors. Workoutnet: A deep learning model for the recognition of workout actions from still images. *2023 3rd International Conference on Intelligent Technologies (CONIT)*; 2023: IEEE. 10.1109/CONIT59222.2023.10205926
18. Dey A, Biswas S, Le D-N. Recognition of Human Interactions in Still Images using AdaptiveDRNet with Multi-level Attention. *International Journal of Advanced Computer Science and Applications*. 2023;14(10).
19. Wu F, Wang Q, Bian J, Ding N, Lu F, Cheng J, et al. A survey on video action recognition in sports: Datasets, methods and applications. *IEEE Transactions on Multimedia*. 2022. 10.1109/TMM.2022.3232034
20. Li W, Nie W, Su Y. Human action recognition based on selected spatio-temporal features via bidirectional LSTM. *IEEE Access*. 2018;6:44211-20. 10.1109/ACCESS.2018.2863943
21. Hussain A, Hussain T, Ullah W, Baik SW. Vision transformer and deep sequence learning for human activity recognition in surveillance videos. *Computational Intelligence and Neuroscience*. 2022;2022. 10.1155/2022/3454167
22. Ravi A, Venugopal H, Paul S, Tizhoosh HR, editors. A dataset and preliminary results for umpire pose detection using SVM classification of deep features. *2018 IEEE Symposium Series on*

- Computational Intelligence (SSCI); 2018: IEEE. 10.1109/SSCI.2018.8628877
23. Ahmad T, Wu J, Alwageed HS, Khan F, Khan J, Lee Y. Human Activity Recognition Based on Deep-Temporal Learning Using Convolution Neural Networks Features and Bidirectional Gated Recurrent Unit With Features Selection. IEEE Access. 2023;11:33148-59. 10.1109/ACCESS.2023.3263155
  24. Wickramasinghe I. Applications of machine learning in cricket: a systematic review. Machine Learning with Applications. 2022;10:100435. 10.1016/j.mlwa.2022.100435
  25. Reddy P S, Santhosh C. Multimodal Spatiotemporal Feature map for Dynamic Gesture Recognition from Real Time Video Sequences. International Journal of Engineering, Transactions B: Applications, 2023;36(8):1440-8. 10.5829/ije.2023.36.08B.04
  26. Pan T-Y, Tsai W-L, Chang C-Y, Yeh C-W, Hu M-C. A hierarchical hand gesture recognition framework for sports referee training-based EMG and accelerometer sensors. IEEE Transactions on Cybernetics. 2020;52(5):3172-83. 10.1109/TCYB.2020.3007173
  27. Ahmad W, Munsif M, Ullah H, Ullah M, Alsuwailam AA, Saudagar AKJ, et al. Optimized deep learning-based cricket activity focused network and medium scale benchmark. Alexandria Engineering Journal. 2023;73:771-9. 10.1016/j.aej.2023.04.062
  28. Das S, Mahmud T, Islam D, Begum M, Barua A, Tarek Aziz M, et al. Deep Transfer Learning-Based Foot No-Ball Detection in Live Cricket Match. Computational Intelligence and Neuroscience. 2023;2023. 10.1155/2023/2398121
  29. Shingrakhia H, Patel H. SGRNN-AM and HRF-DBN: a hybrid machine learning model for cricket video summarization. The Visual Computer. 2022;38(7):2285-301. 10.1007/s00371-021-02111-8
  30. Raval KR, Goyani MM. A survey on event detection based video summarization for cricket. Multimedia Tools and Applications. 2022;81(20):29253-81. 10.1007/s11042-022-12834-y
  31. Nandyal S, Kattimani SL. Cricket Event Recognition and Classification from Umpire Action Gestures using Convolutional Neural Network. International Journal of Advanced Computer Science and Applications. 2022;13(6). 10.14569/IJACSA.2022.0130644
  32. Siddiqui HUR, Younas F, Rustam F, Flores ES, Ballester JB, Diez IdIT, et al. Enhancing Cricket Performance Analysis with Human Pose Estimation and Machine Learning. Sensors. 2023;23(15):6839. 10.3390/s23156839
  33. Zhang Q, Zhang Y, Shao Y, Liu M, Li J, Yuan J, et al. Boosting Adversarial Attacks with Nadam Optimizer. Electronics. 2023;12(6):1464. 10.3390/electronics12061464

#### COPYRIGHTS

©2024 The author(s). This is an open access article distributed under the terms of the Creative Commons Attribution (CC BY 4.0), which permits unrestricted use, distribution, and reproduction in any medium, as long as the original authors and source are cited. No permission is required from the authors or the publishers.



#### Persian Abstract

##### چکیده

بنیابی کامپیوتر کاربردهای گسترده ای در حوزه های مختلف ورزشی دارد و کریکت، یک بازی پیچیده با انواع رویدادهای مختلف، از این قاعده مستثنی نیست. تشخیص سیگنال های داور در طول مسابقات کریکت برای تصمیم گیری منصفانه و دقیق در گیم پلی ضروری است. این مقاله مجموعه داده ویدیوی اکشن داور کریکت (CUAVd) را ارائه می کند. یک مجموعه داده جدید که برای تشخیص وضعیت های داور در مسابقات کریکت طراحی شده است. از آنجایی که داور دارای قدرت قضاوت های مهم در مورد حوادثی است که در زمین رخ می دهد، هدف این مجموعه داده کمک به پیشرفت سیستم های خودکار برای تشخیص داور در کریکت است. شبکه GRU کانولوشن عمیق مبتنی بر توجه پیشنهادی، اقدامات سیگنال داور مختلف را در دنباله های ویدیویی به دقت شناسایی و طبقه بندی می کند. این روش به نتایج قابل توجهی در مجموعه داده های CUAVd آماده شده و مجموعه های داده در دسترس عموم، یعنی HMDB51، Youtube Actions، و UCF101، دست یافت. مدل توجه DC-GRU اثربخشی خود را در گرفتن وابستگی های زمانی و تشخیص دقیق اقدامات سیگنال داور نشان داد. در مقایسه با سایر مدل های پیشرفته مانند معماری های سستی CNN-LSTM، CNN با توجه، و مدل 3DCNN+GRU، مدل پیشنهادی به طور مداوم از آنها در تشخیص اقدامات سیگنال داور برتری داشت. در طبقه بندی صحیح ویدیوهای سیگنال داور، دقت اعتبار بالای 94.38٪ را به دست آورد. این مقاله همچنین مدل ها را با استفاده از معیارهای عملکرد مانند F1-Measure و Confusion Matrix ارزیابی کرد و کارایی آنها را در تشخیص اقدامات سیگنال داور تأیید کرد. مدل پیشنهادی دارای کاربردهای عملی در موقعیت های واقعی مانند آنالیز ورزشی، آموزش داور، و سیستم های خودکار کمک داور است که در آن شناسایی دقیق سیگنال های داور در ویدئوها حیاتی است.



## Automatic Optimization of Initial Blank Shape in Production of All Kinds of Rectangular Parts in Computer Aided Hydroforming Process

R. Mousavipoor, H. Gorji\*, M. Bakhshi-Jooybari, M. Shakeri

*Department of Mechanics, Faculty of Mechanical Engineering, Noshirvani University of Technology, Babol, Iran*

### PAPER INFO

#### Paper history:

Received 30 July 2023

Received in revised form 26 October 2023

Accepted 27 October 2023

#### Keywords:

Deep Drawing

Automatic Optimization

Blank Optimization

Blank Automation Flowchart

### ABSTRACT

In this research, an innovative method has been applied to obtain the shape of initial sheet in the forming of different rectangular geometries. So that we can define rules that automatically determine the optimal shape of the initial sheet at different heights. Sensitivity analysis method was used for optimization, and Python software was used to link with Abaqus software. By examining the geometrical parameters and forming pressure, a flowchart was presented to determine the appropriate pressure. By examining the height changes in different geometries, it was found that the optimization reduces the maximum pressure and the maximum radius of the punch, which were obtained by 4 and 8%, respectively. It was found that the difference in the size of the longitudinal and transverse sides of the section has a direct effect on the changes in the node coordinates to plot the target curve and reduces the number of optimization steps. According to the results, it was shown that by automation and determining the pressure flowchart, the shape of the initial sheet can be determined without repeating the optimization stages and experimental tests. It also prevents material waste.

doi: 10.5829/ije.2024.37.04a.09

## 1. INTRODUCTION

Non-circular parts, particularly those with square and rectangular geometries, are widely used in industry to manufacture main parts in the car body, fuel system components, oil tanks, main components of aircrafts, etc. The production of rectangular and polygonal sheet metal parts is recognized as a complicated activity in industry. The primary method employed for manufacturing such products is metal stamping. However, in traditional processes, achieving consistent production quality with uniform thickness distribution is difficult due to the complexity of the geometries involved. Moreover, several forming stages are required. In certain cases, these parts may feature multiple steps or polyhedral geometries, with sharp corners present at the intersections of these steps or within the part walls. The intricate nature of these features, along with the inherent challenges of material flow in such regions, make it difficult to form the parts by traditional methods such as stamping. By using new methods in production of difficult-to-form sheet parts,

more uniform thickness distribution and higher quality can be achieved.

Sheet hydroforming is a modern sheet metal forming processes that has been used in production of car parts and aircraft bodies since 1980s (1). This process has grown increasingly in recent years in the industry, especially in automobile manufacturing (2). Hydroforming has several advantages such as higher forming limit, better surface quality, higher tensile strength, and higher dimensional accuracy (3, 4). In this process, some preforms may be needed to achieve the proper final shape of the workpiece without defects and excessive material waste (5). Among the various effective parameters in sheet forming processes, the initial shape of the sheet plays a vital role, as optimizing it can significantly impact the production of parts with minimal cost and high quality. Moreover, the optimization of the initial blank increases the drawing ratio, reduces the sheet consumption, and reduces the number of production stages. However, it is very difficult to determine the optimum shape of the initial blank due to the complexity of the material behavior, especially in

\*Corresponding Author Email: [hamidgorji@nit.ac.ir](mailto:hamidgorji@nit.ac.ir) (H. Gorji)

stamping and deep drawing processes in which complicated deformation mechanics are involved.

Currently, according to the different methods provided by researchers, the optimization methods can be divided into two categories: retro-marching and iterative design (6). Slip line field method (7), geometric mapping method (8), area addition and subtraction method (9), inverse finite element method (10), ideal deformation theory (11) and backward finite element tracking (12) are among the methods belong to the retro-marching plan. However, since in this category it is not possible to compensate the shape error which refer to the difference between the desired final shape and the deformed shape, by using finite element analysis (obtained from the predicted initial shape), the mentioned methods provide limited accuracy. But, in iterative designs, the initial shape is guessed and is frequently corrected by considering the shape error until the deformed shape matches the desired final shape. The sensitivity method (13), and the radius vector method (9) belong to this category.

Since the above-mentioned categories provide excellent accuracy and good convergence, they can be used to predict the optimum blank with complicated shapes in processes such as stamping and deep drawing. The methods of sensitivity analysis and radius vector are more useful in each process due to the ease of determining the changes in nodes coordinates and the ability to generalize the relationships based on new parameters. According to the flowchart of the sensitivity analysis method, after determining the target curve related to the flange area, a blank is guessed, the simulation is done, and at the end of the forming process, the amount of deviation of all the nodes from the target curve is obtained (6).

According to the various ranges of commonly used geometries for rectangular parts, stepped geometries are of special importance. Depending on their specific application, these parts can be categorized as side-step parts, middle-step parts, or parts with multiple steps. In all of these cases, due to the existence of the intersections between the steps and the importance of producing a workpiece with complete filling, optimizing the initial dimensions of the sheet can be very important, because it makes it easier for the sheet to flow in the corners, decreases the forming pressure, and reduces the production time.

Research efforts focused on the automatic optimization of the blank shape for all types of parts with a rectangular section have been relatively scarce. Meng et al. (14) investigated the effect of fluid pressure in hydroforming a rectangular aluminum workpiece. They found that the hydroforming process improves the quality of the parts. They also stated that by increasing the fluid pressure, the formability of the part improves. Rahmani et al. (15) investigated the effective parameters in the forming of parts with square sections. These researchers investigated the possibility of achieving the maximum

drawing ratio by considering the effect of pressure parameters, sheet thickness, and friction coefficient. They found that with an increase in friction coefficient, the range of the drawing ratio is limited due to the decrease in the flow of the sheet. Moreover, as the thickness of the sheet increases, a higher drawing ratio is obtained. Mousavipoor et al. (16) investigated the feasibility of forming two-step rectangular parts in a single stage and optimized the dimensions of the blank with experimental investigation and simulation. They found that the effect of forming pressure on the thickness distribution of the part depends on the shape of the product and the type of the hydroforming process. By examining the amount of die filling, they concluded that to achieve complete die filling, the fluid pressure should be increased throughout the process. They also stated that optimization of the sheet blank leads to improve the material flow and a more uniform thickness distribution. Luo et al. (17) presented a new method for forming a rectangular workpiece using a mechanical preforming operation, which was a combination of deep drawing process and superplastic forming. In this research, three different metals have been used: aluminum SPF 5083 with super-plasticity properties, aluminum AA5183, which does not have super-plasticity properties, and AZ31 without super-plasticity properties. The second and third metals were fine-grained through rolling. By comparing the two forming modes with the Hot Draw Mechanical Preforming (HDMP) process and superplastic forming with the obtained pressure curve, it was found that the time of the superplastic forming was longer than that of HDMP. On the other hand, the amount of pressure required in the superplastic forming was lower. Finally, the parts produced using the superplastic forming had rupture in the corners. This was due to the use of the two stages of preforming and final forming, and the control of the strains created in the mentioned combined process. Then, the effects of different parameters on the thickness distribution of the part have been investigated. The results showed that by increasing the diameter of the punch and the drawing depth, the thickness decreases. Vafaesefat (18) examined the optimization of the blank shape for the two geometries of square cup and oil pan drawings made of St14 by using the iterative finite element method. By considering the first square geometry in the analysis, an error occurred due to the lack of sheet flow. Next, by performing iterative finite element analysis, the contours of the target and the formed workpiece coincided with the shape error of 0.9435 mm, the optimum sheet shape was obtained, and the final part was formed. Blount and Fischer (19) investigated the earing phenomenon of aluminum alloy 2048 cup-shaped parts. Using an algorithm, they first simulated the process. After specifying the target curve, the amount of deviation of each node from the target curve was obtained and the average of these values were recorded as an error. Then,

using a coefficient whose value was chosen arbitrarily, the position of each node of the undeformed sheet was changed and the simulation was repeated until the error value was less than the desired value.

In recent years, extensive research has been conducted on various optimization methods for sheet metal parts. However, due to the diverse range of geometries of industrial sheet parts and the variations in drawing depths and final workpiece dimensions, there is a lack of a comprehensive design guide or general relationship to determine the dimensions of the initial sheet for each geometry. Furthermore, manual optimization methods need to be applied separately for circular and rectangular geometries at different depths.

As a result, there is currently no universally applicable method or rule for extracting the initial blank shape for any given geometry. Consequently, there is a need for a method that can automatically establish rules for optimizing the dimensions of the initial sheet by utilizing coding and establishing links between analytical and simulation software. Such a method, with a focus on classifying rectangular geometries, would prove highly beneficial in the industry.

The key figure in this research is that at first, by classifying a group of rectangular workpieces with varying geometries and depths, the initial sheet dimensions are optimized manually and the procedure of changing the nodes coordinates is investigated. Additionally, by checking the parameters and developing a flowchart to determine the proper pressure, by linking Abaqus, Python and MATLAB software and the basic relations of sensitivity analysis, a method is proposed through which, by coding between the software, for any geometry with different depths and dimensions, the initial sheet shape can be extracted automatically. In this research, the sensitivity method is adopted for optimizing the initial sheet shape. This method is chosen due to its practicality and suitability for automation. Moreover, changes in the shape of the initial blank are evaluated based on the alterations in the coordinates of the nodes. The sensitivity method offers a more practical and user-friendly alternative, particularly for the automated optimization of sheet metal parts. In contrast, other optimization methods are parametric and more complex in terms of defining rules and extracting relationships between variables.

## 2. DEFINITION OF PART AND DIE GEOMETRY

To ensure a comprehensive investigation of various rectangular geometries, this research initially focuses on simple rectangular and symmetric stepped geometries. Figure 1 illustrates the geometries employed in the study. The maximum depth of the step for two-step parts is considered in the first stage, which can be formed in a

single hydroforming process. Based on Figure 1, the depth of the first step is 10 and 17 mm, while the depth of the lower step is 20 and 13 mm for the middle-step part and the side-step part, respectively.

## 3. EXPERIMENTAL AND SIMULATION PROCEDURE

The sheet hydroforming process has been modelled using the ABAQUS/Explicit 6-13 software. Due to the symmetry of the defined geometries, only half of the sheet and die components have been 3D modeled. Because of the type of the process and the large deformation of the material, dynamic explicit solution has been employed (20). In the section properties of the software, physical and mechanical properties have been defined for the sheet. Figure 2 shows how to deploy the components of the simulation setup. The contact characteristic used in this research is direct contact. Surface-to-Surface contact is used to define the contacts. Coulomb friction model was used to define the characteristics of the surfaces in contact.

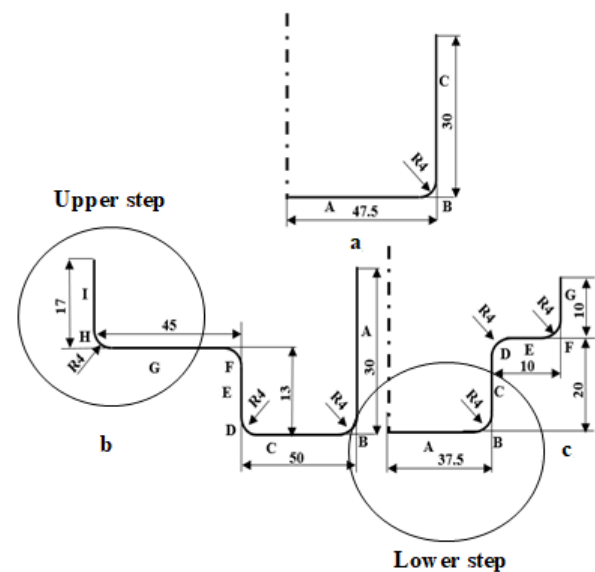


**Figure 1.** Defined geometries, a. Simple workpiece, b. Side-step workpiece, c. Middle-step workpiece

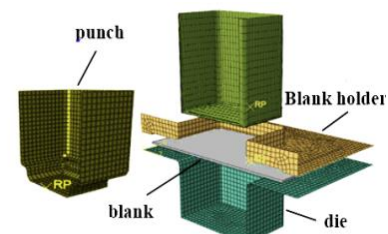


**Figure 2.** Arrangement of the die setup components in Abaqus

According to Zhang et al. (10), the friction coefficient between the punch and the blank is set to 0.14 and that between the blank with the blank holder and the die is considered to be 0.04.

In conducting the tests, a universal testing machine with a capacity of 600 kN, controlled by a computer, was used. Figure 3 shows the manufactured die components. The characteristics and properties of the steel sheet are listed in Table 1. Figure 4 shows the stress-strain diagram of the sheet obtained from the uniaxial tension test. To investigate the anisotropy properties of the sheet material, samples were prepared and tested in the orientations of 0, 45 and 90 degrees to the rolling direction. Due to the insignificant difference of the obtained coefficients, the sheet was considered isotropic. To obtain the optimum pressure path required for the forming of the defined geometries, the path shown in Figure 5 was considered. To examine the filling in the corners of the die, the filling percentage criterion was used. This criterion is defined as the area swept by the formed sheet to the total area of the die cavity in the critical area (as shown in Figure 6) (21).

Based on the purpose of the paper, which focuses on different geometries with rectangular sections, the initial simulation was conducted using a rectangular geometry with an initial depth (h) of 10 mm. Considering the maximum pressure (according to Figure 5) between 12 and 15 MPa and conducting experiments, a rupture occurred in the punch radius area. Then, by increasing the pressure to 18 MPa, the thinning of the wall led to a

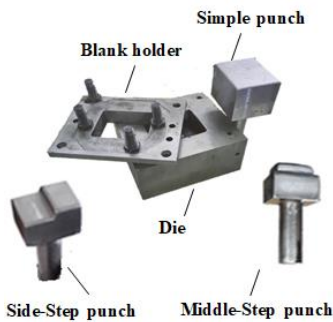


Figure 3. Arrangement of the die setup components in Experimental tests

**TABLE 1.** Mechanical properties of St13 sheet (10)

Yield strength [MPa]	116
Density [kg/m <sup>3</sup> ]	$\rho = 8750$
Poisson's ratio	$\nu = 0.33$
Strength constant [Gpa]	$K=180$
Strain hardening exponent	$n=0.44$
Anisotropy parameters	$R0=1, R45=1.018 R90=1.04$
Young's modulus [Gpa]	$E=210$

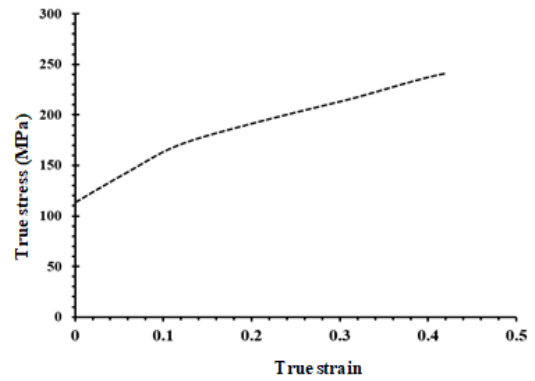


Figure 4. Stress-strain diagram of St13 sheet

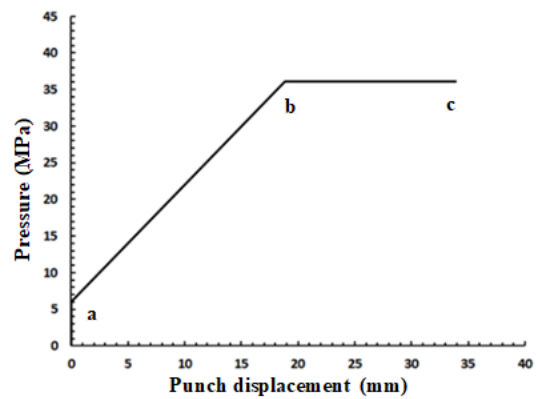


Figure 5. The pressure path used in the research

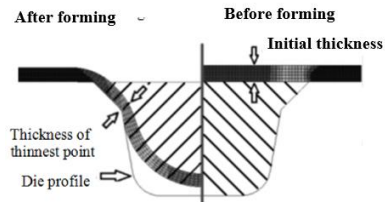
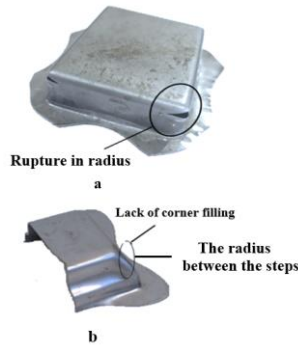


Figure 6. Schematic of determining the percentage of filling in the forming (21)

rupture of the sheet (Figure 7a). Finally, at the pressure of 24 MPa, the sheet material was able to withstand the deformation without rupturing.

To investigate the feasibility of production of stepped parts, by applying the maximum pressure of 24 MPa, it was observed that full filling does not occur in the intersection between the steps. In Figure 7b the rupture and non-filling of the part is shown for the middle-step part at a pressure of 22 MPa. To check the complete forming of the stepped parts, at a depth of 13 mm in the lower step and a maximum pressure of 20 MPa, there is no complete filling in the side-step part and in the middle-step part, and the filling rate is 68 and 60%, respectively. But by increasing the pressure to 40 and 30 MPa, the

filling rate is 84 and 93%, respectively. Finally, by performing the stages of forming stepped parts according to Figure 8, the side-step part was formed and produced at a pressure of 40 MPa. Figure 9 shows the effect of maximum forming pressure of thickness distribution of the deformed part.



**Figure 7.** a. Rupture in the punch radius of a simple part at a pressure of 18 MPa, b. Lack of filling in the middle-step part at a pressure of 22 MPa, obtained from simulation



**Figure 8.** a. Side-step workpiece with a depth of 35 mm and at a pressure of 24 MPa, b. Simple workpiece with a depth of the lower step of 13 mm and at a pressure of 40 MPa, obtained from the experiments

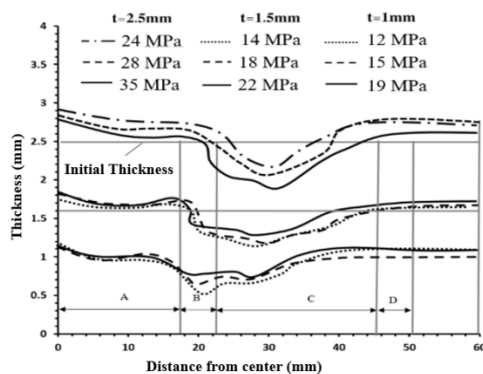


**Figure 9.** Investigating the effects of maximum fluid pressure on the thickness distribution of a simple workpiece with dimensions of 120 × 130 mm, and thicknesses of 1, 1.5 and 2.5 mm with depth of 35mm, obtained from simulation

According to Figure 9, it was determined that by changing the thickness of the part at a fixed depth, the maximum limit of thickness reduction in the area of the punch radius and the upper wall should be reduced by 5%; for a thickness of 1 mm, it will reach from 32% to 30%, the reason is the reduction of the distance between the critical punch radii from each other and less elongation between the walls. Figure 10 shows the formed parts obtained from the simulations.

#### 4. THE PROPER PRESSURE FLOW CHART

A flowchart is written to obtain the proper pressure for the rectangular parts, which is shown in Figure 11. By coding using Python software and by performing the required simulations in ABAQUS software, the proper pressure value is obtained automatically. Many parameters affect the amount of proper forming pressure. In the flowchart, to obtain the proper pressure for a side-step rectangular workpiece with specific material and thickness, according to Figure 11, at first, the simulation was performed with a pressure of 10 MPa and the amount of thinning created in the part ( $t_1$ ) was obtained. If the maximum thinning rate decreases with the increase of pressure, increasing the amount of pressure continues. Investigations showed that the increase in pressure to some extent causes the decrease in thickness, and then with the increase of pressure, the thickness reduction increases. If the thickness reduction increases compared to the previous stage, increasing the pressure value is stopped. Therefore, the amount of pressure should be reduced. Through the investigations, it was determined that the suitable pressure for forming is between the  $n$ th simulation ( $P_n$ ) and  $(n-1)$  th simulation ( $P_{n-1}$ ). Therefore, the pressure value is reduced with a ratio lower than 5 MPa, so that the pressure change is lower than the previous stage. Now, if increasing the pressure by 5 MPa has caused an increase in thickness reduction for the first time, it happens vice versa (left side of the flowchart). In the flowchart,  $t_i$  is the smallest thickness created in the workpiece in each simulation. Using the presented new method, the proper pressure for forming parts a and b was obtained 12 MPa.

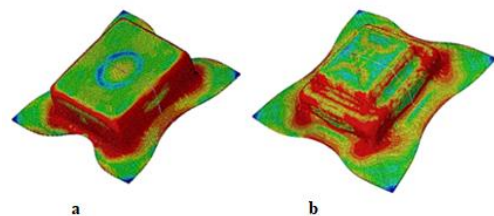


**Figure 10.** a. Simple part with a depth of 30 mm, a thickness of 2.5 mm, and a maximum pressure of 36 MPa, b. Middle-step part at a depth of 13 mm, a thickness of 2.5 mm, and a maximum pressure of 42 MPa, obtained from simulation

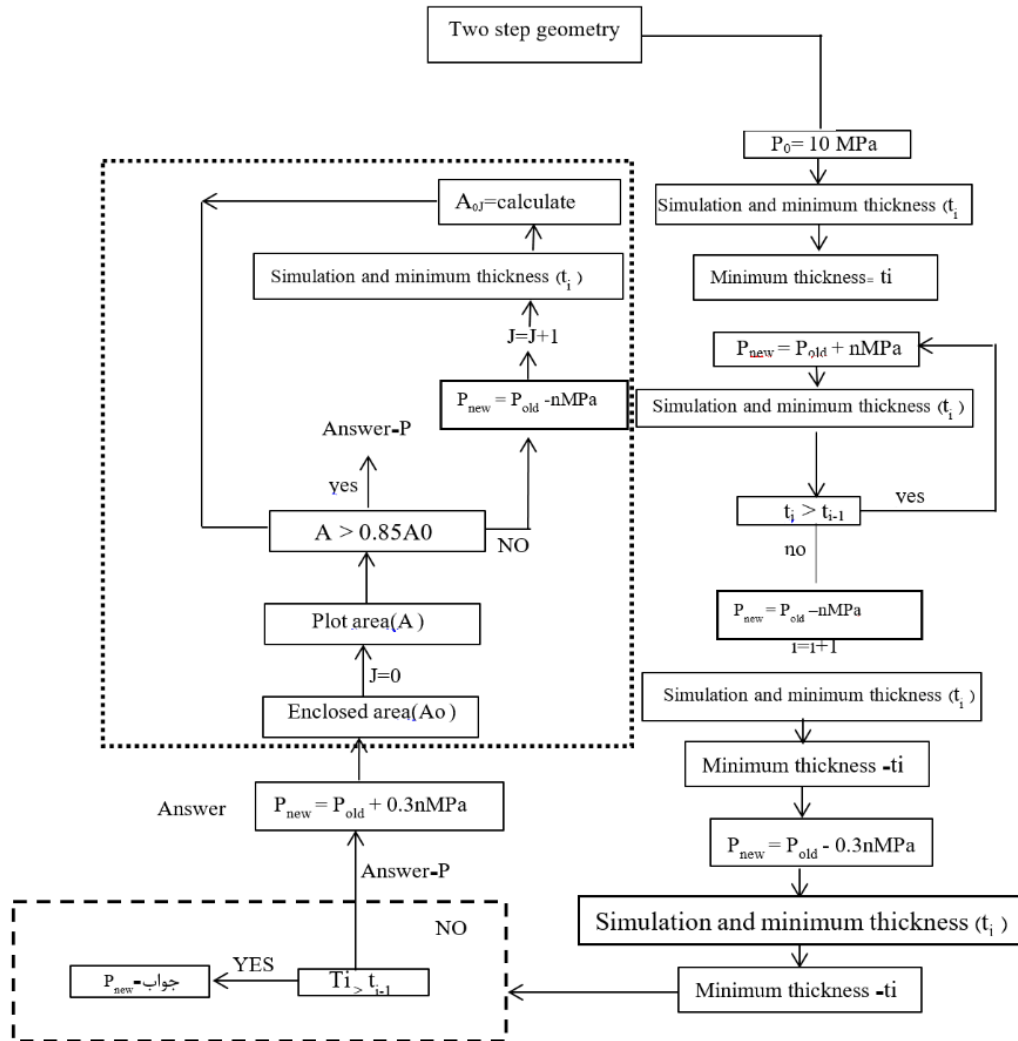


Figure 11. Flowchart of obtaining the proper pressure of a two-step rectangular geometry

5. EFFECT OF FORMING PARAMETERS

**5.1. Change in Depth and Drawing Ratio** In this research, the process of changing the forming parameters for different geometries is performed, so that the general law of the effects of these parameters can be extracted in the form of a flowchart and be used as initial simulation inputs for each determined geometry. To investigate the effect of step depth on thinning, the forming of rectangular workpieces at depths between 10 and 35 mm was investigated. The depth of the first step for stepped parts was considered from 10 to 20 mm. Figure 12 shows rectangular workpieces at different depths. By examining the same process for the two-step parts (side-step part) as seen in Figure 13, by increasing the step depth, due to the increased strain and elongation experienced during the first step, the thinning in the areas of the wall of the first

step and the radius of the corner of the punch increase. Moreover, it was found that the percentage of thickness reduction at step depths of 10, 13, and 20 mm were 7, 11, and 13 percent, respectively. According to the considered thinning criteria, it is observed that there is no rupture in the workpiece.

**5.2. Effect of Punch Radius** Due to the variation in drawing ratio, step depth, and the geometry of rectangular parts, the punch corner radius can have a significant impact on the forming process and the resulting thinning behavior of the part. To study this effect for simple and two-step geometries, the radius of 3, 4, 5, and 7 mm were considered. Figure 14a indicates that for the simple part, when the punch corner radius is increased while maintaining a constant pressure, the maximum thinning decreases and the thickness distribution

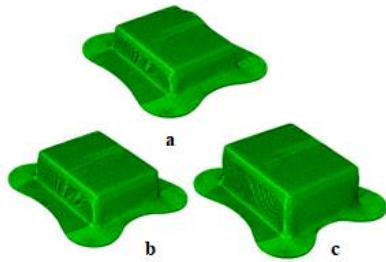


**Figure 12.** Simple part formed with different step depths at the constant pressure of 24 MPa and a thickness of 1.5 mm, a. Depth of 15 mm, b. Depth of 25 mm, c. Depth of 35 mm, obtained from simulation

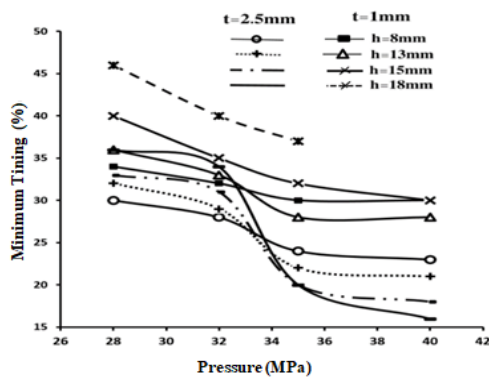


**Figure 13.** Effect of step depth on thickness distribution in for the side-step part, obtained from simulation

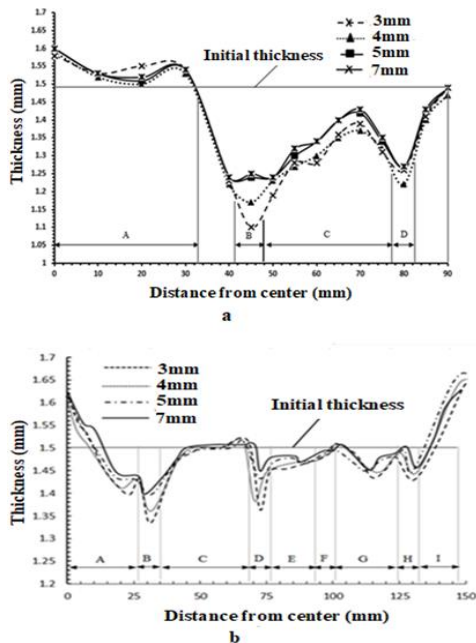


**Figure 14.** Effect of punch corner radius on thickness distribution, a. Simple workpiece at a pressure of 24 MPa, a depth of 35 mm, and a thickness of 1.5 mm. b. Side-step workpiece at a pressure of 40 MPa, a depth of 13 mm, and a thickness of 1.5 mm, obtained from simulation

improves. By increasing the punch corner radius, bending is reduced, and the material flow is facilitated. It is also observed that at the radii smaller than 3 mm, the percentage of thickness reduction exceeds 42%, as a result, the workpiece is prone to tearing in the punch radius area. It is found that the minimum thickness reduction due to the increase in punch corner radius is 5%. By examining the same process for the two-step parts shown in Figure 14b, it is seen that by increasing the punch corner radius in the lower step area, the process of thickness reduction is similar to that of the simple workpiece. Meanwhile, because of more elongation due to the geometry of the upper step and the intersection of the steps, thinning increases up to 7%. Moreover, rupture in the punch corner radius area in the intersection between the steps is reduced by 4% due to the effect of the fluid pressure in filling the die.

## 6. OPTIMIZATION

**6. 1. Optimization with Sensitivity Method** As stated previously, the proper pressure for different geometries has been obtained. In order to examine the process of change of the initial sheet nodes, at first the initial sheet optimization was done manually for three different geometries. To carry out the simulation and experiments, the initial sheet with the dimensions of 152 × 150 mm was considered. To validate the simulation results, several experiments were conducted using the optimized sheet. Figure 15 illustrates the final geometry of the simple workpiece obtained from the optimized initial blank, which was achieved at a pressure of 24 MPa. Figure 16 shows the optimization stages of the middle-step part obtained at a pressure of 30 MPa. Through the experiments, a reasonable correlation was observed between the results obtained from the simulation and the actual experimental results.

The maximum difference between the two was 8%, indicating a relatively good agreement between them. In performing the optimization process for both the middle-step part and side-step part, by applying the sensitivity correction method, during three stages, the dimensions of the initial sheet were modified, and the final curve closely matched the target curve. During the simulation, the maximum fluid pressure to form the middle-step part and the side-step part was obtained as 35 and 40 MPa, respectively. Figure 17 shows the optimized sheet geometry for three different geometries.

**6. 2. The Effects of Optimization** Generally, in forming and stretching in the piece, the amount of strain in the radius and rim areas is more than other areas (22). Optimizing the initial sheet shape is a method to reduce thinning in forming. Figure 18 displays the thickness distribution diagrams obtained with the optimized initial

blank for the three investigated parts. It is evident that in the regions corresponding to the first and second steps, the application of fluid pressure results in the contact between the punch and the sheet, thereby minimizing significant thinning throughout the different stages of optimization.

In the three regions corresponding to the punch corner radius, the maximum thinning occurs due to the tensile bending that takes place. However, through the

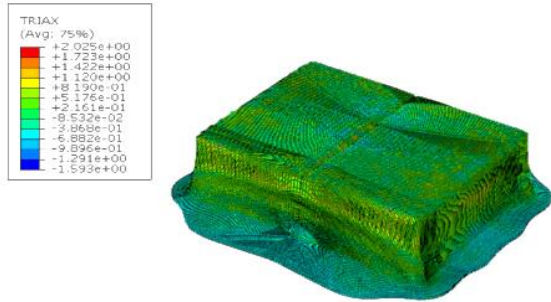


**Figure 15.** The part formed with optimum initial blank with a step depth of 35 mm and a pressure of 24 MPa and a thickness of 1.5 mm, obtained from simulation

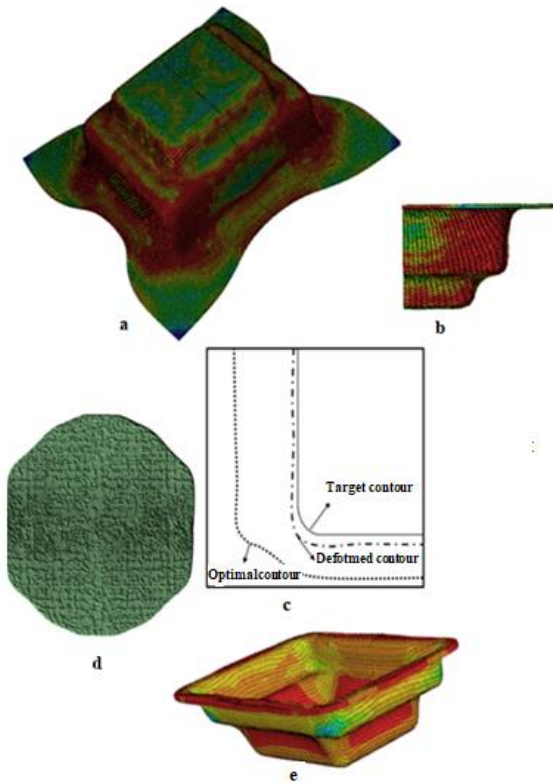


**Figure 16.** Optimizing stages of the middle-step part with a depth of the lower step of 13 mm, a pressure of 30 MPa, and a thickness of 1.5 mm. a. Formed workpiece with the initial blank, b. Formed workpiece inside view, c. Formed curve diagram and target contour, d. Optimized initial sheet, e. Formed part with optimized sheet, obtained from simulation

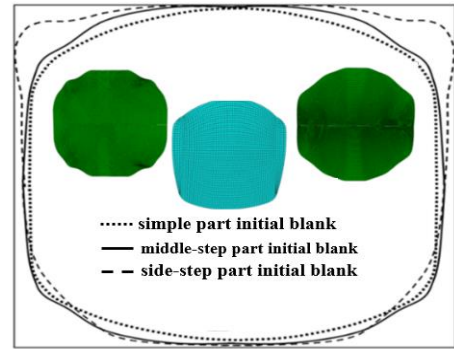


**Figure 17.** Geometry of the optimized initial blank of the simple part, the middle-step part and the side-step part with optimum pressure and constant initial depth, obtained from simulation

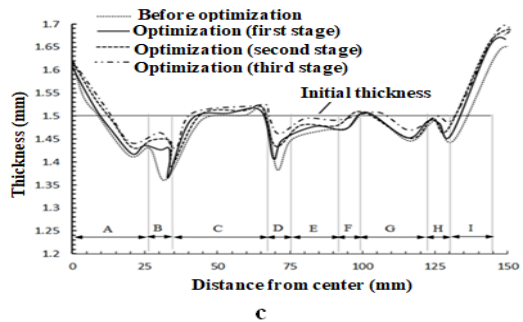
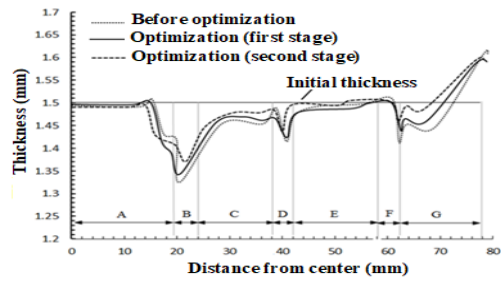
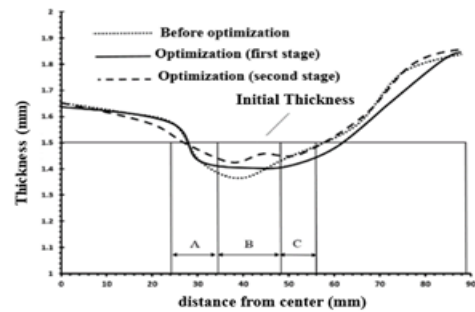


**Figure 18.** Effect of optimizing the shape of the initial blank on the thickness distribution of: a. Simple workpiece at a depth of 35 mm and a pressure of 24 MPa, b. Middle-step workpiece at the depth of 13 mm at the lower step, and a pressure of 30 MPa. c. Side-step workpiece at the depth of 13 mm at the lower step, and a pressure of 40 MPa, obtained from simulation

optimization of the initial dimensions of the sheet, it is possible to reduce the stress concentrations in the corners. This is achieved by removing sharp corners, resulting in a noticeable decrease in the maximum thinning. Figure 19.a shows the initial and formed sheet metal for the simple part. By performing the optimization stages, thinning in the punch corner radius area in the middle-step and the side-step part was reduced by 4 and 8%, respectively. By performing the optimization stages, the maximum thinning in the mentioned area for the middle-step part and the side-step part is reduced by 3 and 4 percent, respectively. Figure 19.b shows the curve of the initial blank and the shape given in the first and second stages of the simple part optimization.

**6. 3. Forming Pressure** To investigate the effect of optimization on forming pressure in rectangular and stepped parts, several stages of experimental testing and simulation were performed. Table 2 shows the amount of pressure reduction obtained for different thicknesses and heights of the simple part and the side-step part with the optimal primary sheet at initial pressures of 28 and 40 MPa, respectively. As the diagram shows, the amount of pressure reduction for a simple part has the same upward trend compared to the original sheet before optimization,

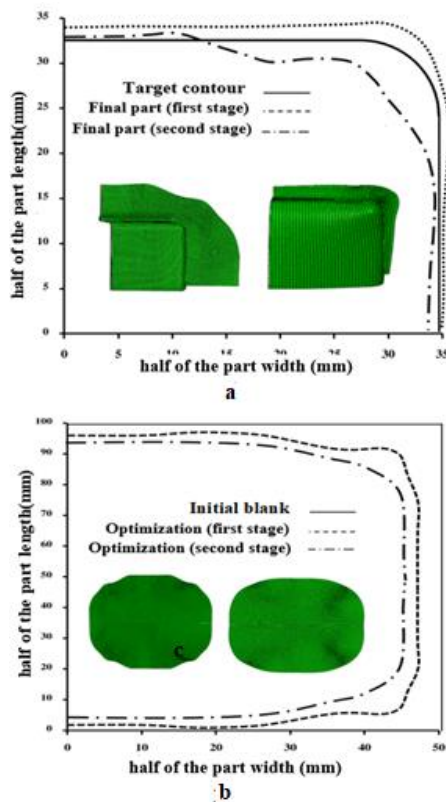


**Figure 19.** a. The initial blank curve of the simple part, b. The formed blank curve for the simple part in the first and second stages of optimization, obtained from simulation

and from a height of more than 25 mm due to greater elongation in the wall and greater flow of the optimized sheet, it decreases by 16%. By examining the same process for the stepped- part according to the diagrams, it is shown that in the two-step part (in the middle of the step and next to the step) due to the creation of the interface between the first and second steps, with an increase in the height of the lower step due to the need for maximum pressure in the final filling, and the high elongation in the lower step has a lower reduction and will reach a maximum of 13%. Figure 20 shows the thickness reduction of the simple part before and after optimization at a constant pressure of 28 MPa.

**TABLE 1.** Pressure reduction achieved by optimizing different thicknesses for the simple piece and the side-step part

Simple part					
Depth (mm)	10	20	25	35	Thickness (mm)
Pressure (MPa)	26	24	22	21	1
	26	25	25	23	1.5
	27	26	25	24	2.5
Side-step-part					
Depth (mm)	8	10	13	20	Thickness (mm)
Pressure (MPa)	37	36	35	34	1
	38	37	36	35	1.5
	39	38	37	37	2.5

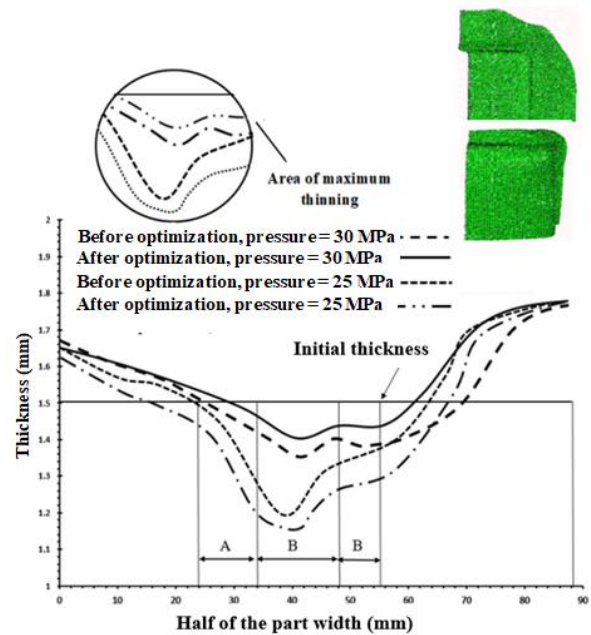


**Figure 20.** A simple rectangular workpiece obtained with an optimized sheet at a pressure of 32 MPa, a depth of 35 mm and a sheet thickness of 2.5 mm, obtained from simulation

**6. 4. Punch Radius** To investigate the effects of optimizing the initial blank on determining the minimum radius, the minimum thickness reduction of the part was investigated in different radii at a constant pressure and depth for the part. By optimization, the amount of the minimum selected radius in the part decreases, since the sheet flow and elongation are reduced in the area of the part walls. So that by optimizing the radius of the part from 5 mm to 4 mm, it will remain constant with no change in thinning. Table 3 shows the obtained thickness distribution values for the final thickness of the workpiece before and after optimization.

**7. CHANGES IN THE SHAPE OF THE INITIAL BLANK AT DIFFERENT DEPTHS**

For each workpiece, the optimal sheet curve changes at different depths. In order to achieve the change process of the initial sheet curve by changing the depth of steps to 15, 20, 25, 30 and 35, simple and two-step rectangular geometries were investigated. Figure 21 shows the zoning of the initial blank to check the material flow. To check the process of changes according to the zoning carried out for three different rectangular geometries, changes in the shape of the initial sheet in the optimization of the simple

and the middle-step parts were examined, which are shown in Figures 22 and 23, respectively. As can be seen, with the change in the shape of the part, the shape of the optimum initial blank will be very different and it is not possible to apply a single optimization process for other geometries and it can't be used for other geometries. So that in the areas of the earring and flange walls in the longitudinal and transverse directions, it needs to change the nodes coordinates (x and y directions) for each geometry. So that, as shown in Figures 24 and 25, if two-step parts have different geometries of the lower step, the flow of material and changes in the coordinates of nodes in the radius and walls are also different. This result was obtained if stepped geometries are considered, depth changes have much more effects on the corners of the optimal sheet and the reason for this is the lack of material flow in the intersection.

With the overview done for the three defined geometries, for the simple rectangular workpiece, due to the initial sheet and the presence of sharp corners, most of the elongation is in the transverse wall. For the side-step workpiece, the material flow is created by removing the nodes in the earring coordinates of the flow in the walls and corners. Three areas: earring area, the transverse wall (the distance between the earrings in the width direction) and the longitudinal wall (the distance between the

**TABLE 3.** Thickness distribution values obtained for the final thickness of the workpiece before and after optimization

Part type	Destruction before optimization	Destruction after optimization	Destruction before the proper punch radius	Destruction after the proper punch radius
Simple	1.26	1.38	1.24	1.41
side-step	1.23	1.35	1.2	1.29
middle-step	1.24	1.41	1.23	1.35

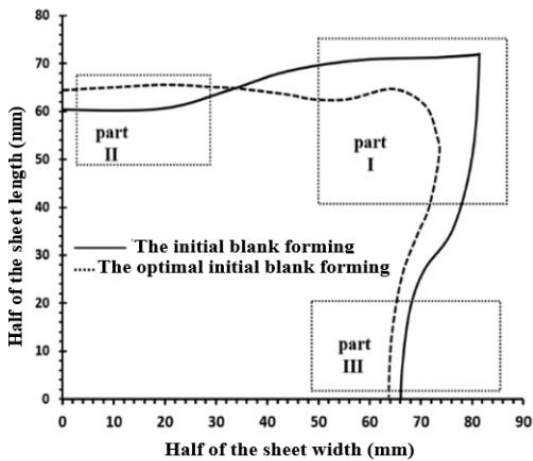


**Figure 21.** Zoning of the initial sheet to check the material flow, I. Corner radius, II. Transverse wall, and III. Longitudinal wall

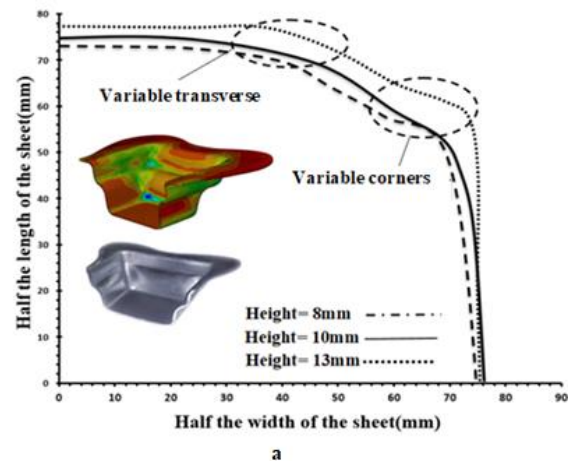


**Figure 22.** Changes in the shape of the initial sheet in the optimization at different depths of the simple part, obtained from simulation

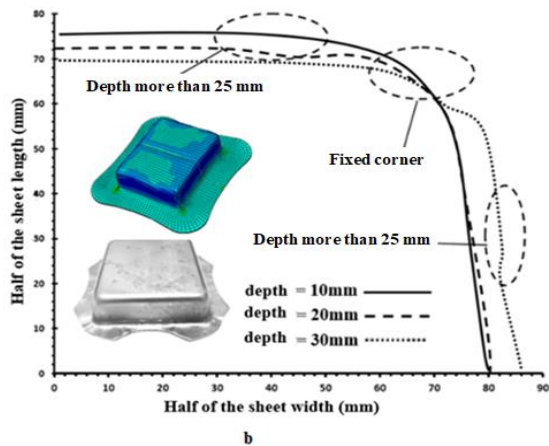


**Figure 23.** Changes in the shape of the initial sheet in the optimization at different depths of the middle-step part, obtained from simulation

earrings in the length direction) and the process of changes in the material flow in the three mentioned areas at different depths were investigated. At the step depths of 10 and 15 mm with the initial sheet, due to the presence of sharp corners in the sheet and lack of material flow due to the short distances of the transverse wall, because strain in the direction of depth in the transverse wall is more than in other areas, by using the sensitivity method and determining the coordinates of the nodes and removing the sharp corner in the earring area, the flow in the three areas has been balanced and by changing the coordinates of the nodes in the earring area, the optimum shape of the sheet has been achieved. Figure 24 shows the trend of changes in nodes coordinates for the middle-step part.

By conducting repeated experimental tests and validating the experimental and simulation results presented in this research, it was shown that by using the flow chart to determine the pressure and the optimal

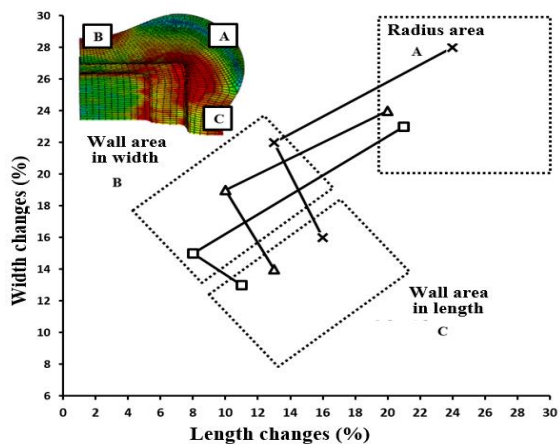


**Figure 24.** The changes of the node's coordinates in three defined areas of the initial sheet for the middle-step part at a pressure of 24 MPa, obtained from simulation

parameters to form a variety of simple and stepped rectangular parts in different heights and geometries, it is possible to determine the optimal shape of the initial sheet automatically. As an example, a simple rectangular geometry with the dimensions of the initial sheet of 152 x 150 mm and a height of 35 mm was considered. Simulation was performed with Abaqus software to determine the sound part. It was done first by using the flowchart to determine the pressure according to Figure 13, then by defining the rules of the flowchart in Abaqus software and the optimal radius at this height obtained from simulation tests. In the next stage, the simulation was done automatically with computer to determine the shape of the initial sheet. It was performed by defining the rules and relationships of the sensitivity analysis method and coding the rules based on the shape flowchart in Python software, with linking Python and Abaqus software. The first stage of simulation was performed based on the definition of the objective function with the coordinates of the nodes. After simulation and matching the curve with the target curve, if there is deviation from the final node, the software calculates the amount of deviation of the nodes and determines the coordinates of the new nodes based on the sensitivity relationships, rules and coding. The simulation was done again after modifying the initial sheet and was repeated until the curve of the formed sheet matches the target curve so that the optimal initial sheet was obtained in the final stage.

### 8. AUTOMATION OF DETERMINING THE INITIAL BLANK SHAPE BY COMPUTER

Because all the findings and the upcoming reviews are only related to a sheet sample with a simple rectangular geometry, obviously, its results cannot be generalized to other geometries. Therefore, after examining the simple geometry by experimental and numerical methods and examining the optimal shape changes in different dimensions, to determine the process of changes and ensure the correctness of the process numerically, the process is determined with the help of a flowchart. It is repeated for other different geometries with two steps. The parameters that are emphasized in this part of the research are optimal pressure and corner radius which are analyzed to produce a sound part and the results are presented in a comparative form.

Finally, after predicting the process of changes in the optimum shape of the sheet by changing dimensions of the samples, by linking Python and Abaqus software and the generalization of the sensitivity analysis relationship, the automatic determination of the optimum sheet shape in the process of hydrodynamic deep drawing with radial pressure will be done by the method of metallurgy. So that, hydrodynamic deep drawing operation is done with radial pressure under different tensile limits by

determining the optimal parameters based on the criterion of maximum thinning for each type of geometry and on the other hand by applying the predicted results in the finite element software, the results are compared with the same experimental test conditions. Figure 25 shows the general flowchart of the work stages.

In this article, after examining the effective parameters in compiling the flowchart and comprehensive review the changes in the shape of the initial blank resulted from the change of these parameters as well as manual optimization of the initial sheet shape for different geometries, by determining the proper pressure flowchart for a group of rectangular parts in simple and two-step mode, by using one of the widely used methods of optimization, a flowchart was developed that can be used by Abaqus software and its outputs and its direct linking with Python software. After determining and specifying the desired geometry for forming, it is possible to perform the stages of determining the proper pressure and finally determining the shape of the initial sheet in a closed loop by computer and in the form of a software package. All the stages of checking the outputs, changing the geometric parameters and checking the shape of the initial sheet that matches the optimal target contour, for any depth and geometric shape, can be done by computer through software linking. According to the investigation of the effective parameters in forming and a comprehensive investigation in this regard for simple and two-step parts in different dimensions and depths, the general results of

the change process of each parameter was considered as initial conditions in coding and automation rules. According to the optimization method considered to start the work, the coordinates of all nodes selected on the sheet are determined and considered as initial coordinates for coding. In the following, in order to categorize and determine the process of nodes coordinates changes numerically and to reduce the optimization process error in determining the automatic execution relationships and to determine the validity of the relationships obtained in the automation method by computer, three points in each area considered in the initial blank (corner radius, transverse wall and longitudinal wall) are as A1, A2, A3, B1, B2, B3 and C1, C2, C3 respectively and the changes of nodes coordinates for simple and two-step parts in different dimensions and depths are determined numerically. Figure 26 shows the determination of nodes coordinates in three areas for the simple segment. In Tables 3 and 4, the numerical coordinates obtained for each node are defined according to the points shown in the simple and middle-step parts, respectively. In Figures 27 and 28, the graphs of the changes obtained from these numbers are shown. Also, in Tables 4, 5, 6 and 7, the thickness distribution in the designated areas of the simple and the middle-step workpieces are shown, respectively.

In conducting the research, we were able to numerically obtain the trend of nodes coordinates changes and determine the optimal pressure parameters through

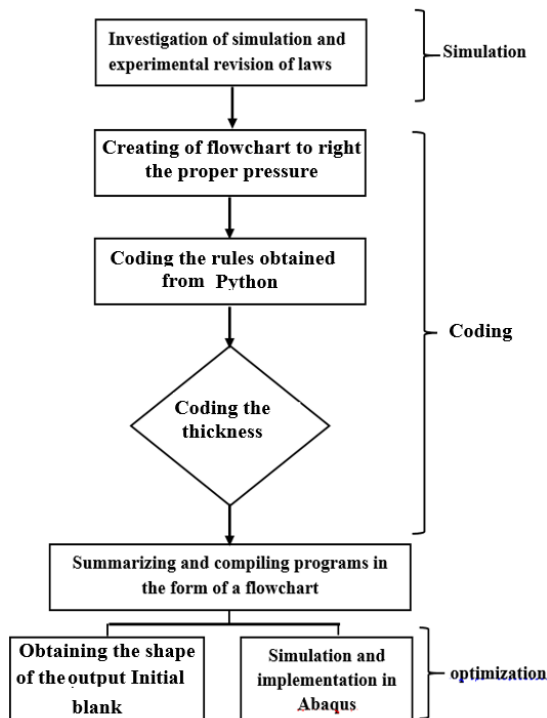


Figure 25. Computer-aided automation process

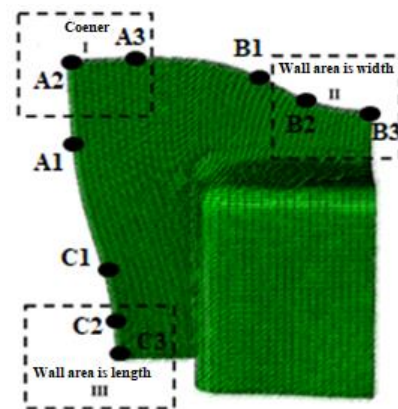


Figure 26. Finding the coordinates of the nodes in the zoning of the simple part in the radius of the punch-A, the transverse wall-B and the longitudinal wall-C

TABLE 4. Thickness distribution values obtained for the final thickness of the simple workpiece

Area	I			II			III		
Node	A1	A2	A3	B1	B2	B3	C1	C2	C3
X	71	73	52	38	31	9	64	57	52
Y	54	69	72	62	54	79	29	21	13

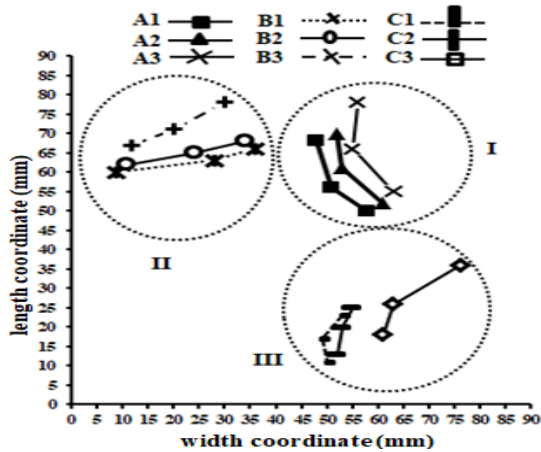


Figure 27. Numerical changes of nodes coordinates in three defined areas of the initial sheet for a simple workpiece at a pressure of 24 MPa and a depth of 35 mm, obtained from simulation

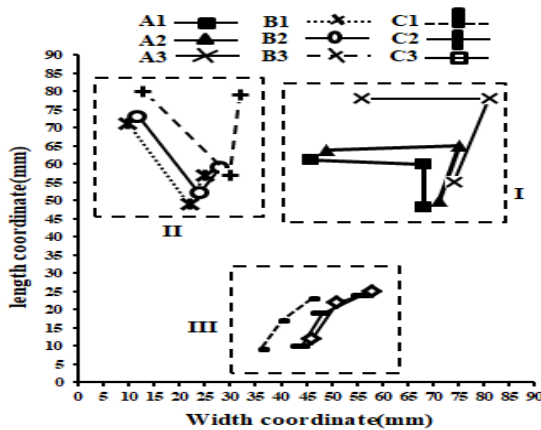


Figure 28. Numerical changes of nodes coordinates in three defined areas of the initial sheet for the middle-step workpiece at a pressure of 30 MPa and a depth of the lower step of 13 mm, obtained from simulation

TABLE 5. Thickness distribution values obtained for the final thickness of the middle-step workpiece

Area	I			II			III		
Node	A1	A2	A3	B1	B2	B3	C1	C2	C3
X	75	79	58	34	28	10	60	52	48
Y	58	71	74	66	58	82	25	19	11

the flowchart, we will determine the proper radius and depth for any simple and rectangular geometry, the parameter rules and the conditions for determining the proper parameters for batch forming of simple and two-step rectangular parts. In order to form any geometry with specific depth and dimensions, the parameters of pressure, radius and approximate dimensions of the initial blank can

TABLE 6. Thickness distribution values obtained for the final thickness of the simple workpiece

Shape	Punch length	Punch width	Punch height	Blank length	Blank width
Simple workpiece	60-75	40-55	H=15-25mm	95	105
			$h \geq 35$ mm	110	125
Simple workpiece	85-110	65-90	H=15-25mm	120	130
			$h \geq 35$ mm	150	152
Simple workpiece	120-160	90-120	H=15-25mm	135	150
			$h \geq 35$ mm	175	185

TABLE 7. Thickness distribution values obtained for the final thickness of the simple workpiece

Shape	Punch length	Punch width	Punch height	Blank length	Blank width
Two-step workpiece	60-75	40-55	$h1 = 15 - 20$ mm, $h1 \leq 13$ mm	135	142
			$h1 = 15 - 20$ mm, $h1 \geq 15$ mm	160	174
Two-step workpiece	85-110	65-90	$h1 = 23 - 27$ mm, $h1 \leq 13$ mm	150	152
			$h1 = 23 - 27$ mm, $h1 \geq 15$ mm	180	195
Two-step workpiece	120-160	90-120	$h1 = 30 - 45$ mm, $h1 \leq 13$ mm	165	180
			$h1 = 23 - 27$ mm, $h1 \geq 15$ mm	195	215

be used to start forming and automatically determine the shape of the initial guessed sheet. To carry out a process to produce the part with the optimal initial sheet shape automatically by computer, based on the general relationships obtained at the beginning, the approximate dimensions of the initial sheet are defined in Abaqus software by defining n points and these points are connected to each other. With the studies done, the rules of the basic relationships of the sensitivity optimization method and the optimal parameters were obtained, which were written in the form of code using the Python programming language. In relations 9 and 10, part of the obtained rules for the parameters and dimensions of the initial blank for simple and two-step parts are shown. Tables 6 and 7 also show the rules for obtaining the dimensions of the initial sheet based on the geometry of the final workpiece and the depth of the drawing. In order to obtain these rules, several stages of simulation were performed to obtain the range of sheet flow changes for each geometry, considering complete forming of the part and the absence of rupture.

Simple part

$$h \leq 20mm, r = 4mm$$

$$\text{if } h \geq 25mm, r = 6mm, P = 24mpa \tag{9}$$

$$\text{if } t \leq 1mm, r = 5mm, P = 22mpa$$

$$\text{if } t \geq 1.5mm, r = 5mm, P = 36mpa$$

Two-step geometry

$$h1 = 22mm, h2 \leq 15, r = 5mm, P = 40Mpa$$

$$\text{if } h \geq 13mm, r = 7mm, P = 42Mpa \tag{10}$$

$$\text{if } t \leq 1mm, r = 8mm, P = 34Mpa$$

$$\text{if } t \geq 2, r = 6mm, P = 46Mpa$$

Also, the basic relationships of how to categorize the coordinates of the nodes and the sensitivity rules used in coding are shown in relationships 11 to 14. According to the initial relationships of the sensitivity method, n points are considered separately based on the dimensions of the initial sheet and the workpiece in positions of the nodes coordinates in forming and are placed in relation 12 with coding and it is defined as a code based on the sensitivity factor with relation 13 and other defined constants. In relation 14, for each coordinate after forming, the new material point is defined and forming continues until reaching the target point for each target contour of a simple or two-step Workpiece.

$$A_{ij} \begin{matrix} X_j^i \\ Y_j^i \end{matrix}, j = [0....120] \tag{11}$$

$$x_j^{i+1} = x_j^i + \delta N \tag{12}$$

$$S = \frac{x_{j_{i+1}} - x_{j_i}}{x_{j_{i+1}} - x_{j_i}} \tag{13}$$

$$x_j^{i+1} = x_j^i - \varepsilon \delta N \tag{14}$$

According to the dimensions of the final part and using the rules obtained from experimental investigations and repeated simulations, the values of the effective parameters were automatically obtained and used in the simulation. On the other hand, simulation using Abaqus software is also coded with Python programming language and proper parameter values were automatically entered into the software. At the end of each simulation, the coordinates of the initial sheet points were entered into the sensitivity analysis relations and a new simulation with coordinate values was obtained automatically. In this research, by obtaining flowcharts and rules and coding done in Python programming language, the optimum initial blank shape is obtained for each rectangular geometry with different dimensions and depths. With the final review of relationships and rules, the final automation flowchart is shown in Figure 29. In order to

validate the obtained rules and coding, by performing the automatic method of determining the shape of the initial blank and forming the simple and two-step part, the dimensions of the optimum initial blanks and the Formed parts are determined with automatic and computer-aided methods and shown in Figure 30 for simple and two-step (middle-step and side-step) geometries.

In this research, according to the rules for determining the geometric parameters and the pressure flow chart and the basic relationships of the Sensitivity analysis, a solution method was presented. First, each geometry is defined with dimensions and height, then the pressure (P) flowchart (Figure 11) determines the method of setting this parameter in the lines of Abaqus software programs through the call codes. The final appropriate pressure is determined through the criterion of maximum thinning (10) and relations of maximum filling (21) (if step

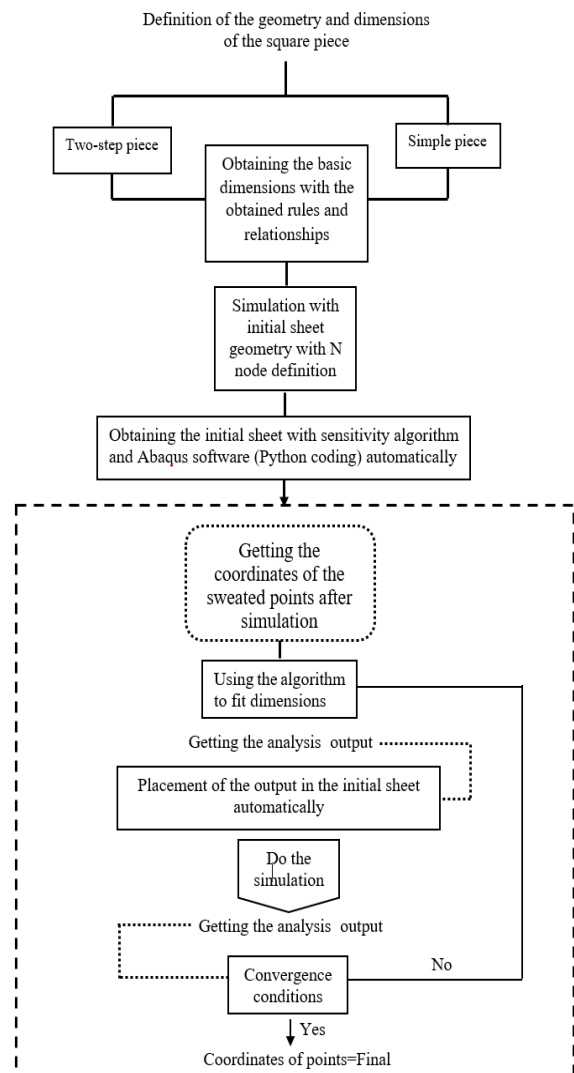
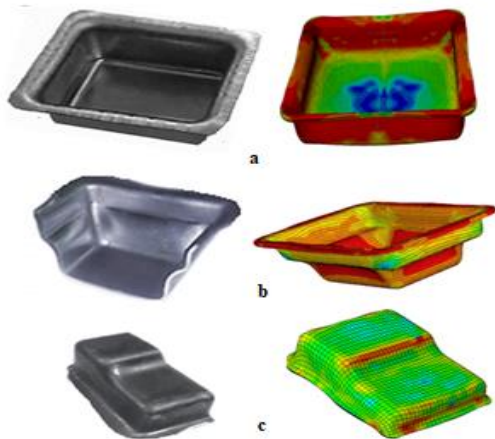


Figure 29. The final flowchart of the initial blank shape automation for all types of rectangular part



**Figure 30.** Final Formed parts with optimal initial sheet in simulation and experimental mode, a. Simple part, b. Middle-step part and c. Side-step part

geometry is defined). Then by defining  $N$  points or nodes  $X$  in the initial sheet and defining the coordinates of the points in the Python software, the simulation of the first step is done with the initial sheet. After checking the coordinates of the shaped sheet  $[X_s]$  with the target curve  $[X_t]$ , the codes defined by Python software of all linked to Abaqus software can determine the deviation nodes from the target curve through the relations of the sensitivity method. Then, the defined codes return to the first line and the simulation is performed until the target curve and the given shape coincide. According to the presented solution method, the amount of deviation of each node is determined with a maximum error of one millimeter. The presented solution method is a new computer-aided method for numerical solution and obtaining the shape of the initial sheet by changing the height and dimensions of various rectangular parts.

## 9. CONCLUSIONS

The following conclusions have been drawn from the current research:

1. By examining the changes in the height and shape of the part, it was found that for each geometry, the shape of the initial sheet in the area of the transverse, longitudinal and radius walls varies, and the amount of changes in the coordinates of the node relative to the target curve deviates with changes in the geometry and height, and the range of changes of node coordinates of simple and stepped parts.
2. In this research, according to the diversity of rectangular parts geometries, the simulation stages and experimental tests to produce a sound part are reduced, and the ability to define rules in Python and Abaqus software was achieved by providing a flowchart to determine the appropriate pressure.

3. According to the parametric examination of forming of the parts to define the rules, it was found that with the change in the thickness and geometric shape of the final part, the amount of forming pressure and the radius of the punch changes. Moreover, it was investigated that, the amount of changes of these parameters can be determined for different dimensions and thicknesses in the form of rules and relationships and can be defined in the automation software.

4. With the increase of the drawing ratio in the parts, the amount of filling in the stepped parts and the amount of thinning at heights of more than 20 mm decrease up to 8%, due to less strain and lack of flow of the sheet in the radius area of the mold. So, forming pressure should be increased.

5. By performing the optimization stages, with more sheet flow due to the removal of the primary sheet corners, the maximum forming pressure at the beginning of the process and at the end of forming is reduced by 10% and 21%, respectively.

6. In this research, by providing automation rules with the use of a computer and the link of Python and Abaqus software, the initial sheet shape can be obtained by specifying the optimal shaping parameters before performing repeated simulations, and it is possible to save time and money.

## 10. SUGGESTION FOR OTHERS

The following suggestions are presented at the end of the paper as future works to be done by other researchers to complete this research:

1. Basic optimization methods such as Radius Vector and Taguchi method, and numerical software solution should be implemented to link with Abaqus software for comprehensive application of software and optimization methods.
2. According to the most important circular and polygonal geometries, it is suggested to investigate the automatic optimization procedures for a group of the mentioned geometries to show the generality of the application of this method.
3. According to the application and development of hydroforming methods in the production of sheet parts in the automotive, aerospace and military industries, it is suggested that automatic methods be used to obtain the optimal forming pressure.

## 11. REFERENCES

1. Zhang S-H. Developments in hydroforming. *Journal of Materials Processing Technology*. 1999;91(1-3):236-44. <https://doi.org/10.1071/mfreview/1999232>

2. Kocańda A, Sadłowska H. Automotive component development by means of hydroforming. *Archives of Civil and Mechanical Engineering*. 2008;8(3):55-72. <https://doi.org/10.5829/ije.2008.22.02b.30>
3. Lange K, Pöhlandt K. Handbook of metal forming. (No Title). 1985. <https://doi.org/10.1080/09507116.1985.581345>
4. Wong C, Dean T, Lin J. A review of spinning, shear forming and flow forming processes. *International Journal of Machine Tools and Manufacture*. 2003;43(14):1419-35. <https://doi.org/10.1016/j.jengfailanal.2011.114348>
5. Kim J, Kang S-J, Kang B-S. Computational approach to analysis and design of hydroforming process for an automobile lower arm. *Computers & Structures*. 2002;80(14-15):1295-304. <https://doi.org/10.1051/mfreview/2002032>
6. Wang H, Gao L, Chen M. Hydrodynamic deep drawing process assisted by radial pressure with inward flowing liquid. *International Journal of Mechanical Sciences*. 2011;53(9):793-9. <https://doi.org/10.1016/j.jengfailanal.2011.114348>
7. Kim T, Yang D-Y, Han S. Numerical modeling of the Multi-stage sheet pair hydroforming process. *Journal of materials processing technology*. 2004;151(1-3):48-53. <https://doi.org/10.1671/mfreview/2004032>
8. Lang L, Danckert J, Nielsen KB. Investigation into hydrodynamic deep drawing assisted by radial pressure: Part I. Experimental observations of the forming process of aluminum alloy. *Journal of Materials Processing Technology*. 2004;148(1):119-31. <https://doi.org/10.1016/j.jengfailanal.2011.114348>
9. Kang B-S, Son B-M, Kim J. A comparative study of stamping and hydroforming processes for an automobile fuel tank using FEM. *International Journal of Machine Tools and Manufacture*. 2004;44(1):87-94. <https://doi.org/10.1016/j.jengfailanal.2011.114348>
10. Zhang S-H, Nielsen KB, Danckert J, Kang D, Lang L. Finite element analysis of the hydromechanical deep-drawing process of tapered rectangular boxes. *Journal of Materials Processing Technology*. 2000;102(1-3):1-8. <https://doi.org/10.1007/s40194-020-00886-3>
11. Wu J, Balendra R, Qin Y. A study on the forming limits of the hydromechanical deep drawing of components with stepped geometries. *Journal of Materials Processing Technology*. 2004;145(2):242-6. <https://doi.org/10.1016/j.jengfailanal.2011.114348>
12. Barlat F, Chung K, Richmond O. Anisotropic plastic potentials for polycrystals and application to the design of optimum blank shapes in sheet forming. *Metallurgical and Materials transactions A*. 1994;25:1209-16. <https://doi.org/10.1007/s40194-020-00886-3>
13. Shim H. Determination of optimal blank shape by the radius vector of boundary nodes. *Proceedings of the Institution of Mechanical Engineers, Part B: Journal of Engineering Manufacture*. 2004;218(9):1099-111. <https://doi.org/10.5829/ije.1994.31.02c.30>
14. Meng B, Wan M, Yuan S, Xu X, Liu J, Huang Z. Influence of cavity pressure on hydrodynamic deep drawing of aluminum alloy rectangular box with wide flange. *International journal of mechanical sciences*. 2013;77:217-26. <https://doi.org/10.1016/j.jengfailanal.2013.102328>
15. Rahmani F, Hashemi SJ, Moslemi Naeini H, Deylami Azodi H. Numerical and experimental study of the efficient parameters on hydromechanical deep drawing of square parts. *Journal of Materials Engineering and Performance*. 2013;22:338-44. <https://doi.org/10.1016/j.jengfailanal.2013.102328>
16. Mousavipoor R, Gorji A, Bakhshi M, Alinejad GM. Experimental and Numerical Study of Effective Parameters in Forming of Double-Stepped Parts and Optimization of the Initial Blank Shape. *Modares Mechanical Engineering*. 2015;15(4). <https://doi.org/10.1016/j.jengfailanal.2013.102328>
17. Luo Y, Luckey S, Friedman P, Peng Y. Development of an advanced superplastic forming process utilizing a mechanical pre-forming operation. *International Journal of Machine Tools and Manufacture*. 2008;48(12-13):1509-18. <https://doi.org/10.1051/mfreview/2015032>
18. Vafaesefat A. Finite element simulation for blank shape optimization in sheet metal forming. *Materials and Manufacturing Processes*. 2011;26(1):93-8. <https://doi.org/10.1016/j.jengfailanal.2013.102328>
19. Blount G, Fischer B. Computerised blank shape prediction for sheet metal components having doubly-curved surfaces. *THE INTERNATIONAL JOURNAL OF PRODUCTION RESEARCH*. 1995;33(4):993-1005. <https://doi.org/10.1016/j.jengfailanal.2013.102328>
20. Xiaojing L, Yongchao X, Shijian Y. Effects of loading paths on hydrodynamic deep drawing with independent radial hydraulic pressure of aluminum alloy based on numerical simulation. *Journal of Materials Sciences and Technology*. 2008;24(03):395. <https://doi.org/10.1007/s40194-009-22886-4>
21. Bakhshi M, Hosseinipour SJ, Gorji A. The Study of effective parameters in hydroforming of fuel cell metallic bipolar plates with parallel serpentine flow field. *Modares Mechanical Engineering*. 2014;14(8):17-27. <https://doi.org/10.1007/s40194-009-22886-4>
22. Panahi Leavoli R, Gorji H, Bakhshi-Jooybari M, Mirnia M. Investigation on formability of tailor-welded blanks in incremental forming. *International Journal of Engineering, Transactions B: Applications*. 2020;33(5):906-15. <https://doi.org/10.5829/ije.2020.33.05b.23>

**COPYRIGHTS**

©2024 The author(s). This is an open access article distributed under the terms of the Creative Commons Attribution (CC BY 4.0), which permits unrestricted use, distribution, and reproduction in any medium, as long as the original authors and source are cited. No permission is required from the authors or the publishers.



---

**Persian Abstract**

---

**چکیده**

در این تحقیق از روشی ابتکاری برای بدست آوردن شکل ورق اولیه در شکل دهی هندسه های مختلف مستطیلی استفاده شده است تا بتوانیم قوانینی را به دست آوریم که به طور خودکار شکل ورق اولیه بهینه را در ارتفاعات مختلف تعیین نمود. از روش آنالیز حساسیت برای بهینه سازی و از نرم افزار پایتون برای لینک با نرم افزار آباکوس استفاده گردید. با بررسی پارامترهای هندسی و فشار شکل دهی، فلوچارت تعیین فشار مناسب ارائه گردید. با بررسی تغییرات ارتفاع در هندسه های مختلف مشخص گردید که بهینه سازی سبب کاهش فشار بیشینه و حداکثر شعاع سنبه می گردد که به ترتیب 4 و 8 درصد بدست آمد. مشخص گردید که اختلاف اندازه اضلاع طولی و عرضی مقطع قطعه تاثیر مستقیم بر روی تغییرات مختصات گره برای انطباق با منحنی هدف دارد و تعداد مراحل بهینه سازی را کاهش می دهد. از نتایج بدست آمده نشان داده شد که با خودکار سازی و تعیین فلوچارت فشار، بدون تکرار در مراحل بهینه سازی و تست های تجربی مکرر، با حداقل مراحل بهینه سازی می توان شکل ورق اولیه را تعیین نمود و از دور بری جلوگیری نمود.

---



# Experimental Study of Open Channel Model of Glass Fiber Reinforced Polymer and Its Flowing Characteristics

S. Hasyim<sup>a\*</sup>, N. Salam<sup>b</sup>, M. Saleh Pallu<sup>a</sup>, F. Maricar<sup>a</sup>

<sup>a</sup> Civil Engineering Department, Faculty of Engineering, Hasanuddin University, Gowa, South Sulawesi Province, Indonesia

<sup>b</sup> Mechanical Engineering Department, Faculty of Engineering, Hasanuddin University, Gowa, South Sulawesi Province, Indonesia

PAPER INFO

Paper history:

Received 01 August 2023

Received in revised form 06 November 2023

Accepted 10 November 2023

Keywords:

Glass Fiber Reinforced Polymer

Open Channel Flume

Experimental Model

Manning Roughness Coefficient

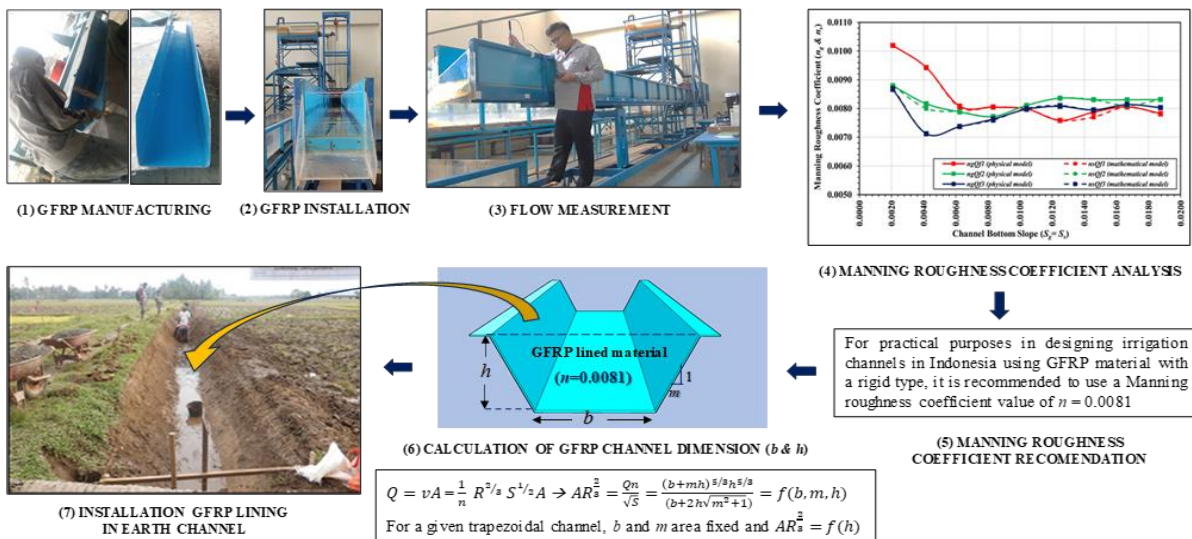
Nash-Sutcliffe Efficiency

ABSTRACT

One of the efforts to reduce water losses in irrigation channels is to provide lined materials in the earth's irrigation channels. Construction of these lined materials in Indonesia requires raw materials (such as sand, gravel, and split stone) mined from nature, and in Indonesia, known as class C excavated materials. Excessive exploitation of class C excavated materials will impact environmental damage. To overcome these problems, therefore, research is needed to find alternative lined materials, and in this research, the alternative lined material is Glass Fiber Reinforced Polymer (GFRP). The study's primary objective was to determine the value of the Manning roughness coefficient for lined channels made of GFRP material. The research involved experimental testing using an open channel model (flume) lined with GFRP material. The flow tests were conducted with three variations of the pump flow discharge and nine variations of the channel bottom slope. The test results from the physical model were compared with the results of the mathematical model simulation using the HEC-RAS software. The model's performance was evaluated using the graphical technique and quantitative statistics specifically the Nash-Sutcliffe Efficiency (NSE) method. Model evaluation with the NSE method shows that the performance of the physical model is "very good". The Manning roughness coefficient value for rigid-lined GFRP material range from 0.0071 to 0.0102. The recommended Manning roughness coefficient value for practical application in the design of irrigation channels in Indonesia is 0.0081.

doi: 10.5829/ije.2024.37.04a.10

Graphical Abstract



\*Corresponding Author Email: [suryadhs@yahoo.com](mailto:suryadhs@yahoo.com) (S. Hasyim)

## 1. INTRODUCTION

One of the efforts to increase the availability of irrigation water is to provide lining for earth irrigation channels so that this will have an impact on reducing the rate of water loss in irrigation channels. Based on Indonesian Irrigation Planning Standards, four types of materials are recommended for use as a lining in irrigation channels in Indonesia, such as stone masonry, concrete, soil-cement, and ferrocement. For irrigation channel planning in Indonesia, the Manning roughness coefficient ( $n$ ) values recommended for use for the four types of lined material are respectively 0.0167, 0.0143, 0.0285 – 0.0222, and 0.0143 (1). Of the four types of lining, only two are the most widely used as lined material in irrigation channels in Indonesia, such as stone masonry lining and concrete lining. Apart from using a mixture of water and cement, the process for construction implementation of two types of lined materials also requires other raw materials such as sand, gravel, and crushed stone, mined from nature, and in Indonesia are known as class C excavated materials. The excessive exploitation of class C excavated materials will impact environmental damage, so it needs to be mitigated (2-4). In practice, also in the project site, the process of making the mixture for the lining of the channels from the stone masonry and concrete has several constraints, such as the difficulty of obtaining class C excavated material sources, the problematic access constraints to transport the mixed material constituents to the work location, the difficulty of obtaining fresh-water that is required for the process of mixing materials in the project site, and the difficulty of controlling the quality of the construction work due to the wide spread of the work locations (5). Figure 1 shows a case example of difficult access conditions for making concrete mixes for tertiary irrigation channel work at the Batang Anai Irrigation Project in West Sumatra Province, Indonesia, which was implemented in 2016.

From these problems, the preliminary research idea arose to find and study alternative materials that do not use cement and class C excavated materials.

One of the products of processed polymer materials is the geomembrane. Geomembrane as a lined channel



**Figure 1.** Construction of concrete lining on tertiary irrigation channels in the Batang Anai Irrigation Project in West Sumatra Province

material has been widely used in various countries. In the United States, geomembrane has been used as a lined material (membrane) in channels that control seepage since 1950s. It is an effective alternative material to replace traditional standard linings methods, such as concrete and compacted soil. One of the first uses of geomembranes for channels was in 1954 in irrigation channels by the U.S. Bureau of Reclamation (USBR) in Fort Collins, Colorado. USBR has extensive experience in geomembrane installation and monitoring for lined channels based on past field testing programs. PVC geomembrane was originally a geomembrane used for lined channels. However, subsequently, Polyethylene (PE) based geomembranes (such as HDPE, LDPE, CSPE, and VLDPE) and several other types of geomembranes (such as EDPM and Polypropylene) are also used as lined channels (6-8). In Portugal, prefabricated membranes for lined channel use are also increasing, especially as a solution for rehabilitating existing concrete channels. The two main types of membranes used in Portugal are bituminous membranes (modified bitumen polymers) and synthetic membranes (PVC) (9).

One of the most essential purposes of scientific research is finding new engineering composites that combine strength and lightweight (10). Polymer matrix composites are used in different industrial applications due to their enhanced mechanical properties and lightweight (11). Fiber-reinforced polymer (FRP) composites have better fatigue and corrosion-resistive performance than metals, reducing the maintenance cost (12). FRP is a composite material made of a polymer matrix reinforced with fibers. The fibers are usually glass, carbon, or aramid. The polymer is usually epoxy, vinyl ester, or polyester thermosetting plastic (13). Because of cost, glass, and carbon are the most widely used reinforcement materials for civil infrastructure composite applications. For applications that require large amounts of materials, glass is the most popular because it is the least expensive (14). The economic analysis indicated that glass fiber is more cost-benefit than carbon fiber in improving the concrete properties, especially for one layer of FRP (15). Polyesters are the most widely used polymers in FRP components for construction/civil infrastructure applications due to their relatively low cost and ease of processing (16). Polyester resins have many advantages, such as suitable adhesive and mechanical properties, better resistance to fatigue and micro cracking, reduced degradation from water ingress, increased resistance to osmosis (surface degradation due to water permeability), and good performance at elevated temperatures (17). Various fabrication techniques, such as hand layup, spray-up, filament winding, lamination, and pultrusion, are used to process polymeric composites (18).

Nowadays, Glass Fiber Reinforced Polymer (GFRP) composites are alternative products for metals due to their superior characteristics like high specific stiffness, corrosion resistance, fatigue resistance, and less weight-to-strength ratio (19). In Indonesia, GFRP materials are currently widely used as building materials in the construction industry. GFRP material generally has strong, lightweight, weather-resistant, and impermeable characteristics, so it is often used as a component of hydraulic structures (such as sliding gates, flap gates, and culverts) in swamp irrigation channels where the water conditions are acidic (Figure 2).

In order to design an irrigation channel using GFRP material lining, it is necessary to know the value of the hydraulic roughness coefficient first. GFRP material is currently also widely used in the manufacture of commercial piping products in various countries. Some of the piping products in the world that have included the value of the hydraulic roughness coefficient in their GFRP piping product specifications include the following:

1. Grandpipe®, a GFRP pipe manufacturing company from Turkey, gives a Manning roughness coefficient  $n = 0.009$  for pipe material products called GRP (Glass-Reinforced Plastics)<sup>1</sup>.
2. Jiubo Composite®, a GFRP pipe manufacturing company from China, gives a Manning roughness coefficient  $n = 0.0084$  for pipe material products called FRP (Fiber-Reinforced Plastics)<sup>2</sup>.

There is still little research using GFRP-lined material in open channels like irrigation channels. In 1975, Malaysia conducted trials on using GFRP material as a lined material in a pilot project for constructing a new tertiary irrigation channel implemented at the Tanjung Karang Irrigation Project. The construction of the tertiary irrigation channels was a typical flume-shape with the characteristics of a rigid GFRP material and was named Fiberglass-Reinforced Polyester (FRP) (20). Japan had also implemented using materials made from GFRP as lined materials to repair existing concrete lining in irrigation channels that had minor cracks. The material lining made of GFRP has flexible characteristics and is



**Figure 2.** Example of using GFRP flap gates in swamp irrigation channels in Central Kalimantan Province, Indonesia

named FFRP (Flexible Fiber Reinforced Plastic). Some samples of the FFRP material were taken to the laboratory to be tested experimentally using an open channel model of a rectangular flume to examine the value of the hydraulic roughness coefficient. The results of their research found that the Manning roughness coefficient is  $n = 0.0094$  (21). Since the idea of using lining with GFRP material in Indonesia is to line earth irrigation channels, the characteristics of the GFRP material must be rigid. Based on this explanation, the final idea of the research was to find the value of the hydraulic roughness coefficient for GFRP material with a rigid type produced by a factory in Indonesia. The primary objectives of the study include:

1. To evaluate the effects of discharge and channel bottom slope changes on flow velocity and flow depth characteristics.
2. To analyze the impact of changes in discharge and channel bottom slope on the value of the Manning roughness coefficient and to interpret the range of Manning roughness coefficient values obtained from the test results.
3. To propose the recommended Manning roughness coefficient value for GFRP material to be used in the design of irrigation channels in Indonesia.

After the innovative value for the Manning roughness coefficient ( $n$ ) for GFRP material resulting from this research has been obtained, the design of irrigation channel dimensions using GFRP lined material can be calculated using the uniform flow formula. Manning's formula and the continuity equation,  $Q = Av$ , form the basic equations for uniform-flow computation. The discharge  $Q$  is given as (22, 23):

$$Q = \frac{1}{n} AR^{2/3} S^{1/2} \quad (1)$$

$$Q = K\sqrt{S} \quad (2)$$

where,

$Q$	=	discharge (m <sup>3</sup> /s)
$A$	=	wetted area (m <sup>2</sup> )
$v$	=	flow velocity (m/s)
$n$	=	Manning roughness coefficient
$R = A/P$	=	hydraulic radius (m)
$P$	=	wetted perimeter (m)
$S$	=	channel bottom slope

$K = \frac{1}{n} AR^{2/3}$  is called the channel's conveyance and expresses the channel's discharge capacity per unit longitudinal slope. For a given channel,  $AR^{2/3}$  is a function of the flow depth. For example, in Figure 3 consider a trapezoidal section of bottom width =  $b$  and side slope  $m$  horizontal: 1 vertical.

<sup>1</sup> <https://grandpipe.com/en/product-information>

<sup>2</sup> <https://www.aldfpr.com/News/Comparison-of-FRP-Pipe-and-pipe-flow-185.html>

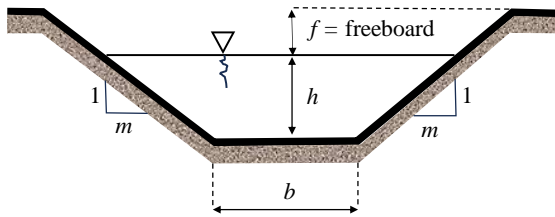


**Figure 3.** Hydraulic parameters on a trapezoidal channel cross section

Then,

$$A = (b + mh)h \quad (3)$$

$$P = (b + 2h\sqrt{m^2 + 1}) \quad (4)$$

$$R = \frac{A}{P} = \frac{(b+mh)h}{(b+2h\sqrt{m^2+1})} \quad (5)$$

$$AR^{\frac{2}{3}} = \frac{Qn}{\sqrt{S}} = \frac{(b+mh)^{5/3}h^{5/3}}{(b+2h\sqrt{m^2+1})} = f(b, m, h) \quad (6)$$

For a given trapezoidal channel,  $b$  and  $m$  are fixed and  $AR^{\frac{2}{3}} = f(h)$ . Since  $AR^{\frac{2}{3}} = \frac{Qn}{\sqrt{S}}$ , and if Manning roughness coefficient ( $n$ ) and channel bottom slope ( $S$ ) are fixed for a channel, the channel have unique depth in uniform flow associated with each discharge. The depth is called the normal depth ( $h$ ).

After this innovative value for the Manning roughness coefficient has been obtained, the advantages that can be obtained from its application in irrigation channels are as follows:

1. The use of GFRP material can reduce the use of class C excavated materials in Indonesia so that the impact of environmental damage can be mitigated.
2. The process of making GFRP material segments can be carried out first in the factory so that it will reduce the constraints, such as the difficulty of obtaining class C excavated material sources, the problematic access constraints to transport the mixed material constituents to the work location, the difficulty of obtaining fresh-water that is required for the process of mixing materials on the project site, and the difficulty of controlling the quality of the construction work.
3. Because the weight of the GFRP material is relatively light, transporting the material to the work location will be cheaper.
4. Because the GFRP material structure design has been created, installing GFRP-lined material segments in earth irrigation channels will be carried out more effectively and efficiently (see Figure 4).

## 2. MATERIAL AND METHOD

The Experimental research conducted at the Hydraulics Laboratory, Civil Engineering Department, Faculty of

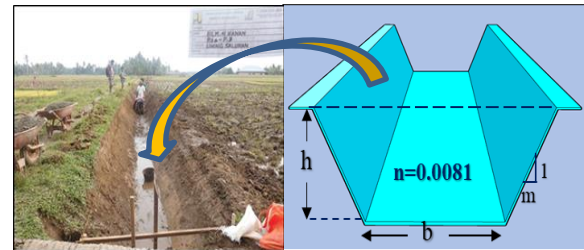


**Figure 4.** Illustration of installing GFRP material segment in an earth irrigation channel

Engineering, Hasanuddin University, South Sulawesi Province, Indonesia. The physical modeling used three pump discharge ( $Q_f$ ) variations as input data flowed into the GFRP flume. The three variations of pump discharge ( $Q_f$ ) are low inflow discharge ( $Q_{f1}$ ), medium inflow discharge ( $Q_{f2}$ ), and high inflow discharge ( $Q_{f3}$ ). The GFRP flume bottom slopes ( $S_g$ ) were also set for nine variations of channel bottom slopes, ranging from  $S_{g1}$  to  $S_{g9}$ .

### 2. 1. Material and Equipment

The primary material used in this study is GFRP (Glass Fiber Reinforced Polymer), produced by one of the factories in Indonesia. As a preliminary stage, measurements, manufacturing, packaging, and installation of the GFRP material into the flume were carried out, as shown in Figure 5.

The equipment used for experimental testing was as follows: a) an open channel (flume) model device lined with GFRP material; b) two submersible water pumps equipped with a pipe network and discharge control valves; c) a flow meter; d) water weighing scale; e) a point gauge; f) The flume's slope adjuster, as shown in Figure 6.

Precisely using this equipment during the experimental testing process is crucial to minimize errors in the hydraulic laboratory. Flow velocity was measured using a mini flow-meter because it can measure at a relatively low flow depth. Flow velocity and flow depth measurements can be seen in Figure 7.



**Figure 5.** (a) Measurements, (b) manufacturing, (c) packaging, and (d) installation of the GFRP material into the flume

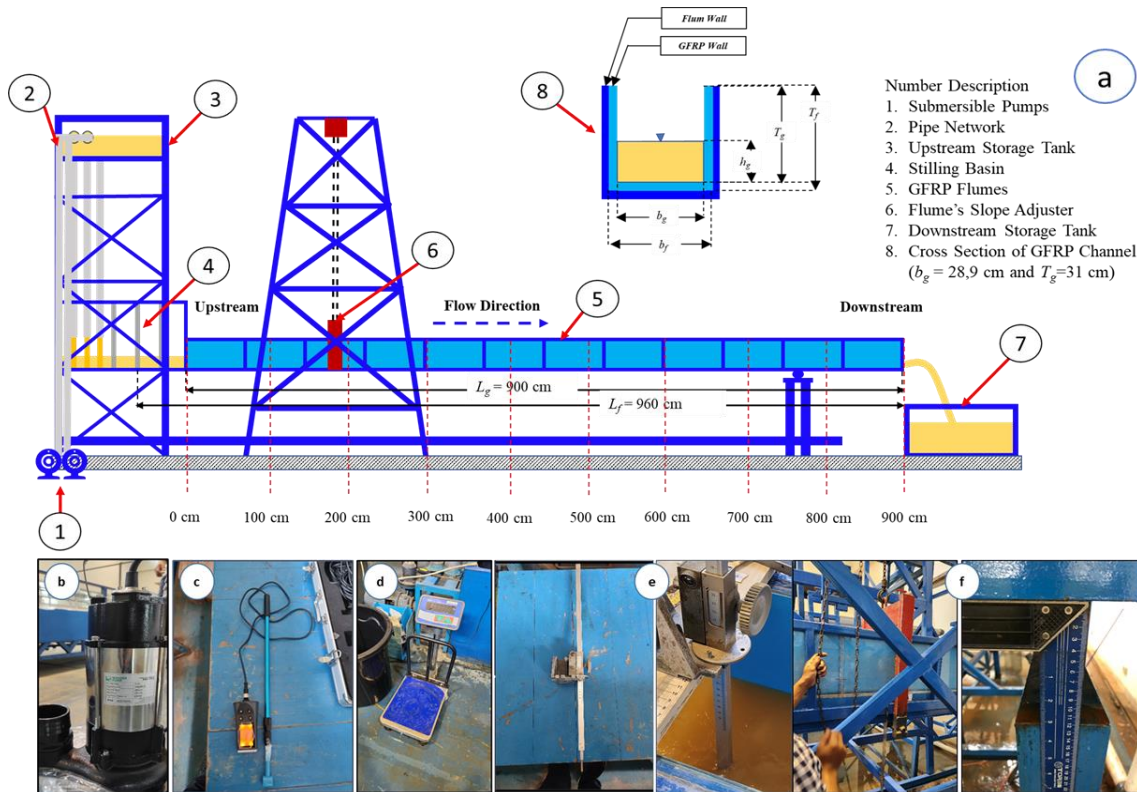


Figure 6. The flume model equipment and other devices used for experimental testing



Figure 7. (a) Flow velocity measurement using a flow meter (left) and (b) flow depth measurement using a point gauge (right)

**2.2. Experimental Test Method** The method used to obtain the Manning roughness coefficient value for GFRP material is by referring to the experimental test method carried out by Mera and Robi (24). They had carried out experimental tests to obtain the Manning coefficient value for PVC (Polyvinyl Chloride) material produced by a commercial company in Indonesia. The research was carried out using a flume device in the hydraulic laboratory at Andalas University in Padang City, West Sumatra Province, Indonesia. Experimental test was carried out using one flow discharge and ten variations of channel bottom slopes. From the implementation of their research, several results were obtained as follows:

1. Graph of the relationship between flow depth and variations in channel bottom slope (Figure 8);
2. Graph of the relationship between the Manning roughness coefficient and variations in channel bottom slopes (Figure 9);
3. From the Figure 9 graph, the Manning roughness coefficient value for PVC material obtained from the results of their research is in the range  $n = 0.010$  to  $0.014$ .

The graph obtained from their research results (25) will later be compared with the graph obtained from this research to verify the accuracy of the proposed method.

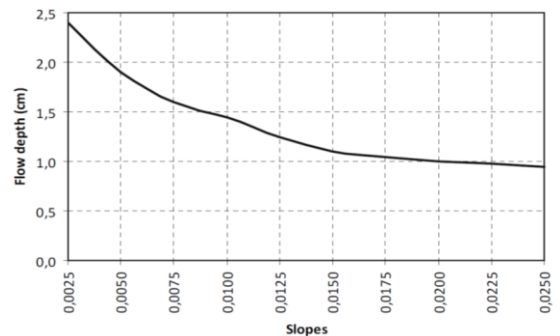
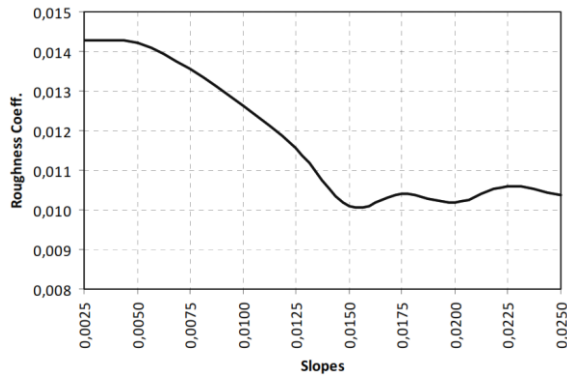


Figure 8. Graph of the relationship between flow depth and variations in channel bottom slope for PVC material (25)



**Figure 9.** Graph of the relationship between the Manning roughness coefficient and variations in channel bottom slope for PVC lined material (25)

### 2. 3. Data Collection

The data collected were dependent variables data and independent variables data. Some of the dependent variable data include: a) the bottom width of the GFRP flume section ( $b_g$ ) of 28.9 cm; b) the flume length ( $L_f$ ) of 960 cm; c) the length of the flume lined with GFRP material ( $L_g$ ) of 900 cm; d) GFRP flume height ( $T_g$ ) of 31 cm; and e) the gravitational constant ( $g$ ) is taken as 9.81 m/s<sup>2</sup>. GFRP flume bottom slope data ( $S_g$ ) was measured by adjusting the flume bottom slopes by increasing the flume elevation in the upstream section at 2 (two) cm intervals for 9 (nine) times to obtain nine different channel/flume bottom slope conditions. By dividing the difference in the height of the upstream and downstream of the flume by the length of the flume ( $L_f = 960$  cm), the values of the nine-bottom slopes of the GFRP flume ( $S_g$ ) are 0.0021; 0.0042; 0.0063; 0.0083; 0.0104; 0.0125; 0.0146; 0.0167; and 0.0188 respectively. Data collections of the independent variables in the GFRP flume were flow depth ( $h_g$ ) and flow velocity ( $v_g$ ). The flow depth in the GFRP flume ( $h_g$ ) was obtained by directly measuring each water flow test's results with a point gauge. The average depth of water flow in the GFRP flume ( $h_r$ ) is the flow depth used to measure the average flow velocity using a flow-meter device measured from the surface of the flow, where the  $h_r$  value is 0.6  $h_g$ . The flow velocity in the GFRP flume ( $v_g$ ) was measured directly using a flow-meter device.

### 2. 4. Data Processing and Analysis

After obtaining the hydraulic data of the water flow in the GFRP flume, then data processing was carried out to obtain the values of other flow parameters data in the flume, such as the wetted area ( $A_g$ ); wetted perimeter ( $P_g$ ), hydraulic radius ( $R_g$ ); discharge that flow in the flume ( $Q_g$ ); Manning roughness coefficient for GFRP materials ( $n_g$ ); critical depth ( $h_{cg}$ ); and flow velocity characteristics that occur using the Froude Number indicator. In the next stage, the calculation results obtained from the experimental test were compared with the results of testing with a mathematical model, i.e.,

HEC-RAS Software (26). If comparing the two models shows good results, it will proceed to the analysis and interpretation of the test data. However, if not, verifying, validating, and calibrating the data will be done first until the model performance shows appropriate results.

### 2. 5. Mathematical Equations

The inflow discharge through the GFRP flume ( $Q_f$ ) was measured using the volumetric method. This method involved measuring the weight of water ( $W_w$ ) flowing out of the downstream end of the GFRP flume using a bucket within a specific time interval ( $\Delta t$ ). The volume of water ( $V_w$ ) was then calculated by dividing the weight of water ( $W_w$ ) by the specific gravity of water ( $\gamma_w = 1$  g/cm<sup>3</sup>). There were three variations setting of pump discharge into the GFRP flume, i.e., low inflow discharge ( $Q_{f1}$ ), medium inflow discharge ( $Q_{f2}$ ), and high inflow discharge ( $Q_{f3}$ ). The water flow setting for these three pump discharge variations was controlled by using two submersible pumps and adjusting valves in the pipeline network. For each of the three water storage experiments conducted in the bucket, the calculation for the pump discharge ( $Q_f$ ) is determined using the following formula:

$$Q_f = \frac{1}{3} \sum_{i=1}^3 \frac{V_{wi}}{\Delta t_i} \quad (7)$$

Measurement of flow parameters in the GFRP flume ( $h_g$  and  $v_g$ ) was conducted in the steady-state flow conditions, and the high-water level is parallel at several points in the middle of the flume segment. Other hydraulic parameters such as wetted area ( $A_g$ ), wetted perimeter ( $P_g$ ), and hydraulic radius ( $R_g$ ) are calculated using the formula (25):

$$A_g = b_g h_g \quad (8)$$

$$P_g = b_g + 2h_g \quad (9)$$

$$R_g = \frac{A_g}{P_g} = \frac{b_g h_g}{b_g + 2h_g} \quad (10)$$

The discharge flowing in the GFRP flume ( $Q_g$ ) is calculated using the following formula:

$$Q_g = v_g A_g \quad (11)$$

The value of the Manning roughness coefficient ( $n_g$ ) obtained from the experimental test results is then determined using the following formula (22, 23):

$$n_g = \frac{1}{v_g} R_g^{2/3} S_g^{1/2} \quad (12)$$

Alternatively, it can also be calculated as follows:

$$n_g = \frac{R_g^{2/3} S_g^{1/2} A_g}{Q_g} \quad (13)$$

The critical depth occurring in the GFRP flume ( $h_{cg}$ ) is calculated using the following equation (26):

$$h_{cg} = \sqrt[3]{\frac{Q_g^2}{b_g^2 g}} \tag{14}$$

If the critical depth ( $h_{cg}$ ) is bigger than the measured flow depth ( $h_g$ ), the flow is then at the super-critical state and otherwise is at the sub-critical state.

**2. 6. Model Evaluation and Performance Assessment**

According to Moriasi et al. (27), based on the recommendations of Legates and McCabe (28) and American Society of Civil Engineer (29) model evaluation involves using graphical techniques and quantitative statistics. The graphical techniques provide a visual assessment of model performance. Utilizing these essential techniques should typically be the first step in model evaluation. A familiar visual fit between observed and simulated constituent data indicates adequate calibration and validation within the simulated constituent range (27, 30). There are various quantitative statistical assessment methods (27), but this study will only use the Nash-Sutcliffe Efficiency (NSE) method. This method involves comparing the model simulation data with quantitative measurement data. The formula for calculating the NSE value is as follows (27, 31, 32):

$$NSE = 1 - \left[ \frac{\sum_{i=1}^n (Y_i^{obs} - Y_i^{sim})^2}{\sum_{i=1}^n (Y_i^{obs} - Y^{mean})^2} \right] \tag{15}$$

where:  $n$  = the total number of observations;  $Y_i^{obs}$  = the  $i$ th observation for the constituent being evaluated;  $Y_i^{sim}$  = the  $i$ th simulated constituent value for the constituent being evaluated;  $Y^{mean}$  = the mean of observed data for the constituent being evaluated.

The best performance values from the predicted value or mathematical model with observational data or the physical model can be obtained if the NSE Index value = 1. A performance rating of the model results is carried out to assess performance in the model's verification and calibration process. The model performance is evaluated as "very good" if the NSE value exceeds 0.75. Model performance is evaluated as "good" if the NSE value ranges from 0.65 to equal/less than 0.75. The model performance is evaluated as "satisfactory" if the NSE value is 0.5 to equal/less than 0.65. The model performance is evaluated as "unsatisfactory" if the NSE value equals/less than 0.5. Table 1 summarizes the relationship between NSE Index and model performance ratings (27).

**TABLE 1.** Performance rating model with the NSE method

No.	Performance Rating	NSE Index
1.	Very good	0,75 < NSE ≤ 1,00
2.	Good	0,65 < NSE ≤ 0,75
3.	Satisfactory	0,5 < NSE ≤ 0,65
4.	Unsatisfactory	NSE ≤ 0,50

**3. RESULTS AND DISCUSSION**

**3. 1. Calculation and Analysis of Pump Discharge Flowing into the GFRP Flume ( $Q_f$ ) using the Volumetric Method**

Calculation and validation of three variations of water pump discharge into the GFRP flume ( $Q_f$ ), i.e., low inflow discharge ( $Q_{f1}$ ), medium inflow discharge ( $Q_{f2}$ ), and high inflow discharge ( $Q_{f3}$ ) using the volumetric method are presented in Table 2.

From Table 2, data were calculated from three validated pump discharge variations that flow into the GFRP flume, such as low inflow discharge ( $Q_{f1}$ ) of 7.83 l/s or 7,830 cm<sup>3</sup>/s; medium inflow discharge ( $Q_{f2}$ ) of 11.60 l/s or 11,600 cm<sup>3</sup>/s; and high inflow discharge ( $Q_{f3}$ ) of 14.88 l/s or 14,880 cm<sup>3</sup>/s.

**3. 2. Calculation and Analysis of Water Flow Data on Physical Models**

After the measurement and validation of the pump discharge have been completed, the flow depth ( $h_g$ ) and flow velocity ( $v_g$ ) that occurs in the flume were measured for each of the three discharge variations that flow into the flume ( $Q_{f1}$ ,  $Q_{f2}$ , and  $Q_{f3}$ ) and on nine variations of flume bottom slope ( $S_g$ ). Using the GFRP flume width ( $b_g$ ) of 28.9 cm, calculating the Manning roughness coefficient value ( $n_g$ ), and analysis of other flow parameters are summarized and presented in Tables 3, 4 and 5, respectively.

From the physical modeling calculation result, the average Manning roughness coefficient ( $n_g$ ) value for the three discharge variations ( $Q_f$ ) is obtained:  $n_{g1}$  = 0.0083,  $n_{g2}$  = 0.0082, and  $n_{g3}$  = 0.0079. Calculations and data analysis will be carried out using a mathematical model to evaluate the reliability of the physical modeling results.

**TABLE 2.** Calculation and validation for low, medium, and high inflow discharge variations

No.	Inflow discharge type	Water Volume	Time Interval	Discharge	Average Discharge	
		$V_w$	$\Delta t$	$Q_f$	$Q_f$	$Q_f$
		l	s	l/s	l/s	cm <sup>3</sup> /s
1	$Q_{f1}$ (Low Inflow Discharge)	28.05	3.64	7.72		
		32.38	4.02	8.05	7.83	7,830
		42.46	5.50	7.72		
2	$Q_{f2}$ (Medium Inflow Discharge)	35.64	3.23	11.03		
		42.29	3.48	12.15	11.60	11,600
		42.97	3.70	11.61		
3	$Q_{f3}$ (High Inflow Discharge)	40.32	2.69	14.99		
		38.27	2.56	14.95	14.88	14,880
		35.58	2.42	14.70		

**TABLE 2.** The results of the calculation of the physical model for water flow parameters at low inflow discharge conditions ( $Q_{I1} = 7,830 \text{ cm}^3/\text{s}$ )

No.	Channel Bottom Slopes	Flow Velocity	Flow Depth	Wetted Area	Wetted Perimeter	Hydraulic Radius	Flow Discharge	Manning Roughness Coefficient	Critical Depth	Characteristic of Flow Velocity
	$S_g$	$v_g$	$h_g$	$A_g$	$P_g$	$R_g$	$Q_g$	$n_{g1}$	$h_{cg}$	$h_{cg}/h_g$
	(cm/cm)	(cm/s)	(cm)	(cm <sup>2</sup> )	(cm)	(cm)	(cm <sup>3</sup> /s)	-	(cm)	
1	0.0021	50.8	5.20	150.28	39.30	3.82	7,634	0.0102	4.14	subcritical
2	0.0042	65.0	3.67	106.06	36.24	2.93	6,897	0.0094	3.87	supercritical
3	0.0063	83.3	3.00	86.70	34.90	2.48	7,223	0.0081	3.99	supercritical
4	0.0083	91.4	2.72	78.61	34.34	2.29	7,188	0.0080	3.98	supercritical
5	0.0104	102.6	2.70	78.03	34.30	2.27	8,007	0.0080	4.28	supercritical
6	0.0125	113.8	2.52	72.83	33.94	2.15	8,287	0.0076	4.38	supercritical
7	0.0146	116.8	2.46	71.09	33.82	2.10	8,307	0.0079	4.38	supercritical
8	0.0167	120.9	2.42	69.94	33.74	2.07	8,456	0.0081	4.44	supercritical
9	0.0188	125.0	2.20	63.58	33.30	1.91	7,945	0.0078	4.26	supercritical
<b>Average of Manning Roughness Coefficient (<math>n_{g1}</math>) =</b>								<b>0.0083</b>		

**TABLE 3.** The results of the calculation of the physical model for water flow parameters at medium inflow discharge conditions ( $Q_{I2} = 11,600 \text{ cm}^3/\text{s}$ )

No.	Channel Bottom Slopes	Flow Velocity	Flow Depth	Wetted Area	Wetted Perimeter	Hydraulic Radius	Flow Discharge	Manning Roughness Coefficient	Critical Depth	Characteristic of Flow Velocity
	$S_g$	$v_g$	$h_g$	$A_g$	$P_g$	$R_g$	$Q_g$	$n_{g2}$	$h_{cg}$	$h_{cg}/h_g$
	(cm/cm)	(cm/s)	(cm)	(cm <sup>2</sup> )	(cm)	(cm)	(cm <sup>3</sup> /s)	-	(cm)	
1	0.0021	62.0	5.77	166.75	40.44	4.12	10,335	0.0088	5.07	subcritical
2	0.0042	85.3	4.70	135.83	38.30	3.55	11,592	0.0082	5.47	supercritical
3	0.0063	100.6	4.07	117.62	37.04	3.18	11,831	0.0079	5.55	supercritical
4	0.0083	112.8	3.70	106.93	36.30	2.95	12,059	0.0077	5.62	supercritical
5	0.0104	117.9	3.58	103.32	36.05	2.87	12,177	0.0081	5.66	supercritical
6	0.0125	121.9	3.40	98.26	35.70	2.75	11,980	0.0084	5.60	supercritical
7	0.0146	128.0	3.19	92.19	35.28	2.61	11,802	0.0083	5.54	supercritical
8	0.0167	133.1	3.03	87.57	34.96	2.50	11,655	0.0083	5.49	supercritical
9	0.0188	138.2	2.92	84.39	34.74	2.43	11,660	0.0083	5.50	supercritical
<b>Average of Manning Roughness Coefficient (<math>n_{g2}</math>) =</b>								<b>0.0082</b>		

**TABLE 5.** The results of the calculation of the physical model for water flow parameters at high inflow discharge conditions ( $Q_{I3} = 14,880 \text{ cm}^3/\text{s}$ )

No.	Channel Bottom Slopes	Flow Velocity	Flow Depth	Wetted Area	Wetted Perimeter	Hydraulic Radius	Flow Discharge	Manning Roughness Coefficient	Critical Depth	Characteristic of Flow Velocity
	$S_g$	$v_g$	$h_g$	$A_g$	$P_g$	$R_g$	$Q_g$	$n_{g3}$	$h_{cg}$	$h_{cg}/h_g$
	(cm/cm)	(cm/s)	(cm)	(cm <sup>2</sup> )	(cm)	(cm)	(cm <sup>3</sup> /s)	-	(cm)	
1	0.0021	66.0	6.41	185.25	41.72	4.44	12,234	0.0087	5.67	subcritical
2	0.0042	101.6	5.07	146.52	39.04	3.75	14,887	0.0071	6.47	supercritical
3	0.0063	114.8	4.62	133.52	38.14	3.50	15,329	0.0074	6.59	supercritical
4	0.0083	122.9	4.27	123.40	37.44	3.30	15,171	0.0076	6.55	supercritical

5	0.0104	130.0	4.18	120.66	37.25	3.24	15,691	0.0080	6.70	supercritical
6	0.0125	136.1	3.92	113.29	36.74	3.08	15,423	0.0081	6.62	supercritical
7	0.0146	142.2	3.58	103.32	36.05	2.87	14,696	0.0080	6.41	supercritical
8	0.0167	147.3	3.52	101.66	35.94	2.83	14,976	0.0081	6.49	supercritical
9	0.0188	153.4	3.32	95.95	35.54	2.70	14,720	0.0080	6.42	supercritical
<b>Average of Manning Roughness Coefficient (<math>n_{g3}</math>) =</b>								<b>0.0079</b>		

### 3. 3. Initial Simulation of Water Flow with Mathematical Models

Initial simulation for calculating and analyzing water flow data with mathematical models will be applied using HEC-RAS software. In the physical model, several water flow parameters (such as flow depth ( $h_g$ ), flow velocity ( $v_g$ ), and inflow discharge ( $Q_f$ )) are measured/calculated first and then inputted as data variables in a mathematical equation to calculate other water flow parameters, including the value of the Manning roughness coefficient ( $n_g$ ). In the mathematical model (using the HEC-RAS application), some of the dependent variable data used in the physical model are also used as input data for model simulation, like the bottom width of the GFRP flume ( $b_g$ ), the height of the GFRP flume ( $T_g$ ), the nine variations of channel bottom slope ( $S_g$ ), and the three variations of inflow discharge ( $Q_f$ ). In addition, data on the Manning roughness coefficient value ( $n_g$ ) obtained from the results of physical modeling were also used as input data in the initial simulation of the HEC-RAS model. After running the model under steady-state flow conditions, the output data from this model simulation process are flow depth ( $h_s$ ), wetted area ( $A_s$ ), wetted

perimeter ( $P_s$ ), hydraulic radius ( $R_s$ ), flow velocity ( $v_s$ ), and critical depth ( $h_{cs}$ ). Initial simulation results for calculating water flow parameters using the HEC-RAS software for each of the three discharge variations ( $Q_{f1}$ ,  $Q_{f2}$ , and  $Q_{f3}$ ) are then summarized and presented in Tables 6, 7 and 8, respectively.

### 3. 4. Comparison and Assessment of Physical Model Performance with Initial Simulation of Mathematical Models

The results of calculating the flow depth ( $h_s$ ) resulting from the initial simulation of the mathematical model (HEC-RAS) are then compared with the results of calculating the flow depth ( $h_g$ ) resulting from physical modeling. The comparison of  $h_s$  and  $h_g$  values for three variations of flow discharge ( $Q_{f1}$ ,  $Q_{f2}$ , and  $Q_{f3}$ ) and nine variations of channel bottom slope ( $S_g$ ) is then displayed in a graphic presented in Figure 10. From the graphic in Figure 10. it can be seen that although the flow depth profile ( $h_g$ ) in the physical model and flow depth profile ( $h_s$ ) in the mathematical model have similar curves, at several locations of the channel bottom slope ( $S_g$ ), there are significant deviations and anomaly conditions of the flow depth values ( $h_g$  and  $h_s$ ).

**TABLE 4.** Calculation results from initial mathematical model simulation (HEC-RAS) for water flow parameters at low inflow discharge conditions ( $Q_{f1} = 7,830 \text{ cm}^3/\text{s}$ )

No.	Channel Bottom Slopes	Manning Roughness Coefficient	Flow Velocity	Flow Depth	Flow Discharge	Wetted Area	Wetted Perimeter	Hydraulic Radius	Critical Depth	Characteristic of Flow Velocity
	$S_s$ (cm/cm)	$n_s$ -	$v_s$ (cm/s)	$h_s$ (cm)	$Q_s$ ( $\text{cm}^3/\text{s}$ )	$A_s$ ( $\text{cm}^2$ )	$P_s$ (cm)	$R_s$ (cm)	$h_{cs}$ (cm)	$h_{cs}/h_s$
1	0.0021	0.0102	53.99	5.02	7,830	145.08	38.94	3.73	4.21	subcritical
2	0.0042	0.0094	71.34	3.79	7,830	109.53	36.48	3.00	4.21	supercritical
3	0.0063	0.0081	74.60	3.63	7,830	104.91	36.16	2.90	4.21	supercritical
4	0.0083	0.0080	90.92	2.98	7,830	86.12	34.86	2.47	4.21	supercritical
5	0.0104	0.0080	95.32	2.84	7,830	82.08	34.58	2.37	4.21	supercritical
6	0.0125	0.0076	105.54	2.57	7,830	74.27	34.04	2.18	4.21	supercritical
7	0.0146	0.0079	98.53	2.75	7,830	79.48	34.40	2.31	4.21	supercritical
8	0.0167	0.0081	118.69	2.28	7,830	65.89	33.46	1.97	4.21	supercritical
9	0.0188	0.0078	124.36	2.18	7,830	63.00	33.26	1.89	4.21	supercritical
<b>Average of Manning Roughness Coefficient from Numeric Simulation (<math>n_{s1}</math>) =</b>								<b>0.0083</b>		

**TABLE 7.** Calculation results from the initial mathematical model simulation (HEC-RAS) for water flow parameters at medium inflow discharge conditions ( $Q_2 = 11,600 \text{ cm}^3/\text{s}$ )

No.	Channel Bottom Slopes	Manning Roughness Coefficient	Flow Velocity	Flow Depth	Flow Discharge	Wetted Area	Wetted Perimeter	Hydraulic Radius	Critical Depth	Characteristic of Flow Velocity
	$S_s$	$n_s$	$v_s$	$h_s$	$Q_s$	$A_s$	$P_s$	$R_s$	$h_{cs}$	$h_{cs}/h_s$
	(cm/cm)	-	(cm/s)	(cm)	( $\text{cm}^3/\text{s}$ )	( $\text{cm}^2$ )	(cm)	(cm)	(cm)	
1	0.0021	0.0088	67.03	5.99	11,600	173.11	40.88	4.23	5.48	subcritical
2	0.0042	0.0082	76.25	5.26	11,600	152.01	39.42	3.86	5.48	supercritical
3	0.0063	0.0079	101.18	3.97	11,600	114.73	36.84	3.11	5.48	supercritical
4	0.0083	0.0077	107.01	3.75	11,600	108.38	36.40	2.98	5.48	supercritical
5	0.0104	0.0081	111.49	3.6	11,600	104.04	36.10	2.88	5.48	supercritical
6	0.0125	0.0084	123.55	3.25	11,600	93.93	35.40	2.65	5.48	supercritical
7	0.0146	0.0083	126.75	3.17	11,600	91.61	35.24	2.60	5.48	supercritical
8	0.0167	0.0083	109.21	3.67	11,600	106.06	36.24	2.93	5.48	supercritical
9	0.0188	0.0083	133.88	2.99	11,600	86.41	34.88	2.48	5.48	supercritical
<b>Average of Manning Roughness Coefficient from Numeric Simulation (<math>n_{s2}</math>) =</b>									<b>0.0082</b>	

**TABLE 8.** Calculation results from the initial mathematical model simulation (HEC-RAS) for water flow parameters at high inflow discharge conditions ( $Q_3 = 14,880 \text{ cm}^3/\text{s}$ )

No.	Channel Bottom Slopes	Manning Roughness Coefficient	Flow Velocity	Flow Depth	Flow Discharge	Wetted Area	Wetted Perimeter	Hydraulic Radius	Critical Depth	Characteristic of Flow Velocity
	$S_s$	$n_s$	$v_s$	$h_s$	$Q_s$	$A_s$	$P_s$	$R_s$	$h_{cs}$	$h_{cs}/h_s$
	(cm/cm)	-	(cm/s)	(cm)	( $\text{cm}^3/\text{s}$ )	( $\text{cm}^2$ )	(cm)	(cm)	(cm)	
1	0.0021	0.0087	73.61	7.00	14,880	202.30	42.90	4.72	6.47	subcritical
2	0.0042	0.0071	91.98	5.60	14,880	161.84	40.10	4.04	6.47	supercritical
3	0.0063	0.0074	112.47	4.58	14,880	132.36	38.06	3.48	6.47	supercritical
4	0.0083	0.0076	121.88	4.23	14,880	122.25	37.36	3.27	6.47	supercritical
5	0.0104	0.0080	126.77	4.06	14,880	117.33	37.02	3.17	6.47	supercritical
6	0.0125	0.0081	136.08	3.78	14,880	109.24	36.46	3.00	6.47	supercritical
7	0.0146	0.0080	143.27	3.60	14,880	104.04	36.10	2.88	6.47	supercritical
8	0.0167	0.0081	145.32	3.54	14,880	102.31	35.98	2.84	6.47	supercritical
9	0.0188	0.0080	153.89	3.34	14,880	96.53	35.58	2.71	6.47	Supercritical
<b>Average of Manning Roughness Coefficient from Numeric Simulation (<math>n_{s3}</math>) =</b>									<b>0.0079</b>	

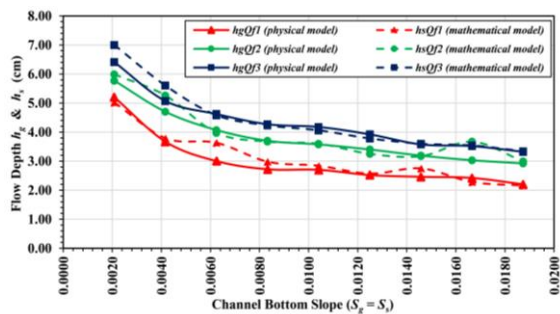


**Figure 10.** Graphic comparison between the flow depth ( $h_s$ ) in the initial simulation of the mathematical model (HEC-RAS) and the flow depth ( $h_g$ ) in the physical model for three variations of inflow discharge ( $Q_f$ )

Furthermore, the results of the calculation of flow velocity ( $v_s$ ) resulting from the initial simulation of the mathematical model (HEC-RAS) are also compared with the results of calculating the flow velocity ( $v_g$ ) resulting from physical model. Comparison of  $v_s$  and  $v_g$  values for the three variations of flow discharge ( $Q_{f1}$ ,  $Q_{f2}$ , and  $Q_{f3}$ ) and the nine variations of channel bottom slope ( $S_g$ ) are then displayed in the graphic presented in Figure 11.

From the graphic in Figure 11, it can be seen that although the flow velocity profile ( $v_g$ ) in the physical model and the flow velocity profile ( $v_s$ ) in the initial simulation of the mathematical model have similar curves at several locations of the channel bottom slope ( $S_g$ ), there are significant deviations and anomaly

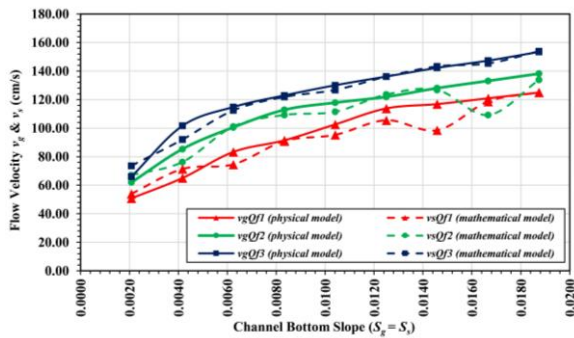


**Figure 11.** Graphic comparison between flow velocity ( $v_s$ ) in the initial simulation of the mathematical model (HEC-RAS) and flow velocity ( $v_g$ ) in the physical model for three variations of inflow discharge ( $Q_f$ )

conditions in the flow velocity values ( $v_g$  and  $v_s$ ). A quantitative accuracy assessment evaluates the performance of the physical model by using the Nash-Sutcliffe Efficiency (NSE) model. The assessment calculates and compares the NSE values for the flow depth ( $h$ ) and flow velocity ( $v$ ) parameters between the physical model and the initial simulation of the mathematical model. The resulting NSE values are then presented in Table 9. Based on the values in Table 9, the NSE index for flow depth ( $h$ ) and flow velocity ( $v$ ) exceeds 0.75. Consequently, the overall performance of the model, considering three variations of inflow discharge ( $Q_f$ ), can be stated as “very good”.

Even though the NSE indexes already have a “very good” performance rating, in order to provide better

**TABLE 9.** Recapitulation of the results of the Quantitative Accuracy Assessment (NSE) between the observed data and the initial simulation results of the mathematical model

No.	Flow Discharge Type	NSE Index for flow depth	Performance Rating	NSE Index for flow velocity	Performance Rating
		NSE ( $h_g$ )		NSE ( $v_g$ )	
1	$Q_{f1}$ (low inflow discharge)	0.908	very good	0.892	very good
2	$Q_{f2}$ (medium inflow discharge)	0.881	very good	0.844	very good
3	$Q_{f3}$ (high inflow discharge)	0.910	very good	0.971	very good

modeling accuracy, the calibration process will still be carried out, especially for some conditions of channel bottom slope ( $S_g$ ) where the flow parameters (flow depth and velocity) provide anomaly condition and different deviation values-quite significant.

Model calibrations are carried out for low inflow discharge conditions ( $Q_{f1} = 7,830 \text{ cm}^3/\text{s}$ ) and medium inflow discharge conditions ( $Q_{f2} = 11,600 \text{ cm}^3/\text{s}$ ) because, apart from having an anomaly and a significant deviation value, the NSE indexes for flow depth and flow velocity are still below 0.9. For conditions of high inflow discharge ( $Q_{f3} = 14,880 \text{ cm}^3/\text{s}$ ), the calibration process is not carried out because the NSE indexes for flow depth and velocity respectively are already reached an exceptionally high value of 0.910 and 0.971 ( $\approx 1$ ).

**3. 5. Model Evaluation and Performance Assessment**

The calibration process involves modifying the input data of the initial Manning roughness coefficient ( $n_g$ ) value in the HEC-RAS simulation to reduce further the deviation profiles and anomaly conditions are shown in Figures 10 and 11 and achieve smooth graphic curves. For low inflow discharge conditions ( $Q_{f1} = 7,830 \text{ cm}^3/\text{s}$ ), the results of calibration are the Manning roughness coefficient values for two-channel bottom slopes ( $S_g$ ) that exhibit relatively high flow depth deviation values ( $h_g$  and  $h_s$ ), specifically  $S_{g3}$  and  $S_{g7}$ .

For the channel bottom slope of the  $S_{g3}$ , the initial  $n_g$  value of 0.0081 is calibrated to  $n_s = 0.0080$ . Similarly, for

the channel bottom slope of the  $S_{g7}$ , the initial  $n_g$  value of 0.0078 is calibrated to  $n_s = 0.0077$ . Once the calibration process for the Manning roughness coefficient value is completed, the HEC-RAS model will be running again and summarize the calculation results obtained from the model simulation. These results are then presented in Table 10.

For medium inflow discharge conditions ( $Q_{f2} = 11,600 \text{ cm}^3/\text{s}$ ), the Manning coefficient values were calibrated on two channel bottom slopes ( $S_g$ ), which had relatively high flow depth deviation values ( $h_g$  and  $h_s$ ), namely  $S_{g2}$  and  $S_{g8}$ . For the channel bottom slope of the  $S_{g2}$ , the initial  $n_g$  value is 0.0082 and calibrated to  $n_s = 0.0080$ . For the channel bottom slope of the  $S_{g8}$ , the initial  $n_g$  value is 0.0083 and calibrated to  $n_s = 0.0081$ . After the calibration process for the Manning roughness coefficient value is carried out, the HEC-RAS model is running again, and the calculation results from the model simulation are summarized and presented in Table 11.

The calibration process was not carried out for high inflow discharge conditions ( $Q_{f3} = 14,880 \text{ cm}^3/\text{s}$ ), so the initial simulation results of the mathematical models in Table 8 will still be used for further data analysis and interpretation. After the calibration process of the Manning roughness coefficient value is carried out, the results of the calculation of the flow parameters resulting from the mathematical modeling are then compared again with the results of the estimation of the flow parameters resulting from the physical modeling.

**TABLE 5.** Calculation results from the next mathematical model simulation (HEC-RAS) for water flow parameters at low inflow discharge conditions ( $Q_{f1} = 7,830 \text{ cm}^3/\text{s}$ )

No.	Channel Bottom Slopes	Manning Roughness Coefficient	Flow Velocity	Flow Depth	Flow Discharge	Wetted Area	Wetted Perimeter	Hydraulic Radius	Critical Depth	Characteristic of Flow Velocity
	$S_s$	$n_{s1}$	$v_s$	$h_s$	$Q_s$	$A_s$	$P_s$	$R_s$	$h_{cs}$	$h_{cs}/h_s$
	(cm/cm)	-	(cm/s)	(cm)	(cm <sup>3</sup> /s)	(cm <sup>2</sup> )	(cm)	(cm)	(cm)	
1	0.0021	0.0102	53.99	5.02	7,830	145.08	38.94	3.73	4.21	subcritical
2	0.0042	0.0094	71.34	3.79	7,830	109.53	36.48	3.00	4.21	supercritical
3	0.0063	0.0080	89.86	3.02	7,830	87.28	34.94	2.50	4.21	supercritical
4	0.0083	0.0080	90.92	2.98	7,830	86.12	34.86	2.47	4.21	supercritical
5	0.0104	0.0080	95.32	2.84	7,830	82.08	34.58	2.37	4.21	supercritical
6	0.0125	0.0076	105.54	2.57	7,830	74.27	34.04	2.18	4.21	supercritical
7	0.0146	0.0077	110.33	2.46	7,830	71.09	33.82	2.10	4.21	supercritical
8	0.0167	0.0081	118.69	2.28	7,830	65.89	33.46	1.97	4.21	supercritical
9	0.0188	0.0078	124.36	2.18	7,830	63.00	33.26	1.89	4.21	supercritical
<b>Average of Manning Roughness Coefficient from Numeric Simulation (<math>n_{s1}</math>) =</b>									<b>0.0083</b>	

**TABLE 11.** Calculation results from next mathematical model simulation (HEC-RAS) for water flow parameters at medium inflow discharge conditions ( $Q_{f2} = 11,600 \text{ cm}^3/\text{s}$ )

No.	Channel Bottom Slopes	Manning Roughness Coefficient	Flow Velocity	Flow Depth	Flow Discharge	Wetted Area	Wetted Perimeter	Hydraulic Radius	Critical Depth	Characteristic of Flow Velocity
	$S_s$	$n_{s2}$	$v_s$	$h_s$	$Q_s$	$A_s$	$P_s$	$R_s$	$h_{cs}$	$h_{cs}/h_s$
	(cm/cm)	-	(cm/s)	(cm)	(cm <sup>3</sup> /s)	(cm <sup>2</sup> )	(cm)	(cm)	(cm)	
1	0.0021	0.0088	67.03	5.99	11,600	173.11	40.88	4.23	5.48	subcritical
2	0.0042	0.0080	77.34	5.19	11,600	149.99	39.28	3.82	5.48	supercritical
3	0.0063	0.0079	101.18	3.97	11,600	114.73	36.84	3.11	5.48	supercritical
4	0.0083	0.0077	107.01	3.75	11,600	108.38	36.40	2.98	5.48	supercritical
5	0.0104	0.0081	111.49	3.6	11,600	104.04	36.10	2.88	5.48	supercritical
6	0.0125	0.0084	123.55	3.25	11,600	93.93	35.40	2.65	5.48	supercritical
7	0.0146	0.0083	126.75	3.17	11,600	91.61	35.24	2.60	5.48	supercritical
8	0.0167	0.0081	133.88	2.99	11,600	86.41	34.88	2.48	5.48	supercritical
9	0.0188	0.0083	133.88	2.99	11,600	86.41	34.88	2.48	5.48	supercritical
<b>Average of Manning Roughness Coefficient from Numeric Simulation (<math>n_{s2}</math>) =</b>									<b>0.0082</b>	

Comparison of the flow depth value ( $h_s$ ) resulting from mathematical modeling with the flow depth value ( $h_g$ ) resulting from physical modeling for three variations of flow discharge ( $Q_{f1}$ ,  $Q_{f2}$ , and  $Q_{f3}$ ) is then displayed again in the graphic as presented in Figure 12.

From the graphic in Figure 12, it can be seen that the flow depth profile ( $h_g$ ) in the physical model and flow depth profile ( $h_s$ ) in the mathematical model still have similar curves, and the deviations that occur at several locations of the channel bottom slope ( $S_g$ ) have also decreased.

Furthermore, the comparison of flow velocity values ( $v_s$ ) resulting from mathematical modeling with flow velocity values ( $v_g$ ) resulting from physical modeling for three variations of flow discharge ( $Q_{f1}$ ,  $Q_{f2}$ , and  $Q_{f3}$ ) are displayed again in the graphic as presented in Figure 13. From the graphic in Figure 13, it can be seen that the flow velocity profiles ( $v_g$ ) in the physical model and the flow velocity profiles ( $v_s$ ) in the mathematical model still have similar curves, and the deviations that occur at several locations of the channel bottom slope ( $S_g$ ) have also decreased.

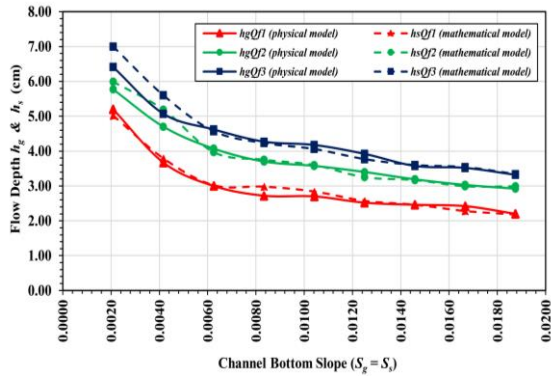


**Figure 12.** Comparison graphic between flow depth ( $h_s$ ) in the mathematical model and flow depth ( $h_g$ ) in the physical model for three variations of inflow discharge ( $Q_f$ ) after the calibration process

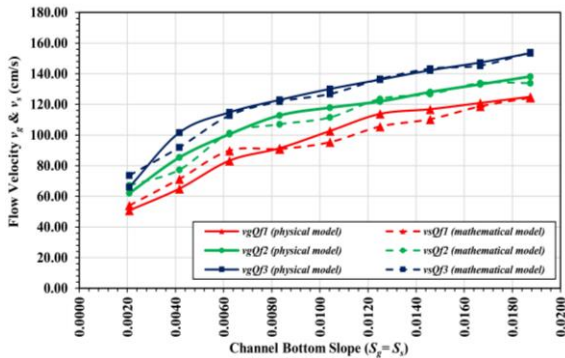


**Figure 13.** Graphic comparison between flow velocity ( $v_s$ ) in the mathematical model and flow velocity ( $v_g$ ) in the physical model for three variations of inflow discharge ( $Q_f$ ) after the calibration process

Finally, the comparison of the calibration value of the Manning roughness coefficient ( $n_s$ ) resulting from mathematical modeling with the value of the Manning roughness coefficient ( $n_g$ ) resulting from physical modeling for three variations of flow discharge ( $Q_{f1}$ ,  $Q_{f2}$ , and  $Q_{f3}$ ) is displayed in the graphic as presented in Figure 14.

The graphic in Figure 14 shows that the profile of the Manning roughness coefficient ( $n_g$ ) in the physical model and the profile of the Manning roughness coefficient ( $n_s$ ) in the mathematical model have similar curves. The deviations at several locations of the channel bottom slope ( $S_g$ ) are also relatively small. After the mathematical model calibration process has been completed, a reassessment of the overall model performance (both the calibration process and the non-calibration process) is carried out using the Nash-Sutcliffe Efficiency (NSE) method.

The results of the calculation of the NSE values for the parameters of flow depth ( $h_g$ ), flow velocity ( $v_g$ ), and Manning roughness coefficient ( $n_g$ ) for three variations

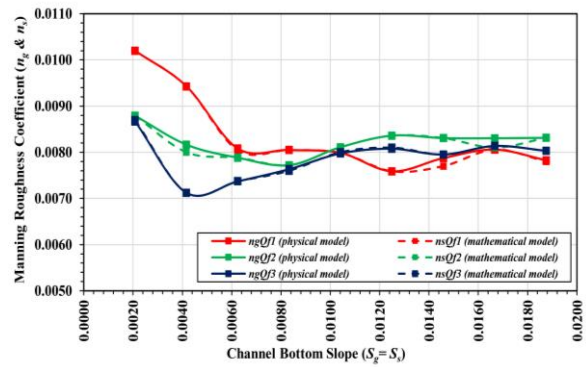


**Figure 14.** Graphic comparison between the Manning roughness coefficient ( $n_s$ ) in the mathematical model and the Manning roughness coefficient ( $n_g$ ) in the physical model for three variations of inflow discharge ( $Q_f$ ) after the calibration process

of inflow discharge ( $Q_{f1}$ ,  $Q_{f2}$ , and  $Q_{f3}$ ) are then presented again in Table 12. Table 12 shows that the NSE Index values for the three flow parameters ( $h_g$ ,  $v_g$ , and  $n_g$ ) are better when compared to the NSE Index values before calibration (see Table 9 again).

### 3. 6. Flow Characteristic and Manning Roughness Coefficient

The final discussion of the flow characteristics and the value of the Manning roughness coefficient is carried out by taking data from the physical model testing, i.e., data in Tables 3, 4 and 5 as well as graphical analysis in Figures 12, 13 and 14. Based on the graphic presented in Figure 12, it can be interpreted that with increasing discharge ( $Q_{f1}$  to  $Q_{f3}$ ), the flow depth ( $h$ ) will also increase. However, as the bottom slope ( $S$ ) increases, the flow depth ( $h$ ) will decrease.

Based on the graphic presented in Figure 13, it can be interpreted that the flow velocity ( $v$ ) will increase with increasing discharge ( $Q_{f1}$  to  $Q_{f3}$ ) and also the bottom slope of the channel ( $S$ ). Based on the data presented in Table 3 (for  $Q_{f1}$ ), Table 4 (for  $Q_{f2}$ ), and Table 5 (for  $Q_{f3}$ ), and regarding the Froude Number indicator, in this modeling, two characteristics of water flow are formed, namely subcritical flow and supercritical flow. Subcritical flow occurs in three conditions of inflow discharge ( $Q_f$ ) but only on the flume's first bottom slope ( $S_{g1}$ ). These results show that in these flow conditions, the effect of inertial forces is still greater than gravitational forces. From the second channel bottom slope ( $S_{g2}$ ) to the ninth channel bottom slope ( $S_{g9}$ ), the flow characteristics change to supercritical flow for the three inflow discharge conditions ( $Q_f$ ). These results show that the effect of gravitational forces is more significant in these flow conditions than inertial forces.

Based on the graphic presented in Figure 14, it can be interpreted that the value of the Manning roughness coefficient ( $n$ ) tends to change (not stable) if the inflow discharge ( $Q$ ) or channel bottom slope ( $S$ ) is changed.

**ABLE 6.** Recapitulation of the results of the quantitative accuracy assessment (Nash-Sutcliffe Efficiency method) after the calibration process with the mathematical model

No.	Flow Discharge Type	NSE Index for flow depth		NSE Index for flow velocity		NSE Index for Manning Roughness Coefficient	
		NSE ( $h_g$ )	PR	NSE ( $v_g$ )	PR	NSE ( $n_g$ )	PR
1	$Q_{f1}$ (low inflow discharge)	0.977	Very good	0.952	Very good	0.995	Very good
2	$Q_{f2}$ (medium inflow discharge)	0.951	Very good	0.960	Very good	0.908	Very good
3	$Q_{f3}$ (high inflow discharge)	0.910	Very good	0.971	Very good	0.999	Very good

(\*) PR = Performance Rating

The value of the Manning roughness coefficient ( $n$ ) tends to be high when the bottom slope of the channel ( $S$ ) is mild. However, starting from the third bottom slope ( $S_{g3} = 0.0063$ ), the value of the Manning roughness coefficient ( $n$ ) tends to be more stable. However, some values of the Manning roughness coefficient ( $n$ ) still tend to increase or decrease, but the value of the deviation that occurs is relatively minor. The stability of the Manning roughness coefficient ( $n$ ) value occurs in supercritical flow conditions.

Based on Tables 3 and 10, for low inflow discharge ( $Q_{f1} = 7,830 \text{ cm}^3/\text{s}$ ), the value of the Manning roughness coefficient ( $n$ ) is in the range of 0.0076 to 0.0102, while the average value is 0.0083. Based on Tables 4 and 11, for medium inflow discharge ( $Q_{f2} = 11,600 \text{ cm}^3/\text{s}$ ), the value of the Manning roughness coefficient ( $n$ ) is in the range of 0.0077 to 0.0088, while the average value is 0.0082. Based on Tables 5 and 8, for high inflow discharge ( $Q_{f3} = 14,880 \text{ cm}^3/\text{s}$ ), the value of the Manning roughness coefficient ( $n$ ) is in the range of 0.0071 to 0.0087, while the average value is 0.0079. Overall, for the three variations of inflow discharge ( $Q_{f1}$ ,  $Q_{f2}$ , and  $Q_{f3}$ ) and nine variations of channel bottom slope ( $S_{g1}$  to  $S_{g9}$ ), the value of the Manning roughness coefficient ( $n$ ) is in the range of 0.0071 to 0.0102, while the average value is 0.0081.

### 3. 7. Verification the Accuracy of the Proposed Method

Two verification methods will be carried out to analyze the accuracy of this proposed research method and the Manning roughness coefficient value obtained from the research results. The first verification was carried out by comparing the results of this research with those conducted by Mera and Robi [28]. To test the accuracy of the proposed method carried out in this research, several graphic analyses of the results of this research will be compared with graphic analyses of the results of research carried out by Mera and Robi [28], which are as follows:

1. For the relationship between flow depth ( $h$ ) and channel bottom slope ( $S$ ), for each of the three variations of flow discharge ( $Q_{f1}$ ,  $Q_{f2}$ , and  $Q_{f3}$ ), the

graphic profile obtained from the results of this experimental test (Figure 12) is similar to the graphic profile obtained from the results of previous research conducted by Mera and Robi [28] (Figure 8).

2. For the relationship between the Manning roughness coefficient ( $n$ ) and the channel bottom slope ( $S$ ), for each of the three variations in flow discharge ( $Q_{f1}$ ,  $Q_{f2}$ , and  $Q_{f3}$ ), the graphic profile obtained from the results of this experimental test (Figure 14) has similarity to the graphic profile obtained from the previous research results of Mera and Robi (24) (Figure 9).

The second verification was carried out by comparing the Manning roughness coefficient ( $n$ ) value for GFRP material obtained from this research with the  $n$  value of GFRP material from commercial piping products Grandpipe®<sup>1</sup> and Jiubo Composite®<sup>2</sup> and the  $n$  value for flexible GFRP material obtained from the results of research conducted by Okazawa et al. (21). The Manning roughness coefficient values ( $n$ ) for the three GFRP material products range from 0.0084 to 0.0094. The value of the Manning roughness coefficient ( $n$ ) for GFRP material obtained from the results of this study ( $n = 0.0081$ ) is slightly smaller than the range of the three  $n$  values.

### 3. 8. The Performance Comparison Between Improved and Traditional Material

A comparative hydraulic analysis will be carried out between the flow depth in the GFRP material ( $n = 0.0081$ ) from experimental test results in the laboratory and the flow depth in the concrete material ( $n = 0.0143$ ) and stone masonry material ( $n = 0.0167$ ) (1) from the results of analytical calculations using the Manning equation. Analysis of flow depth data for the three types of material was carried out using three variations of inflow discharge ( $Q_f$ ) and nine variations of channel bottom slope ( $S_g$ ), where the results of calculations and data processing are presented in Table 13.

The results of processing the flow depth data in Table 13 are then processed further in graphical form, as presented in Figure 15.

<sup>1</sup> <https://grandpipe.com/en/product-information>

<sup>2</sup> <https://www.aldfpr.com/News/Comparison-of-FRP-Pipe-and-pipe-flow-185.html>

**TABLE 7.** Comparison of flow depth ( $h$ ) in the channel for conditions of three variations inflow discharge ( $Q_f$ ) and nine variations of channel bottom slope ( $S_g$ ) among GFRP material, concrete material, and stone masonry material

No.	Channel bottom slope $S_g$	Low Inflow Discharge ( $Q_{f1}$ )			Medium Inflow Discharge ( $Q_{f2}$ )			High Inflow Discharge ( $Q_{f3}$ )		
		Flow Depth (GFRP)	Flow Depth (Concrete)	Flow Depth (Stone Masonry)	Flow Depth (GFRP)	Flow Depth (Concrete)	Flow Depth (Stone Masonry)	Flow Depth (GFRP)	Flow Depth (Concrete)	Flow Depth (Stone Masonry)
		$h_g$	$h_c$	$h_{sm}$	$h_g$	$h_c$	$h_{sm}$	$h_g$	$h_c$	$h_{sm}$
	(cm/cm)	(cm)	(cm)	(cm)	(cm)	(cm)	(cm)	(cm)	(cm)	(cm)
1	0.0021	5.2	6.65	7.41	5.77	8.75	9.77	6.41	10.45	11.7
2	0.0042	3.67	5.26	5.84	4.7	6.87	7.65	5.07	8.17	9.11
3	0.0063	3	4.59	5.09	4.07	5.98	6.65	4.62	7.09	7.9
4	0.0083	2.72	4.18	4.63	3.7	5.43	6.03	4.27	6.43	7.15
5	0.0104	2.7	3.88	4.3	3.58	5.03	5.59	4.18	5.95	6.62
6	0.0125	2.52	3.66	4.05	3.4	4.74	5.26	3.92	5.6	6.22
7	0.0146	2.46	3.48	3.85	3.19	4.5	4.99	3.58	5.31	5.9
8	0.0167	2.42	3.33	3.68	3.03	4.31	4.77	3.52	5.08	5.64
9	0.0188	2.2	3.2	3.54	2.92	4.14	4.59	3.32	4.89	5.42
Average Flow Depth (cm)		2.99	4.25	4.71	3.82	5.53	6.14	4.32	6.55	7.30
Flow depth comparison of $h_g$ to $h_c$ and $h_{sm}$ (%)			70.35	63.48		69.08	62.21		65.95	59.18
Efficiency of using GFRP materials compared to concrete and stone masonry (%)			29.65	36.52		30.92	37.79		34.05	40.82

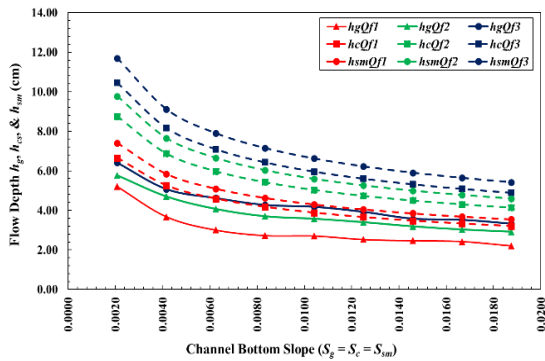


**Figure 15.** Comparison of flow depth ( $h$ ) for conditions of three variations of inflow discharge ( $Q_f$ ) and nine variations of channel bottom slope ( $S_g$ ) among GFRP, concrete, and stone masonry materials

From the results of the data analysis in Table 13 and Figure 15, it can be seen that for conditions with three variations of inflow discharge ( $Q_f$ ) and nine variations of channel bottom slope ( $S_g$ ), as well as a fixed channel/flume bottom width ( $b_g = 28.9$  cm), then the flow depth for GFRP material ( $h_g$ ) is lower than the flow depth for concrete material ( $h_c$ ) and the flow depth for stone masonry material ( $h_{sm}$ ).

By taking the average flow depth value, for low inflow discharge conditions ( $Q_{f1}$ ), the average flow depth value for GFRP material is  $h_g = 2.99$  cm; the average flow

depth value for concrete material is  $h_c = 4.25$  cm; and the average flow depth value for stone masonry material is  $h_{sm} = 4.71$  cm (Figure 16). For medium inflow discharge conditions ( $Q_{f2}$ ), the average flow depth value for GFRP material is  $h_g = 3.82$  cm; the average flow depth value for concrete material is  $h_c = 5.53$  cm; and the average flow depth value for stone masonry material is  $h_{sm} = 6.14$  cm (Figure 17). For high inflow discharge conditions ( $Q_{f3}$ ), the average flow depth value for GFRP material is  $h_g = 4.32$  cm; the average flow depth value for concrete material is  $h_c = 6.55$  cm; and the average flow depth value for stone masonry material is  $h_{sm} = 7.30$  cm (Figure 18).

From the results of the data analysis, for the same values of discharge ( $Q_g$ ), channel bottom width ( $b_g$ ), and channel bottom slope ( $S_g$ ), the flow depth for GFRP material ( $h_g$ ) is lower than the flow depth for lined concrete material ( $h_c$ ) and stone masonry material ( $h_{sm}$ ) or can be written in the form:  $h_g < h_c < h_{sm}$ . Furthermore, for the condition that the bottom width of the cross-section is the same, the wet cross-sectional area of the GFRP material ( $A_g$ ) is smaller than the wet cross-sectional area of the concrete material ( $A_c$ ) as well as the wet cross-sectional area of the stone masonry material ( $A_{sm}$ ), or can be written in the form  $A_g < A_c < A_{sm}$ .

When assessing the outcomes of a performance analysis of channel materials involving GFRP (Glass Fiber Reinforced Polymer) compared to traditional materials such as concrete and stone masonry, it is imperative to evaluate the effectiveness of GFRP's

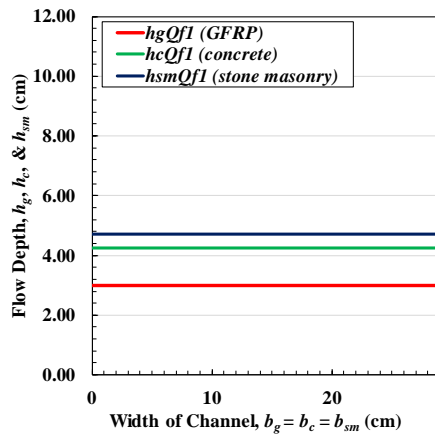


**Figure 16.** Comparison of average flow depth ( $h$ ) for low inflow discharge ( $Q_1$ ) among GFRP, concrete, and stone masonry lined material

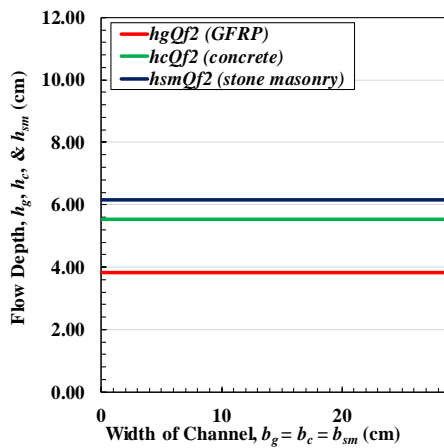


**Figure 17.** Comparison of average flow depth ( $h$ ) for medium inflow discharge ( $Q_2$ ) among GFRP, concrete, and stone masonry lined material

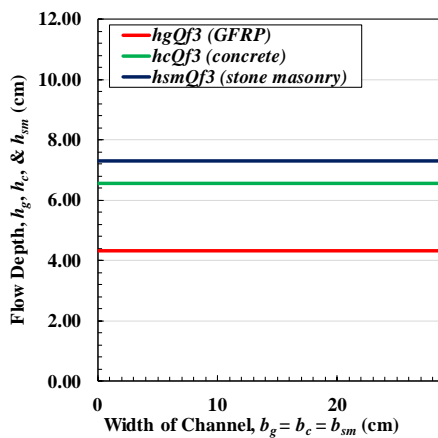


**Figure 18.** Comparison of average flow depth ( $h$ ) for high inflow discharge ( $Q_3$ ) among GFRP, concrete, and stone masonry lined material

performance. This evaluation of performance efficiency primarily focuses on the hydraulic aspect, explicitly comparing the flow depth within GFRP channel linings to that within concrete and stone masonry channel linings. The flow efficiency in a channel is significantly influenced by the Manning coefficient, which characterizes the smoothness or roughness of the channel's surface. In this particular scenario, GFRP exhibits a lower Manning coefficient (0.0081) in contrast to concrete (0.0143) and stone masonry (0.0167), indicating greater efficiency than traditional materials. Based on Table 13, Figure 19 presents a visual representation of the performance efficiency comparison between using GFRP channels and using concrete and stone masonry traditional channels.

Based on the results of this analysis, as shown in Table 13 and Figure 19, it can be concluded that at low inflow discharge, the flow depths in channels with GFRP lining are 29.65% more efficient than in channels with concrete lining and 36.52% more efficient than in channels with stone masonry lining. At medium inflow discharge, the flow depths in channels with GFRP lining are 30.92% more efficient than in channels with concrete lining and 37.79% more efficient than in channels with stone masonry lining. At high inflow discharge, the flow depths in channels with GFRP lining are 34.05% more efficient than in channels with concrete lining and 40.82% more efficient than in channels with stone masonry lining.

From the results of the analysis and interpretation of these data, in general, it can be stated that for the same values of flow discharge, channel bottom width, and channel bottom slope, the cross-sectional dimensions of GFRP material are more efficient than the cross-sectional dimensions of traditional materials (concrete and stone masonry). It can happen because the surface roughness of the GFRP material is smoother than the surface roughness of the concrete lining material and stone masonry lining material.

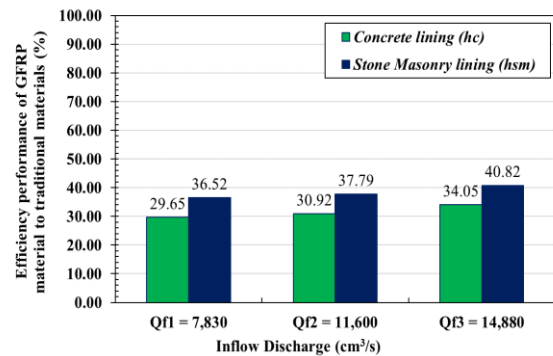


**Figure 19.** Comparative chart of the efficiency performance between the GFRP material and the traditional material (concrete and stone masonry) for three inflow variation discharge

#### 4. CONCLUSION

From the results of the analysis and interpretation of the data between the physical modeling and the mathematical modeling, several conclusions can be written as follows:

1. Before the calibration process was carried out, the performance of the physical model already had "very good" results, where the results of the quantitative accuracy assessment using the Nash-Sutcliffe Efficiency (NSE) method gave a performance index for flow depth ( $h$ ) between 0.881 and 0.910 and a performance index for flow velocity ( $v$ ) is between 0.844 to 0.971. However, because there are relatively large deviation and anomaly values for the two flow parameters in several conditions of the channel bottom slope, the calibration process is still carried out by changing the value of the Manning roughness coefficient input in the mathematical modeling. The results of the re-simulation of water flow with the HEC-RAS software give more minor deviation results, and the graphic of the results of the comparison of the two flow parameters also looks smoother. The final value for the model performance index is also getting better, where the performance index for flow depths ( $h$ ) are between 0.910 to 0.977, the performance index for flow velocities ( $v$ ) are between 0.952 to 0.971, and the performance index for Manning roughness coefficients ( $n$ ) are between 0.908 to 0.999.
2. By regulating three variations of inflow discharge in this experimental test, as the discharge ( $Q$ ) increases, the flow depth ( $h$ ) and flow velocity ( $v$ ) also increase. By adjusting the nine variations of channel bottom slope in this experimental test, as the bottom slope ( $S$ ) increases, the flow velocity ( $v$ ) also increases, but the flow depth ( $h$ ) decreases.
3. In subcritical flow conditions, the value of the Manning roughness coefficient ( $n$ ) tends to be high and unstable. The value of the Manning roughness coefficient ( $n$ ) tends to stabilize at supercritical flow.
4. From the results of this experimental test, the average Manning roughness coefficient ( $n$ ) for low inflow discharge ( $Q_{f1} = 7,830 \text{ cm}^3/\text{s}$ ) is 0.0083; for medium inflow discharge ( $Q_{f2} = 11,600 \text{ cm}^3/\text{s}$ ) is 0.0082; for high inflow discharge ( $Q_{f3} = 14,880 \text{ cm}^3/\text{s}$ ) is 0.0079; and overall, the average value of the Manning roughness coefficient ( $n$ ) is 0.0081.
5. For the discharge, channel bottom width, and channel bottom slope with the same values, the cross-sectional dimensions of GFRP material ( $n = 0.0081$ ) are more efficient than the cross-sectional dimensions of concrete material ( $n = 0.0143$ ) and stone masonry material ( $n = 0.0167$ ) where it can happen because the surface roughness of the GFRP material obtained from the results of this research is smoother than the surface roughness of the concrete material and the

stone masonry material.

6. For practical purposes in designing irrigation channels in Indonesia using GFRP material with a rigid type, it is recommended to use a Manning roughness coefficient value of  $n = 0.0081$ .

#### 5. ACKNOWLEDGMENTS

The authors would like to thank Rita Irmawaty and Hasanuddin University academic staff and Suyudi Akbari Habibi, Arif Dhiaksa, and Haryo Istianto, who have contributed to providing the necessary resources and support for conducting this study.

#### 6. REFERENCES

1. Umum DP. Standar Perencanaan Irigasi. Kriteria Perencanaan Jaringan Irigasi (KP-01). 1986.
2. Anas AV, Suriamihardja D, Pallu MS, Irfan UR. Sustainability analysis of mining management on construction material in Jeneberang River, South Sulawesi. *International Journal of Engineering Research & Technology (IJERT)*. 2013;2(12):191-5. <https://doi.org/10.17577/IJERTV2IS120193>
3. Mattamana BA, Varghese S, Kichu P. River sand inflow assessment and optimal sand mining policy development. *Int J Emergency Technol Adv. Eng.* 2013;3:305-17. [https://www.ijetae.com/files/Volume3Issue3/IJETAE\\_0313\\_52.pdf](https://www.ijetae.com/files/Volume3Issue3/IJETAE_0313_52.pdf)
4. Tahir J, Barat U, editors. Kerusakan Lingkungan Akibat Penambangan Galian Golongan C di Polewali Mandar (Studi Kasus Sungai Mandar di Polewali). *Prosiding Seminar Nasional Biologi*, September; 2017.
5. Hasyim S, Salam N, Pallu MS, Maricar F, editors. Studi Kecepatan Aliran pada Saluran Terbuka dengan Dinding Glass Fiber Reinforced Polymer (GFRP). *Prosiding Seminar Nasional Teknik Sipil UMS*; 2023.
6. Morrison WR, Comer AI. Use of geomembranes in Bureau of Reclamation canals, reservoirs, and dam rehabilitation: Materials Engineering and Research Laboratory Group, Civil Engineering ...; 1995.
7. Swihart J, Haynes J. Canal-lining demonstration project year 10 final report: US Department of the Interior, Bureau of Reclamation, Denver Technical ...; 2002.
8. Stark T, Hynes J. Geomembranes for Canal Lining. *Geosynthetics* 2009. February 25-27 2009, Salt Lake City, Utah. 2009.
9. Morgado F, Lopes GJ, de Brito J, Feiteira J. Portuguese irrigation canals: lining solutions, anomalies, and rehabilitation. *Journal of performance of constructed facilities*. 2012;26(4):507-15. [https://doi.org/10.1061/\(asce\)cf.1943-5509.0000230](https://doi.org/10.1061/(asce)cf.1943-5509.0000230)
10. El-Menshawey O, El-Sissy A, El-Wazery M, Elsad R. Electrical and mechanical performance of hybrid and non-hybrid composites. *International Journal of Engineering, Transactions A: Basics*. 2019;32(4):580-6. <https://doi.org/10.5829/ije.2019.32.04a.16>
11. Jesthi D, Nayak A, Routara B, Nayak R. Evaluation of mechanical and tribological properties of glass/carbon fiber reinforced polymer hybrid composite. *International Journal of Engineering, Transactions A: Basics*. 2018;31(7):1088-94. <https://doi.org/10.5829/ije.2018.31.07a.12>
12. Anish Jafrin Thilak J, Suresh P. Dynamic Response of Glass/Epoxy Laminated Composite Plates under Low-velocity

- Impact. *International Journal of Engineering*. 2022;35(7):1283-90. <https://doi.org/10.5829/ije.2022.35.07a.07>
13. Masuelli MA. Introduction of fibre-reinforced polymers–polymers and composites: concepts, properties and processes. Fiber reinforced polymers-the technology applied for concrete repair: IntechOpen; 2013.
  14. Estrada H, Lee LS. FRP composite constituent materials. *The International Handbook of FRP Composites in Civil Engineering*. 2014:31-2. <https://doi.org/10.1201/b15806-5>
  15. Haj Seiyed Taghia SA, Darvishvand HR, Pourhasan M. An Economic Approach to the Confinement of Different Concrete Classes with Carbon and Glass Fibers Reinforced Polymers. *International Journal of Engineering, Transactions A: Basics*. 2023;36(4):776-87. <https://doi.org/10.5829/ije.2023.36.04a.14>
  16. Zanelidin B. Fiber reinforced polymer materials in construction applications. *J Civ Eng Sci*. 2012;1(4):47-51. <http://paper.academicpub.org/Paper?id=1397>
  17. Mekonnen B, Mamo Y. Tensile and flexural analysis of a hybrid bamboo/jute fiber-reinforced composite with polyester matrix as a sustainable green material for wind turbine blades. *International Journal of Engineering, Transactions A: Basics*. 2020;33(2):314-9. <https://doi.org/10.5829/ije.2020.33.02b.16>
  18. El-Wazery M. Mechanical characterization of glass-basalt-carbon/polyester hybrid composites. *International Journal of Engineering, Transactions A: Basics*. 2018;31(7):1139-45. <https://doi.org/10.5829/ije.2018.31.07a.19>
  19. Prasanth I, Ravishankar D, Manzoor Hussain M. Analysis of milling process parameters and their influence on glass fiber reinforced polymer composites (research note). *International Journal of Engineering, Transactions A: Basics*. 2017;30(7):1074-80. <https://doi.org/10.5829/ije.2017.30.07a.17>
  20. Pang L. Fiberglass Reinforced Polyester Flumes as Tertiary Channels in Malaysian Irrigation Development: *International Rice Research Institute*; 1978.
  21. Okazawa H, Takeuchi Y, Mashino M, Maki T. Coefficient of roughness at an open channel repaired with flexible fiber-reinforced plastic lining. *Journal of Agriculture Science, Tokyo University of Agriculture (Japan)*. 2008;53(3). [https://www.nntechinfo.jp/NNTD/files/0324/0324\\_1102.pdf](https://www.nntechinfo.jp/NNTD/files/0324/0324_1102.pdf)
  22. Chow VT. A note on the Manning formula. *Eos, Transactions American Geophysical Union*. 1955;36(4):688-. <https://doi.org/10.1029/TR036i004p00688>
  23. Manning R, Griffith JP, Pigot T, Vernon-Harcourt LF. On the flow of water in open channels and pipes 1890.
  24. Mera M, Robi R. Technical Notes: Determination of Manning Roughness Coefficient for PVC Gutters. *Jurnal Teknik Sipil ITB*. 2013;20(2):153-60. <https://doi.org/10.5614/jts.2013.20.2.8>
  25. Brunner GW, editor *Hec-ras (river analysis system)*. North American water and environment congress & destructive water; 2002: ASCE.
  26. Te Chow V. *Open channel hydraulics* 1959.
  27. Moriasi DN, Arnold JG, Van Liew MW, Bingner RL, Harmel RD, Veith TL. Model evaluation guidelines for systematic quantification of accuracy in watershed simulations. *Transactions of the ASABE*. 2007;50(3):885-900. <https://doi.org/10.13031/2013.23153>
  28. Legates DR, McCabe Jr GJ. Evaluating the use of “goodness-of-fit” measures in hydrologic and hydroclimatic model validation. *Water resources research*. 1999;35(1):233-41. <https://doi.org/10.1029/1998WR900018>
  29. ASCE Task Committee on Definition of Criteria for Evaluation of Watershed Models of the Watershed Management Committee I, Division D. Criteria for evaluation of watershed models. *Journal of Irrigation and Drainage Engineering*. 1993;119(3):429-42. [https://doi.org/10.1061/\(ASCE\)0733-9437\(1993\)119:3\(429\)](https://doi.org/10.1061/(ASCE)0733-9437(1993)119:3(429))
  30. Singh J, Knapp HV, Arnold J, Demissie M. Hydrological modeling of the Iroquois river watershed using HSPF and SWAT 1. *JAWRA Journal of the American Water Resources Association*. 2005;41(2):343-60. <https://doi.org/10.1111/j.1752-1688.2005.tb03740.x>
  31. Nash JE, Sutcliffe JV. River flow forecasting through conceptual models part I—A discussion of principles. *Journal of hydrology*. 1970;10(3):282-90. [https://doi.org/10.1016/0022-1694\(70\)90255-6](https://doi.org/10.1016/0022-1694(70)90255-6)
  32. Van Liew M, Arnold J, Garbrecht J. Hydrologic simulation on agricultural watersheds: Choosing between two models. *Transactions of the ASAE*. 2003;46(6):1539-51. <https://doi.org/10.13031/2013.15643>

**COPYRIGHTS**

©2024 The author(s). This is an open access article distributed under the terms of the Creative Commons Attribution (CC BY 4.0), which permits unrestricted use, distribution, and reproduction in any medium, as long as the original authors and source are cited. No permission is required from the authors or the publishers.

**Persian Abstract****چکیده**

یکی از تلاش‌ها برای کاهش تلفات آب در کانال‌های آبیاری، تامین مواد آستردهار در کانال‌های آبیاری زمین است. ساخت این مواد آستردهار در اندونزی به مواد خام (مانند شن، ماسه و سنگ شکافی) نیاز دارد که از طبیعت استخراج می‌شود و در اندونزی که به عنوان مواد حفاری کلاس C شناخته می‌شود. بهره برداری بیش از حد از مواد حفاری کلاس C بر آسیب‌های زیست محیطی تأثیر می‌گذارد. بنابراین برای غلبه بر این مشکلات، تحقیقاتی برای یافتن مواد پوشش‌دار جایگزین مورد نیاز است و در این تحقیق، ماده پوشش‌دهنده جایگزین پلیمر تقویت‌شده با الیاف شیشه (GFRP) است. هدف اصلی این مطالعه تعیین مقدار ضریب زبری مانینگ برای کانال‌های اندود شده از مواد GFRP بود. این تحقیق شامل آزمایش تجربی با استفاده از مدل کانال باز (فلوم) پوشیده شده با مواد GFRP بود. آزمایش‌های جریان با سه تغییر دبی جریان پمپ و نه تغییر شیب پایین کانال انجام شد. نتایج آزمون مدل فیزیکی با نتایج شبیه‌سازی مدل ریاضی با استفاده از نرم‌افزار HEC-RAS مقایسه شد. عملکرد مدل با استفاده از تکنیک گرافیکی و آمار کمی به ویژه روش کارایی نش-ساتکلیف (NSE) مورد ارزیابی قرار گرفت. ارزیابی مدل با روش NSE نشان می‌دهد که عملکرد مدل فیزیکی "بسیار خوب" است. مقدار ضریب زبری Manning برای مواد GFRP با روکش صلب از 0.0071 تا 0.0102 متغیر است. مقدار ضریب زبری مانینگ توصیه شده برای کاربرد عملی در طراحی کانال‌های آبیاری در اندونزی 0/0081 است.



## Utilizing a New Voltage Stability Index in Distribution Power System in Presence of Wind Turbine Units

A. H. Foomani, M. Moradlou\*, P. Nazarian

Department of Electrical Engineering, Zanjan Branch, Islamic Azad University, Zanjan, Iran

### PAPER INFO

#### Paper history:

Received 12 August 2023

Received in revised form 08 October 2023

Accepted 02 November 2023

#### Keywords:

Voltage Stability Index

Analytical Hierarchy Process

Active Distribution Network

Multi-criteria Decision Formation

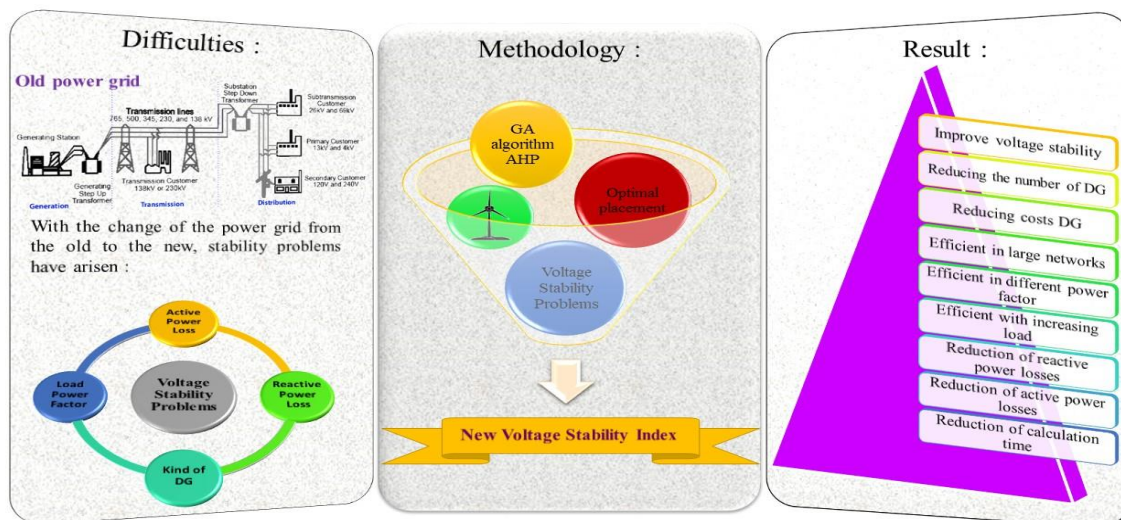
Wind Turbine

### ABSTRACT

Equipping renewable energy resources generation units in the distribution network to reduce economical and emission concerns are the examples of active distribution network (ADN). The other advantages of utilizing distributed generators (DGs) are improving technical constraints of ADN. In this paper multi-benefit functions are defined as main functions. Each of functions illustrates the positive impacts of utilizing wind turbines in the improving technical constraints of the ADN. Voltage stability (VS) is one of the main technical indices of the ADN. Several VSIs are defined to evaluate voltage stability of the ADN. The previous indices could not give the proper results about allocating DGs and accurate evaluating of voltage stability of ADN. This work proposes the new VSI. To this aim active power loss (APL), reactive power loss (RPL) and voltage stability index (VSI) are considered as technical constraints. In order to evaluate the presence of WT on improving APL and RPL, WTs are considered in two operational modes; unified power factor (UPF) and (APF). The main benefit function is solved by implementing genetic algorithm (GA). Multiplying weights to the APL, RPL and VSI (which are improved by attendance WTs) in benefit function formulation, make the multi-criteria decision formation to the proposed optimization problem. By employing analytical hierarchy process (AHP) technique and considering each technical constraints as main criteria, the obtained solutions are arranged. To verify the positive effectiveness of the proposed VSI, its results are compared with the results of other VSIs in the 33, 67 and 118 bus IEEE radial DN.

doi: 10.5829/ije.2024.37.04a.11

### Graphical Abstract



\*Corresponding Author Email: [majid.moradloo@iauz.ac.ir](mailto:majid.moradloo@iauz.ac.ir) (M. Moradlou)

NOMENCLATURE		
<b>Index</b>		
t	Time in second	Pi
i	The counter for the number of WT units	Qi
<b>Parameters</b>		Intr
$\tau$	Planning horizon (year)	Kqv
$\rho$	Price of purchasing/selling of power (\$)	$\alpha$
Vcut-in	The lower bound operational velocity of WT (m/s)	$DLF_{i,t,h}^S$
Vcut-out	The upper bound operational velocity of WT (m/s)	$K_{pv}$
Vrated	Nominal velocity of WT (m/s)	Kqv
T	Planning horizon (hour)	<b>Function</b>
PrWT	Rated power of WT (kW)	VPI
ICWT	The total capital cost of WT	RPLI
OCWT	The total operational cost of WT	VSI
LP	Purchased power from an upstream network	APL
LS	Sold power from upstream network	DNO
IWT	Current of WT	DSM1
Infr	Inflation rate (%)	DSM2
		DSM3
		DSM4

## 1. INTRODUCTION

Due to the lack of fossil fuels and their environmental issues, such as global warming and pollution, energy administrators think of using alternative cheap, available, and clean energy resources. The wind is one of the clean and available resources. By integrating wind turbines (WT), the necessity to install a new central (fossil fuel) power plants is diminished. WT operates in both grid-connected and isolated conditions. Recently equipping distribution networks with WT to improve system technical constraints is the main aim of researchers. The role of WT in improving several technical constraints of distribution network (DN), such as: reliability, voltage stability, active and reactive power loss reduction, are considered in the recent kind of literature. By connecting DGs in the proper buses of DN, besides improving the voltage profile of buses, total active and reactive losses are reduced (1). Optimal integration of distributed generators (DGs), improved the voltage stability of buses (2). Mobashsher et al. (3), introduced an optimal voltage control (OVC) framework for islanded microgrids (MGs) as a unified hierarchical control scheme. Investing in private enterprises in the energy section by installing WTs in the DN was studied by Tooryan et al. (4). Energy not supplied with considering reliability indices in the planning horizon is the primary function as introduced by Yousefipour et al. (5). Integrating WTs and energy storage systems (ESS) to optimal managing of generation and demand by considering WT probabilistic behavior was studied by Wang et al. (6). Elmaadawy et al. (7) studied impacts of utilizing WT on improving voltage stability and reducing active power loss in the 13 and 69

buses, IEEE system. Non-optimal power flow could be caused by the voltage drops and blackouts due to voltage instability of DN (8). An economic dispatch of generation units to calculate the cost of DG installation and system technical constraints is called power flow (9). The destructive effects of installing WT in the DN are; voltage rise and fluctuation stability and increasing short circuit capacity level (10). Presenting the voltage stability index to optimal siting and sizing of DGs are the main aims of the recent kind of literature (11). Azad et al. (12) proposed both of VSI and APLI as primary function of planning problem. Mirjalili et al. (13) also proposed the new indices to improve voltage stability margin (VSM) for both of active and reactive power at the weakest bus after installing WTs. The output power of wind turbines has been injected into the 30 bus system in the South Sulawesi network in order to improve the stability of the network voltage (14). The multi objective performance index (MOPI) is introduced to optimal siting and sizing of DG in the DN. By implementing weighted coefficient, many technical constraints are combined and solved under various operating circumstance (15). Nafeh et al. (16) studied changing parking lot (PL) to the intelligent parking lot (IPL) with installing WT. Onlam et al. (17) obtained the best allocation buses of WTs, the power stability index (PSI) which was proposed with considering 2-bus system with less than the unity margin for a voltage stable operation. Voltage deviation index (VDI) is presented as an absolute value of bus voltage deviation than the unity margin (18). To estimate voltage drop in a power system, voltage collapse prediction index (VCPI) is defined based on the system variables such as the bus voltage magnitude, buses voltage angle, and

admittance matrix of system (19). Hassani et al. (20) introduced the new system sensitivity analyze index (SAI) to measure active and reactive power in the weak buses. To identify the weak bus of radial DN, the bus participation factor (BPF) was proposed by Guerrero et al. (21). Sundarajoo and Soomro (22) proposed an optimal method of load shedding under voltage (UVLS) to optimally predict the amount of shed load and the best place for load shedding. In this work, the stability index (SI) and feed forward back propagation neural network (FFBPNN) are adopted to prevent voltage collapse and blackout by reducing voltage instability following the addition of load in the distribution system. However, in this simulation, the old voltage stability index is still used. Variations in the power factor of different loads as well as the presence of distributed generation have not been investigated in it. Sadeghi and Akbari Foroud(23) considered line length effects on the voltage stability by introducing the new VSI. This index could asses the voltage stability of transmission and distribution network separately and together. Effects of tapchanger and distributed generators on voltage stability of distribution network is analyzed by presenting the new VSI (24).

As it is reviewed from the last literatures, due to importance of technical constraints, authors considered several technical criteria in works. There are different VSIs which were introduced. The presented VSI in the latest researches includes the voltage deviation from the 1 p.u. Therefore, these indices could not give the proper results about allocating DGs and accurate evaluating of voltage stability of DN. In this paper impacts of considering WT in both modes: unity power factor (PF) and adjusted PF on improving technical constraints as: voltage stability (VS), voltage profile and technical constraints such as reactive power loss and active power loss was studied. Figure 1 depicts the concept of main aims of this paper .

The main contributions of this paper are listed as follows:

- Introducing the new voltage stability index
- Optimal siting and sizing of DGs in unified and adjustable power factor
- Applying Analytical Hierarchy Process (AHP) to solve multi-ceria decision problem
- Considering several kinds of loads (residential, industrial and commercial)

The other parts of paper are organized as follows:

In the section 2, problem definition and optimization algorithm has been discussed in details. In section 3, all of obtained results in the different scenarios have been demonstrated. Discussion and conclusion are described respectively in sections 4 and 5.

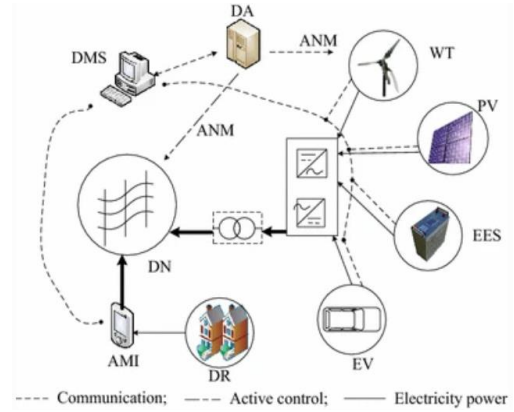


Figure 1. Optimal siting and sizing of DGs

## 2. PROBLEM DEFINITION

In this paper impacts of optimal siting and sizing of DGs on improving voltage stability, active power loss, line flow limitation, reactive power loss and voltage profile index has been studied. Each of indices are defined as follows:

$$DSM_1 = \max \left\{ B_{Total}^{disch\ arg\ e} + B_{Total}^{Load} + B_{Total}^{Loss} + B_{Total}^{WT} - C_{Total}^{inv} \right\} \quad (1)$$

$$DSM_2 = \max \left\{ B_{Total}^{disch\ arg\ e} + B_{Total}^{Load} + B_{Total}^{VSI} + B_{Total}^{WT} - C_{Total}^{inv} \right\} \quad (2)$$

$$DSM_3 = \max \left\{ B_{Total}^{disch\ arg\ e} + B_{Total}^{Load} + B_{Total}^{LFL} + B_{Total}^{WT} - C_{Total}^{inv} \right\} \quad (3)$$

$$DSM_4 = \max \{ W_1 \times DSM_1 + W_2 \times DSM_2 + W_3 \times DSM_3 \} \quad (4)$$

Amounts of archived benefits by installing WT is calculated as follows :

$$B_{Total}^{WT} = \sum_{t=1}^T \sum_{h=1}^{N_h} \sum_{i=1}^{N_b} \sum_{WT=1}^{N_{WT}} (P_{t,h}^{WT} \times \rho_{t,h} \times \tau_{t,h}) \times \left( \frac{1+InfR}{1+IntR} \right)^t \quad (5)$$

The total benefits which are obtained by considering positive impacts of WT are calculated as follows:

$$B_{Total}^{Loss} = \sum_{t=1}^T \sum_{h=1}^{N_h} [(P_{loss,t,h}^{without\ WT} - P_{loss,t,h}^{with\ WT}) \times \rho_{t,h} \times \tau_{t,h}] \times \left( \frac{1+InfR}{1+IntR} \right)^t \quad (6)$$

Amounts of total achieved benefits by reducing the amount of purchased/sold energy from upstream grid is determined as follows:

$$C_{Total}^{Load} = \sum_{t=1}^T \sum_{h=1}^{N_h} (P_{t,h}^{grid} \times \rho_{t,h}^{grid} \times \tau_{t,h}^{grid}) \times \left( \frac{1+InfR}{1+IntR} \right)^t \quad (7)$$

$$R_{Total}^{Load} = \sum_{t=1}^T \sum_{h=1}^{N_h} (P_{t,h}^{Load} \times \rho_{t,h}^{Load} \times \tau_{t,h}^{Load}) \times \left( \frac{1+InfR}{1+IntR} \right)^t \quad (8)$$

$$B_{Total} = R_{Total}^{Load} - C_{Total}^{Load} \quad (9)$$

$$P_{t,h}^{grid} = \begin{cases} P_{t,h}^{Load} + P_{Loss} + P_{charge}^b - P_{WT} \\ P_{t,h}^{Load} + P_{Loss} - P_{discharge}^b - P_{WT} \end{cases} \quad (10)$$

**2. 1. Active Power Loss (APL)** Connecting DG's to the buses, reduce the amount of active power loss. In this section to evaluate DG's role in the reduction of active power loss, the related index is defined as follows (25):

$$APLI = \frac{APL_{Old} - APL_{New}}{APL_{Old}} \quad (11)$$

where :

$$APL_{Old} = \sum R_i \times I_i^2 \quad (12)$$

**2. 2. Rective Power Loss (RPL)** Connecting DG's to the distribution system buses, reduce the amount of reactive power loss, by modifying the value of the buses voltage. The index to evaluate the value of DG's positive impacts in reducing reactive power loss is defined as follows (25):

$$RPL = \frac{RPL_{Old} - RPL_{New}}{RPL_{Old}} \quad (13)$$

Where :

$$RPL_{Old} = \sum X_i \times I_i^2 \quad (14)$$

**2. 3. Line Flow Limitation (LFL)** In this section the new voltage stability index and path of achieving its mathematical model is described. Figure 2 shows the distribution system with both of sending and receiving (feeder and load) parts. Branch current and voltage of receiver section are received by equations (14-17):

$$LFL = \text{Max} \left( \frac{S_{ij}}{CS_{ij}} \right) \quad (15)$$

**2. 4. New voltage stability index (VSI)** To avoid occurring overload in the branches, considering the allowable limit of load flow is important. To evaluate the impacts of connecting DG's on the line's load flow, the line flow limit index is defined as FOLLOWS (26):

$$I_{12} = \left[ \frac{P_2 + jQ_2}{V_2 \angle \delta} \right]^* \quad (16)$$

$$V_2 \angle \delta = V_1 \angle 0 - (R + jX) I_{12} \quad (17)$$

$$V_2 \angle \delta = V_1 \angle 0 - (R + jX) \left[ \frac{P_2 + jQ_2}{V_2 \angle \delta} \right]^* \quad (18)$$

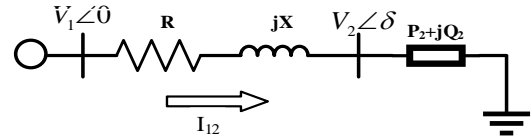


Figure 2. Radial distribution system

$$V_2 \angle \delta = V_1 \angle 0 - (R + jX) \left[ \frac{P_2 - jQ_2}{V_2 \angle \delta} \right]^* \quad (19)$$

By multiplying two sides of Equation 19 in  $V_2 \angle -\delta$ , it will have:

$$V_2^2 = V_1 V_2 \angle -\delta - (R + jX)(P_2 - jQ_2) \quad (20)$$

With rewriting phrase  $V_1 V_2 \angle -\delta$  in complex form, the below equations have been found:

$$V_2^2 = V_1 V_2 \cos \delta - jV_1 V_2 \sin \delta - (R + jX)(P_2 - jQ_2) \quad (21)$$

$$V_2^2 + [P_2 R + Q_2 X + j(P_2 X - Q_2 R)] = V_1 V_2 \cos \delta - jV_1 V_2 \sin \delta \quad (22)$$

With separating the imaginary and real parts, it will be noticed that:

$$V_2^2 = P_2 R + Q_2 X = V_1 V_2 \cos \delta \quad (23)$$

$$(P_2 X - Q_2 R) = -jV_1 V_2 \sin \delta \quad (24)$$

$$R = \frac{P_2 X + V_1 V_2 \sin \delta}{Q_2} \quad (25)$$

With replacing Equation 25 in Equation 23, it will be noticed that:

$$V_2^2 + P_2 \frac{P_2 X + V_1 V_2 \sin \delta}{Q_2} + Q_2 X = V_1 V_2 \quad (26)$$

$$V_2^2 + \left( \frac{P_2 \sin \delta V_1}{Q_2} - V_1 \cos \delta \right) V_2 + \left( \frac{P_2^2}{Q_2} + Q_2 \right) X = 0 \quad (27)$$

It's clear that, buses with stable voltage are received by employing  $b^2 - 4ac \geq 0$  as follows:

$$\left( \frac{P_2 \sin \delta V_1}{Q_2} - V_1 \cos \delta \right)^2 - 4 \left( \frac{P_2^2}{Q_2} + Q_2 \right) X \geq 0 \quad (28)$$

$$1 = \frac{4 \left( \frac{P_2^2}{Q_2} + Q_2 \right) X}{\left( \frac{P_2 \sin \delta V_1}{Q_2} - V_1 \cos \delta \right)^2} \quad (29)$$

The new voltage stability index is defined as follows:

$$VSI = \left| 1 - \frac{4 \left( \frac{P_2^2}{Q_2} + Q_2 \right) X}{\left( \frac{P_2 \sin \delta V_1}{Q_2} - V_1 \cos \delta \right)^2} \right| \quad (30)$$

**2. 5. Wind Turbine** To use wind energy and convert its energy to the electrical energy, WT has been used. Due to probabilistic behavior of wind velocity, the output

power of WT is probabilistic. According to the WT constructions and robustness of WT impeller, lower and upper bond of velocity are defined as  $V_{cut-in}$  and  $V_{cut-out}$  Its output power is calculated as follows (2):

$$P^{Out-WT} = \begin{cases} 0 & V < V_{Cut-in}, V > V_{Cut-out} \\ P_{rated} \frac{V - V_{Cut-in}}{V_{rated} - V_{Cut-in}} & V_{Cut-in} < V < V_{rated} \\ P_{rated} & V_{rated} < V < V_{Cut-out} \end{cases} \quad (31)$$

**2. 6. Load Model** In this paper, non-linear voltage dependence load is considered in beside of daily load. Daily load includes three demand levels (low, basic and peak load) (27):

$$P_{i.t.h}^{D.s} = P_i^D \times DLF_{i.t.h}^S \times (1 + \alpha)^t \quad (32)$$

$$Q_{i.t.h}^{D.s} = Q_i^D \times DLF_{i.t.h}^S \times (1 + \alpha)^t \quad (33)$$

$$S_{i.t.h}^{D.s} = P_{i.t.h}^{D.s} + jQ_{i.t.h}^{D.s} \quad (34)$$

Mathematical model of buses active and reactive power voltage dependency is defined as follows (28):

$$P_i = P_{i.t.h}^{D.s} \times \left(\frac{V_i}{V_{oi}}\right)^{k_{pv}} \quad (35)$$

$$Q_i = Q_{i.t.h}^{D.s} \times \left(\frac{V_i}{V_{oi}}\right)^{k_{qv}} \quad (36)$$

**2. 7. Power Flow** In this section the Newton Raphson-based power flow technique is used to obtain buses voltages and branches current. For each demand level and year of planning horizon, power flow equations are calculated as follows (29):

$$P_{t.h}^{grid} + P_{t.h}^{b} + P_{t.h}^{WT} - P_{t.h}^{De} - V_{i.t.h}^e \sum Y_{ij} V_{i.t.h}^e \times \cos(\delta_{i.t.h}^e - \delta_{i.t.h}^e - Q_{ij}) = 0 \quad (37)$$

$$Q_{t.h}^{grid} - Q_{t.h}^{De} - V_{i.t.h}^e \sum Y_{ij} V_{i.t.h}^e \times \sin(\delta_{i.t.h}^e - \delta_{i.t.h}^e - Q_{ij}) = 0 \quad (38)$$

**2. 8. AHP Technique** Analytical Hierarchy Process (AHP) is the one of most efficient technique to solve multi-criteria problem. This technique by evaluating the problem in the three steps, solve the issues as follows:

- Describing problem
- Listing the various of solving paths with determining alternatives and attributes of them
- Selecting the optimum criteria of solutions among others

Figure 3 illustrates the flowchart of optimization algorithm. Figure 4 illustrates the stages of AHP. As it is seen, the optimization algorithm includes two steps. In the first steps by utilizing GA, problem is solved and in the second step, by utilizing AHP, the optimum criteria

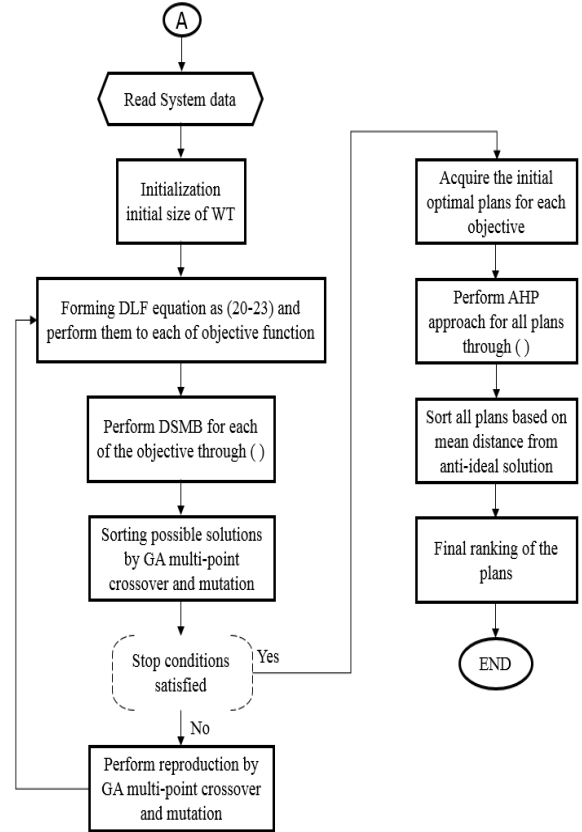


Figure 3. Flowchart of optimization algorithm

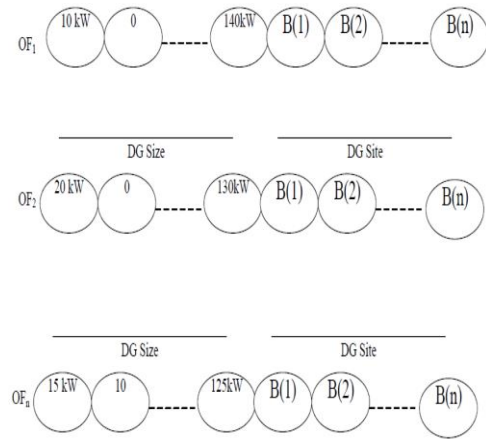


Figure 4. Special chromosome

are selected. Since benefit function is formed by multiplying weights to each technical functions, GA by assigning the larger value to the main technical constraint, start the solving of optimization problem.

**2. 9. Optimization Algorithm** In this paper, genetic algorithm (GA) and AHP are used to solve optimization algorithm. In the first stage, GA obtained the optimal solutions and in the second stage solutions are arranged

by utilizing AHP. Both of GA and AHP are defined as follows :

In this paper to solve multi-criteria optimization problem, multi objective genetic algorithm (MOGA) is used. The routine GA includes three main steps as follows (30):

- Initializing with coding base chromosome with problem variables
- Crossover
- Mutation

The special chromosome which is codified with the problem variables is illustrated in Figure 4. Crossover and mutation are shown in Figure 5.

All stages of AHP technique are listed as follows:

Formation a(ij) Pair-wise comparison matrix:

$$a_{ij} = \begin{bmatrix} a_{11} & a_{12} & a_{13} & \dots & a_{1n} \\ a_{21} & a_{22} & a_{23} & \dots & a_{2n} \\ \dots & \dots & \dots & \dots & \dots \\ a_{n1} & a_{n2} & a_{n3} & \dots & a_{nn} \end{bmatrix} \quad (39)$$

Modelling normalized matrix as:

$$N_{ij} = \begin{bmatrix} \frac{a_{11}}{\sum_{i=1}^n a_{i1}} & \frac{a_{12}}{\sum_{i=1}^n a_{i2}} & \frac{a_{13}}{\sum_{i=1}^n a_{i3}} & \dots & \frac{a_{1n}}{\sum_{i=1}^n a_{in}} \\ \frac{a_{21}}{\sum_{i=1}^n a_{i1}} & \frac{a_{22}}{\sum_{i=1}^n a_{i2}} & \frac{a_{23}}{\sum_{i=1}^n a_{i3}} & \dots & \frac{a_{2n}}{\sum_{i=1}^n a_{in}} \\ \dots & \dots & \dots & \dots & \dots \\ \frac{a_{n1}}{\sum_{i=1}^n a_{i1}} & \frac{a_{n2}}{\sum_{i=1}^n a_{i2}} & \frac{a_{n3}}{\sum_{i=1}^n a_{i3}} & \dots & \frac{a_{nn}}{\sum_{i=1}^n a_{in}} \end{bmatrix} \quad (40)$$

Relative matrix is written as:

$$W_{ij} = \begin{bmatrix} W_1 \\ W_2 \\ W_3 \\ \dots \\ W_n \end{bmatrix} = \begin{bmatrix} \frac{a_{11}}{\sum_{i=1}^n a_{i1}} & \frac{a_{12}}{\sum_{i=1}^n a_{i2}} & \frac{a_{13}}{\sum_{i=1}^n a_{i3}} & \dots & \frac{a_{1n}}{\sum_{i=1}^n a_{in}} \\ \frac{a_{21}}{\sum_{i=1}^n a_{i1}} & \frac{a_{22}}{\sum_{i=1}^n a_{i2}} & \frac{a_{23}}{\sum_{i=1}^n a_{i3}} & \dots & \frac{a_{2n}}{\sum_{i=1}^n a_{in}} \\ \dots & \dots & \dots & \dots & \dots \\ \frac{a_{n1}}{\sum_{i=1}^n a_{i1}} & \frac{a_{n2}}{\sum_{i=1}^n a_{i2}} & \frac{a_{n3}}{\sum_{i=1}^n a_{i3}} & \dots & \frac{a_{nn}}{\sum_{i=1}^n a_{in}} \end{bmatrix} \times \frac{1}{n} \quad (41)$$

Eigenvalue matrix is formed as :

$$N_{ij} = \begin{bmatrix} \frac{V_1}{W_1} \\ \frac{V_2}{W_2} \\ \dots \\ \frac{V_n}{W_n} \end{bmatrix} \quad (42)$$

Matrix  $V_i$  is formed as :

$$V_i = \begin{bmatrix} \frac{V_1}{W_1} \\ \frac{V_2}{W_2} \\ \dots \\ \frac{V_n}{W_n} \end{bmatrix} = \begin{bmatrix} \frac{a_{11}}{W_1} + \frac{a_{12}}{W_2} + \dots + \frac{a_{1n}}{W_n} \\ \frac{a_{21}}{W_1} + \frac{a_{22}}{W_2} + \dots + \frac{a_{2n}}{W_n} \\ \dots \\ \frac{a_{n1}}{W_1} + \frac{a_{n2}}{W_2} + \dots + \frac{a_{nn}}{W_n} \end{bmatrix} \quad (43)$$

Evaluation matrix is formed as :

$$E_{ij} = \begin{bmatrix} \frac{a_{11}}{W_1} & \frac{a_{12}}{W_2} & \frac{a_{13}}{W_3} & \dots & \frac{a_{1n}}{W_n} \\ \frac{a_{21}}{W_1} & \frac{a_{22}}{W_2} & \frac{a_{23}}{W_3} & \dots & \frac{a_{2n}}{W_n} \\ \dots & \dots & \dots & \dots & \dots \\ \frac{a_{n1}}{W_1} & \frac{a_{n2}}{W_2} & \frac{a_{n3}}{W_3} & \dots & \frac{a_{nn}}{W_n} \end{bmatrix} \quad (44)$$

Maximum eigenvalue is achieved as :

$$\tau_{max} = \left[ \frac{V_1}{W_1} + \frac{V_2}{W_2} + \dots + \frac{V_n}{W_n} \right] \times \frac{1}{n} \quad (45)$$

Consistency index is obtained as :

$$CI = \left[ \frac{\tau_{max} - n}{n - 1} \right] \times \frac{1}{n} \quad (46)$$

$n$  is number of criteria. Consistency ratio is achieved as :

$$CR = \frac{CI}{RI} \quad (46)$$

RI is random index.

### 3. RESULTS

In this section all of simulation results are studied in details. Several kinds of technical constraints are considered in the benefit functions. with appropriation the different weights to each function, impacts of technical constraints in total benefits are evaluated. To make a comprehensive analyze, four various scenarios are improvised as follows:

- Scenario 1: Base plan represents the basic structure of the test cases without any WTs
- Scenario 2: Optimal placement of only 1 WT
- Scenario 3: Optimal placement of 2 WTs
- Scenario 4: Optimal placement of 3 WTs

For scenarios 2, 3 and 4 two different states are devised as follows:

- Case-I: Placing WTs operated in unity power factor (UPF)
- Case-II: Placing WTs operated in APF mode

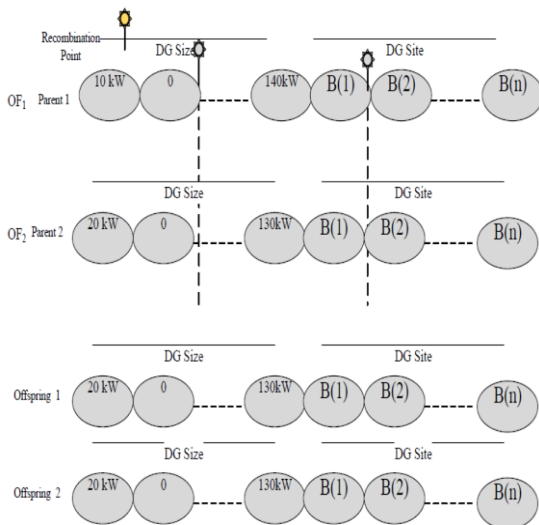
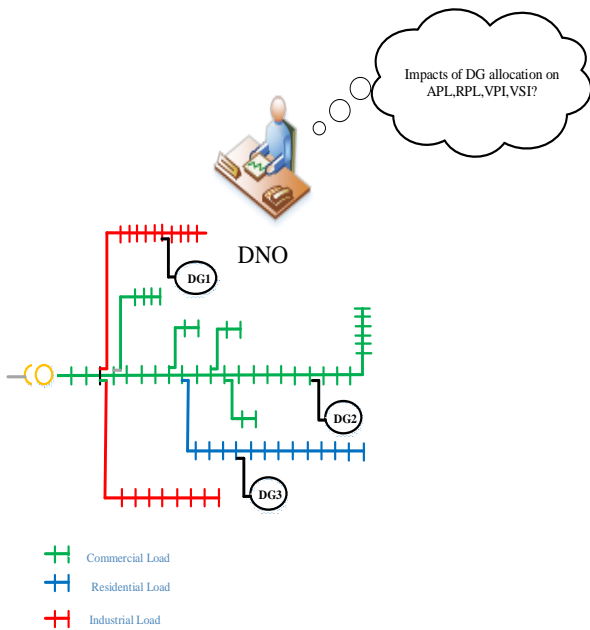


Figure 5. Crossover and mutation process

**3. 1. Input Data** In this paper, 33 bus IEEE system is selected as benchmark system. Figure 6 shows the presented DN by considering three kinds of residential, commercial and industrial loads (31). Total active and reactive power of the mentioned system are 3.72MW and 2.3MVar, respectively. According to the system power, maximum and minimum installing size of DGs are 50% system loads and 200kW, respectively.

Table 1 gives the residential, industrial and commercial loads features. In Table 2, price of exchanging energy has been given. In Table 3, planning parameters are given.



**Figure 6.** The presented DN

**TABLE 1.** Parameters of voltage sensitivity of loads

Load model	Dependency coefficient	
	$k_{pv}$	$k_{qv}$
Constant	0	0
Residential	1.5	2.4
Industrial	0.2	0.7
Commercial	0.5	2.4

**TABLE 2.** Price of sold/purchase power

Parameter	Value	Unit
$\rho_{t,h}$	75	\$/MWh
$\rho_{t,h}^{grta}$	65	\$/MWh
$C_d$	0.001	\$/MWh
$IC_b$	1000	\$/MWh

**TABLE 3.** Parameters of planning problem

Parameter	Value	Unit
$\alpha$	3	%
$V_{min}$	0.9	p.u
$V_{max}$	1.1	p.u
InFR	4	%
InTR	5	%
$\sigma_{t,h}$	$0.1 \times \mu_{i,k}$	--

**3. 2. Optimal Siting and Sizing of WTs with Considering APL as a Main Technical Constraint**

In the presented 33 bus system, feeder 1 is considered as reference bus. Due to budget limitation for operators, three WT with size in [0.2, 20] MW and PF between [0.8,1] p.u are considered in the allocation problem.

As it is given in Table 4, the minimum voltage and active power loss in the base mode is in the bus 18 equal to 0.9038 p.u and 210.98 kW, respectively. Figures (7-9), show the voltage profile for scenarios 2, 3, 4 in mode, respectively. As it can be seen clearly from Figure 8, installing WT with site and size 1.942 MW in bus 8, improve the minimum voltage of bus 18 from 0.91 to 0.948 p.u . Figure 7, illustrates the positive role of installing WT with sizes, 0.857 and 1.204 MW in the buses 13 and 30, in improving the minimum voltage from 0.91 to 0.991. Installing the WTs with sizes 0.749, 0.879 and 0.408 in the buses 14, 25 and 30 improve the voltage profile of buses as Figure 8. In Figure 10 power loss in several scenarios is figured.

Figures 11-13, show the voltage profile for the scenarios 2, 3, 4 in mode 2, respectively. Installing WT (1.911 MW) with the tuned power factor (0.87) improve the voltage profile as Figure 12. Figures 11-13, show the voltage profile for the scenarios 2,3,4 in mode 2, respectively. Installing WT (1.911 MW) with the tuned power factor (0.87) improve the voltage profile as Figure 12. Figure 13 shows the improved voltage profile with installing WT with the size (1.204 MW and 0.857) and tuned power factor (0.9 and 0.87). Equipping DN with three WTs (0.749, 0.879 and 0.408) with tuned power factor in (0.88, 0.92,0.89) improve the buses voltage profile as Figure 14. In Figures 15-16, impacts of increasing the number of WTs on the voltage profile are figured. In Figures 16 and 17, by installing WTs, the voltage magnitude of some buses are more than 1p.u.

In Figures 15-16, impacts of increasing the number of WTs on the voltage profile are figured. In Figures 16 and 17, by installing WTs, the voltage magnitude of some buses are more than 1p.u.

**3. 3. Optimal Siting and Sizing of WTs with Considering VSI as a Main Technical Constraint**

Table 5 gives the results in the conditions which VSI is

considered as main technical constraints. As it can be seen, different scenarios and modes are considered to have a comprehensive study. Results show the positive impacts of injecting reactive power in the adjustable power factor condition, on reducing active power loss and voltage drop. For example, by comparing different modes of scenario 2, the truth of improving voltage domain with 1 WT in the adjustable power factor with injecting reactive power is cleared.

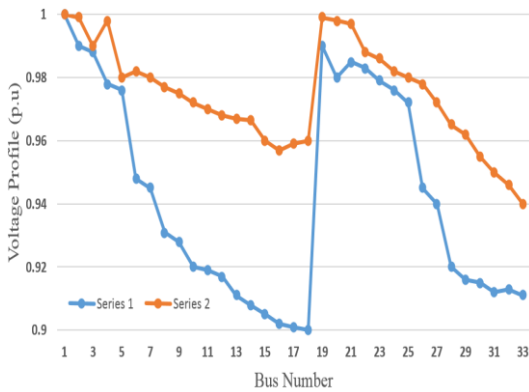


Figure 7. Voltage profile in scenario 2

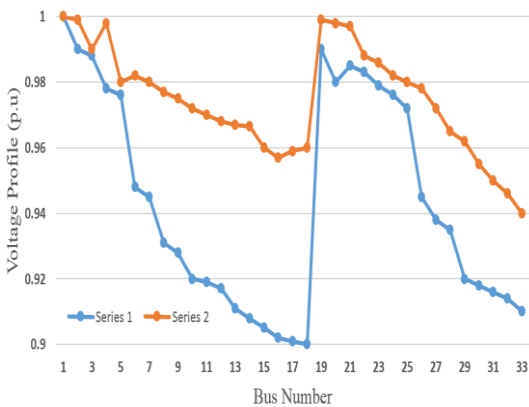


Figure 8. Voltage profile in scenario 3

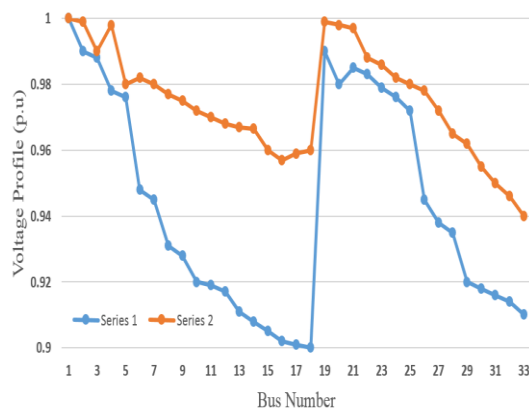


Figure 9. Voltage profile in scenario 4

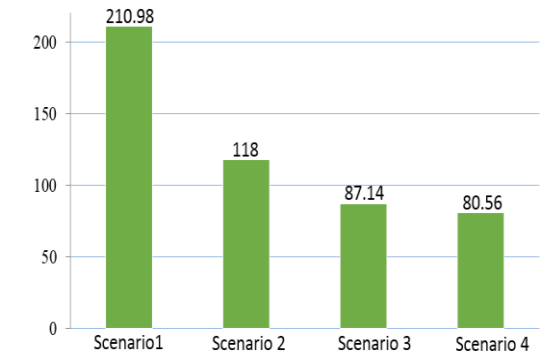


Figure 10. Power loss of each scenario

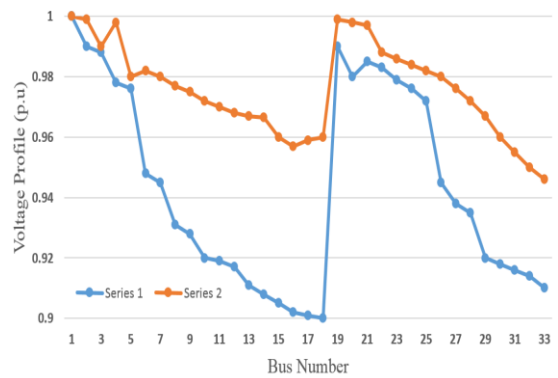


Figure 11. Voltage profile in scenario 2 mode 2

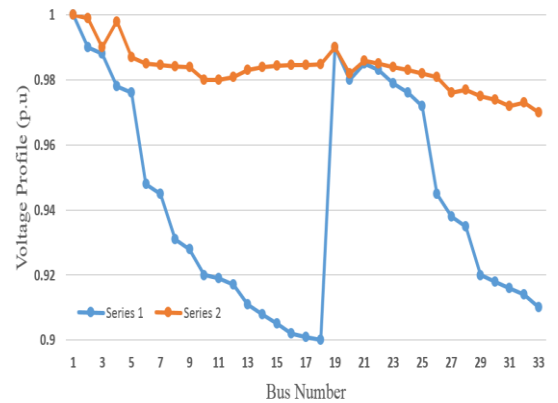


Figure 12. Voltage profile in scenario 3 mode 2

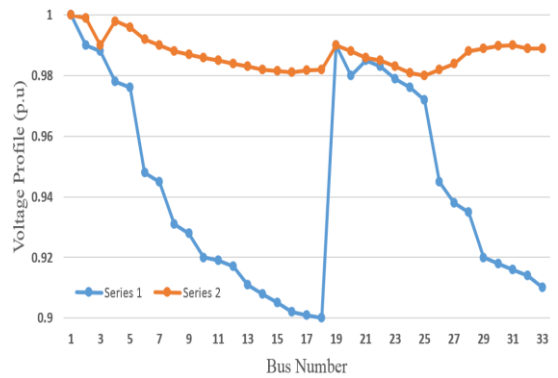


Figure 13. Voltage profile in scenario 4 mode 2

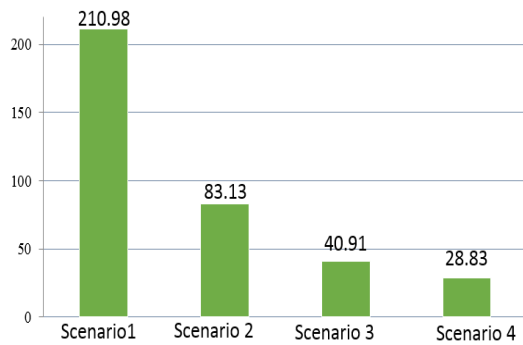


Figure 14. Active power loss in mode 2 (power loss of each scenario)

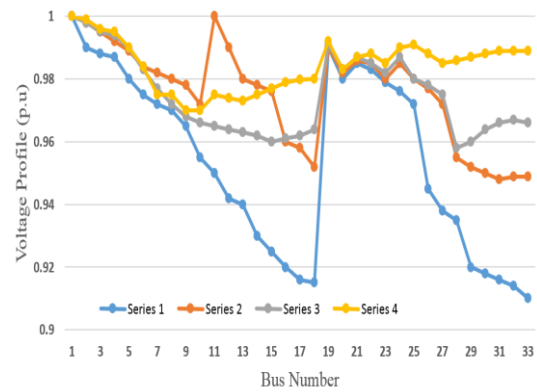


Figure 16. Voltage profile with 1,2,3,4 WT in mode 2

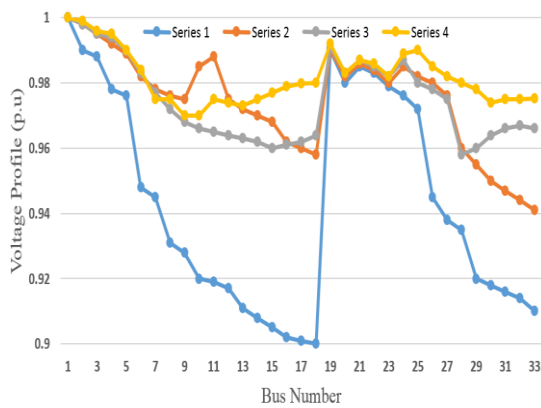


Figure 15. Voltage profile with 1-4 WT in mode 1

### 3. 4. Optimal Siting and Sizing of WTs with Considering LFL as a Main Technical Constraint

In this section optimal configuration of the WTs by solving benefit functions are done with considering LFL as a main technical constraint. Table 6 gives the obtained results.

Amount of achieved benefit functions are given in Table 7. As it is seen clearly, total achieved benefits by considering active power loss as a main technical constraint is more than others.

**3. 5. Employing AHP** Figure 17 illustrates the AHP technique to choose the best solution among the obtained solutions of several scenarios. By considering each of functions as a main technical constraint, all of plans and indices are given in Table 8. After employing AHP, the chosen plans for each of functions are plan 3, plan 2 and plan 5, respectively.

### 3. 6. Evaluating the Proposed VSI in the 118 Bus IEEE System

The IEEE 118 Bus Test Case represents a portion of the American Electric Power System (in the Midwestern US) (32) as shown in Figure 18. By employing the proposed VSI to this system, the minimum value is obtained 0.9521 p.u. Optimal site and size of WTs are obtained buses 12 and 110 with size 0.875 and 1.29 MW, respectively.

TABLE 4. Optimal results with considering active power loss as a main technical constraint

Scenario	Mode	Active Power	Active Power Loss Reduction	Minimum Voltage (p.u)	Optimum Siting and Sizing of WT (MW)	Optimum Power factor
1	Base mode	210.98	-	0.918(B18)	-	-
2	Mode 1	118	44.07	0.9038 (B18)	1.942(B8)	1.00
	Mode 2	83.13	60.6	0.9562 (B33)	1.941(B8)	0.87 (B8)
3	Mode 1	87.17	58.68	0.9670(B33)	0.857(B13)	1.00 (B13)
					1.204(B30)	1.00 (B30)
	Mode 2	40.91	80.6	0.9725(B33)	0.871(B16)	0.87 (B16)
					1.214(B30)	0.9 (B30)
4	Mode 1	80.66	61.77	0.9812 (B25)	0.811(B14)	1.00 (B25)
						1.00 (B31)
	Mode 2	28.83	86.33	0.96745 (B18)	0.749(B14)	0.88 (B14)
					0.879(B25)	0.92 (B25)
				0.408(B30)	0.89 (B31)	

**TABLE 5.** Optimal results with considering VSI as a main technical constraint

Senario	Mode	Active Power	Active Power Loss Reduction	Minimum Voltage (p.u)	Optimum Siting and Sizing of WT (MW)	Optimum Power factor
1	Base mode	210.98	-	0.918 (B18)	-	-
2	Mode 1	118	44.07	0.9038 (B18)	1.911 (B8)	1.00
	Mode 2	83.13	60.6	0.9562 (B33)	1.912 (B8)	0.86 (B8)
3	Mode 1	87.17	58.68	0.9670 (B33)	0.849 (B13)	1.00 (B13)
					1.151 (B30)	1.00 (B30)
	Mode 2	40.91	80.6	0.9725 (B33)	0.86 (B16)	0.85 (B16)
4	Mode 1	80.66	61.77	0.9812 (B25)	1.134 (B30)	0.9 (B30)
					0.728 (B14)	1.00 (B14)
					1.00 (B25)	1.00 (B25)
	Mode 2	28.83	86.33	0.96745 (B18)	0.733 (B14)	0.86 (B14)
					0.847 (B25)	0.9 (B25)
					0.378 (B30)	0.86 (B31)

**TABLE 6.** Optimal results with considering LFL as a main technical constraint

Senario	Mode	Active Power	Active Power Loss Reduction	Minimum Voltage (p.u)	Optimum Siting and Sizing of WT (MW)	Optimum Power factor
1	Base mode	210.98	-	0.9038 (B18)	-	-
2	Mode 1	112	46.67	0.9472 (B33)	1.911 (B8)	1.00
	Mode 2	82.15	60.89	0.9560 (B33)	1.912 (B8)	0.88 (B8)
3	Mode 1	85.41	59.33	0.9643 (B33)	0.849 (B13)	1.00 (B13)
					1.151 (B30)	1.00 (B30)
	Mode 2	39.62	81.13	0.9765 (B25)	0.862 (B16)	0.88 (B16)
4	Mode 1	79.74	62.03	0.95785 (B18)	1.134 (B30)	0.9 (B30)
					0.728 (B14)	1.00 (B14)
					1.00 (B25)	1.00 (B25)
	Mode 2	26.58	87.34	0.9795 (B30)	0.733 (B14)	0.87 (B14)
					0.856 (B25)	0.91 (B25)
					0.421 (B30)	0.88 (B31)

**TABLE 7.** Achieved benefits of different benefit functions with considering LFL as a main technical constraint

Benefits (*10 <sup>7</sup> \$)	Senario			
	1	2	3	4
The benefit of reducing dependency on upstream grid	1.015	1.023	1.038	1.075
The benefits of reducing reactive power loss	1.101	1.108	1.109	1.208
The benefit of reducing power loss	1.428	1.475	1.502	1.678
The benefit of improving voltage stability	1.243	1.305	1.375	1.457
Total benefit (\$)	1.578	1.605	1.642	1.708

#### 4. DISCUSSIONS

In this section the performance of the proposed VSI with two other VSIs is compared. Different VSIs are

determined in 33, 67 and 118 buses IEEE radial distribution system. As it seen from Table 9, the proposed VSI has an efficient role in the determining WT sizes in the improving voltage profile.

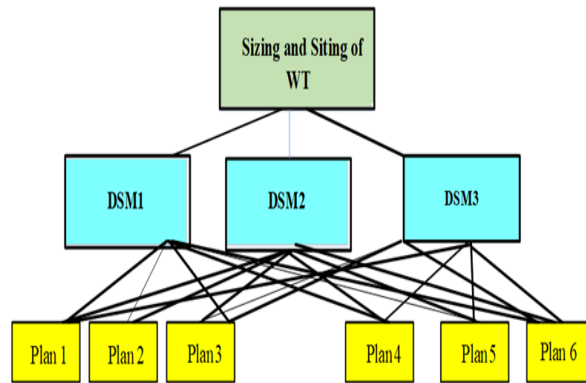


Figure 17. AHP technique with 6 plans

TABLE 8. Alternatives and indices of AHP

OF1= Power Loss Minimization			OF2= Voltage Profile Improvement			OF3= load flow limitation		
$P_{Loss}(x, u) = \sum_k  I_k ^2 R_k$			$VSI = \left[ 1 - \frac{4 \left( \frac{P_2^2 + Q_2}{Q_2} \right) X}{\left( \frac{P_2 \sin \delta V_1}{Q_2} - V_1 \cos \delta \right)^2} \right]$			$LFL = \text{Max} \left( \frac{S_{ij}}{CS_{ij}} \right)$		
Senario	Mode	Plans	Senario	Mode	Plans	Senario	Mode	Plans
2	Case-I	Plan 1	2	Case-I	Plan 7	2	Case-I	Plan 13
	Case-II	Plan 2		Case-II	Plan 8		Case-II	Plan 14
3	Case-I	Plan 3	3	Case-I	Plan 9	3	Case-I	Plan 15
	Case-II	Plan 4		Case-II	Plan 10		Case-II	Plan 16
4	Case-I	Plan 5	4	Case-I	Plan 11	4	Case-I	Plan 17
	Case-II	Plan 6		Case-II	Plan 12		Case-II	Plan 18

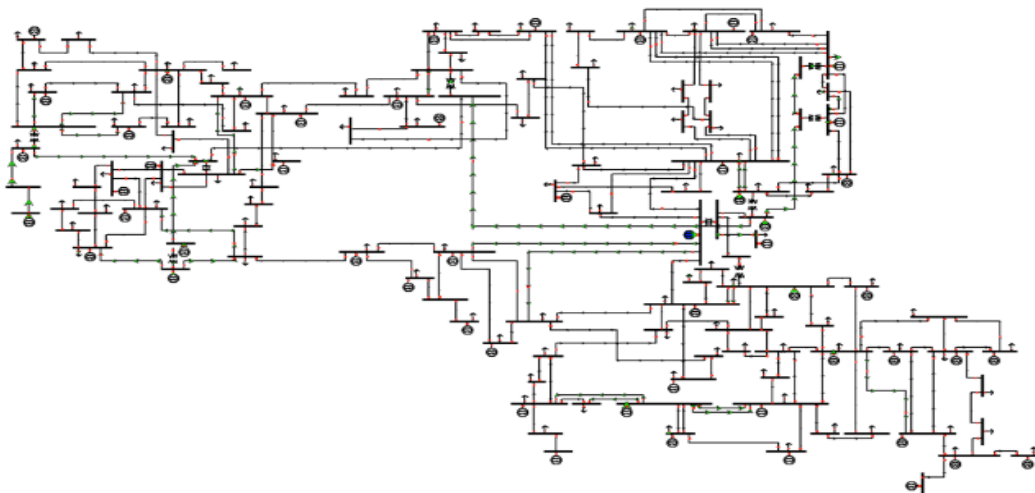


Figure 18. IEEE118 bus test system

Impacts of new VSI performance in improving voltage profile of constant, residential, commercial and industrial loads are shown in Figures 19-22.

It's obviously seen, presence of WT improve the value of nod's VSI in compared with base mode in the several types of load (commercial, industrial and

**TABLE 9.** Comparing different VSI with the proposed index

VSI	33 Bus	67 Bus	118 Bus
The proposed index	0.9725	0.9642	0.9521
$V_{Bus-min} = \max(1 - V_n)$	0.9652	114.3	95.9
$VSI_{(m2)} =  V_{(m1)} ^4 - 4\{P_{(m2)} \times (jj) - Q_{(m2)}r(jj)^2\} - 4\{P_{(m2)} \times r(jj) + Q_{(m2)} \times (jj)\} V_{(m1)} ^2$	0.9672	0.9601	0.9514
$LVSI = \frac{4RP_r}{V_2 \cos\theta - \delta \leq 1}$	0.9651	0.9589	0.9510
$LVSI = \frac{4(Vi Vj \cos\delta - Vj^2 \cos\delta^2)}{Vi^2}$	0.9430	0.9521	0.9641
$LVSI = \sqrt{\frac{V_i^2 - 2Z(Pr \cos\theta + Qr \sin\theta)}{2}}$	0.9285	0.9486	0.9514

residential). The value of minimum VSI in the industrial load is 1.01 in the bus 18 and that corresponding to the absence of WT is 0.8081. in the constant, residential and commercial loads, this value is determined, 1.015, 1.018 and 1.017, respectively.

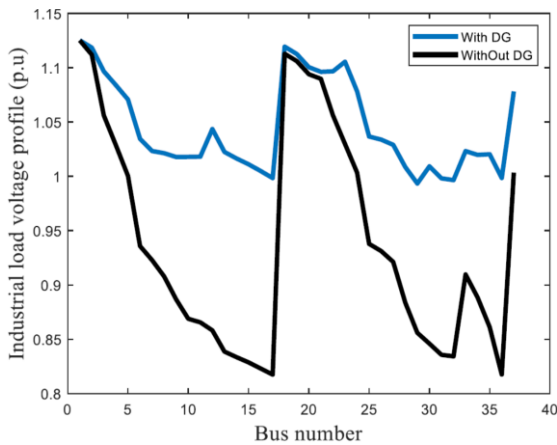


**Figure 19.** Impacts of the new VSI in improving voltage profile of Industrial load

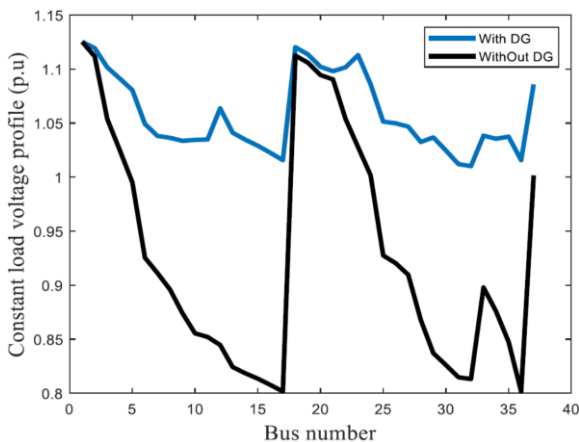


**Figure 20.** Impacts of the new VSI in improving voltage profile of constant load

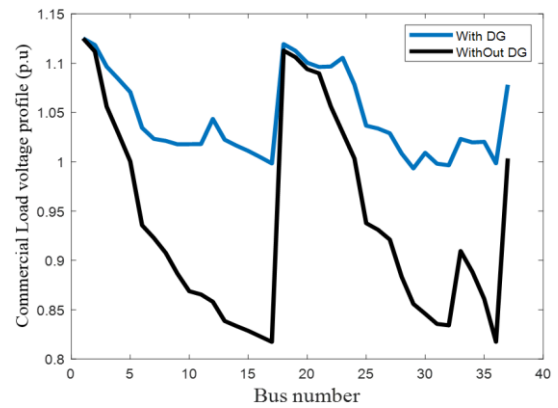


**Figure 21.** Impacts of the new VSI in improving voltage profile of commercial load

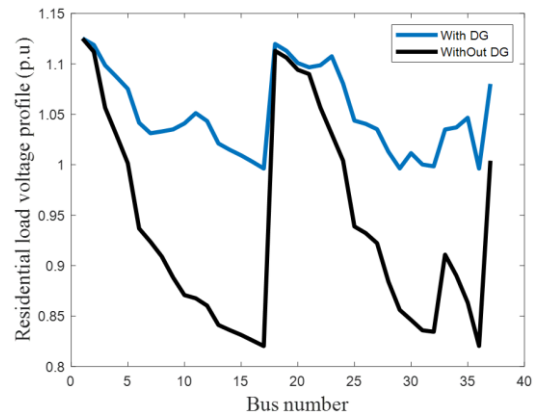


**Figure 22.** Impacts of the new VSI in improving voltage profile of residential load

### 5. CONCLUSION

In this paper new approach is introduced to calculate the voltage stability index under installing WT and in various operational conditions. Besides VSI, active and reactive power loss and voltage profile indices are used as technical constraints. Three main functions, which

include the positive effects of the presence of WT in improving technical constraints and maximizing benefits of the demand side, are defined as objective functions. By multiplying each function in the specified weight and assigning the weight with a high value to the critical technical constraint, the total benefit function is formed. Due to planning problem with the multi-criteria essence, the obtained results of the genetic algorithm (GA) are arranged by applying the AHP technique. Various scenarios are solved in two modes, unified and adjusted power factors. Results verified the efficiency and performance of the proposed GA-AHP optimization algorithm.

## 6. REFERENCES

- Farzinfar M, Jazaeri M. A novel methodology in optimal setting of directional fault current limiter and protection of the MG. *International Journal of Electrical Power & Energy Systems*. 2020;116:105564. 10.1016/j.ijepes.2019.105564
- Sundarajoo S, Soomro DM. Optimal Load Shedding for Voltage Collapse Prevention Following Overloads in Distribution System. *International Journal of Engineering, Transactions A: Basics*. 2023;36(7):1230-8. 10.5829/IJE.2023.36.07A.04
- Mobashsher MM, Keypour R, Savaghebi M. Distributed optimal voltage control in islanded microgrids. *International Transactions on Electrical Energy Systems*. 2021;31(11):e13045. 10.1002/2050-7038.13045
- Tooryan F, HassanzadehFard H, Collins ER, Jin S, Ramezani B. Optimization and energy management of distributed energy resources for a hybrid residential microgrid. *Journal of Energy Storage*. 2020;30:101556. 10.1016/j.est.2020.101556
- Yousefipour A, Rahmani A, Jahanshahi M. Improving the load balancing and dynamic placement of virtual machines in cloud computing using particle swarm optimization algorithm. *International Journal of Engineering, Transactions C: Aspects*. 2021;34(6):1419-29. 10.5829/IJE.2021.34.06C.05
- Wang G, Wang Q, Qiao Z, Wang J, Anderson S. Optimal planning of multi-micro grids based-on networks reliability. *Energy Reports*. 2020;6:1233-49. 10.1016/j.egy.2020.05.007
- Elmaadawy K, Kotb KM, Elkadeem M, Sharshir SW, Dán A, Moawad A, et al. Optimal sizing and techno-enviro-economic feasibility assessment of large-scale reverse osmosis desalination powered with hybrid renewable energy sources. *Energy Conversion and Management*. 2020;224:113377. 10.1016/j.enconman.2020.113377
- Mubaarak S, Zhang D, Wang L, Mohan M, Kumar PM, Li C, et al. Efficient photovoltaics-integrated hydrogen fuel cell-based hybrid system: Energy management and optimal configuration. *Journal of Renewable and Sustainable Energy*. 2021;13(1). 10.1063/1.5141932
- Mehranfar N, Hajiaghaei-Keshteli M, Fathollahi-Fard AM. A novel hybrid whale optimization algorithm to solve a production-distribution network problem considering carbon emissions. *International Journal of Engineering, Transactions C: Aspects*. 2019;32(12):1781-9. 10.5829/IJE.2019.32.12C.11
- Bujal NR, Sulaiman M, Abd Kadir AF, Khatib T, Eltawil N. A Comparison between GSA and IGSA for optimal allocation and sizing of dg and impact to voltage stability margin in electrical distribution system. *Journal of Electrical Engineering & Technology*. 2021;16:2949-66. 10.1007/s42835-021-00829-y
- Mastoi MS, Tahir M, Usman M, Wang D, Zhuang S, Hassan M. Research on power system transient stability with wind generation integration under fault condition to achieve economic benefits. *IET Power Electronics*. 2022;15(3):263-74. 10.1049/pe12.12228
- Azad S, Amiri MM, Heris MN, Mosallanejad A, Ameli MT. A novel analytical approach for optimal placement and sizing of distributed generations in radial electrical energy distribution systems. *Sustainability*. 2021;13(18):10224. 10.3390/su131810224
- Mirjalili S, Gandomi AH, Mirjalili SZ, Saremi S, Faris H, Mirjalili SM. Salp Swarm Algorithm: A bio-inspired optimizer for engineering design problems. *Advances in engineering software*. 2017;114:163-91. 10.1016/j.advengsoft.2017.07.002
- Barnwal AK, Yadav LK, Verma MK. A multi-objective approach for voltage stability enhancement and loss reduction under PQV and P buses through reconfiguration and distributed generation allocation. *IEEE Access*. 2022;10:16609-23. 10.1109/ACCESS.2022.3146333
- Nageswari D, Kalaiarasi N, Geethamahalakshmi G. Optimal Placement and Sizing of Distributed Generation Using Metaheuristic Algorithm. *Comput Syst Sci Eng*. 2022;41(2):493-509. 10.32604/csse.2022.020539
- Nafeh AA, Heikal A, El-Sehiemy RA, Salem WA. Intelligent fuzzy-based controllers for voltage stability enhancement of AC-DC micro-grid with D-STATCOM. *Alexandria Engineering Journal*. 2022;61(3):2260-93. 10.1016/j.aej.2021.07.012
- Onlam A, Yodphet D, Chatthaworn R, Surawanitkun C, Siritaratiwat A, Khunkitti P. Power loss minimization and voltage stability improvement in electrical distribution system via network reconfiguration and distributed generation placement using novel adaptive shuffled frogs leaping algorithm. *Energies*. 2019;12(3):553. 10.3390/en12030553
- Hamid ZA, Jipinus S, Musirin I, Othman MM, Salimin RH. Optimal sizing of distributed generation using firefly algorithm and loss sensitivity for voltage stability improvement. *Indonesian Journal of Electrical Engineering and Computer Science*. 2020;17(2):720-7. 10.11591/ijeecs.v17.i2.pp720-727
- Mehta P, Bhatt P, Pandya V. Optimal selection of distributed generating units and its placement for voltage stability enhancement and energy loss minimization. *Ain Shams Engineering Journal*. 2018;9(2):187-201. 10.1016/j.asej.2015.10.009
- Ahangar ARH, Gharehpetian GB, Baghaee HR. A review on intentional controlled islanding in smart power systems and generalized framework for ICI in microgrids. *International Journal of Electrical Power & Energy Systems*. 2020;118:105709. 10.1016/j.ijepes.2019.105709
- Guerrero JM, Loh PC, Lee T-L, Chandorkar M. Advanced control architectures for intelligent microgrids—Part II: Power quality, energy storage, and AC/DC microgrids. *IEEE Transactions on industrial electronics*. 2012;60(4):1263-70. 10.1109/TIE.2012.2196889
- Sundarajoo S, Soomro DM. Optimal Load Shedding for Voltage Collapse Prevention Following Overloads in Distribution System. *International Journal of Engineering*. 2023;36(7):1230-8. 10.5829/IJE.2023.36.07A.04
- Sadeghi SE, Akbari Foroud A. A general index for voltage stability assessment of power system. *International Transactions on Electrical Energy Systems*. 2021;31(12):e13155. doi.org/10.1002/2050-7038.13155
- Sadeghi SE, Akbari Foroud A. A new approach for static voltage stability assessment in distribution networks. *International Transactions on Electrical Energy Systems*. 2020;30(3):e12203. doi.org/10.1002/2050-7038.12203

25. Bai W, Abedi MR, Lee KY. Distributed generation system control strategies with PV and fuel cell in microgrid operation. *Control Engineering Practice*. 2016;53:184-93. 10.1016/j.conengprac.2016.02.002
26. Samadi A, Eriksson R, Söder L, Rawn BG, Boemer JC. Coordinated active power-dependent voltage regulation in distribution grids with PV systems. *IEEE Transactions on power delivery*. 2014;29(3):1454-64. 10.1109/TPWRD.2014.2298614
27. Jia H, Hou Q, Yong P, Liu Y, Zhang N, Liu D, et al. Voltage stability constrained operation optimization: An ensemble sparse oblique regression tree method. *IEEE Transactions on Power Systems*. 2023. <https://doi.org/10.1109/TPWRS.2023.3236164>
28. Kyomugisha R, Muriithi CM, Nyakoe GN. Performance of various voltage stability indices in a stochastic multiobjective optimal power flow using mayfly algorithm. *Journal of Electrical and Computer Engineering*. 2022;2022. 10.1155/2022/7456333
29. Mahmoud MM, Esmail YM, Atia BS, Kamel OM, AboRas KM, Bajaj M, et al. Voltage quality enhancement of low-voltage smart distribution system using robust and optimized DVR controllers: Application of the Harris hawks algorithm. *International Transactions on Electrical Energy Systems*. 2022;2022. 10.1155/2022/4242996
30. Li B, Hu K, Ma J, Xu S, He Y, Jiao H, et al. The new definitions of loss function for the model-based parameter identification method in power distribution network. *International Transactions on Electrical Energy Systems*. 2022;2022. 10.1155/2022/4197043
31. Hossen MD, Islam MF, Ishraque MF, Shezan SA, Arifuzzaman S. Design and implementation of a hybrid solar-wind-biomass renewable energy system considering meteorological conditions with the power system performances. *International journal of photoenergy*. 2022;2022. 10.1155/2022/8792732
32. Gupta SK. Mathematical Modeling and Analysis of Improved Grey Wolf Optimization Algorithm-Based Multi-Objective Power Flow Optimization for IEEE-118 Bus Test System. *Rivista Italiana di Filosofia Analitica Junior*. 2023;14(2):395-408. 10.52783/tjpt.v44.i2.139

## COPYRIGHTS

©2024 The author(s). This is an open access article distributed under the terms of the Creative Commons Attribution (CC BY 4.0), which permits unrestricted use, distribution, and reproduction in any medium, as long as the original authors and source are cited. No permission is required from the authors or the publishers.



## Persian Abstract

### چکیده

به طور کلی یک شبکه توزیع از ژنراتورها و زیرساخت‌های ارتباطی تشکیل می‌شود. امروزه با توجه به افزایش تقاضای بار و همچنین رشد تولیدات پراکنده، استفاده از این نوع ژنراتورها در شبکه توزیع شدت گرفته است. در مناطقی که سرعت وزش باد مناسب وجود داشته باشد، استفاده از توربین‌های بادی به عنوان یک گام هوشمند در شبکه توزیع تلقی می‌گردد. پایداری ولتاژ همواره به عنوان یک شاخصه اصلی جهت پایداری شبکه و پاسخ‌گویی به نیارهای مصرف‌کننده شناخته شده است. تاکنون شاخص‌های متعددی جهت ارزیابی پایداری ولتاژ معرفی شده است، با این حال هیچ کدام از این شاخص‌ها جواب بهینه‌ای ارائه نکرده‌اند. شاخص ارائه شده در این مقاله تلفات توان اکتیو، راکتیو و پایداری ولتاژ را به عنوان محدودیت‌های فنی مسئله بهینه‌سازی در خود جای داده است. به منظور بررسی تاثیر حضور توربین‌های بادی، مسئله بهینه‌سازی در دو حالت ضریب توان بار واحد و ضریب توان بار تلفیقی با بارهای خطی بررسی شده است. برای حل مسئله بهینه‌سازی از الگوریتم ژنتیک استفاده شده است و با استفاده از تکنیک AHP و در نظر گرفتن هر یک از محدودیت‌های فنی به عنوان معیار اصلی، جواب‌های به دست آمده مرتب می‌شوند. برای تأیید اثربخشی مثبت شاخص پیشنهادی، نتایج آن با نتایج سایر شاخص‌ها در شبکه توزیع شعاعی استاندارد 33-67 و 118 باس IEEE مقایسه شده است.



## Development of Green Product Processes in Textile Industry Using Mathematical Modeling and NSGA-II Metaheuristic Algorithm: A Case Study in Oyaz Industrial Group

Y. Bahrami Kian<sup>a</sup>, F. Harsej<sup>\*a</sup>, M. Molani Aghdam<sup>b</sup>, M. Sadeghpour<sup>c</sup>

<sup>a</sup> Department of Industrial Engineering, Faculty of Engineering, Nour Branch, Islamic Azad University, Nour, Iran

<sup>b</sup> Innovation and Management Research Center, Ayatollah Amoli Branch, Islamic Azad University, Amol, Iran

<sup>c</sup> Department of Industrial Engineering, Qaemshahr Branch, Islamic Azad University, Qaemshahr, Iran

### PAPER INFO

#### Paper history:

Received 05 August 2023

Received in revised form 25 October 2023

Accepted 30 October 2023

#### Keywords:

Green Product Development

Green Process

Mathematical Modeling

Textile Industry

Metaheuristic

NSGA-II Algorithm

### ABSTRACT

The development of green product processes is a strategic approach to minimize the impact of organizational supply chain on the environment while simultaneously expanding its economic performance. To achieve this task, it is crucial to emphasize aspects related to performance in optimizing resource utilization and implementing sustainability principles within an organizational domain. To this end, a multi-objective mixed-integer linear programming model is presented in this study with the objective of minimizing the production time of textiles, transportation costs, and inventory of the products, as well as minimizing the environmental effects of the processes of developing green products. In this model, the constraints and problem parameters are deterministic and solved using weighted sum methods, utilizing real data obtained from the "Oyaz" industrial group. By solving the model, an optimal combination for the values of the objective functions is obtained both collectively and separately. Furthermore, the capability of the proposed model is evaluated for solving large-scale instances using the NSGA-II algorithm. This metaheuristic method has demonstrated satisfactory capabilities compared to the mathematical model because of the slight difference in modeling errors while confirming the accuracy of the developed mathematical model, proving the accuracy and efficiency of the NSGA-II algorithm. Consequently, the sensitivity analysis examines the influence of changing key parameters, such as the maximum storage capacity of production centers, on the decisions of the proposed model. This parameter change is determined through consultation with experts in the textile field. Based on the results obtained, changing the maximum storage capacity has a considerable impact on fibers and cotton. Additionally, if the capacity is changed to the maximum possible value, it has the greatest impact on the purifiers.

doi: 10.5829/ije.2024.37.04a.12

## 1. INTRODUCTION

Global competition in an ever-changing environment has led organizations to recognize the importance of flexibility and demonstrate thoughtful and timely responses (1). In order to survive nowadays, organizations need to globalize and have a presence in this vast arena, even if they aim to have a national or regional presence, they must think globally (2). Therefore, considering green product design is of great importance and became a key issue in both industry and

commerce. Green product design means creating products that have a smaller impact on the environment and natural resources throughout their life cycle (3). Furthermore, green product design should strive to reduce the consumption of natural resources, energy, and water during production, use, and disposal. This includes the use of recycled materials, optimization of the production process, and increased energy efficiency (4). In addition, green product design should contribute to the preservation and protection of the environment and prevent air, water, and soil pollution. This includes

\*Corresponding Author Email: [dr.harsej75@gmail.com](mailto:dr.harsej75@gmail.com) (F. Harsej)

reducing the emission of greenhouse gases, using clean technologies, and proper waste management. In addition to environmental considerations, green product design can have an impact on economic and social aspects. For example, green product design can help increase the efficiency and profitability of businesses (5). Green products can lead to cost savings and increase competitiveness due to the reduction of resource consumption, production and maintenance costs, and improve efficiency. Additionally, green products can have a positive impact on society and contribute to the health and well-being of individuals (6). This includes using materials harmless to human health, designing recyclable products, and reducing product hazards for users. Therefore, green product design considers a proper combination of environmental, economic, and social factors, ultimately benefiting both society and the environment. With the changes in climate and the need for global sustainability, the importance of focusing on green product design is increasing day by day (7).

Mathematical modeling is a powerful tool for developing green product processes in the textile industry, which has various benefits. For example, mathematical modeling helps optimize green product manufacturing processes in the textile industry and minimize resource consumption including water, energy, and recycled materials (8). By optimizing resource consumption, the textile industry can increase its green and sustainable achievements while reducing production costs. Furthermore, it can identify important features and factors that affect product quality and aim to improve it (9). By improving product quality, the textile industry can increase customer satisfaction and enhance its competitiveness in the market (10). Mathematical modeling also helps the textile industry identify and manage various risks associated with green product activities (11). Using mathematical modeling, the effects of changes in different conditions can be simulated, and appropriate solutions for risk management can be provided. Moreover, mathematical modeling assists the textile industry in improving decision-making processes (12). With the use of mathematical modeling, complex problems in this industry can be analyzed, and optimal solutions can be proposed. Considering these benefits, mathematical modeling can significantly contribute to the development of green product processes in the textile industry, as well as environmental sustainability and the improvement of performance in the textile industry (13).

Based on the information mentioned above, the main objective of this research is to provide a mathematical model for optimizing cost and time in the process of developing green products in the textile industry, particularly in Oyaz industrial group. Therefore, the most significant contribution of this research is to propose a multi-objective linear programming model with the aim of minimizing time, cost, and the environmental impacts

of the process of developing green products in the textile industry. In this model, the constraints and problem parameters are deterministic and have been solved using the weighted sum method. Since the model may encounter disruptions in dealing with large-scale issues, metaheuristic methods have been used to cope with this situation.

The remainder of the article is organized in as follows: In second section, a literature review of previous research has been provided. In the third section, mathematical modeling and a metaheuristic approach to solving the problem are demonstrated. In the fourth section, the results of applying the problem to a case study of Oyaz industrial group are presented. Finally, in the fifth section, a general conclusion is provided along with recommendations for future research.

## 2. LITERATURE REVIEW

In this section of research, we have focused on reviewing past studies on the development of Green Product Processes. To this end, Zindani et al. (14) have presented a decision-making framework that makes decisions by modeling the settings of experts using fuzzy sets in a fuzzy environment. This proposed decision-making framework has been examined for identifying the optimal set of process parameters (weight percentage and duration of chemical purification) according to technical, environmental, and economic conditions. The validity, accuracy, and robustness of the ranking have been evaluated through sensitivity analysis and solving previous case studies. This decision-making framework provides a tool for inferring a set of desirable parameters for green composites from agricultural waste, which can be used to examine the possibilities of designing green products and ultimately achieving sustainable goals. Barros(15) investigated the relationship between the circular economy and sustainable jobs in a systematic study and identified the drivers involved.

These drivers include strategic planning, cost management, circular supply chain management, quality management, environmental management, process management, logistics and reverse logistics, service management, and research and development. In addition, the key impact of changes in product development by the circular economy, which helps management achieve greater business sustainability, was presented. Based on the results obtained, adopting a circular economy-based mindset may enable the achievement of sustainable results. Kong and Liu (16) created a new system to justify economic, environmental, and social indicators in their study. According to the evaluation framework, a directed distance function based on the measurement model has been adopted to measure the sustainability of port cities in terms of external impact and internal interaction. For

this purpose, nine port cities in China have been selected as the research domain. Lavuri et al. (17) conducted a study on green factors influencing the purchase of organic products (implication of sustainable development). In this research, they created consumer orientation towards environmentally friendly products, which is considered a social challenge, in the natural components of their products. Furthermore, this study examined how green factors influence customers' intention to purchase organic products. They demonstrated that the mediating role of trust and attitude is crucial in ensuring customers' sustainable orientation towards organic products. Dzikriansyah et al. (18) have addressed the role of green supply chain management practices on environmental performance in small and medium-sized companies in Indonesia in this article. The results indicate that internal factors such as strategic orientation and internal environmental management do not drive companies to consider green supply chain management. Among these, external factors, such as government regulations, play a significant role in adopting green supply chain management. Furthermore, it demonstrates that adopting green supply chain management influences the environmental performance of companies. The findings also establish that internal factors have no impact on environmental performance through green supply chain management. Chakraborty et al. (19) examined the internal factors related to the green supply chain using a structural interpretive modeling approach. In this study, eight factors have been identified that can be controlled within the organization. Among these eight factors, senior management commitment is the most important factor for the highest driving force. The reverse logistics process comes next, followed by storage and materials management at a high level. Soufi et al. (20) have examined the factors influencing the green supply chain in the construction industry of Iran in this study. For this purpose, a descriptive and applied method has been used in this research. The participating experts in the study are senior managers of the construction sector in the municipality of Rasht, Iran, who have relevant academic qualifications and suitable experiences in urban and industrial construction. The experts participated in both qualitative and quantitative stages of the research, which involved examining the factors extracted from the literature and ranking them in ascending order. In the quantitative stage, the step-wise weight assessment ratio analysis (SWARA) was conducted as a new multi-criteria decision-making method to evaluate the drivers of green supply chain acceptance using MATLAB software. Yousof et al. (21) have investigated the mediating roles influencing the green supply chain in relation to environmental sustainability and environmental performance for small companies. The results of this research are useful for managers who intend to manage their companies

sustainably, as they need to understand the mediating roles influencing green supply chains. Wu et al. (22) presented a green supply chain model composed of a capital-constrained manufacturer and a retailer to study the impact of the application of blockchain technology on the manufacturer's financing strategy. Zhu et al. (23) introduced a green sensitivity into the green supply chain system and establish an evolutionary game model between enterprises and consumers. Abbas et al. (24) investigated the complex association that exists between information technology capabilities, green supply chain integration and green innovation on organizational performance in the manufacturing industry. Yang et al. (25) proposed a green product supply chain comprising one dominant manufacturer and one retailer, where the manufacturer can invest to improve a product's green level, and the retailer can make regular-sale promotional efforts.

Based on the accepted reviews in theoretical and empirical studies, a research gap has been observed in the field of providing a mathematical model for optimizing the green product development process, which has not been addressed so far. Therefore, the innovation and contribution of this research are as follows:

1. Simultaneous consideration of cost and time in the green product development process using multi-objective mathematical modeling.
2. Providing a comprehensive model for green product development by formulating its flow through mathematical programming.
3. Utilizing metaheuristic methods to solve the proposed model in large computational dimensions.

Table 1 categorized the literature review related to this work.

**TABLE 1.** Literature review

References	Research objective			
	Cost	Time	Environment	Competitive Advantage
[14]	*	*		
[15]		*	*	
[16]			*	*
[17]	*			*
[18]		*	*	
[19]	*	*	*	
[20]				*
[21]		*	*	
[22]	*			*
[23]		*	*	
[24]	*			*
[25]		*	*	*
Current research	*	*	*	*

### 3. RESEARCH METHODOLOGY

In the present research, a multi-objective model has been proposed for green product production in the textile industry for producing decorative fabrics. The components of this model include manufacturer, supplier, and consumer. As evident from the mentioned components, a green supply chain network has been considered in which the manufacturer is obliged to use environmentally friendly materials such as cotton, hemp, and bamboo in the production of decorative fabrics, as well as controlling chemical wastewater discharge to the environment. Therefore, in this research, we intend to design and optimize a logistics network to save costs in transportation and inventory while considering environmental factors for a decorative fabric manufacturer in the production and supply of green products. In fact, we aim to provide strategic planning for the supply chain from production to distribution of textile products in the form of a network. Figure 1 illustrates the green product production chain.

**3.1. Mathematical Modeling** In this section, all the symbols used to describe sets, parameters, and variables of the problem are explained in Table 2.

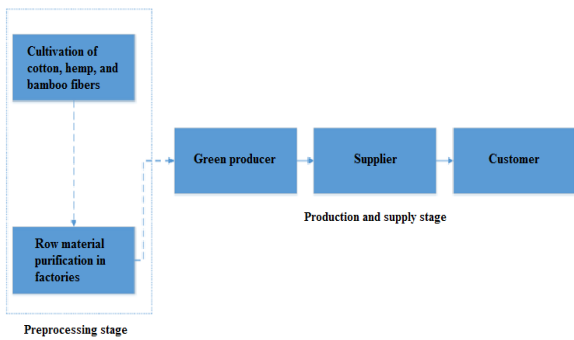


Figure 1. Supply Chain Structure

TABLE 2. Notation for Sets and Indices in the Mathematical Model

Sets	
Symbol	Explanation
$I$	Set of fields required for the production of environmentally friendly raw materials (cotton, hemp, and bamboo) $1, \dots, I$
$J$	Set of purifiers in factories $1, \dots, J$
$P$	Set of environmentally friendly raw materials $1, \dots, P$
$T$	Set of periods $1, \dots, T$
$D$	Set of suppliers $1, \dots, D$
$S$	Set of storage warehouses $1, \dots, S$
$C$	Set of consumers $1, \dots, C$
$H$	Set of factories $1, \dots, H$

Indices	
$i \in I$	Index related to the set of fields
$j \in J$	Set of purifiers
$p \in P$	Set of raw materials
$t \in T$	Set of periods
$d \in D$	Set of suppliers
$s \in S$	Set of storage warehouses
$c \in C$	Set of consumers
$h \in H$	Set of factories

TABLE 3. Notation for Parameters and Variables of the Mathematical Model.

Parameters	
Symbol	Explanation
$capacity_i$	Maximum capacity of field "i"
$Cx_{ijt}$	Cost of transferring raw materials from the field "i" to purifier "j" at time "t"
$Cyj_{jhpt}$	Cost of transferring raw materials from purifier "j" to factory "h" at time "t"
$Cyd_{dcpt}$	Cost of transferring decorative textiles from supplier "d" to consumer at the time "t"
$Cyh_{hdpt}$	Cost of transferring decorative textiles from manufacturer "h" to supplier at the time "t"
$Cds_{dst}$	Cost of transferring textiles from distributor "d" to warehouse "s"
$Csd_{sdt}$	Cost of transferring textiles from warehouse "s" to distributor "d"
$\gamma ds_{dst}$	Percentage of transfer of textiles from distributor "d" to warehouse "s"
$\gamma sd_{sdt}$	Percentage of transfer of textiles from warehouse "s" to distributor "d"
$CI_{jt}$	Cost of importing raw materials to purification center "j" at time "t"
$CIc_{cpt}$	Cost of consuming textiles at consumer centers "c" at the time "t"
$CI d_{dtp}$	Cost of consuming textiles at distribution centers "d" at the time "t"
$CIh_{hpt}$	Cost of consuming raw materials at production centers "h" at the time "t"
$\lambda_{ip}$	Percentage of product quantity "p" (environmentally friendly raw materials) from the input of field "i"
$Dh_{hpt}$	The demand of factory centers "h" for environmentally friendly raw materials "p" in period "t"
$CIhm_{im,h,t}$	Cost of transferring raw materials from import centers "i <sub>m</sub> " to production center "h" at the time "t"
$CI'_{jt}$	Cost of purchasing imported materials to purification center "j" at the time "t"
$CIh'_{hpt}$	Cost of textile production at production centers "h" at the time "t"

Variables	
$x_{ijt}$	The amount of transfer of raw materials from the field "i" to purifier "j" at time "t"
$yh_{jhpt}$	The amount of transfer of organic cotton from purifier "j" to manufacturer "h" at time "t"
$y'h_{jhpt}$	The amount of transfer of hemp from purifier "j" to manufacturer "h" at time "t"
$y''h_{jhpt}$	The amount of transfer of bamboo from purifier "j" to manufacturer "h" at time "t"
$ds_{dst}$	The amount of transfer of textiles from distributor "d" to warehouses.
$sd_{sdt}$	The amount of transfer of textiles from warehouse "s" to distributor "d"
$II_{jt}$	The inventory level of imported raw materials from the field to purification center "j" at time "t"
$Id_{dtp}$	The inventory level of textiles in distribution centers "d" at time "t"

$Ih_{hpt}$	The inventory level of textiles in refinery centers "h" at the time "t"
$Ic_{cpt}$	The inventory level of textiles in warehouse centers "s" for consumption at the time "t"
$II'_{jt}$	The amount of purchased raw materials for purification center "j" at time "t"
$Ih'_{hpt}$	The production quantity of textiles in production centers "h" at time "t"
$Ihm_{im,hpt}$	The amount of imported raw materials from import centers "i <sub>m</sub> " to production center "h" at the time "t"
$tx_{hpt}$	The duration of textiles manufacturing in the factory.

### 3. 1. 1. Objective Function and Constraints

Taking the above factors into consideration, a mathematical model of linear programming has been developed in a deterministic form to represent the mathematical modeling of the problem in the following equations.

$$\begin{aligned}
 A = & \sum_{i \in I} \sum_{j \in J} \sum_{t \in T} x_{ijt} \cdot Cx_{ijt} + \sum_{j \in J} \sum_{d \in D} \sum_{p \in P} \sum_{t \in T} (yh_{jhpt} + y'h_{jhpt} + y''h_{jhpt}) \cdot Cy^j_{jhpt} \\
 & + \sum_{j \in J} \sum_{d \in D} \sum_{p \in P} \sum_{t \in T} (yh_{jhpt} + y'h_{jhpt} + y''h_{jhpt}) \cdot Cyh_{hdpt} + \sum_{j \in J} \sum_{d \in D} \sum_{p \in P} \sum_{t \in T} (yh_{jhpt} + y'h_{jhpt} + y''h_{jhpt}) \cdot Cyd_{dcpt} \\
 & + \sum_{j \in J} \sum_{c \in C} \sum_{p \in P} \sum_{t \in T} ds_{dst} \cdot Cds_{dst} + \sum_{j \in J} \sum_{c \in C} \sum_{p \in P} \sum_{t \in T} sd_{sdt} \cdot Csd_{sdt}
 \end{aligned} \tag{1}$$

$$\begin{aligned}
 B = & \sum_{j \in J} \sum_{t \in T} CI'_{jt} \cdot II'_{jt} + \sum_{j \in J} \sum_{t \in T} CI_{jt} \cdot II_{jt} + \sum_{h \in H} \sum_{t \in T} \sum_{p \in P} CIh'_{hpt} \cdot Ih'_{hpt} + \sum_{c \in C} \sum_{t \in T} \sum_{p \in P} CIc_{cpt} \cdot Ic_{cpt} \\
 & + \sum_{d \in D} \sum_{t \in T} \sum_{p \in P} Id_{dtp} \cdot CId_{dtp} + \sum_{h \in H} \sum_{t \in T} \sum_{p \in P} Ih_{hpt} \cdot CIh_{hpt} + \sum_{h \in H} \sum_{t \in T} \sum_{p \in P} CIh_{im,hpt} \cdot Ih_{im,hpt}
 \end{aligned} \tag{2}$$

$$\begin{aligned}
 C = & \sum_{i \in I} \sum_{p \in P} \lambda_{cp} \cdot (yh_{jhpt} + y'h_{jhpt} + y''h_{jhpt}) + \gamma_{sdt} \cdot (\sum_{j \in J} \sum_{t \in T} CI'_{jt} \cdot II'_{jt} + \sum_{j \in J} \sum_{t \in T} CI_{jt} \cdot II_{jt}) \\
 & + \sum_{h \in H} \sum_{t \in T} \sum_{p \in P} CIh'_{hpt} \cdot Ih'_{hpt} + \sum_{c \in C} \sum_{t \in T} \sum_{p \in P} CIc_{cpt} \cdot Ic_{cpt} + \sum_{h \in H} \sum_{t \in T} \sum_{p \in P} Ih_{hpt} \cdot CIh_{hpt} + \sum_{h \in H} \sum_{t \in T} \sum_{p \in P} CIh_{im,hpt} \cdot Ih_{im,hpt}
 \end{aligned} \tag{3}$$

$$D = \gamma_{dst} \cdot (\sum_{d \in D} \sum_{t \in T} \sum_{p \in P} Id_{dtp} \cdot CId_{dtp}) \tag{4}$$

$$F = tx_{hpt} \cdot (\sum_{h \in H} \sum_{t \in T} \sum_{p \in P} Dh_{hpt}) \tag{5}$$

Equation 1 calculates the cost of transferring raw materials and decorative textiles. For this purpose, it calculates the costs of transferring from the purification center to the factory, from the factory to the supplier, and then from the supplier to the consumer. It also takes into account the costs of transferring from the warehouse to the manufacturer and the supplier. Equation 2 calculates the inventory cost of decorative textiles. To this end, the inventory of raw materials for entering the purification center, as well as the inventory of the factory warehouse, and then the inventory of the supplier's warehouse is

calculated. Equation 3 calculates the level of environmental pollution in production centers. Equation 4 calculates the level of environmental pollution in distribution centers. In addition, in Equation 5, the duration of textile production is considered. In general, the objective functions considered in mathematical modeling in this study are expressed as transportation costs of textiles (A) and inventory costs (B). Additionally, the level of environmental pollution in production centers (C) the level of environmental pollution in distribution centers (D), and the duration of

textile production (F). To overcome the weaknesses of methods when the number of objectives exceeds two, considering the homogeneity of some objectives with each other such as objectives (A), (B), (C), and (D), the sum of these objectives is considered as the final goal, and the problem is transformed into a three-objective

$$\sum_{j \in J} x_{ijt} \leq \text{capacity}_i \quad \forall i \in I, t \in T \quad (6)$$

$$I_{jt} = I_{j,t-1} + \sum_{i \in I} x_{ijt} - \sum_{i \in I} \sum_{p2 \in P} y_{jhpt} - \sum_{c \in C} \sum_{p1 \in P} y_{jhpt}' - \sum_{h \in H} \sum_{p3 \in P} y_{jhpt}'' \quad \forall i \in I, t \in T \quad (7)$$

$$\sum_{i \in I} \sum_{p \in P} (y_{jhpt} + y_{jhpt}' + y_{jhpt}'') \leq \sum_{i \in I} \lambda_{ip} x_{ijt} \quad \forall j \in J, t \in T, p2 \in P \quad (8)$$

$$\sum_{i \in I} \lambda_{ip} x_{ijt} \geq D_{htp} \quad \forall j \in J, t \in T, p3 \in P \quad (9)$$

$$I_{dtp} = \sum_{s \in S} \gamma_{sd} s_{st} - \sum_{s \in S} \gamma_{ds} s_{st} \quad \forall d \in D, t \in T, p2 \in P \quad (10)$$

$$I_{h_{htp}} = I_{h_{h,t-1,p}} + \sum_{h \in H} \sum_{t \in T} I_{hm_{im,ht}} \quad \forall d \in D, t \in T, p2 \in P \quad (11)$$

Constraint 6 ensures that the maximum amount sent from the field to the purifiers is considered. Constraint 7 indicates the inventory level of raw material input from the purifiers. Constraint 8 guarantees that the amount of raw materials to be sent from purifiers "j" to manufacturers should not exceed the maximum desired input of the processed product. Constraint 9 ensures that the quantity of produced textiles to be sent to other distributors meets the required demand for the desired product. Constraint 10 calculates the quantity of textiles available at distribution centers. In constraint 11, the quantity of produced textiles available for supply centers is calculated.

**3.2. Solution Approach: NSGA-II** In this paper, the NSGA-II metaheuristic algorithm has been used to solve the model. One of the positive aspects of this algorithm is that, unlike some other algorithms that only search the solution space in one direction, it simultaneously searches for solutions in multiple directions (24). Another positive feature of this algorithm is its lack of dependence on the continuity and convexity of the objective function. The performance of the NSGA-II algorithm is described below according to the semicode.

//Start

**Step 1:** Generate an initial population

**Begin loop** /\* Loop until a termination condition is met\*/

**Step 2:** Evaluate the fitness of a subset of individuals from the population

problem. Given the mentioned cases above, the sum of Equations 1 and 2 is considered F1, the sum of Equations 3 and 4 is considered F2 and the final objective function is  $E = 0.33 * F1 + 0.33 * F2 + 0.33F$ .

**Step 3:** Select pairs of the fittest individuals for reproduction

**Step 4:** Create offspring using a crossover operator

**Step 5:** Introduce genetic variation in the offspring using a mutation operator

**Step 6:** Replace some of the least fit individuals in the current population with the new offspring

**End loop**

**Finish//.**

Also, the flowchart for its implementation is shown in Figure 2.

## 4. FINDINGS

**4.1. Case Study: Oyaz Textile Group** Jahan Orum Oyaz Company, in the textile industry of the country, was established in 2018 as a young but rich and prosperous company, benefiting from the valuable experience of more than 23 years of continuous presence and activity in the country's textile industry. With relentless efforts and the collaboration of experienced and creative entrepreneurs, relying on their long and valuable experience and private sector investment, the factory of this company was established at the beginning of the road, utilizing the maximum long-term experiences of the board of directors and investors and with sufficient knowledge of the characteristics and conditions of domestic and regional markets. It covers an area of 45,500 square meters and has a nominal production capacity of 33 million and 600 thousand

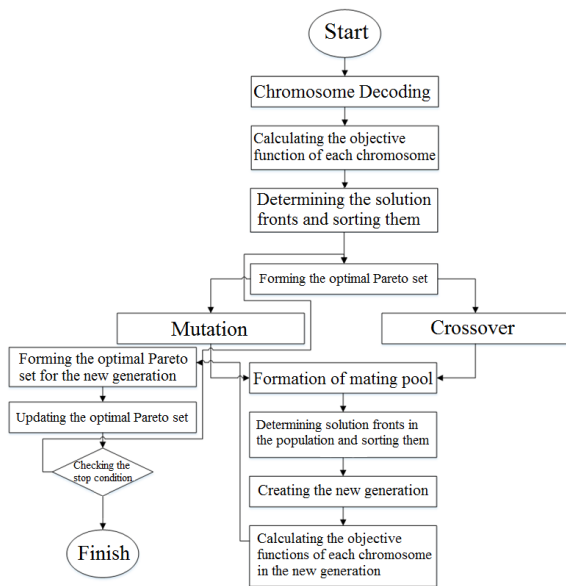


Figure 2. Flowchart of the NSGA-II Algorithm Execution

square meters. After 18 months of construction, it became operational to make positive and effective contributions towards the development of the country and the realization of the valuable aspirations of the esteemed Supreme Leader, including production growth and support for Iranian labor and capital.

Jahan Orum Oyaz is proud to have successfully prevented the outflow of 50 million dollars in currency through its dynamic investments and become a successful regional and global business. In doing so, it contributes to improving the economic indicators of our beloved country, such as Gross Domestic Product and employment. The textile industry is considered one of the most environmentally hazardous industries in the world. Environmental issues arise during certain production processes in the textile industry and directly affect the final product.

**4. 2. Practical Numerical Results** In this section, by considering the specified items in Table 3 as predetermined parameters of the programmed optimization problem for controlling the considered parameters, it is calculated in a small-scale problem as indicated below. The mentioned problem has been executed using GAMS software for the values of the sets specified in Table 4. The feasibility of this problem in this section has been demonstrated by determining a set of solutions based on solving the model in this way.

In this case, the cost of transferring raw materials from the field "i" to purifier "j" at the time "t" ( $x_{ijt}$ ) is calculated according to Table 5.

Based on the calculated results, the total amount of raw material transfer costs, including (fibers, cotton, hemp, and bamboo) is shown in Table 5. The cost of

TABLE 4. Defined Sets for the Problem in Small-Scale

Defined Sets	Value
Field sets for raw material production	$i_1; i_2; i_3$
Purification sets in factories	$j_1; j_2$
Environmentally friendly raw material sets	Cotton, fiber, hemp, and bamboo
Time periods	$t_1; t_2; t_3$
Factories	$h_1; h_2$
Distributors	$d_1; d_2; d_3$
Warehouses	$s_1; s_2$

transferring raw materials from field "i<sub>1</sub>" to the first purification center is zero in the first period. Additionally, this value is zero from the second and third centers to the first and second purification centers in all periods. Furthermore, the highest amount of fluid transfer in the third period from the first field to the first center is equal to 106.080. Moreover, Table 6 displays the inventory value of raw materials transferred from the field to purification center "j" at time "t" ( $II_{jt}$ ).

Based on the results obtained, the value of ( $II_{jt}$ ) indicates that the inventory of raw materials, (including cotton, hemp, flax, and bamboo) entering both purification centers in the first period is equal to zero. Furthermore, the inventory of the purification center in the second period is also equal to zero. In contrast, the inventory of the purification center in the third period is 20.749, which is the highest inventory value during the period. In Table 7, the transfer values of organic cotton from purification center "j" to manufacturer "h" at the time "t" is represented as the variable ( $y_{jhpt}$ ). The transfer value of hemp from purification center "j" to the manufacturer at the time "t" is represented by a variable ( $y'_{jhpt}$ ). Similarly, the transfer value of bamboo from the

TABLE 5. Optimal Value of  $x_{ijt}$

To / From	$j_1$			$j_2$		
	First Period	Second Period	Third Period	First Period	Second Period	Third Period
$i_1$	0	71.489	106.080	85.355	76.101	18.449
$i_2$	0	0	0	0	0	0
$i_3$	0	0	0	0	0	0

TABLE 6. Values of  $II_{jt}$

Purification Center	First Period	Second Period	Third Period
$j_1$	0	0	20.749
$j_2$	0	7.906	13.601

purification center "j" to the manufacturer "h" at time "t" is represented by variable ( $y''h_{jhpt}$ ). Additionally, the transfer value of fibers from the purification center "j" to manufacturer "h" at time "t" is represented by variable ( $y'''h_{jhpt}$ ).

The amount of raw materials from the import centers ( $i_m$ ) to the production center "h" at the time (t), denoted as ( $im_{imdt}$ ), is according to Table 8.

According to the calculated results, the amount of imported raw materials to the first and second factories in the second period is zero. Furthermore, the amount of imported raw materials sent to the first and second factories in the first period have the highest quantity among them, with the highest entry of raw materials from the import section related to the first factory in this

period, which is equal to 55.886. Finally, in Table 9, the values of transferring textiles from the warehouse "s" to the distributor "d", ( $sd_{sdt}$ ), are shown.

By calculating the values above, the value of the objective function is determined according to Table 10. Considering that the problem in this dissertation is multi-objective, it has been calculated using the weighted sum method. The optimum value of the objective function depends on the weights assigned to the objective functions. Since the form of the objective function in the weighted sum problem is represented as ( $w_1f_1 + w_2f_2 + w_3f_3$ ) and the sum of weights is equal to one ( $\sum w_i = 1$ ), different combinations of coefficients can be considered, as shown in Table 9.

TABLE 7. Optimal Values of  $yh_{jhpt}$ ,  $y'h_{jhpt}$ ,  $y''h_{jhpt}$ ,  $y'''h_{jhpt}$ .

Raw Materials	To From	First Period		Second Period		Third Period	
		$h_1$	$h_2$	$h_1$	$h_2$	$h_1$	$h_2$
$(yh_{jhpt})$	$j_1$	0	0	22	0.070	0	12
	$j_2$	7	19.342	0	15.577	0	0
$(y'h_{jhpt})$	$j_1$	0	15	22	0.863	0	14
	$j_2$	7	16.324	0	15.577	0	0
$(y''h_{jhpt})$	$j_1$	0	10.214	22	0.070	0	12
	$j_2$	9	17.247	0	17.542	0	0
$(y'''h_{jhpt})$	$j_1$	0	0	28	0.956	0	24
	$j_2$	5	12.254	0	19.247	0	0

TABLE 8. Values of  $ihm_{imdt}$

from-to	First Period	Second Period	Third Period
$i_1 \rightarrow h_1$	55.886	0	48.150
$i_1 \rightarrow h_2$	51.886	0	9.150
$i_2 \rightarrow h_1$	0	0	0
$i_2 \rightarrow h_2$	39.902	0	0

TABLE 9. Values of  $sd_{sdt}$

from-to	First Period	Second Period	Third Period
$s_1 \rightarrow d_1$	0	0	0
$s_1 \rightarrow d_2$	0	0	0
$s_1 \rightarrow d_3$	0	0	0
$s_2 \rightarrow d_1$	112.960	0	0
$s_2 \rightarrow d_2$	86.760	0	0
$s_2 \rightarrow d_3$	234.104	0	0

TABLE 10. Examination of the Value of the Objective Function for Different Weights

Raw	$w_1$	$w_2$	$w_3$	Value of the Objective function
1	0.1	0.7	0.2	35996.988
2	0.2	0.7	0.1	57969.729
3	0.3	0.5	0.2	76014.309
4	0.5	0.4	0.1	92482.238
5	0.3	0.2	0.5	108570.220
6	0.6	0.2	0.2	12815.680
7	0.7	0.1	0.2	134993.518
8	0.2	0.4	0.4	128171.356
9	0.5	0.3	0.2	161349.194

Based on the obtained results, it can be observed that the value of the objective function is strongly dependent on the weight of the first objective. With an increase in its value, the objective function also increases. On the other hand, the higher the weight of the second objective function, the lower the value of the objective function.

**4. 3. Tuning Parameters of NSGA-II** In order to design experiments in the NSGA-II algorithm, initially, three different levels are defined for its parameters (low with code 1, medium with code 2, and high with code 3). Then, pre-defined experiments in this algorithm are executed for all possible combinations. The suggested values for the parameters of this algorithm are according to Table 11.

Then, using the L9 design, various experiments were conducted on Taguchi and each one was executed with the NSGA-II algorithm. The results of the execution are presented in Table 12. In this table, all possible cases are shown for different levels considered for the factors of the NSGA-II algorithm. For example, in the first experiment, all factors participate at their lowest level. In the second experiment, the factor "PS" is at its lowest level, while other factors are at their average level. Similarly, other possible cases are completed based on the permutation rule in the statistics. By running each

**TABLE 11.** Parameters and Their Levels for the NSGA-II Algorithm

Parameters	Values of Each Level		
	Level 1	Level 2	Level 3
Population size (PS)	50	100	200
Crossover rate (CR)	0.5	0.7	0.9
Mutation rate (MR)	0.2	0.3	0.5
Maximum iterations (Max_iter)	100	150	200

**TABLE 12.** Variable Response Values in the Taguchi design

Execution Number	Parameters of the Algorithm				MID index
	Max_iter	MR	CR	PS	
1	1	1	1	1	0.543
2	2	2	2	1	0.612
3	3	3	3	1	0.537
4	3	2	1	2	0.491
5	1	3	2	2	0.576
6	2	1	3	2	0.637
7	2	3	1	3	0.599
8	3	1	2	3	0.973
9	1	2	3	33	0.642

experiment and calculating the value of the MID index, the desired response level is estimated using this index.

By providing the MINITAB software with these outputs, the S/N chart is presented in Figure 3. Based on the calculated signal-to-noise ratio for all levels considered for each factor, the lower the value for a specific level, the corresponding level is selected for that factor. As shown in Figure 3, the minimum value of signal-to-noise ratio occurs for the factor PS at its high level with code 3. Therefore, the value considered for this parameter in the NSGA-II algorithm is 200. Additionally, the minimum value of the signal-to-noise ratio for the CR index corresponds to the medium level with code 2 for this factor. Hence, the factor CR will have a value of 0.7 in the algorithm. Furthermore, the minimum value for the MR factor corresponds to its low level with code 1. Thus, this factor will have a presence in the algorithm with a value of 0.2. Finally, the Max\_iter factor has a lower value in terms of noise when it is at its high level with code 3. Therefore, this factor will have a value of 200 in the algorithm.

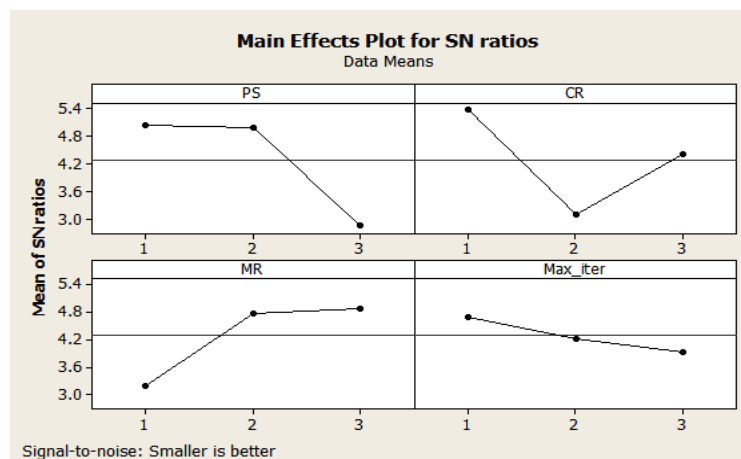


**Figure 3.** MINITAB Output for the Taguchi Method in the NSGA-II Algorithm

Based on the output provided in the above chart, the optimal value for each parameter is specified in Table 12, and other examples are executed with these values of parameters of the algorithm. The optimal values of the parameter are presented in Table 13.

**TABLE 13.** Optimal Values of Variables in NSGA-II

Parameters	Optimal Values
Population size (PS)	200
Crossover rate (CR)	0.7
Mutation rate (MR)	0.2
Maximum iterations (Max_iter)	200

#### 4. 4. Comparison Between Deterministic and Metaheuristic Method

In this section of the research, experiments have been conducted to compare the exact solution with a metaheuristic algorithm on small, medium, and large scales according to Table 14. The numerical sample scales are indicated in this table. As it is evident, there are 10 numerical samples. Samples 1 to 4 correspond to small scales, samples 5 to 8 correspond to medium scales, and samples 9 to 10 correspond to large scales. Naturally, as the scales of the problem increase, the number of problem nodes also increases. These experiments are based on the initial assumptions of the model, which include fields for raw material production, purifiers in manufacturing factories, suppliers, consumers, time periods, and storage warehouses.

**TABLE 14.** Scales of Numerical Samples

Scales	Samples	Fields	Purifiers	Consumers	Periods	Suppliers	Storage Warehouses
Small	Sample 1	1	1	1	1	1	1
	Sample 2	2	2	1	1	2	2
	Sample 3	2	2	1	1	3	2
	Sample 4	2	3	1	1	4	3
Medium	Sample 5	3	3	2	2	3	3
	Sample 6	3	3	2	2	4	3
	Sample 7	4	4	2	2	4	3
	Sample 8	4	4	2	2	3	4
Large	Sample 9	5	5	3	3	4	4
	Sample 10	6	6	4	4	5	5

**TABLE 15.** Comparative Results of Solving in Small and Medium Scales

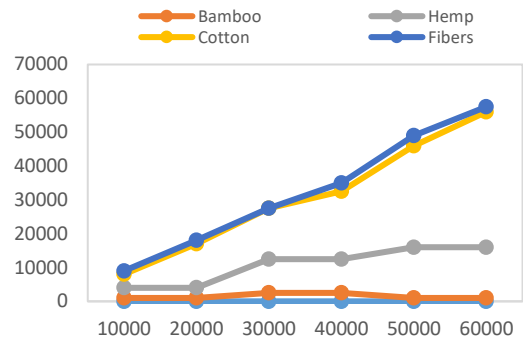
Column	GAMS			Solution Time	NSGA-II			Solution Time	Errors		
	$f_1$	$f_2$	$f_3$		$f_1$	$f_2$	$f_3$		$ARE_1$	$ARE_2$	$ARE_3$
1	509	284.9	1	10	509	284.9	1	5	0	0	0
2	541	300.2	37	12	542	300.2	35	7	0.001	0	0.05
3	649	302.1	49	15	650	303.3	46	12	0.001	0.003	0.06
4	691	320.3	99	17	693	321.9	94	15	0.002	0.004	0.05
5	1454	629	1021	20	1457	631.9	998	18	0.002	0.004	0.02
6	1568	737.5	1413	25	1572	740.4	1398	22	0.002	0.003	0.01
7	1600	804.6	2934	35	1604	806.3	2905	33	0.002	0.002	0.009
8	1909	983.3	7371	50	1911	987.6	7370	45	0.001	0.004	0.0001
9	-	-	-	-	2502	1000.65	76	50	-	-	-
10	-	-	-	-	3546	1125.5	82	55	-	-	-
<b>Mean Errors in Each Objective Function</b>									0.01	0.002	0.018

Table 15 displays the results of solving the model in small, medium, and large sizes. The first four samples correspond to the average model solutions in the small case, the next four samples correspond to the average model solutions in the medium size, and the last two samples are related to the large-scale problem. The last two samples are placed on a large scale because the mathematical model is unable to solve and provide answers for the objective function value. In Table 14, the exact solution results are compared with the results of the NSGA-II method. In the error column, three relative absolute errors are calculated using the formula  $\frac{|mathematical\ model - metaheuristic\ model|}{mathematical\ model}$  developed by Abolghasemian and Darabi (26) which has been recommended by other researchers (27-30). Based on this formula, we can calculate the error between two sets of results. If the calculated computational error between the two sets of data is less than 0.05, the error between the two sets of data will be negligible. Therefore, in this case, we can have confidence in the results of the metaheuristic model in solving large-scale problems. Considering the small difference in the error of the modeling methods and the confirmation of the accuracy of the developed mathematical model, the accuracy and efficiency of the NSGA-II algorithm are proven, and we can rely on NSGA-II for solving large-scale problems. The solution results indicate that as the dimensions of the problem increase, the complexity of the problem increases in both computational methods. This is because the solution time varies and increases from one problem to another. However, the solution time by the NSGA-II metaheuristic algorithm is significantly lower compared to the deterministic method. Therefore, based on the results in Table 14, we can trust the NSGA-II algorithm for solving large-scale problems and predict satisfactory performance.

**4. 5. Sensitivity Analysis**

In this section, the impact of changing key parameters such as the maximum storage capacity of production centers on the decisions of the proposed model is examined. This parameter change has been determined in consultation with experts in the textile field. As shown in Figure 4, changing the maximum storage capacity has a significant impact on fibers and cotton. Figure 4 shows the amount of parameter change for different values in each product.

Also, it is necessary to mention that changing the key parameter affects all examined objective functions. For this purpose, the value of the objective function is calculated for each center. Considering the results of the objective functions, the effect of the maximum capacity parameter was ignored. In Figures 5, 6, and 7, the impact of the maximum capacity parameter on transportation costs, inventory costs, and environmental pollution is shown, respectively. According to Figure 5, if the



**Figure 4.** Change of Capacity Parameter in Relation to the Quantity of Textile Raw Materials

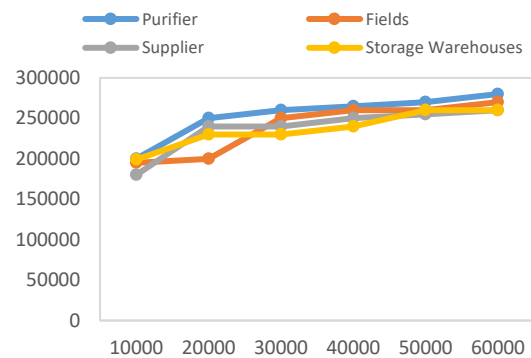


**Figure 5.** The Effect of Capacity on Transfer Costs

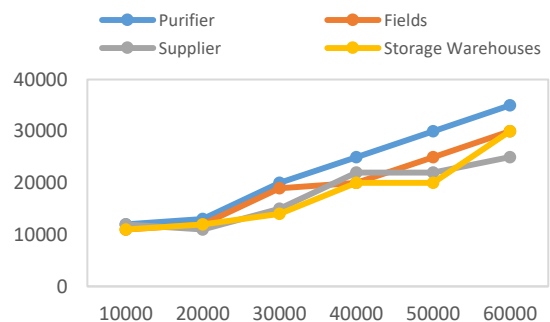


**Figure 6.** The Effect of Capacity on Inventory Cost.

capacity is changed to the maximum possible value, it has the greatest impact on the purifiers. The minimum impact occurs when the capacity increases to 20,000 in which case the least effect is placed on the fields.

According to Figure 6, if the capacity is changed to its maximum possible value, it will have the greatest impact on the purifier. The least impact resulting from a change in capacity occurs when the capacity increases by 50,000. In this case, the minimum inventory cost is incurred in the storage warehouses.

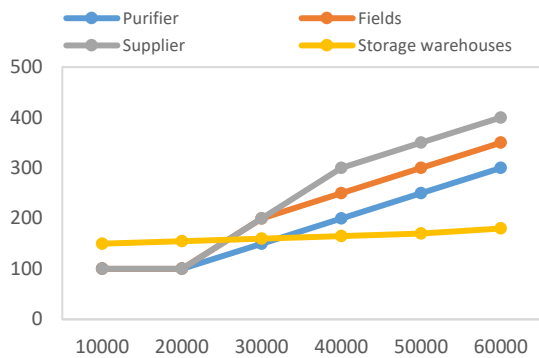


**Figure 7.** The Effect of Capacity on Pollution Level.

According to Figure 7, if the capacity is changed to its maximum value, suppliers will have the greatest impact on pollution. The least impact resulting from a change in capacity occurs when the capacity increases by 10,000 units. In this case, suppliers will make a significant contribution to pollution.

## 5. MANAGERIAL INSIGHT

The managerial insight gained from the current research can be summarized as follows:

- Enhanced Environmental Sustainability:** By incorporating green product processes, organizations like OYAZ Industrial Group can actively contribute to environmental sustainability. Mathematical modeling and the NSGA-II algorithm provide a systematic approach to identify the most effective and eco-friendly practices, helping reduce energy consumption, waste generation, and emissions.
- Optimized Resource Allocation:** The utilization of mathematical modeling and the NSGA-II algorithm allows managers to optimize resource allocation within the textile production processes. This can lead to improved efficiency, lowered costs, and minimized material waste through better planning and scheduling.
- Competitive Advantage:** Adopting green product processes can give OYAZ Industrial Group a competitive advantage in the textile industry. By focusing on sustainability, they can attract environmentally conscious customers while complying with regulations and demonstrating corporate social responsibility.
- Decision Support System:** The integration of mathematical modeling and the NSGA-II algorithm creates a decision support system for managerial decision-making. It provides insights into the trade-offs between different objectives, such as cost, environmental impact, and production efficiency. This empowers managers to make informed decisions aligned with their sustainability goals.

**5. Continuous Improvement:** The application of mathematical modeling and the NSGA-II algorithm enables OYAZ Industrial Group to continuously improve their green product processes. Through iterative optimization, managers can identify bottlenecks, inefficiencies, and areas for further enhancement, allowing for ongoing process optimization and refinement.

## 6. CONCLUSION

In this study, a mathematical modeling method for producing green textiles in a textile company has been presented, focusing on the importance of a green supply chain and reducing environmental pollution. Based on the mathematical modeling proposed for the development of green product processes in the textile industry, it can be concluded that the use of mathematical modeling methods and techniques in the textile industry enables the improvement and optimization of the processes of green product production. Mathematical modeling, using mathematical concepts and computational algorithms, helps analyze and improve process performance.

Therefore, considering the aforementioned points and their significance in this research, a multi-objective mixed-integer linear programming model has been presented with the objective of minimizing production lead time, transportation and inventory costs, and minimizing environmental impacts in the processes of developing green products. In this model, the problem's constraints and parameters are deterministic and have been solved deterministically using weighted sum methods, utilizing real data obtained from the industrial group Oyaz. Furthermore, to evaluate the capability of the proposed model in solving larger instances, the NSGA-II metaheuristic method has been employed. This metaheuristic method has demonstrated desirable performance compared to the mathematical model, as the small difference in modeling errors confirms the accuracy of the developed mathematical model, and the performance and efficiency of the NSGA-II algorithm are proven, making it reliable for solving problems on large scales as well. Finally, the impact of changing key parameters such as the maximum storage capacity of production centers on the decisions of the proposed model has been examined through sensitivity analysis. This parameter change has been determined based on consultation with experts in the textile industry. Based on the results obtained, changing the maximum storage capacity has a significant impact on fibers and cotton. Additionally, if the capacity is changed to the maximum possible value, it will have the greatest impact on the purifiers. The least impact occurs when the capacity increases by 20,000 units, in which case the minimum

impact is placed on the fields. Furthermore, if the capacity is changed to the maximum possible value, it will have the greatest impact on the inventory of the purifiers. The least impact occurs when the capacity increases by 50,000 units, in which case the minimum cost is incurred in the storage warehouses. Finally, if the capacity is changed to the maximum possible value, the suppliers in the chain will have the greatest pollution impact. The least impact occurs when the capacity increases by 10,000 units, in which case the suppliers will make a significant contribution to pollution. It is recommended to use a robust planning approach in the developed model for further research. Additionally, metaheuristic methods should be used to assess the capabilities of the model in small, medium, and large scales.

## 7. REFERENCES

- Torabi N, Tavakkoli-Moghaddam R, Najafi E, Hosseinzadeh-Lotfi F. A two-stage green supply chain network with a carbon emission price by a multi-objective interior search algorithm. *International Journal of Engineering, Transactions C: Aspects.* 2019;32(6):828-34. <https://doi.org/10.5829/ije.2019.32.12c.05>
- Kim HJ, Mun S, Han SH. Corporate social responsibility and the alignment of CEO and shareholders wealth: Does a strong alignment induce or restrain CSR? *Corporate Social Responsibility and Environmental Management.* 2023;30(2):720-41. [10.1002/csr.2384](https://doi.org/10.1002/csr.2384)
- Taheri M, Mahdavi A, Safikhani H. Multi objective optimization of multi-hole orifices using FSI analysis and NSGA II algorithm. *International Journal of Engineering, Transactions B: Applications.* 2021;34(8):2038-44. [10.5829/ije.2021.34.08b.25](https://doi.org/10.5829/ije.2021.34.08b.25)
- Asadpour M, Boyer O, Tavakkoli-Moghaddam R. A blood supply chain network with backup facilities considering blood groups and expiration date: a real-world application. *International Journal of Engineering, Transactions B: Applications.* 2021;34(2):470-9. <https://doi.org/10.5829/ije.2021.34.02b.19>
- Heydari M, Osanloo M. A New Comprehensive Model for Integrating Environmental, Economic, and Social Performance of Deep and Large-scale Open-Pit Copper Mines. *International Journal of Engineering, Transactions A: Basics.* 2024;37(1):1-13. <https://doi.org/10.5829/ije.2024.37.01a.01>
- Nikoohemmat MA, Mazaheri H, H Joshaghani A, Joudaki E. Development of a Novel Super-active Ziegler-Natta Polyethylene Catalyst: Study on Structure, Performance and Application. *International Journal of Engineering, Transactions A: Basics.* 2024;37(1):14-24. <https://doi.org/10.5829/ije.2024.37.01a.02>
- Kamran MA, Kia R, Goodarzian F, Ghasemi P. A new vaccine supply chain network under COVID-19 conditions considering system dynamic: Artificial intelligence algorithms. *Socio-Economic Planning Sciences.* 2023;85:101378. [10.1016/j.seps.2022.101378](https://doi.org/10.1016/j.seps.2022.101378)
- Rezaei Kallaj M, Abolghasemian M, Moradi Pirbalouti S, Sabk Ara M, Pourghader Chobar A. Vehicle routing problem in relief supply under a crisis condition considering blood types. *Mathematical Problems in Engineering.* 2021;2021:1-10. [10.1155/2021/7217182](https://doi.org/10.1155/2021/7217182)
- Chobar AP, Adibi MA, Kazemi A. Multi-objective hub-spoke network design of perishable tourism products using combination machine learning and meta-heuristic algorithms. *Environment, Development and Sustainability.* 2022;1-28. [10.1007/s10668-022-02350-2](https://doi.org/10.1007/s10668-022-02350-2)
- Jahangiri S, Abolghasemian M, Ghasemi P, Chobar AP. Simulation-based optimisation: analysis of the emergency department resources under COVID-19 conditions. *International journal of industrial and systems engineering.* 2023;43(1):1-19. [10.1504/IJISE.2023.128399](https://doi.org/10.1504/IJISE.2023.128399)
- Howldar S, Balaji B, Srinivasa Rao K. Design and Analysis of Hetero Dielectric Dual Material Gate Underlap Spacer Tunnel Field Effect Transistor. *International Journal of Engineering, Transactions C: Aspects.* 2023;36(12):2137-44. [10.5829/ije.2023.36.12c.01](https://doi.org/10.5829/ije.2023.36.12c.01)
- Jahangiri S, Abolghasemian M, Pourghader Chobar A, Nadaffard A, Mottaghi V. Ranking of key resources in the humanitarian supply chain in the emergency department of Iranian hospital: a real case study in COVID-19 conditions. *Journal of applied research on industrial engineering.* 2021;8(Special Issue):1-10. [10.22105/jarie.2021.275255.1263](https://doi.org/10.22105/jarie.2021.275255.1263)
- Abolghasemian M, Kanafi AG, Daneshmand-Mehr M. Simulation-based multiobjective optimization of open-pit mine haulage system: a modified-NBI method and meta modeling approach. *Complexity.* 2022;2022. [10.1155/2022/3540736](https://doi.org/10.1155/2022/3540736)
- Hua C, Chen J, Wan Z, Xu L, Bai Y, Zheng T, et al. Evaluation and governance of green development practice of port: A sea port case of China. *Journal of cleaner production.* 2020;249:119434. [10.1016/j.jclepro.2019.119434](https://doi.org/10.1016/j.jclepro.2019.119434)
- Dorward A. Agricultural labour productivity, food prices and sustainable development impacts and indicators. *Food policy.* 2013;39:40-50. [10.1016/j.foodpol.2012.12.003](https://doi.org/10.1016/j.foodpol.2012.12.003)
- Kong Y, Liu J. Sustainable port cities with coupling coordination and environmental efficiency. *Ocean & Coastal Management.* 2021;205:105534. [10.1016/j.ocecoaman.2021.105534](https://doi.org/10.1016/j.ocecoaman.2021.105534)
- Lavuri R, Jusuf E, Gunardi A. Green sustainability: Factors fostering and behavioural difference between millennial and Gen Z: Mediating role of green purchase intention. *Ekonomia i Środowisko.* 2021.
- Dzikriansyah MA, Masudin I, Zulfikarjah F, Jihadi M, Jatmiko RD. The role of green supply chain management practices on environmental performance: A case of Indonesian small and medium enterprises. *Cleaner Logistics and Supply Chain.* 2023;6:100100. [10.1016/j.clscn.2023.100100](https://doi.org/10.1016/j.clscn.2023.100100)
- Chakraborty A, Al Amin M, Baldacci R. Analysis of internal factors of green supply chain management: An interpretive structural modeling approach. *Cleaner Logistics and Supply Chain.* 2023;7:100099. [10.1016/j.clscn.2023.100099](https://doi.org/10.1016/j.clscn.2023.100099)
- Soufi M, Fadaei M, Homayounfar M, Gheibdoost H, Rezaei Kelidbari H. Evaluating the drivers of green supply chain management adoption in Iran's construction industry. *Management of Environmental Quality: An International Journal.* 2023. [10.1108/MEQ-04-2022-0105](https://doi.org/10.1108/MEQ-04-2022-0105)
- Yousaf Z, Palazzo M, Radulescu M, Javed A. Unleashing the role of greenwashing in the relationship of environmental sustainability thoughts and environmental performance: exploring the importance of generative leadership. *Environment, Development and Sustainability.* 2023;1-20. [10.1007/s10668-023-03473-w](https://doi.org/10.1007/s10668-023-03473-w)
- Wu C, Xu C, Zhao Q, Zhu J. Research on financing strategy under the integration of green supply chain and blockchain technology. *Computers & Industrial Engineering.* 2023;184:109598. [10.1016/j.cie.2023.109598](https://doi.org/10.1016/j.cie.2023.109598)
- Zhu Z, Wang X, Liu L, Hua S. Green sensitivity in supply chain management: An evolutionary game theory approach. *Chaos, Solitons & Fractals.* 2023;173:113595. [10.1016/j.chaos.2023.113595](https://doi.org/10.1016/j.chaos.2023.113595)

24. Abbas A, Luo X, Shahzad F, Wattoo MU. Optimizing organizational performance in manufacturing: The role of IT capability, green supply chain integration, and green innovation. *Journal of Cleaner Production*. 2023;423:138848. 10.1016/j.jclepro.2023.138848
25. Yang H, Chen X, Li L, Sun Y. Supply chain decision-making of green products considering a retailer's fairness concerns under a pre-sale model. *Journal of Cleaner Production*. 2023;414:137457. 10.1016/j.jclepro.2023.137457
26. Abolghasemian M, Darabi H. Simulation based optimization of haulage system of an open-pit mine: Meta modeling approach. *Organizational resources management researchs*. 2018;8(2):1-17. 20.1001.1.22286977.1397.8.2.2.6
27. Abolghasemian M, Ghane Kanafi A, Daneshmandmehr M. A Two-Phase Simulation-Based Optimization of Hauling System in Open-Pit Mine. *Interdisciplinary Journal of Management Studies (Formerly known as Iranian Journal of Management Studies)*. 2020;13(4):705-32. 10.22059/ijms.2020.294809.673898
28. Bayee P, Amani H, Najafpour G, Kariminezhad H. Experimental investigations on behaviour of rhamnolipid biosurfactant as a green stabilizer for the biological synthesis of gold nanoparticles. *International Journal of Engineering, Transactions C: Aspects*. 2020;33(6):1054-60. 10.5829/ije.2020.33.06c.02
29. Kamarudin NH, Harun Z, Othman MD, Hubadillah SK, Jamaluddin M, Yusof K. Preliminary characterization of corn cob ash as an alternative material for ceramic hollow fiber membrane (CHFM/CCA). *International Journal of Engineering, Transactions B: Applications*. 2018;31(8):1389-97. <https://doi.org/10.5829/ije.2022.35.02b.05>
30. Moosavi S, Seifbarghy M. A robust multi-objective fuzzy model for a green closed-loop supply chain network under uncertain demand and reliability (a case study in engine oil industry). *International Journal of Engineering, Transactions C: Aspects*. 2021;34(12):2585-603. <https://doi.org/10.5829/ije.2021.34.12c.03>

#### COPYRIGHTS

©2024 The author(s). This is an open access article distributed under the terms of the Creative Commons Attribution (CC BY 4.0), which permits unrestricted use, distribution, and reproduction in any medium, as long as the original authors and source are cited. No permission is required from the authors or the publishers.



#### Persian Abstract

##### چکیده

توسعه فرآیند محصول سبز یک رویکرد استراتژیک برای به حداقل رساندن اثر زنجیره تأمین سازمانی بر محیط زیست و در عین حال گسترش عملکرد اقتصادی آن است. در انجام این کار، ابعاد متمرکز بر عملکرد در بهینه سازی مصرف منابع و تحقق مفاهیم پایداری در یک زمینه سازمانی ضروری هستند. برای این منظور در این مطالعه یک مدل برنامه ریزی خطی عدد صحیح مختلط چند هدفه با هدف حداقل سازی زمان تولید منسوجات و هزینه های حمل و نقل و موجودی محصول و همچنین کمینه کردن آثار زیست محیطی در فرآیند توسعه محصول سبز در ارائه شده است. در این مدل، محدودیت ها و پارامترهای مساله از نوع قطعی هستند که با استفاده از روش های مجموع وزن دار شده حل شده اند که برای این منظور از داده های واقعی بدست آمده از گروه صنعتی ایاز استفاده شده است. با حل مدل یک ترکیب بهینه برای مقدار توابع هدف به طور ترکیبی و مجزا بدست آمده است. علاوه بر این برای سنجش قابلیت مدل پیشنهادی برای حل نمونه های بزرگ تر از روش فراابتکاری NSGA-II استفاده شده است. این روش فراابتکاری در مقایسه با مدل ریاضی قابلیت مطلوبی را از خود نشان داده است. زیرا، اختلاف کم در خطای روش های مدلسازی ضمن تأیید صحت مدل ریاضی توسعه داده شده، صحت عملکرد و کارایی الگوریتم NSGA-II اثبات می شود و می توان برای حل مسائل در ابعاد بزرگ نیز به NSGA-II اعتماد کرد. سرنجام، تأثیر تغییر پارامترهای کلیدی مانند حداکثر ظرفیت ذخیره سازی مراکز تولیدی بر تصمیمات مدل پیشنهادی از طریق تحلیل حساسیت بررسی شده است. این تغییر پارامتر با استفاده از مشاوره با کارشناسان حوزه نساجی مشخص شده است. براساس نتایج بدست آمده تغییر حداکثر ظرفیت ذخیره سازی تأثیر قابل توجهی بر روی الیاف و پنبه دارد. همچنین، در صورت تغییر ظرفیت به حداکثر مقدار ممکن، بیشترین تأثیر را بر روی تصفیه کننده ها می گذارد.



## Ash Reduction of the Tailings of Agh-Darband Coal Washing Plant by Flotation Method

M. Hosseini Nasab\*

Department of Mining Engineering, Faculty of Engineering, University of Sistan and Baluchestan, Zahedan, Iran

### PAPER INFO

#### Paper history:

Received 20 August 2023

Received in revised form 13 October 2023

Accepted 06 November 2023

#### Keywords:

Agh-Darband Mine

Coal Tailing

Flotation

Experimental Design

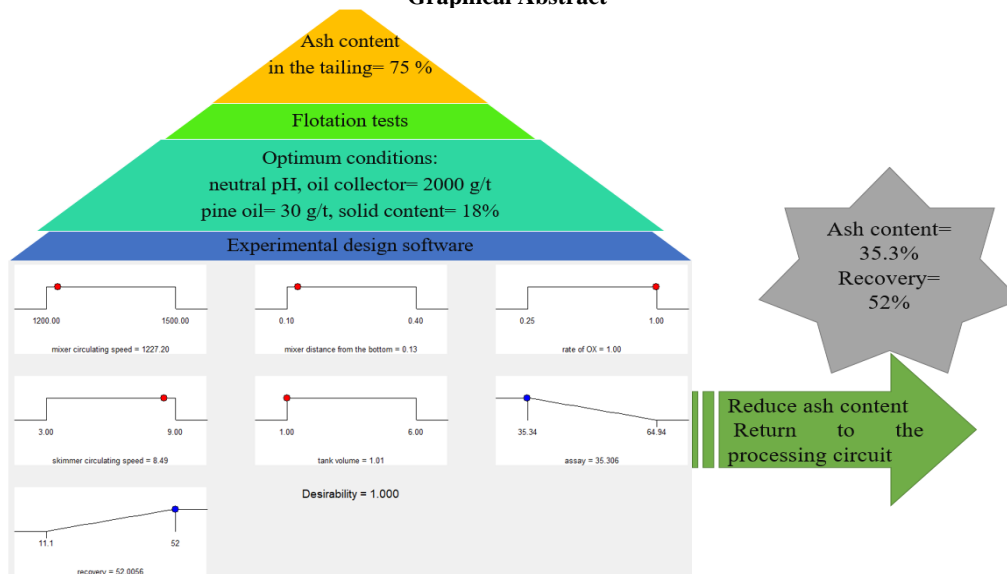
Optimization

### ABSTRACT

One of the major coal mines in the eastern part of Iran is Agh-Darband mine which is located in Sarakhs. Agh-Darband plant works with a content of less than 37% ash at inputs and about 12% ash in the product. Due to the equipment being depreciated and the lack of optimal conditions for the processing system, a large amount of the coal in feed is entered to the tailing part so that ash content in the tailing is about 75%. The purpose of this research is to investigate whether the flotation method can process the mine tailing with 75% ash content and reduce it to return to the processing circuit. For this purpose, various flotation tests were performed on 70 kg of tailing of Agh-Darband mine. The optimum conditions was obtained at neutral pH with 2000 g/t of oil collector, 30 g/t of pine oil as a frother, and a solid content of 18%, which the ash content of coal and recovery were 34% and 45%, respectively. In addition, using the experimental design software (DX7), the mechanical parameters of the cell such as mixer circulating speed, the distance of the mixer from the bottom, the aeration rate, skimmer circulating speed, and cell volume were optimized. Optimal values of parameters were mixer circulating speed= 1227.2 rpm, the distance of the mixer from the bottom= 0.13H, the aeration rate= 1 (completely open), skimmer circulating speed= 8.49 seconds, and the cell volume= 1 L, which resulted in the percentage of ash= 35.34% and the recovery= 52%.

doi: 10.5829/ije.2024.37.04a.13

### Graphical Abstract



\*Corresponding Author Email: [hosseininasab@eng.usb.ac.ir](mailto:hosseininasab@eng.usb.ac.ir) (M. Hosseini Nasab)

## 1. INTRODUCTION

The first fossil fuel that people used as their main source of energy was coal, one of the most significant energy sources in the world. The production of electricity, iron and iron alloy smelting furnaces, coke, liquefied gas, activated carbon production, and other processes like the production of graphite used in electric furnaces, as a pigment in glass production, hard rubbers, and sewage treatment are the most significant uses of coal (1).

**1. 1. Effective Factors in Coal Processing** Clay minerals comprise an average of 60 to 80 percent of all minerals in coal, making them the most important group. In the presence of water, clays, carbonaceous argillite, and clay shales swell. In the processing of coal, the swelling of clay and shale causes a drop in the apparent specific gravity of coal rejects and their proximity to the apparent specific gravity of their separation, leading to the connection of these materials with coal concentrate.

Sulfur is one of the most significant contaminants in coal that its value varies between 0.5 and 11%.

In gravity processing, the density can be altered by the particle size and shape. How particles flow in a fluid (water, air, or heavy media) is determined by their size and form.

However, massive production of coal is conducted by gravity methods (2-4) but flotation is a significant technique of coal processing for fines (<0.5 mm) (5-8).

**1. 2. Coal Flotation** The development and rapid growth of coal flotation are attributable to three factors (9, 10):

- i. Inherent hydrophobicity of coal (organic phase) compared to clay and other minerals in coal
- ii. Flotation by flocculation is one of the most effective methods to reduce water turbidity in a coal preparation plant.
- iii. Relatively low cost of washing by flotation method in comparison to coal's rising value.

**1. 2. 1. Coal Ash from the Flotation Aspect** The amount of coal ash is one of the most important factors in determining the quality of coal (11). The non-combustible components of coal are known as ash. Before utilization, these materials should be cleansed and removed from the operational environment, as they play an undesirable impact. Increasing the ash content of coke has a negative impact on subsequent phases, increases coke consumption, and decreases its efficiency.

In addition to silicate compounds, oxides, and sulfates, coal ash also contains trace amounts of other chemicals. The chemical composition (XRD analysis) of ash in Agh-Darband mine is shown in Table 1.

**1. 2. 2. Inherent Hydrophobicity of Coal** The contact angle determines the hydrophobic properties of coals with various carbonization levels (12). The greater the proportion of the coal functional group (carboxyl, phenolic hydroxide, and acidic group), the more oxidized the coal surface and the less hydrophobic it is (13).

The zero charge point (ZPC) of coal, as determined by research on coals with a low degree of carbonization, is between pH=3.1 and 4.4. When a non-ionic collector is absorbed on the surface of coal, the zero-point charge of the coal is transported to the alkaline area. Thus, depending on the concentration of the collector, the adsorption process between the collector molecule and the coal surface makes coal flotation viable at a pH close to ZPC. Non-ionic collectors are chemically absorbed on the surface of coal with the assistance of covalently stable hydrogen bonds (14).

A significant volume of tailings produced from processing is generally left as permanent features of the landscape after the mining ceases (15). Coal mining is one of the mines that produces many tailings (ash).

The coal washing plant of the Agh-Darband mine is one of the oldest coal concentrate producing facilities in Iran, receiving roughly 60 tons of coal feed per day. This plant's coal processing system is inefficient due to an outdated and suboptimal method. Therefore, a large amount of the coal in feed is entered to the tailing part so that ash content in the tailing is about 75%. The purpose of this research is to investigate whether the flotation method can process the mine tailing with 75 percent ash content and reduce it. Priority was placed on increasing the circuit efficiency of this plant. The way to reach this goal was to analyze the effective chemical parameters in the flotation system and to determine the ideal values for each parameter, as well as to optimize the mechanical parameters of the cell, thereby increasing the flotation efficiency and decreasing ash.

**1. 3. Literature Review** By mechanical flotation, Naik et al. (16) studied the effect of 5 operational parameters, including the amount of collector, the amount of MIBC frother, pH, particle size, and the effect of sodium silicate, in order to optimize the

**TABLE 1.** The chemical composition of ash in Agh-Darband mine

Chemical composition	%	Chemical composition	%
SiO <sub>2</sub>	45.65	CaO	2.86
Al <sub>2</sub> O <sub>3</sub>	28.3	Na <sub>2</sub> O + K <sub>2</sub> O	5.02
TiO <sub>2</sub>	1.95	SO <sub>2</sub>	0.057
Fe <sub>2</sub> O <sub>3</sub>	8.07	MgO	1.39

flotation of non-coking coals with an ash content of 37.7%. In this study, the volume of the collector had the largest impact among the variables, and optimal conditions resulted in 88% recovery and a 25.4% ash percentage.

Tahmasebi et al. examined the decrease of ash in an Agh-Darband coal feed sample in 2006. The sample contained 30% ash on average. Experiments involving vibrating tables were undertaken, including calculating the flow rate of water entering the table and its slope. This technique reduced coal ash by 12.5%. The optimum specific gravity for ash reduction was determined through the use of heavy liquid testing. A concentrate containing 12 percent ash required a medium with a specific gravity of 1.5 g/cm<sup>3</sup> in the fraction -850+212 microns. To identify the best state of the effective parameters, flotation tests were performed. Coal ash decreased by 11.5% in the ideal state.

In 2007, Hacifazlioglu and Sutcu (17) conducted research on the optimization of column flotation operational parameters. Their goal was to accomplish optimal separation as well as a comparison of the column and mechanical cells for the Zonguldak coal mine in Turkey, which has 47.5% ash less than 130 microns in size. Their investigation yielded a product with 15.6% ash and 50.92% recovery by column flotation, and a product with 19.52% ash and 82.32% recovery by mechanical flotation (17).

In the same mine, Hacifazlioglu and Toroglu (18) conducted an additional study on the optimization of Jameson flotation cell design parameters and flotation operational parameters, such as the amount of collector, the amount of frother, and the percentage of solids, in order to achieve the optimal separation of bituminous coal containing 45.3% ash. Under optimal conditions, the influence of the examined parameters resulted in 14.9% ash and 74.2% recovery (18).

Jena et al. (19) compared the fatty alcohols ethanol and butanol. They examined the effect of decreasing coal surface oxidation on the flotation ability of sub-bituminous coals oxidized with 42% ash and particles smaller than 1 mm. This study yielded a product containing 31% ash and 80.4% recovery via mechanical flotation, as well as a product containing 26.6% ash and 66.5% recovery via column flotation (19).

Cinar (20) used column and mechanical flotation cells to investigate the effect of low temperature and no temperature heat treatment on the flotation ability of Turkish Soyak lignite coals in 2009. In this investigation, low-temperature heat treatment was used in both column and mechanical cells to increase recovery and the percentage of ash, even without the use of a collector (20).

Anderson et al. (21) explored flotation in an oscillatory baffled column (OBC). Using a sequence of oscillating sinusoidal baffle plates in the liquid and within the flotation cell, they investigated a new stirring

mechanism. This technique of stirring demonstrated the ability to generate a uniformly distributed shear rate within the cell. The results demonstrated that OBC could increase the flotation speed constant by as much as 60% for fine particles (less than 30  $\mu\text{m}$ ) and by 30% to 40% for larger particles. Therefore, OBC can greatly enhance the flotation rate in typical cells (21).

Shukla et al. (22) evaluated the effect of process variables on gas holdup in a column flotation cell for coal, including feed rate, gasification rate, frother concentration, and solid content. The gas holdup in the collection area was shown to be impacted by both the aeration rate and feeding rate. However, the influence of the feeding rate is negligible in comparison to the gas delivery rate, the gas holdup altered by more than 6 percent when the feeding rate increased from 1 cm/s to 2 cm/s. Furthermore, the addition of frother had a favorable effect. However, as the solids percentage increased, gas holdup dropped (22).

Vapur et al. (23) explored the optimization of a coal flotation system employing modified parameters in a Jameson cell. Using the optimal variables in a Jameson cell, a percentage of recovered combustibles was calculated. The best cell variables were 0.25 mm particle size, 1:1 ratio of vegetable oil to kerosene, 20% solids percentage, and 0.6 l/min washing water flow rate. Finally, in ideal circumstances and an 8-minute flotation time, 94.83% combustible concentrate or 94.86% ash and 17.86% ash were derived (23).

Dashti and Eskandari Nasab (24) studied the impact of hydrodynamic factors on the flotation of coarse coal particles in 2012. The findings of their experiment demonstrated that by increasing the stirrer's speed to 700 rpm, the particles receive sufficient energy to collide and interact with the air bubble, and their recovery rate increases. In addition, the recovery of coarse particles diminishes as the distance of the stirrer from the bottom of the cell increases, as the dead zone under the stirrer expands and the particle suspension becomes less intense. Increasing the concentration of the frother decreased the size of the bubbles and enhanced the stability of the foam phase, resulting in a greater recovery of coarse particles (24).

Pineres and Barraza (25) studied the effect of pH, air velocity, and frother concentration on the recovery of combustible components and the amount of sulfur and ash removed from four samples of Colombian bituminous coal by means of column flotation. The results indicated that the most ash and sulfur were removed from coal from the Guachinate and Nechi regions at acidic pH values of 4 and 5 and air velocities of 1.4 and 1.8 cm/s, respectively. The maximum amount of ash (85.4% and 84.7%) and sulfur (81.1% and 85.1%) removal was obtained in alkaline conditions (pH 9 and 10) with air velocity ranging from 1 to 1.4 cm/s in Creejon and Jagua coals (25).

Chamnet et al. examined the gravimetric and flotation procedures for the Agh-Darband coal mine feed sample. The separation density for the heavy medium test was determined to be 1.53 g/cm<sup>3</sup>, and the coal concentrate obtained from the vibrating table test included 34.5 weight percent and 15.50 percent ash with a recovery rate of 47.2%. The concentrate contains oil collector at a rate of 1,000 grams per ton, pine oil at a rate of 30 grams per ton as a frother in neutral pH with 20% solids, coal with a weight percentage of 56.2% and ash at a rate of 17.59%, with a recovery of 78.63%. Integrated gravity-flotation tests were also conducted, and flowcharts were produced for this purpose in order to improve accuracy and avoid coal waste in tailings. 75.7% of the coal was recovered, yielding a concentrate with a weight percentage of 56.2% and an ash grade of 16.59%.

Other research in recent years resulted in optimizing the flotation process from different aspects. For example, the study of flotation kinetics (26), determination relationships between operating variables and metallurgical responses of industrial coal column flotation circuits (27), examining the performance of feature engineering for concentrate ash content of coal flotation by froth image feature engineering-based prediction method (28) also based on deep learning algorithms and attention mechanism (29, 30). In addition, the optimization of column flotation for fine coal using Taguchi method (31), and using response methodology and central composite rotatable design (CCRD) (32) are other cases of these optimizations.

## 2. MATERIALS AND METHODS

**2. 1. Instruments** The Denver D-12 flotation laboratory cell was used in this study's flotation tests, and the ash content of the sample was measured after coal flotation. Utilizing an oven, moisture was extracted from the sample. The sieves were used to determine the particle-size distribution. The digital scale was applied to measure the weight of samples with a 0.001-gram resolution. The pH meter was used to determine the pulp's pH. The thermometer is used to measure and control the temperature of coal pulp throughout the flotation process. A filter was also employed in this experiment to extract the liquid, dry the sample after the fine-grinding step, and to dry the flotation concentrate. The sample was reduced to diameters smaller than 2 mm using a roll crusher, and then divided into 2 kg, 1 kg, and head sample bags using a rifle. The sample of approximately 1 mm in size, which is unsuitable for flotation, is crushed to approximately 150 microns using a bond rod mill. Using a planetary ball mill, the sample must be reduced to a particle size below 75 microns in order to determine its ash content following the flotation test.

**2. 2. Sample Preparation** The collected sample weighed approximately 70 kg, and the ash content of the tailings measured at approximately 75%. The sample was crushed, the particle size distribution of the crusher product was determined, and the sample was divided and homogenized. The coal tailings were crushed with a roll crusher and sieved through a 2 mm control screen. Half of the 70 kg sample was crushed to less than 600 microns in size. A quarter of the sample was crushed to less than 2 mm, and another quarter was crushed to less than 1 mm. For each fraction, the weight of the remaining material on each sieve was determined, and then the percentage of these materials and cumulative percentage of the remaining materials on each sieve were calculated.

The half of the sample, whose its d80 were smaller than 600 microns, was divided using a riffle, and 2 kg packages were made from it for use in flotation experiments. Another quarter of the samples that were crushed to less than 2 mm and another quarter of the samples that were crushed to less than 1 mm were packaged in 2 kg quantities so that, if necessary, they can be crushed to sizes smaller than 600 micron.

In order to get the needed optimal particle size for flotation, the sample with size smaller than 600 microns was crushed in a bond rod mill at three different times (3, 5 and 10 minutes) and the ash content and recovery was calculated for each time to determine the optimal time.

**2. 3. Flotation Experiment** After wet grinding of 1 kg of the sample by a bond rod mill to the optimal dimensions, and after placing it in a vacuum filter, 0.5 kg of it was used for the flotation tests. Using the Denver D-12 flotation cell, the experiments were conducted. Thus, pulp containing 19% solids is agitated for 5 minutes at a specific speed, and its pH and temperature were monitored at the same time. Then the collector is inserted, followed by the frother two minutes later. After one minute, the air valve was opened and foaming is performed for three minutes at 5-second intervals. At the completion of the foaming period, a 20-gram sample was made from each of the concentrates and tailings acquired after placing each in a vacuum filter and dryer and sending the sample to be ground for 5 minutes until it is ready to be placed in the furnace. In order to calculate the percentage of ash, 1 gram of the sample is heated in a furnace at 950°C for one hour and then the sample taken out of the furnace was weighed. If the discrepancy between the measurements is greater than 0.005 grams, the procedure must be repeated until the requirements are fulfilled. The percentage of ash is determined by comparing the sample's weight before and after being placed in the furnace (Equation 1):

$$A = \frac{(D-B)}{(C-B)} \times 100 \quad (1)$$

A : Ash content (%)

B : Crucible weight (g)

C : Crucible and sample weight (g)

D: Weight of crucible and sample after burning (g)

The experiments were carried out in duplicate, some were randomly repeated for a third time, and the results were then averaged. Error or standard deviation of repeating experiments was logical.

## 2. 4. Flotation Requirements

There are several requirements in coal flotation that are considerably effective in increasing the efficiency of the test if they are fulfilled:

1. The operating temperature should be between 22 and 23°C.
2. The water used is the same water that was used in the laboratory and was determined by pH measurement to be 7.
3. The pulp surface is maintained in every experiment between 12.7 mm and 15.6 mm below the cell edge, which is managed by stirring and aerating.
4. Soaking the coal: Because the sample is dry (not in slurry form), it is necessary to stir it for 5 minutes after mixing it with water and before adding chemicals so that it will float better during the flotation process.
5. Before opening the air flow, chemicals used in flotation are added to the flotation cell. Addition of chemicals (collector and frother) is performed with precision using a pipette or microsyringe.
6. The pH of the pulp is measured prior to the addition of the collector, frother, or any other pre-treatment material.

## 2. 5. Taguchi Test Design for Mechanical Variables

All five investigated parameters are quantitative and each is examined at four distinct levels. The levels of these five parameters are displayed in Table 2.

Using the Taguchi approach, the software developed 16 trials ( $L_{16}$ ) based on the effective parameters. These tests are listed in Table 3 according to their respective levels. All of these trials were conducted in a mechanical laboratory flotation cell. In these studies, the percent of solids, type of frother, type of collector, amount of frother, and amount of collector, etc., were calculated beforehand and considered optimal and consistent.

## 2. 6. Optimal Sizes for Flotation

In order to achieve this objective, one kg of the sample with diameters smaller than 600 microns with one liter of

**TABLE 2.** The examined mechanical parameters and their levels

Parameter level	1	2	3	4
Mixer circulating speed (rpm)	1200	1300	1400	1500
Mixer distance from the bottom	0.1H	0.2H	0.3H	0.4H
Rate of oxygenation	one quarter	half	Three quarters	Full
Skimmer circulating speed (rpm)	20	12	8.6	6.6
Tank volume (lit)	1	2	4	6

Where, H is the cell height.

**TABLE 3.** 16 trials designed by the software (experiment design  $L_{16}$ )

Test number	Mixer circulating speed	Mixer distance from the bottom	Rate of oxygenation	Skimmer circulating speed	Tank volume
1	1	1	1	1	1
2	1	2	2	2	2
3	1	3	3	3	3
4	1	4	4	4	4
5	2	1	2	3	4
6	2	2	1	4	3
7	2	3	4	1	2
8	2	4	3	2	1
9	3	1	3	4	2
10	3	2	4	3	1
11	3	3	1	2	4
12	3	4	2	1	3
13	4	1	4	2	3
14	4	2	3	1	4
15	4	3	2	4	1
16	4	4	1	3	2

water was crushed using a bond rod mill at three different times (2, 5 and 10 minutes). After filtering the crushed samples, the remaining part on the filter was wet-screened. Figures 1-3 depict the particle size distribution of the product of a bond rod mill over periods of 10 minutes, 5 minutes, and 2 minutes, respectively. According to the obtained results and with the aid of interpolation, d80 of samples with a crushing duration of 10 minutes, 76.68 microns, 5 minutes, 151 microns, and 2 minutes, 237.22 microns were derived.

**3. RESULTS**

**3.1. Effect of Particle Size on Ash Content and Coal Recovery**

To perform flotation tests, it is necessary to determine the optimal particle size. Based on this, flotation tests were performed for samples with d80s of 1000, 600, 212, 150 and 75 microns. In all experiments, the percentage of solids for coal and coal tailings were chosen as 19% according to the sources and the tests performed. The chemical parameters used are pH

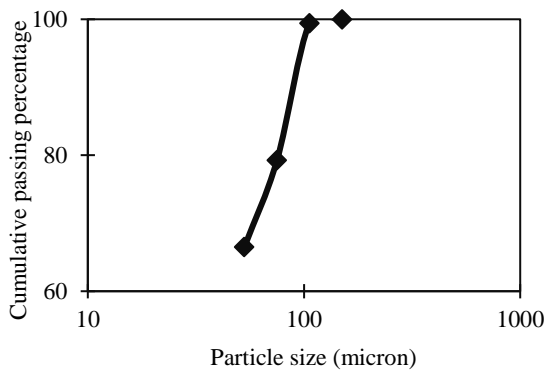


**Figure 1.** Particle size distribution of the product of a bond rod mill (crushing time: 10 minutes)

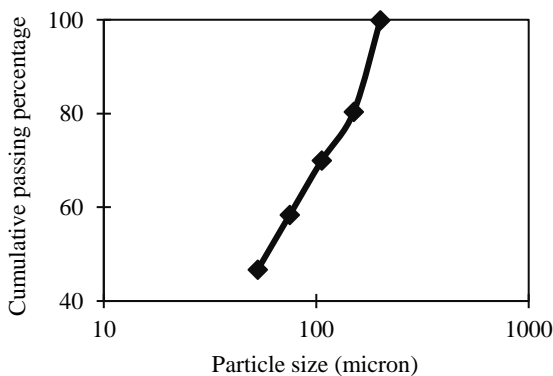


**Figure 2.** Particle size distribution of the product of a bond rod mill (crushing time: 5 minutes)

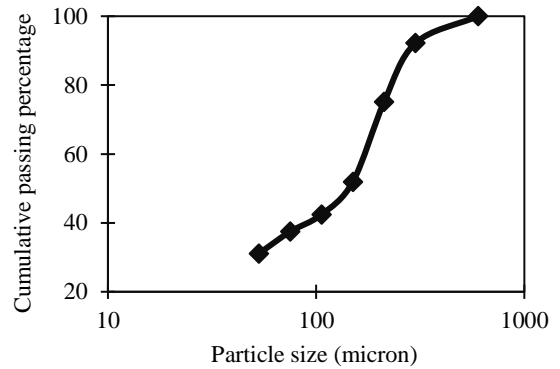


**Figure 3.** Particle size distribution of the product of a bond rod mill (crushing time: 2 minutes)

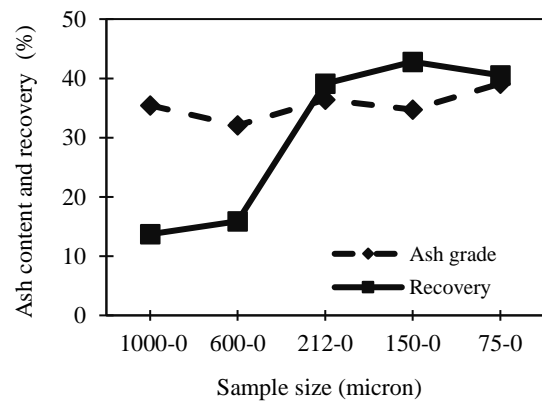
= 7.7, 2000 g/t of oil collector, and 0 g/t of pine oil frother.

Figure 4 compares ash content and coal recovery in concentrate part for various particle size. According to this figure, decreasing the size of the sample increases coal recovery in flotation operations, however the ash content is varied. Coal recovery is extremely poor in samples with d80s of 1000 and 600 microns, and the flotation process is not practicable or possible in these sample sizes.

According to Figure 4 and the calculation of the separation efficiency of various sizes, among the sizes of 212, 150, and 75 microns, 150 microns was chosen as the optimal size due to the decrease in ash content to approximately 35% and the increase in recovery to approximately 45%.

**3.2. Effect of Collector Dosage on Ash Content and Coal Recovery**

Following the measurement of the sample's sizes, the effect of collector concentration was investigated at 1000, 2000, 3000, 4000, and 5000 g/t. Oil collector, solid percentage 19%, pH = 7.7, d80= 150



**Figure 4.** Ash content and coal recovery in concentrate part for different d80s

microns, and pine oil frother in the amount of 0 g/t were used in this series of experiments.

According to Figure 5, the grade of the ash increases as the collector concentration rises. Because when the concentration of the collector increases, some waste are also floating with the coal. At a concentration of 1,000 g/t, coal recovery is poor, but it increases by around 10% at a concentration of 2,000 g/t. From a concentration of 2,000 to 5,000 g/t, the range of recovery is essentially the same and there are no discernible alterations.

In accordance with the graph and the calculation of the separation efficiency for various concentrations, the oil collector with a concentration of 2,000 g/t was selected due to the lower grade of ash (approximately 34%) and higher coal recovery (approximately 43%) in comparison to other options.

**3. 3. Effect of Collector Type on Ash Content and Coal Recovery**

The type of collector was explored after determining the dimensions of the sample and the concentration of the collector. The diesel collector was employed in this series of experiments at concentrations of 1000, 2000, 3000, and 4000 g/t (oil was estimated in the previous step), solid percentage 19%, pH = 7.7, dimensions 150 microns, and 0 g/t of pine oil as a frother.

Figure 6 demonstrates that when the concentration of diesel collector increases, so does the recovery, but to a lesser extent than with the oil collector. As concentration rises, the percentage of ash grade also tends to rise, which is more so than with the oil collector.

Comparing the results of oil and diesel collectors reveals that oil collectors have superior performance.

**3. 4. Effect of Frother Concentration**

In this set of tests, pine oil frother with concentrations of 10, 20, and 30 grams per ton, 19% solids, pH = 7.7, and 150 microns in size, as well as oil collector with a concentration of 2,000 g/t, were utilized.

Figure 7 shows that raising the concentration of frother to 20 and 30 g/t has no noticeable effect on the

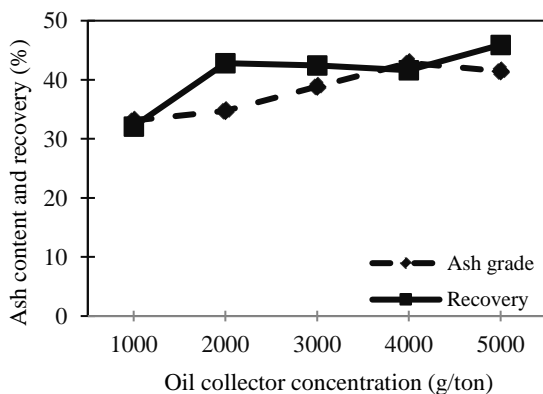


**Figure 5.** The ash content and coal recovery in concentrate for oil collector at various concentrations

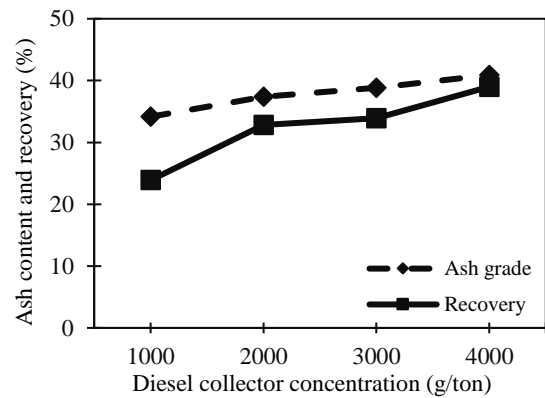


**Figure 6.** Ash content and coal recovery in concentrate for various diesel collector concentrations

ash grade, although the recovery follows a downward and upward trend.

Comparing the results and calculating the separation efficiency led to the selection of 30 g/ton for the pine oil frother.

**3. 5. Effect of Frother Type**

In this set of tests, MIBC frother with concentrations of 10, 20, and 30 grams per ton, 19% solids, pH = 7.7, and 150 microns in size, as well as oil collector with a concentration of 2,000 g/t, were utilized. Results of these tests are depicted in Figure 8.

Comparing the results of pine oil frother and MIBC frother reveals an increase in ash grade and a decrease in recovery. Consequently, pine oil frother yields superior results in terms of both ash content and coal recovery.

**3. 6. Effect of Soluble Salts**

In this series of studies, the influence of soluble salts on coal flotation was explored using pine oil frother, 19% solids, pH = 7.7, 150 micron diameter samples, and a 2000 g/t oil collector concentration. Table 4 demonstrates that as the concentration of soluble salts increases, so do the ash

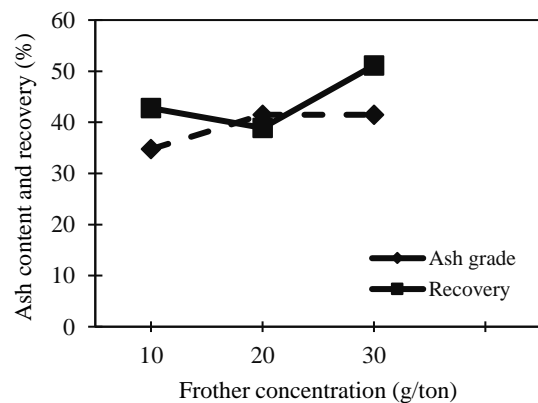


**Figure 7.** Ash content and coal recovery for various concentrations of pine oil frother

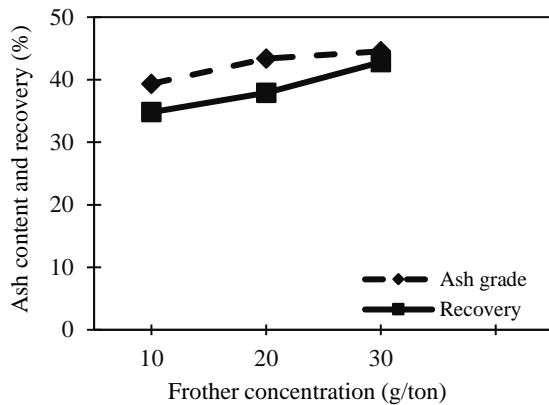


**Figure 8.** Ash content and coal recovery in concentrate as a function of the amount of MIBC frother

grade and coal recovery. However, it can be argued that its function in coal flotation is irrelevant.

### 3. 7. Optimizing the Flotation Cell's Mechanical Parameters

Once the chemical parameters of the cell have been determined through a series of tests, the mechanical parameters are optimized. Experiment design by Taguchi method of Design Expert (DX7) software can be used to determine the percentage of effect of each parameter, the influence of each parameter at each level, the optimal settings for each of these parameters, and the mutual influence of each of these parameters. The software obtained the lowest percentage of the ash in the concentrate and the greatest coal recovery with the fewest tests. The mechanical properties of the cell and its

**TABLE 4.** Effect of soluble salts on ash production and coal recovery

The concentration of dissolved salts (g/ton)	Concentrate (%)			Tailing (%)			Coal content in feed (%)
	Weight	Ash content	Coal recovery	Weight	Ash grade	Coal recovery	
NaCl (1000)	17.9	38.32	40.4	82.1	80.18	59.6	72.69
NaCl (2000)	20.8	42.37	44.4	79.2	81	55.6	72.95
CaCl <sub>2</sub> (1000)	21	46.88	45.6	79	81.06	54.4	73.12
CaCl <sub>2</sub> (2000)	24	47.31	48.1	76	80.04	51.9	71.56
FeCl <sub>3</sub> (1000)	21.5	42.95	42.7	78.5	80.85	57.3	72.56
FeCl <sub>3</sub> (2000)	22.5	44.32	44.2	77.5	81.31	55.8	73.36

surfaces were determined for this purpose using Table 2 in Section 2.5.

Based on the effective parameters, software (DX7) generated sixteen tests using the Taguchi method (L 16). These tests are listed in Table 3 according to their respective levels.

**3. 8. Statistical Analysis of Data** It might be advantageous to present the results of experiments in the form of an experimental model, or a model that expresses the relationship between the response variable and relevant design parameters (33). The technique employed is response surface (historical data). Given that the conducted tests yielded two results (recovery and percentage of ash), the software analyses were also based on these two variables.

#### 3. 8. 1. Variance Analysis of the Proposed Ash Content Model

Table 5 displays the significance of the model and recovery model factors. According to Table 5, the model's P and F values are 0.0001 and 24.89, respectively, which are statistically significant at the 95% confidence level. The greatest value of F is connected to the parameters E (cell volume), BE (the interaction between the distance of the stirrer from the cell bottom and the volume of the cell), and

B(the distance of the stirrer from the cell bottom) as depicted in Figure 9. The remaining F values, from highest to lowest, are connected to the parameters D

**TABLE 5.** ANOVA analysis of variance of ash percentage model

Source	Sum of squares	df	Mean square	F value	Prob>F
Model	1467.11	7	209.59	24.89	<0.0001 significant
A-mixer circulating	135.25	1	135.25	16.06	0.0039
B-mixer distance	161.64	1	161.64	19.2	0.0023
C-rate of ox	28.14	1	28.14	3.34	0.1049
D-skimmer circulating	153.11	1	153.11	18.19	0.0027
E-tank volume	501.92	1	501.92	59.61	<0.0001
BD	126.81	1	126.81	15.06	0.0047
BE	167.51	1	167.51	19.9	0.0021
Residual	67.35	8	8.42		
Cor total	1534.46	15			

(rotation speed of froth collector), A (rotation speed of agitator), BD (mutual impact of agitator distance from the cell bottom and froth collector rotation speed), and C (aeration rate).

Table 6 also displays the model's statistical data. The value of the correlation coefficient derived from the model demonstrates the model's high accuracy.

According to the graph, the projected values and actual values of ash percentage in Figure 10, the distribution of data around the line shows the model's normality and acceptability.

The following is the final equation for the ash percentage of the model based on the parameters of the software code factors:

$$\text{Grade (\%)} = +42.23 +4.25A +4.31B -1.79C +4.05D -7.30E +5.23BD -6.3BE$$

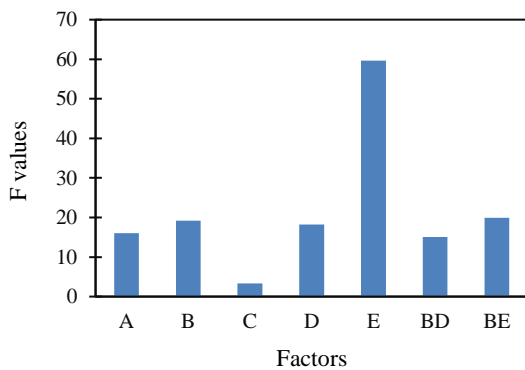


Figure 9. The model's effect of factors in terms of F value

TABLE 6. Statistical criteria of assessing model validity

STD. Dev.	2.9	R-Squared	0.9561
Mean	42.48	Adj R-squared	0.9177
C.V.%	6.83	Pred R-Squared	0.8025
PRESS	303.1	Adeq Precision	15.931

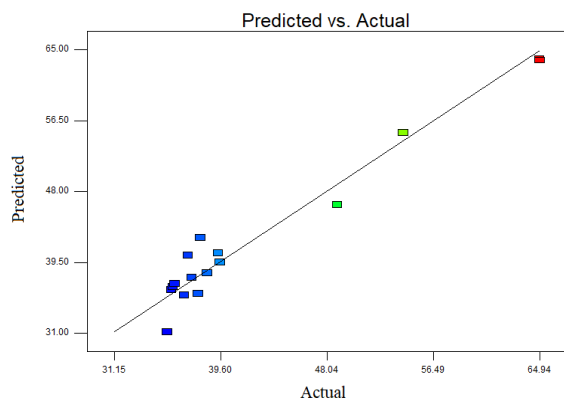


Figure 10. The percentage of actual ash relative to the amount anticipated by the model

**3. 8. 1. 1. Analysis of Geometric Graphs Provided by the Model** Due to the adequacy of the model, the geometric diagrams generated by the model have been evaluated in a single-factor and synchronous manner based on the response-influencing parameters.

**3. 8. 1. 2. The Effect of Single-factor Parameters**

A. Ash's response to stirrer rotating speed.

A linear relationship between stirrer speed and ash quality is depicted in Figure 11; as the speed of the stirrer is increased, so is the ash content.

B. The effect of aeration rate on ash content

As demonstrated in Figure 12, the aeration rate has a minimal impact on the process.

**3. 8. 1. 3. Interaction of Design Parameters with Coal Ash Content**

The software has the capability to examine the effect of parameters under varying circumstances.

A. Mutual effect of the stirrer's distance from the cell bottom and the froth collector's rotation speed on ash (BD)

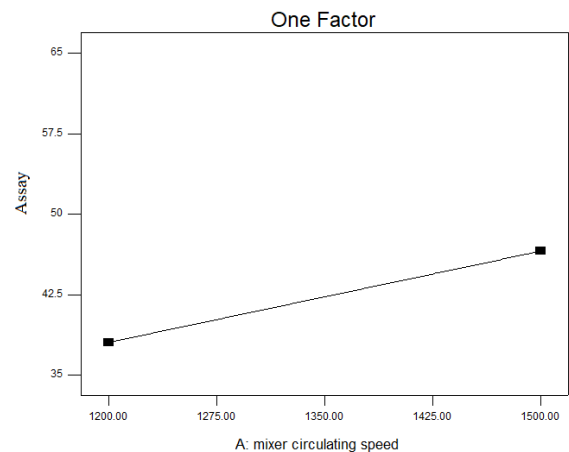


Figure 11. Effect of stirrer rotating speed on coal ash

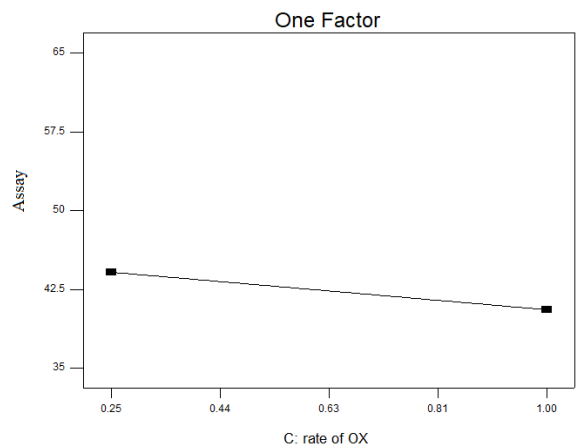


Figure 12. Effect of aeration on coal ash

According to the three-dimensional diagram and contour line in Figure 13, the proportion of ash increases as the stirrer's distance from the cell bottom and the froth collector's rotation speed increase. In such a way that the maximum ash percentage occurs at a stirrer distance of 0.4 H and a rotation speed of froth removal every 9 seconds, and the minimum ash percentage occurs at a stirrer distance of 0.1 H and froth removal every 3 seconds.

B. The mutual effect of the stirrer's distance from the froth and the cell's volume (BE)

Figure 14's three-dimensional diagram and contour line indicate that the distance of the stirrer from the cell bottom and the volume of the cell are inversely correlated. The lowest content of ash is found in cells with the highest volume and the stirrer closest to the bottom.

**3. 8. 2. Variance Analysis of the Proposed Model for Recovery** Table 7, Displays the significance of the model and recovery model parameters.

According to Table 7, the model's P and F values are 0.0009 and 11.49, respectively, which are significant at the 95% confidence level. As shown in Figure 15, the

maximum value of F corresponds to the parameters C (aeration rate). After that, the highest values are related to B<sup>2</sup> (enhanced effect of stirrer distance from the bottom), E (cell volume), D (rotating speed of skimmer), B (stirrer distance from the bottom), and BD (the mutual effect of the distance of the stirrer from the bottom and the rotation speed of the skimmer), respectively.

In Table 8, the model's statistical data are also reviewed. The value of the correlation coefficient derived from the model demonstrates the model's high accuracy.

Figure 16 shows a graph of predicted and actual ash percentage values, and the data distribution around the line proves the model's normality and appropriateness.

Following is the final model recovery equation based on the conditions of software code factors:

$$\text{Recovery (\%)} = +35.44 - 3.78B + 8.92C + 4.28D - 5.08E - 4.38BD - 10.3B^2$$

**3. 8. 2. 1. Analysis of Geometry Diagrams Generated by the Model**

Due to the adequacy of the model, the geometry diagrams generated by the model have been evaluated in a single-factor and simultaneous manner based on the response-influencing variables.

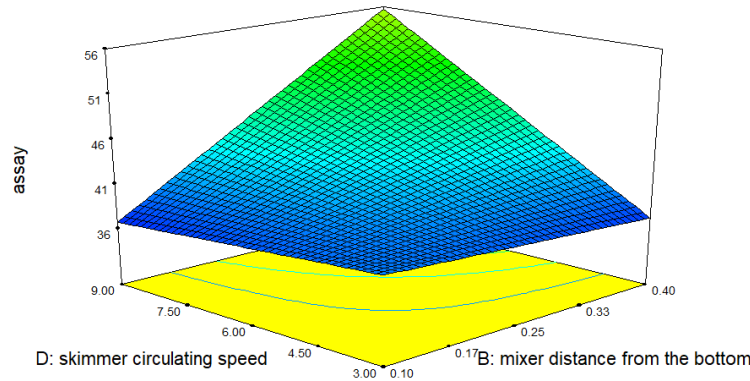


**Figure 13.** The mutual effect of the stirrer's distance from the bottom and the skimmer rotation speed on the percentage of coal ash. A: 3-dimensional B: Contour line

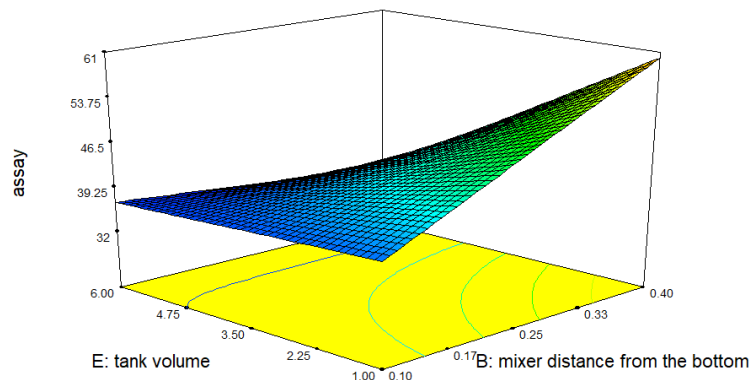


**Figure 14.** The mutual effect of the stirrer's distance from the bottom and the cell volume. A: 3-dimensional B: Contour line

**TABLE 7.** ANOVA analysis of variance recovery model

Source	Sum of squares	df	Mean square	F value	Prob>F	
Model	1657.35	6	276.22	11.49	0.0009	significant
B-mixer distance	126.51	1	126.51	5.26	0.0475	
C-rate of ox	705.27	1	705.27	29.34	0.0004	
D-skimmer circulating	173.84	1	173.84	7.23	0.0248	
E-tank volume	243.19	1	243.19	10.12	0.0112	
BD	95.97	1	95.97	3.99	0.0768	
B <sup>2</sup>	330.86	1	330.86	13.76	0.0048	
Residual	216.36	9	24.04			
Cor total	1873.71	15				

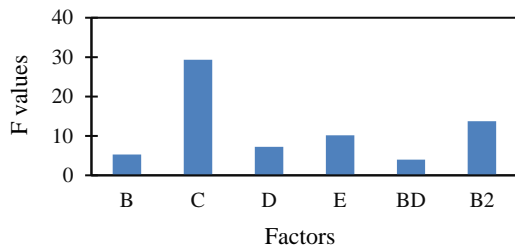


**Figure 15.** The model's influence of factors in terms of F value

**TABLE 8.** Statistical evaluation criteria for model validity

STD. Dev.	4.9	R-Squared	0.8845
Mean	29.99	Adj R-squared	0.8075
C.V.%	16.35	Pred R-Squared	0.5658
PRESS	813.54	Adeq Precision	11.105

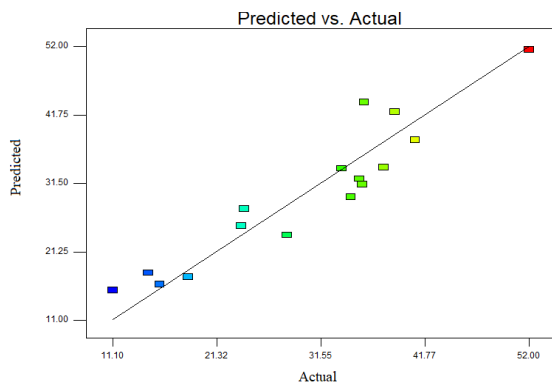


**Figure 16.** Actual recovery compared to the recovery predicted by the model

### 3. 8. 2. 2. Effect of Single Variables

#### A. Aeration rate

As shown in Figure 17, there is a clear correlation between the aeration rate and the recovery, and by raising the aeration rate and fully opening the aeration valve, a substantial improvement in recovery is observed.

#### B. Cell volume

According to Figure 18, the relationship between cell volume and recovery is inverse, with recovery decreasing as cell volume increases.

### 3. 8. 2. 3. Mutual Effects of Design Factors on Coal Recovery

The software includes the capability to examine the effect of parameters under varying circumstances.

A- The mutual effect of the rotation speed of the skimmer and the distance of the stirrer from the froth (BD)

The three-dimensional graphic and contour lines in Figure 19 show that the maximum recovery occurs when the stirrer is about 0.2 H away from the tank bottom and the skimmer rotates once every 9 seconds.

### 3. 8. 3. Optimal Values of Parameters in the Design of Experiments

In order to optimize the software parameters in line with the research objectives, the

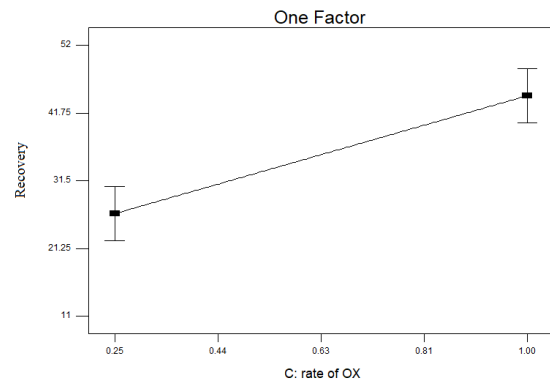


**Figure 17.** Implications of aeration rate on coal recovery

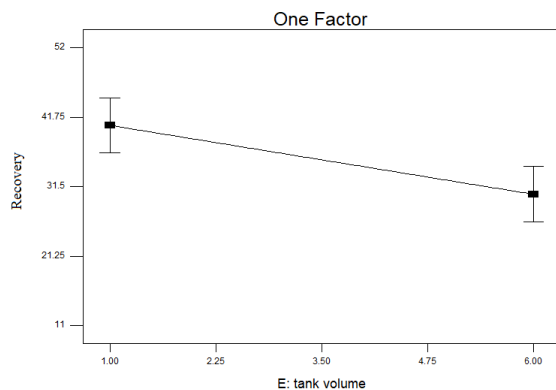


**Figure 18.** Implications of cell volume on coal recovery

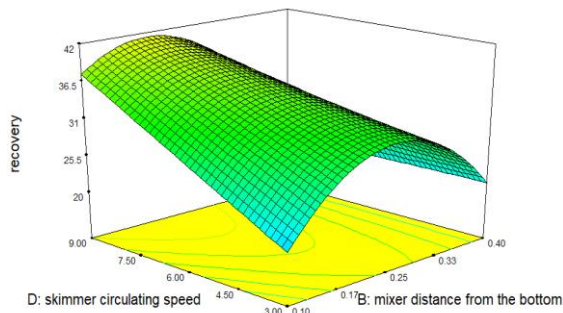


**Figure 19.** The mutual effects between skimmer rotating speed and stirrer distance from tank bottom on coal recovery. A: 3-dimensional B: Contour line

percentage of ash in the minimum state and recovery in the maximum state were considered. Other variables such as the speed of the stirrer, the stirrer distance from the tank bottom, the aeration rate, the speed of the skimmer, and the volume cell were placed within the appropriate range. Figure 20 demonstrates the best mode. The following are the results obtained with a level of utility of 1:

Stirrer rotation speed = 1227.2 rpm

The distance of the stirrer from the tank bottom = 0.13 H

Aeration rate = 1 (fully open)

Rotation speed of skimmer = every 8.49 seconds

Cell volume = 1 liter

Ash percentage = 35.34%

Recovery = 52%

Four experiments were done under the aforementioned conditions to validate its accuracy. In these four experiments, the average recovery and grade of ash were approximately 54% and 33%, respectively.

Ministry of Environment Forest & Climate Change (MoEF&CC) allows use of coal with ash content less than 34% in thermal power plants (34). Therefore, even producing a 34% ash concentrate is valuable and marketable without creating environmental pollution; however, the ash produced in this research returns to the processing circuit.

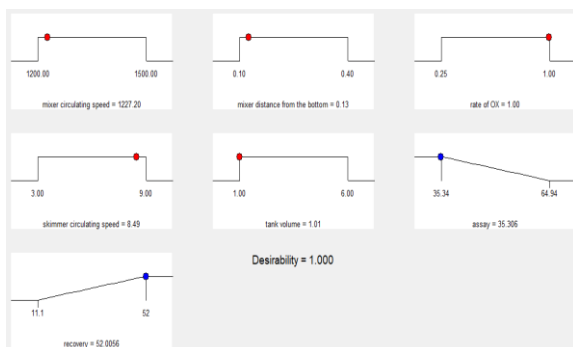


**Figure 20.** Optimal conditions predicted by the statistical model

#### 4. CONCLUSIONS

The coal tailings of Agh-Darband mine with 75% ash so far include a volume of 140,000 tons in the place of the tailings depot from the coal washing plant. Therefore, this research was done in order to reach a product with a grade of 30-35% to return it to the processing circuit. In this regard, flotation tests were performed and the chemical and mechanical parameters of the cell were optimized.

Following are the optimal results of flotation tests (chemical parameters) for achieving the lowest ash content and highest recovery:

Particle size range (d80): 150 microns

Solid percentage: 18%

Oil collector: 2000 grams per ton

Pine oil frother: 30 grams per ton

pH: in the neutral range

After optimizing the chemical parameters, the design expert software was used to optimize the mechanical parameters of the cell, including the rotation speed of the stirrer (A), the distance of the stirrer from the tank bottom (B), the aeration rate (C), the rotation speed of the skimmer (D), and the volume of the cell (E). Software optimization led to a recovery of approximately 52% and an ash content of approximately 35%:

1. Stirrer rotation speed = 1227.2 rpm

2. The distance of the stirrer from the froth = 0.13 H

3. Aeration rate = 1 (completely open)

4. Rotation speed of the skimmer = every 8.49 seconds

5. Cell volume = 1 liter

Following is the final model recovery equation based on the conditions of software code variables:

$$\text{Recovery (\%)} = +35.44 - 3.78B + 8.92C + 4.28D - 5.08E - 4.38BD - 10.3B^2$$

The following is the final equation of the model's ash content according to the requirements of the software code variables:

$$\text{Grade (\%)} = +42.23 + 4.25A + 4.31B - 1.79C + 4.05D - 7.30E + 5.23BD - 6.3BE$$

Using the optimal parameter values, the average recovery and ash content were approximately 54% and 33%, respectively.

Based on the reported experiments and results, the following recommendations can be made to continue the work:

- Using positive laboratory results, it is required to undertake semi-industrial tests so that the responses obtained are as similar as possible to industrial settings, making it easier to make the correct decision.

- In accordance with the ash grade (about 33%) produced by optimizing the chemical and mechanical parameters of the cell, the coal tailing washing product may be used as the input of the processing plant's current

circuit, and consequently, the mine coal tailings can be returned to the circuit.

Therefore, producing a 34% ash concentrate is valuable and marketable without creating environmental pollution.

## 5. REFERENCES

- Leonard III JW. Coal preparation. 1991.
- Yüce E, Güney A, Onal G, Kangal O, Kökkiliç O, Ozer M, et al., editors. Fine coal evaluation by gravity, methods. XXV International Mineral Processing Congress 2010, IMPC 2010; 2010.
- Mijał W, Tora B, editors. Development of dry coal gravity separation techniques. IOP Conference Series: Materials Science and Engineering; 2018: IOP Publishing. 10.1088/1757-899X/427/1/012003
- Phengsaart T, Srichonphaisan P, Kertbundit C, Soonthornwiphat N, Sinthugoot S, Phumkokrux N, et al. Conventional and recent advances in gravity separation technologies for coal cleaning: A systematic and critical review. *Heliyon*. 2023. <https://doi.org/10.1016/j.heliyon.2023.e13083>
- Özbayoğlu G. Coal flotation. *Mineral processing design*. 1987:76-105. [https://doi.org/10.1007/978-94-009-3549-5\\_4](https://doi.org/10.1007/978-94-009-3549-5_4)
- Li L, Lu X, Qiu J, Liu D. Effect of microemulsified collector on froth flotation of coal. *Journal of the Southern African Institute of Mining and Metallurgy*. 2013;113(11):877-80.
- Dong Z, Wang R, Fan M, Fu X. Switching and optimizing control for coal flotation process based on a hybrid model. *Plos one*. 2017;12(10):e0186553. <https://doi.org/10.1371/journal.pone.0186553>
- Feng Q, Wang M, Zhang G, Zhao W, Han G. Enhanced adsorption of sulfide and xanthate on smithsonite surfaces by lead activation and implications for flotation intensification. *Separation and Purification Technology*. 2023;307:122772. <https://doi.org/10.1016/j.seppur.2022.122772>
- Taşdemir T, Taşdemir A. Optimization of floc-flotation process in the removal of suspended particles from wastewater in a Jameson cell using central composite design. *Journal of Water Process Engineering*. 2023;52:103552. <https://doi.org/10.1016/j.jwpe.2023.103552>
- Sokolović J, Misković S. The effect of particle size on coal flotation kinetics: A review. *Physicochemical Problems of Mineral Processing*. 2018;54(4):1172-90. <https://doi.org/10.5277/ppmp18155>
- Tian Q, Wang H, Pan Y. Associations of Gangue Minerals in Coal Flotation Tailing and Their Transportation Behaviors in the Flotation Process. *ACS omega*. 2022;7(31):27542-9. <https://doi.org/10.1021/acsomega.2c02988>
- Leonard JW, Hardinge BC. *Coal Preparation*, Society for Mining, Metallurgy, and Exploration. Inc Littleton, Colorado. 1991:467-70.
- Vamvuka D, Agridiotis V. The effect of chemical reagents on lignite flotation. *International Journal of Mineral Processing*. 2001;61(3):209-24. 10.1016/S0301-7516(00)00034-X
- Akdemir Ü, Sönmez İ. Investigation of coal and ash recovery and entrainment in flotation. *Fuel Processing Technology*. 2003;82(1):1-9. 10.1016/S0378-3820(02)00248-5
- Kumar CL M, KG S, Sunagar P, Noroozinejad Farsangi E. Studies on Contaminated Mine Soil and Its Remediation Using Soil Washing Technique-A Case Study on Soil at Kolar Gold Fields. *International Journal of Engineering, Transactions A: Basics*. 2022;35(1):201-12. 10.5829/IJE.2022.35.01A.19
- Naik PK, Reddy P, Misra VN. Optimization of coal flotation using statistical technique. *Fuel Processing Technology*. 2004;85(13):1473-85. <https://doi.org/10.1016/j.fuproc.2003.10.005>
- Hacifazlioglu H, Sutcu H. Optimization of some parameters in column flotation and a comparison of conventional cell and column cell in terms of flotation performance. *Journal of the Chinese Institute of Chemical Engineers*. 2007;38(3-4):287-93. 10.1016/j.jcice.2007.03.006
- Hacifazlioglu H, Toroglu I. Optimization of design and operating parameters in a pilot scale Jameson cell for slime coal cleaning. *Fuel processing technology*. 2007;88(7):731-6. <https://doi.org/10.1016/j.fuproc.2007.03.003>
- Jena MS, Biswal S, Rudramuniyappa M. Study on flotation characteristics of oxidised Indian high ash sub-bituminous coal. *International Journal of Mineral Processing*. 2008;87(1-2):42-50. <https://doi.org/10.1016/j.minpro.2008.01.004>
- Çınar M. Floatability and desulfurization of a low-rank (Turkish) coal by low-temperature heat treatment. *Fuel Processing Technology*. 2009;90(10):1300-4. <https://doi.org/10.1016/j.fuproc.2009.06.017>
- Anderson CJ, Harris M, Deglon D. Flotation in a novel oscillatory baffled column. *Minerals Engineering*. 2009;22(12):1079-87. 10.1016/j.mineng.2009.04.007
- Shukla SC, Kundu G, Mukherjee D. Study of gas holdup and pressure characteristics in a column flotation cell using coal. *Minerals Engineering*. 2010;23(8):636-42. 10.1016/j.mineng.2010.03.005
- Vapur H, Bayat O, Uçurum M. Coal flotation optimization using modified flotation parameters and combustible recovery in a Jameson cell. *Energy Conversion and management*. 2010;51(10):1891-7. 10.1016/j.enconman.2010.02.019
- Dashti A, Nasab ME. Optimization of the performance of the hydrodynamic parameters on the flotation performance of coarse coal particles using design expert (DX8) software. *Fuel*. 2013;107:593-600. 10.1016/j.fuel.2012.11.066
- Piñeres J, Barraza J. Effect of pH, air velocity and frother concentration on combustible recovery, ash and sulphur rejection using column flotation. *Fuel Processing Technology*. 2012;97:30-7. <https://doi.org/10.1016/j.fuproc.2012.01.004>
- Bao X, Liu J, Wang S, Chen D, Xu W, Zhang D, et al. New Insight into Temperature Effects on Low-Rank Coal Flotation Using Diesel as a Collector. *ACS omega*. 2023;8(17):15479-87. 10.22103/JSSE.2023.3816
- Chelgani SC, Nasiri H, Alidokht M. Interpretable modeling of metallurgical responses for an industrial coal column flotation circuit by XGBoost and SHAP-A “conscious-lab” development. *International Journal of Mining Science and Technology*. 2021;31(6):1135-44. <https://doi.org/10.1021/acsomega.3c00774>
- Wen Z, Zhou C, Pan J, Nie T, Jia R, Yang F. Froth image feature engineering-based prediction method for concentrate ash content of coal flotation. *Minerals Engineering*. 2021;170:107023. <https://doi.org/10.1016/j.mineng.2021.107023>
- Wen Z, Zhou C, Pan J, Nie T, Zhou C, Lu Z. Deep learning-based ash content prediction of coal flotation concentrate using convolutional neural network. *Minerals Engineering*. 2021;174:107251. <https://doi.org/10.1016/j.mineng.2021.107251>
- Yang X, Zhang K, Ni C, Cao H, Thé J, Xie G, et al. Ash determination of coal flotation concentrate by analyzing froth image using a novel hybrid model based on deep learning algorithms and attention mechanism. *Energy*. 2022;260:125027. <https://doi.org/10.1016/j.energy.2022.125027>
- Sachinraj D, Kopparthi P, Samanta P, Mukherjee A. Optimization of Column Flotation for Fine Coal Using Taguchi Method.

- Transactions of the Indian Institute of Metals. 2022;75(5):1255-67. <https://doi.org/10.1007/s12666-021-02512-2>
32. Hazare G, Pradhan SS, Dash N, Dwari RK. Studies on low-grade coking coal characterisation, flotation response and process optimisation. International Journal of Coal Preparation and Utilization. 2023;1-23. 10.1080/19392699.2022.2164572
33. Hosseini Nasab M, Noaparast M, Abdollahi H. Dissolution optimization and kinetics of nickel and cobalt from iron-rich laterite ore, using sulfuric acid at atmospheric pressure. International Journal of Chemical Kinetics. 2020;52(4):283-98. <https://doi.org/10.1002/kin.21349>
34. NITI Aayog. 2020 - Economic and Environmental Impact of Coal Washing in India National Institution for Transforming India (NITI Aayog). India2020 [Available from: <https://policycommons.net/artifacts/2421097/2020/3442689/>].

**COPYRIGHTS**

©2024 The author(s). This is an open access article distributed under the terms of the Creative Commons Attribution (CC BY 4.0), which permits unrestricted use, distribution, and reproduction in any medium, as long as the original authors and source are cited. No permission is required from the authors or the publishers.

**Persian Abstract**

چکیده

یکی از معادن بزرگ زغال‌سنگ در شرق ایران، معدن آق‌دریوند است که در سرخس قرار دارد. کارخانه آق‌دریوند با محتوای کمتر از ۳۷ درصد خاکستر در ورودی و حدود ۱۲ درصد خاکستر در محصول کار می‌کند. به دلیل مستهلک بودن تجهیزات و نبود شرایط بهینه برای سیستم فرآوری، مقدار زیادی از زغال‌سنگ خوراک وارد قسمت باطله می‌شود به طوری که میزان خاکستر در باطله حدود ۷۵ درصد است. هدف از این تحقیق بررسی این موضوع است که آیا روش فلوتاسیون می‌تواند باطله معدن با محتوای خاکستر ۷۵ درصد را فرآوری کرده و محتوای آن را برای بازگشت به مدار فرآوری کاهش دهد. برای این منظور آزمایش‌های مختلف فلوتاسیون بر روی ۷۰ کیلوگرم باطله معدن آق‌دریوند انجام شد. شرایط بهینه در pH خنثی با ۲۰۰۰ گرم در تن کلکتور نفت، ۳۰ گرم در تن روغن کاج به عنوان کف ساز و محتوای جامد ۱۸ درصد به دست آمد که محتوای خاکستر زغال‌سنگ و بازیابی به ترتیب ۳۴ و ۴۵ درصد بود. همچنین با استفاده از نرم افزار طراحی آزمایش (DX7)، پارامترهای مکانیکی سلول مانند سرعت گردش همزن، فاصله همزن از کف سلول، نرخ هوادهی، سرعت گردش کفگیری و حجم سلول بهینه شد. مقادیر بهینه پارامترها عبارت بودند از: سرعت گردش همزن =  $1227/2$  دور در دقیقه، فاصله همزن از کف سلول =  $0/13$  ساعت، نرخ هوادهی = ۱ (کاملاً باز)، سرعت گردش کفگیر = هر  $8/49$  ثانیه، حجم سلول = ۱ لیتر، درصد خاکستر =  $35/34$  درصد و بازیابی ۵۲ درصد بود.



## Seismic Assessment of Concrete Dams, Considering Anisotropy Caused by Lift Joints

R. Saeed\*, A. J. Moradloo

Department of Civil Engineering, Faculty of Engineering, University of Zanjan, Zanjan, Iran

### PAPER INFO

#### Paper history:

Received 21 August 2023  
Received in revised form 02 November  
Accepted 04 November 2023

#### Keywords:

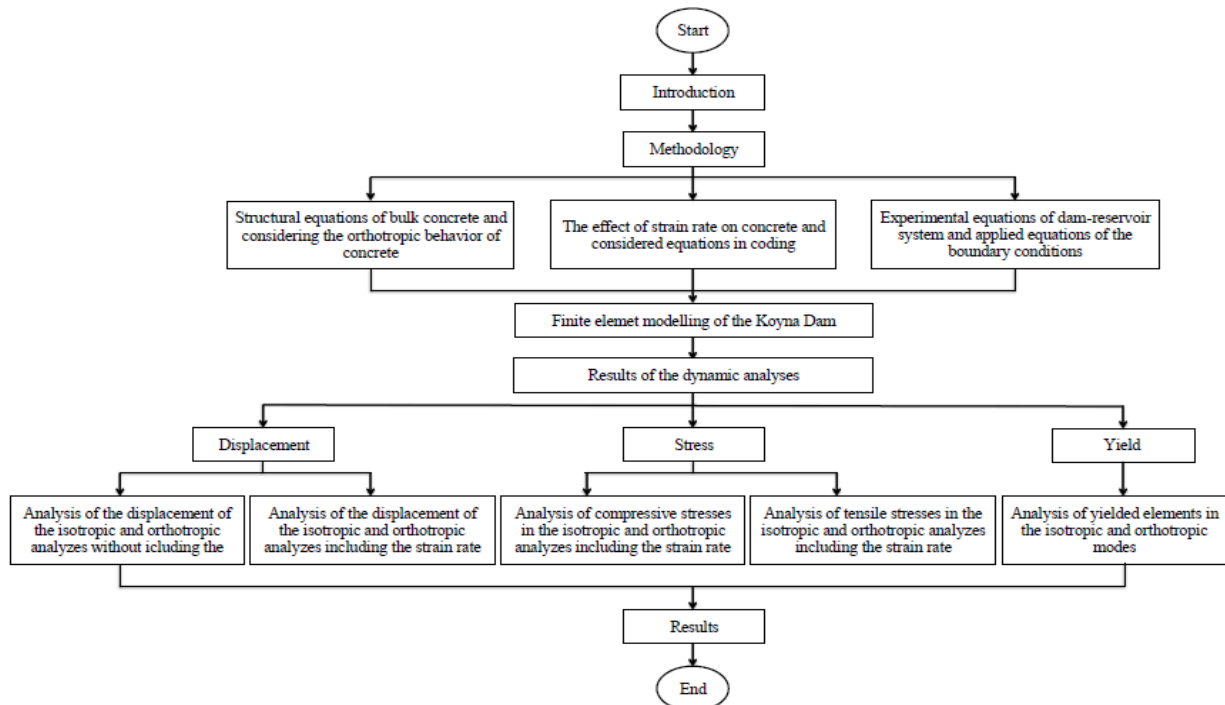
Concrete Anisotropy  
Lift Joints  
Orthotropic Behavior  
Concrete Gravity Dams  
Seismic Loading

### ABSTRACT

Concrete dams are anisotropic due to lift joints that affect their performance. Lift joints are usually ignored in numerical analyses of concrete dams and the dam body is assumed to be homogeneous and isotropic. In this study, the seismic behavior of gravity dams was evaluated considering the anisotropy caused by lift joints, and the orthotropic and isotropic state responses were compared. Moreover, in the seismic loading range, a more detailed evaluation was done by applying the real effects of strain rate. Koyna concrete gravity dam was selected for the case study. The results showed that concrete anisotropy leads to larger dynamic displacements and greater damage to the dam body. By considering the orthotropic properties of concrete can lead to more realistic results. The maximum compressive and tensile stresses also increased in the anisotropic model compared to the homogeneous and isotropic model, indicating the usefulness of incorporating the orthotropic behavior of concrete in seismic analysis. In addition, considering the strain rate in the seismic loading range had an insignificant effect on the results. Therefore, considering the large dynamic increase factor in numerical analyses causes the error.

doi: 10.5829/ije.2024.37.04a.14

### Graphical Abstract



\*Corresponding Author Email: [Rezvan.saeed@znu.ac.ir](mailto:Rezvan.saeed@znu.ac.ir) (R. Saeed)

Please cite this article as: Saeed R, Moradloo AJ. Ash Seismic Assessment of Concrete Dams, Considering Anisotropy Caused by Lift Joints. International Journal of Engineering, A: Basics. 2024;37(04):753-62.

**NOMENCLATURE**

$d\sigma$	Stress increment	$d\varepsilon$	Strain increments
$[D]_0^{\text{Orth}}$	Orthotropic module matrix	$[D]_0^{\text{Iso}}$	Isotropic module matrix
$E_i$	Young's modulus	$G_{ij}$	Shear modulus
$T$	Rotation matrix	$D$	Material matrix
$\nu_{ij}$	Poisson's ratio	$t$	Time
$\dot{\varepsilon}$	Strain rate	$\varepsilon$	Strain
$CDIF$	Compressive DIF	$TDIF$	Tensile DIF
$P$	Hydrodynamic pressure in the reservoir	$C$	Sound propagation speed through fluid
$\bar{a}_{ns}$	Acceleration in the dam-reservoir interface	$q$	Admittance coefficient
$n$	Unit vector	$\ddot{v}_{gn}$	Ground acceleration
$\{R\}$	Matrix of ground motion effect on freedom degrees of structure nodes	$\alpha_b$	Ratio of the reflected wave amplitude to the incident wave
$[M_s]$	Mass matrices of the structure	$[C_s]$	Damping matrices of the structure
$[K_s]$	Stiffness matrices of the structure	$[M_f]$	Mass matrices of fluid
$[C_f]$	Damping matrices of fluid	$[K_f]$	Stiffness matrices of fluid
$\{\ddot{a}\}$	Acceleration vectors	$\{\dot{a}\}$	Velocity vectors
$\{a\}$	Displacement vectors	$Q$	Dam-reservoir interaction matrix

**1. INTRODUCTION**

Dams are structures whose continuous evaluation is of great importance. Due to their large scale, experimental study of concrete dams is difficult and therefore, the numerical simulation is used in the dynamic analysis of such dams more effectively (1). To study the real behavior of these structures, acceptable modeling assumptions should be considered, and simplifying assumptions should be avoided. Based on the construction method of concrete dams, lift joints are inevitable. These joints cause weaker plates in the dam body that induce concrete anisotropy of the dam (2). While, in most studies, the dam body is considered homogenous and isotropic; however, these layers play an important role in the system response which leads to a more realistic response. Moreover, the strain rate is very influential in dynamic evaluation that should be evaluated in the seismic loading accurately and its real effects should be incorporated in the dynamic analyses. Ozturk (3) studied the effects of ground motion speed on the nonlinear displacement response of single degree of freedom (SDOF) systems and the relationship between the maximum nonlinear displacement response and the ground motion speed was evaluated. Fei and Gao (4) performed the dynamic analysis of concrete dams considering nonlinear materials. They developed a strain-dependent model to analyze the Koyna Gravity Dam and the Dagangshan Arch Dam. Based on the obtained results, different values of plastic strains were obtained using the models with and without considering strain rate, with the same distributions. Plastic deformations mainly occurred in areas with maximum tensile stress indicating tensile failure under seismic loads in these areas. Hesari et al. (5) studied the effect of contraction joints and lift joints on the seismic behavior of the Karoun 1 Arch Dam. The dam-reservoir-foundation system was modeled with and without joints, and the effect of contraction joints and lift joints on stress and

displacement response under the effect of the earthquake was studied. According to the dynamic analysis results, considering the joints has a significant effect on the responses. By Hariri-Ardebili et al. (6) seismic evaluation of arch dams was investigated. Dez dam was chosen as the case study and all contraction and peripheral joints were modeled based on as-built drawings. Then, nonlinear seismic analysis of concrete arch dam-reservoir-foundation system considering joints behavior was investigated. The linear and nonlinear seismic analyses of concrete gravity dams were performed by Ouzandja and Tiliouine (7) and the effects of dam-foundation contact conditions on the seismic performance of the Oued Fodda concrete gravity dam were investigated. Alembagheri and Ghaemian (8) studied the seismic performance of arch concrete dams considering contraction joints using the ABAQUS Software for the analysis of the Morrow-Point Dam case study considering three cases of integrated, three-joint, and seven-joint dam models. The results showed that incorporating contraction joints in the analysis had an insignificant effect on main tensile stresses, however, increased compressive stresses. In seismic analyses, an increase in the number of contraction joints generally decreased joint opening and sliding displacements. The opening of contraction joints changes the stress distribution in these structures and increases compressive stress which may result in concrete failure. Contraction joints can significantly decrease damage to the dam body and consequently, increase the seismic safety of the arch concrete dams. Yazdani and Alembagheri (9) studied the dynamic response of solid and cracked gravity dams. Pine Flat Dam was modeled considering a solid foundation and dam reservoir to study the effects of base joints and lift joints. Models of a solid dam, a dam with base joints, and a dam with base joints and two lift joints were developed and the results were compared. The structural stability and safety of the Pine Flat gravity dam located on an inhomogeneous rock foundation under the

static loads of self-weight, hydrostatic, and uplift pressure were evaluated by Ganji and Alembagheri (10). Latorre and Montans (11) presented a new theory for isotropic and anisotropic elastoplastic materials in large strains, which could be applied to elastoplastic metals and soft materials by incorporating strain rate as well. Lu et al. (12) studied the effects of heterogeneity on the nonlinear seismic response of concrete gravity dams and indicated that incorporating concrete heterogeneity can lead to higher damage to the concrete dams. Hai-tao et al. (13) numerically simulated the Koyna Dam under various seismic waves and studied the elastic-plastic seismic response of the Koyna Dam and the results of different scenarios were compared with actual damage to the dam. Ganji et al. (14) performed the seismic analysis of the Pine Flat gravity dam-reservoir-foundation system considering an inhomogeneous foundation. Different foundation characteristics were used and a heterogenic foundation was modeled. Assuming a homogeneous foundation results in a lower average of seismic responses. Hariri Ardebili (15) studied concrete heterogeneity by focusing on concrete dams and indicated that concrete heterogeneity affects progressive failure analysis and therefore, should be included in risk assessments. It was also indicated that crack propagation in macro-heterogeneous materials may differ from homogeneous ones. Therefore, it becomes more important in the case of concrete gravity dams which are more susceptible to heterogeneity due to construction limitations. Guo et al. (16) studied the seismic response of the arch dam considering the vertical and shear joints. The results showed a significant effect of joints on the stress distribution in the nonlinear model, with a significantly increased maximum main tensile stress. Lee and Kwak (17) proposed a strain rate-dependent orthotropic model for reinforced concrete with steel fiber subjected to impact or blast loads. The improved model was an orthotropic model introduced by the same author for plain concrete. Then, the model was analyzed using Ls-Dyna numerical model. The model has minimal dependence on mesh size and can be developed by adding different concrete parameters. Pan (18) developed a complete model of the dam system, foundation, and reservoir to study the effect of concrete heterogeneity on the seismic response of the dam. The Weibull probabilistic distribution assumption was used to define concrete heterogeneity. The results showed that concrete heterogeneity significantly influences the seismic damage to the concrete gravity dams. Lu et al. (19) evaluated damage to the concrete gravity dams considering the heterogeneity of concrete tensile strength and indicated that the possibility of failure increased. Liu et al. (20) studied the effects of concrete heterogeneity on the nonlinear seismic response of concrete gravity dams under different earthquakes. The ABAQUS Software was used to model the Koyna Dam and to include strain

rate, dynamic resistance was assumed 20% higher than the static resistance. The uncertainty of seismic responses and damage patterns were quantified, and the correlation effect between the module and concrete strength was studied. It was concluded that there were significant differences between seismic responses of the homogenous and heterogeneous models, and ignoring the concrete heterogeneity can result in an incorrect estimation of damage pattern to the concrete gravity dams, and the effects of concrete heterogeneity on the nonlinear dynamic response of concrete dams are highly dependent on the input seismic motions. Kadhim et al. (21) studied the behavior of cracked arched concrete dam under moderate intensity earthquake experimentally as well as by using nonlinear analyses. The extended finite element method (XFEM) was described for crack propagation. Li et al. (22) performed a fuzzy analysis of the seismic fragility of gravity dams. Due to different concrete strengths at different dam locations caused by concreting process and concrete heterogeneity, they proposed a method for fuzzy-seismic analysis of dams incorporating local changes in material properties. In this case, the damage to the dam body is intensified which is accompanied by an increase in the number and depth of cracks. They reported that ignoring concrete heterogeneity can lead to an underestimation of the seismic fragility of concrete gravity dams. It can be concluded that, in the construction of gravity dams, the quality of concreting process should be thoroughly observed to reduce local changes in concrete strength. Due to significant financial, fatal and environmental damages, high importance structures are expected to continue their performance after the earthquake. As a result, more research on the seismic performance of these structures is required to achieve their highest level of earthquake resistance (23). In addition, by knowing the behavior of the structure and analyzing it accurately, it is possible to build new structures as well as repair, reconstruct, renovate and retrofit existing structures (24). Based on the technical literature, it is observed that assuming concrete homogeneity and isotropy leads to incorrect results in seismic analyses. Therefore, this has been taken into account in recent evaluations. In many studies, a few layers in the dam height have been modeled to include lift joints. Although the layers are located in sensitive areas in numerical modeling and are determined based on crack profiles of nonlinear seismic finite element analysis, however, there are intermittent lift joints throughout the dam height with different concrete properties. So, modeling based on a limited number of layers is erroneous and despite accurate modeling of the layers, it is accompanied by approximation due to dealing with anisotropic materials. Therefore, lift joints, which are weaker plates with different characteristics than concrete and are alternately present throughout the dam height. Considering limited few lift joints in the dam

height causes errors and leads to incorrect results. Therefore, in the present study, for more accurate modeling, orthotropic material was used to include the lift joints and the mechanical behavior of concrete in the direction perpendicular to the lift joints was considered different from that of the horizontal planes. On the other hand, considering the effect of strain rate in dynamic loading, in the present study, using experimental equations and taking into account the real effects of strain rate in the seismic loading range, strain rate was included in a more precise way in modeling. Therefore, in order to have a more accurate modeling, the effects of loading rate and strain rate were studied. The Finite Element Method (FEM) is widely adopted due to its ability to deal with heterogeneous and anisotropic materials and complex boundaries (25). In the present study, the required elements and subroutines were added to the FEAPPv finite-element model, and a new program called GFEAP was developed. Then, the dynamic behavior of the Koyna Gravity Dam was studied using the developed finite-element numerical model. The geometrical input models,

$$[D]_0^{Orth} = \frac{1}{\Omega} \begin{bmatrix} E_1(1 - \nu_{23}\nu_{32}) & E_1(\nu_{21} + \nu_{23}\nu_{31}) & E_1(\nu_{31} + \nu_{21}\nu_{32}) & 0 & 0 & 0 \\ E_2(\nu_{12} + \nu_{13}\nu_{32}) & E_2(1 - \nu_{13}\nu_{31}) & E_2(\nu_{32} + \nu_{12}\nu_{31}) & 0 & 0 & 0 \\ E_3(\nu_{13} + \nu_{12}\nu_{23}) & E_3(\nu_{23} + \nu_{13}\nu_{21}) & E_3(1 - \nu_{12}\nu_{21}) & 0 & 0 & 0 \\ 0 & 0 & 0 & G_{12}\Omega & 0 & 0 \\ 0 & 0 & 0 & 0 & G_{23}\Omega & 0 \\ 0 & 0 & 0 & 0 & 0 & G_{31}\Omega \end{bmatrix} \quad (2)$$

where

$$\Omega = 1 - \nu_{21}\nu_{12} - \nu_{31}\nu_{13} - \nu_{32}\nu_{23} - \nu_{12}\nu_{23}\nu_{31} - \nu_{21}\nu_{32}\nu_{13} \quad (3)$$

In the above matrix,  $\nu_{ij}$  is Poisson's ratio ( $i, j = 1, 2, 3$ ),  $E_i$  is Young's modulus in the direction  $i$  ( $i = 1, 2, 3$ ), and  $G_{ij}$  is shear modulus in plane  $i-j$  ( $i, j = 1, 2, 3$ ) and is calculated as follows:

$$G_{ij} = \frac{E_i E_j}{E_i(1 + \nu_{ij}) + E_j(1 + \nu_{ji})} \quad (4)$$

By taking into account the effect of lift joints under static and dynamic loads, the material properties can be assumed isotropic in two horizontal directions, and new concrete properties in a direction perpendicular to lift joints can be defined. As a result (2):

$$\frac{\nu_{12}}{E_1} = \frac{\nu_{21}}{E_2}, \frac{\nu_{13}}{E_1} = \frac{\nu_{31}}{E_3}, \frac{\nu_{23}}{E_2} = \frac{\nu_{32}}{E_3} \quad (5)$$

For isotropic materials (29, 30):

$$E_1 = E_2 = E_3 = E, \nu_{12} = \nu_{13} = \nu_{23} = \nu, \quad (6)$$

$$G_{12} = G_{13} = G_{23} = G$$

The isotropic module matrix,  $[D]_0^{Iso}$ , is as follows (29):

assembling matrices, and solver vectors of the original numerical model were used and a three-dimensional 20-node serendipity element as well as a 20-node fluid element were added to the numerical model. Moreover, by adding the required sub-routines, the behavior of the concrete gravity dam under seismic loading was analyzed considering strain rate effects and orthotropic concrete properties.

## 2. METHODOLOGY

### 2. 1. Structural Relationship of Mass Concrete

The overall stress-strain equation can be expressed as follows (26-28):

$$d\sigma = D_0 d\varepsilon \quad (1)$$

where  $d\sigma$  and  $d\varepsilon$  are stress and strain increments, respectively. In the anisotropic case, the module matrix,  $[D]_0^{Orth}$ , is defined as follows:

$$[D]_0^{Iso} = \frac{E}{(1+\nu)(1-2\nu)} \begin{bmatrix} 1-\nu & \nu & \nu & 0 & 0 & 0 \\ \nu & 1-\nu & \nu & 0 & 0 & 0 \\ \nu & \nu & 1-\nu & 0 & 0 & 0 \\ 0 & 0 & 0 & \frac{1-2\nu}{2} & 0 & 0 \\ 0 & 0 & 0 & 0 & \frac{1-2\nu}{2} & 0 \\ 0 & 0 & 0 & 0 & 0 & \frac{1-2\nu}{2} \end{bmatrix} \quad (7)$$

In finite element settings, the incremental stress-strain equation should be converted to a global reference system taking into account orthotropic axes. This can be achieved by using the rotation matrix,  $T$ , as follows (26):

$$D = T^T D_0 T \quad (8)$$

where  $D$  is the material matrix of the overall coordinate system.

### 2. 2. The Effect of Strain Rate on Concrete

To include the effect of strain rate, the empirical dynamic increase coefficients were used (31). For this purpose, the strain obtained at each time step was used to calculate the strain rate. Then, using the empirical DIF equations, the dynamic increase factor for each time step was calculated and applied.

$$\dot{\varepsilon} = \frac{d\varepsilon}{dt} \quad (9)$$

where  $\dot{\varepsilon}$  is the strain rate,  $\varepsilon$  is strain, and  $t$  is time. According to extensive experimental studies by Hao et al. (32), the compressive and tensile DIF equations considered for concrete, based on which the encoding was performed, are as follows (31):

$$CDIF = 0.0419(\log \dot{\varepsilon}) + 1.2165 \text{ for } \dot{\varepsilon} \leq 30/s \quad (10)$$

$$CDIF = 0.8988(\log \dot{\varepsilon})^2 - 2.8255(\log \dot{\varepsilon}) + 3.4907 \text{ for } 30/s < \dot{\varepsilon} \leq 1000/s \quad (11)$$

$$TDIF = 0.26(\log \dot{\varepsilon}) + 2.06 \text{ for } \dot{\varepsilon} \leq 1/s \quad (12)$$

$$TDIF = 2(\log \dot{\varepsilon}) + 2.06 \text{ for } 1/s < \dot{\varepsilon} \leq 2/s \quad (13)$$

$$TDIF = 1.44331(\log \dot{\varepsilon}) + 2.2276 \text{ for } 2/s < \dot{\varepsilon} \leq 150/s \quad (14)$$

The calculated dynamic increase factor is multiplied by the static yield surface to increase the dynamic strength of the structure compared to the static strength and therefore, the dynamic increase factor is applied to the constitutive model.

### 2. 3. Theoretical Equations of Dam-Reservoir System

By assuming a homogeneous, isotropic, non-viscous, and non-rotational fluid, then the governing equation on hydraulic pressure wave propagating in the reservoir (Helmholtz Equation) is as follows (33-37):

$$\nabla^2 P = \frac{1}{c^2} \frac{\partial^2 P}{\partial t^2} \quad (15)$$

where  $P(x, y, z, t)$  is the hydrodynamic pressure in the reservoir, and  $C$  and  $t$  are the sound propagation speed through fluid and time variables, respectively. To solve the above equation for the reservoir, appropriate boundary conditions should be applied, as described in the following.

**Dam-Reservoir Interface:** Because of the same normal fluid and structure velocities in this interface, the boundary condition is expressed as follows:

$$\rho \vec{a}_{ns} = -\frac{\partial P}{\partial n} \quad (16)$$

where  $\vec{a}_{ns}$  is the acceleration in the dam-reservoir interface perpendicular to the dam,  $\rho$  is the volumetric mass of the fluid,  $P$  is the hydrodynamic pressure, and  $n$  is the unit vector perpendicular to the dam surface inwards the reservoir.

**Reservoir-Foundation Interface:** On this surface, due to bed floor sedimentation and sediment properties, a part of the wave energy hitting the bed floor is absorbed and a part is reflected. In this boundary, the following equation is met:

$$\frac{\partial P}{\partial n} = -\rho \dot{v}_{gn} - q \frac{\partial P}{\partial t}; \quad q = \frac{1}{c} \left( \frac{1 - \alpha_b}{1 + \alpha_b} \right) \quad (17)$$

where  $\dot{v}_{gn}$  is the ground acceleration element perpendicular to the boundary,  $q$  is the admittance or damping coefficient on the reservoir floor which is expressed as above using  $\alpha_b$ , and  $\alpha_b$  is the ratio of the reflected wave amplitude to the incident wave.

**Upstream Reservoir Boundary:** By assuming a considerable reservoir length, the following equation can be used for this boundary:

$$\frac{\partial P}{\partial n} = -\frac{1}{c} \frac{\partial P}{\partial t} \quad (18)$$

The physical interpretation of Equation 18 is that a group of dampers is installed in the upstream reservoir boundary.

**Free Surface of the Reservoir:** The surface waves are commonly ignored in tall dams and consequently, the boundary condition of the reservoir's free surface is obtained as follows:

$$P = 0 \quad (19)$$

Considering the static response of the dam-reservoir system as an initial condition, the dam-reservoir system interaction equation for the dynamic response of the system under earthquake is obtained as follows (22, 28, 38, 39):

$$\begin{bmatrix} M_s & 0 \\ \rho Q^T & M_f \end{bmatrix} \begin{Bmatrix} \ddot{a} \\ \ddot{p} \end{Bmatrix} + \begin{bmatrix} C_s & 0 \\ 0 & C_f \end{bmatrix} \begin{Bmatrix} \dot{a} \\ \dot{p} \end{Bmatrix} + \begin{bmatrix} K_s & Q \\ 0 & K_f \end{bmatrix} \begin{Bmatrix} a \\ p \end{Bmatrix} + \begin{Bmatrix} M_s \{R\} \\ \rho Q^T \{R\} \end{Bmatrix} \begin{Bmatrix} \ddot{u}g \\ \ddot{u}g \end{Bmatrix} = 0 \quad (20)$$

where  $[M_s]$ ,  $[C_s]$ , and  $[K_s]$  are the mass, damping, and stiffness matrices of the structure, respectively.  $[M_f]$ ,  $[C_f]$  and  $[K_f]$  are the mass, damping, and stiffness matrices of fluid, respectively; and  $\{\ddot{a}\}$ ,  $\{\dot{a}\}$ , and  $\{a\}$  are acceleration, velocity, and displacement vectors, respectively; and  $\{P\}$ ,  $\{\dot{P}\}$ , and  $\{\ddot{P}\}$  are hydrodynamic pressure, first-order and second-order derivatives of hydrodynamic pressure, respectively. In addition,  $\{R\}$  is the matrix of ground motion effect on freedom degrees of structure nodes,  $\{\ddot{u}g\}$  is the vector of gravity acceleration components in the directions of the coordinate system,  $Q$  is the dam-reservoir interaction matrix, and  $\rho$  is the volumetric mass of the fluid.

### 3. FINITE-ELEMENT MODELING OF THE KOYNA DAM

In the present study, sub-routines were written in Fortran and added to the FEAPpv finite-element numerical model which was called GFEAP. A 20-node 3D serendipity element and a 20-node 3D fluid element with pressure degrees of freedom were added to the numerical

model and used in the modeling. Moreover, sub-routines of the dam-reservoir dynamic interaction using the staggered method, the five-parameter William-Warnke plasticity model as well as a sub-routine for calculation and application of dynamic increase factor were also added to the numerical model (40). The Koyna dam was selected as the case study, which is a concrete gravity dam with a height of 103 m and a foundation width of 70.2 m constructed in India. A 2D model of the dam along with its reservoir (with a length twice the dam height) was developed and a staggered problem-solving pattern was used to solve the dam-reservoir interaction equations. Foundation modelling as well as foundation-structure interaction were ignored. The weight and hydrostatic pressure static loads were applied and used as initial responses in dynamic analyses. The dam body was modeled using 72 three-dimensional brick elements and 592 nodes. Figure 1 shows the finite element mesh of the dam. To show the effect of earthquake on the response of structures, it is necessary to use the time history of earthquake. Earthquake vibration data is required for the design of tall buildings or large-scale structures such as dams or bridges (41). In the present paper, the vertical and horizontal components of the Taft Earthquake were used in dynamic analyses of the Koyna Dam, as shown in Figures 2 and 3. The compressive strength of concrete used in dam construction was 20.4 MPa with a tensile strength of 2 MPa. The concrete density was  $2640 \text{ kg/m}^3$ , sound speed in water was 1440 m/s, and the impedance ratio of the abutments was assumed as 3.44. In the isotropic state, Young's modulus and Poisson's ratio were considered as 26.35 GPa and 0.2, respectively. Considering different concrete properties in a direction perpendicular to joints (compared to other directions) and assuming an anisotropy ratio of 1.2, Young's modulus in the vertical direction was calculated as 21.8 GPa (15).

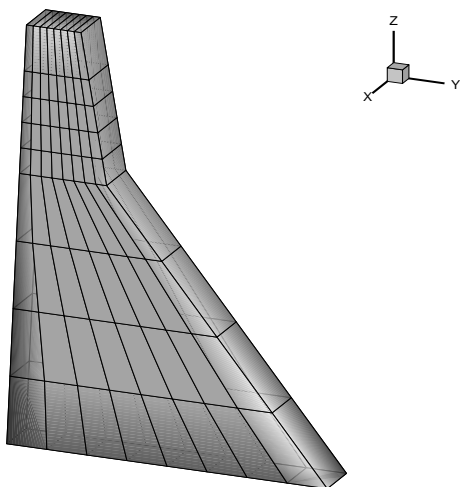


**Figure 1.** Finite-Element Mesh of the Koyna Dam Body

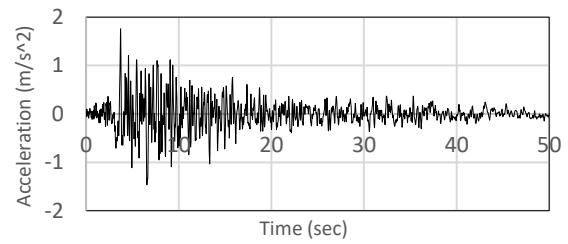


**Figure 2.** Horizontal Component of the Taft Earthquake

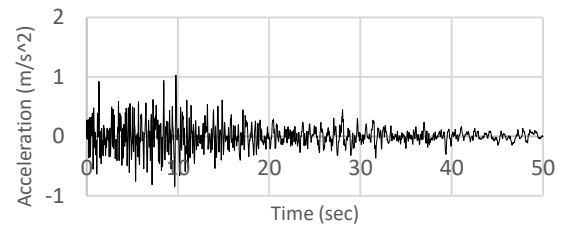


**Figure 3.** Vertical Component of the Taft Earthquake

#### 4. RESULTS OF DYNAMIC ANALYSIS

To study the lift joints, isotropic and orthotropic analyses were performed incorporating the strain rate of the Koyna dam. The time history of a point located on the dam crest in river (longitudinal) directions for the isotropic and orthotropic states considering strain rate is shown in Figure 4. The positive displacement direction is toward downstream. The maximum displacements of the dam crest in the river direction for the isotropic and orthotropic states were 2.32 cm and 2.9 cm, respectively. In the above states, the maximum static displacements in the longitudinal direction were 0.51 cm and 0.61 cm, respectively. The maximum displacements in the dam height (vertical) direction for the isotropic and orthotropic states were 0.64 cm and 0.81 cm, respectively. Considering lift joints and orthotropic state compared to the homogeneous and isotropic state leads to an increase of 24.88% and 25.59% in the longitudinal and vertical directions, respectively. Displacement envelope in the isotropic and orthotropic states considering strain rate is shown in Figures 5 and 6. As can be seen, a similar pattern is observed. The results of the isotropic and orthotropic states were compared without including strain rate and to study the effect of loading rate, the results were compared with the obtained results considering strain rate. The time history of dam crest displacement in the river direction for the isotropic and orthotropic analyses without including strain rate is presented in Figure 7. The maximum displacements in the longitudinal direction for the isotropic and orthotropic states were 2.3223 cm and 2.9015 cm, respectively. Negligible differences occurred with and without considering the strain rate. Using the orthotropic

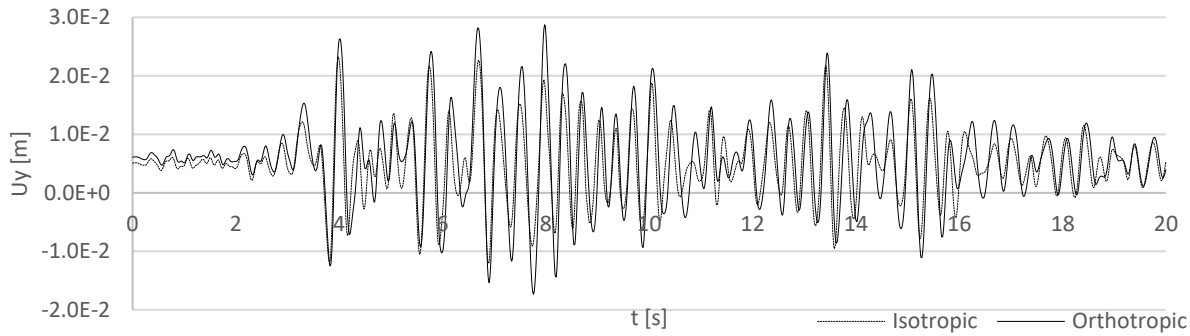


**Figure 4.** Displacement time history at the midpoint of the dam crest in the longitudinal direction for the isotropic and orthotropic analyses considering strain rate

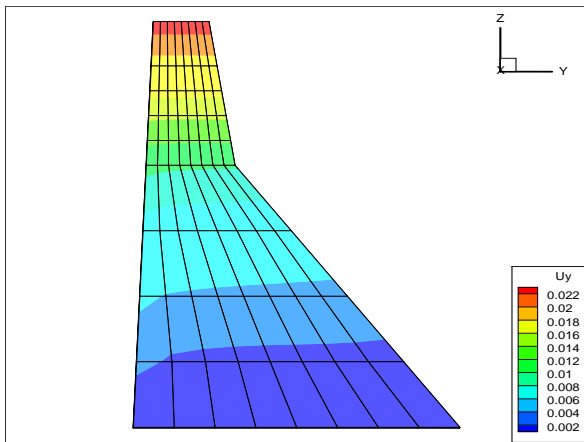


**Figure 5.** Dam Displacement envelope in the Longitudinal Direction for the Isotropic analyses without considering the strain rate

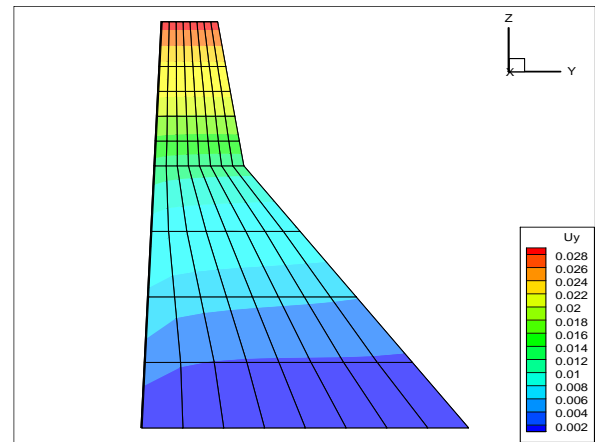


**Figure 6.** Dam Displacement envelope in the longitudinal Direction for the Orthotropic analyses without considering the strain rate

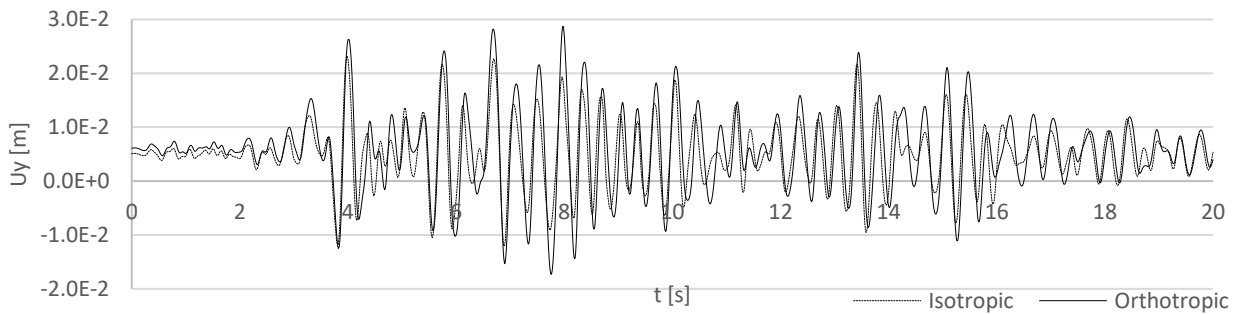


**Figure 7.** Displacement time history at the midpoint of the dam crest in the longitudinal direction for the isotropic and orthotropic analyses without considering the strain rate

state an increase of 24.94% and 25.66% was observed compared to the isotropic one in the longitudinal and vertical directions, respectively. A negligible difference between distribution patterns and values of the displacement envelope was observed with and without considering the strain rate and therefore, is not presented here. The envelope of principal maximum (tensile) and minimum (compressive) stresses on the upstream side of

the dam body in the orthotropic and isotropic analyses including the strain rate are represented in Figures 8 to 11, respectively. As can be seen from Figures 8 and 9, maximum tensile stress in the isotropic and orthotropic states occurred in the dam neck and dam heel. The same distribution pattern was observed in both cases, however, in the orthotropic state a wider distribution occurred throughout the dam body. Maximum tensile stresses in

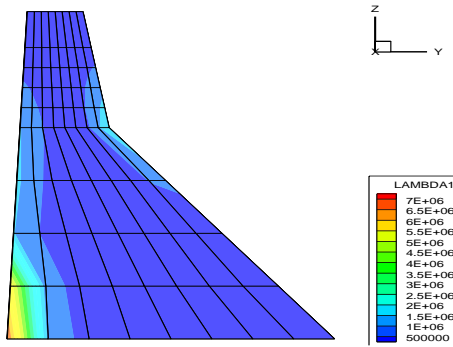


Figure 8. Maximum principal stress (Tensile) envelope in the isotropic state

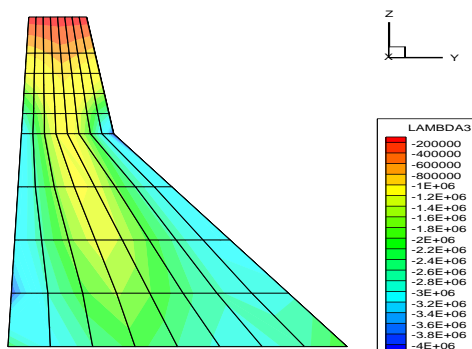


Figure 9. Minimum principal stress (Compressive) envelope in the isotropic state

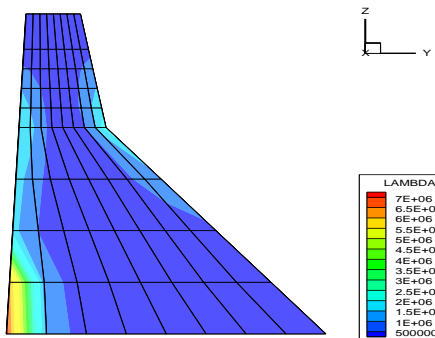


Figure 10. Maximum principal stress (Tensile) envelope in the orthotropic state

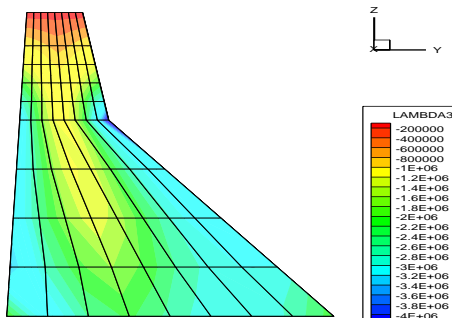


Figure 11. Minimum principal stress (Compressive) envelope in the orthotropic state

the isotropic and orthotropic states were  $7.10E+0$  Pa and  $7.26E+06$  Pa, respectively, indicating an increase of 2.34 percent. Maximum compressive stress in the isotropic and orthotropic states occurred in downstream and dam neck with values of  $-4.14E+06$  Pa and  $4.26E+06$  Pa in the isotropic and orthotropic states, respectively, indicating an increase of 2.78 percent.

The damaged areas of the dam reflect the weak locations. As can be seen, in the isotropic and orthotropic models, the yield function was equal to 0.075 and 0.095, respectively. The yield area is the same as the location with the main tensile stress in the models and in both states, yield areas are focused in the dam heel and slope-changing area in downstream. Yield areas are the same in both the isotropic and orthotropic states with a wider distribution in the orthotropic state. The damaged areas correspond to the tensile stress envelope and the location of maximum tensile stress. Figures 12 and 13 show the yielded areas in both states.

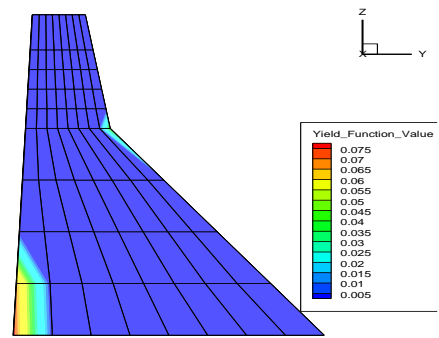


Figure 12. Yielded elements envelope in the isotropic state

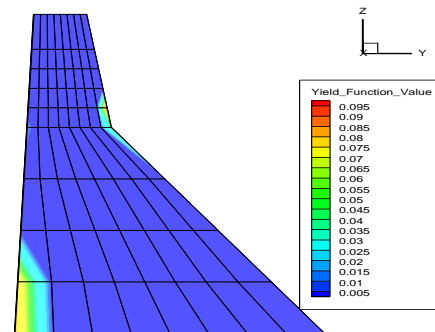


Figure 13. Yielded elements envelope in the orthotropic state

### 5. CONCLUSIONS

In the present paper, based on precise empirical relations of dynamic increase factor, the real effect of strain rate in the seismic loading range on the Koyna concrete gravity dam was studied. Lift joints were also taken into account by applying orthotropic concrete properties

perpendicular to the lift joints. Based on the analyses, the following results were obtained:

1. Obtained displacements in the case of including strain rate were smaller than without strain rate, however, the difference was insignificant so that the strain rate effect can be neglected in seismic loading. Consequently, using large dynamic increase coefficients can lead to errors in the seismic analyses.
2. The time histories of the isotropic and orthotropic models had insignificant differences, however, incorporating anisotropy due to lift joints results in more accurate results. As mentioned before, considering lift joints led to an increase of about 25% in displacements compared to the isotropic model.
3. Tensile and compressive stresses in the orthotropic material state were higher than those in the isotropic one, however, the same distribution pattern was observed. Maximum tensile stress occurred in the dam heel and neck, which are susceptible to damage.
4. A similar damage pattern was observed in the isotropic and anisotropic models with a wider distribution in the orthotropic model. Therefore, ignoring concreting layer can lead to damage underestimation.

## 6. REFERENCES

1. Davani Motlagh A, Sadeghian M, Javid A, Asgari M. Optimization of dam reservoir operation using grey wolf optimization and genetic algorithms (A case study of Taleghan Dam). *International Journal of Engineering*. 2021;34(7):1644-52. <https://doi.org/10.5829/IJE.2021.34.07A.09>
2. Puzrin A. *Constitutive modelling in geomechanics: introduction*; Springer Science & Business Media; 2012.
3. Ozturk B. Investigation of effects of ground motions on SDOF systems using records from the recent earthquakes in Turkey. *New Horizons and Better Practices 2007*. p. 1-8.
4. Fei L, Gao L. Application of thermodynamics-based rate-dependent constitutive models of concrete in the seismic analysis of concrete dams. *Water Science and Engineering*. 2008;1(3):54-64. <https://doi.org/10.3882/j.issn.1674-2370.2008.03.006>
5. Hesari MA, Ghaemian M, Shamsai A. Advanced nonlinear dynamic analysis of arch dams considering joints effects. *Advances in Mechanical Engineering*. 2014;6:587263. <https://doi.org/10.1155/2014/587263>
6. Hariri-Ardebili M, Mirzabozorg H, Estekanchi H. Nonlinear seismic assessment of arch dams and investigation of joint behavior using endurance time analysis method. *Arabian Journal for Science and Engineering*. 2014;39:3599-615. <https://doi.org/10.1007/s13369-014-1027-5>
7. Ouzandja D, Tiliouine B. Effects of Dam–Foundation Contact Conditions on Seismic Performance of Concrete Gravity Dams. *Arabian Journal for Science and Engineering*. 2015;40:3047-56. <https://doi.org/10.1007/s13369-015-1770-2>
8. Alembagheri M, Ghaemian M. Seismic performance evaluation of a jointed arch dam. *Structure and Infrastructure Engineering*. 2016;12(2):256-74. <https://doi.org/10.1080/15732479.2015.1009124>
9. Yazdani Y, Alembagheri M. Effects of base and lift joints on the dynamic response of concrete gravity dams to pulse-like excitations. *Journal of Earthquake Engineering*. 2017;21(5):840-60. <https://doi.org/10.1080/13632469.2016.1185056>
10. Ganji HT, Alembagheri M. Stability of monolithic gravity dam located on heterogeneous rock foundation. *Arabian Journal for Science and Engineering*. 2018;43:1777-93. <https://doi.org/10.1007/s13369-017-2755-0>
11. Latorre M, Montans FJ. A new class of plastic flow evolution equations for anisotropic multiplicative elastoplasticity based on the notion of a corrector elastic strain rate. *Applied Mathematical Modelling*. 2018;55:716-40. <https://doi.org/10.1016/j.apm.2017.11.003>
12. Lu X, Wu Z, Pei L, He K, Chen J, Li Z, et al. Effect of the spatial variability of strength parameters on the dynamic damage characteristics of gravity dams. *Engineering Structures*. 2019;183:281-9. <https://doi.org/10.1016/j.engstruct.2019.01.042>
13. Hai- tao W, Jiayu S, Feng W, Zhiqiang A, Tianyun L. Experimental study on elastic-plastic seismic response analysis of concrete gravity dam with strain rate effect. *Soil Dynamics and Earthquake Engineering*. 2019;116:563-9. <https://doi.org/10.1016/j.soildyn.2018.09.020>
14. Ganji HT, Alembagheri M, Khaneghahi MH. Evaluation of seismic reliability of gravity dam-reservoirinhomogeneous foundation coupled system. *Frontiers of Structural and Civil Engineering*. 2019;13:701-15. <https://doi.org/10.1007/s11709-018-0507-1>
15. Hariri-Ardebili MA. Uncertainty quantification of heterogeneous mass concrete in macro-scale. *Soil Dynamics and Earthquake Engineering*. 2020;137:106137. <https://doi.org/10.1016/j.soildyn.2020.106137>
16. Guo S, Liao J, Huang H, Liang H, Li D, Chen H, et al. The effect of shear sliding of vertical contraction joints on seismic response of high arch dams with fine finite element model. *Advances in Civil Engineering*. 2020;2020. <https://doi.org/10.1155/2020/4353609>
17. Lee M, Kwak H-G. A strain rate dependent nonlinear elastic orthotropic model for SFRC structures. *Journal of Building Engineering*. 2021;42:102466. <https://doi.org/10.1016/j.job.2021.102466>
18. Pan J. Seismic damage behavior of gravity dams under the effect of concrete inhomogeneity. *Journal of Earthquake Engineering*. 2021;25(7):1438-58. <https://doi.org/10.1080/13632469.2019.1581675>
19. Lu X, Pei L, Chen J, Wu Z, Li Z. Comparison of homogenous and random fields of tensile strength effects on the nonlinear dynamical response of Guandi concrete gravity dams under strong earthquake waves. *Structure and Infrastructure Engineering*. 2021;17(12):1684-97. <https://doi.org/10.1080/15732479.2020.1832534>
20. Liu P, Chen J, Fan S, Xu Q, editors. *Uncertainty quantification of the effect of concrete heterogeneity on nonlinear seismic response of gravity dams including record-to-record variability*. Structures; 2021: Elsevier.
21. Kadhim M, Alfatlawi T, Hussein M. Experimental and nonlinear analysis of cracking in concrete arch dams due to seismic uplift pressure variations. *International Journal of Engineering, Transactions B: Applications*. 2021;34(5):1156-66. <http://10.5829/IJE.2021.34.05B.09>
22. Li Z, Wu Z, Chen J, Pei L, Lu X. Fuzzy seismic fragility analysis of gravity dams considering spatial variability of material parameters. *Soil Dynamics and Earthquake Engineering*. 2021;140:106439. <https://doi.org/10.1016/j.soildyn.2020.106439>
23. Saria A, Djermane M, Hadj-Djelloul ND. Three-Dimensional Nonlinear Dynamic Analysis of Base Isolated Cylindrical Steel Tank. *Civil Engineering Journal*. 2022;8(06). <http://dx.doi.org/10.28991/CEJ-2022-08-06-013>

24. Balamuralikrishnan R, Al-Mawaali A, Al-Yaarubi M, Al-Mukhaini B, Kaleem A. Seismic upgradation of RC beams strengthened with externally bonded spent catalyst based ferrocement laminates. *HighTech and Innovation Journal*. 2023;4(1):189-209. <https://10.28991/HIJ-2023-04-01-013>
25. Fadaei-Kermani E, Shojaee S, Memarzadeh R. Numerical Simulation of Seepage Flow through Dam Foundation Using Smooth Particle Hydrodynamics Method (RESEARCH NOTE). *International Journal of Engineering, Transactions A: Basics*. 2019;32(4):484-8. <http://10.5829/IJE.2019.32.04A.04>
26. Balan TA, Spacone E, Kwon M. A 3D hypoplastic model for cyclic analysis of concrete structures. *Engineering Structures*. 2001;23(4):333-42. [https://doi.org/10.1016/S0141-0296\(00\)00048-1](https://doi.org/10.1016/S0141-0296(00)00048-1)
27. Bono G, Campos Filho A, Pacheco A. Modelo 3D de elementos finitos para análise de estruturas de concreto armado. *Revista IBRACON de Estruturas e Materiais*. 2011;4:548-60. <https://doi.org/10.1590/S1983-41952011000400002>
28. Wei K, Chen S, Li G, Han H. Application of a generalised plasticity model in high earth core dam static and dynamic analysis. *European Journal of Environmental and Civil Engineering*. 2020;24(7):979-1012. <https://doi.org/10.1080/19648189.2018.1437777>
29. Hariri-Ardebili M, Mirzabozorg H. Orthotropic material and anisotropic damage mechanics approach for numerically seismic assessment of arch dam-reservoir-foundation system. *Strength of Materials*. 2013;45:648-65. <https://doi.org/10.1007/s11223-013-9501-y>
30. Penado FE. Fracture parameter determination for the orthotropic interface crack with friction. *Engineering Fracture Mechanics*. 2018;204:542-56. <https://doi.org/10.1016/j.engfracmech.2018.10.038>
31. Ye Z, Hao Y, Hao H. Numerical study of the compressive behavior of concrete material at high strain rate with active confinement. *Advances in Structural Engineering*. 2019;22(10):2359-72. <https://doi.org/10.1177/1369433219841174>
32. Hao Y, Hao H, Li Z. Influence of end friction confinement on impact tests of concrete material at high strain rate. *International journal of impact engineering*. 2013;60:82-106. <https://doi.org/10.1016/j.ijimpeng.2013.04.008>
33. Cetin M, Mengi Y. Transmitting boundary conditions suitable for analysis of dam-reservoir interaction and wave load problems. *Applied Mathematical Modelling*. 2003;27(6):451-70. [https://doi.org/10.1016/S0307-904X\(03\)00048-9](https://doi.org/10.1016/S0307-904X(03)00048-9)
34. Omid O, Lotfi V. A symmetric implementation of pressure-based fluid-structure interaction for nonlinear dynamic analysis of arch dams. *Journal of Fluids and Structures*. 2016;69:34-55. <https://doi.org/10.1016/j.jfluidstructs.2016.12.003>
35. Sharma V, Fujisawa K, Murakami A. Space-time FEM with block-iterative algorithm for nonlinear dynamic fracture analysis of concrete gravity dam. *Soil Dynamics and Earthquake Engineering*. 2020;131:105995. <https://doi.org/10.1016/j.soildyn.2019.105995>
36. Moradloo AJ, Naiji A. Effects of rotational components of earthquake on seismic response of arch concrete dams. *Earthquake Engineering and Engineering Vibration*. 2020;19:349-62. <https://doi.org/10.1007/s11803-020-0566-x>
37. Varmazyari M, Sabbagh-Yazdi S-R. Modification of direct-FE method for nonlinear seismic analysis of arch dam-reservoir-foundation system considering spatially varying ground motion. *Soil Dynamics and Earthquake Engineering*. 2021;140:106477. <https://doi.org/10.1016/j.soildyn.2020.106477>
38. Mirzabozorg H, Varmazyari M, Gharehbaghi SA. Seismic evaluation of existing arch dams and massed foundation effects. *Soils and Foundations*. 2016;56(1):19-32. <https://doi.org/10.1016/j.sandf.2016.01.002>
39. Arjmandi SA, Lotfi V. Comparison of three efficient methods for computing mode shapes of fluid-structure interaction systems. *Arabian Journal for Science and Engineering*. 2013;38:787-803. <https://doi.org/10.1007/s13369-012-0523-8>
40. Willam KJ, editor *Constitutive model for the triaxial behavior of concrete*. IABSE Seminar on Concrete Structure subjected Triaxial Stresses; 1974.
41. Hanindya K, Makrup L, Paulus R. Deterministic Seismic Hazard Analysis to Determine Liquefaction Potential Due to Earthquake. *Civil Engineering Journal*. 2023;9(5):1203-16. <https://10.28991/CEJ-2023-09-05-012>

## COPYRIGHTS

©2024 The author(s). This is an open access article distributed under the terms of the Creative Commons Attribution (CC BY 4.0), which permits unrestricted use, distribution, and reproduction in any medium, as long as the original authors and source are cited. No permission is required from the authors or the publishers.



## Persian Abstract

### چکیده

سدهای بتنی به دلیل لایه‌های بتن‌ریزی به صورت ناهمسانگرد می‌باشد و این موضوع بر عملکرد آن‌ها تاثیر می‌گذارد. در این پژوهش با در نظر گرفتن تاثیر ناهمسانگردی ناشی از لایه‌های بتن‌ریزی، رفتار لرزه‌ای سد بتنی وزنی مطالعه شده است و پاسخ حالت‌های ایزوتروپیک و ارتوتروپیک مقایسه شده است. علاوه بر این در محدوده نرخ بارگذاری لرزه‌ای، با اعمال اثرات واقعی نرخ کرنش بررسی دقیق تری صورت گرفته است. سد بتنی وزنی کوئینا به عنوان مطالعه موردی انتخاب شده است. نتایج نشان می‌دهد که ناهمسانگردی بتن منجر به جابجایی‌های دینامیکی بزرگ‌تر و سطح آسیب بیشتر در بدنه سد می‌شود. و در نظر گرفتن خواص ارتوتروپیک بتن سبب نتایج واقعی تر می‌شود. پیشینه تنش‌های کششی و فشاری نیز در مدل ناهمسانگرد نسبت به مدل همگن و ایزوتروپ افزایش می‌یابد که نشان می‌دهد در نظر گرفتن رفتار ارتوتروپیک بتن در آنالیز لرزه‌ای مفید می‌باشد. همچنین در نظر گرفتن نرخ کرنش در محدوده بارگذاری لرزه‌ای تفاوت آشکاری در نتایج ایجاد نمی‌کند. پس در نظر گرفتن ضرایب افزایش دینامیکی بالا در آنالیزهای عددی با خطا همراه است.



## Experimental Investigation on Strength, Durability and Micro Structural Characteristics of Slag-Based Cement Mortar

M. Deepak<sup>\*a</sup>, Y. Ramalinga Reddy<sup>a</sup>, R. Nagendra<sup>b</sup>

<sup>a</sup> School of Civil Engineering, REVA University, Bengaluru, Karnataka, India

<sup>b</sup> Stedrant Technoclinic Pvt Ltd., Bengaluru, Karnataka, India

### PAPER INFO

#### Paper history:

Received 04 September 2023

Received in revised form 23 October 2023

Accepted 04 November 2023

#### Keywords:

Portland Slag Cement

Slag Sand

Cement Mortar

Compressive Strength

Durability

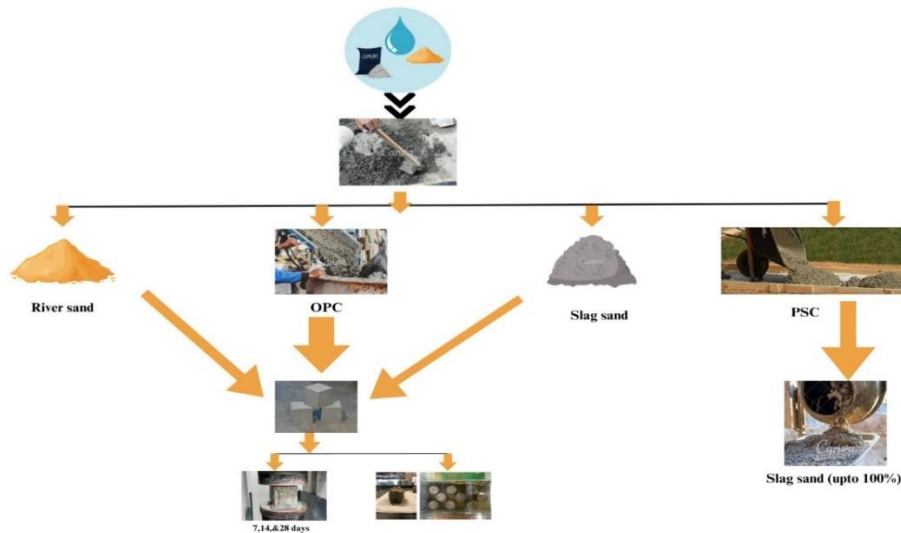
Microstructure

### ABSTRACT

Cement mortar is used as a bonding agent between building materials in the construction of stone masonry and brick masonry. The focus on reducing the environmental burden caused by the high emission of carbon with the consumption of cement has gained interest. In this study, experimental investigations are conducted using two slag-based materials, i.e., Portland Slag Cement (PSC) and Processed Granulated Blast Furnace Slag Sand (PGBFS, iron slag), as a replacement for Ordinary Portland Cement (OPC) and River Sand (RS). The paper aims to investigate the influence of PSC with slag sand on the strength, durability, and microstructure of cement mortar. The present work specifically investigates the strength improvement of cement mortar with slag cement and slag sand by varying the curing period, comparing the results at 7, 14, and 28 days of curing. OPC is replaced fully with PSC, and River sand is replaced partially or fully with slag sand in different percentages, i.e., 0%, 20%, 40%, 60%, 80% and 100% for different types of mixes. Results showed the highest increase in compressive strength and high resistance to acid attack in cement mortar with 100% PSC and 60% Slag Sand replacement. The consumption of proposed materials will benefit the construction industry to achieve the net zero target.

doi: 10.5829/ije.2024.37.04a.15

### Graphical Abstract



\*Corresponding Author email: [deepak.ce@gprec.ac.in](mailto:deepak.ce@gprec.ac.in) (M. Deepak)

Please cite this article as: Deepak M, Ramalinga Reddy Y, Nagendra R. Experimental Investigation on Strength, Durability and Micro Structural Characteristics of Slag-Based Cement Mortar. International Journal of Engineering, A: Basics. 2024;37(04):763-78.

## 1. INTRODUCTION

Cement plays a crucial role in the construction industry; however, its widespread use significantly impacts the environment and contributes significantly to energy consumption. This is primarily due to the harmful emissions of carbon dioxide during the cement manufacturing process, making it a major environmental concern in the realm of construction materials (1). Every year, the global construction industry goes through billions of tonnes of cement. This number is only going to continue to rise if there is a need for both newly built and renovated infrastructures. Cement manufacturing is energy-intensive and emits 5% - 7% CO<sub>2</sub>, according to various reports (2). Cement production is a highly energy-intensive process that involves the extraction of raw materials, such as limestone and clay, and the high-temperature calcination of these materials in kilns to produce cement clinker. The calcination process releases carbon dioxide (CO<sub>2</sub>) as a byproduct, resulting in significant greenhouse gas emissions. In addition, fossil fuels, such as coal, are commonly used as a source of heat in cement kilns, further contributing to CO<sub>2</sub> emissions. It is estimated that the production of one ton of Ordinary Portland cement (OPC) releases about 0.8 tons of carbon dioxide making it a significant contributor to climate change (1-7). The global increase in CO<sub>2</sub> emission and the associated impact on global warming motivated studies seeking to investigate the suitability of certain materials for partial or complete replacements of ordinary Portland cement (OPC) as concrete binders (7, 8). Currently, with the construction projects worldwide developing, plenty of natural materials such as natural sand (RS) are used to produce concrete (9, 10). The over-exploitation of high-quality river sand has not only led to a scarcity of resources, but also to a surge in the price of natural sand materials (11). Cement mortar (CM) is one of the most widely used construction materials; its "green" development is bound to help the construction industry (12, 13). Cement mortars are used in multiple applications in construction, such as plastering/rendering purposes, bonding layers in masonry walls, and fillers in repairing works. Unlike concrete, cement mortars are made with designated cement or supplementary cementitious material (as binder) and fine sand (as filler), where they are mixed in terms of volume/mass ratios to meet the targeted compressive strength and consistency (14). The adoption of sustainable practices during the OPC production phase includes replacement with renewable energy resources and carbon dioxide sequestration techniques is in practice. However, replacing the use of OPC with finding a suitable alternative that can match the performance and cost-effectiveness of conventional cement can be an immediate and effective choice, to achieve the target of net zero. The use of blended cement such as slag-based

cement is environmentally friendly due to the reduction in CO<sub>2</sub> emission during the clinkering process (10). This work enhances the mechanical properties and can help prevent the CO<sub>2</sub> from releases to the atmosphere (4). Eco-friendly materials, waste materials might be incorporated as replacements for aggregate and cement. It has been reported that utilizing waste materials in cementitious composites improved their mechanical characteristics (15). The development of sustainable construction materials based on these waste materials is of great value (11). The use of PSC is known to result in CO<sub>2</sub> emission by 70% compared to OPC but still, the consumption of PSC for construction activities seems significantly less (9). Despite the environmental benefit that can be derived by using PSC, the low rate of heat of hydration and lower early compressive strength development is reasoned for the scarce consumption (3).

Sand forms a major composition for the preparation of cement mortar and concrete. However, the demand for sand has led to several issues, including limited sand supplies, illegal and unsustainable sand mining, and environmental degradation caused by sand mining activities. These issues highlight the need for sustainable and responsible management of sand resources. The ecological balance is disturbed by the ongoing usage of natural sand, which depletes river beds. Thus, research focusing on using industrial wastes as a replacement for conventional river sand has been expanding for a decade (2, 16-18). These studies have also identified that using steel slag as a replacement for river sand will increase the compressive strength of concrete mixes. Cement mortar (CM) is one of the most widely used construction materials; its "green" development is bound to help the construction industry (19). The workability and cohesiveness of mortar are enhanced due to the finer and more consistent grain size of slag sand compared to natural sand. The additional cementitious bond formed by the slag sand reacting with water and calcium content in cement is also known to contribute to the durability (13). Thus, using slag sand will reduce the environmental burden by reducing the demand for the extraction of natural sand and effective waste disposal (20, 21). It is understood that there is lack of extensive studies on the cement mortar prepared with PSC and slag sand, and studying the behaviour of mortar with these environmentally friendly materials will add to the wealth of literature related to the analysis of sustainable material-based mortars. Also, considering the shortcomings of using river sand (RS) and OPC, and the advantages of utilizing slag sand (SS) with PSC, the present study is aimed at assessing the role of slag sand as a replacement for river sand in PSC. The mortar prepared with varying slag sand content with PSC is tested for variation in compressive strength and durability against acid, sulfate, and chloride attack along with microstructural analysis.

## 2. MATERIALS

**2. 1. Cement** Commercially available Ordinary Portland Cement OPC 53 (confirming IS 12269) (22) and Portland Slag Cement (PSC) confirming to IS: 455 (1989) (23) manufactured by Jindal Steel Works, Bellary, India is used in this work. The chemical composition of OPC and PSC determined using X-ray Fluorescence analysis is listed in Table 1. The fresh properties of OPC and PSC are listed in Table 2.

### 2. 2. Fine Aggregate

**2. 2. 1. River Sand** River sand is collected and bought from locally available sand distributors in Kurnool, Andhra Pradesh, India (Figure 1) and slag sand is shown in Figure 2.

**2. 2. 2. Slag Sand** Processed Granulated Blast Furnace Slag (PGBFS) manufactured by JSW Cement Limited, conforming to IS 16714: 2018 (24), is used for the preparation of mortar mix. The sieve analysis of PGBFS is classified as Grading Zone III as per IS:383(2016) (25). The physical properties of river sand and slag sand are shown in Table 3 and the grain size distribution of river sand and slag sand is shown in Figure 3.

**TABLE 1.** Chemical composition of OPC and PSC

Constitutes	Chemical composition (%)	
	OPC 53	PSC
CaO	61.85	43
SiO <sub>2</sub>	20.07	12
Fe <sub>2</sub> O <sub>3</sub>	4.62	12
MgO	0.83	6.7
Al <sub>2</sub> O <sub>3</sub>	5.32	21
SO <sub>3</sub>	2.5	2.59
Lime Saturation Factor	0.91	-
Ratio of Alumina/Iron oxide	1.18	-
Insluble residue % by mass	-	0.37
Loss on ignition % by mass	-	1.66
Chloride content	0.0028	0.0017

**TABLE 2.** Fresh Properties of OPC and PSC

Property	OPC	PSC	
Fineness	220 m <sup>2</sup> /kg	370 m <sup>2</sup> /kg	
Initial Setting Time	34 min	30 min	
Final Setting Time	550 min	600 min	
Compressive Strength	3 days	22 MPa	24 MPa
	7 days	25 MPa	30 MPa
	28 days	52 MPa	58 MPa



**Figure 1.** River sand



**Figure 2.** Slag sand

**TABLE 3.** Physical Properties of RS and SS

Property	River Sand	Slag Sand
Fineness Modulus	2.85 m <sup>2</sup> /kg	2.30 m <sup>2</sup> /kg
Water Absorption	0.8%	0.92%
Apparent Density (Loose)	1595 kg/m <sup>3</sup>	1333 kg/m <sup>3</sup>
Apparent Density (Rodded)	1765 kg/m <sup>3</sup>	1475 kg/m <sup>3</sup>

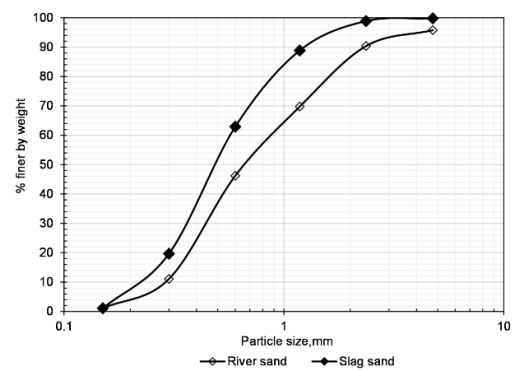


**Figure 3.** Grain size distribution curve fine aggregates

## 3. EXPERIMENTAL METHODS

Initially, the mix design for the cement mortars were set as (1: 3, 1:4 and 1:6) for cement: sand which is the common mortar mixtures prepared (2). The tests conducted on cement mortar mix with 1:3, 1:4 and 1:6 ratio is shown in Figure 4, and cement mortar mix prepared using different materials are shown in Figure 5.

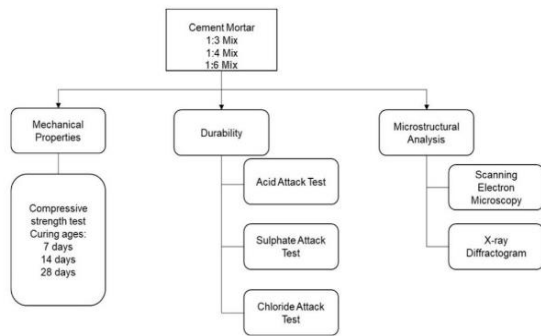


**Figure 4.** Methodology representing the experimental phases

The methodology for laboratory analysis of hardened cement mortar properties with two different proportions to assess the influence of river sand replacement with slag sand, along with detailed micro-level examination, is mentioned as a flowchart (Figure 5).

The designation of cement mortar mix with different proportions is listed in Table 4.

**3. 1. Preparation of Cement Mortar** The dry cement and sand were mixed first followed by mixing with water and intermixed adequately to achieve a homogeneous mortar mix. A water binder ratio of 0.45 is used as a water-cement ratio (w/c) as referred to Jin and Guo (18). The mixtures were filled in cube moulds of size

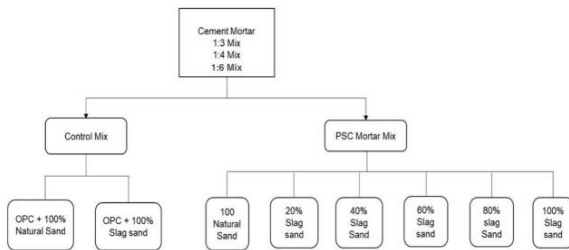


**Figure 5.** Framework showing the materials used for investigation

**TABLE 4.** Designation of cement mortar mixes

Mix Proportion	Designation
OPC+100%RS	OPCRS100
OPC+100%SS	OPCSS100
PSC+0%SS+100%RS	PSCSS0
PSC+20%SS+80%RS	PSCSS20
PSC+40%SS+60%RS	PSCSS40
PSC+60%SS+40%RS	PSCSS60
PSC+80%SS+20%RS	PSCSS80
PSC+100%SS+0%RS	PSCSS100

7.06 x 7.06 x 7.06 cm. The samples were cured as shown in Figure 6.

**3. 2. Compressive Strength** The compressive strength of mortar mix (1:3, 1:4 and 1:6) of OPCRS100, OPCSS100 and PSC with 0%, 20%, 40%, 60%, 80% and 100% SS at w/c of 0.45 at different curing ages i.e., 7-, 14- and 28-days were measured by using the automatic compressive strength testing machine, following the procedure of IS 4031(Part 6): 1988 (18, 23, 26).

**3. 3. Durability** Different methods are used to test the acid, chloride and sulfate attack resistance of concrete, and each method has certain advantages and disadvantages. The durability of the control mortar mix and PSC with SS mortar mix was studied by immersing the cured mortar cubes in the water bath with 5% Sulphuric acid (H<sub>2</sub>SO<sub>4</sub>) and 5% hydrochloric acid (HCl). The mortar cubes were exposed to acid attack for 28 days. The immersed cubes after the corresponding exposure period were removed from the acid solution bath and surfaces were cleaned with a soft nylon wire brush under the running tap water to eliminate weak products and loose material from the surface. The specimens were tested for mass loss and compressive strength after surface drying the mortar cubes.

**3. 4. X-Ray Diffraction Analysis** The X-ray diffractograms of the control mortar and PSC with SS mortar were recorded between diffraction angles (2 theta) of 10° to 80° to identify the hydration product formation in the mortar mix after sufficient curing. Like SEM analysis, specimens were extracted from the samples after compressive strength testing. The X-ray diffractograms of cement mortar mixes (i.e., 1:3, 1:4 and 1:6) with PSC and SS as a replacement to RS are obtained between 2θ = 10° to 80° (25).

**3. 5. Scanning Electron Microscope** A scanning electron microscope (SEM) allows the surface of a sample to be examined in three dimensions by scanning



**Figure 6.** Cement mortar cubes for compressive strength test

the surface with a thin electron beam and generating secondary electrons. Micrographic images of the control mix and PSC mortar with varying percentages of SS as a replacement to RS were obtained for triplicate specimens extracted carefully from compressive strength tested samples. The samples were gold coated using a sputter coater before conducting SEM analysis (27).

Micrographic images of the control mix and PSC mortar with varying percentages of SS as a replacement to RS were obtained for triplicate specimens extracted carefully from compressive strength tested samples. The samples were gold coated using a sputter coater before conducting SEM analysis. Samples collected after compressive strength testing were powdered and gold sputter coated to study the morphological changes in cement mortar mixes prepared with PSC and SS using scanning electron microscopy (SEM). Energy dispersive X-ray analysis (EDAX) was used to characterize the elemental compositions.

**3. 6. Numerical Simulation** Numerical simulation of cement mortar cubes of size 70.6 cm X 70.6 cm X 70.6 cm was carried out using ANSYS software. The material properties used for the simulation is listed in Table 5.

**4. RESULTS AND DISCUSSION**

**4. 1. Compressive Strength** The compressive strength of mortar mix ratio of 1:3 with OPC and 100% RS, 100% SS and PSC with varying dosages of SS are shown in Figure 7. The compressive strength of all samples showed an increase within curing ages and the rate of increase in compressive strength of OPC with 100% RS is 36% and 100% whereas PSC with 100% RS shows an increase of 22% and 122% when curing period is increased from 7 days to 14 and 28 days respectively. The rate of increase is lesser in OPC as well as PSC with 100% SS compared to that mix containing 100% RS. This can be attributed to the low rate of chemical reactivity of slag and the dilution effect as mentioned in earlier research (9). The low rate of chemical reactivity of PSC can be ascribed to the low rate of compressive strength gain compared to OPC. However, with an increase in SS content from 20% to 60%, the strength

gain increased and maximum compressive strength was observed for PSC and 60% SS as a replacement for RS. The compressive strength of PSC with a further higher proportion of SS (i.e., 80% and 100%) reduced and a similar trend of less rate of strength gain is reported elsewhere by Shengtao et al. (16) and Sande et al. (28).

The compressive strength of mortar mix ratio of 1:4 with OPC and 100% RS, 100% SS and PSC with varying dosages of SS are shown in Figure 8. The trend of compressive strength variation is like that observed in 1:3 concrete mix and the strength of PSC with 60% SS is comparable with the strength of OPC with RS without any replacement. The compressive strength of mortar mix ratio of 1:6 with OPC and 100% RS, 100% SS and PSC with varying dosages of SS are shown in Figure 9. The rate of strength reduction in PSC with SS at varying proportions compared to the strength of the control mix is comparatively less compared to that observed in the 1:3 and 1:4 mix which can be attributed to the high bulk density of SS and similar observation is reported.

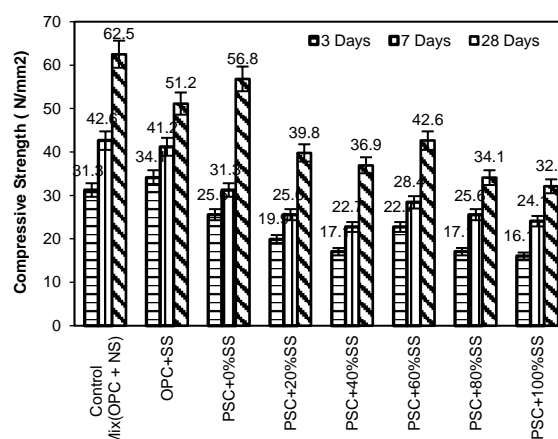


Figure 7. Compressive strength of mortar for 1:3 mix

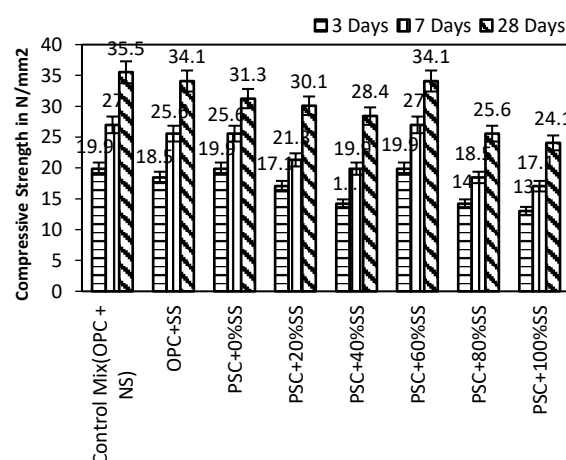


Figure 8. Compressive strength of mortar for 1:4 mix

TABLE 5. Material properties

Material Property	Value
Young's modulus	20000 MPa
Density	1900 kg/m <sup>3</sup>
Poisson's ratio	0.18
Mesh size	1 cm
Load	150

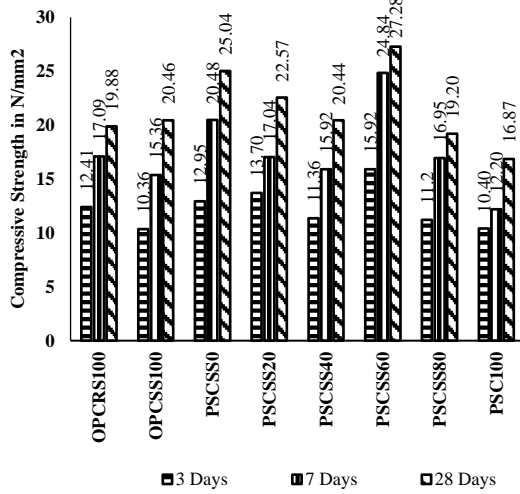


Figure 9. Compressive strength of mortar for 1:6 mix

4. 2. Durability

The durability of control cement mortar cubes and cubes prepared with varying PSC and SS content in the mix ratio of 1:3, 1:4 and 1:6 was evaluated for weight loss and compressive strength variation after exposure to acids.

4. 2. 1. Acid Attack Test

Physical and mechanical changes observed in the cement mortar cubes before and after immersion in sulphuric acid solution are shown in Figures 10a and 10b and Tables 6, 7 and 8. The exposure to acid reduced the compressive strength of the control mortar mix proportion of 1:3 by 45% and a 32% reduction in compressive strength of PSC with RS mortar mix is observed in Figure 11. The exposure of PSC with SS mortar mix showed an increase in the percentage of strength loss but for PSC with 60% SS, there was a reduction in the rate of strength loss. Thus 60% SS as a replacement to RS in PSC will impart high resistance to acid attack and specimens retain high strength during the acid exposure period of 28 days (29-31).



(a)



(b)

Figure 10. a) before and b) after Acid attack

TABLE 6. Change in weight and compressive strength of Mix 1:3 after acid exposure

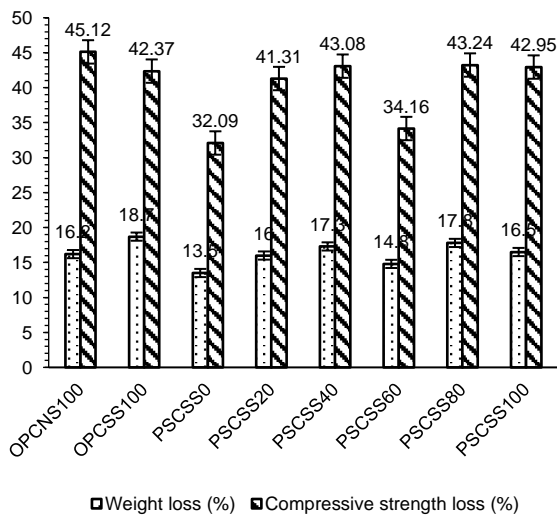
Mix Proportions	Weight before exposure (kg)	Weight after exposure (kg)	Compressive strength before exposure (N/mm²)	Compressive strength after exposure (N/mm²)
OPCRS100	0.741	0.620	62.51	34.17
OPCSS100	0.810	0.658	51.15	29.47
PSCSS0	0.718	0.621	56.83	38.64
PSCSS20	0.730	0.613	39.79	24.27
PSCSS40	0.720	0.595	36.79	20.97
PSCSS60	0.788	0.671	42.62	28.06
PSCSS80	0.730	0.601	34.10	19.35
PSCSS100	0.718	0.599	32.10	13.80

TABLE 7. Change in weight and compressive strength of Mix 1:4 after acid exposure

Mix Proportions	Weight before exposure (kg)	Weight after exposure (kg)	Compressive strength before exposure (N/mm²)	Compressive strength after exposure (N/mm²)
OPCRS100	0.710	0.583	35.52	18.47
OPCSS100	0.730	0.589	34.10	18.84
PSCSS0	0.692	0.593	31.25	20.31
PSCSS20	0.710	0.602	30.09	17.18
PSCSS40	0.705	0.606	28.41	16.47
PSCSS60	0.720	0.629	34.10	22.06
PSCSS80	0.652	0.539	25.57	14.88
PSCSS100	0.688	0.577	24.07	14.48

**TABLE 8.** Change in weight and compressive strength of Mix 1:6 after acid exposure

Mix Proportions	Weight Before Exposure (kg)	Weight After Exposure (kg)	Compressive Strength before Exposure (N/mm <sup>2</sup> )	Compressive Strength After Exposure (N/mm <sup>2</sup> )
OPCRS100	0.67	0.548	19.89	9.98
OPCSS100	0.657	0.531	20.46	11.86
PSCSS0	0.664	0.520	21.82	10.56
PSCSS20	0.670	0.580	22.50	12.02
PSCSS40	0.684	0.582	21.87	12.51
PSCSS60	0.710	0.624	27.28	15.20
PSCSS80	0.620	0.522	20.42	11.60
PSC100	0.580	0.500	18.66	10.24



**Figure 11.** Weight loss and compressive strength loss in 1:3 mix after exposure to hydrochloric acid

The weight loss and compressive strength loss of mortar mix proportion of 1:4 also showed a similar response to acid exposure as that of 1:3 mortar mix. The results are depicted in Figure 12. It is evinced that PSC with no replacement of RS showed the lowest rate of reduction in compressive strength followed by PSC with SS content of 60% and 40% of RS as fine aggregate. This shows that the PSCSS60 sample resists acid attacks like the sample with 100% RS. The results of the weight loss and compressive strength loss of mortar mix proportion of 1:6 are shown in Figure 13.

**4. 2. 2. Sulfate Attack** Sulfate attack on mortar is to determine the resistance of cement mortar under Magnesium sulfate acid exposure. The samples after

curing and after exposure to sulfate attack are shown in Figures 14a and 14b.

The weight loss and compressive strength loss observed after exposure to 5% Magnesium sulfate for 28 days are listed in Tables 9, 10 and 11 for cement mortar of 1:3 mix and 1:4 mix, respectively.

Figures 15, 16 and 17 show the comparison of the rate of strength and weight loss in cement mortar mixes of 1:3, 1:4 and 1:6 proportion with varying cement and fine aggregate content. It is observed that all samples were highly resistant to sulfate attack compared to the hydrochloric acid attack in the case of both 1:3, 1:4 and 1:6 mix proportions. The rate of weight loss is almost in the same range for all samples, but the compressive strength loss is least by 14.2% and 14% for PSC with 100% RS and PSC with 60% SS as a replacement to RS in 1:3 mortar mix samples (Figure 15). The rate of strength loss observed in the 1:4 mix is least by 12% for PSC with 60% SS followed by 15% in PSC with 100% RS and the rate of strength loss observed in the 1:6 mix

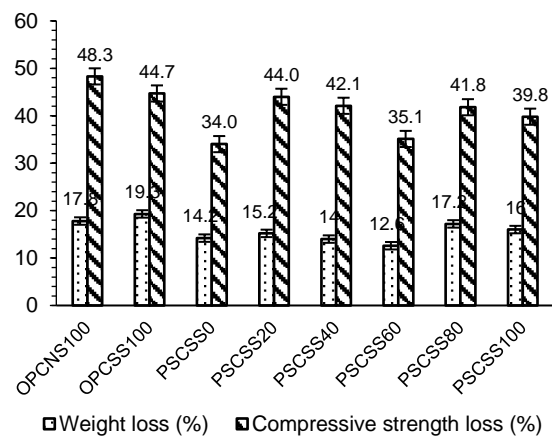


**Figure 12.** Weight loss and compressive strength loss in 1:4 mortar mix after exposure to hydrochloric acid

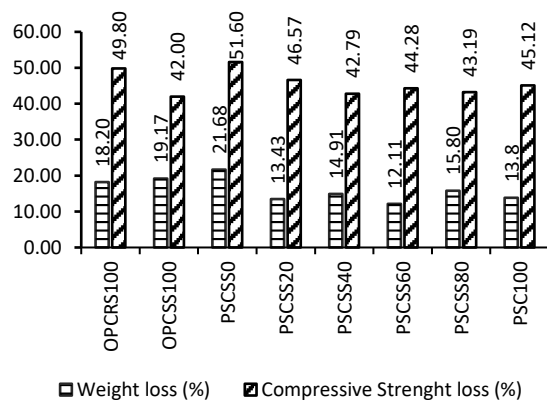


**Figure 13.** Weight loss and compressive strength loss in 1:6 mortar mix after exposure to hydrochloric acid



(a)



(b)

Figure 14. a) before and b) after sulfate attack

TABLE 9. Variation in weight and compressive strength due to sulfate attack 1:3 mortar mix

Mix proportions	Weight before exposure (kg)	Weight after exposure (kg)	Compressive strength before exposure (N/mm <sup>2</sup> )	Compressive strength after exposure (N/mm <sup>2</sup> )
OPCRS100	0.736	0.704	62.51	50.42
OPCSS100	0.738	0.702	51.15	42.58
PSCSS0	0.730	0.702	56.83	48.87
PSCSS20	0.710	0.687	39.79	32.99
PSCSS40	0.748	0.718	36.79	31.27
PSCSS60	0.766	0.737	42.62	35.80
PSCSS80	0.726	0.698	34.10	28.57
PSCSS100	0.724	0.694	32.10	26.64

TABLE 10. Variation in weight and compressive strength due to Sulfate attack test for 1:4 mix

Mix Proportions	Weight before exposure (kg)	Weight after exposure (kg)	Compressive strength before exposure (N/mm <sup>2</sup> )	Compressive strength after exposure (N/mm <sup>2</sup> )
OPCRS100	0.723	0.695	35.52	28.40

OPCSS100	0.690	0.667	34.1	27.62
PSCSS0	0.703	0.683	31.25	26.56
PSCSS20	0.681	0.655	30.09	25.93
PSCSS40	0.690	0.661	28.41	24.04
PSCSS60	0.680	0.657	34.1	30.08
PSCSS80	0.644	0.613	25.57	20.71
PSCSS100	0.682	0.650	24.07	20.56

TABLE 11. Variation in weight and compressive strength due to Sulfate attack test for 1:6 mix

Mix Proportions	Weight Before Exposure (kg)	Weight After Exposure (kg)	Compressive Strength before Exposure (N/mm <sup>2</sup> )	Compressive Strength after Exposure (N/mm <sup>2</sup> )
OPCRS100	0.708	0.682	19.68	16.84
OPCSS100	0.641	0.624	21.82	17.67
PSCSS0	0.638	0.612	18.75	14.34
PSCSS20	0.642	0.624	22.50	20.22
PSCSS40	0.634	0.602	21.62	18.24
PSCSS60	0.612	0.584	23.10	21.02
PSCSS80	0.562	0.532	20.02	17.24
PSC100	0.542	0.522	18.22	15.46

is least by 12% for PSC with 60% SS followed by 15% in PSC with 100% RS. This again confirms the potential of PSC-based mortar with 60% SS to replace RS to resist the acidic environment expected due to contact with industrial effluents etc. and a similar observation is reported (9, 31).

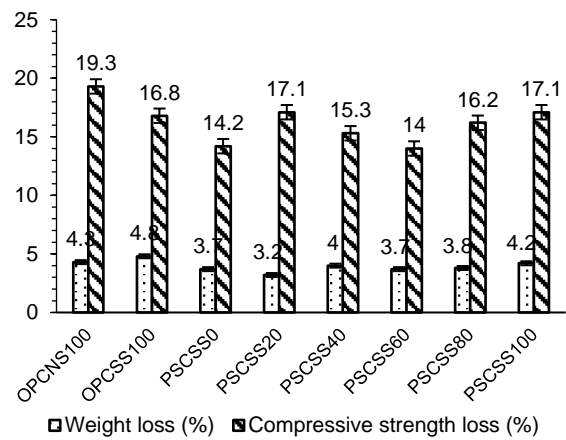


Figure 15. Weight loss and compressive strength loss in 1:3 mortar mix due to sulfate attack

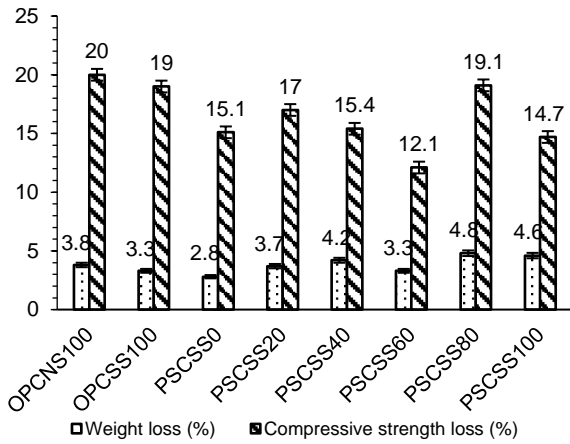


Figure 16. Weight loss and compressive strength loss in 1:4 mortar mix due to sulfate attack

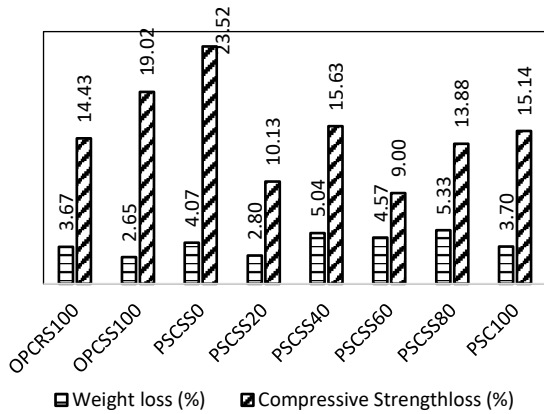


Figure 17. Weight loss and compressive strength loss in 1:6 mortar mix due to sulfate attack

4. 2. 3. Chloride Attack Test

The effect of hydrochloric acid exposure to cement mortar was assessed by weight loss and compressive strength reduction. The mortar samples subjected to chloride attack are shown in Figures 18a and 18b. The loss in weight and compressive strength of samples after exposure to chloride solutions is listed in Tables 12, 13 and 14.

The rate of weight loss and compressive strength of 1:3 mortar after the chloride attack is shown in Figure 19. It can be observed that PSC with 60% SS is only 1.7% whereas it is maximum by 3.1% in conventional cement mortar (i.e., OPCRS100). The strength reduction in mortar after chloride attack is least in PSC with 100% RS followed by PSC with 60%SS.

Table 12 shows the change in weight and compressive strength of 1:4 mortar mixes after exposure to a chloride environment using 5% hydrochloric acid. Figure 20 shows the rate of weight loss and compressive



(a)



(b)

Figure 18 a) before and b) after chloride attack

TABLE 12. Variation in weight and compressive strength due to chloride attack test for 1:3 mix

Mix Proportions	Weight before exposure (kg)	Weight after exposure (kg)	Compressive strength before exposure (N/mm <sup>2</sup> )	Compressive strength after exposure (N/mm <sup>2</sup> )
OPCRS100	0.762	0.738	62.51	57.47
OPCSS100	0.826	0.804	51.15	47.96
PSCSS0	0.720	0.705	56.83	53.98
PSCSS20	0.704	0.688	39.79	37.40
PSCSS40	0.734	0.720	36.79	34.49
PSCSS60	0.740	0.727	42.62	40.07
PSCSS80	0.710	0.692	34.10	31.52
PSCSS100	0.711	0.691	32.10	30.07

TABLE 13. Variation in weight and compressive strength due to chloride attack test for 1:4 mix

Mix Proportion	Weight before exposure (kg)	Weight after exposure (kg)	Compressive strength before exposure (N/mm <sup>2</sup> )	Compressive strength after exposure (N/mm <sup>2</sup> )
OPCRS100	0.706	0.688	35.52	31.25

OPCSS100	0.712	0.692	34.1	30.79
PSCSS0	0.685	0.659	31.25	28.40
PSCSS20	0.708	0.688	30.09	29.06
PSCSS40	0.687	0.673	28.41	26.42
PSCSS60	0.670	0.653	34.1	32.05
PSCSS80	0.684	0.662	25.57	23.27
PSCSS100	0.652	0.629	24.07	22.26

**TABLE 14.** Variation in weight and compressive strength due to chloride attack test for 1:6 mix

Mix Proportions	Weight Before Exposure (kg)	Weight After Exposure (kg)	Compressive Strength before Exposure (N/mm <sup>2</sup> )	Compressive Strength after Exposure (N/mm <sup>2</sup> )
OPCRS100	0.648	0.640	19.89	16.87
OPCSS100	0.665	0.652	22.50	19.70
PSCSS0	0.650	0.622	20.82	16.20
PSCSS20	0.648	0.610	19.86	17.02
PSCSS40	0.666	0.641	21.87	18.50
PSCSS60	0.631	0.610	26.28	23.82
PSCSS80	0.602	0.582	22.42	19.54
PSC100	0.582	0.502	20.02	18.62

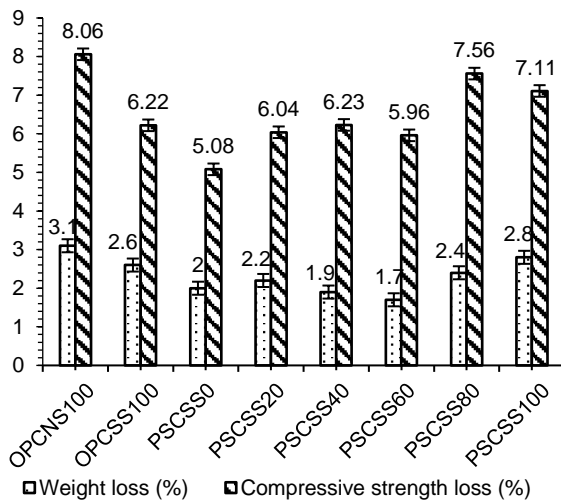


**Figure 19.** Weight loss and compressive strength loss in 1:3 mortar mix due to chloride attack

strength observed in the mortar samples. Table 13 shows the change in weight and compressive strength of 1:6 mortar mixes after exposure to a chloride environment using 5% hydrochloric acid. Figure 21 shows the rate of weight loss and compressive strength observed in the mortar samples.

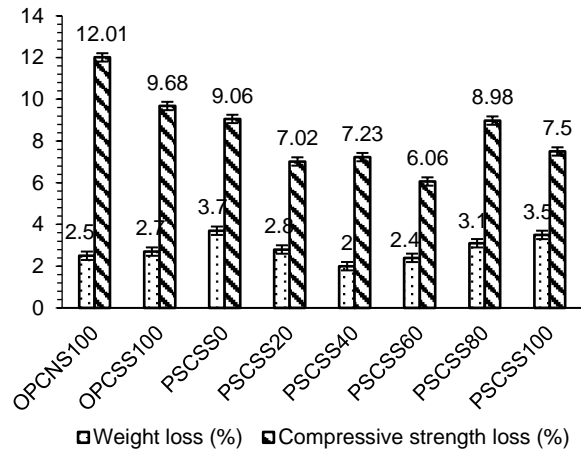


**Figure 20.** Weight loss and compressive strength loss in 1:4 mortar mix due to chloride attack

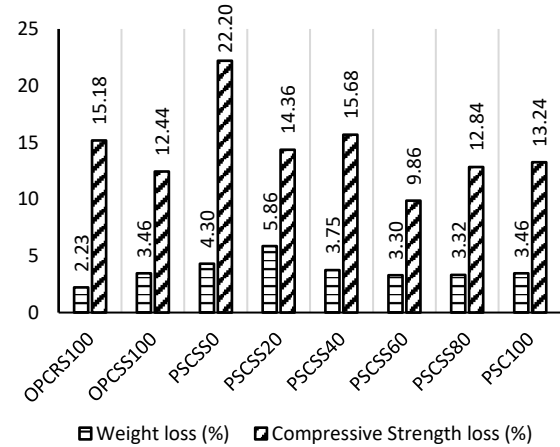


**Figure 21.** Weight loss and compressive strength loss in 1:6 mortar mix due to chloride attack

The weight loss in PSCSS60 mortar is 2.4% which is higher than that observed in 1:3 samples and a similar comparison in rate of compressive strength loss can also be observed.

**4. 2. 4. X-ray Diffractogram Analysis** The XRD pattern of 1:3 cement mortar mixes prepared using PSC mixed with 100% RS and PSC mixed with 60% SS are shown in Figures 22 and 23. In Figure 22, the diffractogram peak intensity of quartz, alite (C<sub>3</sub>S) and belite (C<sub>2</sub>S) are higher than compared to that observed in Figure 23. The reduction in peak intensities can be attributed to the formation of cementing bonds with the fine aggregate and the presence of new peaks is also shown in Figure 23.

The XRD pattern of 1:4 cement mortar mixes prepared using PSC mixed with 100% RS and PSC mixed with 60% SS is shown in Figures 24 and 25. The diffractogram shows a similar observation as that seen in

Figures 22 and 24 indicating the availability of enough silicates as alite, belite and quartz in PSCSS0. The reduction in peak intensities and the presence of newer peaks (Figure 25) confirms the dissolution of silicates and the formation of cementing products with SS in the PSCSS60 mortar mix (32-34).

#### 4. 2. 5. Scanning Electron Microscopic Analysis

The scanning electron microscopic images for 1:3 mortar mix prepared with PSC and 100% RS as well as PSC with 60% SS are shown in Figures 28 (a) and 28 (b). The PSC mortar mix with 100% RS shows the formation of CSH

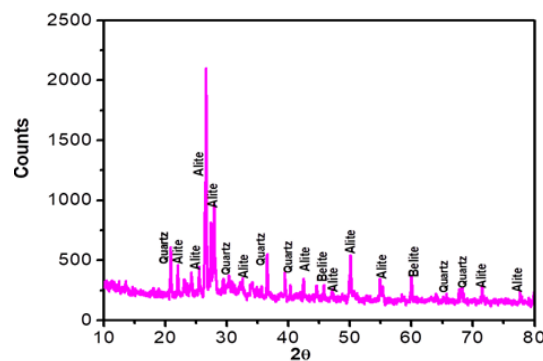


**Figure 25.** X-ray diffractogram of cement mortar mix used in the study of PSCSS60 (1:4)

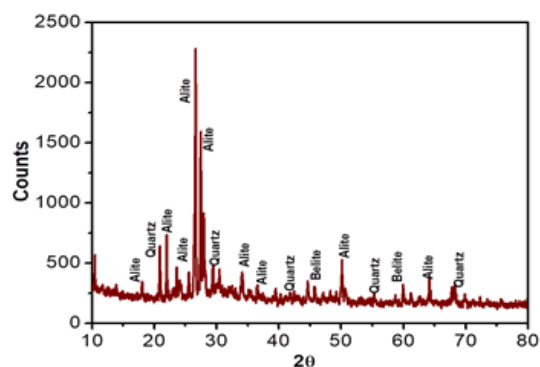


**Figure 22.** X-ray diffractogram of cement mortar mix used in the study of PSCSS0 (1:3)

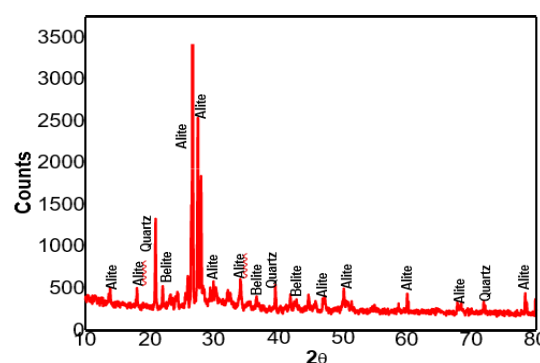


**Figure 26.** X-ray diffractogram of cement mortar mix used in the study of PSCSS0 (1:6)

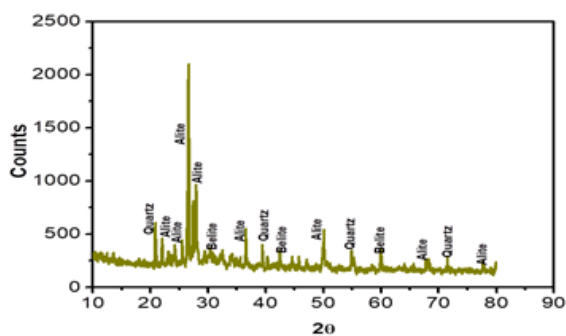


**Figure 23.** X-ray diffractogram of cement mortar mix used in the study of PSCSS60 (1:3)

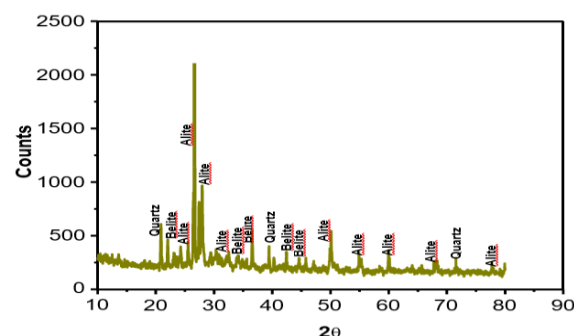


**Figure 27.** X-ray diffractogram of cement mortar mix used in the study of PSCSS60 (1:6)

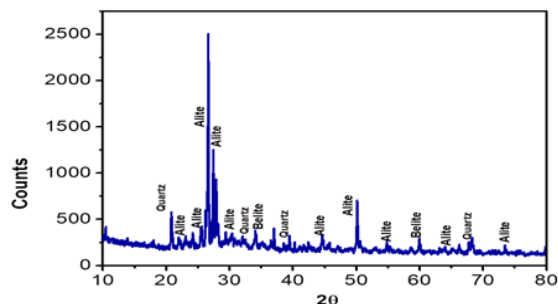


**Figure 24.** X-ray diffractogram of cement mortar mix used in the study of PSCSS0 (1:4)

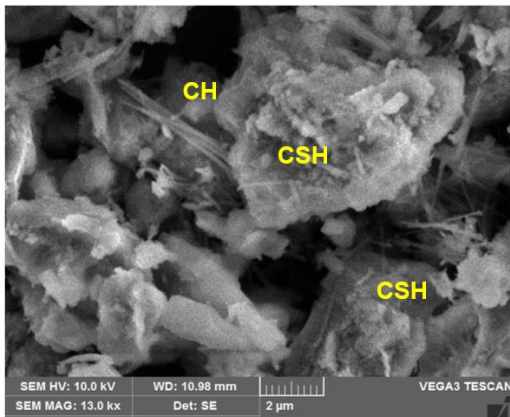
and CH (9, 35, 36). The presence of ettringite as Aft along with CSH is observed in PSC with 60% SS. This can be ascribed to the high strength retention in PSC with SS as a replacement for RS by 60% as observed from durability studies (37, 38).

The comparison of the elemental composition of PSCSS0 and PSCSS60 as shown in Figures 23 and 24 illustrates the reduction in silica and increase in calcium content and the formation of newer peaks representing calcium in PSCSS60. This indicates the reactivity of PSC

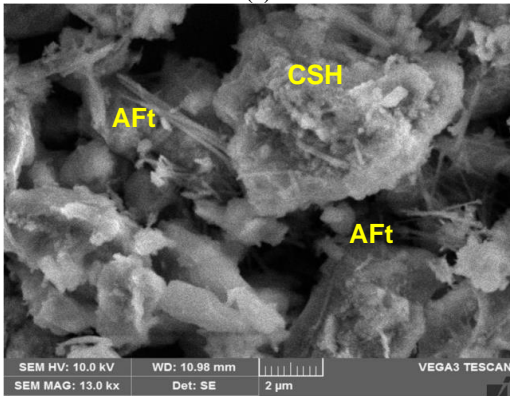
and SS as well along with PSC hydration reaction, that is contributing to enhanced strength and a high rate of strength retention.

The energy dispersive x-ray (EDAX) spectroscopic results of Portland slag cement mortar mix 1:4 prepared with 100% RS and 60% SS as a replacement to RS are shown in Figures 34 and 35.

The elemental compositions obtained from EDAX spectroscopy are used to determine the Calcium (Ca)/Silica (Si) ratio (Table 14). The Ca/Si ratio is approximately 1.00 for all samples indicating the presence of CSH as a tobermorite gel phase and the lower



(a)



(b)

**Figure 28.** Micrographs of 1:3 cement mortar mix a) PSCSS0 b) PSCSS60

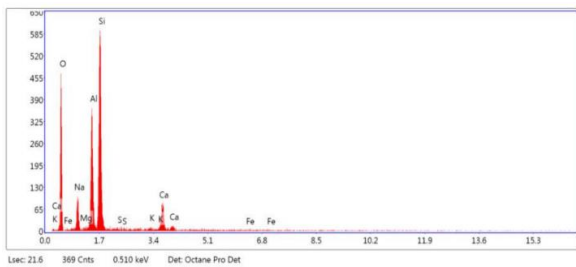


**Figure 29.** EDAX image of 1:3 PSC mortar with 100% RS (PSCSS0)

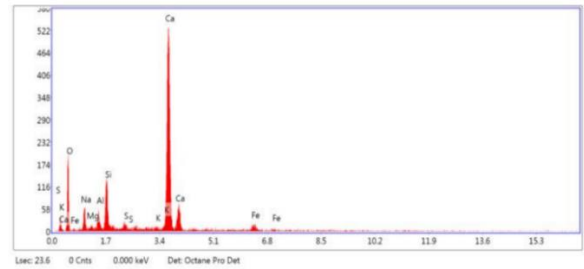


**Figure 30.** EDAX image of 1:3 PSC mortar with 60% SS (PSCSS60)

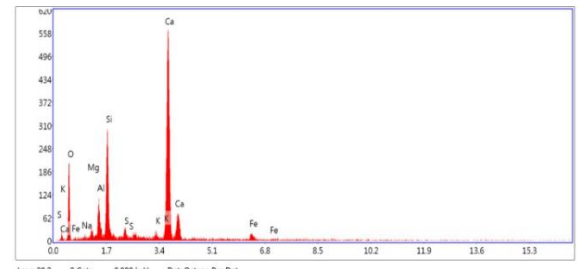


**Figure 31.** EDAX image of 1:4 PSC mortar with 100% RS (PSCSS0)

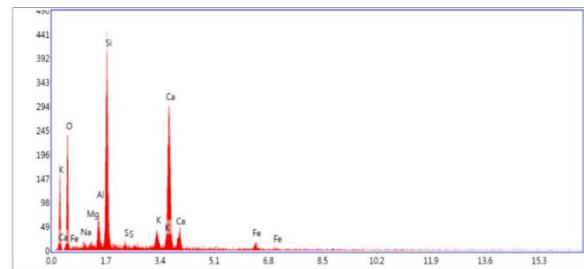
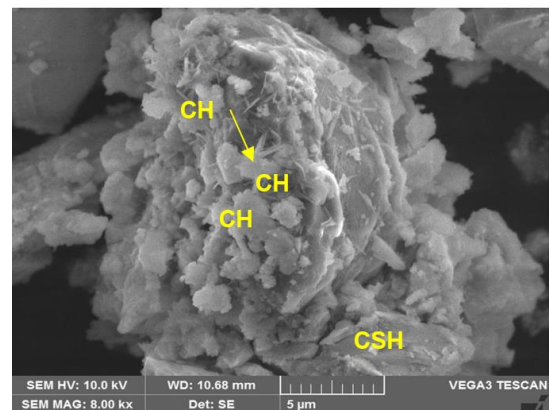
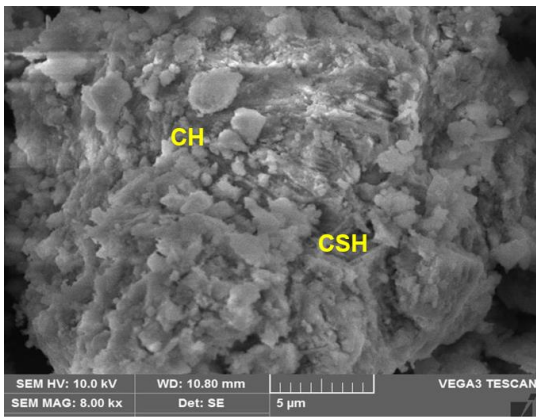


**Figure 32.** EDAX image of 1:4 PSC mortar with 60% SS (PSCSS60)

values of Ca/Si ratio are speculated to correspond to a higher content of CSH resulting in densified mortar matrix (10).



(a)



(b)

Figure 33. Micrographs of 1:4 cement mortar mix a) PSCSS0 b) PSCSS60

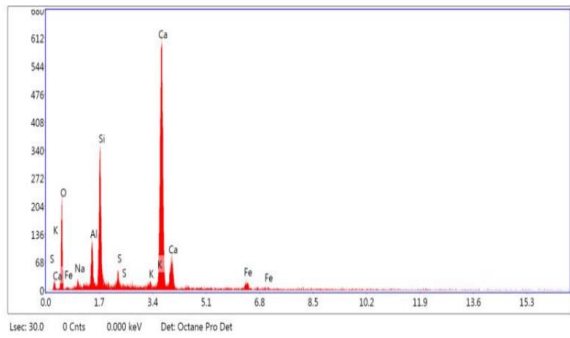


Figure 34. EDAX image of 1:4 PSC mortar with 100% RS (PSCSS0)

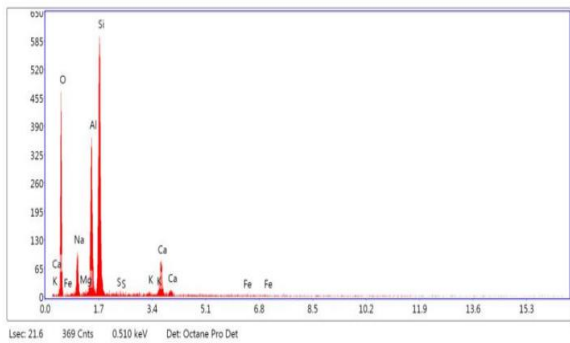


Figure 35. EDAX image of 1:4 PSC mortar with 60% SS (PSCSS60)

TABLE 14. Ca/Si ratio of PSC-based mortar mix

Mix ratio	Sample	Ca/Si
1:3	PSCSS0	1.09
1:3	PSCSS60	1.06
1:4	PSCSS0	1.00
1:4	PSCSS60	0.98

### 5. NUMERICAL STIMULATION

A finite element model (FEM) of the segmental girder specimen under the same conditions as the test is established, as shown in Figure 36 To verify the reliability of the FEM and parameters, the calculated results of the damage pattern and response of the specimen model are compared with the test data. The results are done numerical stimulation by using the Ansys software. Figure 36 shows the variation of stress in the sample under the simulated compressive load. The maximum stress of 50 MPa is exhibited by the proposed cement mortar model which is similar to the experimental values obtained for OPC with SS.

The deformation under the applied load condition showed the maximum of 0.11 mm in the simulated cement mortar cube (See Figure 37).

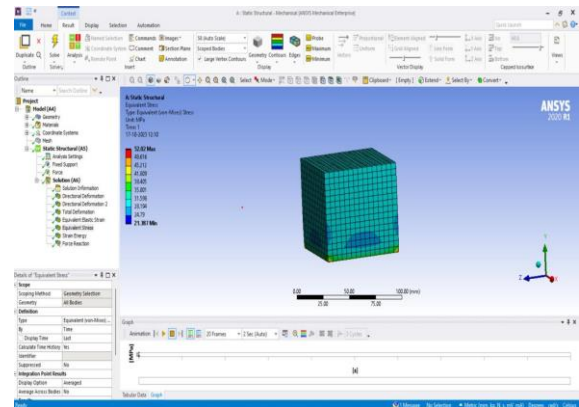


Figure 36. Results of stresses in Ansys model for the cube

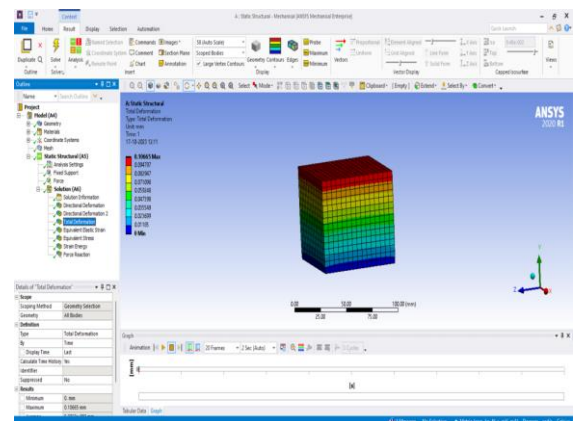


Figure 37. Results of deformations in the cube

### 6. CONCLUSION

The strength and microstructural change in cement mortars with OPC and PSC on partial to full replacement of natural river sand with slag sand has been assessed

based on compressive strength and mass loss after acid attack, sulfate attack and chloride attack along with SEM-EDAX and XRD analysis. Conclusions from the present study can be proposed as follows:

- 1) The 28-day compressive strength of PSC mortar mix with 60% SS as a replacement to RS shows maximum strength gain compared to other percentages of NS replacement. The strength of PSC-based mortar mix is lesser than the strength gain observed in OPC-based mortar mix which can be ascribed to the lower rate of strength gain in PSC-based mortar. The optimum content of SS as fine aggregate for the maximum increase in compressive strength of PSC mortar is 60% with 40% RS.
- 2) Durability studies show that PSC with 60% SS as a replacement to RS shows high resistance to sulfate and chloride exposure compared to the strength loss observed after acid attack testing. This shows that PSCSS60 will be effective in a corrosion-prone environment.
- 3) The formation of cementitious gel phases was observed in XRD as well as EDAX spectroscopy. The SEM image analysis showed the formation of a densified mortar matrix in PSCSS60 with higher CSH formation which is confirmed by Ca/Si ratio  $\approx$  1.0. Thus, the improvement in mechanical properties and durability against aggressive environmental influence is correlated well with the microstructural analysis.
- 4) Numerical simulation of stress deformation analysis by FEM approach using ANSYS software for the optimized cement mortar cube under a compressive load of 150 kN resulted in maximum stress of 50 MPa and deformation of 0.11 mm. The results validate the reliability of experimental results discussed in the present study.

It is understood that the replacement of OPC with PSC and natural river sand with slag sand to prepare cement mortar will satisfy the strength and durability as well as an economically and environmentally sustainable option.

## 6. REFERENCES

1. Arunachalam KP, Avudaiappan S, Maureira N, Garcia Filho FDC, Monteiro SN, Batista ID, et al. Innovative use of copper mine tailing as an additive in cement mortar. *Journal of Materials Research and Technology*. 2023. 10.1016/j.jmrt.2023.06.066
2. Ye W, Fu J. Study on the impermeability and microstructure of cement mortar blended with silicon carbide nanowhiskers. *Case Studies in Construction Materials*. 2023;19:e02334. 10.1016/j.cscm.2023.e02334
3. Dahish HA, Alfawzan M, Tayeh BA, Abusogi MA, Bakri M. Effect of inclusion of natural pozzolan and silica fume in cement-based mortars on the compressive strength utilizing artificial neural networks and support vector machine. *Case Studies in Construction Materials*. 2023;18:e02153. <https://doi.org/10.1016/j.cscm.2023.e02153>
4. Dash MK, Patro SK, Rath AK. Sustainable use of industrial-waste as partial replacement of fine aggregate for preparation of concrete—A review. *International Journal of Sustainable Built Environment*. 2016;5(2):484-516. <https://doi.org/10.1016/j.ijbsbe.2016.04.006>
5. Devi VS, Gnanavel B. Properties of concrete manufactured using steel slag. *Procedia Engineering*. 2014;97:95-104. <https://doi.org/10.1016/j.proeng.2014.12.229>
6. Ferreira VJ, Vilaplana AS-D-G, García-Armingol T, Aranda-Usón A, Lausín-González C, López-Sabirón AM, et al. Evaluation of the steel slag incorporation as coarse aggregate for road construction: technical requirements and environmental impact assessment. *Journal of Cleaner Production*. 2016;130:175-86. <https://doi.org/10.1016/j.jclepro.2015.08.094>
7. Bedoya MA, Tobon JI. Incidence of recycled aggregates and ternary cements on the compressive strength and durability of ecological mortars. *Case Studies in Construction Materials*. 2022;17:e01192. <https://doi.org/10.1016/j.cscm.2022.e01192>
8. Garg R, Bansal M, Aggarwal Y. Strength, rapid chloride penetration and microstructure study of cement mortar incorporating micro and nano silica. *Int J Electrochem Sci*. 2016;11(5):3697-713. [https://doi.org/10.1016/S1452-3981\(23\)17430-X](https://doi.org/10.1016/S1452-3981(23)17430-X)
9. Goyal R, Verma VK, Singh N. Hydration of Portland slag cement in the presence of nano silica. *Construction and Building Materials*. 2023;394:132173. <https://doi.org/10.1016/j.conbuildmat.2023.132173>
10. Guo Y, Xie J, Zhao J, Zuo K. Utilization of unprocessed steel slag as fine aggregate in normal-and high-strength concrete. *Construction and Building Materials*. 2019;204:41-9. <https://doi.org/10.1016/j.conbuildmat.2019.01.178>
11. Guo Y, Xie J, Zheng W, Li J. Effects of steel slag as fine aggregate on static and impact behaviours of concrete. *Construction and Building Materials*. 2018;192:194-201. <https://doi.org/10.1016/j.conbuildmat.2018.10.129>
12. Islam MM, Islam MS, Rahman MA, Das A. Strength behavior of mortar using slag as partial replacement of cement. *MIST INTERNATIONAL JOURNAL OF SCIENCE AND TECHNOLOGY*. 2011;3(1). 10.3329/mist.v3i0.8053
13. Hashempour M, A Samani A, Heidari A. Essential improvements in gypsum mortar characteristics. *International Journal of Engineering, Transactions B: Applications*. 2021;34(2):319-25. 10.5829/ije.2021.34.02b.03
14. Tangadagi RB, Manjunatha M, Bharath A, Preethi S. Utilization of steel slag as an eco-friendly material in concrete for construction. *Journal of Green Engineering*. 2020;10(5):2408-19. 10.1016/j.heliyon.2023.e16288
15. Khan K, Ahmad W, Amin MN, Rafiq MI, Arab AMA, Alabdullah IA, et al. Evaluating the effectiveness of waste glass powder for the compressive strength improvement of cement mortar using experimental and machine learning methods. *Heliyon*. 2023;9(5). <https://doi.org/10.1016/j.cscm.2023.e02264>
16. Li S, Chen X, Zhang W, Ning Y, Casas JR. Utilization of ultra-fine dredged sand from the Yangtze River in alkali-activated slag/fly ash mortars: Mechanical properties, drying shrinkage and microstructure. *Case Studies in Construction Materials*. 2023;19:e02264.
17. Sahith Reddy S, Achyutha Kumar Reddy M. Optimization of Calcined Bentonite Clay Utilization in Cement Mortar using Response Surface Methodology. *International Journal of Engineering, Transactions A: Basics*. 2021;34(7):1623-31. 10.5829/ije.2021.34.07a.07

18. Liu J, Guo R. Applications of steel slag powder and steel slag aggregate in ultra-high performance concrete. *Advances in Civil Engineering*. 2018;2018:1-8. 10.1155/2018/1426037
19. Jebadurai S, Tensing D, Hemalatha G, Siva R. Experimental investigation of toughness enhancement in cement mortar. *International Journal of Engineering, Transactions B: Applications*,. 2018;31(11):1824-9. 10.5829/ije.2018.31.11b.04
20. Pang B, Zhou Z, Xu H. Utilization of carbonated and granulated steel slag aggregate in concrete. *Construction and building materials*. 2015;84:454-67. <https://doi.org/10.1016/j.conbuildmat.2015.03.008>
21. IS 455- 1989 “Indian Standard for Portland Slag cement – Specification”, Bureau of Indian Standards, New Delhi, 1990.
22. IS 12269 (1987): 53 grade ordinary Portland cement [CED 2: Cement and Concrete].
23. IS: 16714-2018. “Ground Granulated Blast Furnace Slag for Use in Cement, Mortar and Concrete, Bureau of Indian Standards, New Delhi.
24. IS 383-2016 “Specification for Tests on Fine aggregate”, Bureau of Indian Standards, New Delhi, 1971.
25. IS 4031-6 (1988) “Methods of Physical Tests for Cement”, Bureau of Indian Standards, New Delhi, 1988.
26. Ahmed SM, Kamal I. Electrical resistivity and compressive strength of cement mortar based on green magnetite nanoparticles and wastes from steel industry. *Case Studies in Construction Materials*. 2022;17:e01712. <https://doi.org/10.1016/j.cscm.2022.e01712>
27. Abdalla A, Salih A. Microstructure and chemical characterizations with soft computing models to evaluate the influence of calcium oxide and silicon dioxide in the fly ash and cement kiln dust on the compressive strength of cement mortar. *Resources, Conservation & Recycling Advances*. 2022;15:200090. <https://doi.org/10.1016/j.rcradv.2022.200090>
28. de Sande VT, Sadique M, Bras A, Pineda P. Activated sugarcane bagasse ash as efficient admixture in cement-based mortars: Mechanical and durability improvements. *Journal of Building Engineering*. 2022;59:105082. <https://doi.org/10.1016/j.jobe.2022.105082>
29. Xu Z, Guo Z, Zhao Y, Li S, Luo X, Chen G, et al. Hydration of blended cement with high-volume slag and nano-silica. *Journal of Building Engineering*. 2023;64:105657. <https://doi.org/10.1016/j.jobe.2022.105657>
30. Wang G, Zong H, Zhang Z, Sun J, Wang F, Feng Y, et al. Application of titanium gypsum as raw materials in cement-based self-leveling mortars. *Case Studies in Construction Materials*. 2023;19:e02536. <https://doi.org/10.1016/j.cscm.2023.e02536>
31. Lekshmi S, Sudhakumar J. An assessment on the durability performance of fly ash-clay based geopolymer mortar containing clay enhanced with lime and GGBS. *Cleaner Materials*. 2022;5:100129. <https://doi.org/10.1016/j.clema.2022.100129>
32. Liao Y, Wang X, Wang L, Yin Z, Da B, Chen D. Effect of waste oyster shell powder content on properties of cement-metakaolin mortar. *Case Studies in Construction Materials*. 2022;16:e01088. <https://doi.org/10.1016/j.cscm.2022.e01088>
33. Seco Meneses A, Castillo JMd, Espuelas Zuazu S, Marcelino Sádaba S, Echeverría AM. Assessment of the ability of MGO based binary binders for the substitution of Portland cement for mortars manufacturing. *Construction And Building Materials* 341 (2022) 127777. 2022. <https://doi.org/10.1016/j.conbuildmat.2022.127777>
34. Chintalapudi K, Pannem RMR. Enhanced chemical resistance to sulphuric acid attack by reinforcing Graphene Oxide in Ordinary and Portland Pozzolana cement mortars. *Case Studies in Construction Materials*. 2022;17:e01452. <https://doi.org/10.1016/j.cscm.2022.e01452>
35. Brekailo F, Pereira E, Pereira E, Farias MM, Medeiros-Junior RA. Red ceramic and concrete waste as replacement of portland cement: Microstructure aspect of eco-mortar in external sulfate attack. *Cleaner Materials*. 2022;3:100034. <https://doi.org/10.1016/j.clema.2021.100034>
36. Liu D, Kaja A, Chen Y, Brouwers H, Yu Q. Self-cleaning performance of photocatalytic cement mortar: Synergistic effects of hydration and carbonation. *Cement and Concrete Research*. 2022;162:107009. <https://doi.org/10.1016/j.cemconres.2022.107009>
37. Han SH, Jun Y, Kim JH. The use of alkaline CO2 solvent for the CO2 curing of blast-furnace slag mortar. *Construction and Building Materials*. 2022;342:127977. <https://doi.org/10.1016/j.conbuildmat.2022.127977>
38. Klyuev S, Fediuk R, Ageeva M, Fomina E, Klyuev A, Shorstova E, et al. Phase formation of mortar using technogenic fibrous materials. *Case Studies in Construction Materials*. 2022;16:e01099. <https://doi.org/10.1016/j.cscm.2022.e01099>

**COPYRIGHTS**

©2024 The author(s). This is an open access article distributed under the terms of the Creative Commons Attribution (CC BY 4.0), which permits unrestricted use, distribution, and reproduction in any medium, as long as the original authors and source are cited. No permission is required from the authors or the publishers.

**Persian Abstract****چکیده**

ملات سیمان به عنوان عامل اتصال بین مصالح ساختمانی در ساخت سنگ تراشی و سنگ تراشی آجری استفاده می شود. تمرکز بر کاهش بار زیست محیطی ناشی از انتشار بالای کربن با مصرف سیمان مورد توجه قرار گرفته است. در این مطالعه، بررسی های تجربی با استفاده از دو ماده مبتنی بر سرباره، یعنی سیمان سرباره پرتلند (PSC) و ماسه سرباره کوره بلند دانه بندی شده پردازش شده (PGBFS، سرباره آهن)، به عنوان جایگزینی برای سیمان پرتلند معمولی (OPC) و ماسه رودخانه انجام شد. (RS) هدف این مقاله بررسی تاثیر PSC با ماسه سرباره بر استحکام، دوام و ریزساختار ملات سیمان است. کار حاضر به طور خاص بهبود مقاومت ملات سیمان با سیمان سرباره و ماسه سرباره را با تغییر دوره پخت بررسی می کند و نتایج را در روزهای ۷، ۱۴ و ۲۸ روزه مقایسه می کند. OPC به طور کامل با PSC جایگزین می شود و ماسه رودخانه به طور جزئی با کامل با ماسه سرباره در درصدهای مختلف جایگزین می شود، یعنی ۰٪، ۲۰٪، ۴۰٪، ۶۰٪، ۸۰٪ و ۱۰۰٪ برای انواع مختلف مخلوط ها. نتایج نشان داد که بیشترین افزایش مقاومت فشاری و مقاومت بالا در برابر حمله اسیدی در ملات سیمان با جایگزینی PSC ۱۰۰٪ و Slag Sand ۶۰٪ وجود دارد. مصرف مصالح پیشنهادی به نفع صنعت ساخت و ساز برای دستیابی به هدف خالص صفر خواهد بود.



## Self-healing Concrete Using Microcapsules Containing Mineral Salts

S. Ghaemifard<sup>a</sup>, H. Khosravi<sup>b</sup>, F. Farash Bamoharram<sup>c</sup>, A. Ghannadiasl<sup>\*a</sup>

<sup>a</sup> Department of Civil Engineering, University of Mohaghegh Ardabili, Ardabil, Iran

<sup>b</sup> Department of Civil Engineering, Hakim Sabzevari University, Sabzevar, Iran

<sup>c</sup> Department of Chemistry, Mashhad Branch, Islamic Azad University, Mashhad, Iran

### PAPER INFO

#### Paper history:

Received 27 September 2017

Received in revised form 17 October 2023

Accepted 04 November 2023

#### Keywords:

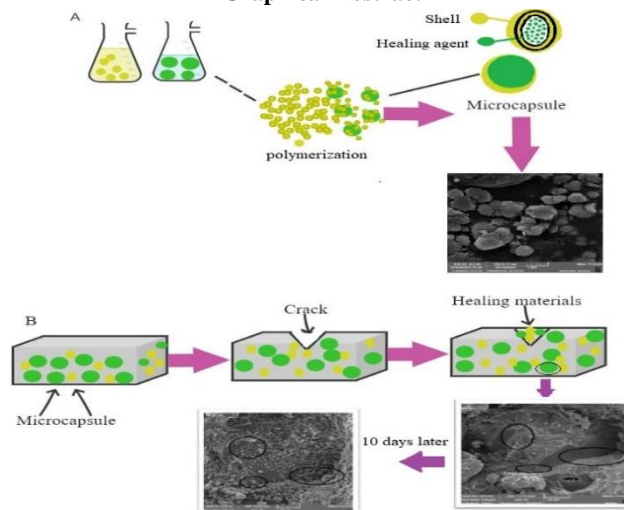
Self-healing  
Microcapsule  
Concrete  
Mineral Salts  
Preyssler  
Calcium Nitrate

### ABSTRACT

Propagating micro-cracks in a structure decreases its load-bearing capacity and leads to the collapse of the entire structure. Addition of various additives in all kinds of concrete or concrete ingredients, as several studies have shown, could significantly make concrete reclaim from the specifications and attributes point of view. A possible manner to the common ruin and expensive preservation of concrete infrastructure, utilizing encapsulating healing factors is helpful for the self-healing of concrete. The self-healing concrete with microencapsulated Preyssler, and calcium nitrate was studied in this paper. Microcapsules were synthesized by in-situ polymerization of urea-formaldehyde as a shell around the core materials inclusive of Preyssler, calcium nitrate. Physicochemical characterization of microcapsules was conducted by Fourier transformation infrared spectroscopy, field emission scanning electron microscopy, and Transmission Electron Microscope. The mechanical assessment of cementitious specimens with different dosages of microcapsules (0%, 0.5%, 1%, 1.5%, and 2%) was performed by compressive tests. Also, by measurement before and after damage after 10 days, the self-healing potential was tested. After the concrete was damaged by exerting 30% of its final load, all samples were incubated by immersion in water. According to the results, the sample containing 0.5% UFN, the sample containing 1.5% UFP, and the sample containing 1.5% UFNP have higher repair rates than others. This scope of research because of its interdisciplinary nature would own several possibilities to be pioneering with making an opening gate to link sciences and engineering such as material, chemistry, science, nanotechnology, and the field of engineering to persuade a wide spectrum of contribution in engineering sciences and usages.

doi: 10.5829/ije.2024.37.04a.16

### Graphical Abstract



\*Corresponding Author Email: [aghamadiasl@uma.ac.ir](mailto:aghamadiasl@uma.ac.ir) (A. Ghannadiasl)

Please cite this article as: Ghaemifard S, Khosravi H, Farash Bamoharram F, Ghannadiasl A. Self-healing Concrete Using Microcapsules Containing Mineral Salts. International Journal of Engineering, A: Basics. 2024;37(04):779-93.

## NOMENCLATURE

P	Preyssler	SEM	Scanning electron microscopy
CN	Calcium Nitrate	TEM	Transmission Electron Microscope
UFN	Urea-formaldehyde calcium nitrate microcapsule	FT-IR	Fourier transform infrared spectrometer
UFNP	Urea-formaldehyde calcium nitrate-Preyssler microcapsule	EDS	Energy Dispersive Spectroscopy
UFP	Urea- formaldehyde Preyssler microcapsule		

## 1. INTRODUCTION

One of the essential building materials used in most of the sections of structures is concrete. Existing crack in concrete structures is so harmful for durability and reliability (1, 2); commonly, this event begins at the atomic area with defects that get more significant and larger that create cracks. In concrete structures, protecting them is controlling and stopping crack diffusion, increasing their yield and dependability, and extending their service lifetime. So, self-healing concrete is an answer for good bases because it may forbid the growth of early life micro cracks into more significant cracks. Without needing human or any kind of manual interference, self-healing materials automatically heal damage (3-5). From the past till today, Micro and Nano-encapsulation are challenging techniques in protecting drugs and healing agents (6, 7). Microcapsule-based self-healing concrete is a novel kind of concrete material that repair micro cracks in concrete and reclaim the strength and stability of concrete (8). The repairing origin of microcapsule self-repairing concrete is typical that when micro cracks of concrete develop and tangency with the microcapsules, the shell of the microcapsules fracture, and the epoxy resin diluted moves into the crack and responds with the curing factor. This fills the cracks and arrives at the target of repairing the cracks (9, 10). Today, researchers have done empirical and simulation investigations on microcapsule-based self-healing concrete. Its efficiency, like its stability compared with ordinary cement, has been of interest to many researchers, and several studies have been carried out on its empirical aspects (11-14). White et al. (9) are the first researchers that report a feasible display of self-healing materials through implanting encapsulated healing agents into a polymer matrix, including diffused catalysts. de Souza Rodrigues et al. (15) investigated the synthesis, characterization, and self-healing qualitative valence of polyurethane microcapsules that include toluene diisocyanate and isophorone diisocyanate as a core factor. The thermal analysis they were determined that the decreasing temperature of the material was higher in TDI-including microcapsules as the core factor. Development and mineralization specifications of *Bacillus subtilis* (BS) detached from marine aquaculture wastewater and its usage in coastal self-healing concrete was investigated by Fu et al. (16). In the research of Wang et al. (17), the strength recovery and acoustic performance of microcapsule self-healing concrete were

used as evaluation indices to assess the damage to the microcapsule self-healing system. They concluded that the self-healing performance was better for the microencapsulated self-healing concrete than the ordinary concrete. Self-healing techniques involve the use of microcapsules containing self-healing agents and catalysts that are dispersed within a structure. In the event of excess load or damage to the structure, the microcapsules detect the damage and release the self-healing agent stored inside them. The self-healing agent then reacts with the previously dispersed catalysts, effectively repairing the damage. Therefore, a stable manufacturing method for the microcapsules containing self-healing agents is crucial in order to repair the damage and ensure the structural stability. Self-healing microcapsules must possess sufficient mechanical strength and thermal stability to be effectively utilized for the repair of composite structures. These properties can be affected by various manufacturing conditions, such as constituent materials, stirring speed, pH, and reaction temperature (18, 19). The speed at which a mixture is stirred is a crucial factor in determining the size and size distribution of microcapsules. The size of these capsules is directly related to their strength. A study by Kosarli et al. (20) examined the mechanical properties, thermal stability, and healing efficiency of microcapsules with five different average diameters, by controlling the stirring speed. The researchers found that microcapsules with smaller diameters showed better thermal stability and lower degradation of mechanical performance.

The different healing factors for crack-healing in cement-based products are displayed in Figure 1 (21). Also, Figure 2 shows that microencapsulation is the most well-known technique accepted for releasing healing components into cement-based products. As we know, for producing concrete with the boosted qualification, utilizing inorganic additives has possessed more consideration worldwide. One of the novel, the environmentally friendly tasks is extending the region of the inorganic additives of compound function via the utilization of heteropolyacids. Heteropolyacids are propounded as a type of inorganic clusters that are built of hydrogen, oxygen, and some transition metals and non-metals (22, 23). In Figure 3, one of the famed forms of heteropolyacids is named Preyssler structures, shows its general formula of it is  $[\text{NaP}_5\text{W}_{30}\text{O}_{110}]^{14}$ . Several researchers investigated the positive factors of organic polymer concrete materials on attributes of concrete. Some of the attributes include excellent vibration

damping, high compressive strength, great vibration damping properties, high particular stiffness and strength, resistance to corrosion and chemicals, fast curing, and the capacity to create involved shapes (24-26). Based on a brief literature review, it has been found that multicomponent concrete with several additives has emerged as a new generation of concrete that is able to maintain the required properties in all operating conditions. The use of multicomponent concretes is growing due to their ability to manage structure formation and show directed quality in properties at all stages of technology (27, 28). For example, Balamuralikrishnan et al. (29) analyzed the flexural, shear, and combined effects of the flexural and shear behavior of reinforced concrete beams that were strengthened with externally bonded ferrocement laminates made with spent catalysts. They compared the results of these beams to control beams that were not strengthened. The testing was conducted under two-point loading conditions. Mohammed et al. (30) investigated how steel fiber-reinforced concrete flat slabs perform when subjected to punching shear force. The experimental results showed that slabs incorporating steel fiber had a 21.8% higher punching shear capacity compared to those without steel fiber. Additionally, the slabs reinforced with steel fiber demonstrated greater ductility than the ones without fiber reinforcement. Nistratov et al. (31) conducted research on waste carbon plastics and unused industrial fiberglass plastics, including office equipment components that contained highly dispersed fibers and laminating coatings with an organo-mineral matrix. The study revealed that adding 1% by weight of fibers to slag blocks and active carbon pellets significantly increases their compressive strength, but the bending strength remains unchanged due to the dispersed reinforcement. As an admixture contributes to the acceleration of the hydration of cement and helps, the increase of the strength of concrete over the long term is calcium nitrate. In our literature survey, we discovered that Polyoxometalates - clusters of early transition metals have not yet been used in concrete microcapsules, specifically Preyssler heteropolyacid (HPA). Given our experience with HPAs and related chemistry (32) and cited references therein, we were inspired to begin investigating this area further. We recently explored the application of different polyoxometalates and Preyssler polyoxometalate in nanotechnology (33), and with our ongoing interest in extending the applications of Preyssler, we feel it is important to examine the potential benefits of using this heteropolyacid as a microcapsule to improve the compressive strength of concrete.

So, moderate dosages of 0.5% to 2% by weight of cement are required to get these advantages. In this paper, the main aim is to evaluate the application of CN, and P that are mineral salt as a healing operators and to define their efficacies in self-healing mechanisms for concrete

materials. To gain this aim, a laboratory test was done to measure the self-healing ability of concrete with CN and P microcapsules and compare the results with samples without microcapsules. In Figure 4 a diagrammatic microcapsule-based self-healing method is displayed.

## 2. EXPERIMENTAL PROCEDURE

The experimental scheme is shown in Figure 5.

**2.1. Materials** Calcium nitrate and Preyssler were used to create UFN, UFP, and UFNP microcapsules. Raw materials used for the experiments have been listed in Table 1.

**2.1.1. Synthesis of Preyssler** In a 250 ml beaker, dissolve 99 g of dihydrate sodium tungstate in 120 ml of distilled water with temperature control between 40-45 °C while stirring, then slowly add 75 ml of phosphoric acid 85% to it and it was refluxed for at least 5 hours. After the reflux period is over, add 5.22 g of KCl salt gradually at room temperature, and at the end, the solution is stirred for 30-40 minutes.

The green precipitate is filtered and crystallized in a minimum amount of water at 70 °C. In the first step, the

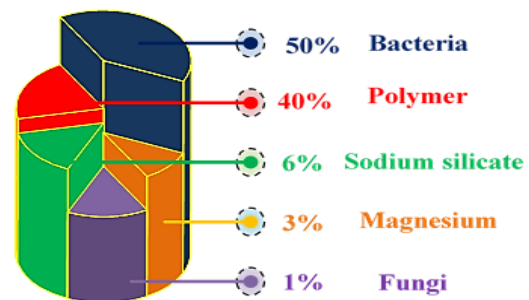


Figure 1. Different methods utilized for the search phrase 'concrete self-healing' event in the Scopus database

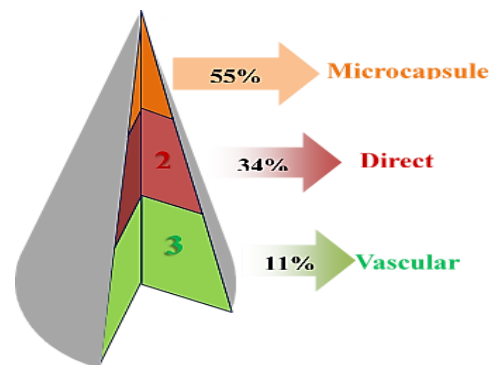


Figure 2. Different techniques of transporting healing factors into the cement-based products for search phrase results in the Scopus database

white crystals of preyssler anion appear on the solution's surface and are separated from the environment by filtering. Figure 6 showed the produced preyssler.

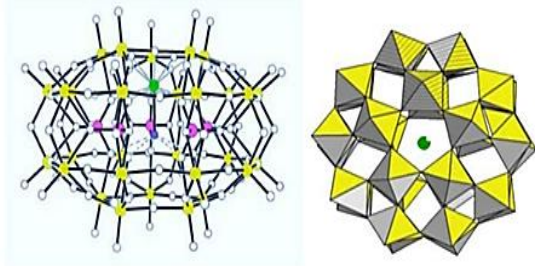


Figure 3. Preyssler [40]

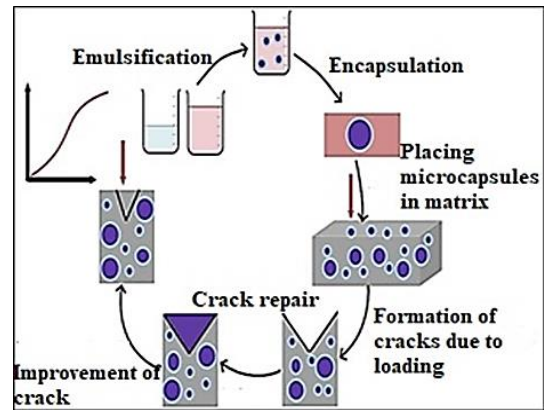


Figure 4. Schematic representing microcapsule-based self-healing method

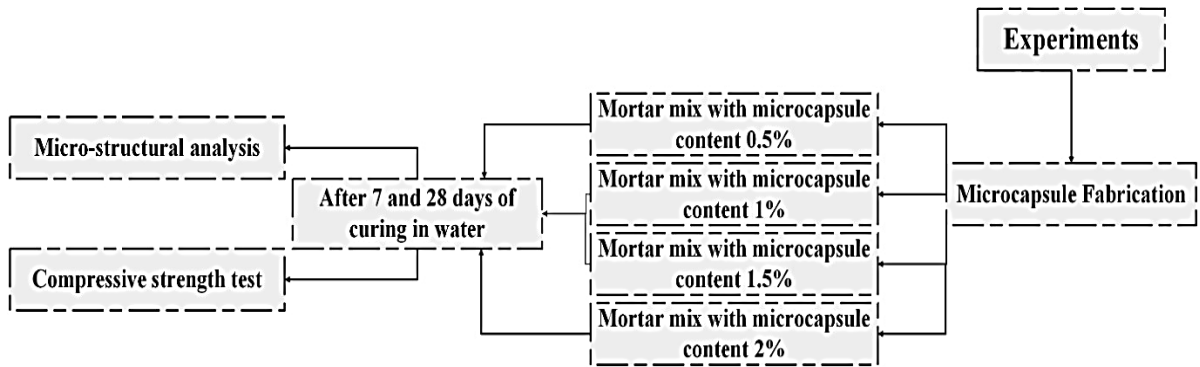


Figure 5. Experimental plan

TABLE 1. Raw materials utilized for the tests

Material Name	Formula	Usage	Pure degree	Manufacturer
Resorcinol	C6H6O2	Preparation of Microcapsules	99.0 % ≤	MERK CO
Formaldehyde	CH2O	Preparation of Microcapsules	37%	MERK CO
Ammonium Chloride	NH4Cl	Preparation of Microcapsules	99%	MERK CO
Urea	CO (NH2)2	Preparation of Microcapsules	99% ≤	MERK CO
Hexane	CH3 (CH2)4CH3	Preparation of Microcapsules	85% <	MERK CO
Sulfonic Acid	R-C6H6-OSO3H R=C10-C13	Preparation of Microcapsules	96%	MERK CO
Span 60	C24H46O6	Preparation of Microcapsules	AR	MERK CO
Calcium Nitrate Tetra hydrate	Ca (NO3)2 × 4 H2O	Preparation of Microcapsules	99-102%	MERK CO
Sodium tungstate dehydrate	Na2WO4.2H2O	Preparation of preyssler	AR	MERK CO
Phosphoric acid	H3PO4	Preparation of preyssler	85%	MERK CO
potassium chloride	KCL	Preparation of preyssler	90% ≤	MERK CO

**2. 2. Synthesis of Microcapsules** The procedure, which uses an in-situ polymerization chemical process to encapsulate CN and P under a water-in-oil emulsion, includes aqueous and continuous phases. The aqueous phase consists of urea, formaldehyde, resorcinol,

ammonium chloride, and calcium nitrate as core materials dissolved in distilled water. In general, the synthesis of self-healing microcapsules is based on the under proceedings.



**Figure 6.** Produced Preyssler

First emulsification, as the aqueous CN, and P are spread into the needful particles, then these spread particles are caught in a shell frame as a result of a chemical response between the surfactants. This act is recognized as polymerization. The synthesis of microcapsule, as introduced in the next part, followed the action reported in literature (34). Figure 7 displays the stages involved during microcapsule making and the final product.

### 2. 2. 1. Calcium Nitrate Self-healing Microcapsules

The procurement method for microcapsules, including CN, was based on prior study conducted by Hassan et al. (34), utilizing a water-in-oil suspension polymerization way that urea formaldehyde is as a shell material. The monomer phase was built of the microcapsules' shell materials and CN as a healing factor.

Part A: For making an aqueous solution containing 0.5 g Resorcinol, 0.5 g Ammonium Chloride, 5 g Urea, 13 g Formaldehyde, and 10 g Calcium Nitrate Tetra hydrate that all of them were mixed in 50 ml of water and stirred at 750 rpm for 1-3 h.

Part B: For making the oil phase (continuous phase), 180 g of hexane with 0.5 g span60 and 0.1g sulfonic acid were mixed at 800-1500 rpm for 24 h at 40 °C. Then, the obtained solution was ultrasonicated for 10 min at 50% amplitude in a pulse regime. The catalyst in this procedure was sulfonic acid, which has a straight effect on the rate of reaction. The reason of utilizing Hexane in the oil phase was cheap and light of it. When it is placed under a vapor hood, its volatility is so helpful because for the collection of the microcapsule, the evaporation and removal of hexane are simple. To ensure that a water-in-oil emulsion was done, it is crucial to protect the ratio between the water and the oil at about 1:3. The oil phase was heated at the preferable temperature between 40-50°C and agitated via a high-shear mixer. Utilizing the high temperatures are forbidden since the temperature straightly acts on the rate of response and is the reason

for the premature formation of the shell wall. The aqueous phase was added dropwise when the temperature was desired, and the polymerization procedure began. The heating time varied from 1-3 h to completion of the in situ condensation of the urea-formaldehyde and also to turn the liquid droplets in the aqueous phase into microcapsules with a solid polymer shell. After the ending of the response, the hexane was discharged, and then the microcapsule slurry was filtered. In the next part, the filtered microcapsules were dried in an oven for two days (48 h) at temperature of 50°C.

### 2. 2. 2. Calcium Nitrate-Preyssler Self-healing Microcapsules

For the synthesis of UFNP, a ratio of 50-50% of CN and P are added to the aqueous solution. All the chemical materials for the aqueous solution were like the synthesis of calcium nitrate microcapsules. Also, the oil phase was similar to the synthesis of UFN.

### 2. 2. 3. Preyssler Self-healing Microcapsules

The method of synthesis of microcapsules containing P is the same as the method of synthesis of microcapsules of calcium nitrate, with the difference that in the aqueous phase, instead of CN, P was added as the core material of the microcapsule.

### 2. 3. FTIR Analysis

FTIR analyses of the specimens were built by utilizing Fourier transform infrared spectrometer in the range 400–4000  $\text{cm}^{-1}$ . FTIR spectra of the CN and P, and their microcapsules are presented in Figures 8-10, respectively. The vibrational band in the area of 3350  $\text{cm}^{-1}$  is related to the tensile bond of H-O and H-N in urea formaldehyde polymer. By comparing the FT-IR spectra of UFN containing it, it can be concluded that the presence of a typical peaks of 833.2 and 1383.46  $\text{cm}^{-1}$ . in CN and microcapsules is evidence of the presence of CN in the urea-formaldehyde microcapsules. By comparing the FT-IR spectra of the P and the microcapsule containing it, it can be concluded that the presence of common peaks of 517.68 and 1164.45  $\text{cm}^{-1}$ . in the P and microcapsule is evidence of the presence of the P in the urea-formaldehyde microcapsule. Also, by comparing the FT-IR spectra of CN-P, and microcapsules containing them, it can be concluded that the presence of a common peak of 3347.18  $\text{cm}^{-1}$ . in CN and prescribers and their microcapsules is evidence of the presence of these two substances in urea-formaldehyde microcapsules.

### 2. 4. SEM Analysis

The microcapsules and concrete structure were done utilizing a Field Emission Scanning Electron Microscope (LMU TESCAN BRNO-MIRA3) operated. Before to used SEM imaging, splashing the gold powder was performed on the samples. According to Figure 11, most of the microcapsules have spherical shaped, while the particles with irregular shapes can be

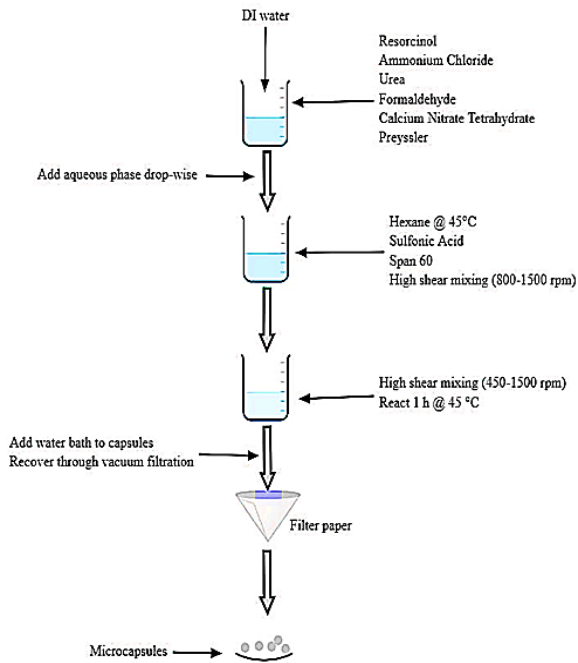


Figure 7. Microencapsulation synthesis process

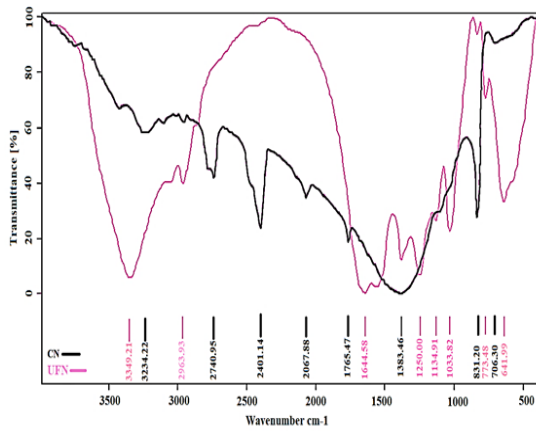


Figure 8. FT-IR spectrum of CN and its microcapsules

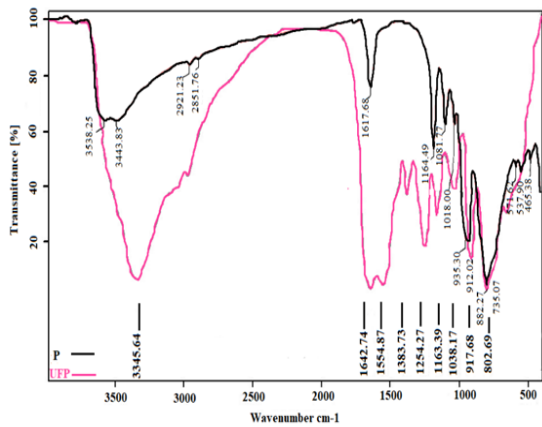


Figure 9. FT-IR spectrum of P and its microcapsules

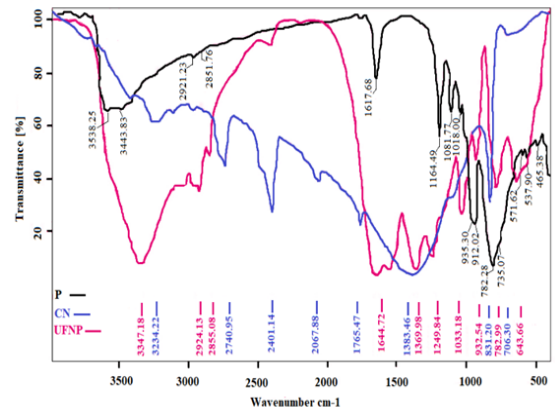
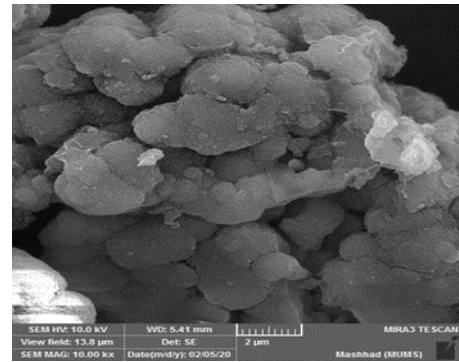
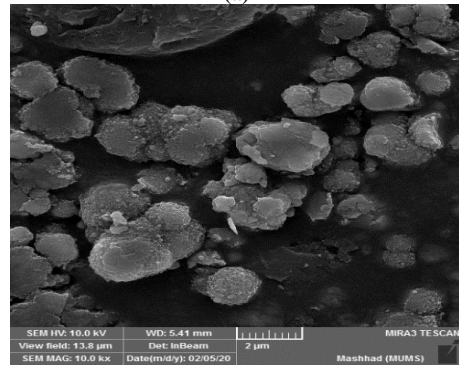


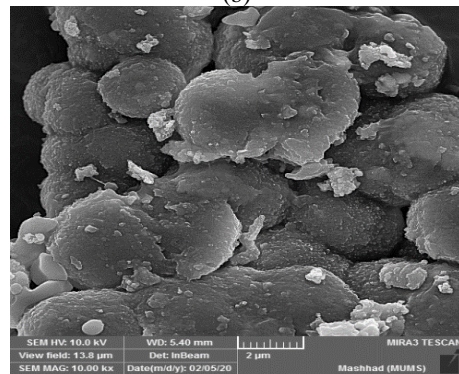
Figure 10. FT-IR spectrum of CN-P and their microcapsules



(a)



(b)



(c)

Figure 11. FESEM images of microcapsules: (a) UFN, (b) UFP, (c) UFNP

found between them. Also, from the EDS analysis can understand that the UFN consists of Ca, O, Na, and C elements.

Therefore, it revealed the existence of urea-formaldehyde (shell material) and nitrate calcium (core material). As shown in Figure 12a, given that the calcium peak intensity in the EDS analysis chart is very high. It can be concluded that the nucleus of the microcapsule contains CN and is well-formed. From the EDS of the UFP, understand that it consists of W, O, N, P, and C elements. Therefore, it revealed the existence of urea-formaldehyde (shell material) and Preyssler (core material). According to Figure 12b, considering that Tungsten (W) is the main constituent of Preyssler and has a high peak, it can be concluded that the core of the microcapsule has an active substance and is well-formed. The EDS of the UFNP shows that it consists of W, Ca, O, N, and P elements. Therefore, it revealed the existence of urea-formaldehyde (shell material) and calcium nitrate- Preyssler (core material). According to Figure 12c, considering that Tungsten (W), the calcium (C), which are the main constituent of Preyssler and calcium, respectively, has a high peak, it can be concluded that the core of the microcapsule has an active substance and is well formed.

## 2. 5. TEM Analysis

TEM observation of the microcapsules was made using a Transmission Electron Microscope (LEO912 AB) operated. This analysis was done to ensure the reliability of producing spherical microcapsules. TEM images of microcapsules are demonstrate in Figure 13.

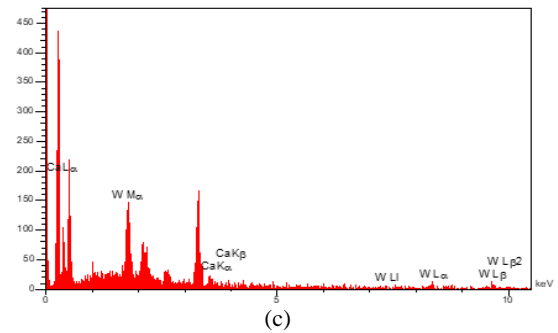
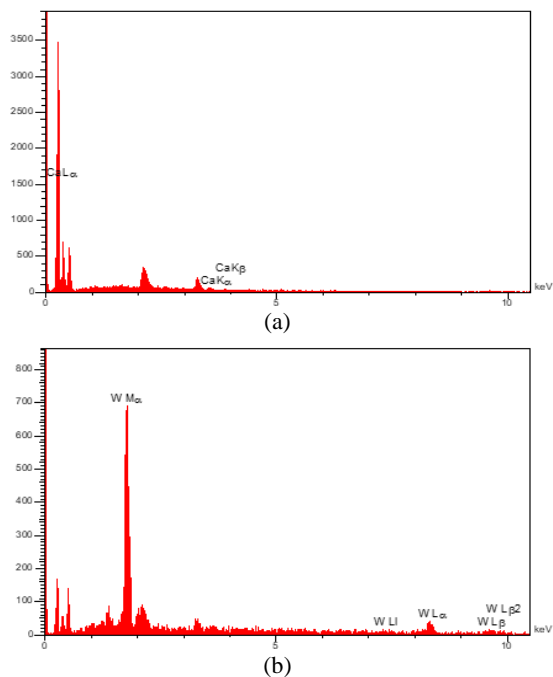


**Figure 12.** EDS analysis: (a) UFN, (b) UFP, (c) UFNP

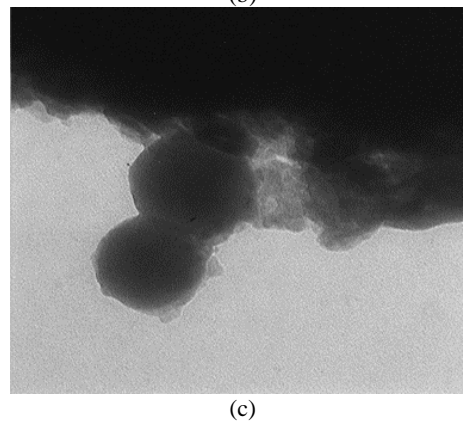
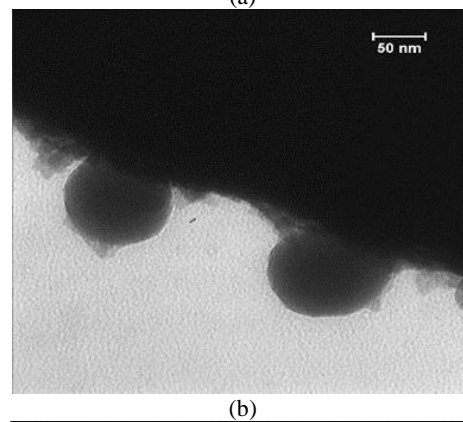
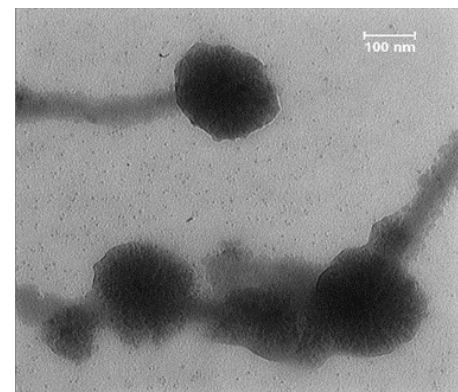


**Figure 13.** TEM images of microcapsules: (a) UFN, (b) UFP, (c) UFNP

**2. 6. MIX Design** For mix design, we utilized concrete’s design process that has a water/cement ratio of 0.23. The amount of materials for the mix design are offered in Table 2. In the present study, the mixing steps are as follows:

1. The weight of all consumables was accurately measured based on the desired percentages.
2. All superplasticizers were mixed with all water consumption.
3. All dry materials were mixed with a mixer for 5 min.
4. By adding 65% of water and lubricant mixture, the materials inside the mixer were mixed at a speed of 1000 rpm for 3 min.
5. The remaining water and superplasticizer were added, and mixing was continued at 1000 rpm for 8 minutes.
- 6 - Finally, the synthesized microcapsules are added to the mixture.

In the next step, the concrete nanocomposites were poured into lubricated molds, and the samples were numbered.

**2. 6. 1. Curing Regime** The specimens were covered via wet sackcloth for 24 h. The drinkable water immersion at room temperature was selected for the curing regime to enable healing.

**3. RESULTS AND DISCUSSIONS**

**3. 1. Testing of Self-healing Concrete** We utilize the microcapsules, including CN, P, as the healing factors in the matrix of concrete to evaluate their self-healing. The efficacy of the number of microcapsules to recognize the excellent condensation by weight of cement was investigated. The concentration experimented were 0.5%, 0.1%, 1.5%, and 2.0%. According to the ASTM C109 standard, compressive strength tests were done for specimens with or without microcapsules, and the cubic testes had dimensions of 50 mm × 50 mm × 50mm.

**3. 2. Concrete Compressive Strength** To evaluate the compressive strength of specimens after 7 and 28

**TABLE 2. Mix design**

Material	Amount in 1 kg/m <sup>3</sup>
Cement(kg)	840
Water(kg)	200
silica sand(kg)	1104
Admixture 1 (Superplasticizer)	42
Admixture 2 (Microcapsule concentration <sup>1</sup> (%))	0.5,1,1.5 and 2%
Micro silica	202

<sup>1</sup> Concentration is given as a percentage by weight of cement

days of curing in a humidity chamber was conducted, and the efficacy of the microcapsules on the standard properties of the concrete was evaluated. The average testing results of three samples of each design samples are listed in Figures 14-16, which showed that the number of microcapsules have a significant impact on compressive strength. Considering that the compressive strength of concrete has a direct relationship with the density of concrete, it can be said that the denser the concrete, the higher its compressive strength. For example, according to Figures 17-19, which shows the density of samples with different weight percentages of microcapsules (0, 0.5, 1, 1.5, 2), in the sample containing UFN from 1% to2%, the density of the samples It has no microcapsules more than the sample.

Also, the sample containing 0.5 and 2% UFP and the samples containing UFN in the range of 0.5 to 1.5% have a higher density than the sample without microcapsules. For this reason, it can be concluded that the higher the density value, the higher the density of the sample and the higher the strength.

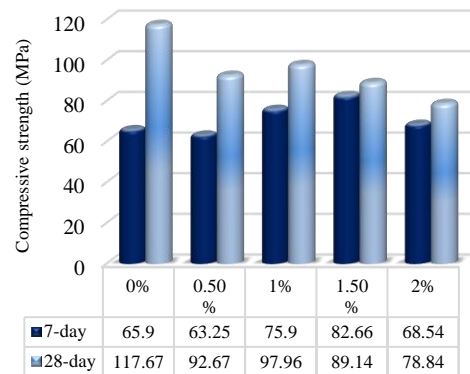


**Figure 14.** Compressive strength of concretes containing UFN at different ages

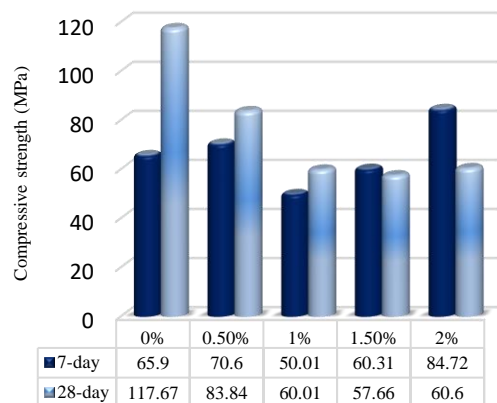


**Figure 15.** Compressive strength of concretes containing UFP at different ages

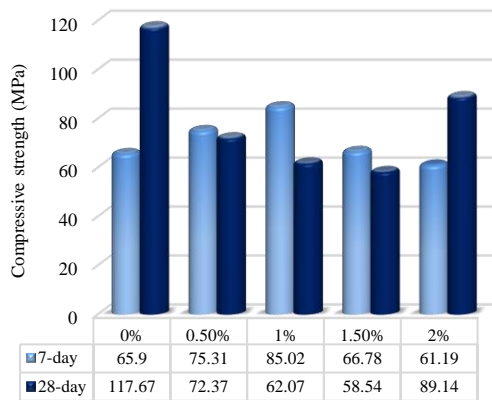


**Figure 16.** Compressive strength of concretes containing UFP at different ages

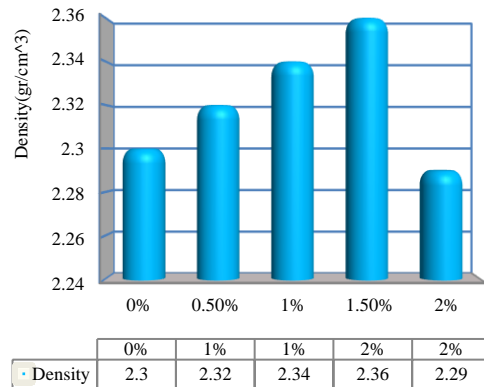


**Figure 19.** Density of samples with different percentages of UFNP

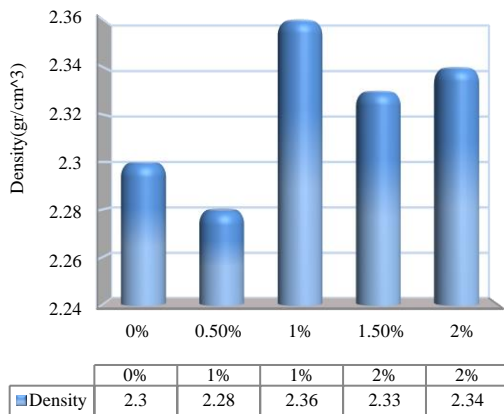


**Figure 17.** Density of samples with different percentages of UFN

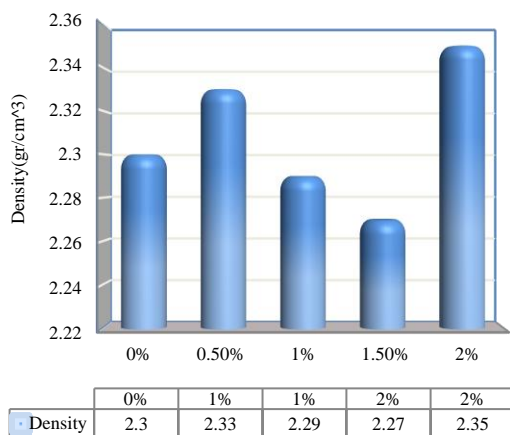


**Figure 18.** Density of samples with different percentages of UFP

Figures 20 and 21 compare 7 and 28-day compressive strength performance of concrete samples containing various microcapsules. According to the figures, the following results can be inferred.

- The concrete sample containing 0.5% UFN has the greatest 7-day compressive strength compared to the other types.
- The concrete sample containing 1% UFN has the greatest 7-day compressive strength compared to the other types.
- The concrete sample containing 1.5% UFN has the greatest 7-day compressive strength compared to the other types.
- The concrete sample containing 2% UFP has the greatest 7-day compressive strength compared to the other types.
- The concrete sample containing 0.5% UFN has the greatest 28-day compressive strength compared to the other types.
- The concrete sample containing 1% of UFN has the greatest 28-day compressive strength compared to the other types.
- The concrete sample containing 1.5% UFN has the greatest 28-day compressive strength compared to the other types.
- The concrete sample containing 2% UFNP has the greatest 28-day compressive strength compared to the other types.

### 3. 3. Recovery of Compressive Strength of Concrete Samples Containing Various Microcapsules

In order to check the final compressive strength after repair, other concrete samples containing different percentages of microcapsules were damaged after a 28-day curing period with 30% of the final loading obtained in the previous section. At first, a group of concrete samples were damaged for 2 h. The water was kept at room temperature until the repair

process was established. After 2 h, the samples were again loaded and broken, and their resistance was considered as the initial strength of the repair. Another group of concrete specimens were situated in water for 10 days to make the repair procedure more complete, and their resistance was considered the final strength of the repair was recorded.

To obtain the recovery rate, the relationship introduced by Dong et al. (35) has been used.

$$\text{Strength recovery rate} = \frac{\text{final strength of the restoration} - \text{Initial strength to repair}}{\text{Initial strength to repair}}$$

Also, the equation introduced by Li et al. (36) can be used to obtain the amount of resistance restoration.

$$\text{Strength recovery rate} = \frac{\text{Maximum strength to reloading}}{\text{Initial strength}}$$

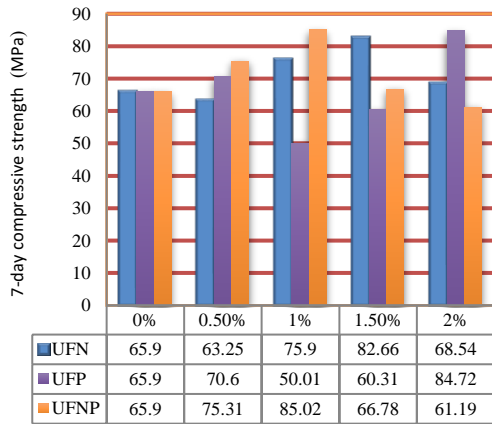


Figure 20. Comparison of 7-day compressive strength performance of concrete samples containing different microcapsules

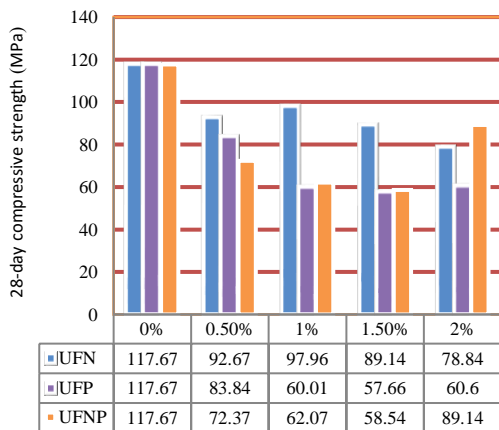


Figure 21. Comparison of 28-day compressive strength performance of concrete samples including various microcapsules

In the following, for example, the compressive strength test results of samples containing UFN, UFP, and UFNP with a loading of 30% of the final load are given.

**3. 3. 1. Compressive Strength Test Results of Samples Containing UFN With the Loading of 30% of the Final Loading**

According to Table 3, it can be concluded that the concrete specimens including 0.5% by weight of UFN, have a higher strength repair rate than other percentages by weight of microcapsules. Also, in Figure 22 the average compressive strength of the samples, containing different percentages of UFN under 30% loading of the final strength is displayed.

**3. 3. 2. Compressive Strength Test Results of Samples Containing UFP with the Loading of 30% of the Final Loading**

According to Table 4, it can be concluded that the concrete sample containing 1.5% by weight of UFP has a higher repair rate than other percentages by weight of microcapsules. In Figure 23, for

TABLE 3. The recovery rate of compressive strength of concrete samples, containing UFN with different percentages under 30% final loading

Percentage of microcapsules	Maximum initial compressive strength (MPa)	Final compressive strength after 10 days of restoration (MPa)	Resistance recovery rate
0.5%	33.46	81.80	1.44
1%	36.54	83.55	1.28
1.5%	37.60	89.30	1.37
2%	39.19	90.005	1.29

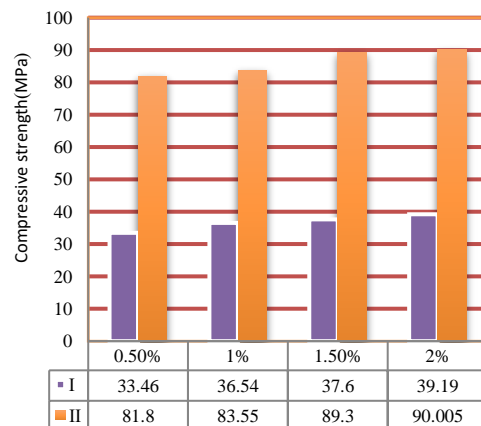
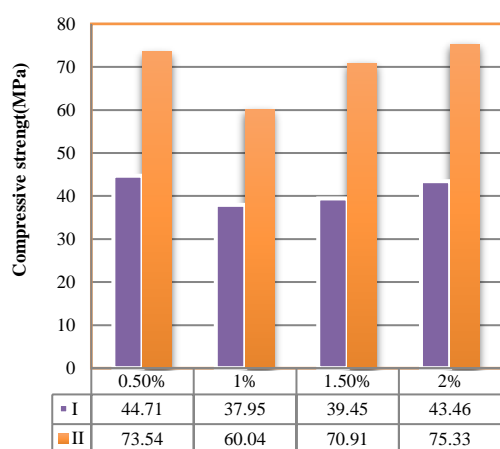


Figure 22. The average compressive strength of the samples, containing different percentages of UFN under 30% loading of the final strength (MPa): (I) Initial compressive strength after two hours, (II) Final compressive strength after 10 days of restoration

**TABLE 4.** The recovery rate of compressive strength of concrete specimens, including UFP with various percentages under 30% final loading

Percentage of microcapsules	Maximum initial compressive strength (MPa)	Final compressive strength after 10 days of restoration (MPa)	Resistance recovery rate
0.5%	44.71	73.54	0.64
1%	37.95	60.04	0.58
1.5%	39.45	70.91	0.79
2%	43.46	75.33	0.73

**Figure 23.** The average compressive strength of the specimens, including various percentages of UFP under 30% loading of the final strength (MPa): (I) Initial compressive strength after two hours, (II) Final compressive strength after 10 days of restoration

UFP microcapsule, the average compressive strength of the samples under 30% loading of the final strength is shown.

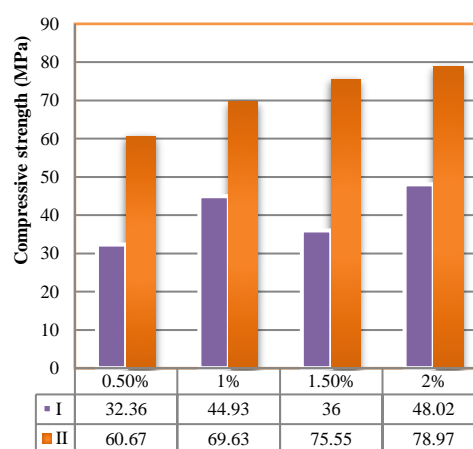
### 3. 3. 3. Compressive Strength Test Results of Samples Containing UFNP with the Loading of 30% of the Final Loading

According to Table 5, it can be concluded that the concrete sample containing 1.5% by weight of UFNP has a higher strength recovery rate than other percentages by weight of microcapsules.

**3. 4. Concrete Microstructure** After compressive strength analysis, the specimens that expressed the greatest concrete compressive strength of the sample, contained different microcapsules, were analyzed under SEM to evaluate the concrete microstructure and crack repairing process. Figure 24 illustrated the average compressive strength of the specimens, including various percentages of UFNP under 30% loading of the final strength

**TABLE 5.** The recovery rate of compressive strength of concrete specimens, including UFNP with various percentages under 30% final loading

Percentage of microcapsules	Maximum initial compressive strength (MPa)	Final compressive strength after 10 days of restoration (MPa)	Resistance recovery rate
0.5%	32.36	60.67	0.87
1%	44.93	69.63	0.54
1.5%	36	75.55	1.09
2%	48.02	78.97	0.64

**Figure 24.** The average compressive strength of the specimens, including various percentages of UFNP under 30% loading of the final strength (MPa): (I) Initial compressive strength after two hours, (II) Final compressive strength after 10 days of restoration

### 3. 4. 1. The Repair Process in a Concrete Sample Containing UFN

The first sample contains UFN. In this sample, on the first day after cracking, the following cracks were selected so that the repair process could be observed on them after 10 days. As shown in the Figure 25, after 10 days, the specified cracks have been repaired. In Figure 26, EDS is used to show the existence of the repair factor in the crack area. According to the result of the EDS, it can be said that the presence of the Ca element indicates the repair of the crack area by calcium nitrate microcapsules in the cement matrix.

### 3. 4. 2. The Repair Process in a Concrete Sample Containing UFP

The second sample includes UFP. In this sample, on the first day after failure, the following cracks were selected so that the repair process could be observed on them after 10 days (Figure 27). Figure 28 shows the EDS analysis to show the existence of the repair factor in the crack area. According to the result of the elemental analysis, it can be said that the

presence of W and P elements indicate the repair of the crack area by UFP in the cement matrix because these elements are not ordinarily present in cement.

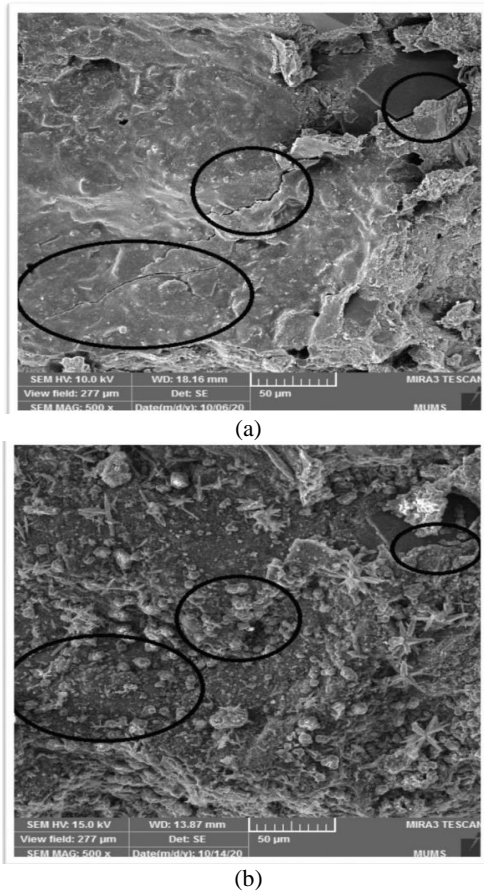


**Figure 25.** (a) Specifying the number of cracks to check the repair on them, (b) SEM image of crack repair in a sample containing UFN after 10 days

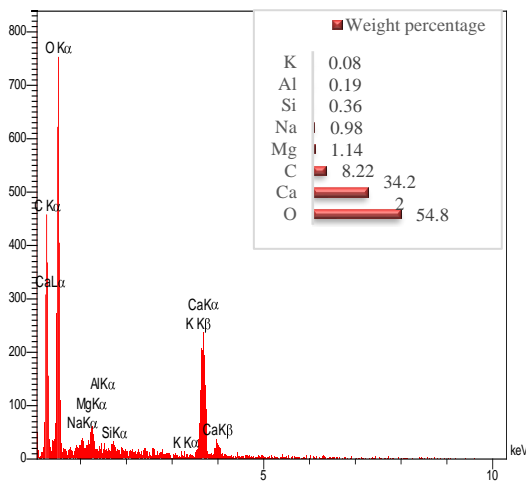


**Figure 26.** EDS analysis of the cracked area

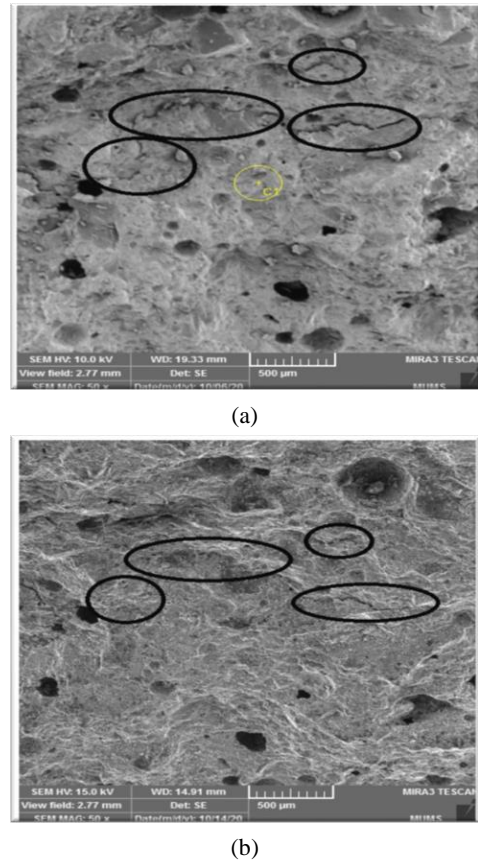


**Figure 27.** (a) Specifying the number of cracks to check the repair on them, (b) SEM image of crack repair in a sample containing UFP after 10 days

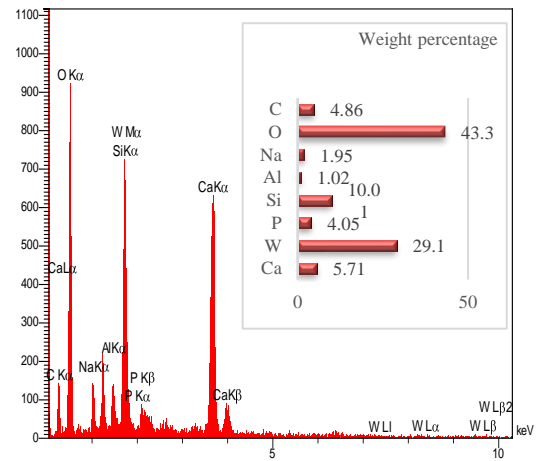
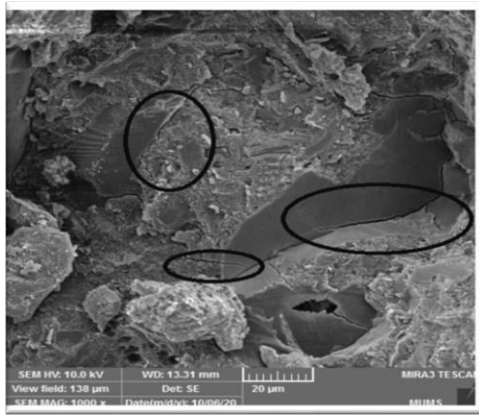


**Figure 28.** EDS analysis of the cracked area

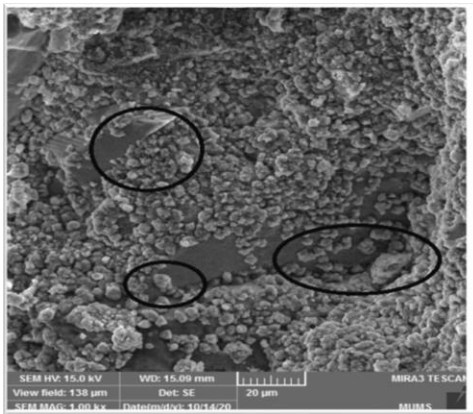
### 3. 4. 3. The Repair Process in a Concrete Sample Containing UFNP

The third sample includes UFNP. In this example, on the first day after failure, the following cracks were selected so that the repair process

could be observed on them after 10 days (Figure 29). Figure 30 shows the EDS analysis to show the existence of the repair factor in the crack area. According to the



(a)



(b)

**Figure 29.** (a) Specifying the number of cracks to check the repair on them, (b) SEM image of crack repair in a sample containing UFNP after 10 days

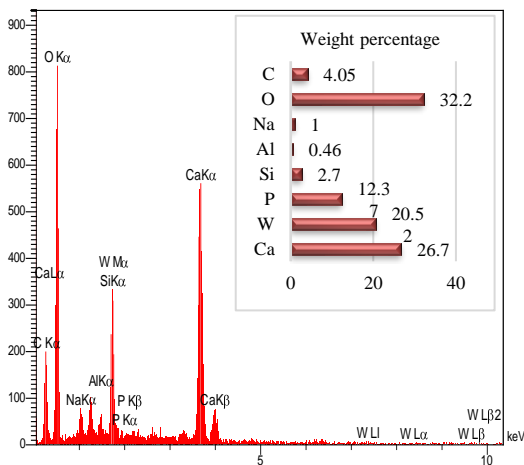
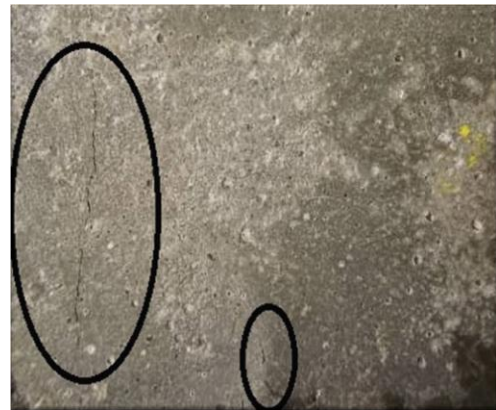
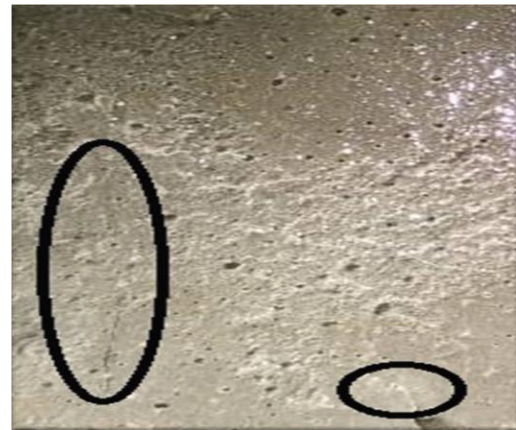


**Figure 30.** EDS analysis of the cracked area

result of the elemental analysis, it can be said that the presence of W, P, and Ca elements indicates the repair of the crack area by UFNP in the cement matrix because these elements are not ordinarily present in cement. Also, in Figure 31, the repair of cracks in concrete containing microcapsules is shown.



(a)



(b)

**Figure 31.** (a) existed the crack, (b) Repair the crack

#### 4. CONCLUSION

In this paper, for self-healing of concrete, the microcapsules were synthesized by an in situ technique utilizing urea-formaldehyde as a shell and mineral salts as the core. The healing yield of concrete by the microcapsules prepared was assessed in terms of the strength restoration as well as the healing microstructure. Some outcomes can be described as follow:

1. Compared to other types of microcapsules, UFN has considerable efficacy in increasing the compressive strength of 7 and 28-day specimens.
2. Among the samples containing UFN, the sample containing 1% microcapsules had the highest 28-day compressive strength, which was 16.75% higher than the

control sample, and the sample containing 1.5% microcapsules, had the highest 7-day compressive strength, 25.44% less than the control sample.

3. Among the samples containing UFP, the sample containing 1.5% microcapsules had the highest 28-day compressive strength, which was 28.75% higher than the control sample, and the sample containing 2% microcapsules had the highest 7-day compressive strength, which was 28.57% less than the control sample.

4. Among the samples containing UFNP, the sample containing 2% microcapsules had the highest 28-day compressive strength, which was 24.25% higher than the control sample, and the sample containing 1% microcapsules had the highest 7-day compressive strength, which was 29.01%. Less than the control sample.

At the end of article can say that the effect of using magnetic water instead of urban drinking water used in this research on the mechanical properties of concrete, including compressive strength, should also be considered by those interested. Also, investigating the effect of using other polyoxometalates as microcapsules can be a very effective suggestion in the continuation of this research.

## 5. REFERENCES

- Danish A, Mosaberpanah MA, Salim MU. Past and present techniques of self-healing in cementitious materials: A critical review on efficiency of implemented treatments. *Journal of Materials Research and Technology*. 2020;9(3):6883-99.
- Taheri S. A review on five key sensors for monitoring of concrete structures. *Construction and Building Materials*. 2019;204:492-509. 10.1016/j.conbuildmat.2019.01.172
- Wool RP. Self-healing materials: a review. *Soft Matter*. 2008;4(3):400-18.
- Shahsavari H, Baghani M, Naghdabadi R, Sohrabpour S. A thermodynamically consistent viscoelastic-viscoplastic constitutive model for self-healing materials. *Journal of Intelligent Material Systems and Structures*. 2018;29(6):1065-80.
- Ramavath S, Suryawanshi S, ASHISH A. Experimental Study on Self-compacting and Self-healing Concrete with Recycled Coarse Aggregates. *International Journal of Engineering*. 2023:-.
- Musyanovych A, Landfester K. Polymer micro-and nanocapsules as biological carriers with multifunctional properties. *Macromolecular bioscience*. 2014;14(4):458-77. 10.1002/mabi.201300551
- Ahangaran F, Navarchian AH, Picchioni F. Material encapsulation in poly (methyl methacrylate) shell: A review. *Journal of applied polymer science*. 2019;136(41):48039. 10.1002/app.48039
- Bekas D, Tsirka K, Baltzis D, Paipetis AS. Self-healing materials: A review of advances in materials, evaluation, characterization and monitoring techniques. *Composites Part B: Engineering*. 2016;87:92-119. 10.1016/j.compositesb.2015.09.057
- White SR, Sottos NR, Geubelle PH, Moore JS, Kessler MR, Sriram S, et al. Autonomic healing of polymer composites. *Nature*. 2001;409(6822):794-7. 10.1038/35057232
- Van Tittelboom K, De Belie N. Self-healing in cementitious materials—A review. *Materials*. 2013;6(6):2182-217. 10.3390/ma6062182
- Zhang M, Xing F, Shi KY, Du XX, editors. Study on organic microcapsule based self-healing cementitious composite. *Advanced Materials Research*; 2011: Trans Tech Publ.
- Wang X, Xing F, Zhang M, Han N, Qian Z. Experimental study on cementitious composites embedded with organic microcapsules. *Materials*. 2013;6(9):4064-81. 10.3390/ma6094064
- Wang X, Zhang J, Han R, Han N, Xing F. Evaluation of damage and repair rate of self-healing microcapsule-based cementitious materials using electrochemical impedance spectroscopy. *Journal of Cleaner Production*. 2019;235:966-76. 10.1016/j.jclepro.2019.06.294
- Blaiszik B, Caruso M, McIlroy D, Moore J, White S, Sottos N. Microcapsules filled with reactive solutions for self-healing materials. *Polymer*. 2009;50(4):990-7. 10.1016/j.polymer.2008.12.040
- de Souza Rodrigues VH, Carrara AE, Rossi SS, Silva LM, Dutra RdCL, Dutra JCN. Synthesis, characterization and qualitative assessment of self-healing capacity of PU microcapsules containing TDI and IPDI as a core agent. *Materials today communications*. 2019;21:100698. 10.1016/j.mtcomm.2019.100698
- Fu Q, Liu M, Zhang S, Lu L, Fang N, Chen J, et al. Growth and mineralization characteristics of *Bacillus subtilis* isolated from marine aquaculture wastewater and its application in coastal self-healing concrete. *Materials Today Communications*. 2023;35:105654. 10.1016/j.mtcomm.2023.105654
- Wang Y, Lin Z, Tang C, Hao W. Influencing factors on the healing performance of microcapsule self-healing concrete. *Materials*. 2021;14(15):4139. 10.3390/ma14154139
- Mufrodi Z, Shitophyta L, Sulisty H, Aziz M. Reaction of Carbon Dioxide Gas Absorption with Suspension of Calcium Hydroxide in Slurry Reactor. *Emerging Science Journal*. 2023;7(2):328-38. 10.28991/ESJ-2023-07-02-02
- Yoon SH, Cha JH. Optimal manufacturing method for self-healing microcapsules in damaged composite structures. *Composite Structures*. 2021;263:113748. 10.1016/j.compstruct.2021.113748
- Kosarli M, Bekas DG, Tsirka K, Baltzis D, Vaimakis-Tsogkas DT, Orfanidis S, et al. Microcapsule-based self-healing materials: Healing efficiency and toughness reduction vs. capsule size. *Composites Part B: Engineering*. 2019;171:78-86. 10.1016/j.compositesb.2019.04.030
- Sidiq A, Setunge S, Gravina RJ, Giustozzi F. Self-repairing cement mortars with microcapsules: A microstructural evaluation approach. *Construction and Building Materials*. 2020;232:117239. 10.1016/j.conbuildmat.2019.117239
- Gumerova NI, Rompel A. Synthesis, structures and applications of electron-rich polyoxometalates. *Nature Reviews Chemistry*. 2018;2(2):0112. 10.1038/s41570-018-0112
- Long D-L, Burkholder E, Cronin L. Polyoxometalate clusters, nanostructures and materials: From self assembly to designer materials and devices. *Chemical Society Reviews*. 2007;36(1):105-21. 10.1039/B502666K
- Kumar R. A review on epoxy and polyester based polymer concrete and exploration of polyfurfuryl alcohol as polymer concrete. *Journal of Polymers*. 2016;2016. 10.1155/2016/7249743
- Altalib F, Tavakoli HR, Hashemi SK. The Post-fire Behavior of Lightweight Structural Concrete is Improved by Nano-SiO<sub>2</sub> and Steel Fibers. *International Journal of Engineering*. 2023;36(11):1942-60. 10.5829/ije.2023.36.11b.01

- [https://www.ije.ir/article\\_175959\\_b9bb66f14bf197c890006d3aa118e693.pdf](https://www.ije.ir/article_175959_b9bb66f14bf197c890006d3aa118e693.pdf)
26. Sivamani J, Thiyaneswaran MP, Navaneethan KS. Performance Studies on Glass Fiber Reinforced Recycled Aggregate Concrete. *International Journal of Engineering*. 2023;36(5):904-13. 10.5829/ije.2023.36.05b.07  
[https://www.ije.ir/article\\_166827\\_ba5f6a3de83823d90e315166815e223a.pdf](https://www.ije.ir/article_166827_ba5f6a3de83823d90e315166815e223a.pdf)
  27. Al-Hindawi LAA, Al-Dahawi AM, Sh. J. Al-Zuheriy A. Use of Waste Materials for Sustainable Development of Rigid Pavement. *International Journal of Engineering*. 2023;36(10):1919-31. 10.5829/ije.2023.36.10a.16  
[https://www.ije.ir/article\\_175335\\_a9112d2f48c1b49b9e55bdcf18f465b2.pdf](https://www.ije.ir/article_175335_a9112d2f48c1b49b9e55bdcf18f465b2.pdf)
  28. Esparham A, Mehrdadi N. Effect of Combined Different Sources of Alumina Silicate on Mechanical Properties and Carbonation Depth of Environmentally Friendly Geopolymeric Composite Based on Metakaolin. *International Journal of Engineering*. 2023;36(7):1383-97. 10.5829/ije.2023.36.07a.18  
[https://www.ije.ir/article\\_170844\\_54d8a448092f54c9f1166f26532307e0.pdf](https://www.ije.ir/article_170844_54d8a448092f54c9f1166f26532307e0.pdf)
  29. Balamuralikrishnan R, Al-Mawaali A, Al-Yaarubi M, Al-Mukhaini B, Kaleem A. Seismic Upgradation of RC Beams Strengthened with Externally Bonded Spent Catalyst Based Ferrocement Laminates. *HighTech and Innovation Journal*. 2023;4(1):189-209. 10.28991/HIJ-2023-04-01-013
  30. Mohammed AH, Mubarak HM, Hussein AK, Abulghafour TZ, Nassani DE. Punching Shear Characterization of Steel Fiber-Reinforced Concrete Flat Slabs. *HighTech and Innovation Journal*. 2022;3(4):483-90. 10.28991/HIJ-2022-03-04-08
  31. Nistratov AV, Klimentov NN, Pustynnikov IV, Vu LK. Thermal regeneration and reuse of carbon and glass fibers from waste composites. *Emerging Science Journal* 2022;6:967-84. 10.28991/ESJ-2022-06-05-04
  32. Bamoharram FF. Role of polyoxometalates as green compounds in recent developments of nanoscience. *Synthesis and Reactivity in Inorganic, Metal-Organic, and Nano-Metal Chemistry*. 2011;41(8):893-922.
  33. Saneinezhad S, Bamoharram FF, Mozhdehi AM, Sharifi AH, Ayati A, Pordel M, et al. Functionalized cellulose-preyssler heteropolyacid bio-composite: An engineered and green matrix for selective, fast and in-situ preparation of Pd nanostructures: synthesis, characterization and application. *Arabian Journal of Chemistry*. 2020;13(3):4644-60. 10.1016/j.arabjc.2019.10.006
  34. Hassan MM, Milla J, Rupnow T, Al-Ansari M, Daly WH. Microencapsulation of Calcium Nitrate for Concrete Applications. *Transportation Research Record*. 2016;2577(1):8-16. 10.3141/2577-02  
<https://journals.sagepub.com/doi/abs/10.3141/2577-02>
  35. Dong B, Fang G, Ding W, Liu Y, Zhang J, Han N, et al. Self-healing features in cementitious material with urea-formaldehyde/epoxy microcapsules. *Construction and Building Materials*. 2016;106:608-17. 10.1016/j.conbuildmat.2015.12.140
  36. Li W, Jiang Z, Yang Z, Zhao N, Yuan W. Self-healing efficiency of cementitious materials containing microcapsules filled with healing adhesive: Mechanical restoration and healing process monitored by water absorption. *PloS one*. 2013;8(11):e81616. 10.1371/journal.pone.0081616

**COPYRIGHTS**

©2024 The author(s). This is an open access article distributed under the terms of the Creative Commons Attribution (CC BY 4.0), which permits unrestricted use, distribution, and reproduction in any medium, as long as the original authors and source are cited. No permission is required from the authors or the publishers.

**Persian Abstract****چکیده**

انتشار ریز ترک ها در سازه، ظرفیت باربری آن را کاهش داده و منجر به فروریختن کل سازه می شود. همانطور که مطالعات متعدد نشان داده است، افزودن مواد افزودنی مختلف در انواع بتن یا اجزای بتن، می تواند به طور قابل توجهی از نظر مشخصات و ویژگی ها، بتن را بازیابی کند. یک روش احتمالی مفید برای جلوگیری از خرابی رایج و حفظ گران قیمت زیرساخت های بتنی، استفاده از عوامل التیام دهنده کپسوله سازی برای خود ترمیمی بتن است. بتن خود ترمیم شونده با پرایسler و نیترات کلسیم میکرو کپسوله شده در این مقاله مورد بررسی قرار گرفت. میکروکپسول ها با پلیمریزاسیون درجا اوره فرمالدئید به عنوان پوسته در اطراف مواد هسته شامل پرایسler، نیترات کلسیم سنتز شدند. خصوصیات فیزیکوشیمیایی میکروکپسول ها توسط طیف سنجی مادون قرمز تبدیل فوری، میکروسکوپ الکترونی روبشی، میکروسکوپ الکترونی عبوری انجام شد. ارزیابی مکانیکی نمونه های سیمانی با دوزهای مختلف میکروکپسول (0، 0.5، 1، 1.5 و 2 درصد) با آزمایش های مقاومت فشاری انجام شد. همچنین با اندازه گیری قبل و بعد از آسیب پس از 10 روز، پتانسیل خود ترمیمی مورد آزمایش قرار گرفت. پس از اینکه بتن با اعمال 30 درصد بار نهایی خود آسیب دید، تمام نمونه ها با غوطه وری در آب انکوبه شدند. با توجه به نتایج، نمونه حاوی 0.5٪ UFN، نمونه حاوی 1.5٪ UFP و نمونه حاوی 1.5٪ UFNP نسبت به سایرین نرخ تعمیر بالاتری دارند. این گستره تحقیقات به دلیل ماهیت بین رشته ای خود، دارای امکانات متعددی برای پیشگامی در ایجاد دروازه های برای پیوند علوم و مهندسی مانند مواد، شیمی، علم، فناوری نانو و رشته مهندسی برای متقاعد کردن طیف گسترده ای از مشارکت در مهندسی و علوم و کاربردها است.



## Effect of Varying Glass Powder Size on Performance of Cement Mortar: Microstructural and Compressive Strength Assessment at High Temperatures

S. S. Patil<sup>a</sup>, Y. D. Patil<sup>b</sup>

<sup>a</sup> Research Scholar, Department of Civil Engineering, S. V. National Institute of Technology, Surat, Gujarat, India

<sup>b</sup> Associate Professor, Department of Civil Engineering, S. V. National Institute of Technology, Surat, Gujarat, India

### PAPER INFO

#### Paper history:

Received 27 September 2023

Received in revised form 31 October 2023

Accepted 04 November 2023

#### Keywords:

Glass Powder

Pozzolanic Activity

Residual Compressive Strength

Strength Activity Index

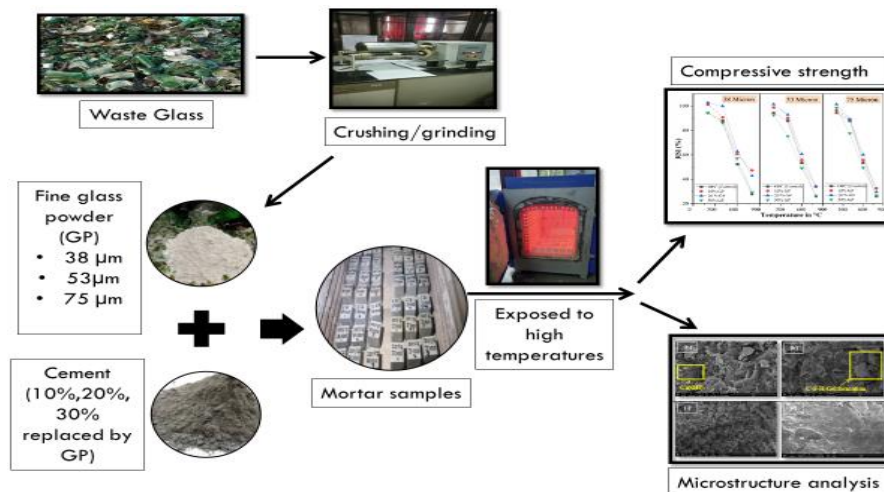
Thermo Gravimetric Analysis

### ABSTRACT

This study employs fine glass powder as a partial replacement for ordinary Portland cement in order to better understand the complex effects of high temperature on the microstructure and compressive strength of cement mortar. The study aims to identify the optimal mix that maximizes the benefits of glass powder incorporation by experimenting with different glass powder sizes (38  $\mu\text{m}$ , 53  $\mu\text{m}$ , and 75  $\mu\text{m}$ ) and replacement rates (10%, 20%, and 30%). At 25°C, 200°C, 400°C, 600°C, and 800°C, mortars containing glass powder were subjected to compressive strength tests. Mortar samples were examined using X-ray diffraction (XRD), scanning electron microscopy (SEM), and Thermo Gravimetric analysis (TGA) to gain insight into their behavior at high temperatures. Mortar mixes containing 10% glass powder (38  $\mu\text{m}$  size) performed best at temperatures below 400°C, with an average residual strength index value of 90.7% compared to 87.8% in the reference sample. The glass powder mortars with 10% and 20% replacement rates functioned better at higher temperatures of 800°C, losing just 52-57% of their strength as opposed to 72% in the control sample. The increased pozzolanic activity attributable to the addition of glass powder is shown by XRD and SEM analyses to account for the increased strength of mortar by consuming more portlandite ( $\text{Ca}(\text{OH})_2$ ). TGA study has shown that at temperatures exceeding 400°C, tobermorite and other hydrated products become dehydrated, which may account for the strength reduction.

doi: 10.5829/ije.2024.37.04a.17

### Graphical Abstract



\*Corresponding Author Email: [sachinpatil180784@gmail.com](mailto:sachinpatil180784@gmail.com) (S. S. Patil)

## 1. INTRODUCTION

The concrete industry, heavily reliant on non-renewable resources and CO<sub>2</sub>-intensive processes, presents a significant opportunity for sustainability through the exploration of alternative materials (1). Concrete, a primary construction material, typically contains 10-15% Portland cement (OPC), with the remainder being aggregates, water, and other additives. However, OPC production is environmentally taxing due to its high CO<sub>2</sub> emissions—0.7 to 1 ton per ton of OPC—and its heavy reliance on natural resources like limestone (2). Additionally, Portland cement-based concretes have durability issues, leading to 40-50% of construction budgets being spent on repairs. This underscores the need for alternative cement materials that are more sustainable and address OPC's shortcomings (3). Such environmental awareness has heightened interest in converting industrial by-products into concrete ingredients. Using these wastes not only conserves materials and energy but can also enhance concrete performance. To this end, supplementary cementitious materials (SCMs) such as fly ash, ground granulated blast furnace slag, or glass powder are used to replace cement, reducing both consumption and environmental impact (4, 5).

One of the major issues faced by concrete is the elevated temperatures which can significantly compromise the structural integrity and durability of concrete. When exposed to high temperatures, concrete undergoes physicochemical transformations, leading to a loss of compressive strength, spalling, and changes in its microstructure (6). Supplementary cementitious materials (SCMs) play a pivotal role in mitigating these adverse effects. Incorporating SCMs enhances the thermal stability of concrete (7). They not only improve the concrete's resistance to high temperatures but also aid in preserving its mechanical properties, making it more resilient to temperature-induced degradation (8). However, with the increasing use of supplementary cementitious materials (SCMs) in concrete, its high temperature performance has become more complicated. Therefore, investigating the influence of concrete constituents such as SCMs at high temperatures is of great significance.

The use of fine glass powder, derived from waste glass, as a partial replacement for cement in concrete production, has recently gained attention due to its potential benefits in enhancing the mechanical and durability properties of concrete while promoting sustainability (9). Several studies have investigated the impact of fine glass powder on the compressive strength of concrete at ambient temperature conditions. Aliabdo et al. (10) found that the inclusion of glass powder at 10% as a cement replacement could enhance the compressive strength of mortar by 9%. Similarly, Nagrockienė and

Barkauskas (11) found that adding 5% waste glass powder to cement-based mortar can improve its performance for civil engineering applications. Fine glass particles, when ground to less than 75 μm, can enhance concrete strength and durability due to their pozzolanic reactivity. This reactivity increases with the surface area of particles, improving the concrete microstructure (12). Moreover, finely ground glass powder (GP) with a particle size below 100 μm does not trigger alkali-silica reactions due to rapid pozzolanic reaction, a common issue with larger glass aggregates (13). However, the potential of glass powder as a supplementary cementitious material, especially its impact on cement hydration and microstructure at elevated temperatures, remains largely unexplored and warrants further investigation. Few studies have investigated the mechanical properties, durability, and thermal stability of concrete incorporating glass powder, showcasing potential avenues for sustainable and resilient construction materials. Yang et al. (14) found that cement mortar with glass powder showcased less degradation under high temperatures compared to traditional mortar. It is attributed to the vitreous nature of glass which tends to resist thermal degradation to a certain extent. The spalling behavior of concrete is a significant concern at high temperatures. Research conducted by Ali et al. (15) highlights that the use of glass powder can mitigate spalling, primarily due to its influence in modifying the pore structure of the concrete, thereby facilitating better thermal strain accommodation. While some research points to an initial decrease in strength with increased glass powder content (16), others suggest a possible enhancement in strength upon optimizing the particle size and blending proportions at high temperatures above 400°C (17). It is highly important to note that temperatures as high as 800°C can induce phase transformations in the concrete matrix. This often requires a thorough understanding of the formation of new phases and the decomposition of existing phases at high temperatures, which can affect the durability of the concrete. Scanning Electron Microscopy (SEM) analyses performed by Dyer and Dhir (18) showed that fine glass powder-blended concretes possessed denser microstructures, even after exposure to high temperatures. This is attributed to the pozzolanic reaction of the glass powder, which fills the micro voids in the matrix. However, existing literature insufficiently explores the microstructural alterations in glass powder concrete under high temperatures, particularly concerning the influence of glass powder fineness.

Therefore, this research aims to investigate the impact of high temperature on the microstructure properties and its subsequent effects on the compressive strength of glass powder-cement mortar. To achieve this, fine glass powder with varying granule sizes such as 38 μm, 53 μm, and 75 μm has been utilized as a substitute for cement at

replacement rates of 10%, 20%, and 30% to pinpoint the best substitution level for glass powder, emphasizing its role in enhancing cement mortar properties. The residual strength of glass powder-cement mortar after thermal exposure is also evaluated. The testing of residual compressive strength of cement mortar at temperatures up to 800°C is essential for safety assessments, material development, and a deeper understanding of the material's behavior under extreme conditions. The results of this study have the potential to improve building safety by contributing to the creation of fireproof concrete.

## 2. MATERIALS

**2.1. Cement and Aggregate** In this study, OPC-53 grade Portland cement, conforming to IS 12269:2013 (19), was procured from a local market. Its basic properties and chemical composition determined through X-ray Fluorescence (XRF) analysis, are detailed in Tables 1 and 2, respectively. The chemical composition of cement highlights a predominant CaO content of around 60%. Locally sourced river sand, meeting IS 650:1991 (20) criteria, served as the fine aggregate with a specific gravity of 2.49. Potable water was utilized for both mixing and curing procedures.

**2.2. Glass Powder** Greyish-white glass powder with a specific gravity of 2.61 was produced from mixed

waste glass sourced locally, undergoing crushing, and grinding processes. The powder was then segregated into three distinct categories through a sieving process involving three different sieves: GP-A with an average size of less than 38  $\mu\text{m}$ , GP-B with less than 53  $\mu\text{m}$ , and GP-C with less than 75  $\mu\text{m}$ . Sieve analysis data illustrates a uniform gradation in the particle size analysis, revealing that all glass powder types contain particles smaller than 75  $\mu\text{m}$  (Figure 1). XRF analysis (Table 2) indicates a SiO<sub>2</sub> content increase in the sequence GP-A > GP-B > GP-C, attributed to decreasing particle size. As per ASTM-C618 requirements (25) outlined in Table 3, all three glass powder variants meet the chemical composition criteria for pozzolanic materials, presenting a viable option to substitute cement in mortar preparation.

**2.3. Mixing and Casting Procedure** Table 4 shows the mix proportion that was used for preparing 240 samples of mortar in which fine glass powder of varying sizes was substituted for OPC cement. In addition, 45 control samples were made using a ratio of 1 part Portland cement (100%) to 3-part sand by weight (26). The experimental work used a w/b ratio of 0.42 for the flow of mix  $110 \pm 5.0$ . Mortar samples were made by substituting 10%, 20%, and 30% of the cement with glass powder. Mortar sample composition, mixing, and casting were all carried out in accordance with IS 4031 (part 6):1988 (26) and IS 1727:1967 (27) standards. After thoroughly combining the dry ingredients, water was added in accordance with a predetermined w/b ratio. Later, using the steel trowel, the components were mixed by hand to ensure consistency. To test the compressive strength of mortar in accordance IS 4031 (part 6):1988 (26), a 70.6 mm cube mold was filled with a fresh mortar

**TABLE 1.** Physical properties of cement

Standard consistency	30.5	IS:4031 (Part-4) (21)
Initial setting time	155 minutes	IS:4031 (Part-5) (22)
Final setting time	234 minutes	
Soundness	1.00%	IS:4031 (Part-3) (23)
Fineness by Blaine surface	278 m <sup>2</sup> /kg	IS:4031 (Part-2) (24)
Specific gravity	3.15	

**TABLE 1.** Chemical composition of raw materials (%)

Raw material	OPC	GP-A	GP-B	GP-C
SiO <sub>2</sub>	15.7	70	68.7	67.6
CaO	71.8	7.46	7.85	7.46
Al <sub>2</sub> O <sub>3</sub>	2.01	1.6	2.03	1.45
Fe <sub>2</sub> O <sub>3</sub>	5.39	0.99	0.237	1.08
SO <sub>3</sub>	2.65	0.59	0.124	0.69
K <sub>2</sub> O	0.69	0.3	0.279	0.26
MgO	-	1.99	3.25	1.41
TiO <sub>2</sub>	0.72	0.069	-	0.06
Na <sub>2</sub> O	-	16.5	17.5	19.34
MnO	0.05	0.044	-	0.052

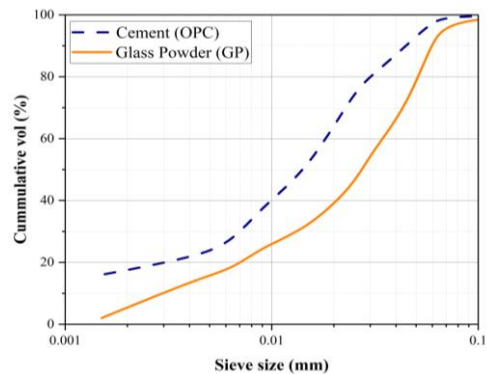


**Figure 1.** Grain size distribution

**TABLE 3.** ASTM C618 requirements for pozzolanic binders

ASTM C618	Value	GP-A	GP-B	GP-C
SiO <sub>2</sub> +Al <sub>2</sub> O <sub>3</sub> +Fe <sub>2</sub> O <sub>3</sub>	≥ 70%	72.59	70.96	70.13
SO <sub>3</sub>	≤ 4 %	0.59	0.12	0.69

**TABLE 4.** Mix proportion of mortars with different (%) of glass powder

Mix	Components (g)			
	Cement	Sand	GP	Water
OPC (Control)	600	1800	0	252
10%GP-A*	540	1800	60	252
20%GP-A*	480	1800	120	252
30%GP-A*	420	1800	180	252

(\*same mix proportion used for GP-B and GP-C)

mix and vibrated on a vibration table to achieve compaction. Fresh samples were stored for 24 hours at room temperature before demolding and curing for 7 and 28 days in water, respectively.

To analyze the impact of high temperatures on the mortar samples, water-cured 28-day samples were first dried in an oven at 105°C for 24 hours to prevent unstable spalling. Subsequently, they underwent a high-temperature exposure process where they were subjected to temperatures of 200°C, 400°C, 600°C, and 800°C at a steady increase of 10°C/min in an electric furnace. Each sample was maintained at the target temperature for a 2-hour soaking period before the furnace was turned off. The samples were then removed and cooled naturally in open air. Additionally, all samples were tested under room temperature conditions at 25°C for comparison.

### 3. TEST PROCEDURES

The specimens for compressive strength were tested in the compression testing machine under a controlled loading rate of 35 N/mm<sup>2</sup>/min before and after exposure to high temperatures. The results presented correspond to the average of a minimum of three specimens. XRD patterns were obtained using a high-resolution X-Ray diffractometer (Rigaku SmartLab, Japan). The samples were crushed and dried just before running the tests. Diffraction analyses were made from 10° to 80° 2θ using copper K radiation at a rate of 5° per min. The excitation voltage was 40 kV at 40 mA and the minerals and compounds in each specimen were determined using the “MATCH-3” software. The underlying internal changes in the microstructure were identified using 1-cm<sup>3</sup> specimens obtained from the compressive strength tested mortar samples by performing SEM analysis using a Carl Zeiss supra 55 FESEM model (Germany) with an energy dispersive X-ray spectroscopy (EDS) detector. A TG/DTG thermal analysis was performed on a simultaneous TA Instruments SDT-Q600 equipment. Samples were analyzed under an oxygen atmosphere (100 ml/min) at a heating rate of 10°C/min using alumina crucibles.

## 4. RESULTS AND DISCUSSION

### 4. 1. Effect of Glass Powder Size on the Strength Activity Index (SAI)

According to ASTM C618 (25), the strength activity index (SAI) should be calculated using an 80:20 cement-to-additive mass ratio, with a minimum acceptable value of 75% for any pozzolan. This index is determined by comparing the compressive strength of pozzolan additive-inclusive samples to that of reference samples (10). Figure 2 illustrates the SAI for three different GP-inclusive mortar mixtures such as 80% OPC combined with 20% GP-A, GP-B, or GP-C at 7 and 28 days of period. Complying with the code, 20%GP-A exceeded the 75% threshold at both 7 and 28 days of curing. In contrast, 20%GP-B and 20%GP-C fell short of the criteria at 7 days but demonstrated significant improvement with SAI values of 89.2% and 88%, respectively at 28 days. The inconsistency in activity indices among the different glass powders can be attributed to variations as reported in literature (28). Specifically, GP-A, which contains a higher proportion of particles under 38 μm, offers a greater specific surface area (SSA), thereby resulting in better compressive strength compared to GP-B and GP-C.

### 4. 2. Effect of Glass Powder Size on Compressive Strength of Mortar

Figure 3 shows the influence of curing age and glass powder size on the strength of GP-mortars with 10%, 20%, and 30% glass powder replacement levels at ambient temperature. Initially, at a 7-day curing age, all three variations of glass powder substitution resulted in decreased compressive strength compared to the control sample (C) with 40 MPa strength, likely due to a dilution effect (29). However, after a 28-day curing period, GP-mortars with 10% and 20% glass powder replacements demonstrate similar or superior strength levels to the control (58.12 MPa), owing to enhanced pozzolanic activity, promoting the

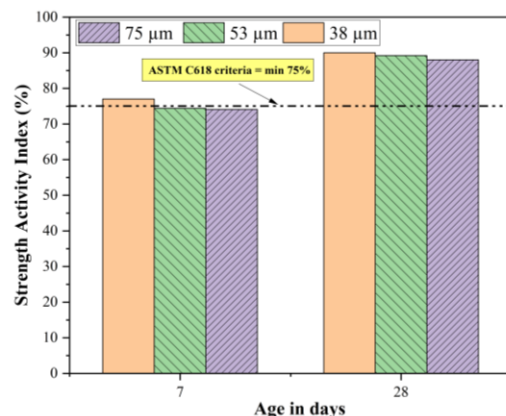


**Figure 2.** Effect of GP size on strength activity index

formation of more hydration and pozzolanic products (30). Notably, there is a decrement in strength with increasing glass powder size (38µm to 75µm) and replacement ratio (10% to 30%), irrespective of the curing duration. Particularly, the 10%GP-A mortar exhibits optimal performance, with its strength exceeding 10%GP-B and 10%GP-C strength values by 1.02 and 1.04 units respectively at 28 days, indicating it as the most efficient substitution ratio.

Figure 4 shows the behavior of compressive strength of the different mortars when exposed to an elevated temperature range between 200°C and 800°C. In general, all mortars lose strength as the temperature increases. The primary causes of this are the dissociation of hydration phases and thermal incompatibility at higher temperatures, both of which result from physical and chemical changes (31). If the cement mortar containing glass powder is exposed to temperatures near or above the transition temperature of the glass, the glass particles could soften. This could potentially lead to a reduction in the compressive strength of the mortar due to the softening of the glass particles, which would no longer contribute to the strength of the matrix as effectively. In the present study, the effect of temperature causes a significant loss in strength for all the mortars upto 800°C, but the residual compressive strength of GP-mortar for 10% and 20% replacement levels is found to be much higher with much less strength loss than 30% and control samples upto 400°C regardless of glass powder size. In particular, the decreased calcium hydroxide (CaOH<sub>2</sub>) content due to the pozzolanic effect is responsible for the greater strength of the 10%GP and 20%GP replacement levels compared to the control. Higher temperatures accelerate the pozzolanic reaction, which results in the development of additional calcium silicate hydrate (C-S-H) phases in GP-mortars (16). This finding agrees with prior research that has found similar behavior of compressive strength as a result of elevated temperatures (14, 32). However, when the mortar samples are exposed to temperatures greater than 400°C, the compressive strength reduces dramatically in all samples mainly due to the microstructure changes in the material and glass transition temperature of glass.

In addition, it was determined that the residual compressive strength of the fine glass powder (GP-A) was more prominent than that of the relative coarse glass powders (GP-B and GP-C) because the pozzolanic activity increased with glass powder fineness (33). In comparison to GP-B, GP-C, and control samples, the residual compressive strength of 10%GP-A at 200°C was 4.68%, 9.17%, and 13.27% greater, respectively. Also, compared to GP-B, GP-C, and control samples, 10%GP-A at 800°C exhibited higher residual compressive strength by 42.4%, 51.3%, and 78.89%. The subsequent microstructure analysis further explains the possible mechanisms for the results obtained at elevated temperatures in this study.

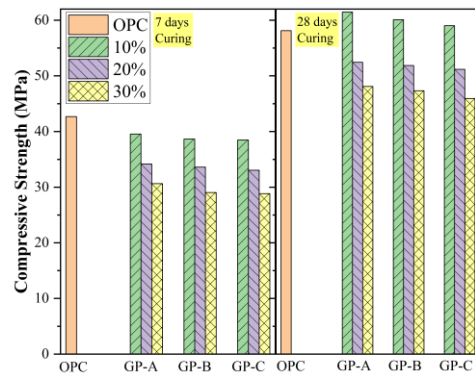


Figure 3. Effect of glass powder size on compressive strength at room temperature condition

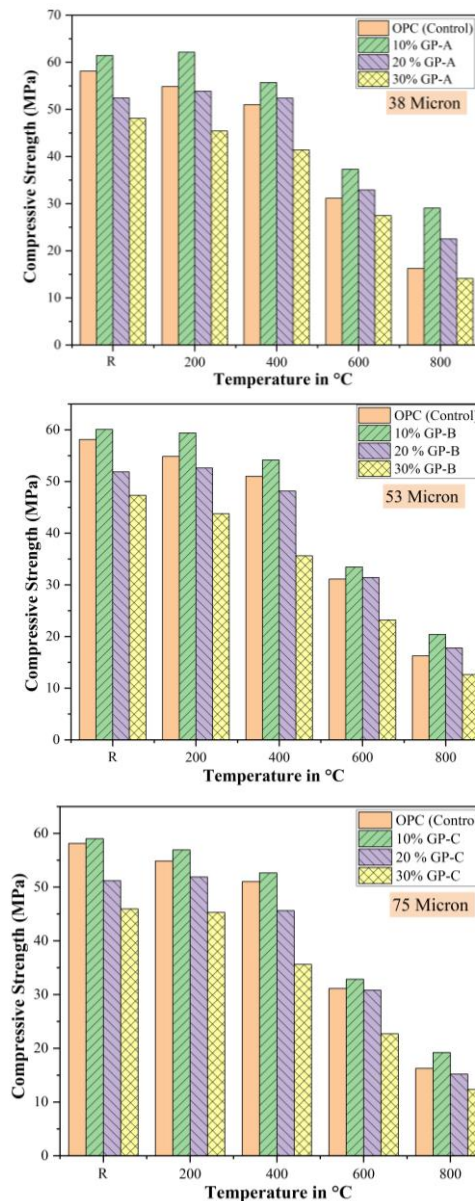
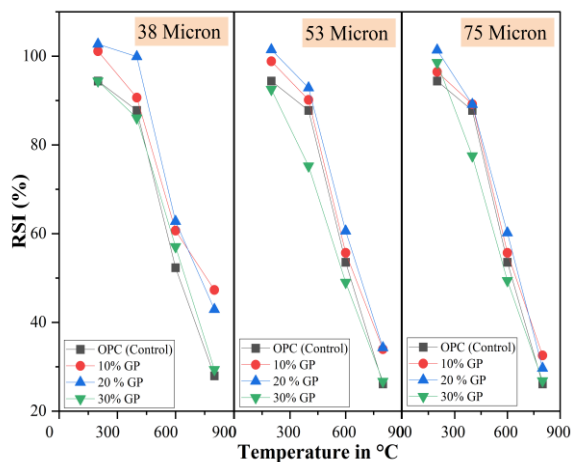


Figure 4. Effect of fine GP size on compressive strength of mortar at elevated temperatures

**4. 3. Residual Strength Index (RSI)** The residual strength index (RSI) for different GP-mortars as shown in Figure 5 was calculated as the percentage ratio of residual strength at elevated temperature to the initial strength at room temperature [7]. With an RSI of 101.1% and 102.7%, respectively, GP-A mortar with a 10% and 20% replacement rate exhibited excellent original strength at 200°C temperature, in comparison to OPC mortar. Up to 400°C, strength loss was minimal for both GP-B and GP-C mortars as well. The RSI value of GP-mortars drops considerably as the temperature increases from 400°C to 600°C and 800°C, but 10%GP-A and 20%GP-A continue to perform better than control mortar, losing only 37-39% and 52-57% of their strength, respectively, at 600°C and 800°C compared to 47.7% and 72% strength loss for the control sample. The lower thermal conductivity of glass powder provides better fire resistance and maintains its structure and strength properties, and the enhanced pozzolanic activity of glass powder leads to the formation of a denser matrix as well as additional pozzolanic/hydration gels (34, 35). These two are the possible reasons for the higher RSI values for GP-mortars compared to control. The 30% substitution of OPC with GP in mortar proved less efficient, leading to a greater decrease in compressive strength. This is primarily due to the dilution effect: the higher replacement rate and reduced cement content result in lower formation of hydration products compared to the control sample.

**4. 4. XRD Analysis** The XRD spectra of 28 days cured OPC mortars before and after exposure to 200°C and 800°C temperatures are demonstrated in Figure 6. These mortar samples were chosen to analyze the strength behavior across a range of thermal exposures. The diffractograms reveal that the intensity variations in



**Figure 5.** Effect of glass powder and varying temperature on RSI of mortar

the peaks corresponding to portlandite, alite, and belite across all samples are a result of the thermal effects on the hydrated OPC mortar, with a notable decrease in peak height as temperatures escalate from 25°C to 800°C (36). This alteration is attributed to the transformation of portlandite into carbonate or lime. Furthermore, the XRD analysis confirms the formation of hydration products such as ettringite and dense C-S-H gel at room temperature, evidenced by their distinct peaks at  $2\theta$ -29.6°, 32.5° and 47.4° (37). However, these peaks diminish at 800°C, indicating the dehydration of crystalline structures at lower temperatures of 200°C-400°C and the disappearance of amorphous hydrated products from the XRD pattern. Notably, at the extreme temperature of 800°C, the C-S-H undergoes a transition to thermally stable forms of alite and belite (31).

Figure 6 also shows the XRD spectra of GP-A, GP-B, and GP-C mortars at 10% optimum replacement level for temperature exposure to 25°C, 200°C, and 800°C. The temperature-induced alterations in crystalline phases appear consistent between cement paste and GP-mortars. Notably, the glass powder particle size significantly influences the peak heights of crystalline products, with the intensity of portlandite, alite, and belite in the order of GP-C>GP-B>GP-A (8). Glass powder, a pozzolanic substance, interacts with the portlandite produced in the cement system, promoting C-S-H formation. This reaction not only creates a denser structure, as evidenced by the XRD patterns but also enhances the fire resistance of GP-mortar, indicated by the diminished portlandite peaks (38). At 800°C, portlandite peaks are nearly eliminated. Furthermore, the data reveals an increase in C-S-H peaks for GP-mortars at 200°C, particularly for GP-A mortar, suggesting enhanced compressive strength compared to the control. However, at 800°C, these peaks display reduced intensity, indicating a decrease in the C-S-H concentration.

**4. 5. SEM Analysis** Figure 7 illustrates the morphological changes in 28-day cured samples of OPC mortar and 10%GP mortars at various temperatures. Figures 6(a) and 6(b) depict the room temperature and 200°C exposure states of control sample, characterized by hexagonal portlandite plates that signify the microstructure of the samples (39). However, at 800°C, these plates are absent, indicating portlandite decomposition as shown in Figure 6(c). This thermal exposure also induces micro-cracks surrounding unhydrated particles and leads to the loss of distinct crystal structures in hydrated phases, resulting in the prevalence of irregular and amorphous agglomerates throughout the sample. Figures 6(d), 6(g), and 6(j) reveal that GP mortars at room temperature maintain a crystalline phase, evidenced by large plates similar to those in cement paste, with visible micrometer-sized

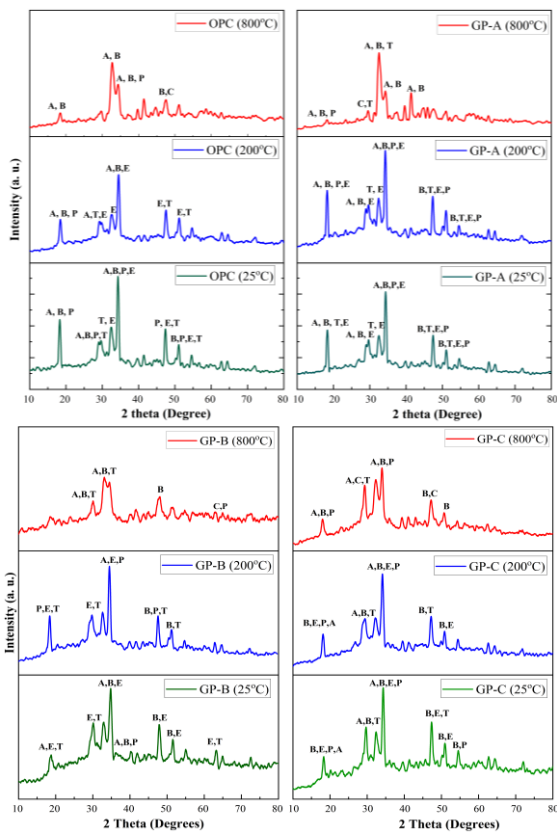


**Figure 6.** XRD analysis of OPC mortar and GP-mortars (A=Alite, B=Belite, C=Calcite, E=Ettringite, P=Portlandite and T=Tobermorite)

spherical glass powders dispersed uniformly across the sample. Additionally, all three GP-mortar variants exhibited the presence of C-S-H gel. Notably, higher temperature exposures caused the disappearance of platelike crystals, although some intact GP particles were occasionally observed within the sample.

**4. 6. TGA Analysis**

The TG analysis curves of OPC mortar and GP-A mortar specimens after hydration of 28 days are shown in Figure 8. The weight loss of mortar samples was found by heating them continuously from 20°C to 900°C. Water evaporation and the dehydration of C-S-H hydrates accounted for the mass loss observed across all samples between 50°C and 200°C (40). Within this temperature range, OPC lost 3.59% of its weight while GP-A lost 4.31% for samples exposed to 200°C.

The greater percentage of weight loss seen with GP-A mortar indicates the highest level of gel formation. As gypsum and other gel products decomposed at 350°C–500°C in mortar samples, mass loss was significant in this range (36). In addition, portlandite  $Ca(OH)_2$  melts at 500°C–600°C. Thus, all samples lost mass because of deformation at high temperature. Lastly, albite and  $CaCO_3$  decomposed at 600°C–800°C, causing mass loss. The maximum GP-A mix weight-loss percentage during these peaks was 2.31%. Greater weight loss showed the highest carbonate content in the GP-A sample, which explains its (10) higher mechanical properties.

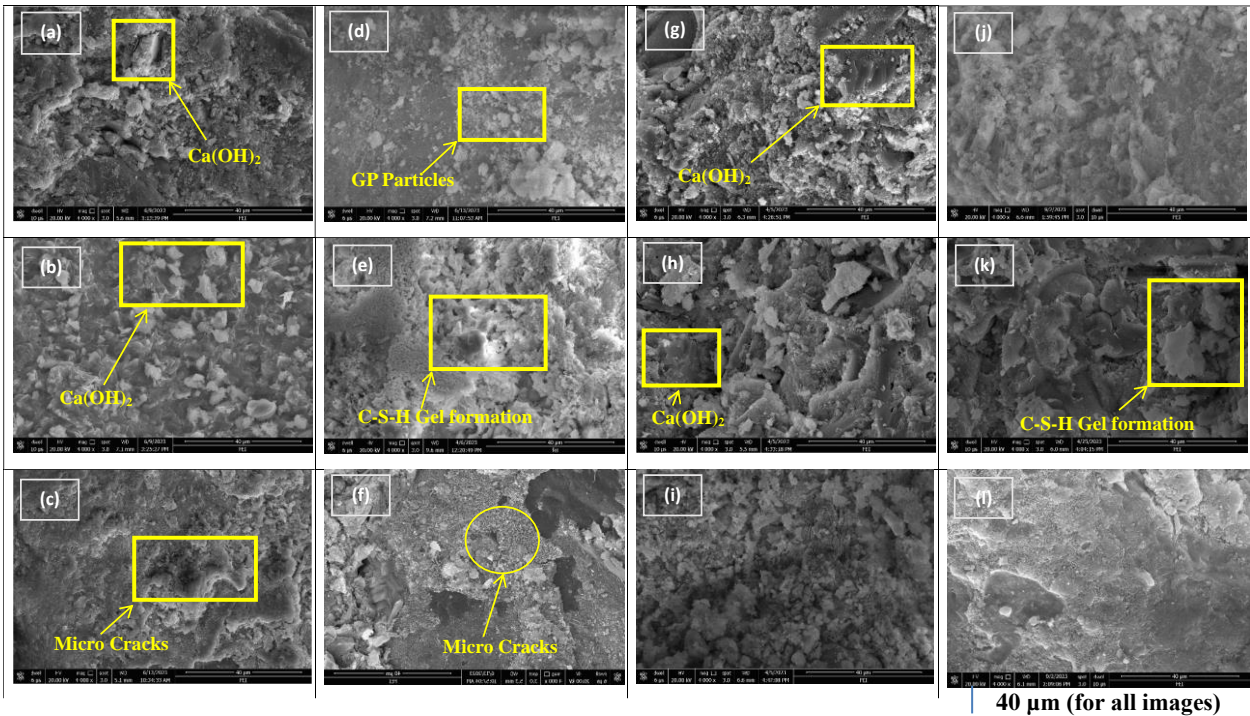


**Figure 7.** SEM analysis of OPC mortar and GP-mortars [(a),(b),(c)-OPCmortar; (d),(e),(f)-GP-A; (g),(h),(i)-GP-B; (j),(k),(l)-GP-C]

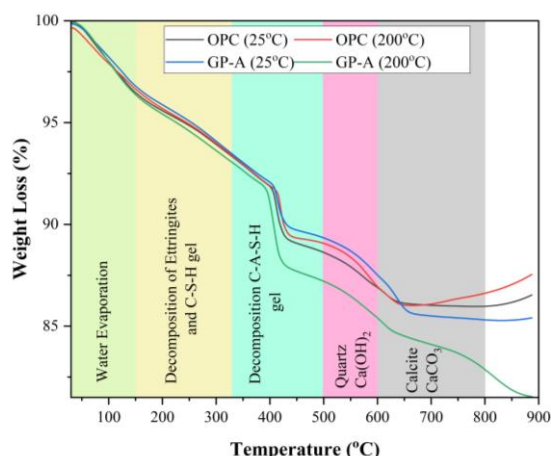


Figure 8. TG analysis of OPC mortar and GP-A mortar

## 5. CONCLUSION

Using cementitious mortars with 10%, 20%, and 30% replacement rates of glass powder of varying fine particle sizes, this study illustrates the influence of increased temperatures on the properties of the mortars. The following conclusions are drawn:

- Compressive strength testing indicated that 38 $\mu$ m particle size GP substitution in cement mortar was the most effective. At 200°C, 10% replacement increases the residual compressive strength by 13.27% compared to the control mortar.
- When exposed to temperatures above 400°C, mortar samples, including GP, show a decline in compressive strength. However, 10%GP-A and 20%GP-A performed better by achieving a higher RSI value than the others.
- XRD and SEM analysis demonstrate that the inclusion of GP increases the pozzolanic activity, which causes more portlandite to be consumed in GP mortars, resulting in greater strength. Dehydration of main hydration products and portlandite, as verified by TGA analysis, may account for the strength loss at temperatures above 400°C.

With its low thermal conductivity and pozzolanic character, GP is a great cement alternative because it helps cement mortar withstand high temperatures and maintain its strength. More study on the fire resistance of structural members built from concrete incorporating glass powder and its behavior at high temperatures is needed.

## 6. REFERENCES

1. Goaz HA, Shamsaldeen HA, Abdulrehman MA, Al-Gasham T. Evaluation of steel fiber reinforced geopolymer concrete made of

- recycled materials. *International Journal of Engineering, Transactions A: Basics.* 2022;35(10):2018-26. <https://doi.org/10.5829/ije.2022.35.10a.19>
2. Taherkhani R, Alviri M, Panahi P, Hashempour N. Low Embodied Carbon and Energy Materials in Building Systems: A Case Study of Reinforcing Clay Houses in Desert Regions. *International Journal of Engineering, Transactions B: Applications.* 2023;36(8):1409-28. <https://doi.org/10.5829/ije.2023.36.08b.02>
3. Nikkiah H, Tavakoli H, Fallah N. Experimental investigation of the effects of using waste rubber ash on mechanical properties of plain concrete. *International Journal of Engineering, Transactions C: Aspects.* 2023;36(3):450-6. <https://doi.org/10.5829/ije.2023.36.03c.03>
4. Omotayo O, Arum C. Challenges and Prospects of Widespread Adoption of Pozzolans for Building Construction: A Statistical Assessment. *International Journal of Engineering, Transactions A: Basics.* 2022;35(10):1929-40. <https://doi.org/10.5829/ije.2022.35.10a.12>
5. Maraghechi H, Maraghechi M, Rajabipour F, Pantano CG. Pozzolanic reactivity of recycled glass powder at elevated temperatures: Reaction stoichiometry, reaction products and effect of alkali activation. *Cement and Concrete Composites.* 2014;53:105-14. <https://doi.org/10.1016/j.cemconcomp.2014.06.015>
6. Altalib F, Tavakoli H, Hashemi S. The Post-fire Behavior of Lightweight Structural Concrete is Improved by Nano-SiO<sub>2</sub> and Steel Fibers. *International Journal of Engineering, Transactions B: Applications.* 2023;36(11):1942-60. <https://doi.org/10.5829/ije.2023.36.11b.01>
7. Ramzi S, Hajiloo H. The Effects of Supplementary Cementitious Materials (SCMs) on the Residual Mechanical Properties of Concrete after Exposure to High Temperatures. *Buildings.* 2022;13(1):103. <https://doi.org/10.3390/buildings13010103>
8. Saavedra WGV, de Gutiérrez RM. Performance of geopolymer concrete composed of fly ash after exposure to elevated temperatures. *Construction and Building Materials.* 2017;154:229-35. <https://doi.org/10.1016/j.conbuildmat.2017.07.208>
9. Federico L, Chidiac S. Waste glass as a supplementary cementitious material in concrete—critical review of treatment methods. *Cement and concrete composites.* 2009;31(8):606-10. <https://doi.org/10.1016/j.cemconcomp.2009.02.001>
10. Aliabdo AA, Abd Elmoaty M, Aboshama AY. Utilization of waste glass powder in the production of cement and concrete. *Construction and Building Materials.* 2016;124:866-77. <https://doi.org/10.1016/j.conbuildmat.2016.08.016>
11. Nagrockienė D, Barkauskas K. Utilization of waste glass powder in cement mortar. *Environmental Sciences Proceedings.* 2021;9(1):25. <https://doi.org/10.3390/envirosciproc2021009025>
12. Patel D, Tiwari R, Shrivastava R, Yadav R. Effective utilization of waste glass powder as the substitution of cement in making paste and mortar. *Construction and Building Materials.* 2019;199:406-15. <https://doi.org/10.1016/j.conbuildmat.2018.12.017>
13. Zheng K. Pozzolanic reaction of glass powder and its role in controlling alkali-silica reaction. *Cement and Concrete Composites.* 2016;67:30-8. <https://doi.org/10.1016/j.cemconcomp.2015.12.008>
14. Yang S, Lu J-X, Poon CS. Recycling of waste glass in cement mortars: Mechanical properties under high temperature loading. *Resources, Conservation and Recycling.* 2021;174:105831. <https://doi.org/10.1016/j.resconrec.2021.105831>
15. Ali MH, Dinkha YZ, Haido JH. Mechanical properties and spalling at elevated temperature of high performance concrete

- made with reactive and waste inert powders. *Engineering Science and Technology, an International Journal*. 2017;20(2):536-41. <https://doi.org/10.1016/j.jestch.2016.12.004>
16. Du H, Tan KH. Waste glass powder as cement replacement in concrete. *Journal of Advanced Concrete Technology*. 2014;12(11):468-77. <https://doi.org/10.3151/jact.12.468>
  17. Ma Q, Guo R, Zhao Z, Lin Z, He K. Mechanical properties of concrete at high temperature—A review. *Construction and Building Materials*. 2015;93:371-83. <https://doi.org/10.1016/j.conbuildmat.2015.05.131>
  18. Dyer TD, Dhir RK. Chemical reactions of glass cullet used as cement component. *Journal of Materials in Civil Engineering*. 2001;13(6):412-7.
  19. Standard I. 12269: Ordinary Portland Cement, 53 Grade—Specification (First Revision). Bureau of Indian Standards, New Delhi. 2013.
  20. IS 650, “Indian Specification for Standard Sand for Testing of Cement”, Bureau of Indian Standards, New Delhi, (1991), 1–11.
  21. IS 4031 (Part 4), “Indian Standard, Methods Of Physical Tests for Hydraulic Cement, Part 4, Determination of Consistency of Standard Cement Paste”, Bureau of Indian Standards, New Delhi, (1988).
  22. IS 4031 (Part 5) IS, Methods Of Physical Tests for Hydraulic Cement, Part 5, Determination of initial and Final Setting Times”, Bureau of Indian Standards, New Delhi, (1988).
  23. IS 4031 (Part 3), “Indian Standard, Methods Of Physical Tests for Hydraulic Cement, Part 3 Determination of soundness”, Bureau of Indian Standards, New Delhi (1988).
  24. IS 4031 (Part 2), “Indian Standard, Methods of Physical Tests For Hydraulic Cement, Part 2 determination of fineness by blaine air permeability method”, Bureau of Indian Standards, New Delhi, (1999).
  25. Concrete ACC-o, Aggregates C. Standard specification for coal fly ash and raw or calcined natural pozzolan for use in concrete: ASTM international; 2013.
  26. IS: Methods of physical tests for hydraulic cement—Part 6: Determination of compressive strength of hydraulic cement other than masonry cement, (first revision). Bureau of Indian Standards, New Delhi. 2005:1-3.
  27. – I. Methods of test for Pozzolan materials. 2004.
  28. Serpa D, Silva AS, de Brito J, Pontes J, Soares D. ASR of mortars containing glass. *Construction and Building Materials*. 2013;47:489-95. <https://doi.org/10.1016/j.conbuildmat.2013.05.058>
  29. Sankar B, Ramadoss P. Experimental and statistical investigations on alccofine based ternary blended high-performance concrete. *International Journal of Engineering, Transactions B: Applications*. 2022;35(8):1629-40. <https://doi.org/10.5829/IJE.2022.35.08B.19>
  30. Islam GS, Rahman M, Kazi N. Waste glass powder as partial replacement of cement for sustainable concrete practice. *International Journal of Sustainable Built Environment*. 2017;6(1):37-44. <https://doi.org/10.1016/j.ijbsbe.2016.10.005>
  31. Pan Z, Tao Z, Murphy T, Wuhler R. High temperature performance of mortars containing fine glass powders. *Journal of Cleaner Production*. 2017;162:16-26. <https://doi.org/10.1016/j.jclepro.2017.06.003>
  32. Mirzahosseini M, Riding KA. Influence of different particle sizes on reactivity of finely ground glass as supplementary cementitious material (SCM). *Cement and Concrete Composites*. 2015;56:95-105. <https://doi.org/10.1016/j.cemconcomp.2014.10.004>
  33. Paul SC, Šavija B, Babafemi AJ. A comprehensive review on mechanical and durability properties of cement-based materials containing waste recycled glass. *Journal of Cleaner Production*. 2018;198:891-906. <https://doi.org/10.1016/j.jclepro.2018.07.095>
  34. Lu J-X, Yan X, He P, Poon CS. Sustainable design of pervious concrete using waste glass and recycled concrete aggregate. *Journal of cleaner production*. 2019;234:1102-12. <https://doi.org/10.1016/j.jclepro.2019.06.260>
  35. Bisht K, Ramana P. Sustainable production of concrete containing discarded beverage glass as fine aggregate. *Construction and Building Materials*. 2018;177:116-24. <https://doi.org/10.1016/j.conbuildmat.2018.05.119>
  36. Karim MR, Chowdhury FI, Zabed H, Saidur M. Effect of elevated temperatures on compressive strength and microstructure of cement paste containing palm oil clinker powder. *Construction and Building Materials*. 2018;183:376-83. <https://doi.org/10.1016/j.conbuildmat.2018.06.147>
  37. Serelis E, Vaitkevicius V. Effect of waste glass powder and liquid glass on the Physico-Chemistry of Aluminum-Based Ultra-Lightweight concrete. *Construction and Building Materials*. 2023;390:131615. <https://doi.org/10.1016/j.conbuildmat.2023.131615>
  38. Althoey F, Zaid O, Majdi A, Alsharari F, Alsulamy S, Arbili MM. Effect of fly ash and waste glass powder as a fractional substitute on the performance of natural fibers reinforced concrete. *Ain Shams Engineering Journal*. 2023:102247. <https://doi.org/10.1016/j.asej.2023.102247>
  39. Stutzman P. Scanning electron microscopy imaging of hydraulic cement microstructure. *Cement and Concrete Composites*. 2004;26(8):957-66. <https://doi.org/10.1016/j.cemconcomp.2004.02.043>
  40. Jagad G, Modhera C, Patel D, Patel V. Mechanical and Microstructural Characteristics of Manufactured Sand-Based High-Strength Geopolymer Concrete and Its Environmental Impact. *Practice Periodical on Structural Design and Construction*. 2023;28(4):04023036. <https://doi.org/10.1061/ppscfx.sceng-1308>

**COPYRIGHTS**

©2024 The author(s). This is an open access article distributed under the terms of the Creative Commons Attribution (CC BY 4.0), which permits unrestricted use, distribution, and reproduction in any medium, as long as the original authors and source are cited. No permission is required from the authors or the publishers.

**Persian Abstract****چکیده**

این مطالعه از پودر شیشه ریز به عنوان جایگزینی جزئی برای سیمان پرتلند معمولی به منظور درک بهتر اثرات پیچیده دمای بالا بر ریزساختار و مقاومت فشاری ملات سیمان استفاده می‌کند. هدف این مطالعه شناسایی ترکیب بهینه ای است که مزایای ترکیب پودر شیشه را با آزمایش با اندازه های مختلف پودر شیشه (۳۸ میکرومتر، ۵۳ میکرومتر و ۷۵ میکرومتر) و نرخ جایگزینی (۱۰٪، ۲۰٪ و ۳۰٪) به حداکثر می‌رساند. در دماهای ۲۵، ۲۰۰، ۴۰۰، ۶۰۰ و ۸۰۰ درجه سانتی گراد، ملات های حاوی پودر شیشه تحت آزمایش مقاومت فشاری قرار گرفتند. نمونه های ملات با استفاده از پراش اشعه ایکس (XRD)، میکروسکوپ الکترونی روبشی (SEM) و تجزیه و تحلیل ترموگراویمتری (TGA) برای به دست آوردن بینشی در مورد رفتار آنها در دماهای بالا مورد بررسی قرار گرفتند. مخلوط ملات حاوی ۱۰ درصد پودر شیشه (اندازه ۳۸ میکرومتر) در دمای کمتر از ۴۰۰ درجه سانتیگراد با میانگین مقدار شاخص مقاومت باقیمانده ۹۰.۷ درصد در مقایسه با ۸۷.۸ درصد در نمونه مرجع بهترین عملکرد را داشتند. ملات پودر شیشه با نرخ جایگزینی ۱۰٪ و ۲۰٪ در دماهای بالاتر ۸۰۰ درجه سانتیگراد عملکرد بهتری داشتند و تنها ۵۲-۵۷٪ از مقاومت خود را در مقایسه با ۷۲٪ در نمونه شاهد از دست دادند. افزایش فعالیت پوزولانی که به افزودن پودر شیشه نسبت داده می‌شود، توسط تجزیه و تحلیل های XRD و SEM نشان داده شده است که افزایش استحکام ملات را با مصرف بیشتر پرتلندیت (Ca(OH)<sub>2</sub>) نشان می‌دهد. مطالعه TGA نشان داده است که در دماهای بیش از ۴۰۰ درجه سانتیگراد، برموریت و سایر محصولات هیدراته دچار خشکی می‌شوند که ممکن است دلیل کاهش مقاومت باشد.



## Computational Framework Development to Investigate Al Matrix with Low-Velocity Impact Behavior at Varied Temperatures for Cold Spray Composite Coating Design: Al/TiN Case

P. Chupong, K. Tuchinda\*

Mechanical Engineering Simulation and Design Mechanical and Automotive Engineering, The Sirindhorn International Thai-German Graduate School of Engineering, King Mongkut's University of Technology North Bangkok, Thailand

### PAPER INFO

#### Paper history:

Received 11 September 2023

Received in revised form 09 October 2023

Accepted 27 November 2023

#### Keywords:

Cold Spray

Low-pressure Cold Spray

Finite Element

Aluminum Particle

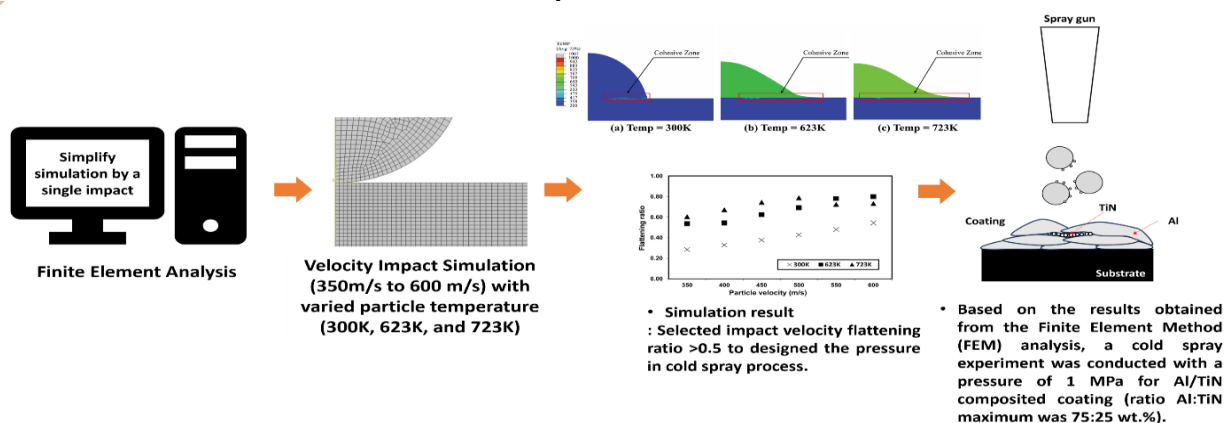
Hardened SKD11

### ABSTRACT

Cold spray (CS) with Metal matrix composite (MMC) is an alternative process for improving surface properties, which is crucial in plastic manufacturing. Understanding of particle behavior during impact is required for CS. This study focused on developing a simplified computational framework using the single-shot particle impact model to predict the adherence of matrix particles in the low-velocity impact. In this work, the hardened SKD11 coated with Al matrix/TiN reinforcement composite was selected, aiming to verify the proposed framework. Al particle impact at different temperatures (300K, 623K, and 723K) under the low-velocity range of 350–600 m/s were simulated, revealing the particle temperature affects the cohesive area. As the particle temperature increases, the areas also increase under similar velocity. The flattening ratio was calculated from the simulation and found to be influenced by the particle velocity. The CS of pure Al and Al/TiN (75:25 wt.%) on the hardened SKD11 under 623K and 723K was carried out under the experiment with the estimated pressure based on the flattening ratio and particle behavior. The results suggest the coatings could be developed using estimated pressure. Al/TiN coating was deposited at different initial particle temperatures. Results reveal that low coating porosity (<0.01%) could be obtained for both cases, and the higher particle temperature reveals higher thickness and %porosity, which agree well with the computational results. The developed framework shows high potential for designing CS for MMC coating, provided the reinforcement particles do not significantly affect the matrix particle flow or impact conditions.

doi: 10.5829/ije.2024.37.04a.18

### Graphical Abstract



\*Corresponding Author's email: [karuna.t@tggs.kmutnb.ac.th](mailto:karuna.t@tggs.kmutnb.ac.th) (K. Tuchinda)

Please cite this article as: Chupong P, Tuchinda K. Computational Framework Development to Investigate Al Matrix with Low-Velocity Impact Behavior at Varied Temperatures for Cold Spray Composite Coating Design: Al/TiN Case. International Journal of Engineering, A: Basics. 2024;37(04):804-17.

## 1. INTRODUCTION

Steel is a versatile material with extensive applications across various industries. SKD11 holds an outstanding position in the production of plastic molds. One commonly employed method for enhancing material properties is heat treatment. Surface treatment is a step in the heat treatment process that increases surface properties and extends the materials' lifetime. Surface heat treatment involves various methods, such as nitriding, which can make the material's surface harder and increase wear resistance. Moreover, surface heat treatment processes such as physical vapor deposition (PVD), cathode arc physical vapor deposition (CAPVD), chemical vapor deposition (CVD), and plasma-assisted chemical vapor deposition (PACVD) are actively employed. These techniques use various coating materials, including AlCrN, CrN, TiAlN, TiC, AlTiN, and TiN, to augment the surface properties of molds. The heat treatment process enhances material properties and can also be employed to regenerate carbon and glass fibers from waste composites. While surface heat treatment offers numerous advantages in terms of improved properties, it also has the drawback of potential distortion due to the high temperatures exceeding 700°C or the long duration of the process (1-5). Another method involves applying a different material as a coating on the substrate's surface without allowing diffusion between the two layers. These methods offer rapid improvements, such as thermal spray, cold spray, and cold plasma. Thermal spray techniques, including flame spray and plasma spray, are widely employed for applying surface coatings. These processes involve the controlled melting of deposited particles onto the substrate (6, 7). In addition, the sacrificial anodes for cathodic protection method are widely used to protect steel from chloride attack (8). The cold spray (CS) coating was initially developed in the mid-1980s, which uses a high velocity and low temperature for solid powder, impinges on the substrate, and creates a surface coating (9).

Cold spray is a new branch of surface engineering that relates to surface improvement by applying powder particle coating on a substrate with high velocity (300–1200 m/s) through a de Laval nozzle at a temperature below the melting point of the spray material. At or above a critical velocity of particles, the particle plastic deformation rate suggests adherence of deformation particles on the substrate and with each other to form the coating. Critical velocity is the lowest velocity at which solid particles impinge or deform on the substrate. The critical velocity varies for each solid powder due to particle density and specific heat (10-13). The CS process typically uses 5–50 μm powder particles. The CS had two categories, High-pressure and Low-pressure, at typical stagnation pressure ranges of 2–5 MPa and 0.3–1 MPa, respectively. High-pressure cold spray (HPCS) typically

generates particle velocities of 800-1400 m/s using higher-density particles. The lower gases, such as nitrogen or helium, are the preferred propellant gases in this system. The low-pressure (LPCS) system generates particle velocities of 300–600 m/s and uses lighter-density particles; air or nitrogen allow propellant gases (14-16). In addition, particle velocity depends on particle size, density, and morphology. HPCS and LPCS processes for coating formation include two stages: particle-substrate and particle-particle interaction. The HPCS process bonding mechanism has a high particle velocity that allows for adiabatic shear band formation and bonding at the interface. For the LPCS process, the bonding mechanism is followed by i) breaking the oxide film by preliminary particle impact, ii) impact particle consolidation, and iii) densification from deformation and consolidation of particle collection due to the shot peening effect (17). The material particles generally use cold spray processes such as Al, Ti, Ni, Mg, etc. Because the properties of these materials can improve the wear and corrosion resistance of substrate materials, they are easy to deposit on substrates. However, these materials had limited mechanical properties, like Al, which can be susceptible to corrosion by galvanic or wear by abrasives (18-21). To improve the mechanical and physical properties of the base material particles, a metal matrix composite coating could be considered to increase hardness, wear resistance, and corrosion resistance.

The ceramic particles or hard particles used for reinforcement of the material included TiN, Al<sub>2</sub>O<sub>3</sub>, SiC, etc. Al, Cu, and Ni are widely utilized for matrix particles. The complex particle only peens on the layers or is embedded in a soft matrix (22). Al-based MMC with TiN by HPCS increases deposit hardness, has a low friction coefficient, and has a low wear rate compared to Al5356. TiN has higher hardness, electrical, and optical properties (23-25).

The computational technique, i.e., finite element method (FEM), could be used to study the effect of impact velocity on particle impact associated with the CS process. The model could be used for investigation of the particle characteristics after impinging, predicting critical velocity, predicting temperature between cohesion zones, predicting porousness in the coating, etc. (26-36). To comprehend adiabatic shear and plastic flow localization, it is crucial to recognize these phenomena as major contributors to particle/substrate bonding during the cold spray process. The flattening ratio serves as an indicator of the extent of particle deformation resulting from the impact, and it can provide valuable guidance for selecting the appropriate process pressure.

The objective of this study is to develop a simplified computational framework to predict the adherence of MMC coating by focusing on soft matrix. The results could be useful in the design of the CS process conditions to develop a specific MMC coating to improve the

surface properties of substrate material. SKD11 material with an Al/TiN coating was selected due to the high potential of Al/TiN coatings in protecting against thermal oxidation on the substrate. FEM was used as a tool to understand the deformation behavior of matrix particles, i.e., Al particles, on hard substrates. The effect of particle temperature and impact velocity was investigated. The impact of a single Al particle was modeled to investigate its behavior. It is expected that the behavior of single particle impact is sufficient to select a critical velocity that identifies the process temperature and pressure associated with obtaining Al/TiN coating, provided that the CS equipment performance is known. Notably, it is assumed that the presence of TiN particle does not significantly affect the Al particle flow or impact conditions. Experimental work was carried out to verify the technique proposed. The CS of pure Al coating and Al/TiN coating with different Al:TiN ratios were studied.

In this paper, the model descriptions are presented in the second section, providing a comprehensive overview of the theoretical framework. The third section covers experiment details, offering insights into the practical aspects of the study. The fourth section presents and discusses the computational results. The fifth section is dedicated to the discussion of the cold spray experiment results. Finally, the paper concludes in the last section, summarizing the key findings and their implications.

## 2. MODEL DESCRIPTION

**2.1. Finite Element Modeling** The study of a single CS particle's behavior upon impacting a substrate was conducted employing the widely used FEM software, ABAQUS/Explicit version 2017, which has seen extensive utilization in CS research (29-35). The model was simplified as a two-dimensional (2D) axisymmetric model was used for Arbitrary Lagrangian–Eulerian (ALE) analyses to simulate the large deformation processes that would occur during particle impact, with  $R$  representing radius,  $L$  representing length, and  $W$  representing width. The subscript  $p$  was assigned to distinguish the particle, as shown in Figure 1(a). Considering the axisymmetric nature of the normal impact process, the boundary conditions employed involved fixing the bottom of the substrate with the constraints ( $U_1=U_2=U_3=0$ ), and XSYMM, signifying symmetry about a plane X, as illustrated in Figure 1(b). The thermal and mechanical effects were assessed using two procedures available in ABAQUS: the Coupled Temperature Displacement procedure and the Dynamic Temperature Displacement Explicit procedure. Given the requirement for handling large deformations, the Dynamic Temperature Displacement Explicit procedure was deemed more suitable for this study. Accordingly, it was utilized to investigate the adiabatic stress effect (29).

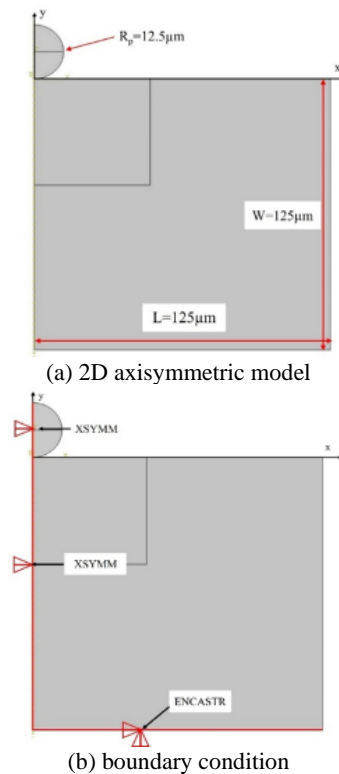
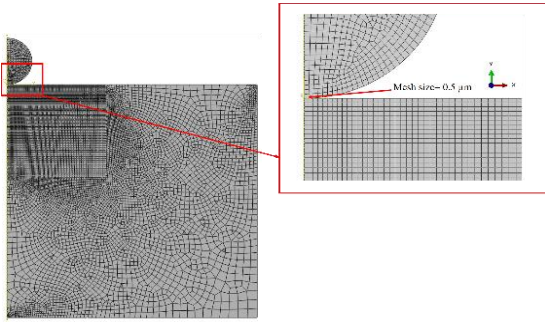


Figure 1. Schematic diagram

For 2D, the particle/substrate interaction was executed by using the surface-to-surface contact (Explicit) penalty contact algorithm, choosing balance master-slave weighting contact for two element-based deformable surfaces that contact each other, and a finite sliding formulation (general and allows any arbitrary motion of the surfaces). The penalty contact algorithm aims to balance the weighting of forces on both the master and slave contact surfaces. In cold spray impact, the particle surface and substrate surface begin to slide relative to each other. The kinematic friction coefficient ( $\mu_k$ ) should be used instead of the static friction coefficient ( $\mu_s$ ) and is generally lower than  $\mu_s$ . The friction coefficient ( $\mu_k$ ) was set to be 0.3 (29). The time increment used for this study was 60 ns. The particle velocity varied from 350 to 600 m/s for low-pressure cold spray. The initial substrate temperature was 300K, while particle temperature varied at 300K, 623K, and 723K.

The element type CAX4RT (A 4-node thermally coupled axisymmetric quadrilateral, bilinear displacement and temperature, reduced integration, and viscoelastic hourglass control) was used for the study, as shown in Figure 2. The meshing size at the contact between the particles and substrate was  $0.5 \mu\text{m}$  for  $25 \mu\text{m}$  particles (a meshing resolution of  $1/50D_p$ ). To reduce resulting computational errors, Arbitrary Lagrangian–Eulerian (ALE) adaptive remeshing was performed to avoid mathematical truncation errors due to substantially



**Figure 2** Mesh structure of 2D axisymmetric model

deformed elements [29]. This method was used to remesh the model 100 times in each increment.

**2. 2. Materials Properties** The numerical model uses the Johnson-Cook plasticity model to estimate the effects of strain-hardening, strain-rate hardening, and the equivalent flow stress, which can be expressed as follows (26):

$$\sigma = [A + B\varepsilon_p^n][1 + C \ln(\dot{\varepsilon}_p / \dot{\varepsilon}_0)][1 - (T^*)^m] \quad (1)$$

where  $\sigma$  is the flow stress,  $\varepsilon_p^n$  and  $\dot{\varepsilon}_p$  are the equivalent plastic strain and strain rate, respectively, and  $\dot{\varepsilon}_0$  is normalized reference strain rate. The constant A is yield stress, B is the strain-hardening parameter, C is strain-rate hardening, n is the power exponent of strain hardening, and m is the thermal softening constant.  $T^*$  is normalization temperature defined as follows:

$$T^* = \begin{cases} 0; & T < T_{trans} \\ (T - T_{trans}) / (T_{melt} - T_{trans}); & T_{trans} \leq T \leq T_{melt} \\ 1; & T_{melt} < T \end{cases}$$

where  $T_{trans}$  is a reference transition temperature at or below which there is no temperature dependence of the

**TABLE 1.** Material properties used in FE mode (26, 31)

Parameters	Al	SKD11
Density (kg/m <sup>3</sup> )	2710	8400
Young's modulus (GPa)	68.9	208
Poisson's ratio	0.33	0.30
Heat capacity (J/kg.K)	904	461
Melting temperature (K)	916	1733
A (MPa)	148.4	1766
B (MPa)	345.5	904
n	0.183	0.39
C	0.001	0.012
m	0.895	3.38
Reference temperature (K)	293	298
Reference strain rate (s <sup>-1</sup> )	1	1

response, and  $T_{melt}$  is the melting temperature. All constant parameters depend on materials and are shown in Table 1.

### 3. EXPERIMENT

**3. 1. Materials and Deposition Process** First, the cold spray (CS) of pure aluminum (Al) was carried out at 1 MPa, at a temperature of 623K (supported by Impact-Innovations GmbH in Germany) with an Impact spray machine model 5/11. Nitrogen was used as an accelerating gas with a 30 mm stand-off distance and a nozzle travel speed of 20 mm/s. Pure Al coating was deposited with a 3-pass process. The discussion of CS conditions will be provided in a subsequent text.

For the metal matrix composite coating experiment, TiN particles (0.8-1.2  $\mu\text{m}$ , H.C. STARCK, USA) with spherical shapes for feedstock powders were used to produce TiN reinforcement in Al coating. Figure 3 presents the morphologies of Al-mixed TiN particles. The particles were mechanically mixed for 8 hours for deposition at an Al:TiN ratio of 75:25 wt.%, following the work of Wen-Ya Li (23). The low cold spray system installed at the University of the Witwatersrand, South Africa (Centreline, Center Line model SST PX, Canada) was used for composite coating development in this work. Low-pressure compressed air was used as an accelerating gas at 1 MPa with a 30 mm stand-off distance with deposition temperatures of 623K and 723K. A nozzle traveling speed of 12 mm/sc was employed to minimize porosity, as suggested by preliminary tests.

**3. 2. Characterization** The cross-section microstructure of the deposited coating was examined by scanning electron microscopy (SEM) (JSM 6610LV, JEOL, Japan), including an energy-dispersive X-ray spectroscope (EDS) (INCA-xart, Oxford, UK). The average percentage of particles and voids were evaluated using IMAGE J analysis with SEM imagery. The X-ray diffraction pattern was identified by X-ray diffraction (XRD) (SmartLab, Rigaku, Japan) analysis with Cu  $K\alpha_1$  radiation under the condition of 40 kV and 30 mA in 30-80° scanning 2 $\theta$  ranges and incidence angle of 0.5°. The microhardness of the top surface was tested by Vickers hardness indenter (SINOWON, China) with a load of 100 gf and a holding time of 15 s. Ten measurements on the polish cross-section were averaged to determine the average surface hardness. Note that this preliminary study did not include adhesive strength testing.

### 4. COMPUTATIONAL RESULTS AND DISCUSSION

**4. 1. Effect of Particle Impact Velocity and Particle Temperature on Deformation Behavior** The initial energy of particles with different impact velocities

predicted by the computational model is shown in Figure 4. The graph shows that increasing the particle velocity increases the kinetic energy. The energy transfer from the particle to the substrate was observed when the particle initiated contact with the substrate at 10 ns. Later, at approximately 30 ns, the particle deformation process starts, and the particle adheres to the substrate as there is insufficient energy for the particle to rebound.

The deformation of particles during impact could also be predicted. Figure 5 shows the typical results of equivalent plastic strain (PEEQ) distribution for different impact particle velocities at a constant initial temperature of 623 K (process temperature). The results show that particles will stretch out when the impact velocity is increased, eventually forming a sheet-like shape that adheres to the substrate. Hence, a certain particle velocity called critical velocity is required for the coating to be deposited successfully. At the contact surface, a metal "surface-scrubbing" jet is created. The lack of separation between the powder particle and the substrate at the contact surface suggests that there was no rebound or detachment of the particles from the substrate because of the impact. This agrees with work on critical velocity previously reported for Al on the hard substrate [30]. Further, a jetting phenomenon for 300 K starts at the edge of the particle at an impact velocity above 500 m/s.

In theory, the critical velocity may be described using particle temperature and material properties following

Equation 2 for known material (28). Notably, the equation does not include the effect of the substrate material. This equation is used for estimating the critical velocity of soft particles on a soft substrate, the reference material, i.e.:

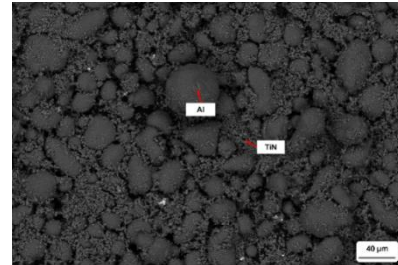


Figure 3. SEM micrograph of Al mixed TiN

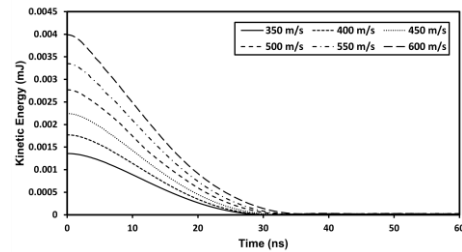


Figure 4. Kinetic energy of Al impact at varying impact velocity

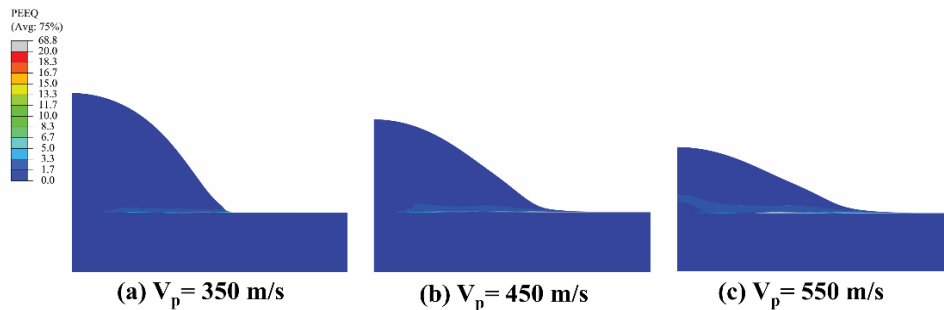


Figure 5. Simulation contour of PEEQ at 36ns of 25 μm Al particles upon an SKD11 hardening substrate at varying particle velocity (particle temperature at 623K)

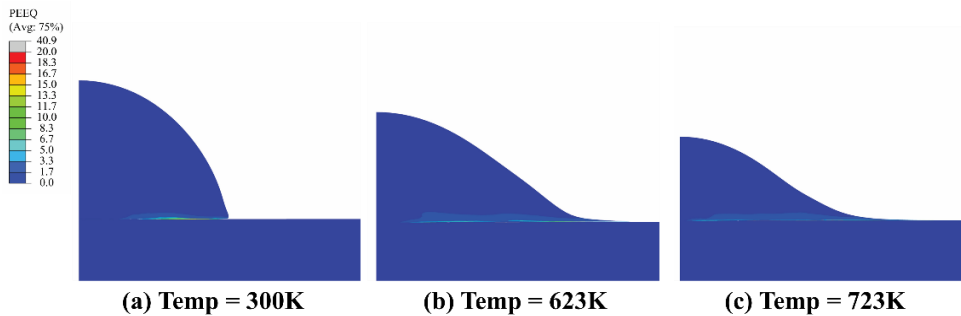


Figure 6. Simulation contour of PEEQ at 36ns of 25 μm Al particles upon an SKD11 hardening substrate at varying particle temperature (particle velocity at 450 m/s)

**TABLE 2.** Critical velocity of pure Al particle calculation from Equation 2

Initial particle temperature (K)	Critical velocity (m/s)
300	665
623	460
723	370

$$V_{cr} = 0.64 \sqrt{\left( \frac{16\sigma_{TS}}{\rho_p(T_m - 293)} + C_p \right) [T_m - T_{pi}]} \quad (2)$$

where  $C_p$  is the particle-specific heat,  $T_m$  is the particle melting temperature,  $\rho_p$  is the particle density,  $\sigma_{TS}$  is the particle tensile strength, and  $T_{pi}$  is the particle impact temperature (28). The results are shown in Table 2.

The  $V_{cr}$  different temperatures could be estimated using Equation 2. For example, the particle velocity at 300K is approximately 665 m/s (see Table 2). It could be seen that  $V_{cr}$  decreases as particle temperature increases, as shown in Table 2. When considering the plastic strain equivalent (PEEQ) result, Figure 5 shows that the Al particles start adhering to the substrate at a particle velocity of 350 m/s, while the critical velocity determined by Equation 2 suggests a higher value of critical velocity. The deposition of soft particles onto a hard substrate typically demands a lower critical velocity, as demonstrated in the research conducted by Bae et al. (30). In their study, they determined that for scenarios involving particle sizes of 25  $\mu\text{m}$  and a process temperature of 300K, the critical velocity was 775 m/s for Al particles on an Al substrate and 365 m/s for Al particles on a steel substrate. The current work observed that the critical velocity initiation occurred at approx. 400 m/s for 300K (see detail later in the text), which aligns with the work previously reported (30). This indicated that the simulated critical velocity was lower than the calculated value due to substrate effects. Specifically, when the substrate is harder than the particle, it has the potential to reduce the critical velocity.

It should be noted that the effect of particle size  $V_{cr}$  has also been discussed by Dowding et al. (37), suggesting increasing  $V_{cr}$  with decreasing particle size. This is because the small particle size has a higher surface area-to-volume ratio. It should be noted that Equation 2 does not include such an effect. The effect of particle size could be investigated in more detail using the current model to predict impact behavior.

The results of increasing temperature on the particle (see Figure 6) present the contour of PEEQ at the same particle velocity at various particle temperatures. The result shows that the particle increased surface area and deformed more when increasing particle temperature. Increasing the temperature of Al particles could result in particle softening and particles being easier to deform. Thus, an increase in particle temperature could increase particle flat length from 15  $\mu\text{m}$  to 35  $\mu\text{m}$ , 133% from its initial temperature (300K to 723K). This could also help in the deposition of the particle in the following impact.

Figure 7 provides a graph showing the relationship between plastic strain equivalent (PEEQ) and impact time for different particle temperatures. It could be seen that an increase in strain developed when increasing the temperature up to the melting point. With a process temperature equal to or higher than the melting temperature, the particle would start melting, and wetting phenomena may take place. Hence, Al material spreading out is expected. The deformation behavior of the particle, therefore, could result in a change in coating layer thickness depending on the particle geometry after impact.

**4. 2. Effect of Particle Impact Velocity and Particle Temperature on Interface Temperature**

Figure 8 (a)-(c) presents the temperature distribution in the particle and substrate during impact (at 36ns) for cases with an impact velocity of 450m/s. Figure 8(a) shows the result for an initial particle temperature of 300 K. It could be seen that the cohesive zone was small, and the temperature of a particle during impact at 36 ns was 823 K. The cohesive zone size increases by approximately 86% and 143%, and the temperature of a particle during impact at 36 ns rise to 1066 K and 1000K when the initial particle is 623 K and 723 K, respectively (see Figure 8b). The change in the cohesive zone and interface temperature could affect adhesion behavior,

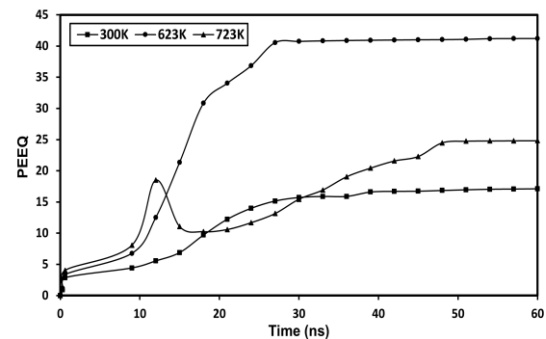


**Figure 7.** Time history of PEEQ for Al impact at different particle temperatures (Impact velocity of 450 m/s)

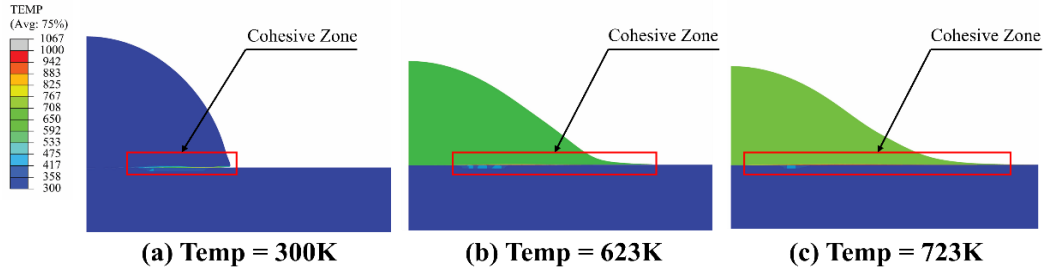


Figure 8. Temperature contour particle and substrate at 36ns, 450m/s with different particle temperatures

i.e., gap and adhesion strength, at the interface between the coating and the substrate. Figure 9 shows the relationship between particle temperatures at the interface with impact time for different initial particle temperatures. The particle temperature during impact would affect the particle deformation behavior during impact and in turn, result in a change in the critical velocity of Al particles as observed as a result of changing initial particle velocity, i.e., decreasing in the critical velocity is expected for higher initial particle velocity. As temperature rises, particles acquire greater kinetic energy, leading to increased vibrational intensity. As gas temperature increases, particles gain kinetic energy, resulting in higher speeds. Consequently, particles collide with surfaces more frequently and with greater impact.

**4. 3. Influence of Particle Impact Velocity and Particle Temperature on Flattening Ratio**

The flattening ratio represents the severity of particle deformation after impact in a clearer aspect. Deposits with heavily deformed particles are likely to have less porosity, a high bonded area, and high cohesive strength, as described earlier. Thus, the flattening ratio can be examined as a "diagnostic" microstructure property. It acts as a benchmark for the general quality of cold-spray coating. Hence, the effect of particle impact on the flattening ratio is also investigated.

Figure 10 shows the typical characteristics of particles before and after impact. As the flattening ratio is closer to 1, less porosity is expected. This is because as the particles deformed flatter, the gap between the two colliding particles should be reduced, resulting in a denser coating.

On the other hand, the resulting coating will be highly porous if the flattening ratio is close to 0. In general, the elongation characteristics of a particle depend on particle velocity. High particle velocity results in a high flattening ratio. The flattening ratio can be calculated following Equation 4.

$$Flattening\ Ratio = 1 - \frac{h_p}{D_p} \tag{4}$$

where  $h_p$  is the height of the particle after impact and  $D_p$  is the diameter of the particle before impact.

For the flattening ratio, the relationship between the particle velocity and the flattening ratio can be plotted as shown in Figure 11, which shows the relationship between the particle velocity and the flattening ratio at different temperatures of the obtained coating predicted by the computational analysis. When increasing particle temperature, the flattening ratio increases to approximately 60% of room temperature. High particle velocity should be selected, or a flattening ratio approaching 1 should be chosen to reduce coating porosity and improve adhesion behavior. As shown in Figure 8, the flattening ratio, as indicated by the temperature contour, decreases as particle temperature increases, resulting in an expanded cohesive zone.

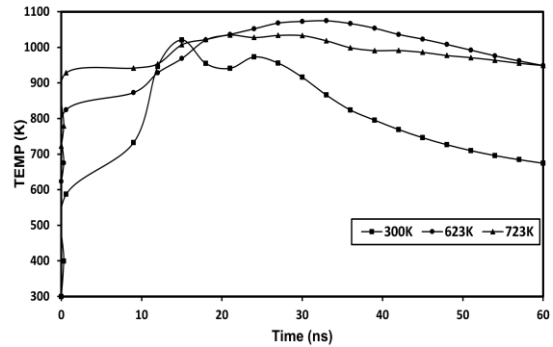


Figure 9. Time history of temperature for Al impact at different particle temperatures (Impact velocity of 450 m/s)

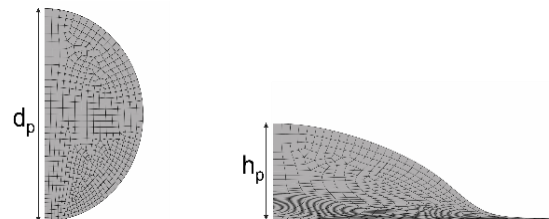
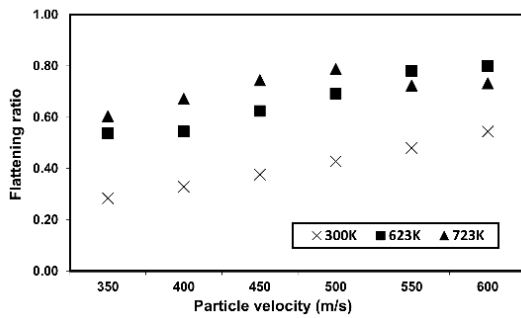


Figure 10. Characteristics of particles before and after impact on the substrate



**Figure 11.** Relationship between the particle velocity and the flattening ratio at different temperatures

### 5. COLD SPRAY EXPERIMENT

To investigate the capability of the computational model, the experiment was performed. A process temperature of 623K was selected. The preliminary study of the cold spray of pure Al on SKD11 was first carried out. The pressure in the experiment could be determined by using the equation shown in Equation 5 (10) for a required particle velocity,  $V_p$ . The desired particle velocity was chosen based on computational results for 623K using the flattening ratio results. The particle velocity should be greater than the critical velocity,  $V_{cr}$ , which gives the flattening ratio greater than 0.5. Notably, the flattening ratio was approximately 0.5 when the particle velocity was equal to critical velocity  $V_{cr}=V_p$  (28). This is to ensure that a coating with low porosity would be developed. The desired velocity of 450 m/s was selected.

$$V_p = \frac{1}{\frac{1}{M} \sqrt{\frac{M_{gas}}{\gamma RT}} + 0.85 \sqrt{\frac{D}{x}} \sqrt{\frac{\rho_p}{\rho_0}}} \quad (5)$$

where  $M$  is the local Mach number and  $\gamma$  is the ratio of specific heat. For monatomic gases (He, Ar),  $\gamma$  is 1.66, and for diatomic gases ( $N_2$ , air),  $\gamma$  is typically 1.4.  $R$  is the gas constant (8314 J/kmol K).  $T$  is gas temperature. Local Mach number  $M$  only depends on the inner form of the nozzle.  $M_{gas}$  is the molecular weight of the gas used in the process.  $P_0$  is the supply pressure measured at the entrance of the nozzle, while  $\rho_p$  is the particle density,  $D$  is the particle diameter, and  $x$  is the axial position.

The calculated pressure for the desired particle velocity is shown in Table 3a, while the particle velocity developed for a pressure of 1 MPa (the low pressure was chosen in this work due to the limitation of the CS machine) is shown in Table 3b. In Table 3b, the initial particle temperature affects the particle velocity in the process; as the temperature increases, particle velocity also increases. Temperature plays a significant role in adding energy to the spraying process in the form of heat. Elevated gas temperature enhances gas expansion through the nozzle, resulting in higher particle velocities.

This observation is also related to the flattening ratio. Additionally, as the temperature increases, so does the temperature of the particles, leading to a greater degree of particle softening. This, in turn, increases the likelihood of plastic deformation during impact, ultimately improving deposition efficiency.

#### 5. 1. Cold Spray of Pure Al Coating

The characteristics of the sample after cold spray as shown in Figure 12. The sample was cross-sectioned by wire cutting to measure the thickness, as shown in Figure 13. The coating thickness was found to be  $180 \pm 55 \mu m$ , while the hardness was  $29.3 \pm 5 HV_{0.1}$ .

The preliminary experimental (pure Al) results confirmed that the computational model could be used to estimate the initial desired velocity, which was later used to select the process pressure for different particle temperatures based on particle deformation and interface behavior, i.e., flattening ratio. On the other hand, for a case with pressure limitation due to machine specification/performance, the required impact velocity for different particle temperatures could be estimated, which can be helpful in the design of the process parameters or improvement of the heating and pumping

**TABLE 3a.** Process pressure estimated for particle velocity of 450 m/s for different initial particle temperatures

Initial particle temperature (K)	Particle velocity	Pressure (MPa)
300	450	1.4
623	450	0.95
723	450	0.86

**TABLE 3b.** Particle velocity developed for a process pressure of 1 MPa for different initial particle temperatures

Initial particle temperature (K)	Pressure (MPa)	Particle velocity
300	1	387
623	1	457
723	1	471



**Figure 12.** Appearance of pure Al-coated specimen carried out at Impact-Innovations GmbH in Germany



**Figure 13.** Optical micrographs for a cross-section of pure Al-coated specimen carried out at Impact-Innovations GmbH in Germany (magnitude 5x)

system. The effect of particle size should also be investigated with no major difficulty, which could be used as a guideline to reduce the process temperature and pressure.

**5. 2. Cold Spray of Al/TiN Coating** To improve the hardness of Al coating, TiN hard particles were added for reinforcement. To investigate the ability of the computational framework for the prediction of coating achievement based on Al particle impact behavior, the composite coatings deposition was performed. The selected size of TiN was smaller than pure Al to minimize the effect of TiN particles on Al particle flow and impact behavior. In this experiment, TiN was expected to disperse in a soft matrix and not deform. TiN particles are hard to deform or implant on a hard substrate at low velocity. The critical velocity and particle velocity of TiN (size 10 μm) could be estimated theoretically following the methodology previously described. The TiN critical velocity was approximately twice that of the Al particle,  $V_{crAl}$ , and the particle velocity of TiN was approximately  $1.2V_{pAl}$  (particle velocity of Al particle). Thus, TiN particles are expected to require higher energy for deformation on a hard substrate.

For the composite coating, the experiment used the same condition desired for pure Al (Pressure of 1 MPa, Temperature of 623K). Preliminary tests with 2 Al:TiN ratios (25 wt.% and 50 wt.% TiN) were investigated to study the upper limit of % TiN that could be deposited based on the critical velocity predicted for pure Al.

It was found that 50wt.% TiN was the limit of TiN fraction for conditions of pressure =1 MPa and temperature = 623K. It was also found that the average thickness of coating obtained for this case was approximately  $18.7 \pm 4.6\mu\text{m}$ , which was too thin, and the specimens were unevenly coated. This may be due to the effect of TiN particles on particle flow, which could reduce the travelling velocity and impact velocity of Al particles. It should be noted that the number of TiN particles is higher with a higher percentage of TiN. The micrograph presented in Figure 14 (a & b) shows an SEM

(backscattered electron mode) micrograph of the cross-section of Al/TiN composite coating at a process temperature of 623K with magnitudes of 100x and 1000x, respectively.

A gap between the coating and substrate can be observed in Figure 14(b). The coating hardness was found to be  $75.3 \pm 26.2 \text{ HV}_{0.1}$ . The effect of the hard substrate could be expected due to the thin coating developed. Increasing the process pressure and temperature or reducing the TiN size may improve the coating process, resulting in an increase in coating thickness.

For a ratio of Al=75wt.%: TiN = 25%, the average coating thickness was found to be approximately  $234.7 \pm 51 \mu\text{m}$ , and the average coating hardness was  $63.6 \pm 8.8 \text{ HV}_{0.1}$ . Figure 15 presents a micrograph showing a cross-section of Al/TiN (fraction Al=75wt.%: TiN = 25wt.%).

The coating appears denser and thicker than that observed with a fraction of Al=50wt.%: TiN = 50wt.%. It could be said that the computational prediction of critical velocity and particle velocity of Al could be used for Al/TiN composite coating for the case with insignificant effect of TiN on Al impact behavior. Notably, the %TiN limitation is expected to be changed with process conditions and particle size. For this work, the TiN and Al particle sizes are 10 μm and 25 μm, respectively, and the process pressure and temperature are 1 MPa and 623K, respectively.

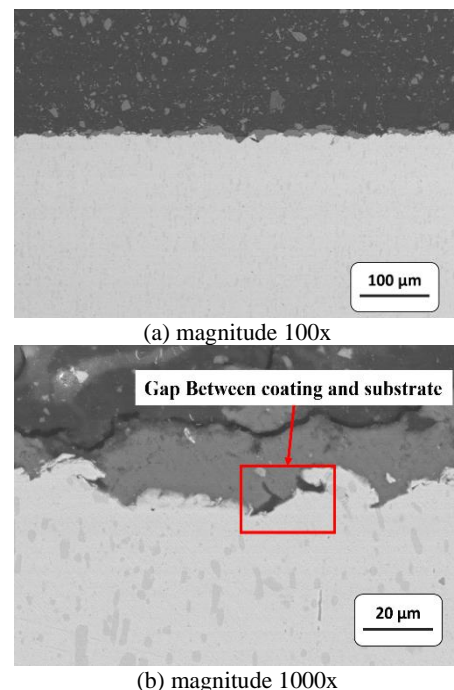


**Figure 14.** SEM (Back Scattered Electron mode with magnitude 100x and 1000x) micrograph showing a cross-section of Al/TiN (fraction Al=50wt.%: TiN = 50wt.%) (Centreline Center Line model SST PX)

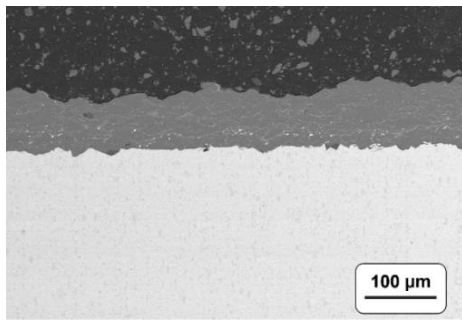
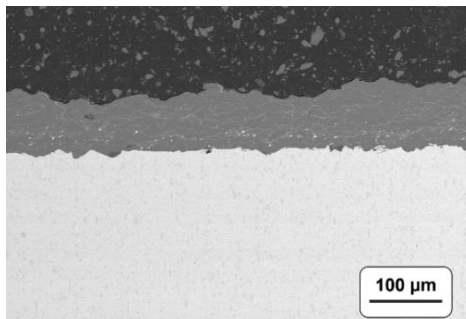


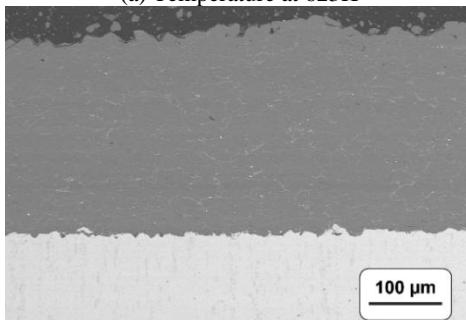
**Figure 15.** SEM (Back Scattered Electron mode with magnitude 100x) micrograph showing a cross-section of Al/TiN (fraction Al=75wt.%: TiN = 25wt.%) (Centreline Center Line model SST PX)

For the experimental study of the effect of initial particle temperature, tests were performed at 623K and 723K for an Al:TiN ratio of 75 wt.:%:25 wt.%. The pressure for both cases was fixed at 1 MPa.

A micrograph of Al/TiN composite coating in Figure 16 (a & b) shows an SEM (backscattered electron mode) micrograph of the cross-section of Al/TiN composite coating at process temperatures of 623K and 723K, respectively. The EDS mappings, as depicted in Figure 17, displayed the presence of pure aluminum (a) on the deposit side, along with nitrogen (b) and titanium (c).



(a) Temperature at 623K



(b) Temperature at 723K

**Figure 16.** SEM (Back Scattered Electron mode with magnitude 100x) micrograph showing a cross-section of Al/TiN composite coating at different process temperatures (Centreline Center Line model SST PX)

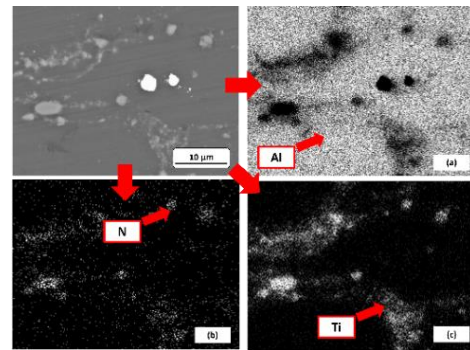


**Figure 17.** EDS mapping (Energy Dispersive Spectroscopy with magnitude 3000x) of the cold-sprayed Al/TiN composite coating at a process temperature of 723K.

The X-ray diffraction analysis of the Al/TiN composite coating was conducted, and the findings are presented in Figure 18. Based on the XRD analysis, the coating primarily consisted of aluminum (Al), with a limited presence of titanium nitride (TiN). The X-ray diffraction (XRD) analysis revealed the absence of impurities, additional phases, or significant phase alterations, thus confirming the absence of oxidation during the cold spray process. The results further confirmed the embedding of TiN particles within the Al matrix.

A micrograph showing a cross-section of Al/TiN reveals that the Al particles deformed flat and were deposited layer by layer. TiN particles were embedded around pure Al particles and were uniformly dispersed in the matrix (see Figure 19 (a)). Because the impact energy for particles of the soft component is high enough to adhere to the substrate, the impact energy of hard material is sufficient to adhere to the surface previously covered by soft material due to mechanical embedding (31). The volume fraction of TiN in the deposit was approximately 10% for both conditions. This differs slightly from the findings of Li et al. (24), who investigated TiN composite coating with high-pressure

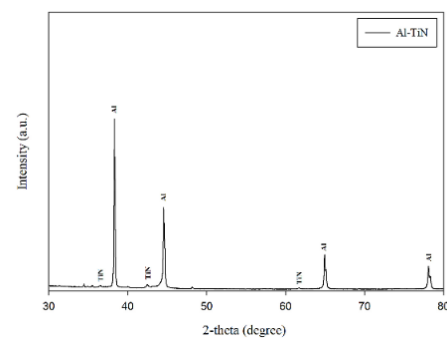


**Figure 18.** X-ray diffraction pattern of Al/TiN composite coating

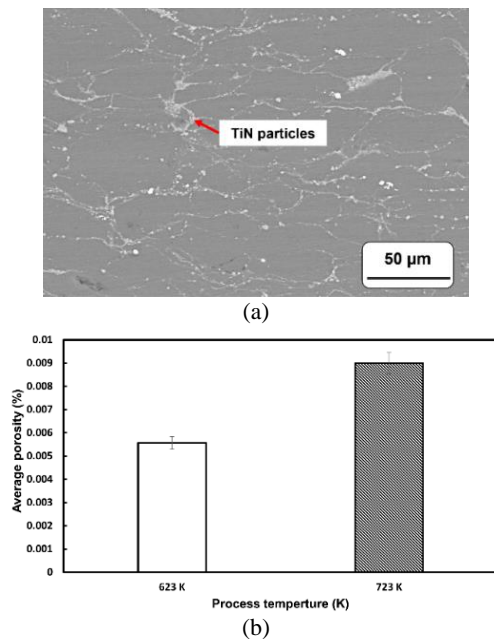


**Figure 19.** SEM (Back Scattered Electron mode with magnitude 500x) micrograph showing a cross-section of Al/TiN composite coating at a process temperature of 723K (a) and Al/TiN porous coating on SKD11 hardened by cold spraying (b)

cold spray at 25 wt.% TiN (resulting in a volume fraction of 13.9% in the deposit). It is evident that the flattening ratio results from simulations have utility in designing experimental conditions.

The results suggested that the temperature in the process affects coating porosity and thickness, as predicted by computational investigation. It was found that increasing the process temperature increases the thickness, and a dense Al/TiN composite coating was expected with this flattening ratio ( $> 0.5$ ). The average percentage of voids was evaluated using IMAGE J analysis with SEM imagery. The result found that the porosity of the Al/TiN composite coating was less than 0.01% at both process temperatures (see Figure 19(b)). The results show that at a process temperature of 723 K, there is a higher percentage of porosity compared to 623 K. This observation may be attributed to the particle expansion and contraction behavior, as depicted in Figure 7 (Time history of PEEQ for Al impact at different particle temperatures (Impact velocity of 450 m/s)). At 723 K, particles initially expand from 0 to 10 seconds, then contract briefly before expanding again after 15 seconds. This cyclic behavior can create voids in the coating, resulting in a higher porosity at the higher process temperature of 723 K as compared to 623 K.

The coating thickness is presented in Figure 20. A higher particle temperature could increase particle velocity at the same process pressure, resulting in a thicker coating. This is because high particle velocity

would result in flatter particles after impact, which could promote particles adhering during the impact of the following particle, i.e., the next particle layer.

The highest microhardness of Al/TiN composites was  $74.2 \pm 6.5$  HV<sub>0.1</sub> at 723 K. The hardness of the Al/TiN composite coating was higher than the Al deposit by 65% (the hardness of the pure Al deposit was  $29.6 \pm 5.1$  HV<sub>0.1</sub>), as expected (23-25). Figure 21 shows that increasing the particle temperature could result in a coating with higher surface hardness. This is due to the effect of thicker coating with higher deformation obtained at higher temperatures, as the particles deform more easily, showing flatter particle geometry after each impact. The results align with those from Li et al. (24), who examined Al5356/TiN composite coating in high-pressure cold spray. They found that TiN particles increased the hardness of the matrix coating by 50%. For instance, with a TiN fraction of 25 wt.%, the hardness of Al5356/TiN reached approximately 140.38 HV<sub>0.2</sub>, while Al5356 alone had a hardness of 68.7 HV<sub>0.2</sub>. In terms of adhesive strength, Al5356 had a strength of 32 MPa, while Al5356/TiN exhibited an even higher strength exceeding 50 MPa (24, 25). Based on the Li et al. (24) study, the adhesive strength can be estimated to fall within the range of 30 MPa to 50 MPa. Note that this preliminary study did not include adhesive strength testing, but this aspect will be addressed in future work as the experimental conditions are refined.

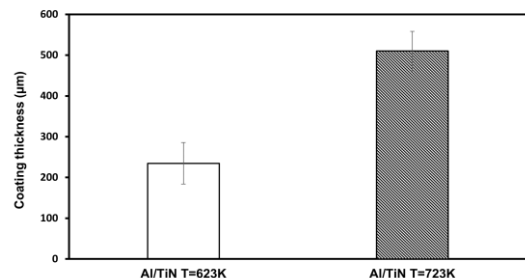


**Figure 20.** The average coating thickness of the composite coating

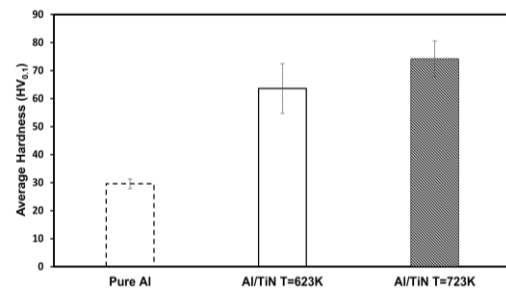


**Figure 21.** Average coating hardness of pure Al coating and composite coating

## 6. CONCLUSIONS

A simplified computational framework to predict the adherence of MMC coating was proposed, i.e. a model for a single impact of a single matrix particle. The deformation behavior of matrix particles could be investigated to provide information for CS process conditions to be selected for cases with the insignificant effect of hard reinforcement particles. The critical velocity, characteristic of particles during impact, and porosity in the coating could be predicted. Al/TiN coating was studied in this work. The effects of particle temperature and impact velocity were investigated. The results showed that:

- Single-shot particle impact modelling could be used to show representative composite coating deposition performance for the case of hard reinforcement particles as long as no significant effect of hard particles on matrix particle velocity is observed. For the Al/TiN coating studied in this work (TiN and Al particle sizes of approx. 10  $\mu\text{m}$  and 25  $\mu\text{m}$ , respectively), 25wt.% TiN was suggested.
- Particle temperature directly affects the cohesive zone; by increasing particle temperature, the cohesive zone area increases as well. This could confirm that the particles adhere to the substrate.
- The flattening ratio can be determined computationally, which can then be used as a guideline to predict the coating porosity.
- Particle deformation increases with increasing impact velocity and initial temperatures. Hence, the coating could be easier to deposit with higher particle velocity or higher initial temperature.

## 7. ACKNOWLEDGMENTS

The author would like to express the deepest appreciation to the Research and Researchers for Industries-RRI of the Thailand Research Fund and to Metalfine (Thailand) Ltd. for funding under the Research Scholar Grant (No.PHD59I0021 and RDG6150009). Sincere thanks are also extended to Professor Natasha Sacks at Stellenbosch University in South Africa for her advice and suggestions. Special thanks to the Material Manufacturing and Surface Engineering Research Center (MaSE lab) for providing laboratory support.

## 8. REFERENCES

1. Gapsari F, Hidayatia N, Setyarini P, Alan MP, Subagyo R, Andoko A. Hydroxyapatite coating on stainless steel 316l using flame spray technique. *International Journal of Engineering, Transactions B: Applications*. 2021;34(2):493-9. 10.5829/IJE.2021.34.02B.22
2. Afshar A, GHORBANI G, Ehsani N, Saeri M, Sorrell C. A STUDY OF ZETA POTENTIAL OF PLASMA SPRAYED HYDROXY AP ATITE COATING IN FOUR SIMULATED PHYSIOLOGICAL SOLUTIONS. *International Journal of Engineering*. 2003;16(4):343-54.
3. Ebrahimi N, Sedaghat Ahangari Hosseinzadeh A, Vaezi M, Mozafari M. Evaluation of corrosion resistance of bi-layered plasma-sprayed coating on titanium implants. *International Journal of Engineering, Transactions A: Basics*. 2022;35(4):635-43.
4. Poursaeidi E, Salarvand A. Comparison of properties of ti/tin/ticn/tialn film deposited by cathodic arc physical vapor and plasma-assisted chemical vapor deposition on custom 450 steel substrates. *International Journal of Engineering, Transactions A: Basics*. 2016;29(10):1459-68. 10.5829/idosi.ije.2016.29.10a.17
5. Nistratov AV, Klimenko NN, Pustynnikov IV, Vu LK. Thermal regeneration and reuse of carbon and glass fibers from waste composites. *Emerg Sci J*. 2022;6:967-84. 10.28991/ESJ-2022-06-05-04
6. Fauchais PL, Heberlein JV, Boulos MI. *Thermal spray fundamentals: from powder to part*: Springer Science & Business Media; 2014.
7. Khadayeir AA, Wannas AH, Yousif FH. Effect of Applying Cold Plasma on Structural, Antibacterial and Self Cleaning Properties of  $\alpha$ -Fe<sub>2</sub>O<sub>3</sub> (HEMATITE) Thin Film. *Emerging Science Journal*. 2022;6(1):75-85. 10.28991/ESJ-2022-06-01-06
8. Astuti P, Rafdinal RS, Yamamoto D, Andriamisaharimanana V, Hamada H. Effective Use of sacrificial zinc anode as a suitable repair method for severely damaged RC members due to chloride attack. *Civil Engineering Journal*. 2022;8(7):1535-48. 10.28991/CEJ-2022-08-07-015
9. Pawlowski L. *The science and engineering of thermal spray coatings*: John Wiley & Sons; 2008.
10. Huang R, Ma W, Fukunuma H. Development of ultra-strong adhesive strength coatings using cold spray. *Surface and Coatings Technology*. 2014;258:832-41. 10.1016/j.surfcoat.2014.07.074
11. Schmidt T, Gärtner F, Assadi H, Kreye H. Development of a generalized parameter window for cold spray deposition. *Acta materialia*. 2006;54(3):729-42. 10.1016/j.actamat.2005.10.005
12. Sansoucy E, Kim G, Moran A, Jodoin B. Mechanical characteristics of Al-Co-Ce coatings produced by the cold spray process. *Journal of Thermal Spray Technology*. 2007;16:651-60. 10.1007/s11666-007-9099-3
13. Huang R, Sone M, Ma W, Fukunuma H. The effects of heat treatment on the mechanical properties of cold-sprayed coatings. *Surface and Coatings Technology*. 2015;261:278-88. 10.1016/j.surfcoat.2014.11.017
14. Wu J, Fang H, Yoon S, Kim H, Lee C. Measurement of particle velocity and characterization of deposition in aluminum alloy kinetic spraying process. *Applied surface science*. 2005;252(5):1368-77. 10.1016/j.apsusc.2005.02.108
15. Moridi A, Hassani-Gangaraj SM, Guagliano M, Dao M. Cold spray coating: review of material systems and future perspectives. *Surface Engineering*. 2014;30(6):369-95. 10.1179/1743294414Y.0000000270
16. Hussain T. Cold spraying of titanium: a review of bonding mechanisms, microstructure and properties. *Key engineering materials*. 2013;533:53-90. 10.4028/www.scientific.net/KEM.533.53
17. Maev RG, Leshchynsky V. Low-pressure cold spray (LPCS). *Cold-Spray Coatings: Recent Trends and Future perspectives*. 2018:95-142. 10.1007/978-3-319-67183-3\_4
18. Wang Q, Birbilis N, Zhang M-X. Process optimisation of cold spray Al coating on AZ91 alloy. *Surface engineering*. 2014;30(5):323-8. 10.1179/1743294413Y.0000000224

19. Irissou E, Legoux J-G, Arsenault B, Moreau C. Investigation of Al-Al<sub>2</sub>O<sub>3</sub> cold spray coating formation and properties. *Journal of Thermal Spray Technology*. 2007;16(5-6):661-8. 10.1007/s11666-007-9086-8
20. Meng F, Hu D, Gao Y, Yue S, Song J. Cold-spray bonding mechanisms and deposition efficiency prediction for particle/substrate with distinct deformability. *Materials & Design*. 2016;109:503-10. 10.1016/j.matdes.2016.07.103
21. Hodder K, Nychka J, McDonald A. Comparison of 10 µm and 20 nm Al-Al<sub>2</sub>O<sub>3</sub> metal matrix composite coatings fabricated by low-pressure cold gas dynamic spraying. *Journal of thermal spray technology*. 2014;23:839-48. 10.1007/s11666-014-0094-1
22. Yu M, Li W. Metal matrix composite coatings by cold spray. *Cold-Spray Coatings: Recent Trends and Future perspectives*. 2018:297-318. 10.1007/978-3-319-67183-3\_10
23. Li W-Y, Zhang G, Liao H, Coddet C. Characterizations of cold sprayed TiN particle reinforced Al<sub>2</sub>319 composite coating. *Journal of materials processing technology*. 2008;202(1-3):508-13. 10.1016/j.jmatprotec.2007.09.045
24. Li WY, Zhang G, Guo X, Liao H, Coddet C. Characterizations of Cold-sprayed TiN Particle-reinforced Al Alloy-based Composites—from Structures to Tribological Behaviour. *Advanced Engineering Materials*. 2007;9(7):577-83. 10.1002/adem.200700085
25. Li W-Y, Zhang G, Zhang C, Elkedim O, Liao H, Coddet C. Effect of ball milling of feedstock powder on microstructure and properties of TiN particle-reinforced Al alloy-based composites fabricated by cold spraying. *Journal of thermal spray technology*. 2008;17:316-22. 10.1007/s11666-008-9182-4
26. Xie J, Nélias D, Walter-Le Berre H, Ogawa K, Ichikawa Y. Simulation of the cold spray particle deposition process. *Journal of Tribology*. 2015;137(4):041101. 10.1115/1.4030257
27. King PC BG, Zahiri SH, Jahedi M, Lee C. An experimental and finite element study of cold spray copper impact onto two aluminum substrates. *Journal of thermal spray technology*. 2010 19(4):620-34. 10.1007/s11666-009-9454-7
28. Assadi H, Schmidt T, Richter H, Kliemann J-O, Binder K, Gärtner F, et al. On parameter selection in cold spraying. *Journal of thermal spray technology*. 2011;20:1161-76. 10.1007/s11666-011-9662-9
29. Li W-Y, Zhang C, Li C-J, Liao H. Modeling aspects of high velocity impact of particles in cold spraying by explicit finite element analysis. *Journal of Thermal Spray Technology*. 2009;18:921-33. 10.1007/s11666-009-9325-2
30. Bae G, Xiong Y, Kumar S, Kang K, Lee C. General aspects of interface bonding in kinetic sprayed coatings. *Acta Materialia*. 2008;56(17):4858-68. 10.1016/j.actamat.2008.06.003
31. Sova A, Maestracci R, Jeandin M, Bertrand P, Smurov I. Kinetics of composite coating formation process in cold spray: Modelling and experimental validation. *Surface and Coatings Technology*. 2017;318:309-14. 10.1016/j.surfcoat.2016.06.084
32. Zhou H, Li C, Bennett C, Tanvir H, Li C. Numerical Analysis of Deformation Behavior and Interface Bonding of Ti6Al4V Particle After Subsequent Impact During Cold Spraying. *Journal of Thermal Spray Technology*. 2021;30:1093-106. 10.1007/s11666-021-01188-w
33. Yu M, Li W-Y, Wang F, Liao H. Finite element simulation of impacting behavior of particles in cold spraying by Eulerian approach. *Journal of thermal spray technology*. 2012;21:745-52. 10.1007/s11666-011-9717-y
34. Li J, Jing L, Chen M. An FEM study on residual stresses induced by high-speed end-milling of hardened steel SKD11. *Journal of Materials Processing Technology*. 2009;209(9):4515-20. 10.1016/j.jmatprotec.2008.10.042
35. Assadi H, Gärtner F, Stoltenhoff T, Kreye H. Bonding mechanism in cold gas spraying. *Acta materialia*. 2003;51(15):4379-94. 10.1016/S1359-6454(03)00274-X
36. Schmidt T, Assadi H, Gärtner F, Richter H, Stoltenhoff T, Kreye H, et al. From particle acceleration to impact and bonding in cold spraying. *Journal of thermal spray technology*. 2009;18:794-808. 10.1007/s11666-009-9357-7
37. Dowding I, Hassani M, Sun Y, Veysset D, Nelson KA, Schuh CA. Particle size effects in metallic microparticle impact-bonding. *Acta Materialia*. 2020;194:40-8. 10.1016/j.actamat.2020.04.044

**COPYRIGHTS**

©2024 The author(s). This is an open access article distributed under the terms of the Creative Commons Attribution (CC BY 4.0), which permits unrestricted use, distribution, and reproduction in any medium, as long as the original authors and source are cited. No permission is required from the authors or the publishers.

**Persian Abstract****چکیده**

اسپری سرد (CS) با کامپوزیت زمینه فلزی (MMC) یک فرآیند جایگزین برای بهبود خواص سطحی است که در ساخت پلاستیک بسیار مهم است. درک رفتار ذرات در هنگام ضربه برای CS مورد نیاز است. این مطالعه بر توسعه یک چارچوب محاسباتی ساده شده با استفاده از مدل ضربه ذره تک شات برای پیش‌بینی پایبندی ذرات ماتریس در ضربه با سرعت پایین متمرکز بود. در این کار، SKD11 سخت پوشیده شده با کامپوزیت تقویت‌کننده ماتریس Al/TiN با هدف تأیید چارچوب پیشنهادی انتخاب شد. تأثیر ذرات Al در دماهای مختلف ۳۰۰ K، ۶۲۳ K و ۷۲۳ K در محدوده سرعت پایین ۳۵۰-۶۰۰ متر بر ثانیه شبیه‌سازی شد، که نشان داد دمای ذرات بر ناحیه منسجم تأثیر می‌گذارد. با افزایش دمای ذرات، مناطق نیز با سرعت مشابه افزایش می‌یابند. نسبت مسطح شدن از شبیه‌سازی محاسبه شد و مشخص شد که تحت تأثیر سرعت ذرات قرار دارد. CS از Al و Al/TiN خالص (۷۵:۲۵ درصد وزنی) روی SKD11 سخت شده تحت ۶۲۳ K و ۷۲۳ K تحت آزمایش با فشار تخمین زده شده بر اساس نسبت مسطح و رفتار ذرات انجام شد. نتایج نشان می‌دهد که پوشش‌ها را می‌توان با استفاده از فشار تخمینی توسعه داد. پوشش Al/TiN در دماهای اولیه ذرات مختلف رسوب داده شد. نتایج نشان می‌دهد که تخلخل پوشش کم (>۰.۱٪) را می‌توان برای هر دو مورد به دست آورد، و دمای ذرات بالاتر ضخامت و درصد تخلخل بیشتری را نشان می‌دهد، که به خوبی با نتایج محاسباتی مطابقت دارد. چارچوب توسعه‌یافته پتانسیل بالایی برای طراحی CS برای پوشش MMC نشان می‌دهد، مشروط بر اینکه ذرات تقویت‌کننده به طور قابل توجهی بر جریان ذرات ماتریس یا شرایط ضربه تأثیر نگذارند.

## AIMS AND SCOPE

The objective of the International Journal of Engineering is to provide a forum for communication of information among the world's scientific and technological community and Iranian scientists and engineers. This journal intends to be of interest and utility to researchers and practitioners in the academic, industrial and governmental sectors. All original research contributions of significant value focused on basics, applications and aspects areas of engineering discipline are welcome.

This journal is published in three quarterly transactions: Transactions A (Basics) deal with the engineering fundamentals, Transactions B (Applications) are concerned with the application of the engineering knowledge in the daily life of the human being and Transactions C (Aspects) - starting from January 2012 - emphasize on the main engineering aspects whose elaboration can yield knowledge and expertise that can equally serve all branches of engineering discipline.

This journal will publish authoritative papers on theoretical and experimental researches and advanced applications embodying the results of extensive field, plant, laboratory or theoretical investigation or new interpretations of existing problems. It may also feature - when appropriate - research notes, technical notes, state-of-the-art survey type papers, short communications, letters to the editor, meeting schedules and conference announcements. The language of publication is English. Each paper should contain an abstract both in English and in Persian. However, for the authors who are not familiar with Persian, the publisher will prepare the latter. The abstracts should not exceed 250 words.

All manuscripts will be peer-reviewed by qualified reviewers. The material should be presented clearly and concisely:

- *Full papers* must be based on completed original works of significant novelty. The papers are not strictly limited in length. However, lengthy contributions may be delayed due to limited space. It is advised to keep papers limited to 7500 words.
- *Research notes* are considered as short items that include theoretical or experimental results of immediate current interest.
- *Technical notes* are also considered as short items of enough technical acceptability with more rapid publication appeal. The length of a research or technical note is recommended not to exceed 2500 words or 4 journal pages (including figures and tables).

*Review papers* are only considered from highly qualified well-known authors generally assigned by the editorial board or editor in chief. Short communications and letters to the editor should contain a text of about 1000 words and whatever figures and tables that may be required to support the text. They include discussion of full papers and short items and should contribute to the original article by providing confirmation or additional interpretation. Discussion of papers will be referred to author(s) for reply and will concurrently be published with reply of author(s).

## INSTRUCTIONS FOR AUTHORS

Submission of a manuscript represents that it has neither been published nor submitted for publication elsewhere and is result of research carried out by author(s). Presentation in a conference and appearance in a symposium proceeding is not considered prior publication.

Authors are required to include a list describing all the symbols and abbreviations in the paper. Use of the international system of measurement units is mandatory.

- On-line submission of manuscripts results in faster publication process and is recommended. Instructions are given in the IJE web sites: [www.ije.ir](http://www.ije.ir)-[www.ijeir.info](http://www.ijeir.info)
- Hardcopy submissions must include MS Word and jpg files.
- Manuscripts should be typewritten on one side of A4 paper, double-spaced, with adequate margins.
- References should be numbered in brackets and appear in sequence through the text. List of references should be given at the end of the paper.
- Figure captions are to be indicated under the illustrations. They should sufficiently explain the figures.
- Illustrations should appear in their appropriate places in the text.
- Tables and diagrams should be submitted in a form suitable for reproduction.
- Photographs should be of high quality saved as jpg files.
- Tables, Illustrations, Figures and Diagrams will be normally printed in single column width (8cm). Exceptionally large ones may be printed across two columns (17cm).

## PAGE CHARGES AND REPRINTS

The papers are strictly limited in length, maximum 8 journal pages (including figures and tables). For the additional to 8 journal pages, there will be page charges. It is advised to keep papers limited to 3500 words.

### **Page Charges for Papers More Than 8 Pages (Including Abstract)**

For International Author ***	\$55 / per page
For Local Author	100,000 Toman / per page

## AUTHOR CHECKLIST

- Author(s), bio-data including affiliation(s) and mail and e-mail addresses).
- Manuscript including abstracts, key words, illustrations, tables, figures with figure captions and list of references.
- MS Word files of the paper.



THOMSON REUTERS

WEB OF SCIENCE



Scopus®



CAS®

A DIVISION OF THE  
AMERICAN CHEMICAL SOCIETY



Scientific Indexing Services

Google  
Scholar